

REACTION STRATEGIES USING SURFACE-FUNCTIONALIZED NANOPARTICLES

Inauguraldissertation

zur

Erlangung der Würde eines Doktors der Philosophie
vorgelegt der
Philosophisch-Naturwissenschaftlichen Fakultät
Der Universität Basel

von

Sven Armin Freimann

2023

Originaldokument gespeichert auf dem Dokumentenserver der Universität Basel
edoc.unibas.ch

Genehmigt von der Philosophisch-Naturwissenschaftlichen Fakultät

auf Antrag von

Prof. Dr. E. C. Constable

Prof. Dr. C. Sparr

Prof. Dr. J. Llorca Pique

Basel, 13.12.2022

Prof. Dr. Marcel Mayor

Dekan der Philosophisch-
Naturwissenschaftlichen Fakultät

TABLE OF CONTENTS

Table of Contents	I
Acknowledgements	V
Figure Acknowledgements	VI
Abbreviations and Units	VII
Materials and Methods	X
Chemicals	X
Instruments	XI
Abstract	XIII
Chapter I: Introduction	1
1.1 Motivation to be sustainable	1
1.2 Nanomaterials	2
1.2.1 General definition	2
1.2.2 Classification	3
1.2.3 Nanomaterials in history	4
1.3 Nanomaterial production methods	5
1.3.1 Mechanical milling	5
1.3.2 Laser ablation	6
1.3.3 Ion sputtering	6
1.3.4 Nanolithography	7
1.3.5 Thermal decomposition	7
1.3.6 Solid-state methods	7
1.3.7 Liquid-state methods	8
1.3.8 Gas-phase methods	9
1.3.9 Biosynthesis	9
1.3.10 Other methods	10
1.4 Surface-functionalized nanomaterials	11
1.4.1 General functionalization principles	11
1.4.2 Non-covalent surface functionalization	12
1.4.3 Covalent surface functionalization	14
1.5 Applications and current research	16
Chapter II: The SALSAC Approach	19
Comparing Solvent Dispersed Nanoparticles with Nanoparticulate Surfaces	19
2.1 Summary	19
2.2 Paper	20
2.2.1 Abstract	21

2.2.2 Introduction.....	21
2.2.3 Experimental.....	22
2.2.4 Results and discussion.....	24
2.2.5 Conclusion.....	30
2.2.6 References.....	31
2.3 Supplementary.....	33
Chapter III: Standing Still.....	52
Catalytic Studies Using Ligand and Metal-Complex Functionalized TiO₂ Nanoparticles.....	52
3.1 Motivation.....	52
3.2 Cobalt-catalysed cross coupling.....	52
3.2.1 Results and discussion.....	52
3.2.2 Experimental, Co(3)@TiO ₂	54
3.2.3 Experimental, Co(3)(8)@TiO ₂	54
3.2.4 Experimental, cross-coupling of 2-chloropyridine and phenylboronic acid.....	54
3.2.5 Experimental, cross-coupling of 2-chloropyridine and phenylboronic acid using f-NPs.....	55
3.3 Nickel-catalysed dimerization.....	55
3.3.1 Results and discussion.....	55
3.3.2 Experimental, Ni(3)@TiO ₂ NPs.....	56
3.3.3 Experimental, Ni(3) ₂ @TiO ₂ NPs.....	57
3.3.4 Experimental, Ni(3)(glyme)@TiO ₂ NPs.....	57
3.3.5 Experimental, reductive dimerization of 2-bromoethylbenzene.....	57
3.4 Ruthenium complex photoredox-catalysed atom-transfer radical addition.....	57
3.4.1 Results and discussion.....	57
3.4.1 Experimental Ru@TiO ₂	59
3.4.2 Experimental photoredox-catalysed atom-transfer radical addition using Ru@TiO ₂	60
3.5 Conclusion.....	60
Chapter IV: Turning over on Sticky Balls.....	61
Preparation and Catalytic Studies of Surface-Functionalized TiO₂ Nanoparticles.....	61
4.1 Summary.....	61
4.2 Paper.....	63
4.2.1 Abstract.....	63
4.2.2 Introduction.....	63
4.2.3 Experimental.....	64
4.2.4 Results and discussion.....	67
4.2.5 Conclusion.....	72
4.2.6 References.....	73
4.3 Supplementary.....	74

Chapter V: Attraction in Action	96
Reduction of Water to Dihydrogen Using.....	96
Surface-Functionalized TiO₂ Nanoparticles	96
5.1 Summary.....	96
5.2 Paper	97
5.2.1 Abstract	97
5.2.2 Introduction.....	97
5.2.3 Materials and methods	98
5.2.4 Results and discussion.....	103
5.2.5 Conclusion.....	109
5.2.6 References	109
5.3 Supplementary	112
Chapter VI: Where the Sun does Shine	134
Water Reduction Using Surface-Functionalized BaTiO₃ and SrTiO₃ Nanoparticles ..	134
6.1 Motivation.....	134
6.2 Results	134
6.2.1 Nanoparticle surface activation	134
6.2.2 Nanoparticle surface ligand functionalization.....	136
6.2.3 Nanoparticle surface complexation.....	139
6.2.4 Dihydrogen generation.....	144
6.3 Experimental.....	144
6.3.1 Nanoparticle surface activation using HNO ₃ (SrTiO ₃ -a, BaTiO ₃ -a)	144
6.3.2 Nanoparticle surface activation using H ₂ O ₂ (SrTiO ₃ -OH, BaTiO ₃ -OH).....	145
6.3.3 Nanoparticle surface ligand functionalization (9 @SrTiO ₃ -a, 9 @SrTiO ₃ -OH, 9 @BaTiO ₃ -a, 9 @BaTiO ₃ -OH).....	145
6.3.4 Nanoparticle surface complexation (Ru @SrTiO ₃ , Ru @BaTiO ₃).....	146
6.3.5 Nanoparticle surface complexation (rR @SrTiO ₃ -a, rR @SrTiO ₃ -OH, rR @SrTiO ₃ -OH-A, rR @BaTiO ₃ -a, rR @BaTiO ₃ -OH, rR @BaTiO ₃ -OH-A).....	146
6.3.6 Dihydrogen generation.....	148
6.4 Conclusion	148
Chapter VII: A Peek at Transition Metal Oxides	149
Functionalization of Tungsten, Tin, Zirconium and Zinc Oxide Nanoparticles.....	149
7.1 Motivation.....	149
7.2 Results and discussion	149
7.2.1 Anchoring ligand functionalization.....	149
7.2.2 Competition between different pairs of anchors on NPs.....	157
7.3 Experimental.....	158
7.3.1 General functionalization method.....	158

7.3.2 General competitions experiment method.....	159
7.3.3 Functionalized ZnO NP complexation	160
7.7 Conclusion	160
Chapter VIII: Catalysis and Deuteration	162
Using Metal Oxide Deposited ZnO Nanoparticles	162
8.1 Motivation.....	162
8.2 Results and discussion	163
8.2.1 Functionalization of ZnO NPs using $RuCl_3 \cdot 3H_2O$	163
8.2.2 Deuteration experiments	163
8.2.3 Alcohol oxidation	164
8.3 Experimental.....	165
8.3.1 ZnO NP functionalization ($Ru@uZnO$ NPs)	165
8.3.2 General procedure for deuteration experiments	165
8.3.3 Alcohol oxidation	166
8.4 Conclusion	167
Chapter IX: Modifying Surface Characteristics.....	168
Introduction of Polymerizable Thiophenes	168
9.1 Motivation.....	168
9.2. Results and discussion	169
9.2.1 TiO_2 NP complexation forming $Ru(21)(bpy)@TiO_2$ and $Ru(21)_2@TiO_2$	169
9.2.2 $9@TiO_2$ NPs polymerization attempts using $FeCl_3$ or $FeCl_3$ and H_2O_2 in suspension.....	170
9.2.3 $9@TiO_2$ NPs vapour phase polymerization using $FeCl_3$ or $PTSa$	172
9.3 Experimental.....	175
9.3.1 TiO_2 NPs complexation with <i>bpy</i> and ligand 21	175
9.3.2 Attempt at thiophene surface polymerization using $FeCl_3$	176
9.3.3 Attempt at thiophene surface polymerization using $FeCl_3$ and H_2O_2	176
9.3.4 Vapor-phase surface polymerization using <i>TTh</i>	177
9.4 Conclusion	179
Chapter X: Conclusions.....	180
Supplementary Materials:	182
References	183

ACKNOWLEDGEMENTS

Initially I was very uncertain about doing a PhD but having worked within this group during my masters changed my opinion quickly. It goes to show how important a great work environment is and how rare it is to find. However, with Prof. Dr. Catherine Housecroft and Prof. Dr. Edwin Constable as outstanding ever interested supervisors I always felt welcome and supported. I would like to thank you profusely for the opportunity to do my PhD within your group. You always had an open door to ask about any problem and gave interesting project directions and ideas while leaving the freedom to explore my own. I also would like to thank you for proof-reading my publications and thesis with incredible speed and detail. I really do not know how you do that.

I would like to thank Prof. Dr. Christof Sparr not only for being my co-examiner but also for discussions during assessments. They always helped to gain an outside perspective on the project. I would further like to thank Prof. Dr. Jordi Llorca for being my external examiner, I am very interested to also hear your perspective and thoughts on my work during the past years.

A big thank you to the whole Constable research group current and former members for this great, helpful, smart and friendly working atmosphere which is something very hard to achieve. Whenever there was a problem, I would find someone to help me with it. I would further like to thank everybody keeping the instruments and lab running and helping with general duties. I specifically like to thank the coffee break enjoyers, always having time to shift the mind from PhD problems to coffee and games for a little while. Just having fun sometimes was very welcome and important to keep a fresh mind.

Special thanks to following current and former group member goes to Marco Meyer for being an accomplice in crime, blasting the lab with awful music for countless hours and enjoying terrible jokes together. I would further like to thank you for your utmost helpfulness within shared and not shared responsibilities and being always available to discuss any problems. You always went out of your way to help someone. I would further like to thank you and Fabian Brunner for introducing me to the LEC subgroup's instruments and responsibilities. Giacomo Manfroni I would like to thank for sharing many funny and frustrating moments within our lab and helping me with single crystal and powder X-Ray. Thank you to Mariia Becker for having the patience to introducing me to EIS and help me with the Sun simulator.

Markus Lenz from the FHNW I would like to thank for carrying out the ICP-MS measurements, answering questions and being great to work with in general. I would like to thank Prof. Dr. Daniel Häussinger for keeping the NMR machines up and running and for measuring and explaining DOSY spectroscopy and ^2H NMR spectroscopy to me. Thank you to the Palivan/Meier Group for letting me use several of their devices. Special thanks to Dalin Wu and Serena Rigo for introducing me into the AFM and for a great help at the beginning of my project.

Dr. Bernhard Jung any interaction with you was pleasant, be it in the lab during my first bachelor years or later when I was an assistant in the 1st and 2nd semester chemistry practicals. You always had funny or interesting stories to tell, and I truly enjoyed giving practicals to new students. Teaching students is part of the PhD program, and I enjoyed it more than I thought. I would additionally like to thank you and the whole IT team for the support you all gave the group and me. While anything PC related can be frustrating and some University machines are dated, I always felt you cared to solve any problem that might occur.

The amazing team from the nanoimaging lab Dr. Markus Dürrenberger, Evi Bieler, Susanne Erpel, Daniel Mathys, Dr. Marcus Wyss and Dr. Monica Schönenberger I would like to thank for teaching and demonstrating your instruments and measuring my samples. It always was a pleasure to work with you and use your broad expertise and enthusiasm in the field of microscopy to my advantage for my project.

I would like to thank the analytics team Jonas Zurflüh, Sylvie Mittelheisser and Michael Pfeffer for the fast and reliable support regarding analytical measurements. I further would like to thank Dr. Alessandro Prescimone for measuring and resolving my crystal structures. Markus Ast, Pascal Andrek, Andreas Sohler and Hisni Meha from the workshop team I would like to thank for their amazing support. Any problem always felt like it was your priority no matter how big or small a task was. Another big thank you goes to Beatrice Erismann and Isa Worni for administrative assistance. I would also like to thank Reisfond of the Ressort Nachwuchsförderung Basel for enabling me to attend the ISPPCC conference while COVID was very restrictive during my PhD years, at least I could enjoy the experience once fully without having to worry about money too much.

Special thanks goes to friends outside of University, it was always great meeting up, getting other impressions and not thinking about any academic problems. Lastly, I would like to thank my family who always have encouraged me to keep following my dreams, supported me throughout my journey and helped me wherever possible.

FIGURE ACKNOWLEDGEMENTS

In this Section I would like to acknowledge copyright holders for permission to reuse or alter the following Figures, or pictures. The specific link to each license is given as a reference in the figure caption. Figure 1 was adapted and is licenced under © Crown Copyright 2021. Information provided by the National Meteorological Library and Archive – Met Office, UK. Figure 2 is licensed under CC0 1.0 Universal (CC0 1.0) Public Domain Dedication. For Figure 3 all adapted illustrations are licensed under Attribution-ShareAlike 3.0 Unported, (CC BY-SA 3.0), I acknowledge Michael Ströck for part a), Danylo Zherebetsky for part b), Jordi Marchn for part c). The adapted Figure 4 is licensed under Attribution-NonCommercial-ShareAlike 2.0 Generic (CC BY-NC-SA 2.0) for Egyptian blue and I acknowledge Dan Diffendale, Attribution-ShareAlike 4.0 International (CC BY-SA 4.0) for the photograph of Actinolite and I acknowledge Didier Descouens, Attribution-ShareAlike 4.0 International (CC BY-SA 4.0) for the photograph of the Lycurgus cup illuminated from outside and I acknowledge the British Museum Collection and CC0 1.0 Universal (CC0 1.0) Public Domain Dedication for the photograph of the Lycurgus cup illuminated from inside. Figure 6 adapted from Xiaohu Xia, Hsin-Chieh Peng, Kyle D. Gilroy, et al., Seed-Mediated Growth of Colloidal Metal Nanocrystals, *Angew. Chem., Int. Ed. Engl.*, **2017**, *56*, 60 – 95 with permission from John Wiley and Sons. Figure 7 adapted and licensed under Attribution 4.0 International (CC BY 4.0) and I acknowledge Xin Zhao et al., Graphene-Based Nanocomposites for Neural Tissue Engineering, *Molecules*, **2019**, *24*, 658. Figure 8 was reprinted from Jing Zhan, Zhendong Lei, Yong Zhang, Non-Covalent interactions of graphene surface: Mechanisms and application, *Chem*, **2022**, *8*, 947 – 979 with permission from Elsevier.

ABBREVIATIONS AND UNITS

°C	degree Celsius
Å	ångström
<i>a, b, c</i>	crystallographic unit cell axes
a.u.	arbitrary units
amu	atomic mass units
a-NP	activated nanoparticles
ATRA	atom transfer radical polymerization
au	atomic units
bp	boiling point
bpy	2,2'-bipyridine
calc.	calculated
CFCs	chlorofluorocarbons
CHCA	α -cyano-4-hydroxycinnamic acid
cm	centimetre
COSY	correlation spectroscopy
d	day; doublet
dap	2,9-dianisyl-1,10-phenanthroline
dd	doublet of doublets
ddd	doublet of doublets of doublets
DFT	density functional theory
DMF	<i>N,N</i> -dimethylformamide
DMSO	dimethyl sulfoxide
DOSY	diffusion-ordered spectroscopy
dt	doublet of triplets
<i>e.g.</i>	for example
EDX	energy-dispersive X-ray spectroscopy
eq.	equivalent
ESI-MS	electrospray ionization mass spectrometry
Et	ethyl, -C ₂ H ₅
<i>et al.</i>	and others
Et ₂ O	diethyl ether
EtOH	ethanol
eV	electron volts
f-NP	functionalized nanoparticle
g	gram
GC-MS	gas chromatography–mass spectrometry
glyme	dimethoxyethane
GS	ground state
h	hour
HCFCs	hydrochlorofluorocarbons
HFCs	hydrofluorocarbons

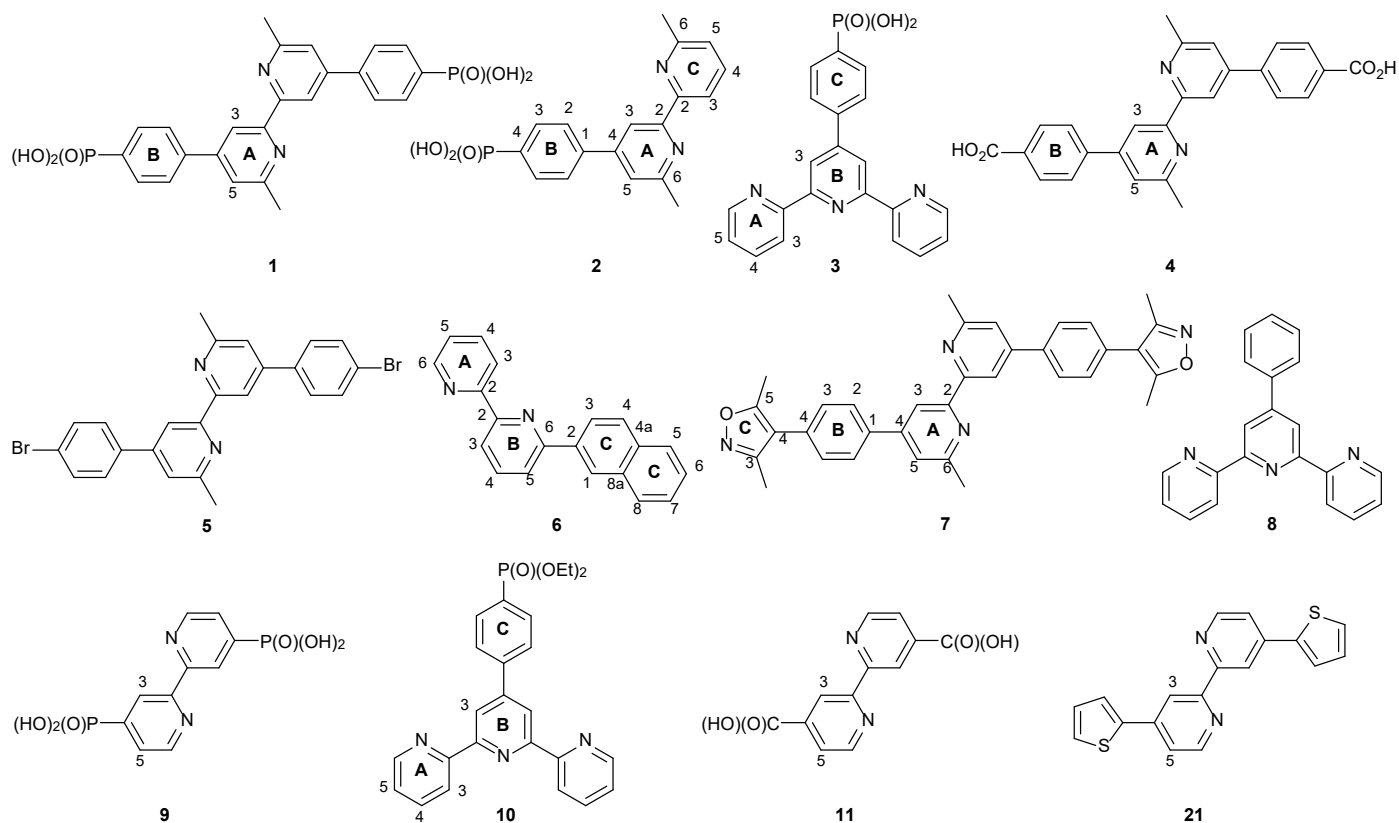
HMBC	heteronuclear multiple bond correlation
HMQC	heteronuclear multiple quantum correlation
HOMO	highest occupied molecular orbital
Hz	hertz
ICP-MS	inductively coupled plasma-mass spectrometry
<i>i</i> Pr	isopropyl
IR	infrared
<i>J</i>	coupling constant
K	kelvin
K ₂ HPO ₄	dipotassium hydrogen phosphate
<i>K_d</i>	dissociation constant
KOMe	potassium methoxide
L	litre
LC	liquid chromatography
LUMO	lowest unoccupied molecular orbital
m	meter; multiplet
M	molarity
m.p.	melting point
<i>m/z</i>	mass to charge ratio
MALDI-TOF	matrix-assisted laser desorption ionization - time of flight
Me	methyl
MeOH	methanol
Mes	mesityl, 1,3,5-trimethylphenyl, -C ₆ H ₂ Me ₃
mg	milligram
MHz	megahertz
min	minutes
mL	millilitre
MLCT	metal-to-ligand charge transfer
mmol	millimole
mol	mole
MS	mass spectrometry
MW	microwave
NBS	<i>N</i> -bromosuccinimide
NIS	<i>N</i> -iodosuccinimide
nm	nanometre
NMR	nuclear magnetic resonance
NOESY	nuclear Overhauser effect spectroscopy
NP	nanoparticle
OAc	acetate
Pd/C	palladium on charcoal
PEDOT:PSS	poly(3,4-ethylenedioxythiophene):poly(styrenesulfonate)
PEG	Polyethylene glycol
PFGE	pulsed field gradient spin-echo
Ph	phenyl, -C ₆ H ₅

phen	1,10-phenanthroline
ppm	parts per million
PTFE	polytetrafluoroethylene
PTSa	<i>p</i> -toluenesulfonic acid
QQQ	triple quadrupole
quant.	quantitative
rt	room temperature
s	second; singlet
SALSAC	surface as ligand surface as complex
SEM	scanning electron microscope
sept	septet
sh	shoulder
T	temperature
t	triplet
<i>t</i> Bu	<i>tert</i> -butyl
<i>t</i> BuOH	<i>tert</i> -butanol
TEM	transmission electron microscopy
TEOA	triethanolamine
TFA	trifluoroacetic acid
TGA-MS	thermogravimetric analysis-mass spectrometry
THF	tetrahydrofuran
TMS	trimethylsilyl
tpy	2,2';6',2"-terpyridines
TTh	2,2':5',2"-terthiophene
TWh	terawatt hour
UV	ultraviolet
V	volt
Vis	visible
W	watt
Z	number of formula units in the unit cell
α, β, γ	crystallographic unit cell angle
δ	chemical shift
ϵ	<i>extinction coefficient</i>
λ	<i>wavelength</i>
λ_{exc}	excitation wavelength
μg	microgram
μL	microlitre
μmol	micromole
μs	microsecond
v	frequency

MATERIALS AND METHODS

Chemicals

Commercial compounds were purchased from Acros Organics, Sigma Aldrich, Johnson Mathey, Materials Technology UK, Evonik Industries, Oxkem Ltd, Apollo Scientific Ltd, or Alfa Aesar GmbH & Co. Non-commercial ligands and complexes (4-(4-bromophenyl)-6,6'-dimethyl-2,2'-bipyridine¹, **1**², **3**³, **4**⁴, **5**², **6**⁵, **8**⁶, **9**⁷⁻¹¹, **10**³, **21**¹², [Cu(MeCN)₄][PF₆]¹³, [Cu(**5**)₂][PF₆]², [Fe(**8**)₂][PF₆]₂¹⁴, *cis*-[Ru(bpy)₂Cl₂]¹⁵) were prepared according to the literature. Their spectroscopic data matched those previously reported. Average NP radius sizes were <50 nm for SrTiO₃, WO₃, SnO₂, ZrO₂, ZnO while BaTiO₃ had average NP radius sizes of 25 nm. The spherical TiO₂ NPs used, had an average radius of 10.5 nm¹⁶ and an average surface area-to-volume ratio of 0.28 nm⁻¹. The number of equivalents of NPs is defined as 0.28 × the total number of TiO₂ formula equivalents in the mass given, i.e. the effective surface concentration of TiO₂.¹⁷ Similarly, when clarifying equivalents or mmol of functionalized NPs, it refers to the estimated amount of ligand or complex bound to the surface. Other NP sizes follow the same assumption and calculations are based on their average radii.



Scheme 1: Labelling of ligands.

Note the labelling of ligands and complexes in this thesis was chosen for consistently with Scheme 1; however, publications in **Chapters IV** and **V** use different labels and numbering as defined in the publications.

Instruments

^1H NMR, $^{13}\text{C}\{^1\text{H}\}$ NMR and $^{31}\text{P}\{^1\text{H}\}$ NMR spectra were measured at 298 K on a Bruker Avance III-500 or Bruker Avance III-600 NMR spectrometer. ^1H and ^{13}C chemical shifts were referenced to residual solvent peaks with respect to $\delta(\text{TMS}) = 0$ ppm for ^1H and $^{13}\text{C}\{^1\text{H}\}$; and ^{31}P chemical shifts were referenced with respect to $\delta(\text{H}_3\text{PO}_4 \text{ 85\% aqueous}) = 0$ ppm. For DOSY experiments a Gaussian fit to the diffusion peak intensity was performed to determine the diffusion constant of the signal. The PFGSE experiments were performed using a bipolar gradient pulse sequence. The sigmoidal intensity decrease was fitted with a two-parameter fit (I_0 and diffusion coefficient D) with the DOSY routine implemented in topspin 4.0 (Bruker Biospin GmbH, 2016). The ^2H NMR experiments were performed on a Bruker Avance III HD four-channel NMR spectrometer, which operated at 92.12 MHz deuterium frequency. The instrument was equipped with a helium cooled cryogenic 5 mm four-channel QCI probe (H/C/N/F) with self-shielded z-gradient. The experiments were performed at 298 K and calibrated using a MeOH standard showing accuracy within ± 0.2 K. The ^2H NMR experiments were recorded with 16 scans in fully protonated solvents without deuterium lock and were referenced relative to TMS using the natural abundance deuterium signal of the solvent.

Reactions and procedures under microwave conditions were carried out in a Biotage Initiator 8 reactor. Microwave vials (5 mL and 20 mL) were from Biotage and were selected depending on the required solvent volume. Autoclave reactions were done in a 23 mL Model 4749 Acid Digestion Vessel (Parr Instrument Company) using a forced convection chamber furnace (Nabertherm NA15/65). The methods used are described in the experimental sections of each chapter where applicable. For centrifugation an Eppendorf Centrifuge 5415 R or a Hettich Centrifuge Universal 320 was used with 2-, 10- and 50 mL samples. Experiments done in a glovebox used a UniLab glovebox from mBraun under N_2 .

Solution absorption spectra were recorded on an Agilent Cary 5000 spectrophotometer and for solid-state absorption spectra, a diffuse reflectance accessory was added to the spectrophotometer. For solid-state absorption spectrum presented in **Chapters II - IV**, baseline (100%) and zero (0%) corrections were done with the appropriate NP precursor and a black background. In **Chapter V**, activated NPs were used for the baseline (100%) correction. For solid-state absorption spectroscopy in all other chapters, a baseline correction (100%) was made with commercial NPs as the reference sample. Fluorescence emission spectra were measured on a Shimadzu RF-6000 spectrofluorometer with an excitation slit width of 3 – 10 nm and an emission slit width of 3 – 10 nm. For emission spectroscopy, the NPs were dispersed in water with a concentration of 0.1 mg / mL. FTIR spectra were recorded on a Perkin Elmer UATR Two spectrophotometer.

Irradiation experiments were done in a Biotage 5 mL microwave vial with a LOT Quantum Design LS0811 instrument as light source at 1200 W m^{-2} . The simulated light power was calibrated with a silicon reference cell. Gas chromatography was performed on a Model 8610C Gas Chromatograph from SRI instruments equipped with a flame ionization detector (FID/meth 300C hi gain), thermal conductivity detector (TCD100C low current), Haysep D 3 m 1/8" AD 2 mm ID Mesh 80/100 column and a HT2000H headspace autosampler from HTA S.R.L. The method used a constant column temperature of 90 °C, 3 minutes event time, N_2 carrier gas at 10 mL min^{-1} and 1 mL isocratic sampling. The GC integral was measured, adjusted for pre-existing nitrogen volume, sampling amount and then converted to volume in mL using an H_2 GC measured blank curve. GC-MS in **Chapter III** was performed using a quadrupole GCMS-QP2020 from Shimadzu.

Electrospray ionization (ESI) mass spectrometry (MS) and high-resolution ESI MS were measured on a Shimadzu LCMS-2020 or a Bruker maXis 4G instrument, respectively. MALDI-TOF mass spectra were measured using a Shimadzu MALDI-8020 with α -cyano-4-hydroxycinnamic acid (CHCA) solution as matrix for sample preparation. Thermogravimetric analysis (TGA) was performed on a TGA5500 (TA Instruments) instrument under N_2 or air. For TGA-MS the instrument was coupled to a MKII mass spectrometer. Initially, the temperature was held at 30 °C for 10 min before heating at a rate of 10 °C/min to 120 °C. This temperature was maintained for 30 min to remove all traces of water. Afterwards the sample was heated to 900 °C at a rate

of 10 °C/min. After maintaining the temperature at 900 °C for 30 min, the sample was cooled to ambient temperature. For **Chapter II** the same method was used but with a TGA/SDTA851 (Mettler Toledo) instrument. NP sample analysis with triple quadrupole inductively coupled plasma mass spectrometry (ICP-QQQ-MS) was performed on an 8800 ICP-QQQ MS system (Agilent) using the general-purpose operational settings. Samples were digested in aqueous HNO₃ (69%, semiconductor grade, PanReac AppliChem), diluted with milliQ water to a final HNO₃ concentration of 3% and quantification was performed via multi-element standards (Sigma-Aldrich). To account for matrix effects ⁸⁹Y was used as an internal standard. ⁴⁷Ti, ¹⁰¹Ru and ¹⁰³Rh were quantified operating the ICP-MS system in single-quad mode using helium as the collision gas.

Scanning electron microscopy (SEM) was performed using a Hitachi S-4800 instrument with an acceleration voltage of 5 kV and a working distance of 4 mm. Particle sizes were measured with a nanoimaging tool from the Nano Imaging Lab, University of Basel. TEM images were recorded under high vacuum on a Philips CM100 instrument. The instrument is equipped with a tungsten electron column and a CCD camera using an acceleration voltage of ~100 kV. The images were recorded using bright field mode. STEM images were recorded on a JEOL JEM-F200 cFEG instrument. The instrument is equipped with a cold field emission gun as well as an EDX detector for EDX mapping. Images were recorded at high vacuum and an acceleration voltage of 200 kV using bright field mode.

Single crystal data in **Chapter IV** were collected on a Bruker APEX-II diffractometer (CuK α radiation) with data reduction, solution and refinement using the programs APEX,¹⁸ ShelXT,¹⁹ Olex2²⁰ and ShelXL v. 2014/7.²¹ Structure analysis including the ORTEP representation, used CSD Mercury 2020.1.²²

ABSTRACT

Chapter I: The Chapter introduces motivation to work with smart nanomaterials, presents general definition and classification, describes current and past uses, how to synthesize and functionalize them using various methods and examples.

Chapter II: The Chapter summarizes published work which investigated NP surface activation with HNO₃, established functionalization methods anchoring ligands and found suitable characterization methods of TiO₂ NPs.¹⁷ The Chapter further studied the application of the SALSAC 'surface-as-ligand, surface-as-complex' method using several homoleptic copper(I) and iron(II) complexes with f-NPs.

Chapter III: This Chapter attempts to transfer literature homogeneous catalytic reactions onto TiO₂ f-NPs. The methods learned included (i) forming a metal complex catalyst directly on the NP surface instead of using an in-situ method, (ii) testing metal-to-ligand ratios that might be beneficial, (iii) more cautiously considering the impact of different ligand functional groups, (iv) moisture-sensitive reactions can be problematic.

Chapter IV: This summarizes published work²³ which used stepwise synthesised Rh(3)₂@TiO₂ NPs as catalyst to perform an alcohol oxidation with 1-phenylethanol. The Rh(3)₂@TiO₂ NPs were used to compare their catalytic activity in contrast to the homogeneous counterpart, [Rh(3)₂]Cl₃. It was confirmed that catalytic activity was not lost upon surface-binding. The stability of Rh(3)₂@TiO₂ NPs was remarkable as they were able to withstand reaction temperatures of up to 100 °C for 24 days without degradation.

Chapter V: This Chapter focuses on a previously reported system for water reduction under simulated sunlight irradiation Lehn and Sauvage utilized [Ru(bpy)₃]²⁺ and [Rh(bpy)₃]³⁺ as photo- and electrocatalysts.²⁴ The homogeneous catalysts were replaced with a heterogeneous version anchored onto TiO₂ NPs. Using these ruthenium(II) and rhodium(III) metal complex f-NPs (rR@TiO₂ NPs), greater efficiency for the immobilised systems over the previously reported homogeneous systems was demonstrated and published.²⁵

Chapter VI: This explores water reduction catalysis under the same conditions and metal complex preparations but now using SrTiO₃ and BaTiO₃ NPs instead of TiO₂. The Chapter further investigated H₂O₂ surface activation compared to previous studies with HNO₃ activation. Thereby it was found that the metal complex H₂O₂ activated BaTiO₃ and SrTiO₃ NPs were inactive for water reduction. Acid activated NPs were both active during water reduction, and SrTiO₃ NPs being the most efficient while performing worse than comparable TiO₂ NPs. The Chapter further studied pH influence during complexation.

Chapter VII: This Chapter focuses on functionalization of commercial WO₃, ZrO₂, SnO₂, TiO₂ and ZnO NPs with anchoring ligand bearing phosphonic or carboxylic acids using methods established in **Chapter II**. Overall, successful functionalization was established with each type of metal oxide NPs. Anchoring ligand binding preferences were studied by carrying out competition experiments concluding a better binding with phosphonic acid bearing anchors in most cases.

Chapter VIII: This takes a closer look at ruthenium functionalized ZnO (Ru@uZnO) NPs. They were able to perform two catalytic reactions relatively well, namely the deuteration of bpy or 4'-aminobenzo-15-crown-5 (**12**), and the oxidation of 1-phenylethanol (**13**). However, the material characterization of Ru@uZnO NPs using TGA-MS was insufficient to fully characterize the material and further measurements are required to provide insights into the catalytic activity.

Chapter IX: Ruthenium-complex functionalized TiO₂ NPs with 2-(thiophen-2-yl)-2,2'-bipyridine (**21**) and/or 2,2'-bipyridine (bpy) as ancillary ligands were prepared. Ligand **21** was selected with the aim of using the pendant thienyl groups to investigate solution or vapour polymerizations. The project was more successful in using vapour phase polymerization (VPP) with using either FeCl₃ or *p*-toluenesulfonic acid (PTSA) as oxidant and 2,2':5',2"-terthiophene (TTh) as building block.

Chapter X: Summarizes the conclusion of each Chapter but being more thorough in its approach than the work presented here.

CHAPTER I: INTRODUCTION

1.1 Motivation to be sustainable

The last seven consecutive years are the warmest years (global mean temperature) on record since 1880, when recording started. The year-to-year course is illustrated in Figure 1 with data plotted from six different major climate organizations. Although 2021 managed a lower ranking due to successive La Niña events at the end of the year which led to a less pronounced warming, this did not disrupt the upwards trend. The year 2021 still places as the sixth warmest year on record with 2018, showing a global mean temperature of 0.76 °C above the 1961 – 1990 average and 1.1 °C above the 1850 – 1900 average. It is especially clear to see that individual decades have been warmer than previous one since the 1980s. Hence, year-to-year variability in global average temperatures now far exceed naturally occurring climate fluctuations. Temperature is one of the indicators for climate change, with others including ocean heat content, ocean pH, glacial mass, sea ice extent and global mean sea level. Long term global warming is caused mainly by greenhouse gases in the atmosphere with the main contributors being CO₂, CH₄, N₂O and fluorocarbons (e.g. CFCs, HCFCs, HFCs, SF₆ etc.). When looking at these greenhouse gases year-to-year, it is not surprising that all of them rise in concentration. In 2021 CO₂ rises to 415.7 ppm while CH₄ reached 1908 ppb and N₂O 334.5 ppb and compared to pre-industrial values they are 149%, 262% and 124% higher, respectively. As current efforts to limit global warming and greenhouse gas emission are not yet having impact, this trend will likely continue, and earth will reach the 2.0 °C increase mark easily by 2100. Projections suggest a temperature rise of 2.0 – 4.9 °C with a 3.2 °C median. They further give achieving the goal of the Paris Climate Agreement (temperature rise until 2100 below 2.0 °C, 1.5 °C) a chance of 5% and 1% respectively. While a difference of 0.5 °C might not seem a lot, the impact it will have on the climate is highly significant. Some of these impacts are 2.6 times increase the global population exposed to extreme heat, ten times increase in ice-free summers, 38% more melted permafrost and 29% greater decline of coral reefs. The earth will face more and more devastating climate events such as droughts, heavy precipitations, flooding and storms.²⁶⁻³²

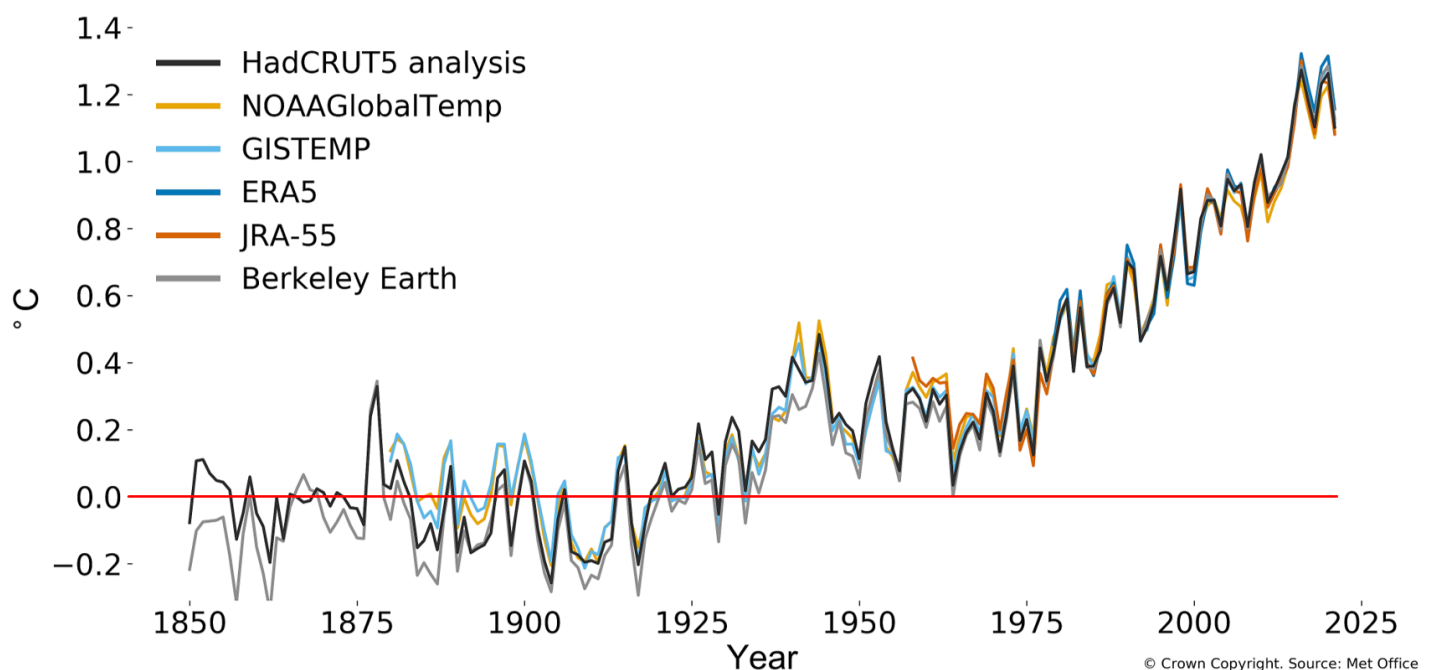


Figure 1: Global mean temperature difference from 1850 – 1900 in °C.²⁷

CO₂, mainly produced by the combustion of fossil fuels such as natural gas, oil and coal is one of the long lifetime greenhouse gases and will affect the climate for thousands of years even if all production were to be halted today.³³ 'Sustainability' can be described as meeting the needs of today without hindering future generations from meeting theirs. As such, sustainable practices and devices have to be developed using green methods and renewable, recyclable and smart materials. New materials have to be more and more highly specialized and as efficient and renewable as possible for their given task. Materials development must use non-toxic, earth-abundant, cleaner materials and ideally be energy neutral in their manufacture. Figure 2 shows plot of the abundance (on a logarithmic scale) of elements in the Earth's crust, against the atomic number, the most sustainable elements being in the green region.³⁴

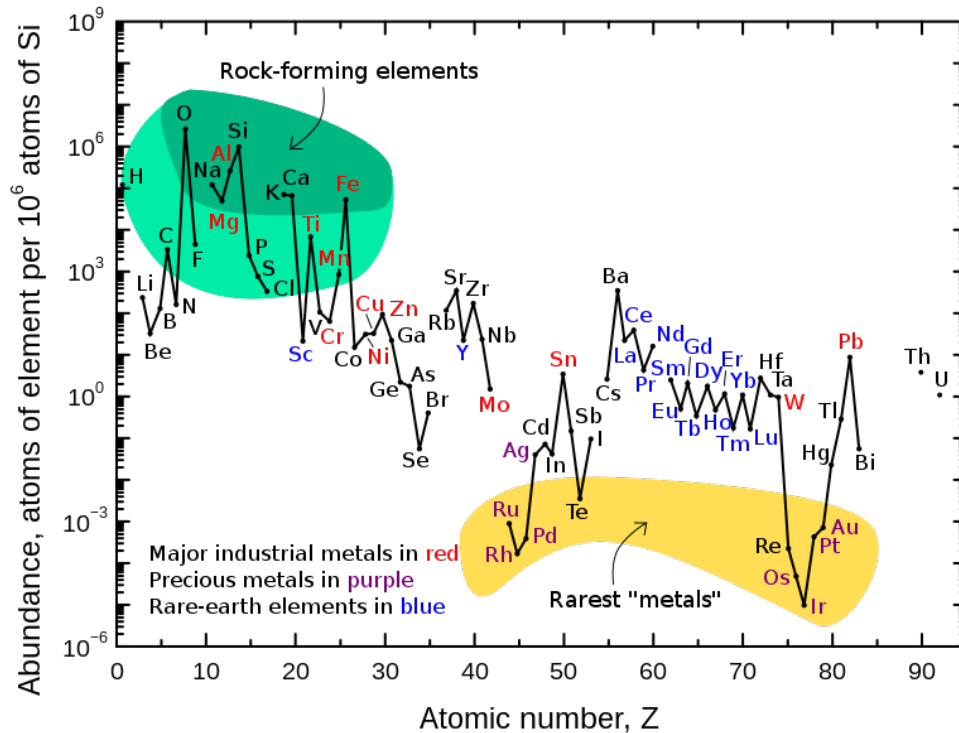


Figure 2: Atomic number, Z vs abundance of elements per 10⁶ of Si atoms.³⁵

1.2 Nanomaterials

1.2.1 General definition

Nanomaterials which include nanoparticles (NPs) or nanostructured materials are widely used and prevalent in a wide variety of research fields. The detailed definition of nanomaterials may vary between organizations but they are typically defined as a manufactured or natural materials consisting of unbound, aggregated or agglomerated particles which have at least one external dimensions between 1 – 100 nm.³⁶ The word nano originates from the Greek and describes dwarf or small and is today used to indicate 10⁻⁹ of a unit.³⁷ Nanomaterials unique properties (e.g. size distribution, morphology, surface reactivity) originate from their small size. The smaller a particle, the larger the surface area to volume ratio (AtV) gets; while a spherical micrometre particle has a modest AtV of 0.003 nm⁻¹ a nanometre particle possesses a AtV of 3 nm⁻¹. Hence, nanomaterials can bridge the gap between the molecular and bulk phases.³⁸ A further contributing factor for their value and popularity is their adaptability, both physical (e.g. shape and size) and physiochemical (e.g. wettability, melting point, catalytic activity, light absorption, scattering, electrical and thermal conductivity) properties can be adjusted. Having such precise and wide control over the material properties gives the possibility to adjust the nanomaterial to any problem, often resulting in an enhanced performance over their bulk counterparts.^{39,40}

1.2.2 Classification

Nanomaterials made by biological species or non-anthropogenic activities (e.g. dust, smoke particles) can be classified as natural nanomaterials. The most commonly manufactured nanomaterials are classified into carbon-based nanomaterials, inorganic-based nanomaterials, organic-based nanomaterials and composite-based nanomaterials.^{36,41,42}

Carbon-based nanomaterials comprise carbon and can be spherical or near-spherical species in the case of fullerenes, two dimensional in the case of graphene, aggregated spheres in the case of carbon black or cylindrical stacked cones, cups or plates in the case of carbon nanofibres or even perfect cylinders labelled carbon nanotubes. All examples have their own unique features and can be utilised as single layered or multi-layered structures. Fullerenes are assemblies of 28 to 1500 sp^2 hybridized carbon atoms and can be either single layered or multi-layered (i.e onion like) reaching sizes of 0.7 to 8.2 nm and 4 to 36 nm respectively.^{43,44} Fullerenes are inert, non-toxic, can transmit light based on intensity and find uses as semiconductors, conductors, superconductors or for targeted drug delivery.^{41,45} A single graphene sheet has a thickness of 1 nm but can be multi-layered if desired and graphenes, possess excellent thermal and electrical conductivity, can withstand outstanding physical force and absorb light.⁴⁶ Carbon nanotubes have diameters of at least 0.7 nm for single layered wires and 100 nm for multi-layered wires and can be up to several millimetres long in the other dimension. Carbon nanotubes and nanofibres have similar characteristics to graphene (e.g. electrical, thermal conductivity, mechanical strength) while being flexible and elastic if desired. Since the material consist mostly of carbon, they are highly resistant to UV degradation a feature utilized in carbon black pigments.

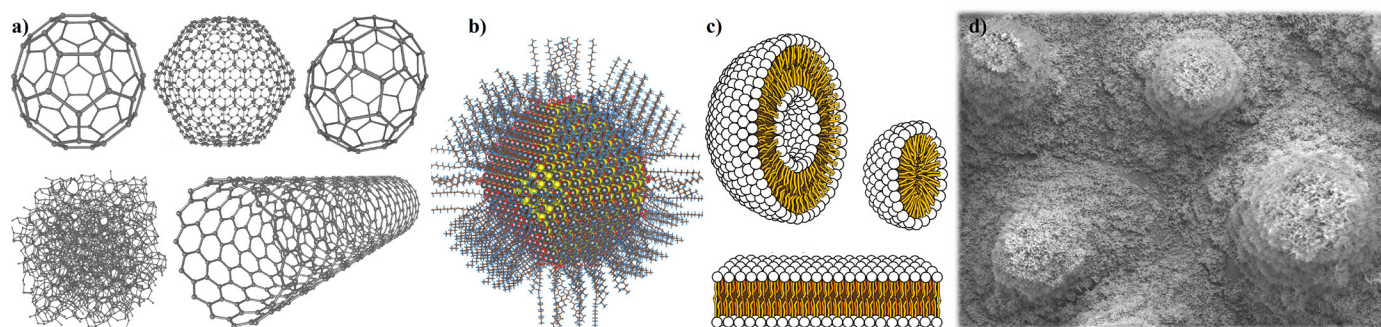


Figure 3: Comparison of carbon-based nanomaterials (a, model of fullerenes, amorphous carbon and carbon nanotube), inorganic-based nanomaterials (b, atomistic model of oleic acid, oleyl amine and hydroxyl ligand passivated colloidal lead sulphide nanoparticle, quantum dot), organic-based nanomaterials (c, model of micelles, liposomes, bilayer sheets) and natural nanomaterials (d, SEM imaging of lotus leaf cuticle nanostructure).⁴⁷⁻⁴⁹

Inorganic-based nanomaterials can be from metals (e.g Pt NPs, Au NPs, Ag NPs) or metal oxides (e.g. TiO_2 NPs, WO_3 NPs, ZnO NPs, CeO_2 NPs, Fe_2O_3 NPs and Fe_3O_4 NPs). Metal-based nanomaterials are made using constructive (or bottom-up) methods such as sol-gel, chemical vapour deposition and biosynthesis or destructive (or top-down) methods such as mechanical milling, nanolithography, and sputtering. Since various methods and almost any metal is suitable to make metal-based nanomaterials, their distinctive properties can be fine-tuned. Physical properties such as pore sizes, shape, colour, crystallinity, surface charge and charge density as well as chemical properties like toxicity, flammability, reductivity or air, moisture, heat, pH, and sunlight reactivity and stability can be adjusted depending on the aimed application.⁴¹ Typical examples of applications include anti-bacterial activity of Ag NPs to UV-filtering by Zn NPs. Metal-oxide-based nanomaterials can often exhibit enhanced beneficial properties (e.g. reactivity, efficiency, sensitivity and stability) over their metal counterparts while being lower priced. Metal-oxide-based nanomaterials can also be prepared using bottom-up approaches (e.g. sol-gel and pyrolysis) or top-down methods (e.g. mechanical milling, laser ablation and thermal decomposition), fine-tuning is possible and applications are broad. Typical examples range from Al_2O_3 to ZnO NPs.

Organic-based nanomaterials use noncovalent interactions and clever molecule design for self-assembly into micelles, liposomes, polymer NPs or dendrimers. Often used in the biomedical field, these nanomaterials can be designed to be biodegradable, non-toxic or featuring a hollow core.⁴¹ Organic-based nanomaterials can be sensitive to thermal and electromagnetic radiation or pH and can be injected into various parts of the body. Depending on the application, a nanomaterial is chosen that can either absorb or entrap a drug. These properties make them ideal for targeted drug delivery. Each type of nanomaterial (carbon-based, inorganic-based or organic-based) can be combined to create composite-based materials. Generally, when one part of a composite is a nanomaterial, the composite as a whole is considered a nanomaterial. This mixture of bulk and nanomaterials often enhances the overall material advantages or reduces its price. More complicated composites such as metal-organic-frameworks (MOFs) exist and are being used as they bring their own unique benefits including permanent porosity, diverse chemical functionalities and well-defined 3D architectures.^{36,41,50}

1.2.3 Nanomaterials in history

Considering these advantages and broad characteristics, nanomaterials have been used to achieve a certain goal or enhance and replace certain materials for centuries. Nanomaterials found use as pigments, construction materials or later as heterogeneous catalysts in the petrochemical industry even before the properties or synthesis of NPs were understood and characterization methods had been developed. The earliest uses go back as far as 7000 years ago when humans in Cyprus and Greece used clay minerals with a thickness of a few nanometres to bleach wools and clothes.⁵¹ Natural asbestos nanofibres (Figure 4, middle left) found use to reinforce ceramic matrixes over 4500 years ago.⁵² Pb S NPs with a 5 nm diameter were synthesized and utilized to dye hair by the Ancient Egyptians.⁵³ Cu NPs that coloured glass red through surface plasmon excitation were found in Italy dating back 3000 years ago.⁵⁴ Roughly 2500 years ago Egyptians were also known for the synthesis and use of Egyptian blue (Figure 4, left), a nanometre-sized pigment consisting of quartz (SiO_2) and glass ($\text{CaCuSi}_4\text{O}_{10}$). The pigment was widely used in arts as well as architecturally to colour ceilings and walls.⁵⁵ An excellent and famous use of NPs is the Lycurgus Cups made in the Roman Empire (300 – 400 AD). The cups are fascinating as they change colour, depending on the direction of the light that passes through it. This is achieved with Ag-Au alloy NPs dispersed in the glass, giving the cup a dichroic effect appearing green when light gets reflected (Figure 4, middle right) and red when light is transmitted (Figure 4, right) through it.^{36,56,57}



Figure 4: Left to right; Egyptian blue, natural asbestos nanofibres, the Lycurgus Cup illuminated from outside and inside.⁵⁸⁻⁶¹

While history is filled with the use of nanostructured materials, the first deliberate synthesis of a nanomaterial was arguably reported in 1857 when Michael Faraday discovered Au colloid NPs and described their dissimilar optical characteristics from the bulk material. This phenomenon was later explained by Gustav Mie in 1908.⁶² The invention of electron microscopy methods such as transmission electron microscopy (TEM) in the 1930s and scanning electron microscopy (SEM) in the 1940s led to the first visual confirmation of NPs

and started its detailed research.⁶³ However, it took over a century from Faraday's discovery before the NP field gained significant attention, most likely initiated with availability of characterization techniques suitable for analysis at the nanometre scale. The field gained attention slowly but gained strong momentum when metal and semiconductor NPs were studied in the late 1990s. The NPs showed excellent plasmonic and excitonic properties and the material was therefore highly popularized for use in industrial applications and research within the scientific community.⁶⁴

1.3 Nanomaterial production methods

The creation of nanomaterials is heavily studied and available the methods are versatile and continuously improved and adjusted depending on the desired nanomaterial properties (e.g. size, shape, porosity, density, conductivity, reactivity or stability). For example, precisely designing the plasmonic properties of nanomaterials allows to even control selectivity and catalytic properties among different crystal surfaces.⁶⁴ Hence, characteristics of the bulk material are aimed to be outperformed by not only making improvements in nanomaterial synthesis but also in purification methods and post synthetic modifications.³⁶

Nanomaterials synthesis ranges from various bottom-up or top-down methods that can be performed in solid, liquid or gas phase. Top-down methods (Figure 5) use bulk materials and reduces their material size using physical or chemical treatments. The methods are simple but also heavily limited in the minimal sizes they can achieve and unique shapes they can produce. They further can have unwanted effects on surface chemistry and physicochemical properties.⁴² Common methods include ball milling, laser ablation, thermal decomposition and ion sputtering. Bottom-up approaches produce nanomaterials from atoms, smaller molecules, or particles to build clusters and then the final product. The methods can be differentiated depending on the used phase, hence there are solid (physical and chemical vapour deposition), liquid (sol-gel, hydrothermal, solvothermal and seed mediated growth) or gas (spray, laser or flame pyrolysis) phase methods. Additional bottom-up methods include biological (e.g. bioreduction, use of bacteria or fungi) or other methods (e.g. electrochemical deposition, galvanic replacement, coreduction, microwave assisted, supercritical fluid technology and ultra sound technique) that are difficult to put into other categories.⁴² However, more complex structures often require several methods. Bimetallic NPs provide an example of a nanomaterial requiring a combination of methods, often a combination of seed-mediated growth and coreduction or thermal decomposition.⁶⁵

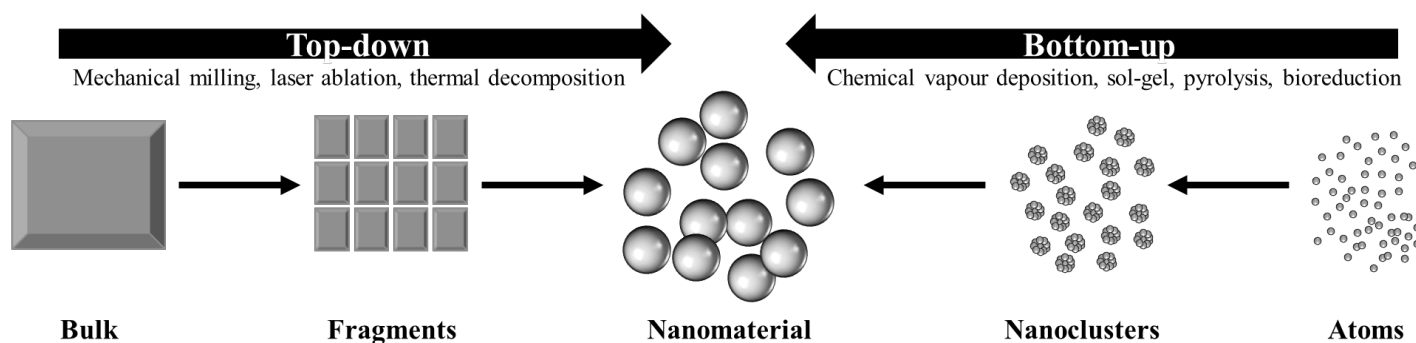


Figure 5: Top-down methods compared to bottom-up methods.

1.3.1 Mechanical milling

Mechanical milling can be separated into ball milling and mechanochemical synthesis. Both methods have their advantages, disadvantages and applications. Ball milling adds the bulk material as a powder into a container with several heavy (usually steel) balls. There are several types of ball mills (e.g. planetary ball mill, vibrating ball mill, low energy tumbling mill, high-energy ball mill) but all have the same general working

principle. The free moving heavy balls crush the bulk material either by rolling over it or impacting it. This method is useful for large-scale production of high purity NPs with optimal physical properties (e.g. better solubility) but requires high energy, long milling times and can lead to contamination due to the used balls (e.g. iron). A typical example is the preparation of elemental aluminium powder or β -silicon carbide.⁶⁶⁻⁶⁸ Mechanochemical synthesis uses the same ball mills but instead combines precursors through repeated deformation, cold welding and fracturing of the stoichiometrically mixed starting materials. Forming these materials using the bulk precursors usually requires high temperature but only low temperature when using a ball mill. The method is both efficient and simple to setup. However, displacement reactions do occur and purification is required. Contamination is a problem and small particles require very long milling times. A typical example is the use of iron chloride and sodium carbonate to form ferric oxide NPs (Fe_2O_3). One-step ball milling was also used by Y. Chen, L. Soler et al. to form H_2 producing a Pd/TiO₂ NPs photocatalyst in which Pd_x clusters gave a metal-support interface which could rearrange producing Pd NPs during photocatalysis. Ball milling was essential and when a calcination treatment was used, the unique properties of Pd/TiO₂ interface was lost. Hence, the mechanochemical strategy can be used to stabilize the material without the use of organic compounds.^{42,69-71}

1.3.2 Laser ablation

Using pulsed laser irradiation, a condensed plasma plume is created which fragments a solid target material immersed in liquid media, producing nanometre scale particles. Pulse frequency, laser wavelength, energy, laser fluency, ablation time and liquid media can be adjusted to influence relative amount, efficiency and characteristics of the particles produced. The formed particles remain in the liquid as a colloid. Typical lasers are neodymium-doped yttrium aluminium garnet (Nd:YAG), titanium-doped sapphire or copper vapour lasers. The major advantage of the method is the tuneability of the produced NPs by adjusting the parameters. As the liquid media can be either organic solvent or water, the method can be considered a green process. The method is further rather effective at producing large amounts of particles in a short amount of time. However, it is, in turn, limited to short ablation times as high amounts of NPs in the liquid media block the laser path, thereby reducing the efficiency. Common examples of products of laser ablation include Al₂O₃ nanomaterial coatings or silicon NPs.⁷²⁻⁷⁵

1.3.3 Ion sputtering

Sputtering is used to deposit nanoclusters on surfaces. The target surface is fixed within a vacuum chamber, and acts as an anode. Sputtered materials must be electrically conductive and examples include C, Au, Pt or W plates located at the cathode. After establishing a high vacuum in the chamber, sputtering gas (e.g. Ar, Ne, He, Kr and Xe) is released and ionized through alternating high current. The created argon plasma has enough energy upon collision with the coating plate to surpass the binding energy of the material atoms, thereby dislodging nanoclusters forming a diffuse cloud of particles. Hence, the fixed target surface is coated with an evenly distributed film of the dislodged nanomaterial. The thickness of the coating can be precisely controlled by adjusting the sputtering time. The versatile technique is advantageous as it does not alter the target material and sputtered nanocluster composition in the process while being cheap to comparable methods. The process further forms relatively pure coatings with only minor measurable effects on surface morphology and optical properties caused by the used sputtering gas. The method finds extensive use on surfaces of catalysts, photovoltaics, hydrophobic coatings or for sample preparation of non-conductive sample in electron microscopy.^{42,76,77}

1.3.4 Nanolithography

Nanolithography can be separated into photolithography (e.g. optical, multiphoton, extreme ultraviolet light and X-ray), scanning lithography (e.g. electron-beam, proton beam and scanning probe) and soft lithography (e.g. nanoimprint and patterning by etching at the nanoscale). The general principle of each method is the same: printing a structure or shape onto a light sensitive substrate. Blueprints or masks are used in many lithography methods to print a pattern onto the substrate, and often techniques are used to further shrink the mask to form nanomaterials on the desired scale. The printing could either selectively modify the surface so that unwanted material can be washed away, etch the surface into the desired shape or directly print the material in the desired shape onto the substrate depending on the used method. The method can print structures from single NPs with resolutions of 3 – 5 nm although, the equipment for most nanolithography methods is very expensive. One of the most important applications of nanolithography, using extreme ultraviolet light lithography, is the production of the most advanced microchips. However, the price to start making these chips shows the drawback of the method, as the required equipment, which is made by a single company, costs over 150 million dollars.^{41,78-82}

1.3.5 Thermal decomposition

Thermal decomposition is an endothermic chemical decomposition method, which is also called thermolysis and creates nanocrystals by breaking chemical bonds within an organometallic compound. The method is performed under anaerobic conditions in organic solvents. After the decomposition of the organometallic compound within the reaction vessel, the NP nucleation begins. Usually, the nucleation process continues for several hours to let the NPs grow to the desired size (aging). While the specific decomposition temperature depends on the compound, both mono- and bimetallic nanocrystals can be made. The NPs created can be tuned (e.g. shape, size and composition) by varying temperature, pressure, reactants, reaction time, annealing temperature, solvents and surfactants. A further influence on the nanocrystal formation is the use of capping agents such as carboxylic acids, alkyl amines or acetylacetonates. An example reaction uses iron(III) oleate in 1-octadecene under argon for iron oxide NP formation. The experiment first reaches an intermediate at temperatures around 150 – 200 °C while NP nucleation was reported to start at 250 °C. Reaching the desired NP size took 24 hours in this case.^{41,83,84}

1.3.6 Solid-state methods

Solid state bottom-up methods mainly consist of physical and chemical vapour deposition. Both methods are used to deposit a thin film on a substrate. In physical vapour deposition, thermal evaporation, sputtered deposition or laser ablation is used to prepare the thin films. While the method is limited by the low volume of generated material and high price, it does find use in preparing thin films of lanthanum strontium cobalt, tungsten selenides, solar cells or platinum-ruthenium NPs.^{42,85,86} Chemical vapour deposition is more commonly used and there are various subcategorized methods such as thermally active, plasma enhanced and photo initiated chemical vapour deposition. In general, a chemical reaction of a substrate with a target molecule in the gas phase forms the thin films. The thin films deposited on the substrate can be recovered and used. Chemical vapour deposition methods allow for tuneable nanostructure surface morphology and crystal structure, they yield durable highly pure uniform thin films and are easy to scale up. Major drawbacks of using chemical vapour deposition are the production of hazardous gases during the deposition (highly toxic, corrosive and explosive) and challenging or impossible to use for multicomponent materials.^{41,42,87}

1.3.7 Liquid-state methods

Liquid state bottom-up methods mainly consist of sol-gel, hydrothermal, solvothermal and seed mediated growth methods. One of the most favoured methods to synthesize NPs is the sol-gel method, as it is simple and versatile. The method starts from a homogeneous pH-controlled precursor solution and is initiated by a catalyst. The four main temperature controlled steps of the method are (i) hydrolysis followed (ii) by condensation, (iii) chain growth and (iv) particle agglomeration. The “sol” refers to the colloid that forms after hydrolysis and condensation and which slowly transform into a gel during the chain growth and agglomeration. Precursors that can be used with the sol-gel method are typically alkoxides, metal oxides, metal chlorides or alkoxy silanes. Purification involves either filtration, centrifugation or sedimentation while moisture removal of the product material is done by drying. The method is rather simple and gives great control over particle size and morphology by tuning the reaction conditions which explains its popularity.^{41,42}

Hydrothermal methods are more difficult to control and sometimes struggle with reliability and reproducibility. The method uses an aqueous mixture of precursors under high pressure and temperature in an autoclave. This process leads to saturated vapour which produces highly pure crystalline nanomaterials in a one-step reaction without requirement annealing treatments. While hydrothermal methods often show rather low yields they do work with a wide range of nanomaterials and their characteristics can be modified by adjusting the reaction conditions (e.g. precursors, precursor concentration, stabilizing agents, temperature, pressure and reaction time).^{42,88,89} The solvothermal method produces high quality crystallized monodispersed nanocrystals with narrow size distributions. The method is generally very similar to the hydrothermal method and is performed at high temperature and pressure, often in an autoclave. Its main advantage is the possibility to use organic solvents like methanol, ethanol or polyol for the reaction. Typical nanomaterials prepared by the solvothermal method are TiO₂ NPs, graphene and MOFs.^{42,90-92}

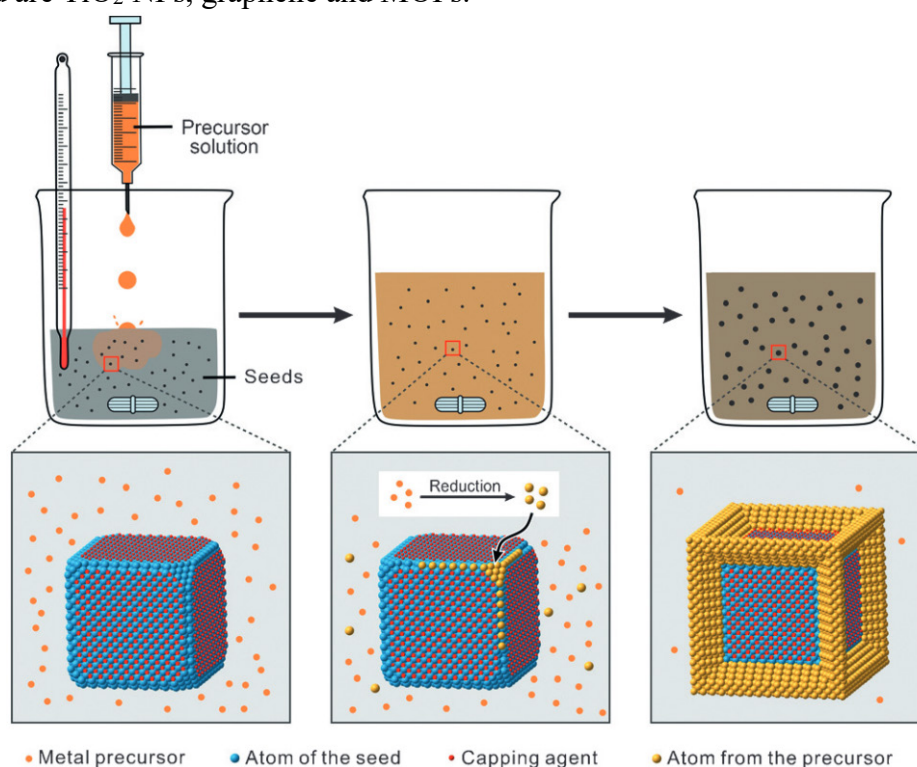


Figure 6: Seed-mediated growth method, step by step illustration; with precursor solution injection into reaction vessel suspension (reductant, capping agents, colloidal stabilizer and seeds); metal precursor reduction (or decomposition) and heterogeneous nucleation at seed surface; formation of defined nanocrystals through continued growth.⁹³

Seed-mediated growth is a method for synthesizing a broad range of bimetallic core-shell, dendritic and heterostructured nanocrystals with staggering degree of control over size, shape, structure and composition of

nanocrystals. The method illustrated in Figure 6, uses a reaction vessel containing a mixture of reductant, capping agent, seeds and colloidal stabilizer. The metal precursor solution is then injected into the vessel and will either get reduced or decomposed to form zero-valent atoms (charge neutral atoms). The zero-valent atoms nucleate heterogeneously on the surface of the seeds. The continuous growth leads to well-defined nanocrystals depending on the seeds.⁶⁵ The method may be performed as a homogeneous or heterogeneous nucleation. Generally, however homogeneous nucleation is used to generate defined seeds and heterogeneous nucleation is used to direct and control nanocrystal growth. Because the main control for the reaction is gained by using defined seeds, a homogeneous nucleation would be problematic since it leads to diverse sizes, shapes, morphologies and internal structures. For homogeneous nucleation to occur the reactant concentration needs to be supersaturated while heterogeneous nucleation makes use of the preformed seeds as primary sites and supersaturation is not required. Concentrations have to be precisely controlled to avoid both processes from happening at once. A further important parameter is that the metal precursor has a lower reduction potential than the seed otherwise a redox reaction between precursor and seed will occur leading to galvanic replacement instead.⁹³

Galvanic replacement might be unwanted during seed-mediated growth however, it is a rather unique and useful method on its own. It is one of the few methods that can be used to form hollow bimetallic nanocrystals. Using previous methods hollow nanocrystals cannot be formed. Galvanic replacement is an electrochemical process which utilizes differences in reduction potentials between two elements. The method first forms a sacrificial metal template (e.g. Ag nanocrystals) with the desired size of the empty space then the metal precursor (e.g. HAuCl₄) with the higher reduction potential is introduced. The introduction of the metal precursor will oxidize the metal ions of the template slowly covering the exterior with the reduced target metal while slowly dissolving the interior into solution. This leads to a hollow bimetallic nanostructure (e.g. hollow gold nanocubes) in the shape of the initial template. An example of this procedure was demonstrated by J. Patarroyo et al., forming hollow PdAg-CeO₂ heterodimer nanocrystals. The method commenced with initial Ag nanocrystal formation and subsequent CeO₂ deposition which was then used as a sacrificial template with K₂PdCl₆ and HNO₃ to form hollow nanostructures.^{65,93,94}

1.3.8 Gas-phase methods

Typical gas phase methods to form nanomaterials (e.g. NPs) are spray, laser or flame pyrolysis. For spray pyrolysis, a vaporized precursor is introduced into a hot reactor using a nebulizer. NPs are formed within the thermostatically controlled tubular reactor and collected with a precipitator. Typical precursors are metal acetates, nitrates or chlorides. The method is relatively simple and cheap and finds use in forming TiO₂ or ZnO NPs.^{95,96} Homogeneous nucleation reactions to form NPs can be triggered by irradiating a supersaturated vaporized precursor using a laser (laser pyrolysis), with an infrared CO₂ laser being most typically used. Laser pyrolysis is a rather clean method that allows for particle size control by modifying the vapour flow rate.⁷⁶ Problems for these methods are precursors with very low vapour pressures making them difficult to vaporize. In such cases, flame pyrolysis can be modified by directly spraying a liquid precursor or a solution of the precursor into a flame. The method is very effective, and precursors can be sprayed into the flame dissolved in organic or aqueous solvents.⁴²

1.3.9 Biosynthesis

Increasing demand for greener material synthesis put focus on biosynthesis for nanomaterial formation. New methods need to be more cost efficient, be environmentally friendly, possible to scale up and must not require high pressures, temperatures or toxic materials. There are many biosynthetic methods being studied and improved to fit these criteria, including bioreduction or biosorption with both methods being used to form

NPs using bacteria, fungi or plant products. Bioreduction uses microorganisms to reduce metal ions into biologically stable metallic nanostructures while biosorption utilizes stable cell wall or peptide interactions by combining metal cations with cell walls of organisms to form stable NPs. One example is *E. coli* forming NPs such as Pd, Pt or Ag through extracellular reduction. Hence, the microorganism (bacteria) rapidly multiplies under extreme conditions forming tuneable (size and shape) NPs. Modifications can be controlled through changing cultivation conditions such as temperature, pH, growth medium, incubation time and oxygenation.^{97,98} Enzymes and proteins from fungi can be used as reducing agents with certain metals can bind to the cytoplasmic membrane through electrostatic interactions. Methods that use fungi have the advantage that they can be scaled up, offer a large surface area to work with and are more efficient than bacteria as they secrete larger amounts of proteins.^{99,100} Alternatively, plant or plant products can be extracted for their primary and secondary metabolites (e.g. phenolic acids, terpenoids and alkaloids) and the compounds used as reducing agents and capping agents to synthesize NPs. For the NP synthesis, the purified bio-reducing agents are mixed in aqueous solution with a metal precursor. Plant extracts are advantageous as they are readily available, eco-friendly and suitable for bulk production. This method does, however, require high temperatures.^{101,102}

1.3.10 Other methods

Methods of NP synthesis that do not fit within the categories already described are summarised in this Section. These include electrochemical deposition, co-reduction, microwave assisted, supercritical fluid technology and ultrasound techniques. For electrochemical deposition a three terminal potentiostat is used together with dissolved metal salts in either acidic or basic baths. Ion etching can be used in addition to form porous membranes. The resultant nanomaterials deposit over time under a slight voltage on the electrode. The method is fast, inexpensive and simple allowing control of the nanomaterial (NPs, nanowires, nanorods) size and morphology. A further advantage can be the direct attachment of the nanomaterial to the electrodes.¹⁰³⁻¹⁰⁵

For bimetallic nanocrystals, coreduction can be used. Hence, bimetallic nanocrystals are produced by simultaneous reduction of two metal precursors. The zero-valent (charge neutral) atoms nucleate and grow to form the bimetallic nanocrystals. A final inert atmosphere annealing is often performed to obtain homogeneous alloys. The method allows control over composition shape and size by fine-tuning experimental parameters (reducing agent, use of coordinating ligands, reaction temperature, capping agents, and the reduction potentials of the metal ions).⁶⁵

Microwave assisted synthesis is a simple and rapid method which can decrease reaction times dramatically. The method uses metal precursors together with reducing agents to produce NPs under homogeneous heating. However, shorter reaction times result in shorter crystallization and nucleation times which can lead to less control over shape and size of the NPs.¹⁰⁶⁻¹⁰⁸

Ultrasound techniques and in specific sonochemistry is an eco-friendly, fast, green and simple method which uses acoustic cavitation to form nanostructures from metal precursors. When a liquid (any less volatile organic solvent) is exposed to ultrasound, oscillating microscopic bubbles form caused by alternating expansive and compressive acoustic waves. The bubbles act as plasma chemical microreactors and offer a unique extreme environment of high temperature (~ 5000 K) and high pressure (~ 1000 bar) with fast heating and cooling rates ($>10^{10}$ K s⁻¹) inside the bubbles, allowing access to unique chemical reaction spaces. The method can be used to prepare nanostructures from noble metal salts without the need for reducing agents and allows the preparation of several types of nanostructures, including carbides, metals, oxide and sulfides. Typical examples include nanostructures such as TiO₂, ZnO, CeO₂, BiPO₄ or more specialized materials such as the bimetallic Fe-Co NPs made from Co(CO)₃NO and Fe(CO)₅.^{42,109,110}

Running a reaction at the interface between the gas phase and liquid phase is possible through supercritical fluid technology. By varying the pressure or temperature the reaction can run in the gas phase or liquid phase, causing a change in the physiochemical properties. One important aspect of this method is the vast difference

in density between the two phases. When making NPs the rapid expansion from liquid to gaseous can be utilized to create fine powders. This fast, low cost, simple method, does not require organic solvents while maintaining high solubility through the use of supercritical solvents (CO_2 , H_2O). The method finds use in preparing nanotubes, core shell particles and NPs.^{107,111}

1.4 Surface-functionalized nanomaterials

1.4.1 General functionalization principles

As **Section 1.3** showed, there are many methods available for the preparation of nanomaterials and most give outstanding control over their characteristics (e.g. size, shape, surface charge, stability and composition etc.) yielding hyper-specialized nanomaterials capable of dealing with any task. However, a large area of nanomaterial research involves post-treatments to functionalize or modify the surface to further enhance their physical and chemical properties, adjust them to do something new or to protect them. As such, nanomaterials can be enhanced to make them more biocompatible by introducing steric stabilization through the use of hydrophilic polymers such as PEG to prevent protein absorption. Imaging qualities of nanomaterials can be enhanced by functionalizing the surface with fluorescent molecules. Further surface functionalization gives control over porosity, wettability, solubility, surface acidity, mechanical and thermal resistance. Using clever surface functionalization, nanomaterials can be modified to hinder fast agglomeration, an often unwanted feature due to their excessive surface activity in liquid media. Furthermore, some nanomaterials (e.g. metal NPs) can corrode or passivate if kept unprotected against which surface modifications are employed.^{112,113}

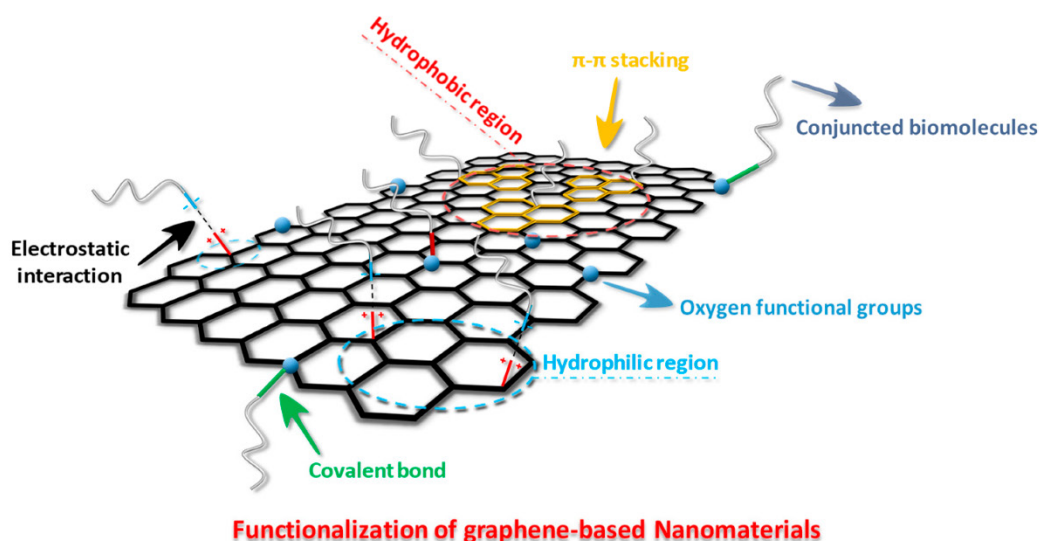


Figure 7: Overview of non-covalent and covalent surface functionalization in of graphene-based nanomaterials.¹¹⁴

In general, there are two approaches to functionalize nanomaterials, through non-covalent bonding (e.g. electrostatic, ionic, hydrophobic interactions, π - π stacking, hydrogen bonds or van der Waals interactions) or covalent bonding with the use of either bifunctional linkers and mediator linkers (e.g. R-COOH , R-NH_2 , R-SH , R-PO(OH)_2 , R-Si(OMe)_3), grafting, ligand exchange or adapter molecules and coordinate binding. Graphene-based nanomaterials (Figure 7) are excellent examples of both approaches as they permit most functionalization methods due to their special surface properties. Both approaches have advantages in various fields of application. The technique is selected based upon which properties are desired and which groups are present on the nanomaterial surface. As such, binding affinities have to be considered, as the appropriate functionalization leads to critical improvements of the functionalization degree. Non-covalent bonding is simple and does not permanently alter the surface structure of the nanomaterial. Non-covalent interaction can be

used to deposit a load designed to be released on the nanomaterial, as the bonding can be tuned to be sensitive to pH, temperature or irradiation and the medical field utilises this for targeted drug release. Covalent bonding has increased functionalization stability which allows for sequential functionalization, and this is of major importance in various fields. Furthermore, keeping the nanomaterial properties unchanged can be beneficial (as in non-covalent bonding) the opposite can be of use too, this is best achieved using covalent surface functionalization.^{112,113,115,116}

1.4.2 Non-covalent surface functionalization

Non-covalent interactions that can be used for surface functionalization are shown in Figure 8 again using graphene, graphene oxide and reduced graphene oxide as example. One of the most investigated non-covalent interactions for surface functionalization involves ionic or electrostatic interactions, often used to bind polymers. The method involves two opposite charged species (e.g. polymers, inorganic NPs, nucleic acids) and can be divided into direct, desalting and layer-by-layer depositions. The direct addition is simple and mixes both precursors together to form an aggregate of the opposite charged components. This method is rapid but can yield unordered results. An example of a preparation overcoming this drawback describes the formation of uniform raspberry-like particles by dropwise addition of positively charged amine-modified polystyrene particles (154 nm diameter) to a negatively charged silica or gold NPs suspension. The smaller adsorbed inorganic particles were located within the electrostatic double layer of the large polymeric particles. Hence, the entire surface of the polystyrene sphere acted as multivalent counter-ions ensuring uniform distribution of the inorganic NPs.¹¹⁷⁻¹¹⁹

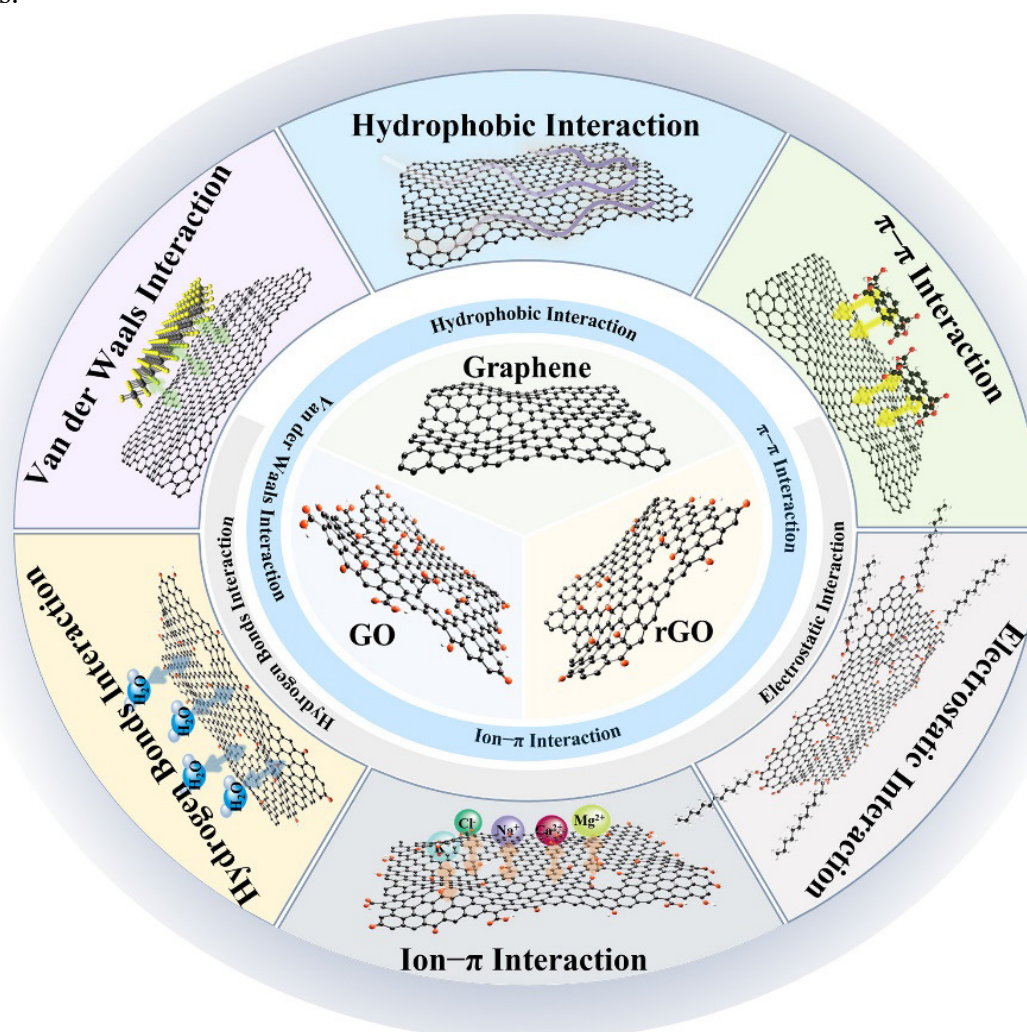


Figure 8: Non-covalent surface interactions for pristine graphene, graphene oxide (GO) and reduced graphene oxide (rGO).¹²⁰

More ordered nanomaterials can be obtained by dispersing the components in a solution containing salts. The non-covalent binding is inhibited in the presence of the salt and can be controlled by ions slowly desalting. The greatest order, allowing highly controlled coatings and hierarchical morphologies, can be gained through the most time-consuming method – layer-by-layer deposition. This method involves, as the name would suggest, alternate addition of oppositely charged compounds into a nanomaterial suspension. The method is repeated several times and purified (to remove weakly bound species) after each cycle. Thereby layers of opposing charge are created. The method was used by Takahashi et al. to prepare polyethyleneimine functionalized bovine serum albumin modified gold nanorods. The nanomaterial showed increased cellular uptake and binding as agglomeration was prevented due to greater stability in the electrolyte buffer solution. The layer-by-layer deposition technique can also be modified to form hybrid hollow NPs, used in the biomedical field. The method utilizes colloidal templates together with NPs and polymers. The hollow NP wall thickness and, capsule structure can be controlled by changing the layering cycles and the colloid template morphology and size. An example using this technique is the preparation of Fe₃O₄/Pd/polyelectrolyte. This uses melamine resin particles as removable colloid template, poly(sodium *p*-styrenesulfonate) and poly(allylamine hydrochloride) as negatively and positively charged polyelectrolytes, hydrolysed negatively charged Pd NPs as catalyst and Fe(NO₃)₃ under reducing conditions to deposit Fe₃O₄. The hollow NPs were formed by removing the colloid template under acidic conditions (0.1 M HCl). Further examples in the literature include ZnO nanorod/Ag, ZnO nanorod/CeO₂ and ZnO nanorod/CdS.^{117,121-126}

A similar method using electrostatic interactions which allows for immobilization control of structural complex biomolecules (proteins) uses avidin or streptavidin and biotin modified NPs and compounds. The method, mostly used in bio-nanotechnology makes use of the zwitterionic receptor avidin, which can be easily non-covalently bound to negatively charged NPs while compounds modified with the small molecule, biotin can be obtained through biotinylation of carbohydrates or thiol moieties. Biotin and avidin compounds offer high affinity (K_d around 10^{-14}) due to four identical subunits within avidin, yielding four binding pockets that specifically recognize biotin making them excellent non-covalent binders. The binding is extremely stable and can resist harsher chemical and temperature fluctuations than other non-covalent bonding interactions. The method finds use in NP based biosensors.^{118,127}

Hydrophobic coupling describes the adsorption of lipophilic compounds onto nanomaterials. The method is widely used in medicine. The weak hydrophobic interaction can be utilized for specific compound release (targeted drug release) and can be further enhanced by encapsulating the nanomaterial with an amphiphilic polymer or capsule. As the core and functionalization can act independently after separation the material can be used for two purposes; (i) the NP could act as imaging agent while (ii) the adsorbed compound could be therapeutic. The method causes only minimal changes to the nanomaterial surface through the functionalization. Common compounds that are attached to hydrophobic nanomaterials are fluorophores, proteins and antibodies but in general any lipophilic compound will work. However, for proteins and antibodies, conformational change resulting from by binding might change their native structure and activity. Similarly, hydrophilic interactions can be used to achieve a non-covalent binding. This method is less common, but an example is the preparation of orientation locked hybrid NPs with an ulterior goal of future functionalization and creation of asymmetric particles with two distinct parts (Janus morphologies). Jiang et al. used hydrophilic fused silica NPs and adsorbed them to the oil-water interface of a molten wax and water emulsion. The particles were frozen into position by cooling the oil phase thereby creating a template, which could be used during chemical modifications making it impossible for the adsorbed particles to change their orientation.^{118,128}

1.4.3 Covalent surface functionalization

Similar to non-covalent functionalization covalent bonding is done to either introduce new properties, change solubility or stabilize the NPs against agglomeration, corrosion or oxidation. Covalent surface functionalization can be separated to chemical treatments introducing new functional groups, grafting of synthetic polymers and ligand exchange techniques. However, most methods are used together to build the desired surface modification. Using chemical treatments, surface functionalization can build various covalent bonds through different reactions, which depend on the groups present on the NPs. For -OH groups Figure 9 shows an overview of surface modifications that can be done. The reactions include esterification, epoxide opening, isocyanate or isothiocyanate addition, silanization and phosphonic esterification. One of the more commonly used strategies, salinization is a useful method to improve the dispersion stability of NPs in various solvents or polymer matrices compared to unmodified NPs.¹²⁹ An example of this method was done by Suzuki et al. who modified TiO₂ NP surfaces with silane coupling agents, such as 3-aminopropyltriethoxysilane and n-propyltriethoxysilane gaining suppressed photocatalytic activity to use the material as inorganic UV filter while Cheng et al. modified ZnO surfaces with 3-methacryloxypropyltrimethoxysilane gaining better dispersion and increased performance in absorbing UV light.^{130,131}

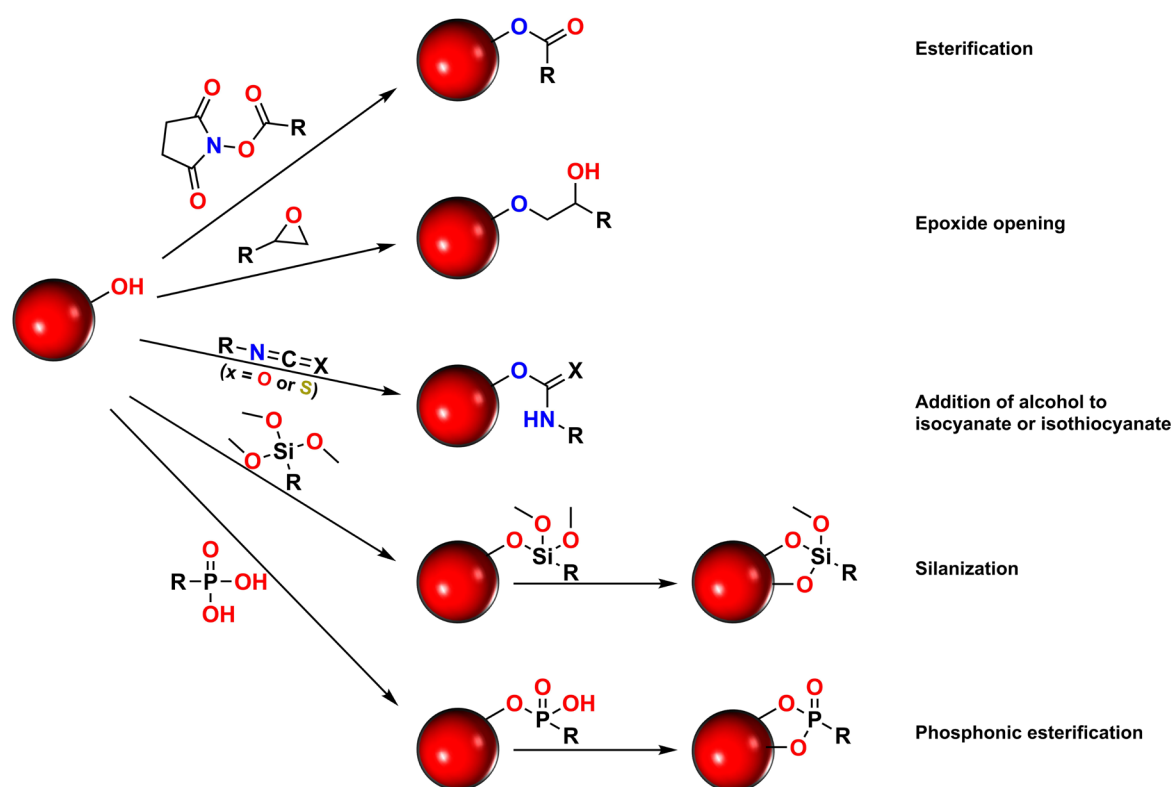


Figure 9: Covalent bond reaction strategies for nanomaterial functionalization with pre-existing hydroxyl groups. Figure was redrawn from M. A. Hood et al., Synthetic Strategies in the Preparation of Polymer/Inorganic Hybrid Nanoparticles, *Materials*, 2014, 7, 4057 – 4087.

Another studied approach is using esterification often with carboxylic acid or phosphonic acid derivatives. This approach has seen wide application in implementing dye structures onto semiconductor metal oxides for dye-sensitized solar cells making use of the mild reaction conditions, excellent stability and unhindered photocatalytic activity. It has to be noted that covalent binding can be affected by the reaction conditions including used anchoring molecule, solvent, pH and NP pre-treatment. Hence not only is the covalent bonding shown in Figure 9 (e.g. with phosphonic acids) possible, but also a range of binding modes including monodentate,

bidentate chelating and bidentate bridging are accessible. Covalently bound silane moieties can be interconnected to form a stable silica shell around the nanomaterial (e.g silane inorganic polymers). Similarly, to pre-existing hydroxyl -OH groups in Figure 9 the NPs could be designed to have -NH₂ on its surface. This opens up different reactions pathways shown in Figure 10 that can be used for further purposes.^{127,132}

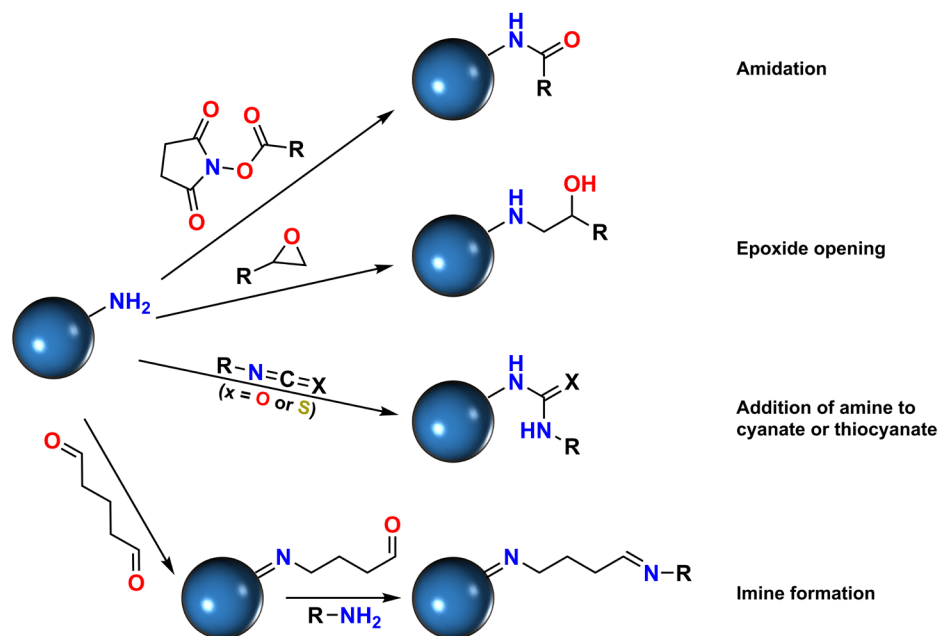


Figure 10: Covalent bond reaction strategies for nanomaterial functionalization with pre-existing amine groups. Figure was redrawn from M. A. Hood et al., *Synthetic Strategies in the Preparation of Polymer/Inorganic Hybrid Nanoparticles*, *Materials*, **2014**, *7*, 4057 – 4087.

One important aspect of surface functionalization is grafting of synthetic polymers. The method can be separated into 'grafting to', 'grafting from' and 'grafting through'. All methods alter the surface topology of inorganic or organic nanomaterials and enhances their chemical functionality, thereby creating nanocomposites. 'Grafting to' can be described as reacting fully grown polymer chains with appropriate reactive groups on the nanomaterial surface while 'grafting from' often has initiating functionality on the nanomaterial surface then introduces monomers to build the polymer on the nanomaterial. 'Grafting through' uses nanomaterials with polymerizable groups on the surface and initiator monomers in solution; each monomer is capable of acting as a linker and thus, a nanomaterial polymer network can form. 'Grafting to' methods often make use of functional groups already functionalized on the nanomaterial surface which allows the method to bind polymers. Hence, further covalent bonding strategies shown in Figure 11 and methods that were shown in Figure 9 and Figure 10 are important to couple any desired polymer to nanomaterial surfaces. The ease of using click chemistry allows for high efficiency and mild conditions and the resulting functionalization gives access to for many 'grafting to' examples. Examples include (i) TiO₂ NPs coupling with phosphonate and click chemistry to then graft polystyrene to the surface, (ii) radical in situ polymerizations, to create highly tailored materials or (iii) with thiol-ene reactions to modify nanocellulose crystals and couple them into the matrix of composite materials. A special form of 'grafting to' creates hierarchical hybrid NPs, which involves two NPs with one of them carrying the polymer. An example was demonstrated by Agrawal et al. using amino-functionalized CdTe nanocrystals. The nanocrystals were amide coupled with a carbodiimide, to carboxylic-terminated poly(N-isopropyl acrylamide) microgel NPs. A further example of this method was the click chemistry coupling of azide functionalized Au NPs with acetylene functionalized polymer NPs.¹³³⁻¹³⁸

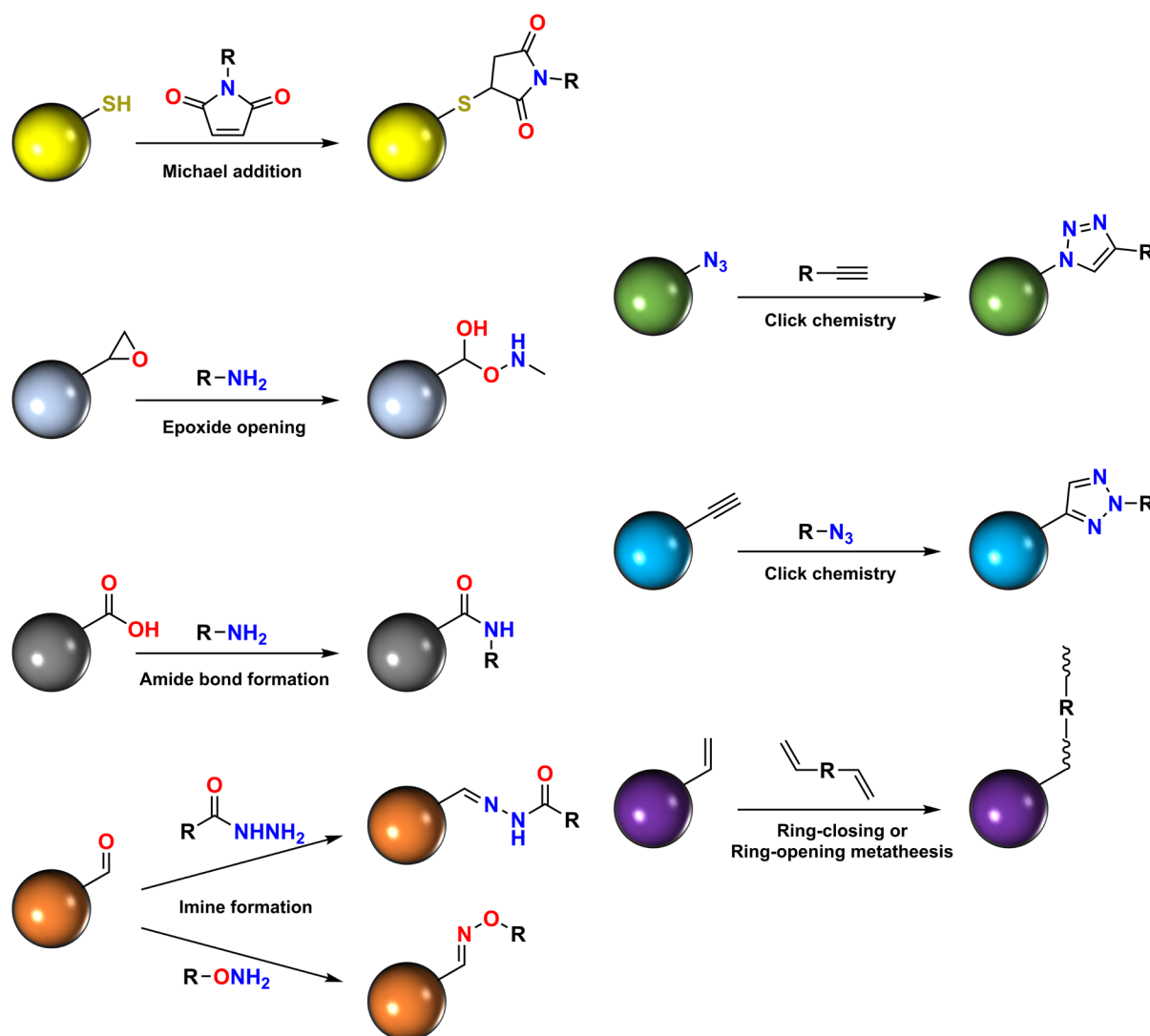


Figure 11: Covalent bond reaction strategies for nanomaterial functionalization with other pre-existing groups. Figure was re-drawn from M. A. Hood et al., Synthetic Strategies in the Preparation of Polymer/Inorganic Hybrid Nanoparticles, *Materials*, **2014**, 7, 4057 – 4087.

Polymer chains can be propagated directly from the nanomaterial surface by functionalizing its surface with initiating groups. The method, 'grafting from' leads to a higher percentage of successful grafts and can use various polymerization methods such as radical, anionic or cationic.¹¹⁶ For example the method uses TiO₂ NPs adsorbed with hydroperoxide macroinitiators and radically polymerizes styrene and methyl methacrylate on the surface.¹³⁹ Another demonstration of the method used TiO₂ nanoparticles and photocatalytically polymerized methyl methacrylate on the NP surface.¹⁴⁰ Magnetic iron, cobalt and nickel NPs can be also used in a similar fashion hence styrene and methyl methacrylate were polymerized under irradiation onto the NPs.¹⁴¹ 'Grafting to' was also demonstrated using a biomimetic imitator functionalized on TiO₂ NP surfaces which reacted with methyl methacrylate to form the polymer nanocomposite.¹⁴² Biocompatible polymers can also be formed as such a radical polymerization between 2-methacryloyloxyethyl phosphorylcholine and azo silica nanomaterial surfaces was performed.¹⁴³

1.5 Applications and current research

Throughout the previous sections some uses of nanomaterials have been discussed but nanomaterials have seen broad use from 1000 commercial products in 2012 to over 5000 to 10000 products in 2022 depending on the used database. Figure 12 compares the main nanomaterials and shows in which area they are being used.

Nanomaterials based on silver, TiO_2 and SiO_2 were the most reported. However, while the distribution of used nanomaterials is highly interesting it has to be noted that many manufacturers did not disclose which nanomaterial they used. Nanomaterials found use in every area of life from agriculture and automotive industry to construction and cosmetics with many products in electronics and medicine as well as several in the renewable energy sector.¹⁴⁴⁻¹⁴⁶ As such, this Section will focus presenting some applications in industry and research. Products include nano-encapsulated zinc oxide as fertilizers in agriculture. Here, the zinc has an essential role for plant growth and by using the unique properties of zinc oxide NPs it is possible to achieve fast absorption but slow-release from the nano-capsules. This saves consumption and reduces environmental impact. The automotive industry utilizes NPs in several areas of the production of a car. They find use as clear coatings for metallic and non-metallic paints to enhance the polish finish and scratch resistance to fillers in tyres for improving adhesion. Construction industries uses nanomaterials to improve UV resistance, corrosion resistance, thermal conductivity, isolation and also for smart windows to reduce energy consumption by blocking solar radiation. The food industry found clever uses as sensors to indicate product ripeness detecting released aromas by the fruit.¹⁴⁶ In electronics Samsung uses Ag NPs as antibacterial material for air conditioners, air purifiers, refrigerators, washing machines and vacuum cleaners.¹⁴⁷ While quantum dots which are excitonic nanocrystalline semiconducting luminescent material for display applications and bioimaging. The excellent electronic, photophysical and optoelectronic properties of quantum dots change as a function of shape and size because of their symmetric and narrow emission spectra properties. Hence, they find use with several manufacturers of displays (e.g. flat panel TVs).⁶⁴ However, their tunability goes further than traditional NP size/shape manipulation and studies the use of heterostructuring of the quantum dots. Nanocrystal functionalities can therefore be controlled including interface engineering (suppression of Auger recombination) of quantum dot LEDs and lasers, intraband relaxation (improved carrier multiplication) for quantum dot photovoltaics and Stokes-shift engineering useful for large-area luminescent solar concentrators.¹⁴⁸ The properties of quantum dots are outstanding. They often contain toxic cadmium or lead or use rare elements. To cut the manufacturing costs and improve the environmental friendliness of quantum dots, research groups have started to work on synthesis in aqueous media while other groups have begun to develop non-toxic quantum dots using earth abundant metals. One of those examples is hydrophilic graphene-based quantum dots which emit blue light and are non-toxic.^{146,149,150} In the medical field the use of nanomaterials ranges from disinfection to medical supplies, pharmaceuticals and analytics. As such, superparamagnetic NPs are studied as contrast agents in magnetic resonance imaging (MRI). Using an alternating magnetic field these NPs are used as magnetic fluid hyperthermia agents where they convert magnetic energy into thermal energy to treat cancer.¹⁵¹

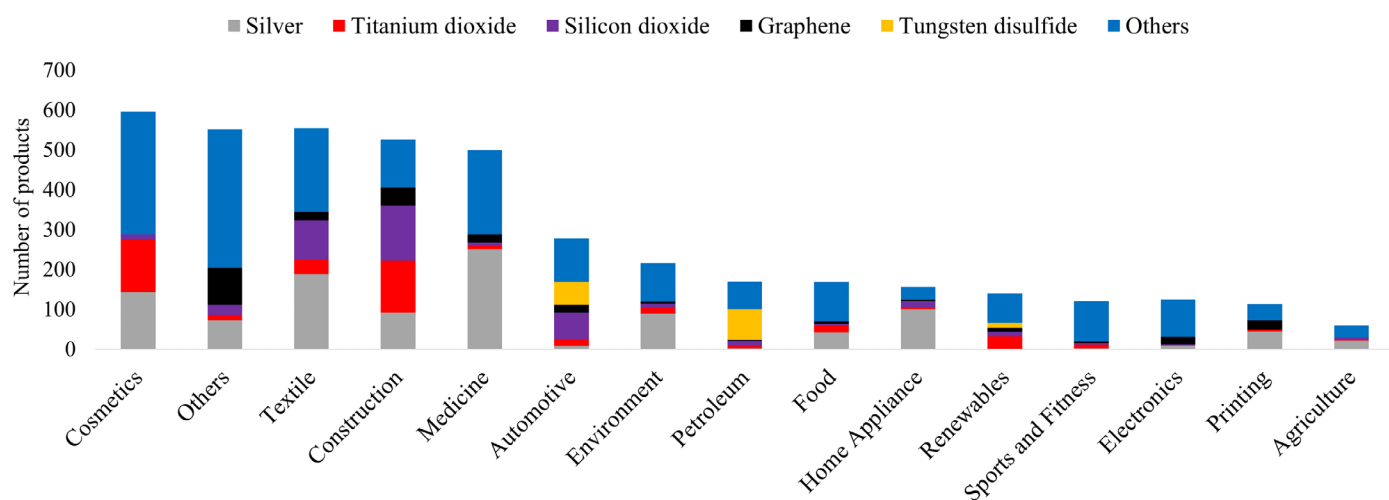


Figure 12: Type of nanomaterials reported to be used in different product categories. Data from product.statnano.com.

Nanomaterial based materials also find use in dye-sensitized solar cells (DSSCs) which were first introduced 1991 in Nature by M. Grätzel and B. O'Regan. Grätzel took advantage of nanocrystalline TiO_2 semiconductors onto which the dye molecules could be adsorbed which was the critical advance to make the technique work. The specific characteristics of NPs with their higher surface area solved the problem atomically flat semiconductors had by allowing much higher dye coverage. The material is now commercially used in certain solar cells and even accessible in smaller gadgets such as the solar powered keyboards.^{152,153} A further use for nanomaterials is within battery development. As such, one example exploring advancement with lithium-ion batteries uses hollow $\text{Mn}_x\text{Fe}_{3-x}\text{O}_4$ as anode. The particle size, hollow morphology, crystal structure, composition all contribute to benefits in lithium-ion batteries yielding excellent electrical conductivity, ability to buffer volume changes during cycling, cycling performance, structural stability and lithium kinetics.¹⁵⁴ Overall, research always comes into play before anything can reach the commercial market. Hence, it is important to invest heavily into finding new sustainable materials, improving current ones and replacing environmentally damaging ones.

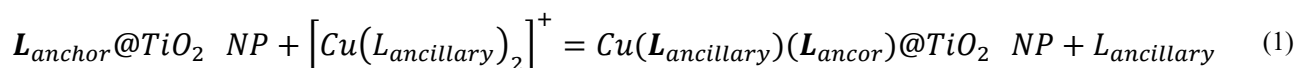
CHAPTER II: THE SALSAC APPROACH

COMPARING SOLVENT DISPERSED NANOPARTICLES WITH NANOPARTICULATE SURFACES

2.1 Summary

The project that led to the following paper¹⁷ was to investigate the application of the SALSAC 'surface-as-ligand, surface-as-complex' method previously used for annealed nanoparticulate TiO₂ surfaces to dispersed NPs in solution. During this work, NP surface activation, functionalization and suitable characterization methods were established which led to this work being a cornerstone for the subsequent Chapters of this thesis.

The paper includes functionalization of TiO₂ NPs with anchoring ligands **1** – **4**. The anchoring was performed in a microwave reactor at elevated temperatures in water using either phosphonic acid or carboxylic acid anchoring groups. Competitive binding experiments of anchoring ligands to the NP surface showed preferential binding of phosphonic acid over carboxylic acid anchors. The phosphonic acid anchors showed binding orders **3** > **1** > **2**. The SALSAC approach was demonstrated by subsequently forming heteroleptic copper (I) and iron (II) complexes on the NP surface-functionalized with ligand **1**, **2**, **4** (for copper(I)) or ligand **3** (for iron(II)) (shown in Figure 13). Overall, several homoleptic complexes ([Cu(**5**)₂][PF₆], [Cu(**6**)₂][PF₆], [Cu(**7**)₂][PF₆] or [Fe(**8**)₂][PF₆]₂) were prepared to use with anchoring ligand-functionalized NPs (f-NP) according to Equation (1). The equation describes the general process and nomenclature used here and in following Chapters. As such, @ represents 'attached to the surface' while text before and after the @ sign describe functionalization and NP, respectively. It must, however, be noted that the protonation state of the surface-attached phosphonic acid is not known and it is represented through the thesis in the acid form. However, mono- or bis-deprotonated species are also possible and, where there is a formal positive charge on the complex, it may well be that the species is neutral with the charge compensated by deprotonation of a phosphonic acid.



NP functionalization was investigated using ¹H NMR spectroscopy, FTIR spectroscopy, solid-state absorption spectroscopy, TGA and SEM.

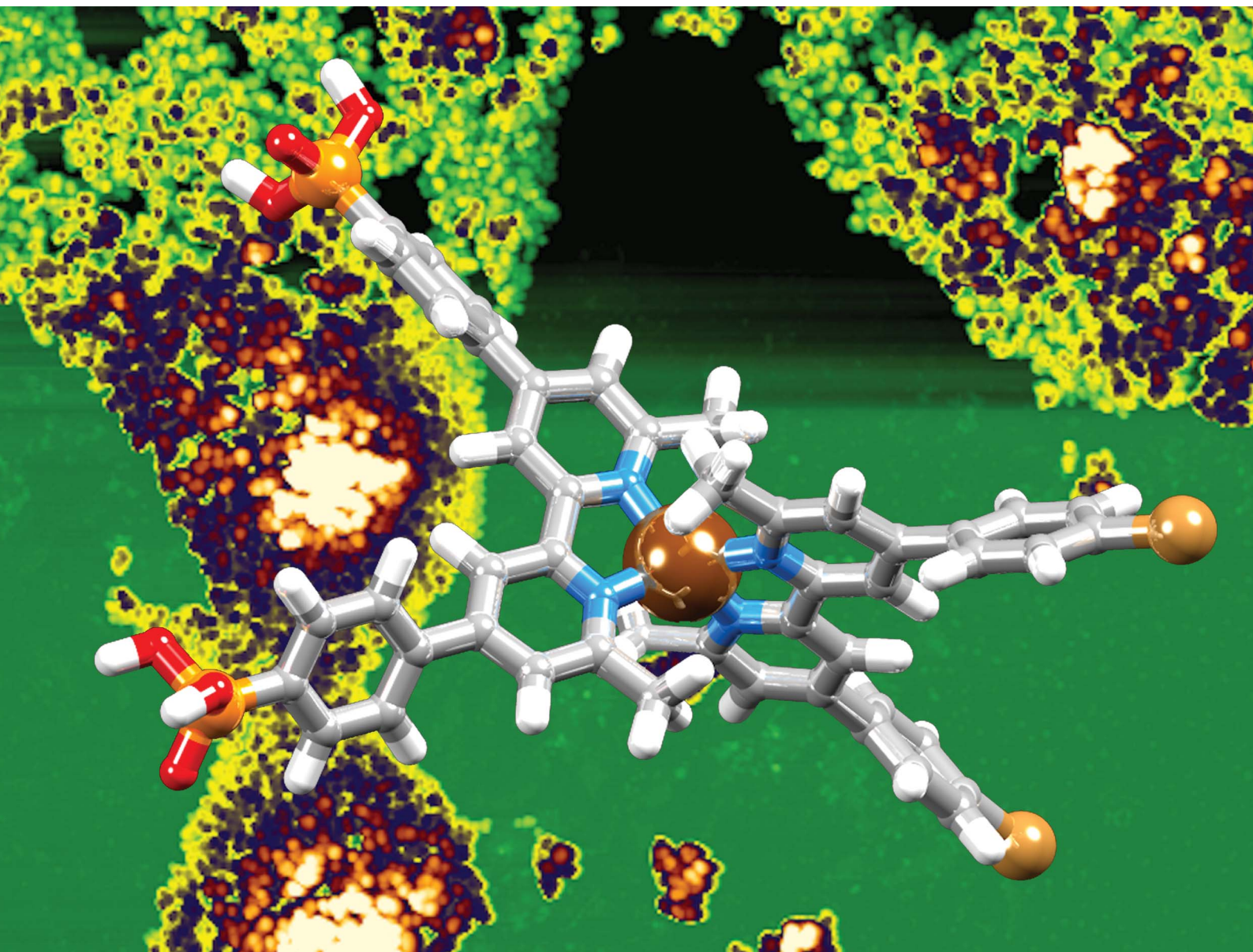


Figure 13: Photographs of activated TiO₂ NPs from left to right: functionalized with **1** and **3**; and after treatment with [Cu(**5**)₂][PF₆]; [Cu(**7**)₂][PF₆]; [Cu(**6**)₂][PF₆]; [Fe(**8**)₂][PF₆]₂.¹⁷

Nanoscale Advances

Volume 2
Number 2
February 2020
Pages 523–914

rsc.li/nanoscale-advances




ISSN 2516-0230

PAPER

Edwin C. Constable *et al.*
The SALSAC approach: comparing the reactivity of
solvent-dispersed nanoparticles with nanoparticulate
surfaces

Cite this: *Nanoscale Adv.*, 2020, 2, 679

The SALSAC approach: comparing the reactivity of solvent-dispersed nanoparticles with nanoparticulate surfaces†

Sven A. Freimann,  Davood Zare,  Catherine E. Housecroft 
and Edwin C. Constable *

We demonstrate that the 'surface-as-ligand, surface-as-complex' (SALSAC) approach that we have established for annealed nanoparticulate TiO₂ surfaces can be successfully applied to nanoparticles (NPs) dispersed in solution. Commercial TiO₂ NPs have been activated by initial treatment with aqueous HNO₃ followed by dispersion in water and heating under microwave conditions. We have functionalized the activated NPs with anchoring ligands 1–4; 1–3 contain one or two phosphonic acid anchoring groups and 4 has two carboxylic acid anchors; ligands 1, 2 and 4 contain 6,6'-dimethyl-2,2'-bipyridine (Me₂bpy) metal binding domains and 3 contains a 2,2':6',2''-terpyridine (tpy) unit. Ligand functionalization of the activated NPs has been validated using infrared and ¹H NMR spectroscopies, and thermogravimetric analysis. NPs functionalized with 1, 2 and 4 react with [Cu(MeCN)₄][PF₆]₂ and those with 3 react with FeCl₂·4H₂O; metal binding has been investigated using solid-state absorption spectroscopy and scanning electron microscopy (SEM). Competitive binding of ligands 1–4 to TiO₂ NPs has been investigated and shows preferential binding of phosphonic acid over carboxylic acid anchors. For the phosphonic acids, the binding orders are 3 > 1 > 2 which is rationalized in terms of relative pK_a values (phosphonic acid and [HMe₂bpy]⁺ or [Htpy]⁺) and the number of anchoring groups in the ligands. Ligand exchange between ligand-functionalized NPs and homoleptic metal complexes gives NPs functionalized with heteroleptic copper(i) or iron(ii) complexes.

Received 8th August 2019
Accepted 12th December 2019

DOI: 10.1039/c9na00488b

rsc.li/nanoscale-advances

Introduction

Numerous methodologies have been developed for the synthesis of hierarchical structures^{1–4} at interfaces, including self-assembled monolayers,^{5–7} self-organization and self-assembly^{8,9} through van der Waals forces^{10–12} supramolecular chemistry,¹³ templating,¹⁴ sol–gel deposition techniques,¹⁵ pyrolysis⁴ and dye-stamping.¹⁶ In most cases the methods are either highly specific to the target structure, are dependent upon the preparation of complex soluble or volatile covalent structures or have significant elements of serendipity in the outcome.¹⁷

In the context of our research into dye-sensitized solar cells (DSCs), we developed a methodology^{18–20} which we have termed

'surfaces-as-ligands, surfaces-as-complexes' (SALSAC). This extends 'simple' self-assembly and self-organization at surfaces to the stepwise and hierarchical building up of new pre-defined and easily tailored architectures. Our inspiration and motivation lie in an appreciation of the exquisite complexity of biological systems and at the same time a desire to utilize self-assembly and self-organization strategies to achieve similar levels of complexity in synthetic systems. An added value of this approach is that the increasing complexity of the architectures can lead to emergent properties²¹ not found in the individual components. The concept of this paper relates to the transferability of modification reactions between extended surfaces and nanoparticulate materials.

Although we developed the SALSAC approach for the assembly of heteroleptic copper(i) dyes on the surface of semiconductor nanostructured surfaces for use in DSCs,²⁰ it is clear that the experimentally simple approach of sequentially reacting a surface with components leading to a hierarchical assembly has wider applications. In its mature form, SALSAC has been developed into a powerful atom-efficient methodology allowing the preparation of multiply and specifically functionalized surfaces through step-wise assembly of structures incorporating anchoring ligands, metal ions and ancillary ligands.²⁰ The SALSAC approach is illustrated in Fig. 1: a nanoparticulate

Department of Chemistry, University of Basel, BPR 1096, Mattenstrasse 24a, CH-4058 Basel, Switzerland. E-mail: edwin.constable@unibas.ch

† Electronic supplementary information (ESI) available: Instrument details; Fig. S1–S6: mass spectrum and NMR spectra of 2; Fig. S7: DOSY fits; Fig. S8 and S9: IR spectra of NPs functionalized with 1 and 3; Fig. S10: TGA curve of 1; Fig. S11–S13 and S15: NMR spectra of competition experiments; Fig. S14: photographs of activated TiO₂ NPs functionalized 2 and 4; Fig. S16–S21: mass spectrum and NMR and IR spectra of 7; Fig. S22–S29: NMR and IR spectra of [Cu(6)₂][PF₆]₂ and [Cu(7)₂][PF₆]₂; Fig. S30: absorption spectrum of NPs functionalized with 3 after treatment with [Fe(8)₂][PF₆]₂. See DOI: 10.1039/c9na00488b



surface is modified with a compound (L_{anchor}) which combines an anchoring group specific to the surface (e.g. carboxylic acid, carboxylate, phosphonic acid or phosphonate for a metal oxide) and a metal-binding domain such as 2,2'-bipyridine (bpy) or 2,2':6',2''-terpyridine (tpy). Subsequent reaction with a metal ion (e.g. copper(I) in the case of DSC applications²⁰) and concurrent or consecutive reaction with ancillary ligands ($L_{\text{ancillary}}$) gives a surface functionalized with a heteroleptic metal complex containing both L_{anchor} and $L_{\text{ancillary}}$ ligands. An alternative strategy is to introduce metal ion and $L_{\text{ancillary}}$ by ligand exchange from a homoleptic complex.

Although we have focused on the addition of a single type of ancillary ligand in optimizing DSCs, we have also demonstrated that surfaces can be modified by sequential addition of two different ancillary ligands.²² Further development of this approach has the potential to introduce secondary surface sites which act purely to spatially separate the primary surface sites. In DSC applications, this translates to the introduction of co-adsorbants which can also bind to the metal oxide surface, typically through carboxylic acid or carboxylate, to inhibit molecular-dye aggregation.²³ Spatial separation may also be important in preventing metal-binding domains of surface-attached anchoring ligands from binding the same metal ion, generating surface-bound homoleptic complexes rather than the desired heteroleptic species.²⁴

Although numerous studies have described the attachment of anchor-functionalized complexes to surfaces, few studies relate to initial ligand functionalization of a surface through an anchor.²⁵ While ligand functionalized surfaces have been subsequently metallated,^{26,27} to the best of our knowledge, there has been no systematic investigation of the SALSAC methodology and combined use to introduce functionality through the ancillary ligand other than our own work in the context of copper(I) DSCs. We now explore how the principles established for annealed nanoparticulate TiO_2 surfaces (i.e. working electrodes in DSCs) can be extended to nanoparticles (NPs) of the same material dispersed in fluid phase. The fabrication and applications of functionalized metal oxide NPs is well

established,²⁸ but hierarchical assembly strategies are less well explored. It should be noted that when an anchoring ligand with an acidic functionality such as $-\text{CO}_2\text{H}$ or $-\text{PO}_3\text{H}_2$ is introduced, the protonation state and binding mode of the ligand is typically not well-defined, although the properties of the assembly are critically dependent on the protonation state.²⁹⁻³¹ The functionalization of metal chalcogenide nanoparticles with carboxylic and phosphoric acids has attracted much recent attention and a few reports of selectivity and exchange of surface-bound ligands have been published.³²⁻⁴¹

Experimental

General

Details of instrumentation are given in the ESI.†

The complex $[\text{Cu}(\text{MeCN})_4][\text{PF}_6]$ was prepared by the method of Kubas.⁴² 4-(4-Bromophenyl)-6,6'-dimethyl-2,2'-bipyridine,¹⁸ **1**,⁴⁴ **3**,³⁰ **4**,⁴³ **5**,⁴⁴ **6**,⁴⁵ **8**,⁴⁶ $[\text{Fe}(\mathbf{8})][\text{PF}_6]_2$,⁴⁷ and $[\text{Cu}(\mathbf{5})][\text{PF}_6]$ ⁴⁴ were prepared according to literature and their spectroscopic data matched those previously reported.

TiO_2 nanoparticles (AEROXIDE TiO_2 P25) were purchased from Evonik Industries. The spherical NPs have an average radius of 10.5 nm,⁴⁸ leading to a surface area-to-volume ratio of 28%. In the Experimental section, the number of equivalents of NPs are defined as $0.28 \times$ the total number of TiO_2 formula equivalents in the mass given, i.e. the effective surface concentration of TiO_2 .

Compound 2a

Solid 4-(4-bromophenyl)-6,6'-dimethyl-2,2'-bipyridine (340 mg, 1.00 mmol, 1 eq.), Cs_2CO_3 (1.629 g, 5 mmol, 5 eq.) and $[\text{Pd}(\text{PPh}_3)_4]$ (57.8 mg, 0.05 mmol, 0.05 eq.) were placed in a 20 mL microwave vial under N_2 . Diethyl phosphonate (552 mg, 511 μL , 4 mmol, 4 eq.) and 15 mL dry THF were added. The mixture was degassed by bubbling N_2 for 5–10 min and then the vial was capped. The reaction mixture was heated in the microwave reactor for 5 h at 130 °C and then cooled to room temperature, filtered through Celite and evaporated to dryness. The resulting yellow oil was dissolved in MeCN and the product isolated as pale-yellow crystals which were collected by filtration, washed with cold Et_2O and dried under vacuum (200 mg). The crude product was used in the next step without further purification (see text).

Compound 7

5 (582 mg, 1.18 mmol, 1.0 eq.), Cs_2CO_3 (2.31 g, 7.08 mmol, 6.0 eq.) and $[\text{Pd}(\text{PPh}_3)_4]$ (136 mg, 0.118 mmol, 10 mol%) were added to a microwave vial under N_2 . 3,5-Dimethyl-4-(4,4,5,5-tetramethyl-1,3,2-dioxaborolan-2-yl)isoxazole (1.05 g, 4.72 mmol, 4.0 eq.) and anhydrous toluene (20 mL) were added to another vial and N_2 was bubbled through the solution for 15 min. The contents of the two vials were combined into one microwave vial and N_2 was bubbled through the mixture for 10 min. The vial was sealed and the reaction mixture was heated to 110 °C for 4 h in a microwave reactor, after which time it was allowed to cool to room temperature. Then H_2O (40 mL) was

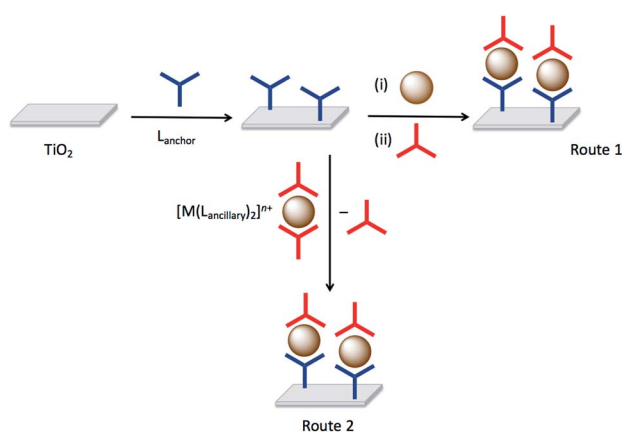


Fig. 1 Surface modification (e.g. nanoparticulate TiO_2) with a single anchor, single metal ion and an ancillary ligand (route 1), or with a single anchor followed by ligand exchange using a homoleptic metal complex (route 2).



added and the reaction mixture was extracted with CH_2Cl_2 (3×50 mL) and dried over anhydrous MgSO_4 . The solvent was removed under reduced pressure to yield an off-white solid. The residue was dissolved in hot CHCl_3 (1 mL), and the product was precipitated by addition of EtOH (10 mL). The precipitate was washed with EtOH (50 mL) and acetone (50 mL) to yield **7** as a beige solid (205 mg, 1.18 mmol, 33%). ^1H NMR (500 MHz, CDCl_3) δ /ppm: 8.55 (d, $J = 1.6$, 2H, $\text{H}^{\text{A}3}$), 7.85 (dd, $J = 8.3$, $J = 1.7$, 4H, $\text{H}^{\text{B}2}$), 7.44 (d, $J = 1.6$, 2H, $\text{H}^{\text{A}5}$), 7.40 (dd, $J = 8.2$, $J = 1.7$, 4H, $\text{H}^{\text{B}3}$), 2.74 (s, 6H, H^{MeA}), 2.47 (s, 6H, H^{MeC}), 2.33 (s, 6H, H^{MeC}). $^{13}\text{C}\{^1\text{H}\}$ NMR (126 MHz, CDCl_3) δ /ppm: 165.4 ($\text{C}^{\text{C}3/\text{C}5}$), 158.8 ($\text{C}^{\text{C}3/\text{C}5}$), 158.7 ($\text{C}^{\text{A}6}$), 156.7 ($\text{C}^{\text{A}2}$), 149.0 ($\text{C}^{\text{A}4}$), 138.1 ($\text{C}^{\text{B}1}$), 131.2 ($\text{C}^{\text{B}4}$), 129.8 ($\text{C}^{\text{B}3}$), 127.8 ($\text{C}^{\text{B}2}$), 121.2 ($\text{C}^{\text{A}5}$), 116.7 ($\text{C}^{\text{A}3}$), 116.3 ($\text{C}^{\text{C}4}$), 25.0 (C^{MeA}), 11.8 (C^{MeC}), 11.1 (C^{MeC}). ESI-MS: m/z 527.19 $[\text{M} + \text{H}]^+$ (calc. 527.24). HR ESI-MS: m/z 527.2440 $[\text{M} + \text{H}]^+$ (calc. 527.2440).

[Cu(6)₂][PF₆]

Compound **6** (15 mg, 0.053 mmol, 2 eq.) was dissolved in acetone (0.5 mL) and $[\text{Cu}(\text{MeCN})_4][\text{PF}_6]$ (9.9 mg, 0.027 mmol, 1.0 eq.) was added to the solution. The solution was stirred for 10 min and then Et_2O (3 mL) was added. The precipitate that formed was removed by centrifugation to yield $[\text{Cu}(6)_2][\text{PF}_6]$ as a dark-red solid (17 mg, 0.02 mmol, 83%). No further purification was required. ^1H NMR (500 MHz, acetone- d_6) δ /ppm: 8.87 (dd, $J = 5.1$, $J = 1.2$, 2H, $\text{H}^{\text{A}6}$), 8.21 (td, $J = 8.0$, $J = 1.6$, 2H, $\text{H}^{\text{A}3}$), 8.16 (dd, $J = 7.9$, $J = 1.6$, 2H, $\text{H}^{\text{A}4}$), 8.02 (s, 2H, $\text{H}^{\text{C}1}$), 7.77 (m, 2H, $\text{H}^{\text{A}5}$), 7.75–7.72 (overlapping m, 4H, $\text{H}^{\text{B}4/\text{C}5}$), 7.67 (m, 2H, $\text{H}^{\text{C}3}$), 7.64 (m, 2H, $\text{H}^{\text{B}3}$), 7.54 (m, 2H, $\text{H}^{\text{B}5}$), 7.64 (m, 2H, $\text{H}^{\text{C}6}$), 7.41 (d, $J = 8.4$, 2H, $\text{H}^{\text{C}4}$), 7.36 (ddd, $J = 8.1$, $J = 6.8$, $J = 1.2$, 2H, $\text{H}^{\text{C}7}$), 7.24 (d, $J = 8.1$, 2H, $\text{H}^{\text{C}8}$). $^{13}\text{C}\{^1\text{H}\}$ NMR (126 MHz, acetone- d_6) δ /ppm: 157.9 ($\text{C}^{\text{B}6}$), 153.2, ($\text{C}^{\text{A}2}$) 152.9 ($\text{C}^{\text{B}2}$), 149.6 ($\text{C}^{\text{A}6}$), 138.8 ($\text{C}^{\text{A}4/\text{B}4}$), 137.7 ($\text{C}^{\text{C}2}$), 134.1 ($\text{C}^{\text{C}4\text{a}}$), 133.1 ($\text{C}^{\text{C}8\text{a}}$), 128.8 ($\text{C}^{\text{C}8}$), 128.4 ($\text{C}^{\text{C}4/\text{C}5}$), 128.3 ($\text{C}^{\text{C}4/\text{C}5}$), 127.9 ($\text{C}^{\text{C}1/\text{C}6}$), 127.8 ($\text{C}^{\text{C}1/\text{C}6}$), 127.3 ($\text{C}^{\text{A}5/\text{C}7}$), 125.8 ($\text{C}^{\text{B}5}$), 125.3 ($\text{C}^{\text{C}3}$), 123.3 ($\text{C}^{\text{A}3}$), 120.7 ($\text{C}^{\text{B}3}$). UV-vis (CH_2Cl_2 , 2.02×10^{-5} mol dm^{-3}), λ/nm ($\epsilon/\text{dm}^3 \text{ mol}^{-1} \text{ cm}^{-1}$): 235 (103 500), 260 (64 700), 305 (36 600), 430 (5500), 554 (2300). ESI-MS: m/z 627.2 $[\text{M} - \text{PF}_6]^+$ (calc. 627.2). Found C 61.68, H 3.95, N 7.17; $\text{C}_{40}\text{H}_{28}\text{CuF}_6\text{N}_4\text{P}$ requires C 62.14, H 3.65, N 7.25.

[Cu(7)₂][PF₆]

Compound **7** (15 mg, 0.038 mmol, 2 eq.) was dissolved in acetone (0.5 mL) and $[\text{Cu}(\text{MeCN})_4][\text{PF}_6]$ (5.31 mg, 0.019 mmol, 1.0 eq.) were added to the solution. The solution was stirred for 10 min and then Et_2O (3 mL) was added. The precipitate that formed was separated by centrifuge to yield $[\text{Cu}(7)_2][\text{PF}_6]$ as a red solid (14 mg, 0.010 mmol, 78%). No further purification was required. ^1H NMR (500 MHz, acetone- d_6) δ /ppm: 9.15 (d, $J = 1.6$, 4H, $\text{H}^{\text{A}3}$), 8.20 (dd, $J = 8.1$, $J = 1.7$, 8H, $\text{H}^{\text{B}2}$), 8.11 (d, $J = 1.5$, 4H, $\text{H}^{\text{A}5}$), 7.66 (d, $J = 8.1$, $J = 1.7$, 8H, $\text{H}^{\text{B}3}$), 2.52 (s, 12H, H^{MeA}), 2.48 (s, 12H, H^{MeC}), 2.31 (s, 12H, H^{MeC}). $^{13}\text{C}\{^1\text{H}\}$ NMR (126 MHz, acetone- d_6) δ /ppm: 165.4 ($\text{C}^{\text{C}3/\text{C}5}$), 158.9 ($\text{C}^{\text{C}3/\text{C}5}$), 158.7 ($\text{C}^{\text{A}6}$), 153.6 ($\text{C}^{\text{A}2}$), 150.7 ($\text{C}^{\text{A}4}$), 137.0 ($\text{C}^{\text{B}1}$), 133.3 ($\text{C}^{\text{B}4}$), 130.8 ($\text{C}^{\text{B}3}$), 128.8 ($\text{C}^{\text{B}2}$), 124.5 ($\text{C}^{\text{A}5}$), 118.8 ($\text{C}^{\text{A}3}$), 116.5 ($\text{C}^{\text{C}4}$), 25.5 (C^{MeA}), 11.7 (C^{MeC}), 10.9 (C^{MeC}). UV-vis (CH_2Cl_2 , 3.33×10^{-5} mol dm^{-3}) λ/nm ($\epsilon/\text{dm}^3 \text{ mol}^{-1} \text{ cm}^{-1}$): 285 (81 600), 325 (52 200), 495 (12 800).

ESI-MS: m/z 1115.4 $[\text{M} - \text{PF}_6]^+$ (calc. 1115.4). HR ESI-MS: m/z 1115.4013 $[\text{M} - \text{PF}_6]^+$ (calc. 1115.4028). Satisfactory elemental analysis was not obtained.

Functionalization of commercial (non-activated nanoparticles): Procedure A

Ligand **1** (10 mg, 1 eq.) was dissolved in dry DMSO (10 mL). Commercial TiO_2 NPs (48.2 mg, 8.4 TiO_2 eq.) were added to the solution and dispersed with sonication for 10 min. The mixture was stirred at room temperature (*ca.* 295 K) for 48 h. Then the particles were separated by centrifugation (10 min, 9000 rpm) and washed with DMSO (3×5 mL) and EtOH (1×5 mL). The NPs were dried under high vacuum and the white powder was stored under N_2 in a sealed vial.

Activation of commercial nanoparticles

Commercial TiO_2 NPs (1 g) were dispersed in dilute aqueous HNO_3 (15 mL, 13.6%) then the mixture was sonicated for 15 min and stirred for 30 min. The NPs were separated by centrifugation and washed once with water (15 mL). Afterwards the NPs were dispersed through sonication (10 min) in water (20 mL) and stirred overnight. The NPs were separated with centrifugation, washed twice with water (2×20 mL) and then dried over high vacuum. The activated NPs (950 mg) were stored in a sealed vial under N_2 .

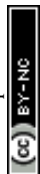
Functionalization of activated nanoparticles (Procedure B)

Ligand **1** (3.73 mg, 1 eq.) was placed in a microwave vial and milliQ water (13 mL) was added. The mixture was dispersed by sonication for 1 min. Activated TiO_2 NPs (60.0 mg, 28 TiO_2 eq.) were added to the solution and dispersed with sonication for 10 min. The microwave vial was sealed and the reaction mixture was heated to 130 °C for 3 h in the microwave reactor. The reaction mixture was allowed to cool to room temperature. The functionalized NPs were separated from the solvent by centrifugation (10 min, 9000 rpm). Then the functionalized NPs were dried under high vacuum yielding a slightly yellow powder.

Analogous procedures were used to functionalize activated NPs with ligands **2**, **3** or **4** starting with **2** (2.56 mg, 1 eq.), **3** (2.92 mg, 1 eq.), **4** (3.19 mg, 1 eq.) and activated TiO_2 NPs (60.0 mg, 28 TiO_2 eq.). For **4**, the functionalized NPs were washed with DMSO (3×10 mL) and EtOH (3×10 mL); see discussion in manuscript. The functionalized NPs were dried under high vacuum and the white powder was stored under N_2 in a sealed vial.

Functionalization of activated nanoparticles: competition between anchoring ligands (Procedure C)

Ligands **1** (3.73 mg, 1 eq.) and **2** (2.56 mg, 1 eq.) were placed in a microwave vial and milliQ water (13 mL) was added. The mixture was dispersed by sonication for 1 min. Activated TiO_2 NPs (60.0 mg, 28 TiO_2 eq.) were added to the solution and dispersed with sonication for 10 min. The microwave vial was sealed and the reaction mixture was heated to 130 °C for 3 h in a microwave reactor. The reaction mixture was allowed to cool



to room temperature. The water was then removed under high vacuum and then some of the residue was dispersed in DMSO- d_6 in an NMR tube.

An analogous procedure was used with combinations of ligands **1** (3.73 mg, 1 eq.) and **3** (2.92 mg, 1 eq.), or ligands **1** (3.73 mg, 1 eq.) and **4** (3.19 mg, 1 eq.) with activated TiO₂ NPs (60.0 mg, 28 TiO₂ eq.).

Functionalization of activated nanoparticles: competition between anchoring ligands (Procedure D)

Ligand **4** (3.19 mg, 1 eq.) was placed in a microwave vial and milliQ water (13 mL) was added. The mixture was dispersed by sonication for 1 min. Activated TiO₂ NPs (60.0 mg, 28 TiO₂ eq.) were added to the solution and dispersed with sonication for 10 min. The microwave vial was sealed and the reaction mixture was heated to 130 °C for 3 h in the microwave reactor. The reaction mixture was allowed to cool to room temperature. The water was then removed under high vacuum and then some of the residue was dispersed in DMSO- d_6 in an NMR tube and the ¹H NMR spectrum was recorded. The remaining residue was washed by dispersing it in DMSO (3 × 10 mL) and EtOH (3 × 10 mL). The washed residue was collected by centrifugation and was dried under high vacuum. Then some of the residue was dispersed in DMSO- d_6 . The NMR spectrum revealed that no excess free ligand was left on the functionalized NPs. Ligand **1** (2.49 mg, 1 eq.) was placed in a microwave vial and milliQ water (13 mL) was added. The mixture was dispersed by sonication for 1 min. The previously obtained NPs functionalized with **4** (40 mg) were added to the solution and dispersed with sonication for 10 minutes. The microwave vial was sealed and the reaction mixture was heated to 130 °C for 3 h in the microwave reactor. The reaction mixture was allowed to cool to room temperature. The water was then removed under high vacuum to yield a residue, a portion of which was dispersed in DMSO- d_6 in an NMR tube.

Complexation of nanoparticles functionalized with anchored ligands

Stock solutions of [Cu(MeCN)₄][PF₆]₂ (5.59 mg, 10 mL, 1.5 mM in acetone) and FeCl₂·4H₂O (2.88 mg, 10 mL, 1.5 mM in acetone) were prepared.

Activated NPs functionalized with ligands (10 mg) (Procedures B or C above) were dispersed by sonication (15 s) in water (1.35 mL) and the stock solution of [Cu(MeCN)₄][PF₆]₂ in the case of **1**, **2** or **4** (0.15 mL) or of FeCl₂·4H₂O in the case of **3** (0.15 mL) was added. The solutions in the sample vials were stirred for 72 h. The coloured NPs were separated by centrifugation (10 min, 13 200 rpm), then washed with acetone (3 × 1 mL) and dried under high vacuum.

SALSAC assembly of heteroleptic copper(i) complexes on activated nanoparticles

Stock solutions of [Cu(5)₂][PF₆]₂, [Cu(6)₂][PF₆]₂ and [Cu(7)₂][PF₆]₂ (1.5 mM in acetone) were prepared. NPs functionalized with **1** (10 mg, see Procedure B) were dispersed in water (1.35 mL) by sonication (15 s) and then a portion (0.15 mL) of the stock

solution of [Cu(5)₂][PF₆]₂ was added. The mixture was stirred for 72 h. The orange-red NPs were separated from the supernatant liquid by centrifugation (10 min, 13 200 rpm), then washed with acetone (3 × 1 mL) and dried under high vacuum. The procedure was repeated using [Cu(6)₂][PF₆]₂ or [Cu(7)₂][PF₆]₂.

SALSAC assembly of heteroleptic iron(II) complexes on activated nanoparticles

A stock solution of [Fe(8)₂][PF₆]₂ (1.5 mM in acetone) was prepared. NPs functionalized with **3** (10 mg, see Procedure B) were dispersed in water (1.35 mL) by sonication (15 s) and then a portion (0.15 mL) of the stock solution of [Fe(8)₂][PF₆]₂ was added. The mixture was stirred for 72 h. The purple NPs were separated from the supernatant liquid by centrifugation (10 min, 13 200 rpm), then washed with acetone (3 × 1 mL) and dried under high vacuum.

Results and discussion

Choice of anchoring ligands

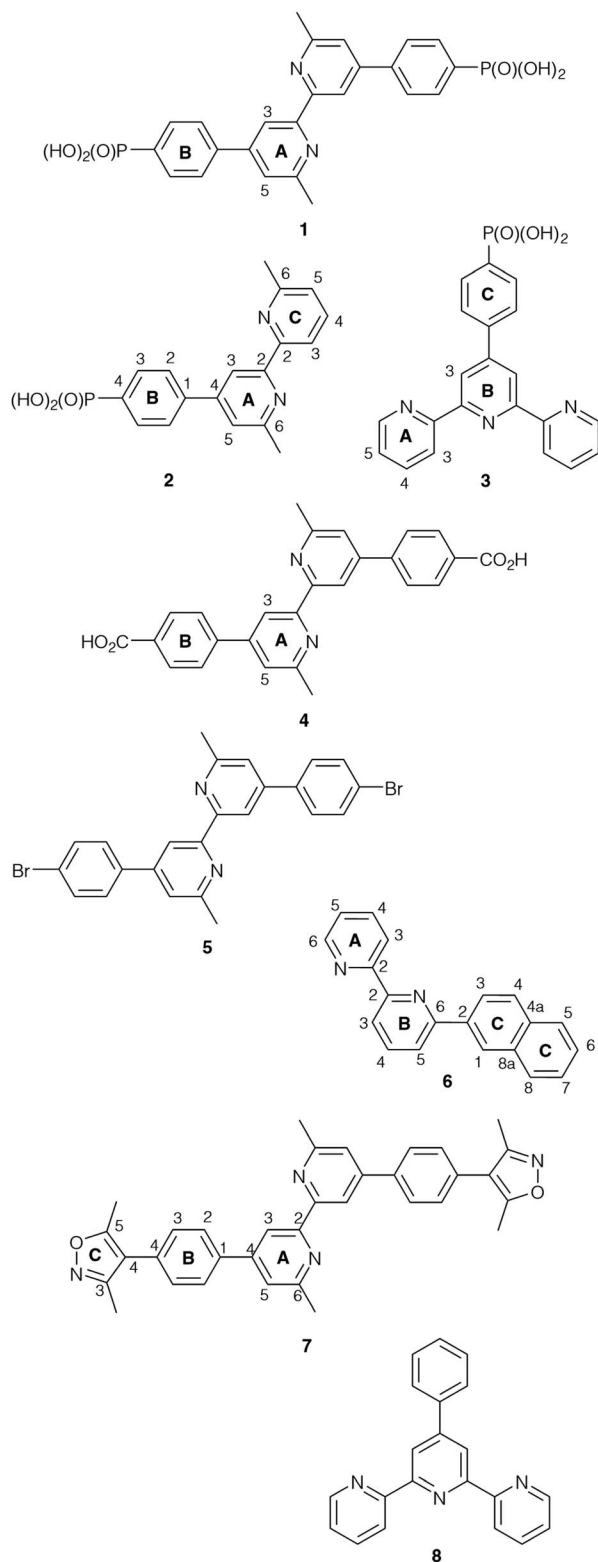
Based on our previous experience of functionalizing TiO₂ surfaces,^{19,20,24} anchoring ligands **1** and **4** (Scheme 1) were selected for the present investigation to provide a comparison of carboxylic *versus* phosphonic acid anchors. The DSC community consider that phosphonic acid anchors give more stable attachment to TiO₂ surfaces than carboxylic acids.⁴⁹ Both **1** and **4** contain a bpy metal-binding domain for coordination to copper(i).¹⁹ The presence of the 6,6'-dimethyl substituents stabilizes a bis(diimine)copper(i) complex against oxidation by inhibiting a geometrical change from tetrahedral (favoured by Cu⁺) to square planar (favoured by Cu²⁺).^{50,51} Ligand **2** was designed to allow a comparison of mono- *versus* bis(phosphonic acid) anchors (**2** *versus* **1**) bearing the same bpy metal-binding domains. Both **2** and **3** carry one phosphonic acid group, but differ in the metal-binding unit; bpy and 2,2':6',2''-terpyridine (tpy) can be addressed by copper(i) and iron(II), respectively. Each of ligands **1**–**4** contains a phenylene spacer between the anchoring group and the metal-binding units.

Compound **2** was prepared as described in the Experimental section. The base peak in the electrospray mass spectrum at *m/z* 339.06 (Fig. S1†) was assigned to [M – H][–]. The ¹H and ¹³C NMR spectra of **2** (Fig. S2 and S3†) were assigned by COSY, NOESY, HMQC and HMBC methods (Fig. S4–S6†) and were consistent with the structure shown in Scheme 1.

Nanoparticle activation and general procedure for functionalization

Our initial attempts to replicate TiO₂ surface-functionalization using commercial NPs (AEROXIDE TiO₂ P25) suspended in DMSO in place of screen-printed and annealed (commercial or in-house fabricated) surfaces following previously published protocols^{20,52} met with variable success. A significant observation came from DOSY experiments on a DMSO- d_6 solution of **1** and a DMSO- d_6 suspension of dried commercial NPs after treatment with **1** (Procedure A in the Experimental section). Fig. 2 shows a comparison of the ¹H NMR spectra of the two





Scheme 1 Structures of compounds 1–8. Atom numbering schemes are given where required for NMR spectroscopic assignments.

samples. Apart from small changes (<0.1 ppm) in the chemical shifts of signals, the spectra are essentially identical and the signals remain sharp. This strongly suggests that free ligand **1** is

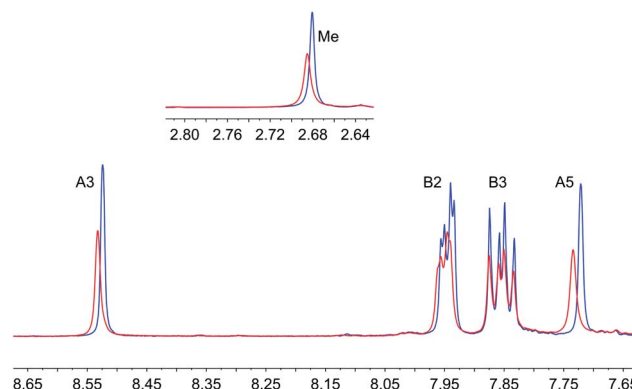


Fig. 2 ^1H NMR spectrum (500 MHz, $\text{DMSO}-d_6$, aromatic region with methyl region inset) of **1** (blue) and of the NPs after treatment with **1** following Procedure A in Experimental section (red). Chemical shifts in δ/ppm .

present in the solution containing dispersed NPs. To unambiguously confirm this proposal, PFGSE spectra of **1** before and after exposure to commercial NPs were recorded. The proton signal at δ 8.525 ppm was selected to determine the diffusion coefficient by a two-parameter fit to the DOSY intensities. For **1** in $\text{DMSO}-d_6$, a diffusion coefficient of $1.355 \times 10^{-10} \text{ m}^2 \text{ s}^{-1}$ was determined (Fig. S7a †), and for the solution containing the dispersed NPs the diffusion coefficient was $1.326 \times 10^{-10} \text{ m}^2 \text{ s}^{-1}$ (Fig. S7b †), identical to the previous value within experimental error. These data are consistent with either some or all of **1** remaining non-anchored during attempts to functionalize the NPs using Procedure A detailed in the Experimental section. This illustrates a general problem with non-activated NPs, that simple washing does not suffice to remove surface-adsorbed or aggregated ligand from NPs with anchored ligand.

We therefore decided to *activate* the commercial TiO_2 NPs prior to *functionalization* with the ligand. Literature activation procedures⁵³ include treatment with HNO_3 (ref. 54) and ultrasound sonication for to optimize particle dispersion.⁵⁵ Initial tests revealed that replacing DMSO by water was advantageous for NP functionalization, and that reducing the amount of anchoring ligand with respect to the quantity of NPs was also beneficial. We therefore modified the procedure by an initial treatment of the commercial NPs with aqueous HNO_3 (see Experimental section). Following this, the activated NPs were added to an aqueous suspension of **1**, **2**, **3** or **4** and dispersed with sonication before the suspension was heated at 130°C for 3 h under microwave conditions before being separated from the solvent by centrifugation (see Procedure B in the Experimental section). Fig. 3 compares part of the FT-IR spectra of the activated NPs, free ligand **1** and activated NPs functionalized with **1**; the full spectra are given in Fig. S8. † The spectrum of the functionalized NPs exhibits bands at 1629, 1601, 1570 and 1545 cm^{-1} . While the bands appear to be characteristic of free ligand **1**, closer inspection of Fig. 3 shows differences with the spectroscopic signature of pristine **1** which has absorptions at 1645, 1624, 1598 and 1545 cm^{-1} . Significantly, this pattern of absorptions is retained in a mixture of commercial NPs (non-



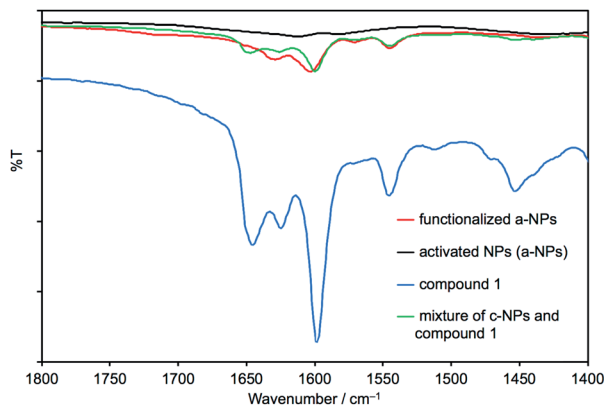


Fig. 3 Solid-state IR spectra of activated NPs (a-NPs), pristine **1**, a-NPs functionalized with **1** following Procedure B in the Experimental section, and a mixture of commercial NPs (c-NPs) and **1**. The full IR spectra are presented in Fig. S8.†

activated) and **1** (1647, 1624, 1600 and 1543 cm^{-1} , Fig. 3). Thus, the IR spectroscopic data provide evidence that ligand **1** is anchored to the TiO_2 . A comparison of the IR spectra of ligand **3** and NPs functionalized with **3** is shown in Fig. S9.† Thermogravimetric analysis (TGA) of the activated NPs and those functionalized with **1** was carried out, and the results are displayed in Fig. 4. Both samples show a weight loss of about 2% in two steps (isotherm maxima $<120^\circ\text{C}$ and $<330^\circ\text{C}$) attributed to the loss of physisorbed and chemisorbed water, respectively. The non-functionalized NPs undergo no further change in mass, even after being heated at 900°C for 30 minutes. In contrast, the NPs functionalized with **1** exhibit a further 2% weight loss above *ca.* 430°C ascribed to decomposition of the ligand. The profile of the TGA curve above 430°C (red curve in Fig. 4) is similar to that of the thermal decomposition of **1** (Fig. S10†). Three measurements were made for the functionalized NPs to confirm reproducibility of the data.

Further evidence for NP functionalization came from a comparison of the ^1H NMR spectra of the pristine ligands **1**, **2** or **3** in $\text{DMSO}-d_6$ with those of suspended NPs functionalized with **1**, **2** or **3** (Fig. 5, S11 and S12†). The functionalized NPs were prepared according to Procedure B in the Experimental section.

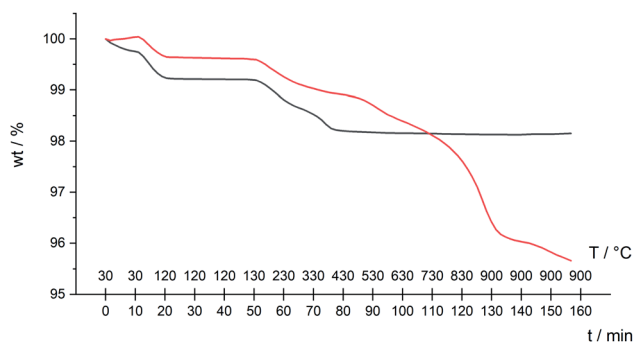


Fig. 4 TGA curves for activated NPs only (black line), and activated NPs functionalized with **1** following Procedure B in the Experimental section (red line).

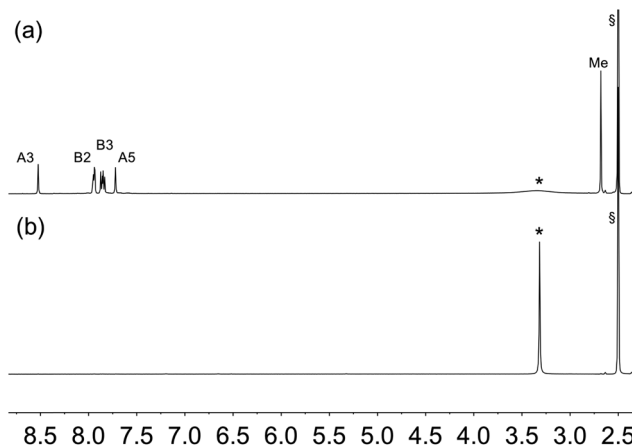


Fig. 5 ^1H NMR (500 MHz, $\text{DMSO}-d_6$, 298 K) of (a) ligand **1** and (b) suspended residue after activated TiO_2 NPs had been after activated TiO_2 NPs were functionalized with **1** following Procedure B in Experimental section, separated by centrifugation and dried. See Scheme 1 for atom labelling. Chemical shifts in δ/ppm . ξ = residual $\text{DMSO}-d_5$. * = water.

After centrifugation and drying, the functionalized NPs were not washed. The ligand anchored to the NP is NMR silent, and Fig. 5b confirms that all of ligand **1** (shown to be present in the IR study of the same material) is anchored to the TiO_2 surface. In the case of ligand **4**, the bulk residue showed a signal due to free **4** and the material had to be thoroughly washed with DMSO and EtOH to completely remove traces of free ligand (Fig. S13†). This indicates that the carboxylic acid anchoring ligand **4** adsorbed less efficiently to the surface of the TiO_2 NPs than the phosphonic acids **1**, **2** and **3**. We return to this later.

To confirm that the functionalized NPs bear anchored ligands capable of coordination to metal ions, NPs functionalized as described above with **1**, **2**, **3** or **4** were dispersed in water by sonication and an acetone solution of $[\text{Cu}(\text{MeCN})_4][\text{PF}_6]$ (for **1**, **2** and **4**) or $\text{FeCl}_2 \cdot 4\text{H}_2\text{O}$ (for **3**) was added. Colour changes were observed after about five minutes and the intensity of colour increased over a period of an hour (Fig. 6 and S14†). The orange and purple colours are, respectively, characteristic of

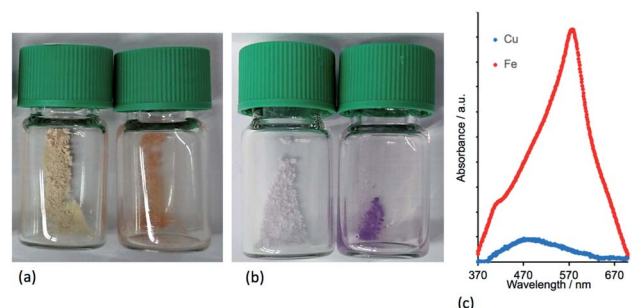


Fig. 6 Photographs of (a) activated TiO_2 NPs functionalized with **1** (left) and after treatment with $[\text{Cu}(\text{MeCN})_4][\text{PF}_6]$ (right), and (b) activated TiO_2 NPs functionalized with **3** (left) and after treatment with $\text{FeCl}_2 \cdot 4\text{H}_2\text{O}$ (right). (c) Solid-state absorption spectra of the NPs functionalized with **1** or **3** and treated with $[\text{Cu}(\text{MeCN})_4][\text{PF}_6]$ (blue curve) and $\text{FeCl}_2 \cdot 4\text{H}_2\text{O}$ (red).



$[\text{Cu}(\text{diimine})_2]^+$ and $[\text{Fe}(\text{tpy})_2]^{2+}$ chromophores, and imply that addition of the metal ion results in coordination by two adjacent ligands on a single NP or two ligands on adjacent NPs. Solid-state absorption spectra of the samples (Fig. 6c) exhibit metal-to-ligand charge transfer (MLCT) bands at 489 and 579 nm which, along with the band profiles, are typical of $[\text{Cu}(\text{diimine})_2]^+$ and $[\text{Fe}(\text{tpy})_2]^{2+}$ chromophores, respectively. Scanning electron microscopy (SEM) was used to image the TiO_2 NPs before (Fig. 7a) and after functionalization with **1** and $[\text{Cu}(\text{MeCN})_4][\text{PF}_6]$ (Fig. 7b). The 'halo' around each NP in Fig. 7b is interpreted as the sheath of organic ligand **1**. The dimensional relationship between the TiO_2 NP and the 'halo' supports this proposal.

The ligand-functionalized NPs can be stored as dry solids under N_2 for periods of months without loss of activity.

Competition between different pairs of anchors on NPs

In applying the SALSAC approach to DSCs, we have demonstrated that devices incorporating dyes with phosphonic acid anchors outperform those with analogous dyes with carboxylic anchors.^{56,57} Similarly, Grätzel and coworkers have observed strong surface adhesion of ruthenium(II) dyes bearing phosphonic acid anchoring groups.⁵⁸ Despite this latter finding being reported as early as 1995, the DSC community continues to favour the use of carboxylic acid anchoring units.

We decided to investigate the competitive binding to TiO_2 NPs of pairs of ligands **1** and **3**, **1** and **4**, and **1** and **2** to gain insight into preferential binding of phosphonic and carboxylic acid anchors, and competition between spatially different ligands bearing phosphonic acids. Equimolar amounts of each pair of ligands (**1** and **3**, **1** and **4**, or **1** and **2**) were added to water and then TiO_2 NPs, activated as described above were added and dispersed with sonication (see Procedure C in the Experimental section). Each mixture was heated to 130 °C for 3 hours in a microwave reactor. After cooling and removal of water *in*

vacuo, part of the residue was dispersed in $\text{DMSO}-d_6$ in an NMR tube and ^1H NMR spectra of the suspended residues were then recorded. Once again, ligands anchored to the NP surface will not be observed. Fig. 8 displays the ^1H NMR spectra of pristine ligands **1**, **3** (Fig. 8a and b) and the suspended residue after activated NPs had been treated with a 1 : 1 molar mixture of **1** and **3** (Fig. 8c). Signals in Fig. 8c are attributed to ligands that are not bound to the surface. Fig. 8c shows both free ligands **1** and **3** in solution, and the small changes in chemical shifts on going from Fig. 8a or 8b to 8c are consistent with those described in the previous section. The molar ratio of ligands **1** : **3** in the solution investigated in Fig. 8c is 2 : 1 based on the relative integrals of the signals for protons H^{A3} and H^{A5} in each ligand (see Scheme 1 and Fig. 8c). This indicates that the TiO_2 NPs preferentially bind **3**. Three portions of the washed and dried functionalized NPs (shown to contain no free ligand, Fig. 8d) were dispersed in water by sonication and an acetone solution of $[\text{Cu}(\text{MeCN})_4][\text{PF}_6]$ was added to one portion, an acetone solution of both $[\text{Cu}(\text{MeCN})_4][\text{PF}_6]$ and $\text{FeCl}_2 \cdot 4\text{H}_2\text{O}$ to the second, and an acetone solution of $\text{FeCl}_2 \cdot 4\text{H}_2\text{O}$ to the third. Fig. 9a shows the visual difference between the samples, but definitive evidence that both **1** and **3** are bound to the surface comes from a comparison of the IR spectra (Fig. 9b) of NPs functionalized with **1**, with **3** or after activated TiO_2 NPs were functionalized with a 1 : 1 mixture of **1** and **3** following Procedure C in the Experimental section. The IR spectrum of the latter exhibits diagnostic absorptions of both ligands.

Next, we investigated the functionalization of TiO_2 NPs with a 1 : 1 molar mixture of **1** and **2**. Both ligands contain a 6,6'- Me_2bpy unit, but ligand **1** contains two phosphonic acid groups while **2** contains one (Scheme 2). In the ^1H NMR spectrum of the suspension of functionalized NPs in $\text{DMSO}-d_6$ (Fig. S15c†) the ratio of integrals of signals for protons H^{A3} (or of H^{A5}) of each ligand in solution is *ca.* 1 : 1. This is consistent with there being approximately twice as much **2** as **1** remaining in solution after activated TiO_2 NPs have been treated with a 1 : 1 mixture of **1** and **2**. Thus, **1** is preferentially bound to the surface.

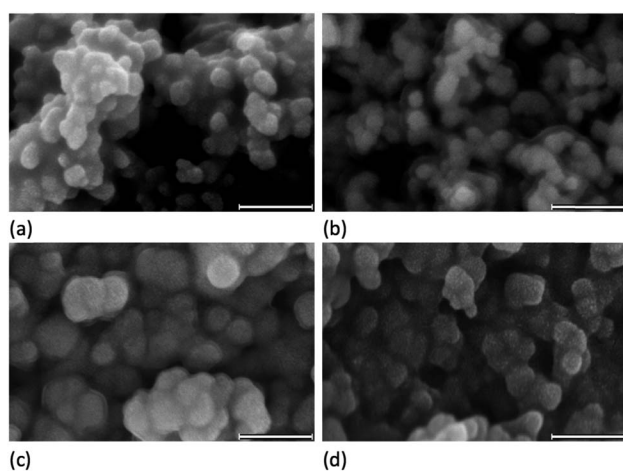


Fig. 7 SEM images of (a) activated TiO_2 NPs, and (b) activated TiO_2 NPs functionalized with **1** and treated with $[\text{Cu}(\text{MeCN})_4][\text{PF}_6]$. Activated TiO_2 NPs functionalized with **1** and after treatment with (c) $[\text{Cu}(\text{5})_2][\text{PF}_6]$ or (d) $[\text{Cu}(\text{7})_2][\text{PF}_6]$. Each scale bar = 100 nm.

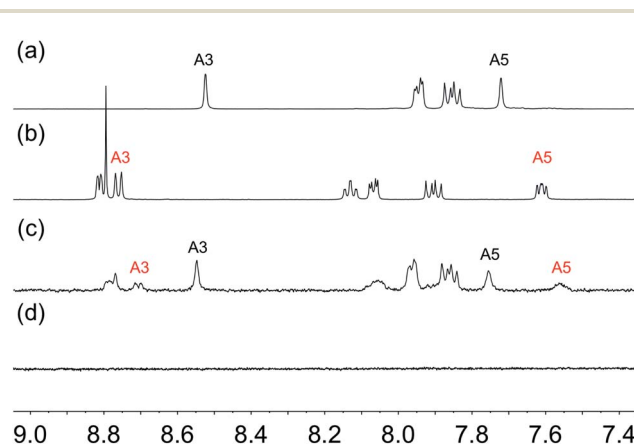


Fig. 8 Aromatic regions of the ^1H NMR (500 MHz, $\text{DMSO}-d_6$, 298 K) of (a) ligand **1**, (b) ligand **3**, (c) suspended residue after activated TiO_2 NPs were functionalized with **1** and **3** following Procedure C in the Experimental section, (d) residue after washing. See Scheme 1 for atom labelling. Chemical shifts in δ/ppm .



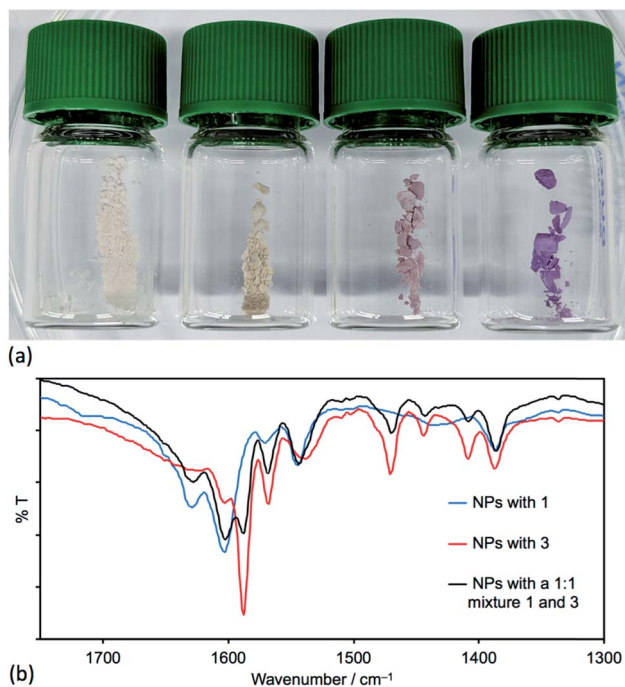
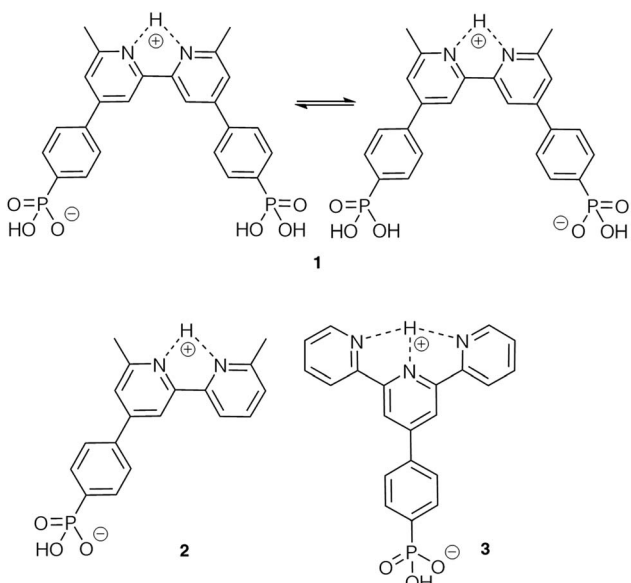


Fig. 9 (a) Photographs of (left to right) activated TiO_2 NPs after functionalized with a 1 : 1 mixture of **1** and **3**, after one portion has been further treated with $[\text{Cu}(\text{MeCN})_4][\text{PF}_6]$, after another portion has been further treated with $[\text{Cu}(\text{MeCN})_4][\text{PF}_6]$ and $\text{FeCl}_2 \cdot 4\text{H}_2\text{O}$, and after a final portion has been further treated with $\text{FeCl}_2 \cdot 4\text{H}_2\text{O}$. (b) Solid-state FT-IR spectra of NPs functionalized with ligand **1** only, with **3** only, and activated TiO_2 NPs functionalized with **1** and **3** following Procedure C in the Experimental section.

In order to rationalize the results of the competition experiments, it is pertinent to note that we have previously demonstrated that in $\text{DMSO}-d_6$, ligand **1** exists as a zwitterion.³¹ This is consistent with known values of $\text{p}K_a = 4.4$ for $[\text{Hbpy}]^+$,⁵⁹ and of



Scheme 2 Zwitterionic structures of ligands **1**–**3**.

$\text{p}K_a(\mathbf{1}) = 1.86$ for $\text{PhPO}(\text{OH})_2$.⁶⁰ On the other hand, the 6,6'-dimethyl substituents in **1** will render the Me_2bpy unit a weaker base than bpy , as is observed for 1,10-phenanthroline ($\text{p}K_a$ for $[\text{Hphen}]^+ = 4.86$ (ref. 61)) and 2,9-dimethyl-1,10-phenanthroline ($\text{p}K_a$ for $[\text{HMe}_2\text{phen}]^+$ is reported as 5.85 (ref. 62) and 6.17 (ref. 61)). The zwitterionic form of **1** should exhibit a *cis*-configuration arising from hydrogen bonding⁶³ (Scheme 2). Similarly, we expect **2** to exist as a zwitterion in water and DMSO (Scheme 2). Values of $\text{p}K_a = 4.54$ and 3.57 for $[\text{Htpy}]^+$ and $[\text{H}_2\text{tpy}]^{2+}$ (measured in 0.2 M aqueous KCl at 298 K)⁶⁴ indicate that **3** is also likely to show zwitterionic behaviour (Scheme 2), as has also been reported for 2,2':6',2''-terpyridin-4'-ylphosphonic acid.⁶⁵ We expect the availability of phosphonate groups in the zwitterionic forms of the ligands to favour surface binding³¹ and the observed binding orders of $\mathbf{3} > \mathbf{1} > \mathbf{2}$ can be rationalized in terms of the relative $\text{p}K_a$ values and the number of anchoring groups in the ligands.

When activated TiO_2 NPs were treated under microwave conditions with a 1 : 1 mixture of ligands **1** and **4**, we observed that only carboxylic acid **4** remained in solution (Fig. 10). The strong adsorption of the phosphonic acid **1** to NPs dispersed in solution is consistent with what we and Grätzel have observed for annealed TiO_2 surfaces.^{56–58} The preferential binding of **1** with respect to **4** was also demonstrated by ligand displacement. Activated TiO_2 NPs were dispersed in an aqueous suspension of **4** and then heated under microwave conditions at 130°C for 3 hours. After cooling, the water was removed, and part of the residue was suspended in $\text{DMSO}-d_6$. Sharp signals in the ^1H NMR spectrum were consistent with the presence of non-anchored ligand (Fig. 10a). The remaining residue was thoroughly washed until, NMR analysis of a part of the residue dispersed in $\text{DMSO}-d_6$ revealed no signal for free ligand **4** (Fig. 11b). We demonstrated that some **4** ligand remained and was surface-bound by treating the residue with $[\text{Cu}(\text{MeCN})_4][\text{PF}_6]$. The observation of an orange colour (see the photograph in Fig. 11) is characteristic of the formation of a $[\text{Cu}(\text{diimine})_2]^+$ chromophore (see earlier). The functionalized NPs were then treated with **1** in aqueous solution under microwave conditions (see Procedure C in the Experimental

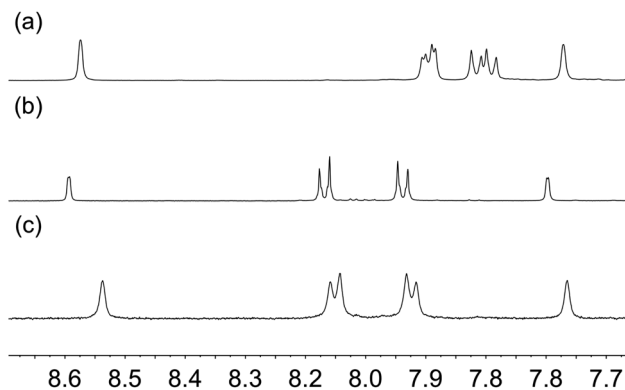


Fig. 10 ^1H NMR (500 MHz, $\text{DMSO}-d_6$, 298 K) of (a) ligand **1**, (b) ligand **4**, (c) suspended residue after activated TiO_2 NPs had been treated with a 1 : 1 mixture of **1** and **4** following Procedure C in the Experimental section.



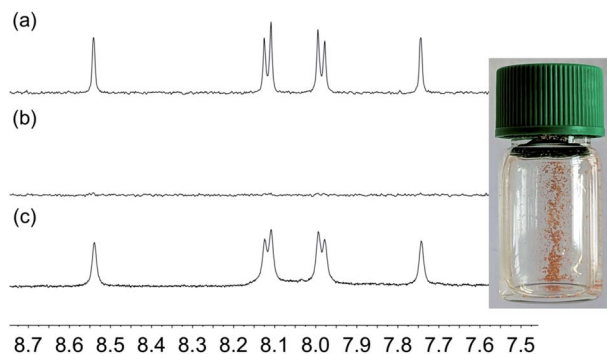
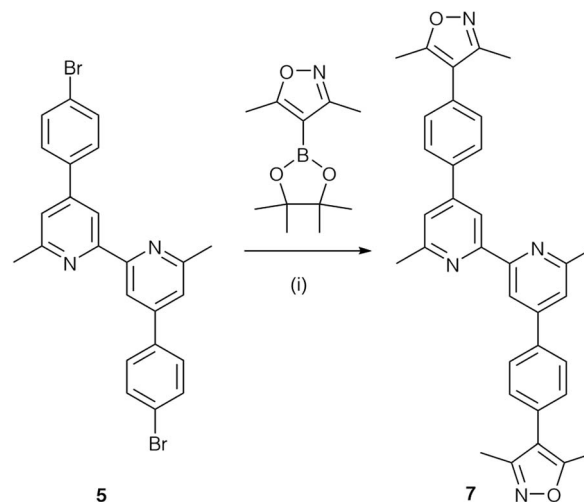


Fig. 11 ^1H NMR (500 MHz, $\text{DMSO}-d_6$, 298 K) of (a) suspended residue after activated TiO_2 NPs had been treated with **4**, (b) suspended residue after thorough washing (see text), and (c) suspended residue after NPs functionalized with **4** had been treated with **1** following Procedure D in the Experimental section. Chemical shifts in δ/ppm . The photograph shows the residue from (b) after treatment with $[\text{Cu}(\text{MeCN})_4][\text{PF}_6]$ (see text).

section). After removal of water, the residue was analysed by ^1H NMR spectroscopy (Fig. 11c). The spectrum exhibited sharp signals with the signature of ligand **4**. No free ligand **1** (compare with Fig. 10a) was observed, confirming the displacement of surface-bound **4** by **1**.

Application of SALSAC: preparation and characterization of homoleptic copper(i) complexes

To test the application of the SALSAC approach to the functionalization of NPs, we first prepared the homoleptic compounds $[\text{Cu}(\text{L}_{\text{ancillary}})_2][\text{PF}_6]$ and $[\text{Fe}(\mathbf{8})_2][\text{PF}_6]_2$. The iron(II) complex was prepared as previously described.⁴⁷ The general method for the copper(i) complexes was the reaction of $[\text{Cu}(\text{MeCN})_4][\text{PF}_6]$ with two equivalents of $\text{L}_{\text{ancillary}}$ followed by precipitation of $[\text{Cu}(\text{L}_{\text{ancillary}})_2][\text{PF}_6]$. $[\text{Cu}(\mathbf{5})_2][\text{PF}_6]$ has previously been described.⁴⁴ Reaction of ligand **6** (ref. 45) with $[\text{Cu}(\text{MeCN})_4][\text{PF}_6]$ yielded $[\text{Cu}(\mathbf{6})_2][\text{PF}_6]$. Ligand **7** was prepared as shown in Scheme 3 and was characterized by ^1H and ^{13}C NMR spectroscopy (Fig. S16–S19[†]) with assignment of the signals by 2D methods (see Experimental section), electrospray MS (Fig. S20[†]) and IR spectroscopy (Fig. S21[†]). $[\text{Cu}(\mathbf{7})_2][\text{PF}_6]$ was isolated as a red solid. The ESI mass spectra of $[\text{Cu}(\mathbf{6})_2][\text{PF}_6]$ and $[\text{Cu}(\mathbf{7})_2][\text{PF}_6]$ showed peaks at m/z 627.2 $[\text{M} - \text{PF}_6]^+$ and 1115.4, respectively, arising from the $[\text{M} - \text{PF}_6]^+$ ion. The ^1H and ^{13}C $\{^1\text{H}\}$ NMR spectra of $[\text{Cu}(\mathbf{6})_2][\text{PF}_6]$ and $[\text{Cu}(\mathbf{7})_2][\text{PF}_6]$ were assigned by COSY, NOESY, HMQC and HMBC methods and selected spectra are shown in Fig. S22–S28.[†] The solid-state IR spectra of the compounds (Fig. S29[†]) exhibit a characteristic strong absorption at 833 cm^{-1} from the $[\text{PF}_6]^-$ ion. The solution absorption spectra of the two compounds (Fig. 12) exhibit intense absorption bands below *ca.* 340 nm arising from spin-allowed ligand-centred $\pi^* \leftarrow \pi$ transitions. The broad absorption band centred at 495 nm in $[\text{Cu}(\mathbf{7})_2][\text{PF}_6]$ is assigned to an MLCT transition and is typical of homoleptic bis(diimine)copper(i) complexes in which the 6,6'-substituents are methyl groups.^{19,66} In contrast, $[\text{Cu}(\mathbf{6})_2][\text{PF}_6]$ exhibits two bands at 430 and 554 nm which are reminiscent of those



Scheme 3 Synthetic route to compound **7**. Conditions: (i) Cs_2CO_3 , catalytic amount of $[\text{Pd}(\text{PPh}_3)_4]$, toluene, $110\text{ }^\circ\text{C}$, 4 h in a microwave reactor; isolated in 33% yield.

at 423 and 573 nm in $[\text{CuL}_2][\text{PF}_6]$ where $\text{L} = 4,4'$ -bis(4-bromophenyl)-6,6'-diphenyl-2,2'-bipyridine.⁴⁴ The profile of the spectrum and the red-shift in absorption maximum are consistent with the effects of introducing phenyl substituents adjacent to the nitrogen donors in $[\text{Cu}(\text{dpp})_2]^+$ ($\text{dpp} = 2,9$ -diphenyl-1,10-phenanthroline),^{67,68} and have been attributed to the flattened, low-symmetry structure of the complex.⁶⁸

Application of SALSAC: NPs functionalized with heteroleptic copper(i) and iron(II) complexes

Route 2 in Fig. 1 summarized the SALSAC approach for TiO_2 surface modification using ligand exchange between a surface-anchored ligand and one ligand from a homoleptic bis(diimine) copper(i) complex to produce a surface functionalized with a heteroleptic copper(i) complex (eqn (1)).

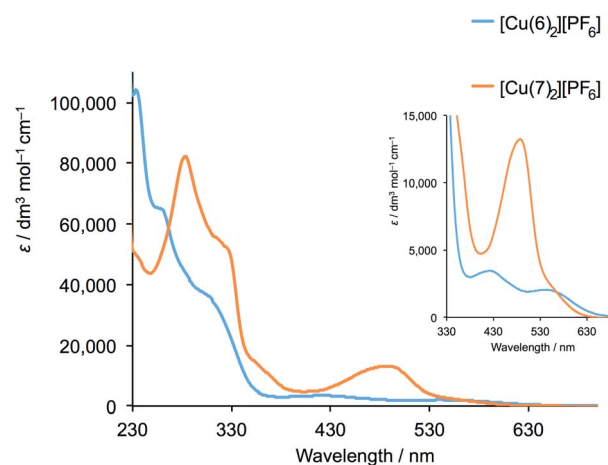


Fig. 12 Solution absorption spectra of $[\text{Cu}(\mathbf{6})_2][\text{PF}_6]$ ($2.02 \times 10^{-5}\text{ mol dm}^{-3}$) and $[\text{Cu}(\mathbf{7})_2][\text{PF}_6]$ ($3.33 \times 10^{-5}\text{ mol dm}^{-3}$) in CH_2Cl_2 . The inset shows an expansion of the MLCT region.



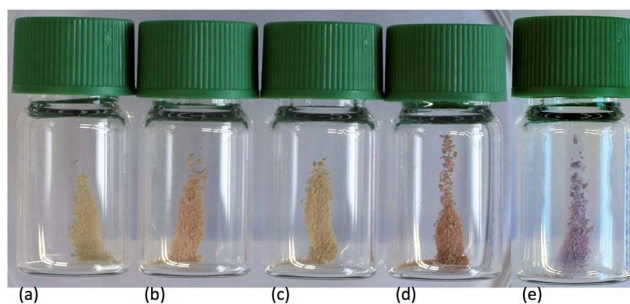
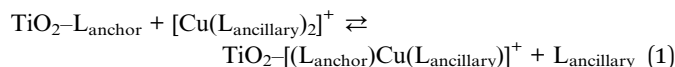


Fig. 13 Photographs of activated TiO₂ NPs functionalized (a) with **1**, and after treatment with (b) [Cu(5)₂][PF₆], (c) [Cu(7)₂][PF₆], (d) [Cu(6)₂][PF₆] and (e) [Fe(8)₂][PF₆]₂.



To date, we have applied this strategy to annealed nanoparticulate TiO₂ surfaces, and we now demonstrate an extension to TiO₂ NPs dispersed in solution. NPs functionalized with **1** were dispersed in water, and an acetone solution of [Cu(5)₂][PF₆], [Cu(6)₂][PF₆] or [Cu(7)₂][PF₆] was added (see Experimental section). During a 72 hour period of stirring, the NPs became orange-red. A similar procedure was followed for ligand exchange between [Fe(8)₂][PF₆]₂ and NPs functionalized with **3** which resulted in purple-coloured NPs. The NPs were separated by centrifugation, and were washed and dried. The observed colours of the NPs (Fig. 13) are diagnostic of [Cu(diimine)₂]⁺ and [Fe(tpy)₂]²⁺ chromophores, and their solid-state absorption spectra are shown in Fig. 14 and S30.† Absorption maxima are observed at 491, 498 and 488 nm for the copper(i) complexes with L_{ancillary} = 5, 6 and 7, respectively, and at 577 nm for the surface bound iron(ii) complex. That the latter arise from ligand exchange and not from residual homoleptic complexes is best demonstrated by comparing the solid-state spectrum of NPs functionalized with **1** after treatment with [Cu(6)₂][PF₆] with that of the homoleptic [Cu(6)₂][PF₆]. As discussed earlier, significant red-shifting is observed in the solution absorption spectrum of [Cu(6)₂][PF₆] due to flattening of the copper(i)

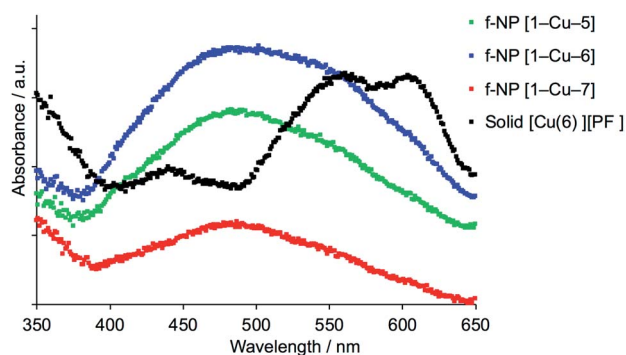


Fig. 14 Solid-state absorption spectra of NPs functionalized with **1** after treatment with [Cu(5)₂][PF₆], [Cu(6)₂][PF₆] or [Cu(7)₂][PF₆], and, for comparison, the solid-state absorption spectrum of homoleptic [Cu(6)₂][PF₆].

coordination sphere, and this is also observed in the solid-state with an MLCT band centred at *ca.* 580 nm (Fig. 14).

SEM images of the TiO₂ NPs functionalized with **1** after treatment with [Cu(5)₂][PF₆] and [Cu(7)₂][PF₆] are displayed in Fig. 7c and d. Comparison with the images in Fig. 7a and b reveals an increase in particle size after reaction with the homoleptic copper complexes, consistent with the functionalization step in eqn (1).

Conclusions

We have demonstrated that the SALSAC approach to the hierarchical assembly of heteroleptic bis(dimine)copper(i) complexes that we have previously established for annealed nanoparticulate TiO₂ surfaces²⁰ can be extended to NPs dispersed in solution. We have presented a general procedure for the activation of commercial TiO₂ NPs by initial treatment with aqueous HNO₃. After dispersion in water, the activated NPs were functionalized with anchoring ligands **1–4** by heating under microwave conditions, and the functionalized NPs were investigated using FT-IR, TGA, and ¹H NMR spectroscopy. Ligands **1–3** contain phosphonic acid anchoring groups while **4** has two carboxylic acid anchors; ligands **1, 2** and **4** contain 6,6'-Me₂bpy and **3** contains tpy metal binding domains. NPs functionalized with **1, 2** and **4** react with [Cu(MeCN)₄][PF₆] and those with **3** react with FeCl₂·4H₂O; metal binding has been investigated using solid-state absorption spectroscopy and SEM.

By reacting the activated NPs with mixtures of ligands, competitive binding of ligands to TiO₂ has been investigated. For the phosphonic acids, the binding orders are 3 > 1 > 2 which can be rationalized in terms of relative pK_a values (phosphonic acid and [HMe₂bpy]⁺ or [Htpy]⁺) and the number of anchoring groups in the ligands. Competition experiments between **1** and **4** confirmed preferential binding of phosphonic over carboxylic acid anchors.

The final step in the SALSAC strategy is ligand exchange between ligand-functionalized NPs and homoleptic metal complexes to yield TiO₂ NPs functionalized with heteroleptic complexes. We have demonstrated that this is successful for NPs functionalized with **1** reacted with three different [Cu(L_{ancillary})₂][PF₆] complexes and for NPs functionalized with **3** reacted with [Fe(8)₂][PF₆]₂. This approach provides a versatile hierarchical approach to the formation of metal complex-functionalized NPs, and we are currently employing the SALSAC strategy in catalysis and sensing applications.

Conflicts of interest

There are no conflicts to declare.

Acknowledgements

We are grateful to the Swiss National Science Foundation (grant number 200020_182000) and the University of Basel for financial support. DOSY spectroscopy was performed by PD Dr D. Häussinger. TEM and SEM images were measured with the assistance of Susanne Erpel and Evi Bieler, respectively, at the



Nano Imaging Lab, University of Basel and we also thank Dr Markus Dürrenberger. Ligands **3** and **6** were prepared by Alexandra Wiesler and Fabian Brunner (University of Basel), respectively. We also thank Mariia Karpacheva (University of Basel) for supplying $[\text{Fe}(\mathbf{8})_2][\text{PF}_6]_2$.

References

- Z. Ren, Y. Guo, C.-H. Liu and P.-X. Gao, *Front. Chem.*, 2013, **1**, 1.
- Modern Inorganic Synthetic Chemistry*, ed. R. Xu and Y. Xu, Elsevier, Amsterdam, 2nd edn, 2017.
- Hierarchical Nanostructures for Energy Devices*, ed. S. H. Ko and C. P. Grigoropoulos, RSC Nanoscience & Nanotechnology, No. 35, RSC, Cambridge, 2015.
- S. Whitelam, *Adv. Mater.*, 2015, **27**, 5720.
- S. Casalini, C. A. Bortolotti, F. Leonardi and F. Biscarini, *Chem. Soc. Rev.*, 2017, **46**, 40.
- A. Ulman, *Chem. Rev.*, 1996, **96**, 1533.
- J. J. Gooding, F. Mearns, W. Yang and J. Liu, *Electroanalysis*, 2003, **15**, 81.
- A. Iyer and K. Paul, *IET Nanobiotechnol.*, 2015, **9**, 122.
- E. Mattia and S. Otto, *Nat. Nanotechnol.*, 2015, **10**, 111.
- F. Tao, *Pure Appl. Chem.*, 2008, **80**, 45.
- S. De Feyter and F. C. De Schryver, *J. Phys. Chem. B*, 2005, **109**, 4290.
- A. Kumar, K. Banerjee and P. Liljeroth, *Nanotechnology*, 2017, **28**, 082001.
- D. N. Reinhoudt, *Perspectives in Supramolecular Chemistry*, Wiley, Chichester, 2008, vol. 20.
- S. Stepanow, N. Lin, J. V. Barth and K. Kern, *J. Phys. Chem. B*, 2006, **110**, 23472.
- A. E. Danks, S. R. Hill and Z. Schnepf, *Mater. Horiz.*, 2016, **3**, 91.
- G. M. Whitesides, E. Ostuni, S. Takayama, X. Jiang and D. E. Ingber, *Annu. Rev. Biomed. Eng.*, 2001, **3**, 335.
- R. E. P. Winpenny, *J. Chem. Soc., Dalton Trans.*, 2002, 1.
- E. Schönhofer, B. Bozic-Weber, C. J. Martin, E. C. Constable, C. E. Housecroft and J. A. Zampese, *Dyes Pigm.*, 2015, **115**, 154.
- C. E. Housecroft and E. C. Constable, *Chem. Soc. Rev.*, 2015, **44**, 8386.
- F. J. Malzner, C. E. Housecroft and E. C. Constable, *Inorganics*, 2018, **6**, 57.
- From system complexity to emerging properties*, ed. M. Aziz-Alaoui and C. Bertelle, Springer, Berlin/Heidelberg, 2009.
- F. J. Malzner, A. Prescimone, E. C. Constable, C. E. Housecroft and M. Willgert, *J. Mater. Chem. A*, 2017, **5**, 4671.
- S. Y. Brauchli, F. J. Malzner, E. C. Constable and C. E. Housecroft, *RSC Adv.*, 2014, **4**, 62728.
- C. E. Housecroft, C. G. Palivan, K. Gademann, W. Meier, M. Calame, V. Mikhalevich, X. Zhang, E. Piel, M. Szponarski, A. Wiesler, A. Lanzilotto, E. C. Constable, A. Fanget and R. L. Stoop, *Chimia*, 2016, **70**, 402.
- For an overview, see: A. Winter, S. Hoepfner, G. R. Newkome and U. S. Schubert, *Adv. Mater.*, 2011, **23**, 3484.
- See for example: W. R. McNamara, R. C. Snoberger, G. Li, J. M. Schleicher, C. W. Cady, M. Poyatos, C. A. Schmuttenmaer, R. H. Crabtree, G. W. Brudvig and V. S. Batista, *J. Am. Chem. Soc.*, 2008, **130**, 14329.
- S. P. Hill, T. Banerjee, T. Dilbeck and K. Hanson, *J. Phys. Chem. Lett.*, 2015, **6**, 4510.
- See for example: S. Takahashi, S. Hotta, A. Watanabe, N. Idota, K. Matsukawa and Y. Sugahara, *ACS Appl. Mater. Interfaces*, 2017, **9**, 1907; J. Sun, E. J. Petersen, S. S. Watson, C. M. Sims, A. Kassman, S. Frukhtbeyn, D. Skrtic, M. T. Ok, D. S. Jacobs, V. Reipa, Q. Ye and B. C. Nelson, *Acta Biomater.*, 2017, **53**, 585; R. Bhandary, J. G. Alauzun, P. Hesemann, A. Stocco, M. In and P. H. Mutin, *Soft Matter*, 2017, **13**, 8023; J. Kirschner, J. Will, T. J. Rejek, L. Portilla, M. Berlinghof, P. Schweizer, E. Spiecker, H.-G. Steinrück, T. Unruh and M. Halik, *Adv. Mater. Interfaces*, 2017, **4**, 1700230; L. Zeininger, L. M. S. Stiegler, L. Portilla, M. Halik and A. Hirsch, *ChemistryOpen*, 2018, **7**, 282 and references therein.
- See for example: M. Nilsing, S. Lunell, P. Persson and L. Ojamäe, *Surf. Sci.*, 2005, **582**, 49; C. Queffelec, M. Petit, P. Janvier, D. A. Knight and B. Bujoli, *Chem. Rev.*, 2012, **112**, 3777.
- V. Spampinato, N. Tuccitto, S. Quici, V. Calabrese, G. Marletta, A. Torrisi and A. Licciardello, *Langmuir*, 2010, **26**, 8400.
- A. J. Stephens, F. J. Malzner, E. C. Constable and C. E. Housecroft, *Sustainable Energy Fuels*, 2018, **2**, 786.
- R. Calzada, C. M. Thompson, D. E. Westmoreland, K. Edme and E. A. Weiss, *Chem. Mater.*, 2016, **28**, 6716.
- J. De Roo, K. De Keukeleere, Z. Hens and I. Van Driessche, *Dalton Trans.*, 2016, **45**, 13277.
- J. De Roo, Z. Zhou, J. Wang, L. Deblock, A. J. Crosby, J. S. Owen and S. S. Nonnenmann, *Chem. Mater.*, 2018, **30**, 8034.
- L. Du, W. Wang, C. Zhang, Z. Jin, G. Palui and H. Mattoussi, *Chem. Mater.*, 2018, **30**, 7269.
- C. Goldmann, F. Ribot, L. F. Peiretti, P. Quaino, F. Tielens, C. Sanchez, C. Chanéac and D. Portehault, *Small*, 2017, **13**, 1604028.
- V. Grigel, L. K. Sagar, K. De Nolf, Q. Zhao, A. Vantomme, J. De Roo, I. Infante and Z. Hens, *Chem. Mater.*, 2018, **30**, 7637.
- M. L. Kessler, H. E. Starr, R. R. Knauf, K. J. Rountree and J. L. Dempsey, *Phys. Chem. Chem. Phys.*, 2018, **20**, 23649.
- R. R. Knauf, J. C. Lennox and J. L. Dempsey, *Chem. Mater.*, 2016, **28**, 4762.
- M. La Rosa, T. Avellini, C. Lincheneau, S. Silvi, I. A. Wright, E. C. Constable and A. Credi, *Eur. J. Inorg. Chem.*, 2017, **2017**, 5143.
- A. Ritchhart and B. M. Cossairt, *Inorg. Chem.*, 2019, **58**, 2840.
- G. J. Kubas, *Inorg. Synth.*, 1979, **19**, 90.
- A. Hernández Redondo, Ph.D. thesis, University of Basel, 2009, http://edoc.unibas.ch/diss/DissB_8757.
- B. Bozic-Weber, S. Y. Brauchli, E. C. Constable, S. O. Furer, C. E. Housecroft, F. J. Malzner, I. A. Wright and J. A. Zampese, *Dalton Trans.*, 2013, **42**, 12293.



- 45 F. Brunner, S. Graber, Y. Baumgartner, D. Häussinger, A. Prescimone, E. C. Constable and C. E. Housecroft, *Dalton Trans.*, 2017, **46**, 6379.
- 46 J. Wang and G. S. Hanan, *Synlett*, 2005, 1251.
- 47 E. C. Constable, J. Lewis, M. C. Liptrot and P. R. Raithby, *Inorg. Chim. Acta*, 1990, **178**, 47.
- 48 <https://www.aerosil.com/sites/lists/RE/DocumentsSI/TI-1243-Titanium-Dioxide-as-Photocatalyst-EN.pdf>, accessed 31 July 2019.
- 49 L. Zhang and J. M. Cole, *ACS Appl. Mater. Interfaces*, 2015, **7**, 3427.
- 50 M. K. Eggleston, D. R. McMillin, K. S. Koenig and A. J. Pallenberg, *Inorg. Chem.*, 1997, **36**, 172.
- 51 N. A. Gothard, M. W. Mara, J. Huang, J. M. Szarko, B. Rolczynski, J. V. Lockard and L. X. Chen, *J. Phys. Chem. A*, 2012, **116**, 1984.
- 52 Y. M. Klein, M. Willgert, A. Prescimone, E. C. Constable and C. E. Housecroft, *Dalton Trans.*, 2016, **45**, 4659.
- 53 S. P. Pujari, L. Scheres, A. T. M. Marcelis and H. Zuilhof, *Angew. Chem., Int. Ed.*, 2014, **53**, 6322.
- 54 B. Kim, S. W. Park, J.-Y. Kim, K. Yoo, J. A. Lee, M.-W. Lee, D.-K. Lee, J. Y. Kim, B. S. Kim, H. Kim, S. Han, H. J. Son and M. J. Ko, *ACS Appl. Mater. Interfaces*, 2013, **5**, 5201.
- 55 See for example: A. Estrada-Monje, R. Zitzumbo-Guzmán, J. A. Bañuelos-Díaz and E. A. Zaragoza-Contreras, *Mater. Chem. Phys.*, 2019, **235**, 121760.
- 56 B. Bozic-Weber, E. C. Constable, C. E. Housecroft, P. Kopecky, M. Neuburger and J. A. Zampese, *Dalton Trans.*, 2011, **40**, 12584.
- 57 B. Bozic-Weber, V. Chaurin, E. C. Constable, C. E. Housecroft, M. Meuwly, M. Neuburger, J. A. Rudd, E. Schönhofer and L. Siegfried, *Dalton Trans.*, 2012, **41**, 14157.
- 58 P. Péchy, F. P. Rotzinger, M. K. Nazeeruddin, O. Kohle, S. M. Zakeeruddin, R. Humphry-Baker and M. Grätzel, *J. Chem. Soc., Chem. Commun.*, 1995, 65.
- 59 A. Moissette, Y. Batonneau and C. Brémard, *J. Am. Chem. Soc.*, 2001, **123**, 12325.
- 60 *Metal Phosphonate Chemistry: From Synthesis to Applications*, ed. A. Clearfield and K. Demadis, RSC Publishing, 2011, ch. 5, p. 166.
- 61 G. Clauti, G. Zassinovich and G. Mestroni, *Inorg. Chim. Acta*, 1986, **112**, 103.
- 62 G. D. Stevens and R. A. Holwerda, *Inorg. Chem.*, 1984, **23**, 2777.
- 63 See for example: A. D. Burrows, R. W. Harrington and M. F. Mahon, *Acta Crystallogr., Sect. C: Cryst. Struct. Commun.*, 1999, **55**, 1921; W. S. Wu, *Acta Crystallogr., Sect. E: Struct. Rep. Online*, 2011, **67**, o2070; E. C. Constable, C. E. Housecroft, M. Neuburger, P. Rösel, G. E. Schneider, J. A. Zampese, F. Monti, N. Armaroli, R. D. Costa and E. Orti, *Inorg. Chem.*, 2013, **52**, 885.
- 64 E. Farkas, É. A. Enyedy, G. Micera and E. Garribba, *Polyhedron*, 2000, **19**, 1727.
- 65 M. K. Nazeeruddin, S. M. Zakeeruddin, R. Humphry-Baker, T. A. Kaden and M. Grätzel, *Inorg. Chem.*, 2000, **39**, 4542.
- 66 See for example: F. J. Malzner, S. Y. Brauchli, E. C. Constable, C. E. Housecroft and M. Neuburger, *RSC Adv.*, 2014, **4**, 48712; A. Büttner, S. Y. Brauchli, E. C. Constable and C. E. Housecroft, *Inorganics*, 2018, **6**, 40.
- 67 A. K. Ichinaga, J. P. Kirchoff, D. R. McMillin, C. O. Dietrich-Buchecker, P. A. Marnot and J. P. Sauvage, *Inorg. Chem.*, 1987, **26**, 4290.
- 68 M. T. Miller, P. K. Gantzel and T. B. Karpishin, *Inorg. Chem.*, 1998, **37**, 2285.



Supporting Information

The SALSAC Approach: Comparing the reactivity of solvent-dispersed nanoparticles with nanoparticulate surfaces

Sven A. Freimann,^a Davood Zare,^a Catherine E. Housecroft^a and Edwin C. Constable*^a

^a Department of Chemistry, University of Basel, BPR 1096, Mattenstrasse 24a, CH-4058 Basel, Switzerland.
email: edwin.constable@unibas.ch

Experimental Details of Instruments

¹H NMR, ¹³C{¹H} NMR and ³¹P{¹H} NMR spectra were measured at 298 K on a Bruker Avance III-500 NMR spectrometer. ¹H, ¹³C and ³¹P chemical shifts were referenced to residual solvent peaks with respect to $\delta(\text{TMS}) = 0$ ppm for ¹H and ¹³C{¹H} and $\delta(\text{H}_3\text{PO}_4 \text{ 85\% aqueous}) = 0$ ppm for ³¹P{¹H}. A Gaussian fit to the diffusion peak intensity was done to determine the diffusion constant of the signal. The PFGSE experiments were performed using a bipolar gradient pulse sequence.¹ The sigmoidal intensity decrease was fitted with a two-parameter fit (I_0 and diffusion coefficient D) with the DOSY routine implemented in topspin 4.0 [Bruker Biospin GmbH, 2016].

Reactions under microwave conditions were carried out in a Biotage Initiator 8 reactor. An Eppendorf Centrifuge 5415 R was used for 2 mL samples while a Hettich Centrifuge Universal 320 was used for 10 mL samples.

Solution absorption spectra were recorded on an Agilent Cary 5000 spectrophotometer and for solid-state absorption spectra, a Diffuse Reflectance Accessories was added to the spectrophotometer. For each solid-state absorption spectrum, a baseline correction was done with the respective nanoparticle precursor. Infrared spectra were recorded on a Perkin Elmer UATR Two spectrometer. Electrospray ionization (ESI) mass spectra and high resolution ESI MS were measured on a Shimadzu LCMS-2020 or a Bruker maXis 4G instrument, respectively.

Scanning electron microscopy (SEM) was performed using an Hitachi S-4800 instrument with an acceleration voltage of 5 kV and a working distance of 4 mm. Particle sizes were measured with a nanoimaging tool from the Nano Imaging Lab, University of Basel.

Thermogravimetric analysis (TGA) was performed on a TGA/SDTA851 (Mettler Toledo) instrument under nitrogen. Initially, the temperature was held at 30 °C for 10 min before heating at a rate of 10 °C/min to 120 °C. This temperature was maintained for 30 min to remove all traces of water. Afterwards the sample was heated to 900 °C at a rate of 10 °C/min. After maintaining the temperature at 900 °C for 30 min, the sample was cooled to ambient temperature.

1. D.H. Wu, A.D. Chen and C.S.J. Johnson, *Magn. Reson. A*, 1995, **115**, 260-264.

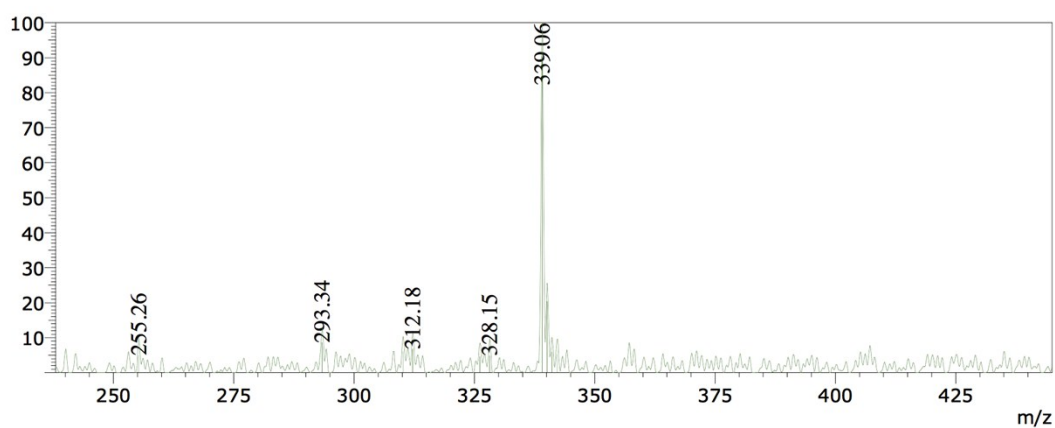


Fig. S1. Electrospray mass spectrum of **2** (with aqueous NH_3 , negative mode).

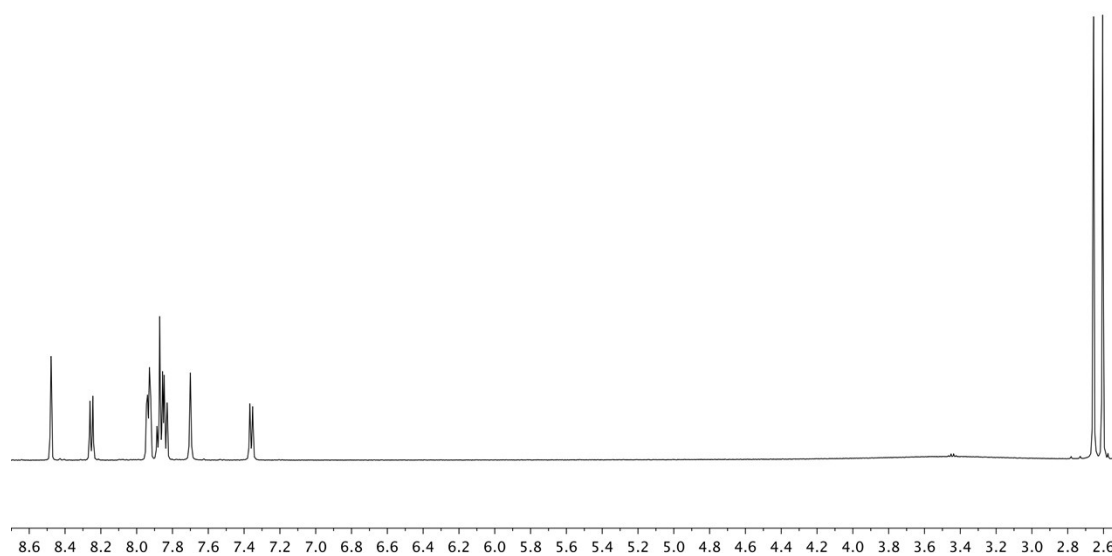


Fig. S2. ^1H NMR (500 MHz, DMSO-d_6 , 298 K) spectrum of compound **2**. δ / ppm.

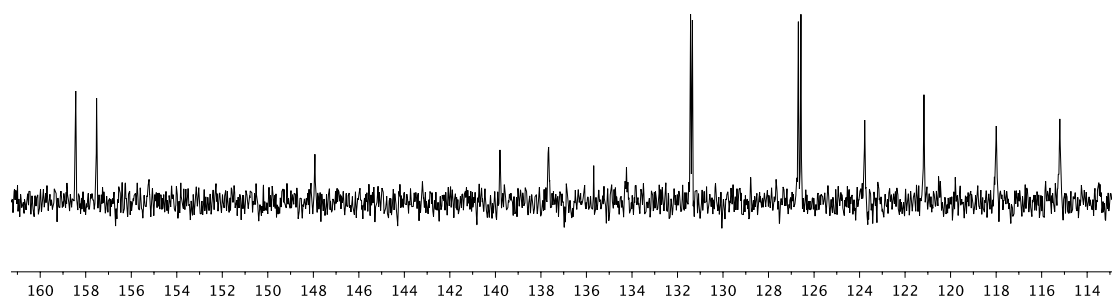


Fig. S3. $^{13}\text{C}\{^1\text{H}\}$ NMR (126 MHz, DMSO-d_6 , 298 K) spectrum (aromatic region) of compound **2**. δ / ppm.

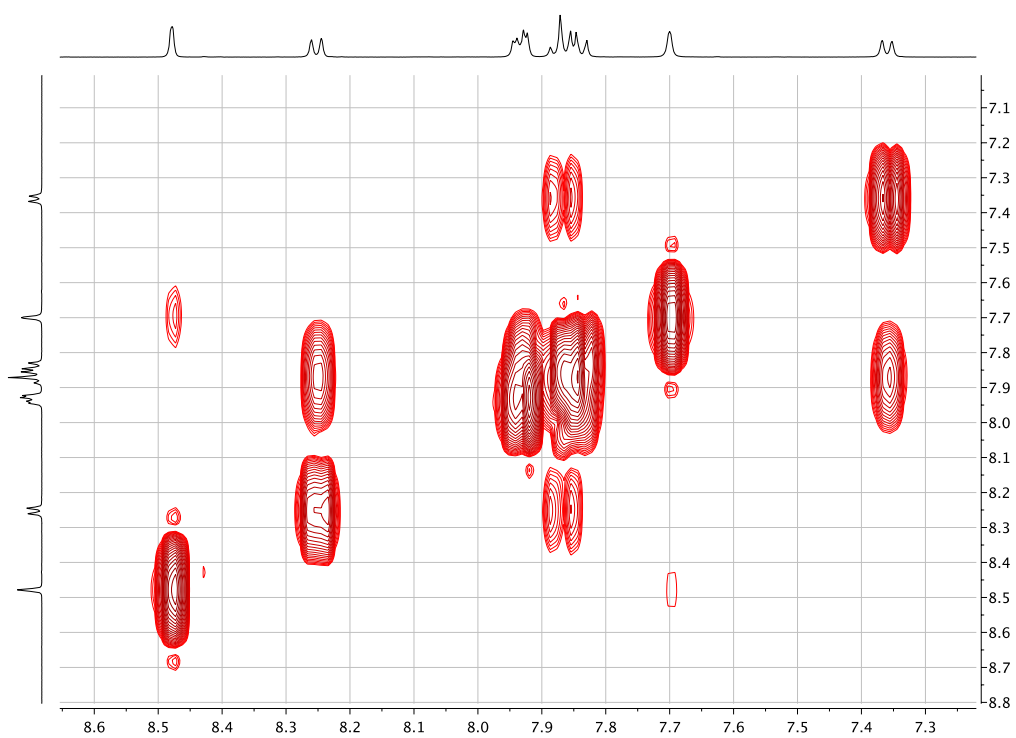


Fig. S4. COSY (500 MHz, DMSO-d₆, 298 K) spectrum of compound **2**. δ / ppm.

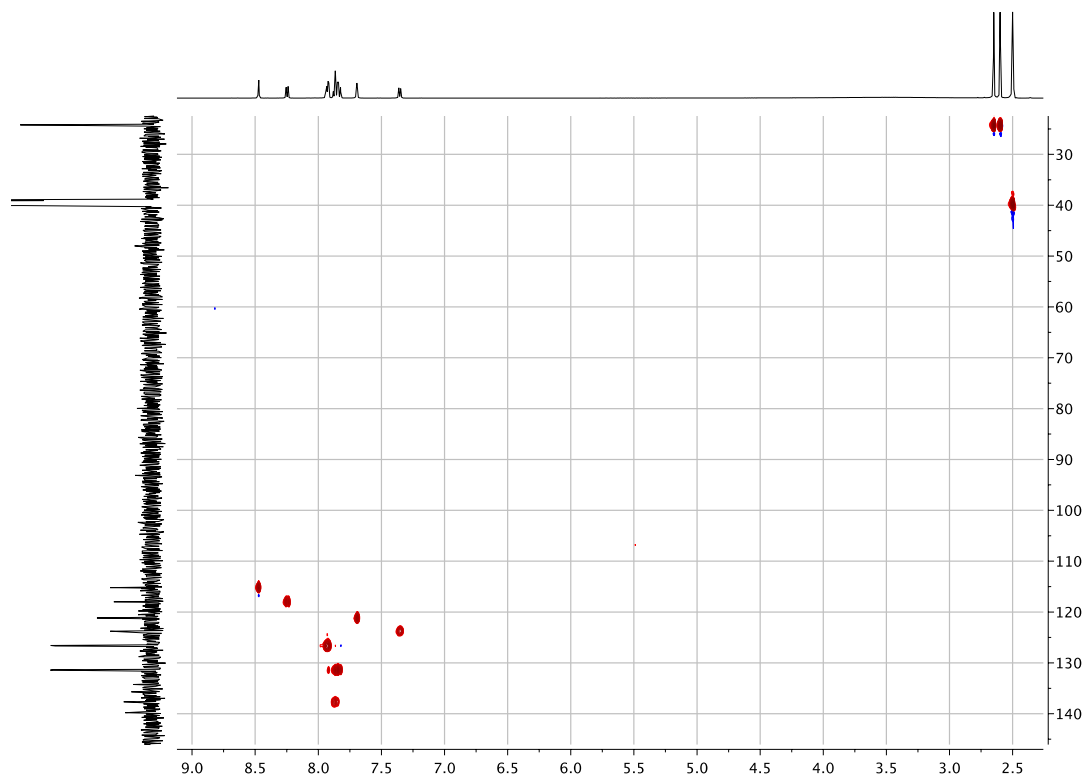
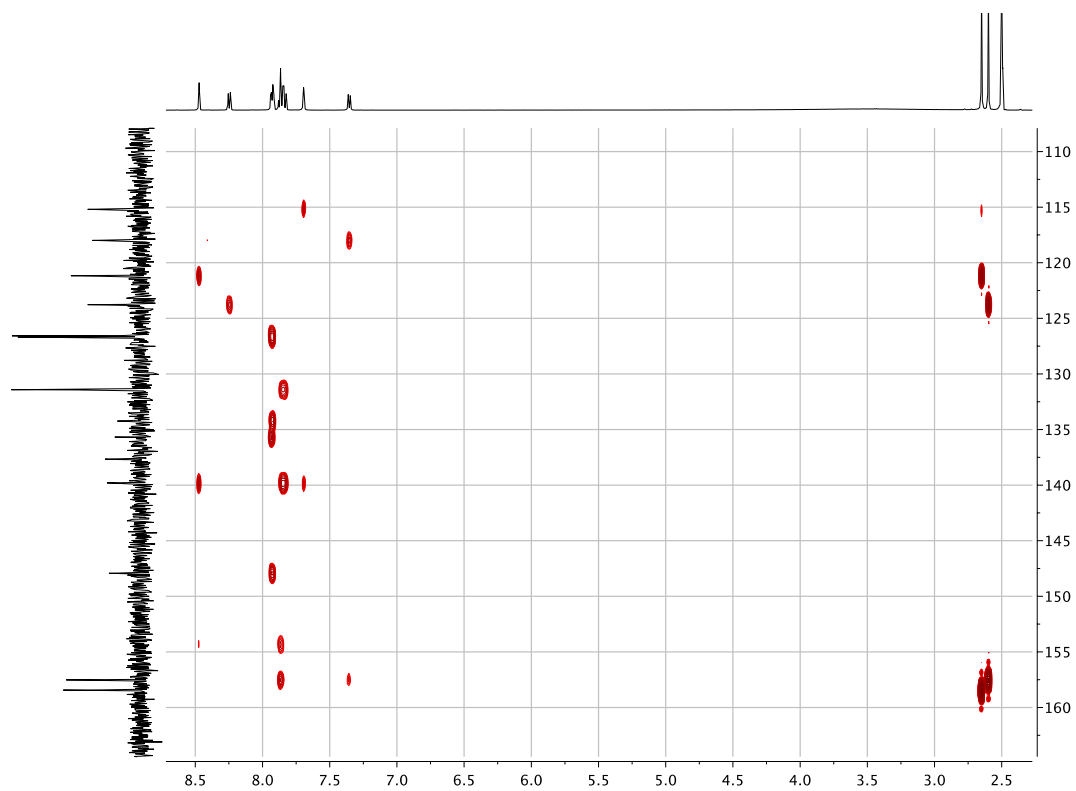
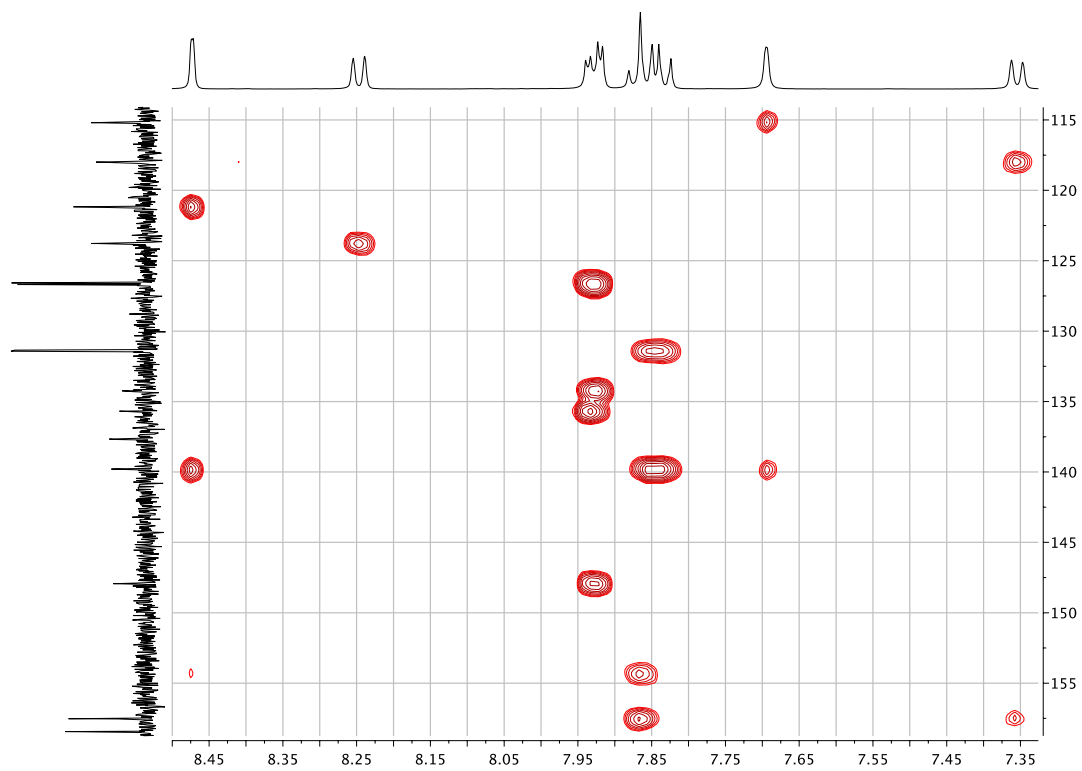


Fig. S5. HMQC (500 MHz ¹H, 126 MHz ¹³C, DMSO-d₆, 298 K) spectrum of compound **2**. δ / ppm.

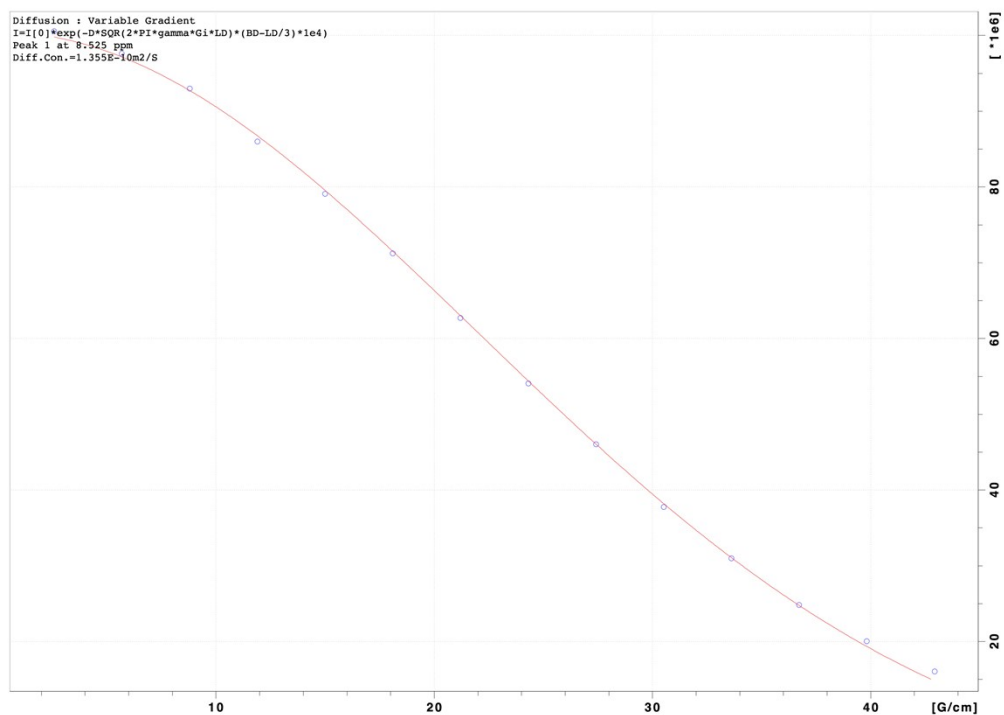


(a)

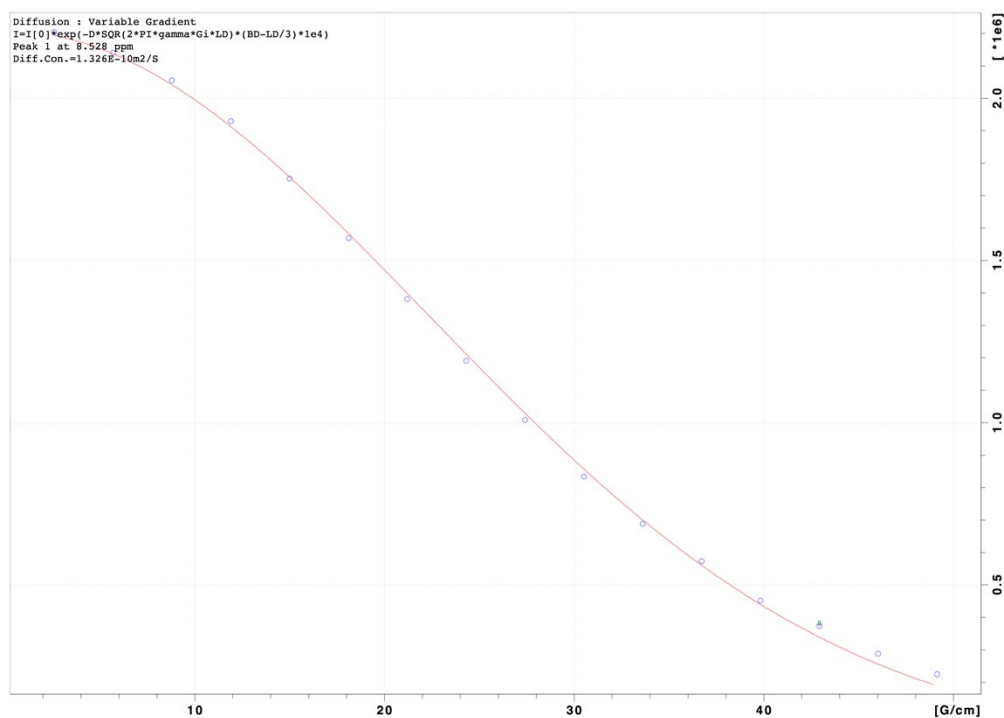


(b)

Fig. S6. (a) HMBC (500 MHz ^1H , 126 MHz ^{13}C , DMSO- d_6 , 298 K) spectrum of compound **2**, and (b) an expansion of the aromatic region. δ / ppm.



(a)



(b)

Fig. S7. Fits to the DOSY intensities for (a) ligand **1** in DMSO- d_6 , and (b) a DMSO- d_6 solution containing dispersed NPs which had been treated with **1** following Procedure A in the Experimental Section.

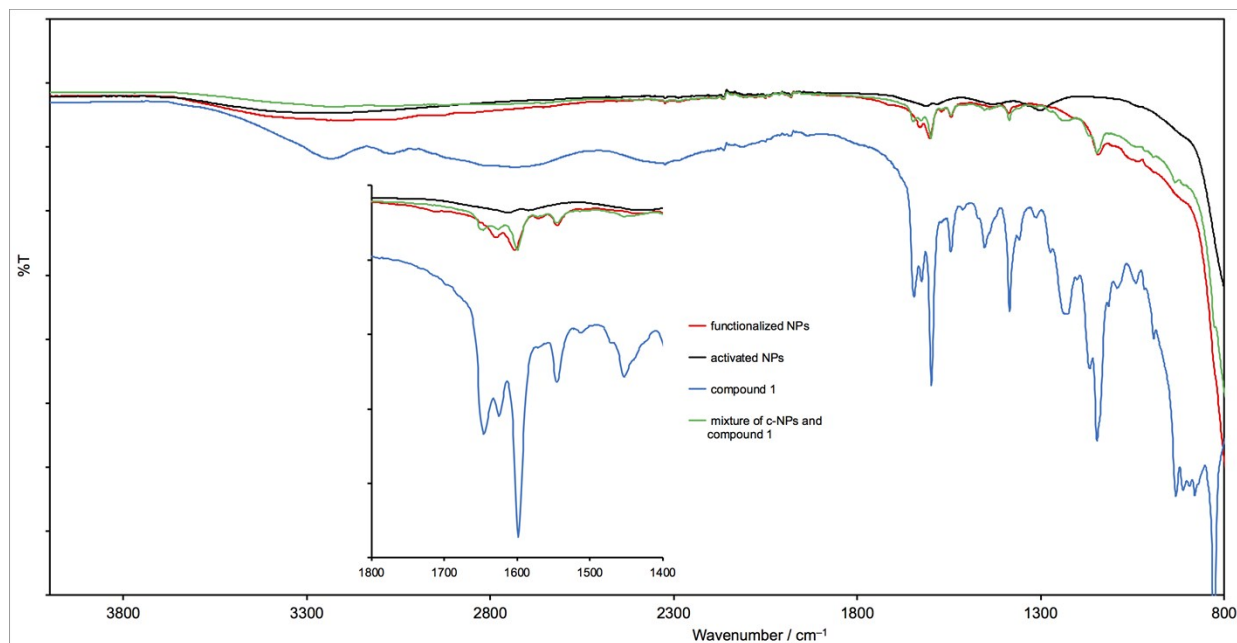


Fig. S8. Solid-state IR spectra of activated NPs (a-NPs), pristine **1**, a-NPs functionalized with **1** following Procedure B in the Experimental Section, and a mixture of commercial NPs (c-NPs) and **1**.

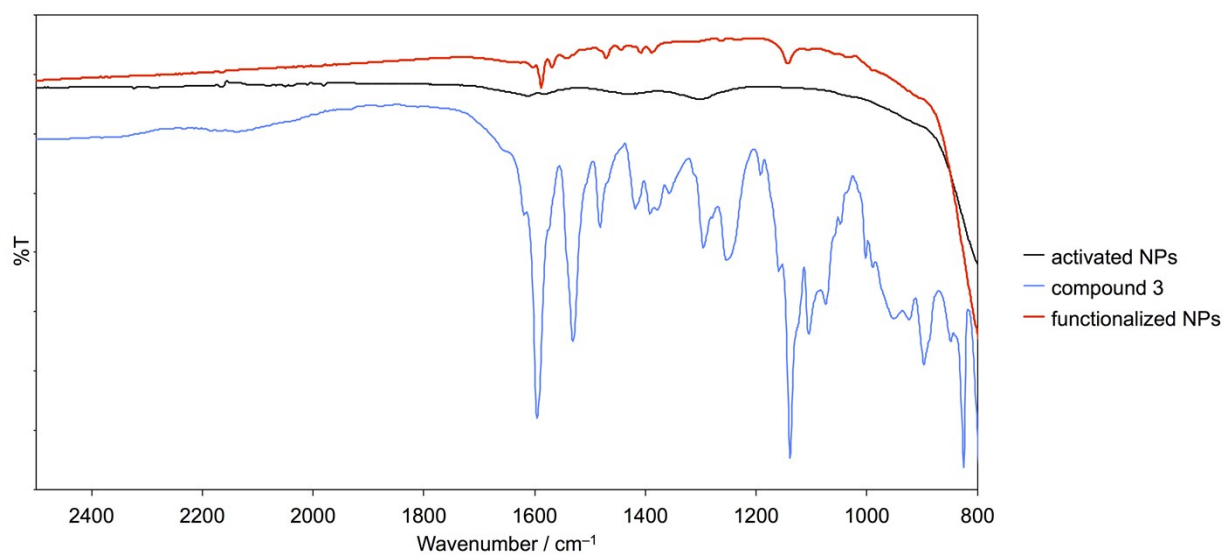


Fig. S9. Solid-state IR spectra of activated NPs, pristine **3**, and NPs functionalized with **3** following the Procedure B in the Experimental Section.

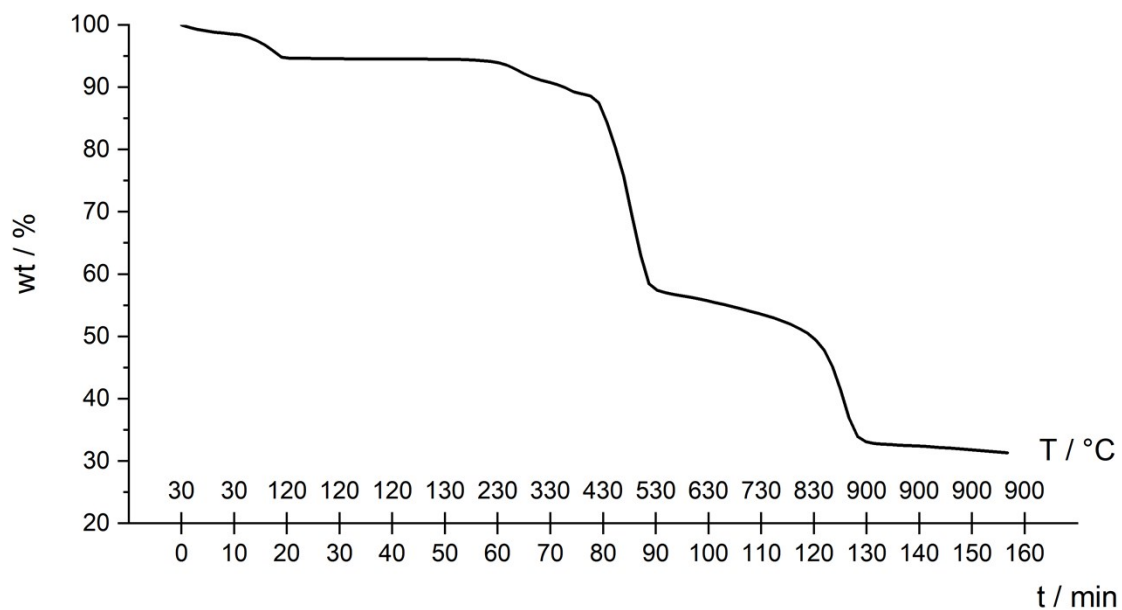


Fig. S10. TGA curve for ligand 1.

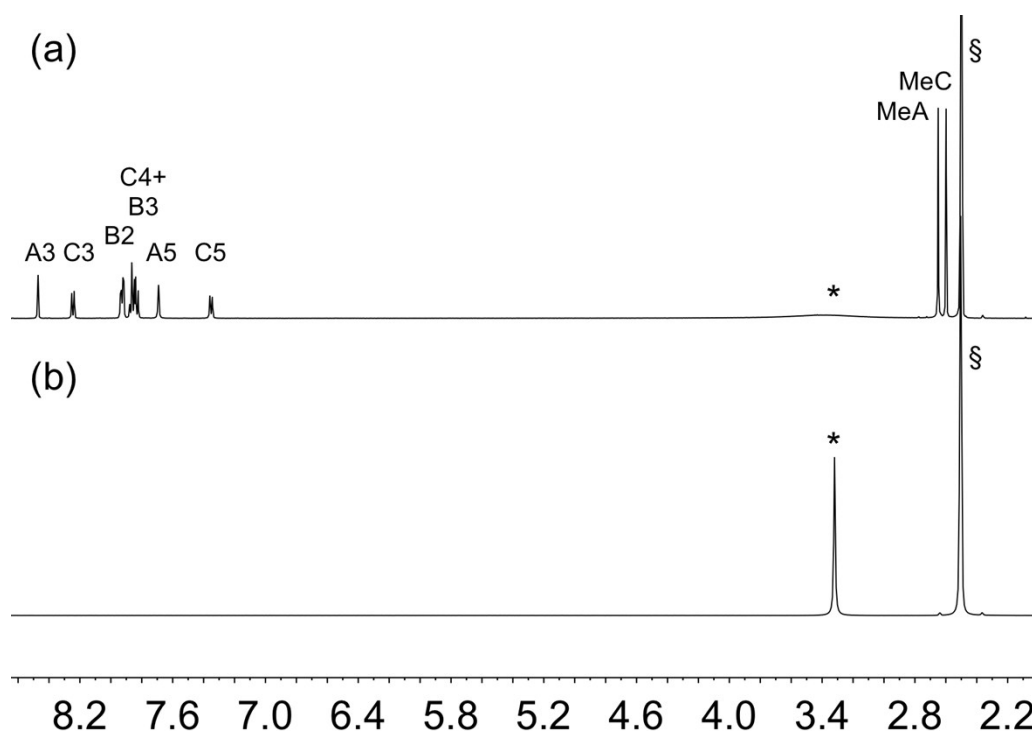


Fig. S11. ¹H NMR (500 MHz, DMSO-*d*₆, 298 K) of (a) ligand 2 and (b) suspended residue after activated TiO₂ NPs had been functionalized with 2 following Procedure B in the Experimental Section. See Scheme 1 for atom labelling. Chemical shifts in δ / ppm. § = residual DMSO-*d*₅. * = water.

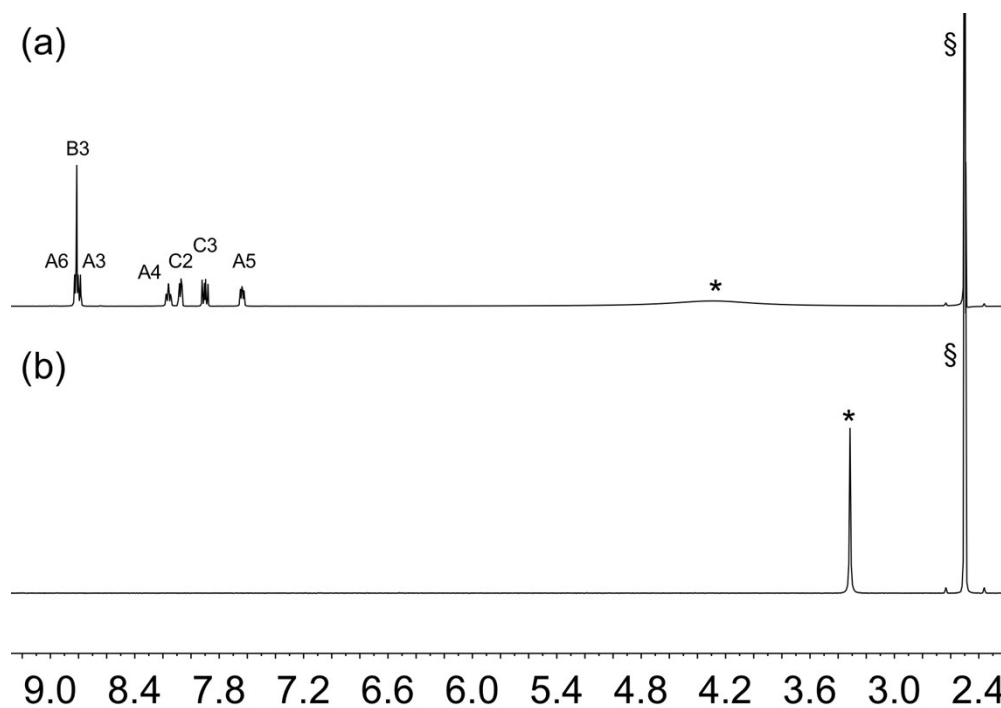


Fig. S12. ¹H NMR (500 MHz, DMSO-*d*₆, 298 K) of (a) ligand **3** and (b) suspended residue after activated TiO₂ NPs had been functionalized with **3** following Procedure B in the Experimental Section.. See Scheme 1 for atom labelling. Chemical shifts in δ / ppm. § = residual DMSO-*d*₅. * = water.

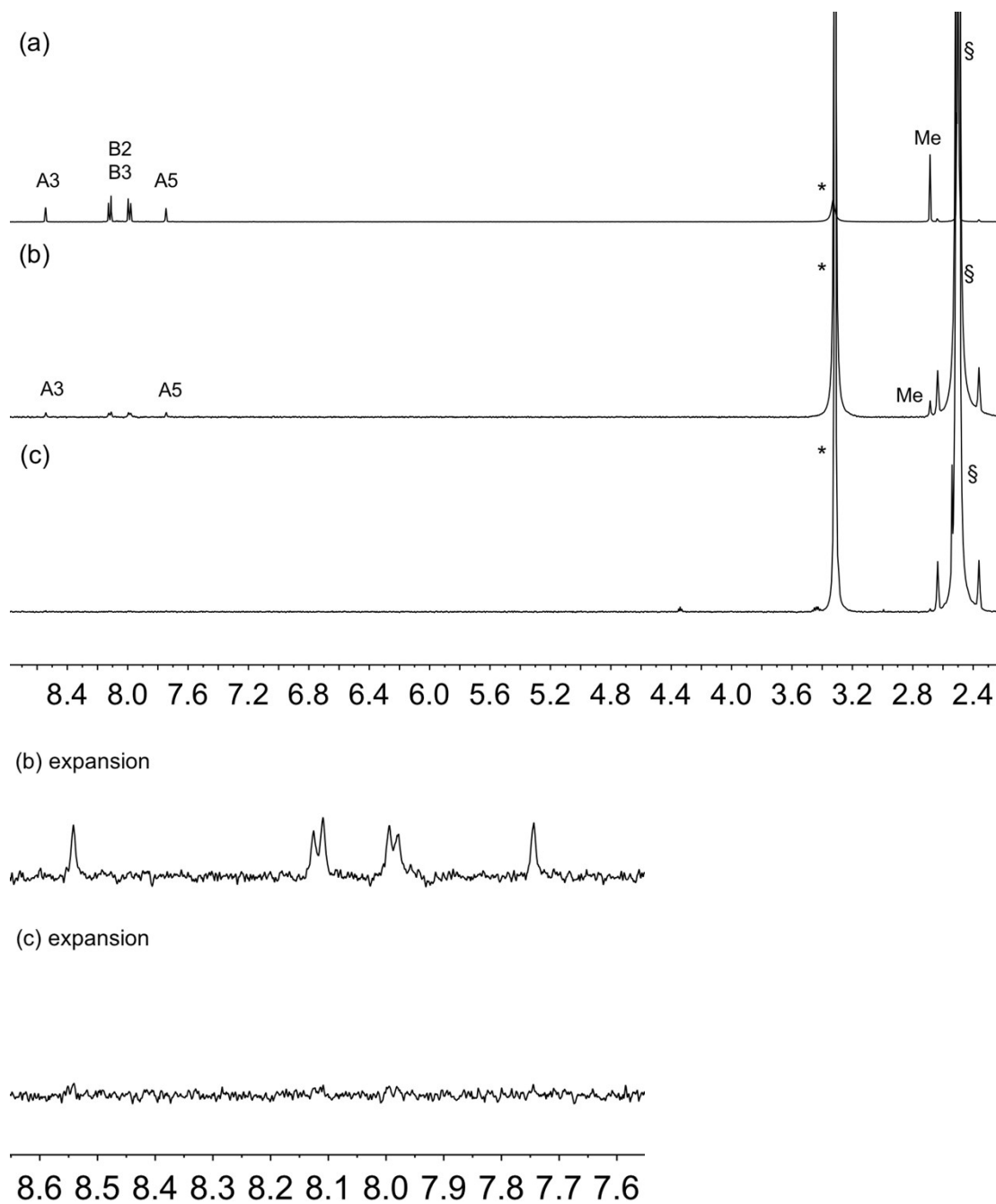


Fig. S13. ^1H NMR (500 MHz, $\text{DMSO-}d_6$, 298 K) of (a) ligand **4**, (b) suspended residue after activated TiO_2 NPs had been functionalized with **4** following Procedure B in the Experimental Section, and (c) the same residue after washing with DMSO and EtOH. Expansions of the aromatic region in (b) and (c) are also shown. See Scheme 1 for atom labelling. Chemical shifts in δ /ppm. § = residual $\text{DMSO-}d_5$. * = water.

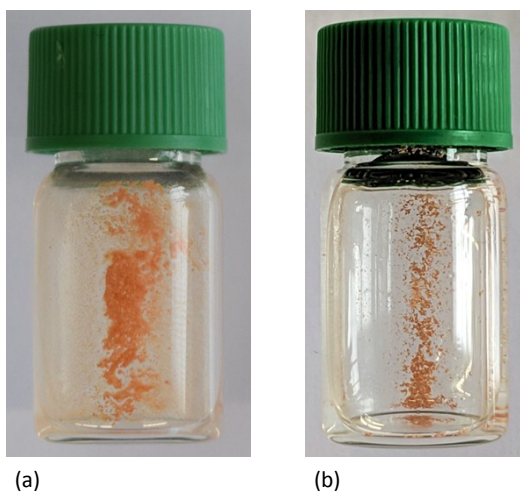


Fig. S14 Photographs of activated TiO₂ NPs functionalized (a) with **2** and after treatment with [Cu(MeCN)₄][PF₆], and (b) with **4** and after treatment with [Cu(MeCN)₄][PF₆].

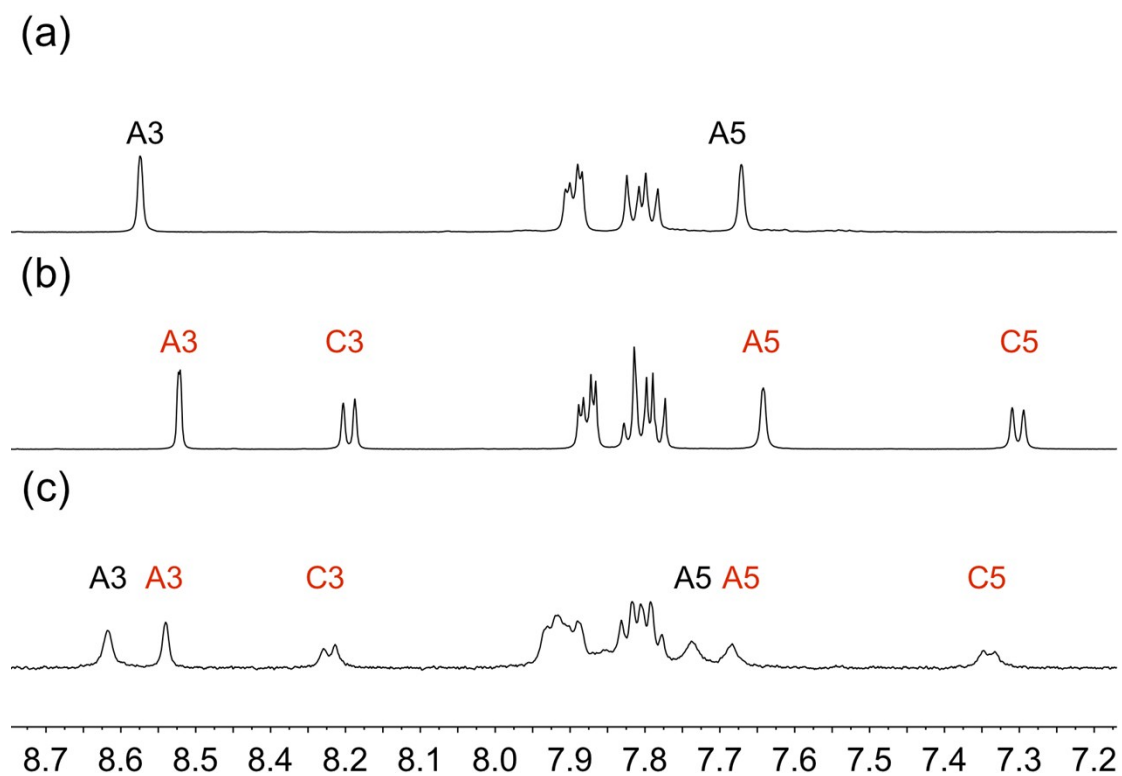


Fig. S15. ¹H NMR (500 MHz, DMSO-*d*₆, 298 K) of (a) ligand **1**, (b) ligand **2**, (c) suspended residue after activated TiO₂ NPs had been functionalized with a 1:1 mixture of **1** and **2** following Procedure C in the Experimental Section. See Scheme 1 for atom labelling. Chemical shifts in δ/ppm.

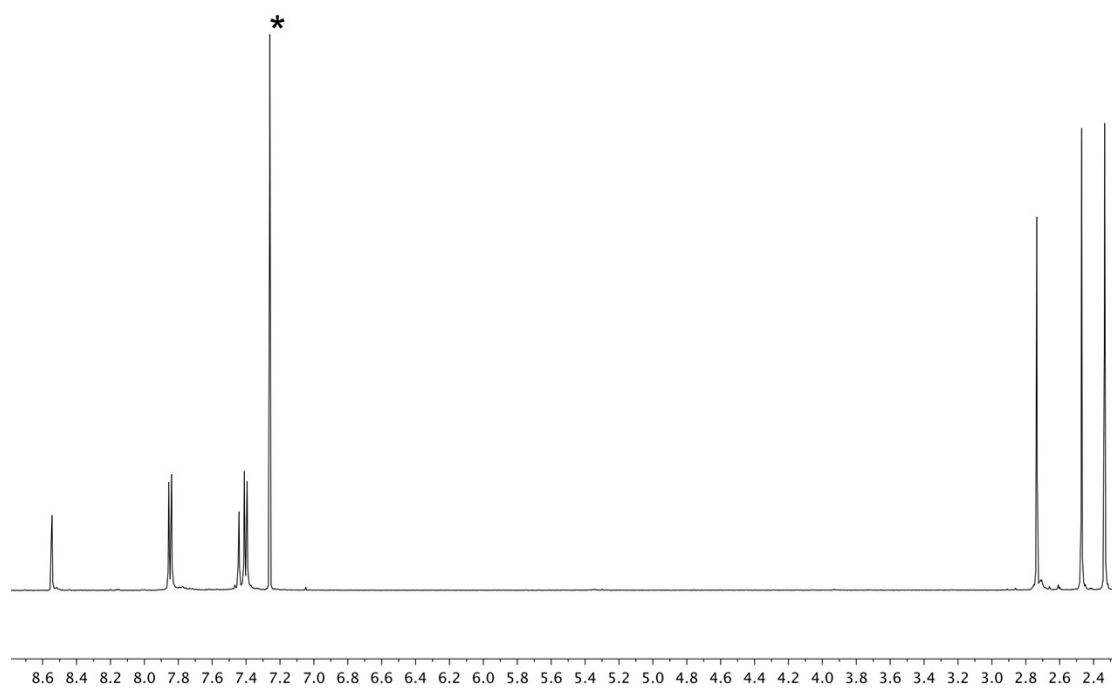


Fig. S16. ^1H NMR (500 MHz, CDCl_3 , 298 K) spectrum of compound 7. * = residual CHCl_3 . δ / ppm.

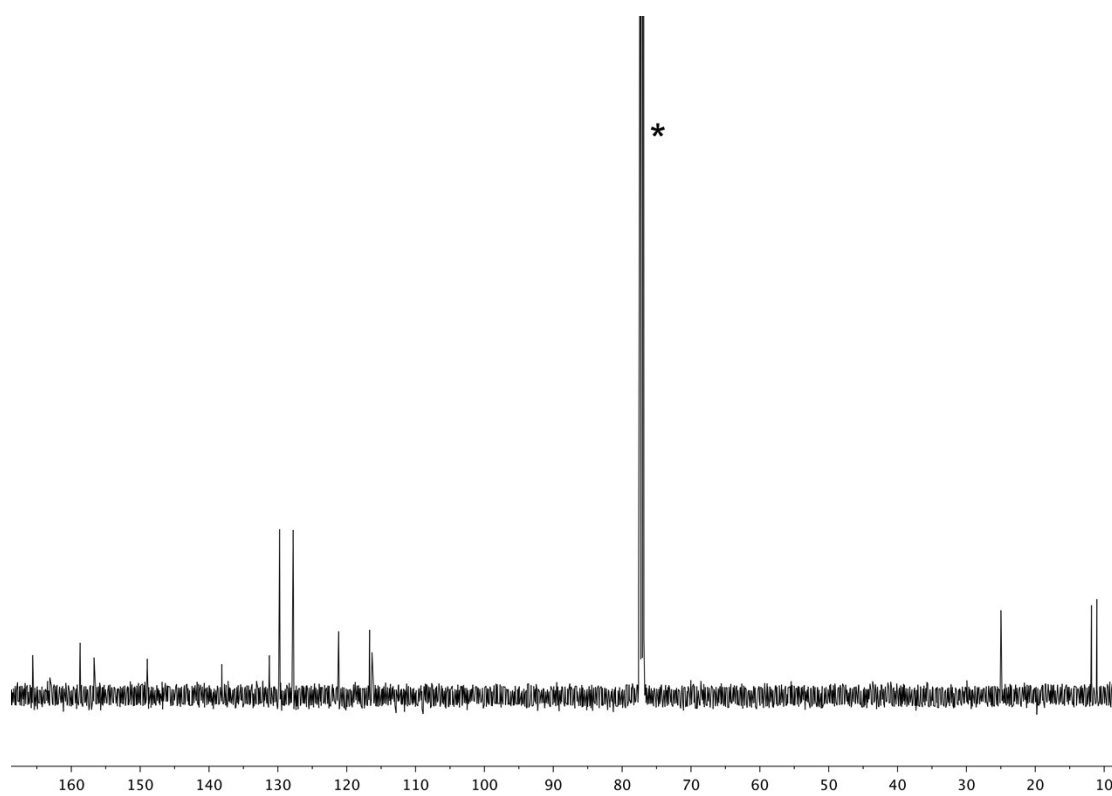
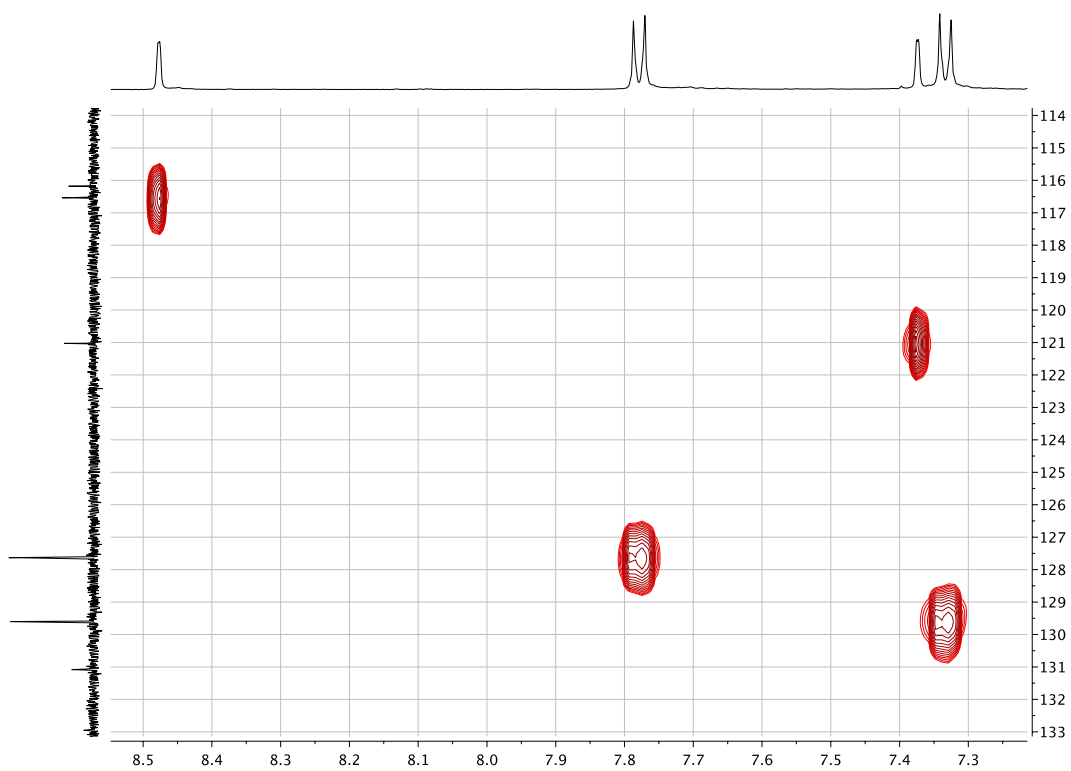
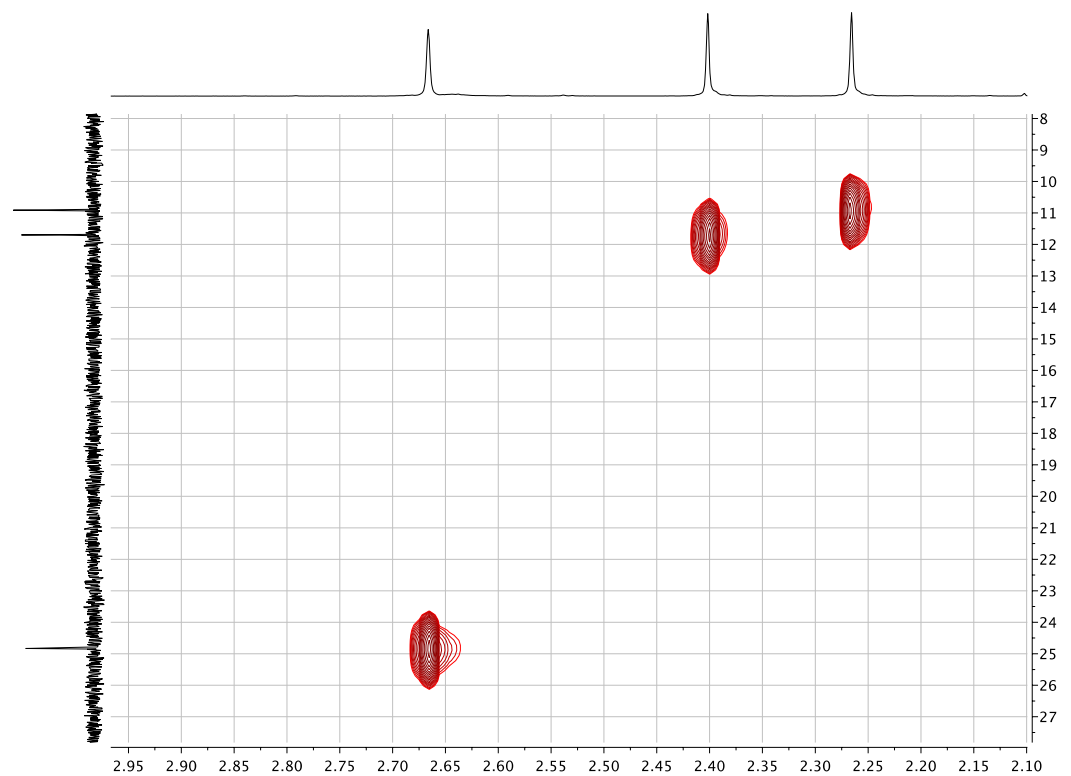


Fig. S17. $^{13}\text{C}\{^1\text{H}\}$ NMR (126 MHz, CDCl_3 , 298 K) spectrum of compound 7. * = CDCl_3 . δ / ppm.



(a)



(b)

Fig. S18. HMQC (500 MHz ^1H , 126 MHz ^{13}C , CDCl_3 , 298 K) spectrum of compound 7: (a) aromatic region, (b) methyl signals. δ / ppm.

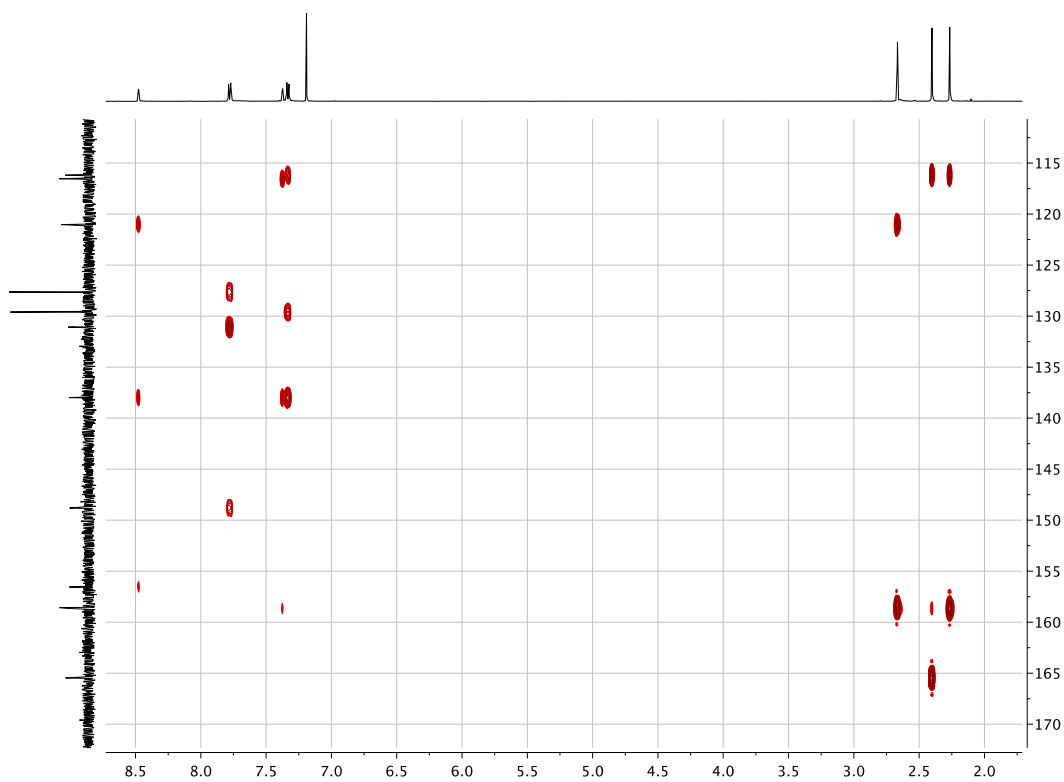
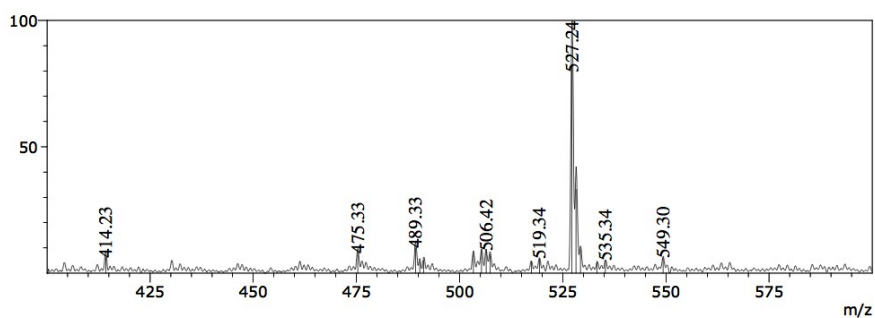


Fig. S19. HMBC (500 MHz ^1H , 126 MHz ^{13}C , CDCl_3 , 298 K) spectrum of compound **7**. δ / ppm.



Line#:1 R.Time:----(Scan#:----) MS Spectrum Positive Full Scan Zoomed View
 MassPeaks:17
 Spectrum Mode:Averaged 0.017-0.100(3-13) Base Peak:527.24(1317767)
 BG Mode:Averaged 0.150-2.933(19-353) Segment 1 - Event 1

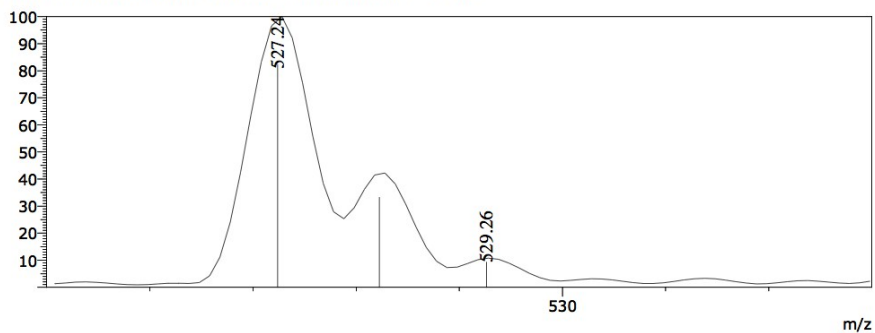


Fig. S20. Electrospray mass spectrum of **7** (with formic acid, positive mode).

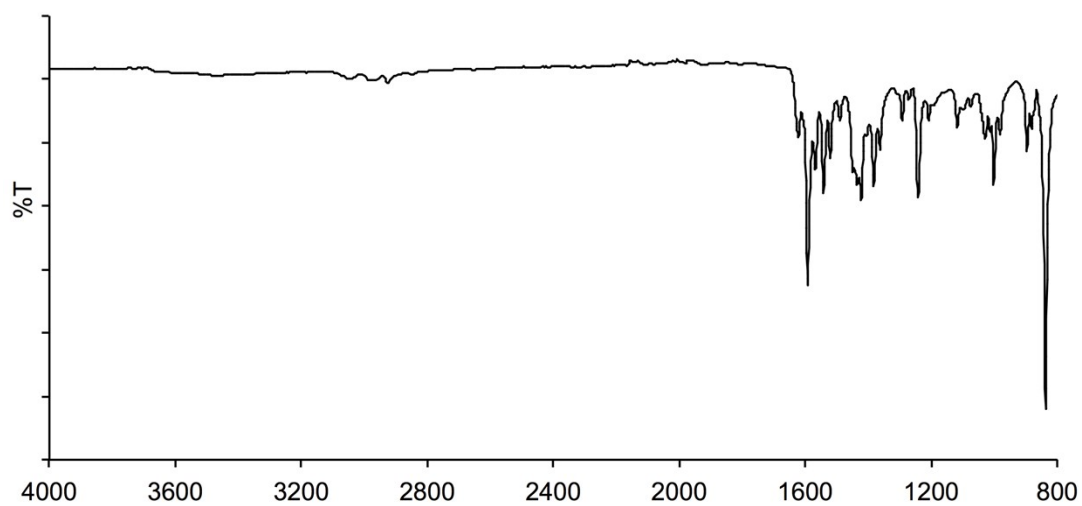


Fig. S21. FT-IR spectrum of solid 7.

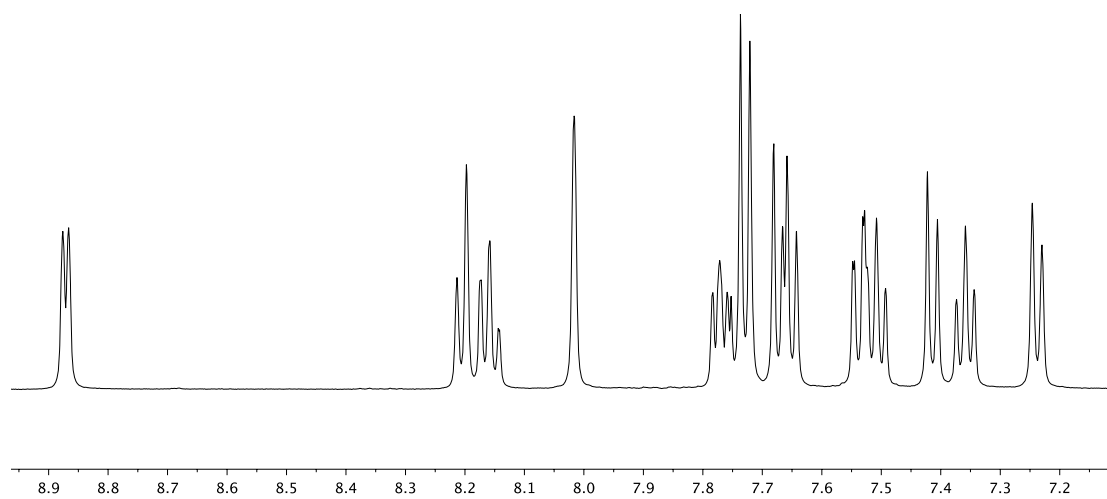


Fig. S22. ^1H NMR (500 MHz, acetone- d_6 , 298 K) spectrum (aromatic region) of $[\text{Cu}(\mathbf{6})_2][\text{PF}_6]$. δ / ppm.

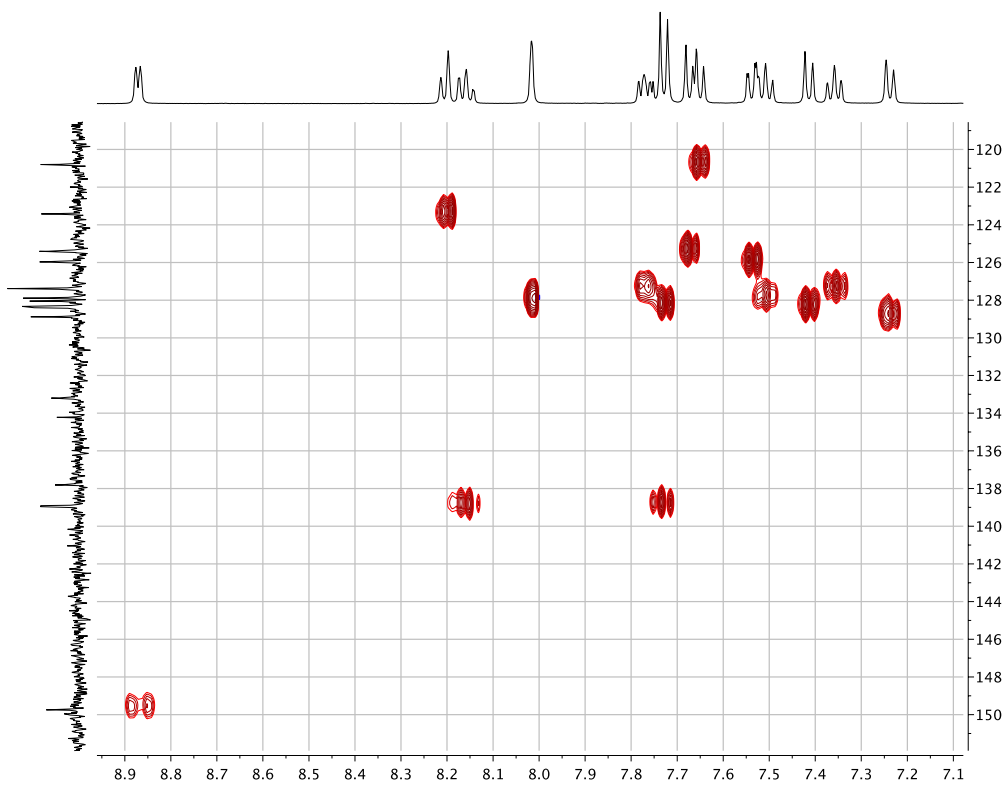


Fig. S23. HMQC (500 MHz ^1H , 126 MHz ^{13}C , acetone- d_6 , 298 K) spectrum of $[\text{Cu}(\mathbf{6})_2][\text{PF}_6]$. δ / ppm.

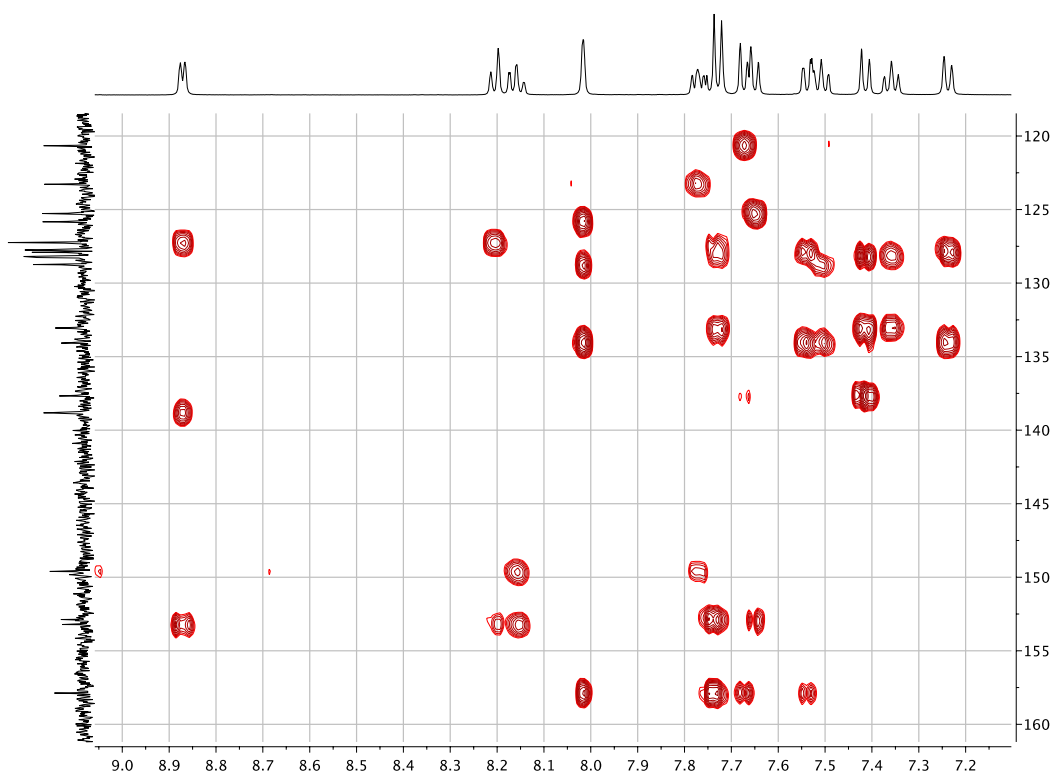


Fig. S24. HMBC (500 MHz ^1H , 126 MHz ^{13}C , acetone- d_6 , 298 K) spectrum of $[\text{Cu}(\mathbf{6})_2][\text{PF}_6]$. δ / ppm.

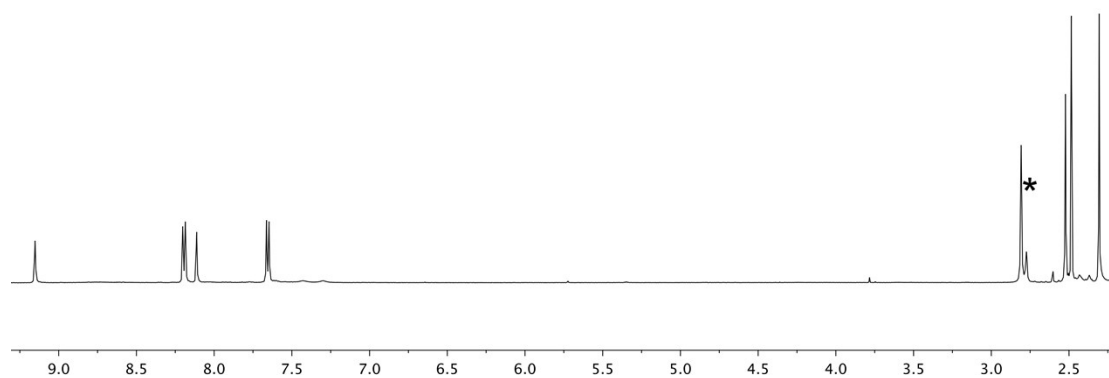


Fig. S25. ^1H NMR (500 MHz, acetone- d_6 , 298 K) spectrum of $[\text{Cu}(\mathbf{7})_2][\text{PF}_6]$. * = H_2O , HOD. δ / ppm.

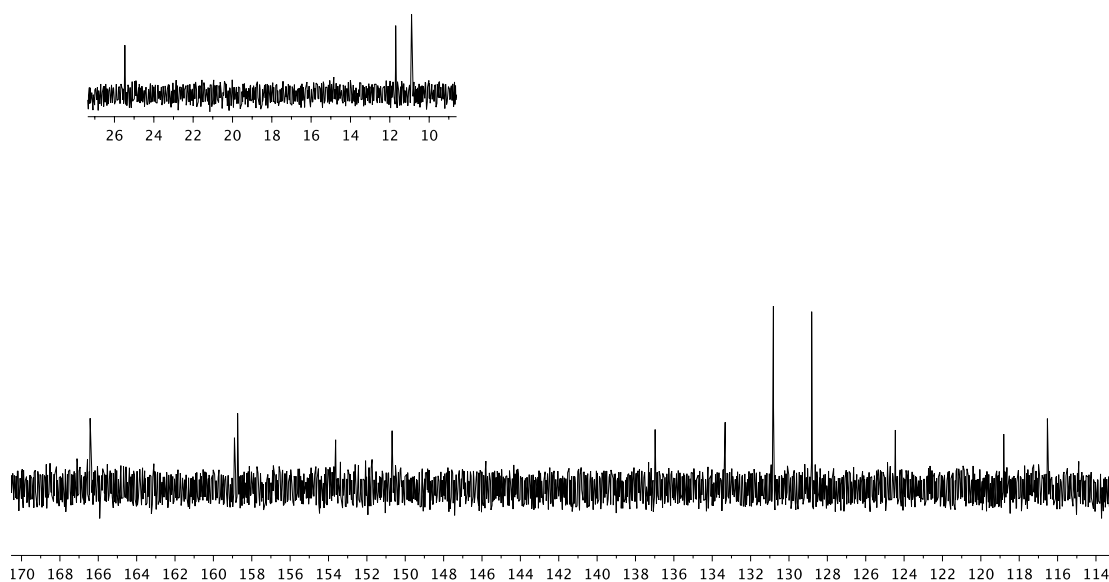


Fig. S26. $^{13}\text{C}\{^1\text{H}\}$ NMR (126 MHz, acetone- d_6 , 298 K) spectrum of $[\text{Cu}(\mathbf{7})_2][\text{PF}_6]$, aromatic region with methyl region inset. δ / ppm

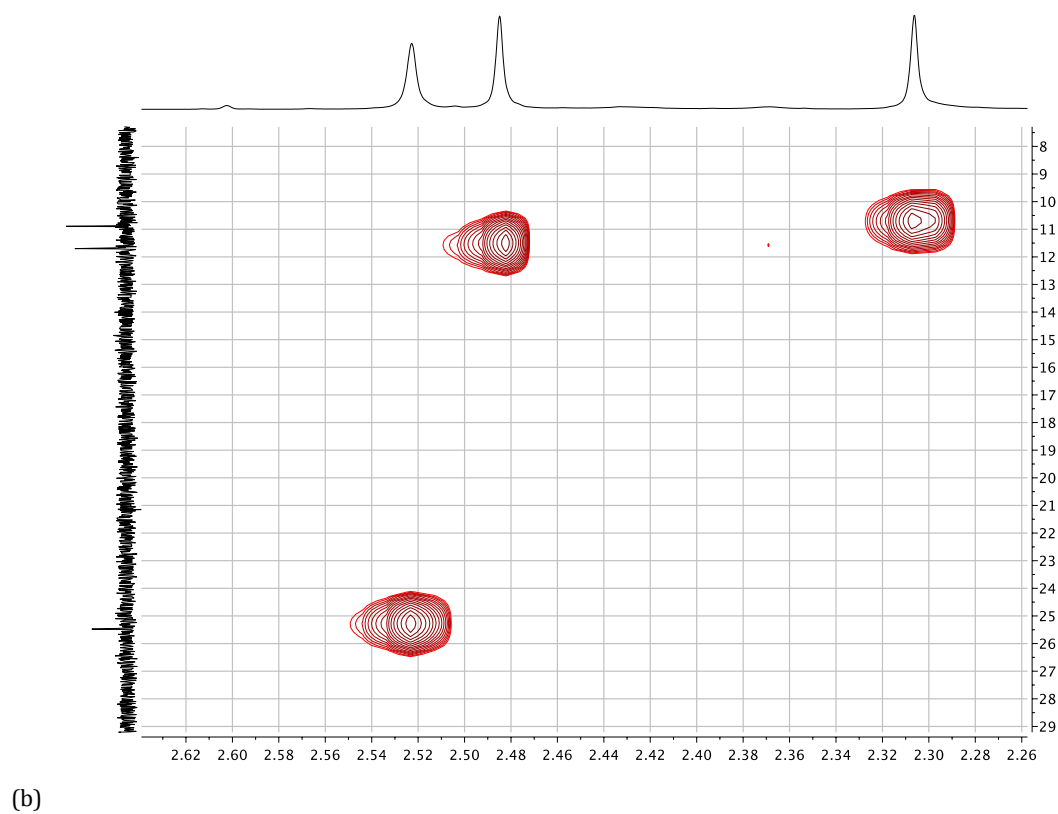
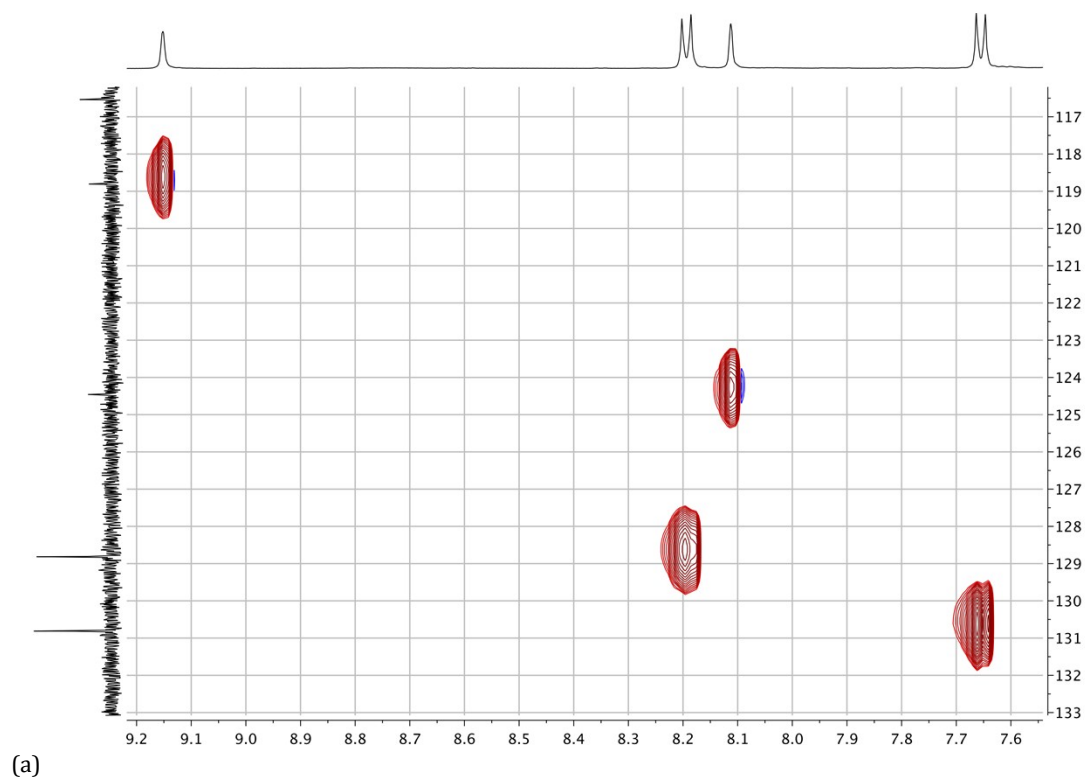


Fig. S27. HMQC (500 MHz ^1H , 126 MHz ^{13}C , acetone- d_6 , 298 K) spectrum of $[\text{Cu}(\mathbf{7})_2][\text{PF}_6]$: (a) aromatic region, (b) methyl signals. δ / ppm.

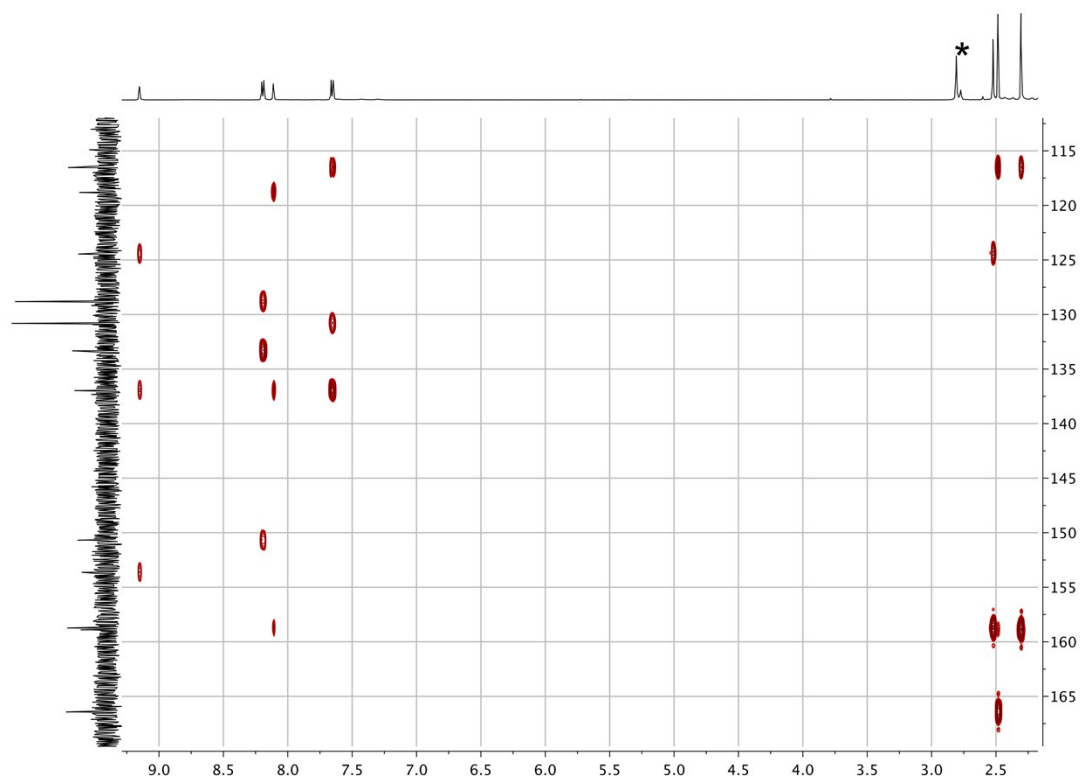


Fig. S28. HMBC (500 MHz ^1H , 126 MHz ^{13}C , acetone- d_6 , 298 K) spectrum of $[\text{Cu}(\mathbf{7})_2][\text{PF}_6]$. * = H_2O , HOD. δ / ppm.

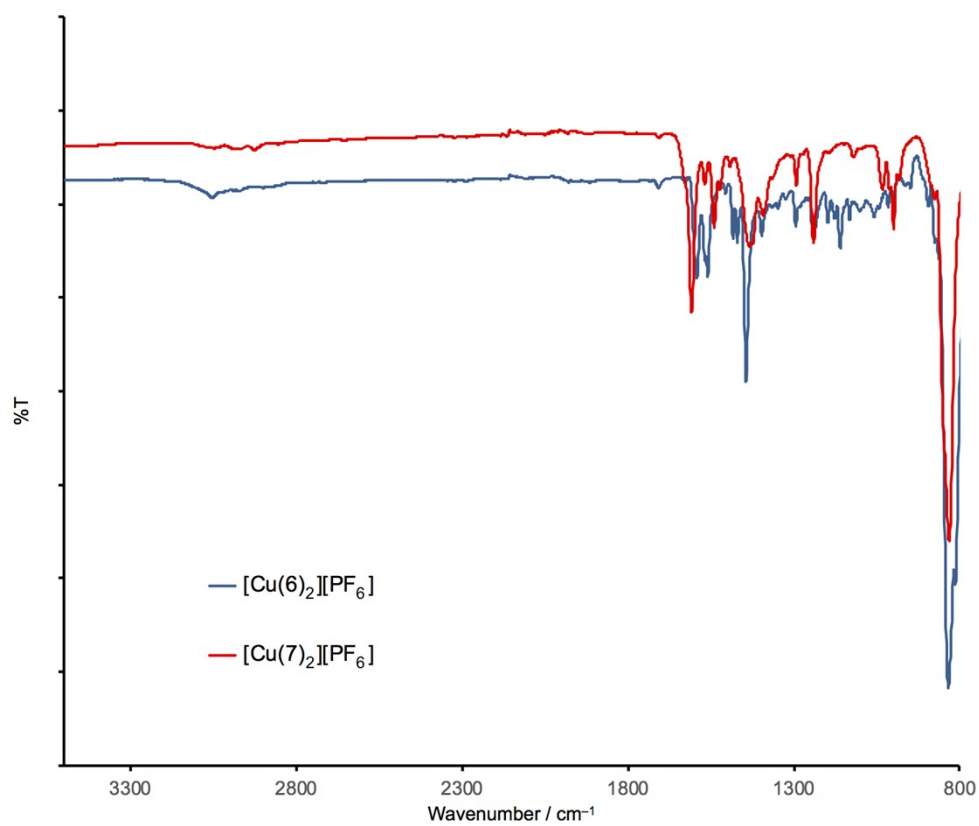


Fig. S29. Solid-state IR spectra of $[\text{Cu}(\mathbf{6})_2][\text{PF}_6]$ and $[\text{Cu}(\mathbf{7})_2][\text{PF}_6]$.

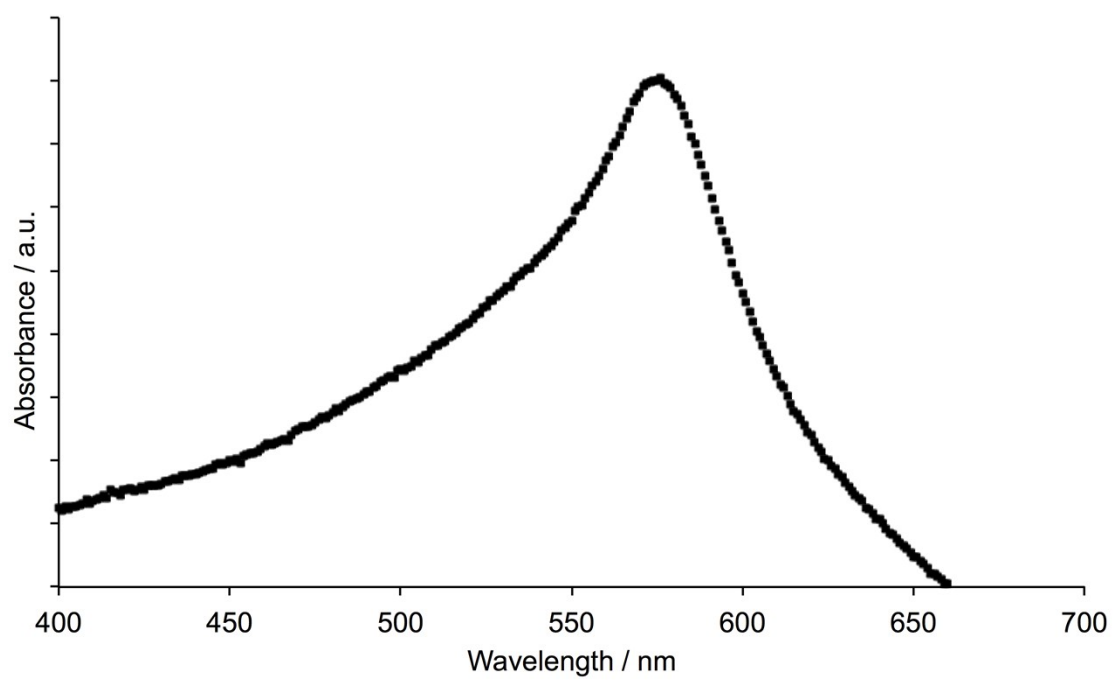


Fig. S30. Solid-state absorption spectrum of NPs functionalized with **3** (following Procedure B in the Experimental Section) after treatment with $[\text{Fe}(\mathbf{8})_2][\text{PF}_6]_2$.

CHAPTER III: STANDING STILL

CATALYTIC STUDIES USING LIGAND AND METAL-COMPLEX FUNCTIONALIZED TiO₂ NANOPARTICLES

3.1 Motivation

As shown in **Chapter II**, f-NPs are capable of forming metal coordination compounds and this motivated investigations into a wide range of possible applications. There was particular interest in discovering examples of reactions in which conventional homogeneous catalytic solution processes could be transferred to heterogeneous catalytic systems using an NP platform. Working with NPs necessarily means that an anchoring group must be built into the ligand. Phosphonic acid groups were the most beneficial for successful anchoring. However, incorporating the phosphonic acid meant that it was not always possible to exactly reproduce the ancillary ligand in the catalyst upon going from homogeneous to heterogeneous conditions.

2,2'-Bipyridines (bpy) and 2,2';6',2''-terpyridines (tpy) have been widely used for catalysis due to their good σ -donor and strong π -acceptor characteristics and known coordination chemistry with all metals in the periodic table. Examples involve d-block metals such as Ni, Cu, Ru, Pd, Rh, Fe, Mn and Co allowing a broad choice of a suitable candidate which can be optimised for operating conditions.¹⁵⁵ Furthermore, TiO₂ NPs have the benefit that they incorporate earth abundant elements, are relatively cheap, thermodynamically stable, pH resistant, temperature resistant and non-toxic. TiO₂ NPs can also be specifically and repeatedly prepared in a wide variety of sizes and shapes. This makes them a desirable choice for further investigation as a substrate for catalytic centres.

Homogeneous catalysts have the advantage that all of the catalytic centres are potentially active, whereas in heterogeneous catalytic systems, only the surface catalytic sites of solid phases are active whilst interior sites are inactive.¹⁵⁶ This can be addressed by using the solid catalyst in a finely divided form, distributed over a carrier material such as zeolite. This gives catalytically active material possessing a very large surface area, although this process is often very challenging, especially in terms of stability in aqueous media.¹⁵⁷ Reactions with solid phase heterogeneous catalyst, can often only take place at their interfaces rather than the bulk of the material hence fine tuning of the porosity may be required.^{157,158} Heterogeneous catalysts also have significant benefits in terms of catalyst recovery, a feature gaining increasing environmental and economic importance. Hence, it is often easier to separate the products of heterogeneous catalysis from the spent catalyst than in the case of homogeneous catalysis.^{159,160} Ideally, one would have a catalyst with both characteristics active throughout the material with all metal centres catalytically active and easily recoverable. NP immobilized catalysts have the potential of bridging the gap between these two types of catalysis.

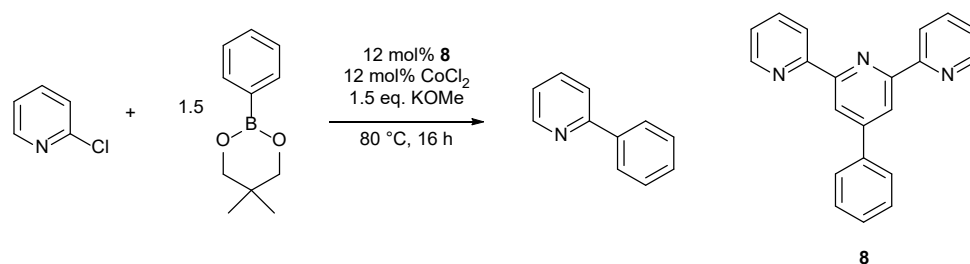
In this Chapter, focus was placed on transferring three different homogeneous catalytic reactions to heterogeneous conditions using f-NPs. The reactions used Co, Ni or Ru metal complexes to perform cross-coupling, dimerization and atom-transfer radical addition reactions. The reactions were investigated by binding the catalytic metal complex to the NPs using phosphonic acid based anchoring ligands.

3.2 Cobalt-catalysed cross coupling

3.2.1 Results and discussion

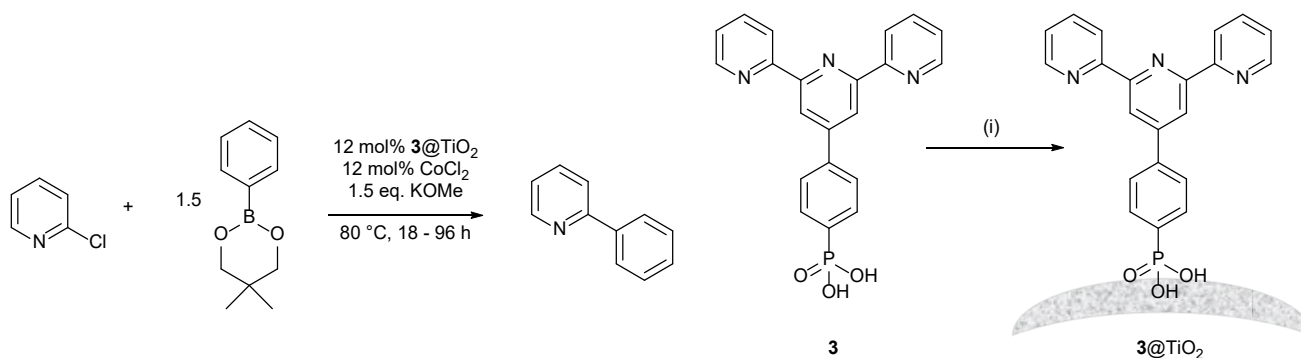
As a starting point for this project, the Co(II)-catalysed reaction shown in Scheme 2 was selected from the literature.¹⁶¹ The literature reaction shown is a CoCl₂ and **8** (Scheme 2) catalysed cross-coupling between an aryl halide (2-chloropyridine) and an arylboronic ester (phenylboronic acid neopentylglycol ester) using potassium methoxide as base. The literature report shows that the reaction proceeds with a yield of 91% after

extraction and flash column chromatography. The reaction was performed under strictly inert conditions in a glovebox. The authors of the initial report were able to cross-couple a broad range of heteroaryl halides and aryl halides. The reaction was either done in DMF or THF although neither kinetic experiments nor catalyst recycling experiments were performed.



Scheme 2: Cobalt-catalysed cross coupling reaction conditions reported in the literature.¹⁶¹

The catalyst prepared for this project incorporates the tpy-based ligand **8** and was modelled using a cobalt(II) complex containing NP-anchored **3** (Scheme 3) and ligand **8** to form a heteroleptic complex attached to the NP surface (experimental details described in **Sections 3.2.2** and **3.2.3**). The functionalization of TiO₂ NPs with ligand **3** was already established in **Chapter II**, and ligand **8** was also available. The main goal of this project was a working method for performing an analogous reaction using functionalized **3@TiO₂** NPs to catalyse the reaction heterogeneously. The reaction strategy can be seen in Scheme 3. Once the success of this step had been established, the aim was to carry out catalyst recycling and kinetic experiments. The execution of the literature reaction as a general test (described in **Section 3.2.4**) made it very clear that any water present in the reaction severely hindered its success. Thus, CoCl₂ was dried under harsh conditions and work was primarily done in the glovebox. This was a first indication that a successful reaction using f-NPs might be difficult because previous TGA-MS measurements had shown that NPs always carry a certain amount of surface and chemisorbed water.



Scheme 3: Cobalt-catalysed cross coupling reaction conditions and catalyst, (i) TiO₂ NPs, H₂O, 130 °C, 3 h, MW complete conditions described in **Chapter II**.

Section 3.2.5 describes the experimental details of the heterogeneous NP-supported cobalt-catalysed cross coupling reaction attempts. GC-MS was used to estimate the reaction success, and this showed that only trace amounts of the desired product were produced when replacing **8** by **3@TiO₂**. Several conditions were tested including changes to temperature, solvents, reaction times and catalyst pre-stirring time. Changing the solvent from dry THF to DMF yielded slight improvements while increasing the temperature from 80 °C to 120 °C did not improve the yield. The best results were obtained with **Method 2** in **Section 3.2.5**. Further small improvements were seen when the catalyst and NPs were pre-stirred for up to 3 days. It was assumed that the improvements resulted from the formation of increased amounts of a cobalt(II)/tpy complex (presumed to be [Co(**3**)Cl]²⁺) on the **3@TiO₂** NP surface. While these findings were interesting, the yields were

still low (<1%) and the project was ultimately discontinued in favour of other work in progress. Later, the project was revisited using new NPs which were functionalized with the pre-formed Co(II) complex. Different methods were applied to directly form the complex on the surface including making a heteroleptic version on the f-NP with ligand **8** (see **Sections 3.2.2** and **3.2.3**). However, while making the f-NPs was successful and straightforward, characterization of the functionalized NPs was non-trivial and, for time efficiency, was not carried out in detail.

The difficulty of reproducing the homogeneous results using an NP-based heterogeneous catalyst could be due to several things. The phosphonic acid functional group required for anchoring to the NP in **3@TiO₂** could hinder the catalytic performance. The formation of the metal complex on the NP surface could be too slow leading to only small amounts of active species being present. The catalytic process requires the labile heteroleptic cobalt chloride complex and the functionalization could form a stable homoleptic complex on the surface. This possible problem was minimized by making an assumption of the maximum amount of ligand that could be present, and by using a 1:1 ratio of CoCl₂. Finally, surface and chemisorbed water on the NPs could cause severe deactivation of the catalysis.

3.2.2 Experimental, *Co(3)@TiO₂*

3@TiO₂ (281.2 mg, 1.0 eq.) and anhydrous CoCl₂ (4.2 mg, 32 μmol, 1.0 eq.) were added to a vial. H₂O (5.0 mL) and EtOH (3.0 mL) were added, and the mixture was thoroughly dispersed using sonication and stirring. The suspension was transferred to an autoclave with a PTFE liner with additional EtOH (2.0 mL). The autoclave was sealed and then heated in an oven with 320 °C/h to 160 °C. The autoclave was left at 160 °C for 1 h. After cooling down, the autoclave was opened and the suspension was centrifuged (20 min, 7000 rpm). The resulting NPs were washed with H₂O (3 × 10 mL) and EtOH (1 × 10 mL) and dried under high vacuum. The NPs were isolated as a pale yellow powder (257.1 mg).

3.2.3 Experimental, *Co(3)(8)@TiO₂*

3@TiO₂ (280.9 mg, 1.0 eq.), anhydrous CoCl₂ (4.2 mg, 32 μmol 1.0 eq.) and **8** (9.9 mg, 32 μmol, 1.0 eq.) were added to a vial. H₂O (5.0 mL) and EtOH (3.0 mL) were added, and the mixture was thoroughly dispersed using sonication and stirring. The suspension was transferred to an autoclave with a PTFE liner with additional EtOH (2.0 mL). The autoclave was sealed and then heated in an oven with 320 °C/h to 160 °C. The autoclave was left at 160 °C for 1 h. After cooling down, the autoclave was opened and the suspension was centrifuged (20 min, 7000 rpm). The resulting NPs were washed with H₂O (3 × 10 mL) and EtOH (1 × 10 mL) and dried under high vacuum. The NPs were isolated pale pink powder (262.8 mg).

3.2.4 Experimental, *cross-coupling of 2-chloropyridine and phenylboronic acid*

Dry THF (1.0 mL), heat-vacuum dried CoCl₂ (7.4 mg, 12 mol%), KOMe (52.6 mg, 0.750 mmol, 1.5 eq.) and **8** (17.6 mg, 12 mol%) were added to a dried reaction tube in a glovebox. The mixture was allowed to stir at rt (ca. 22 °C) for 5 minutes. A second vial was prepared in the glovebox with dry THF (1.0 mL), 2-chloropyridine (0.50 mmol, 1.0 eq.) and phenylboronic acid neopentylglycol ester (0.75 mmol, 1.5 eq.). The solution from vial 2 was transferred to the reaction tube and sealed. The tube was removed from the glovebox and heated for 16 h at 80 °C. 10 mg of the reaction suspension was removed from the vial to measure GC-MS. This reaction and characterization method were repeated using dry DMF.

3.2.5 Experimental, cross-coupling of 2-chloropyridine and phenylboronic acid using *f*-NPs

Method 1

Dry THF (2.0 mL), heat vacuum dried CoCl_2 (1.7 mg, 12 mol%), KOMe (10.5 mg, 0.150 mmol, 1.5 eq.) and $\mathbf{3@TiO}_2$ (100.9 mg, 12 mol%) were added to a dried reaction tube in a glovebox. The mixture was allowed to stir at rt for 5 minutes. A second vial was prepared in the glovebox with dry THF (1.0 mL), 2-chloropyridine (0.10 mmol, 1.0 eq.) and phenylboronic acid neopentylglycol ester (0.150 mmol, 1.5 eq.). The solution from vial 2 was transferred to the reaction tube and sealed. The tube was removed from the glovebox and heated for 16 h at 80 °C. 10 mg of the reaction suspension was removed from the vial to measure GC-MS. This reaction was repeated using dry DMF or higher reaction temperature (120 °C).

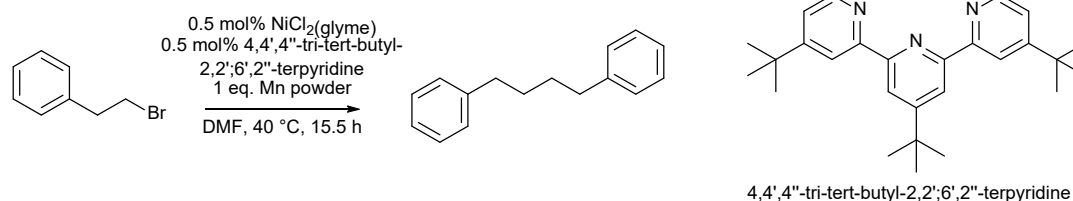
Method 2

Dry DMF (2.0 mL), heat vacuum dried CoCl_2 (1.7 mg, 12 mol%) and $\mathbf{3@TiO}_2$ (100.9 mg, 12 mol%) were added to a dried reaction tube in a glovebox. The mixture was allowed to stir at rt for 60 minutes. The vial was opened and KOMe (10.5 mg, 0.150 mmol, 1.5 eq.) was added. A second vial was prepared in the glovebox with dry DMF (1.0 mL), 2-chloropyridine (0.10 mmol, 1.0 eq.) and phenylboronic acid neopentylglycol ester (0.150 mmol, 1.5 eq.). The solution from vial 2 was transferred to the reaction tube and sealed. The tube was removed from the glovebox and heated for 16 h at 80 °C. 10 mg of the reaction suspension was removed from the vial to measure GC-MS. This reaction was repeated using dry MeOH, EtOH or toluene. This reaction was also repeated allowing CoCl_2 and the NPs to stir for a prolonged time of 3 days at room temperature (ca. 22 °C) before addition of base and reactants.

3.3 Nickel-catalysed dimerization

3.3.1 Results and discussion

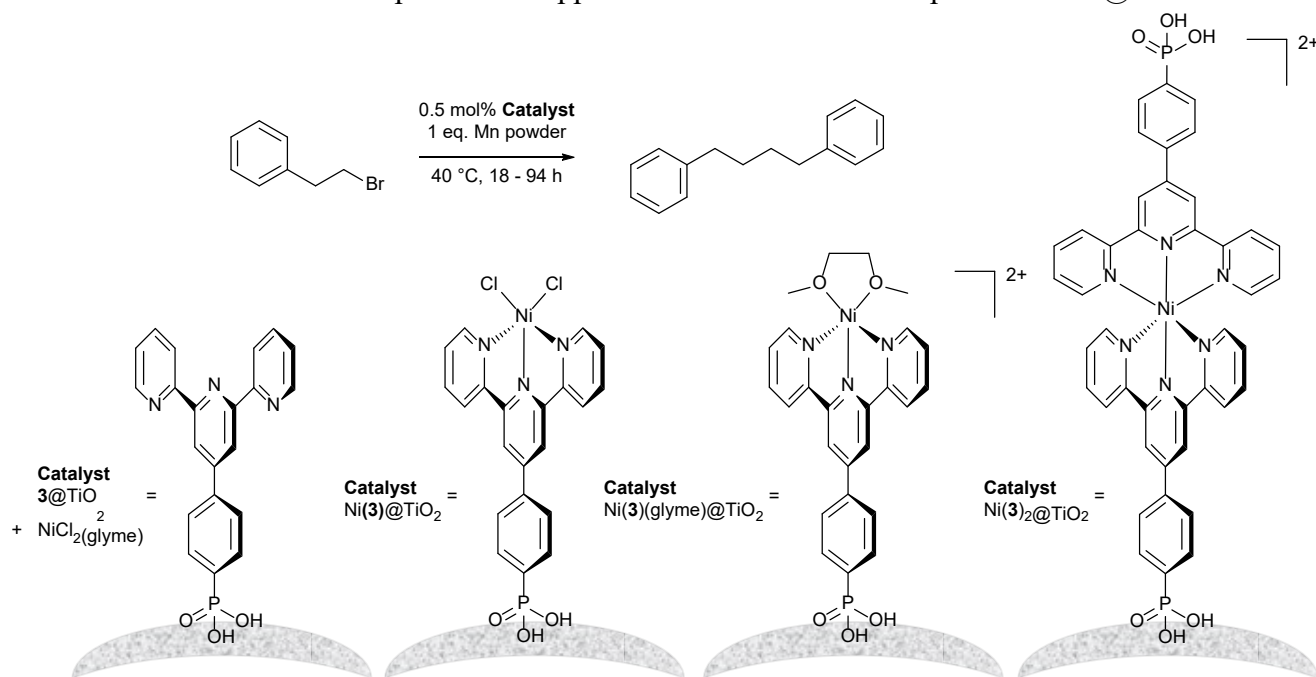
The literature reaction¹⁶² in Scheme 4 demonstrates a $[\text{NiCl}_2(\text{glyme})(4,4',4''\text{-tri-}t\text{-butyl-}2,2';6',2''\text{-terpyridine})]$ catalysed reductive dimerization of 2-bromoethylbenzene using Mn powder as reducing agent. After a silica plug filtration with diethyl ether, the yield of 1,4-diphenylbutane was 98% after 15.5 h in air and 95% after 17 h under inert conditions in a glovebox under N_2 . The literature report also tests the influence of several reaction components within the catalytic system (no ligand, no nickel or no manganese) with each having a severe effect (<1% yield) although, kinetic or recycling experiments were not performed. Accordingly, this catalytic process was selected for this Chapter for further investigation and transfer to *f*-NPs.



Scheme 4: Nickel-catalysed dimerization reaction conditions reported in the literature.¹⁶²

The advantage of this reaction was that it was possible to work under air which would hopefully rule out problems caused by surface or chemisorbed water on the TiO_2 NPs. A potential disadvantage was that the ligand used in the homogenous reaction (Scheme 4) was electronically quite different from the anchoring ligand $\mathbf{3}$ required for TiO_2 surface binding. Hence, the project was deemed interesting and focused on a heterogeneous adaptation using $\mathbf{3@TiO}_2$ NPs to catalyse the reaction as shown in Scheme 5. For the catalysis,

the in-situ approach to forming metal complexes as the active species (as used in the literature model reaction) was replaced in favour of a surface-bound metal complex on the TiO₂ NPs formed before the catalytic reaction. **Sections 3.3.2-3.3.4** describe the procedures applied to form the metal complexes with **3**@TiO₂ NP.



Scheme 5: Nickel-catalysed dimerization reaction conditions and f-NP immobilised catalysts.

Section 3.3.5 describes the experimental details of the heterogeneous nickel-catalysed dimerization attempts. ¹H NMR spectroscopy and MALDI mass spectrometry were used to follow the reaction progress. Overall, the reaction shown in Scheme 5 was tested using three different f-NPs (Ni(**3**)@TiO₂, Ni(**3**)₂@TiO₂ and Ni(**3**)(glyme)@TiO₂). It must be noted that binding of the ligands for the catalyst Ni(**3**)₂@TiO₂ is unclear and cannot be represented perfectly by Scheme 5, as both ligands could be bound to the same or separate NPs. Analysing the ¹H NMR spectroscopic results of the crude reaction mixture using Ni(**3**)@TiO₂ showed no product formation after 21 h reaction time and only traces <1% after 69 h. When using Ni(**3**)₂@TiO₂, traces of product (<1%) were observed after 21 h and the yield was estimated to be about 2% after 69 h. **Method 2** performed similarly showing <1% and 2% of product after 19 h and 94 h, respectively. After silica filtration, the ratio of product to starting material was roughly 1:10. When using Ni(**3**)(glyme)@TiO₂ with **Method 1**, after 18 h roughly 10% product was observed by NMR spectroscopy in the crude reaction suspension. After silica filtration (see **Section 3.3.5**) only the desired product and solvent impurities remained. The identity of the product was confirmed from the ¹³C {¹H} NMR spectrum in which each peak matched the literature data.¹⁶²

Even though the product yields were quite low, this project yielded interesting findings. The increased yield when using Ni(**3**)(glyme)@TiO₂ provided further evidence that a prior formation of the metal complex on the NP surface was important for catalysis. The decrease in efficiency of the catalyst is probably due to the replacement of a ligand with electron-donating *tert*-butyl groups which are not present in anchoring ligand **3**.

3.3.2 Experimental, Ni(**3**)@TiO₂ NPs

NiCl₂·6H₂O (6.0 mg, 25 μmol, 1 eq.) was heated in a sealable glass vial under vacuum until the solid turned bright yellow. The solid was allowed to cool under vacuum and the vial was filled with N₂. The solid was dissolved in dry EtOH (2.5 mL). Dried **3**@TiO₂ NPs (220.3 mg, 1.0 eq.) were added to the vial and the NPs were dispersed by sonication for 5 minutes. The vial was sealed and heated at 100 °C for 72 h. The Ni(**3**)@TiO₂ NPs were separated from the solvent by centrifugation (10 min, 9000 rpm) and then washed with EtOH (2 × 2.0 mL) and then dried under high vacuum yielding a yellow powder (187.3 mg).

3.3.3 Experimental, Ni(**3**)₂@TiO₂ NPs

NiCl₂·6H₂O (3.0 mg, 13 μmol, 1 eq.) was heated in a sealable glass vial under vacuum until the solid turned bright yellow. The solid was allowed to cool under vacuum and the vial was filled with N₂. The solid was dissolved in dry DMF (2.0 mL). Dried **3**@TiO₂ NPs (220.0 mg, 2 eq.) were added to the vial and the NPs were dispersed by sonication for 5 minutes. The vial was sealed and heated at 100 °C for 72 h. The Ni(**3**)₂@TiO₂ NPs were separated from the solvent by centrifugation (10 min, 9000 rpm) and then washed with EtOH (2 × 2 mL) and then dried under high vacuum yielding a yellow powder (107.4 mg).

3.3.4 Experimental, Ni(**3**)(glyme)@TiO₂ NPs

3@TiO₂ (219.7 mg, 1.0 eq.) and [NiCl₂(glyme)] (5.5 mg, 25 μmol, 1.0 eq.) were added to a vial. H₂O (5.0 mL) and EtOH (3.0 mL) were added, and the mixture thoroughly dispersed using sonication and stirring. The suspension was transferred to an autoclave with a PTFE liner with additional EtOH (2.0 mL). The autoclave was sealed and then heated at a rate of 320 °C/h to 160 °C. The autoclave was left at 160 °C for 1 h. After cooling, the autoclave was opened and the suspension was centrifuged (20 min, 7000 rpm). The resulting NPs were washed with H₂O (3 × 10 mL) and EtOH (1 × 10 mL) and then dried under high vacuum. Ni(**3**)(glyme)@TiO₂ was isolated as a yellow powder (196.8 mg).

3.3.5 Experimental, reductive dimerization of 2-bromoethylbenzene

Method 1

Ni(**3**)@TiO₂ NPs (88.0 mg, 0.5 mol%) was added to a vial. Dry DMF (2 mL) was added, and the mixture was thoroughly dispersed using sonication for 10 minutes. 2-Bromoethylbenzene (280 μL, 2.00 mmol) and Mn powder (111.0 mg, 2.00 mmol, 325 mesh) were added to the vial. The vial was sealed and heated at 40 °C for 94 h. After 18 h to 94 h the reaction mixture was checked using ¹H NMR spectroscopy and MALDI mass spectrometry. The suspension was filtered through an Et₂O pre-wetted silica plug. The plug was washed with additional Et₂O (50 mL) and the concentrated liquid was analysed using ¹H NMR spectroscopy and MALDI mass spectrometry. This reaction was repeated using Ni(**3**)₂@TiO₂ NPs or Ni(**3**)(glyme)@TiO₂ instead of Ni(**3**)@TiO₂. The reaction with Ni(**3**)(glyme)@TiO₂ yielded 1,4-diphenylbutane (39.3 mg, 0.185 mmol, 9.2%). ¹H NMR (500 MHz, CDCl₃) δ / ppm: 7.30-7.12 (m, 10 H), 2.64 (m, 4 H), 1.67 (m, 4 H). ¹³C{¹H} NMR (126 MHz, CDCl₃) δ / ppm: 142.7, 128.6, 128.4, 125.8, 36.0, 31.2.

Method 2

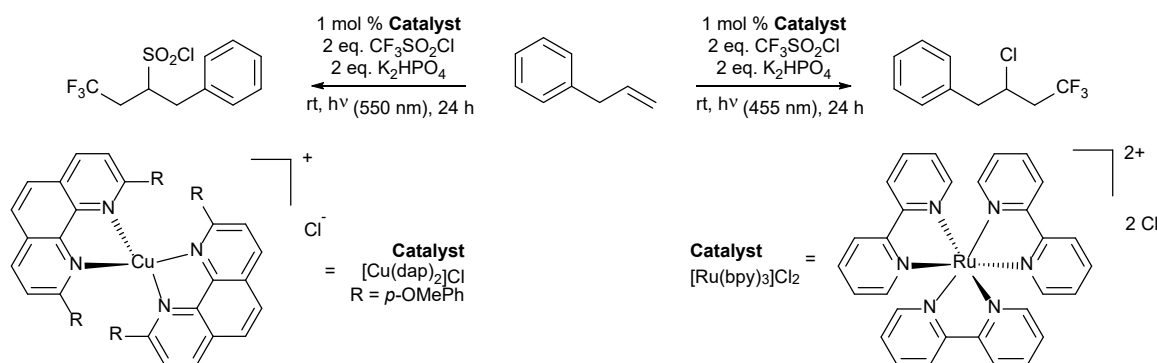
3@TiO₂ (88.0 mg, 0.5 mol%) and [NiCl₂(glyme)] (2.2 mg, 10 μmol, 0.50 mol%) were added to a vial. Dry DMF (2 mL) was added, and the mixture was thoroughly dispersed using sonication for 10 minutes. 2-Bromoethylbenzene (280 μL, 2.00 mmol) and Mn powder (111.0 mg, 2.00 mmol, 325 mesh) were added to the vial. The vial was sealed and heated at 40 °C for 94 h. After 18 h and 94 h the reaction mixture was checked using ¹H NMR spectroscopy and MALDI mass spectrometry. The suspension was filtered through an Et₂O pre-wetted pipette silica plug. The plug was washed with additional Et₂O (50 mL) and the concentrated liquid was analysed using ¹H NMR spectroscopy and MALDI mass spectrometry.

3.4 Ruthenium complex photoredox-catalysed atom-transfer radical addition

3.4.1 Results and discussion

Photoredox-catalysed atom transfer radical additions are interesting since, depending on the catalyst and wavelength of the light source, the reaction can be selectively directed to two products as shown in Scheme 6 either the chloride or sulfonyl chloride can be obtained. The literature reaction presented here^{163,164} is the

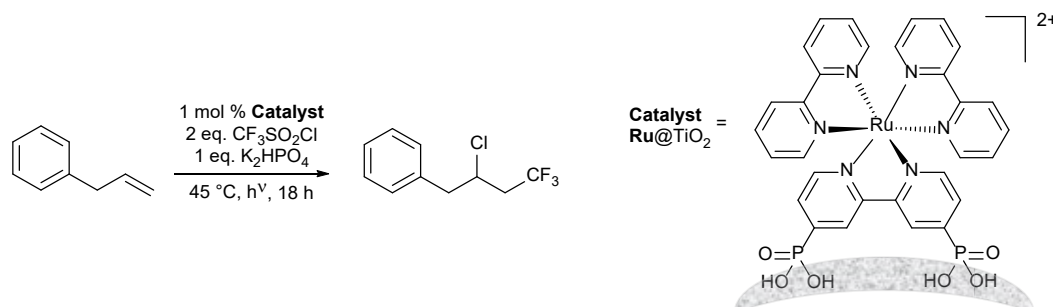
conversion of allylbenzene, using either a $[\text{Cu}(\text{dap})_2]\text{Cl}$ catalyst together with 550 nm light to primarily form 4,4,4-trifluoro-1-phenylbutan-2-sulfonyl chloride with a 86% yield after column chromatography purification, or a $[\text{Ru}(\text{bpy})_3]\text{Cl}_2$ catalyst together with 455 nm light to form (2-chloro-4,4,4,-trifluorobutyl)benzene with a 84% yield after column chromatography. K_2HPO_4 was used as a weak base. The reaction was sealed within a glovebox and then removed.

Scheme 6: Ruthenium-catalysed ATRA.^{163,164}

By modifying a ligand in either of these catalysts with a phosphonic acid anchoring group, it would be possible to test the feasibility to perform this reaction using f-NPs immobilized catalysts. Considering the reaction in Scheme 6, it was decided to focus on the ruthenium(II)-containing catalyst and prepare $\text{Ru}@\text{TiO}_2$ since introducing a phosphonic acid group to a bpy domain would be rather trivial compared to modifying a dap ligand. Scheme 7 shows the reaction conditions and photocatalyst studied in this section. In analogy to the literature reactions,^{163,164} the reaction of allylbenzene with $\text{CF}_3\text{SO}_2\text{Cl}$ was targeted and $\text{Ru}@\text{TiO}_2$ NPs (see Scheme 7) were used as a photocatalyst and K_2HPO_4 as a weak base to form (2-chloro-4,4,4,-trifluorobutyl)benzene under blue light and elevated temperature (45 °C).

The photocatalytic $\text{Ru}@\text{TiO}_2$ NPs were already being studied in this thesis as described in **Chapter V**. The procedure for the preparation of $\text{Ru}@\text{TiO}_2$ NPs is described in **Chapter V** but it is also given in **Section 3.4.1** of this Chapter for convenience.

Figure 14 shows that, based on ^1H NMR spectroscopy, the starting material was completely consumed under the reaction conditions as indicated by the disappearance of the allylic protons. The complete consumption of the starting material was certainly astonishing, but detailed interpretation of the data was extremely difficult. The products even after silica plug filtration were a combination of many compounds as confirmed in the $^{19}\text{F}\{^1\text{H}\}$ NMR spectrum which showed at least 30 peaks. Possibilities for the ^{19}F signals could be a dimerization of the starting material leading to a product with several isomers or CF_3 addition at different positions in the starting material.



Scheme 7: Ruthenium-catalysed ATRA.

Further, investigations to understand if the catalyst caused this behaviour alone could have been done by running two test reactions. These were (i) let the starting material run under the reaction conditions with just

the catalyst and, (ii) let the reaction run with all components minus the catalyst. This would have provided evidence to the activity of the heterogeneous catalyst. Unfortunately, the reaction would remain very unpredictable, hence it was decided to abandon this project.

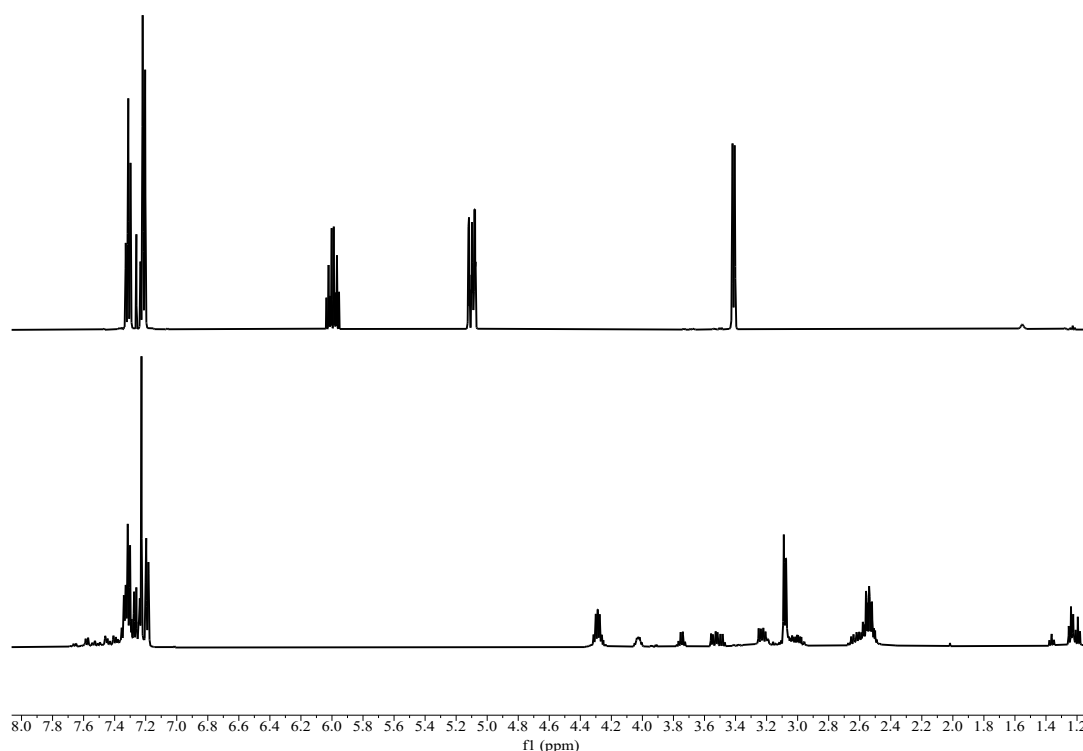
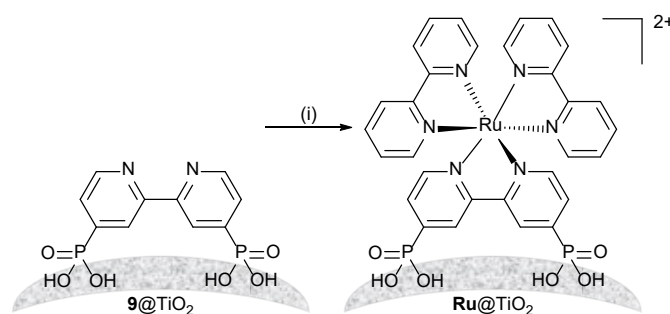


Figure 14: ^1H NMR (500 MHz, CDCl_3 298 K) spectrum of allylbenzene (starting material) (top), Reaction products measured after Section 3.4.2 (bottom). Chemical shifts in δ/ppm .

3.4.1 Experimental $\text{Ru}@\text{TiO}_2$



Scheme 8: Assembly of ruthenium(II) metal complex ($\text{Ru}@\text{TiO}_2$) starting from NPs functionalized with **9**. Conditions: (i) $\text{RuCl}_3 \cdot 3\text{H}_2\text{O}$, bpy, $\text{EtOH}:\text{H}_2\text{O}$, 160°C , 1 h autoclave.

The metal complex was formed directly on the NP surface (Scheme 8). $\mathbf{9}@\text{TiO}_2$ (45.9 mg), $\text{RuCl}_3 \cdot 3\text{H}_2\text{O}$ (1.03 mg, $3.94 \mu\text{mol}$) and 2,2'-bipyridine (1.56 mg, $10.0 \mu\text{mol}$) were added to a vial. H_2O (5.0 mL) and EtOH (3.0 mL) were added and the mixture was thoroughly dispersed using sonication and stirring. The suspension was transferred to an autoclave with a PTFE liner with additional EtOH (2.0 mL). The autoclave was sealed and then heated in an oven with heating rate of $320^\circ\text{C}/\text{h}$ to 160°C . The autoclave was left at 160°C for 1 h. After cooling, the autoclave was opened and the suspension was centrifuged (20 min, 7000 rpm). The resulting NPs were washed with H_2O ($3 \times 10 \text{ mL}$) and EtOH ($1 \times 10 \text{ mL}$) and dried under high vacuum. $\text{Ru}@\text{TiO}_2$ was isolated as a dark orange powder. ^1H NMR spectroscopy, MALDI mass spectrometry, TGA-MS, FTIR spectroscopy, ICP-MS and solid-state absorption spectroscopy were performed on the NPs. TGA: weight loss / %, 1.5 ($<380^\circ\text{C}$), 4.6 ($380 - 900^\circ\text{C}$). TGA-MS: amu, 18 ($<380^\circ\text{C}$), 18, 44

(380 – 900 °C). FTIR spectroscopy: 1640, 1604, 1465, 1447, 1423, 1398, 1156 and 1049 cm^{-1} . ICP-MS: ruthenium present. Solid-state absorption spectroscopy: 400 – 490 nm, 490 – 700 nm (broad). MALDI m/z : 414.1 $[\text{Ru}(\text{bpy})_2]^+$ (calc. 414.0), 535.1 $[\text{Ru}(\mathbf{9}) + \text{TiO}_2 + \text{K} - 2 \text{H}]^+$ (calc. 534.8), 570.1 $[\text{Ru}(\mathbf{9})(\text{bpy}) - 4 \text{H}]^+$ (calc. 569.9), 602.1 $[\text{Ru}(\text{bpy})_2 + \text{CHCA} - \text{H}]^+$ (calc. 602.1), 728.9 $[\text{Ru}(\mathbf{9})(\text{bpy})_2 - \text{H}]^+$ (calc. 729.0).

3.4.2 Experimental photoredox-catalysed atom-transfer radical addition using $\text{Ru}@\text{TiO}_2$

Dry MeCN (2.5 mL), allylbenzene (0.10 mL, 0.75 mmol, 1.0 eq.), $\text{CF}_3\text{SO}_2\text{Cl}$ (254 mg, 1.51 mmol, 2.0 eq.), K_2HPO_4 (132 mg, 0.758 mmol, 1.0 eq.) and $\text{Ru}@\text{TiO}_2$ (89.4 mg, 1 mol%) were added to a dried reaction tube in a glovebox. The mixture was removed from the glovebox, heated to 45 °C and irradiated with a blue LED (470 nm) for 24 h. The suspension was filtered through an Et_2O pre-wetted pipette silica plug. The plug was washed with additional Et_2O (15 mL) and the concentrated liquid was analysed using ^1H and ^{19}F NMR spectroscopies.

3.5 Conclusion

This Chapter showed several attempts to transfer literature homogeneous catalytic reactions onto TiO_2 f-NPs. It showed that in many cases, transferring reactions from homogeneous to heterogenous conditions can bring new and unexpected challenges. Although the projects in this Chapter did not yield publishable results, they helped immensely in understanding the limitations of the systems, but more importantly, they aided the development of techniques for analysis of the NP-supported systems. Knowing these limitations and methods was crucial to finding suitable candidates for future projects.

The methods learned included (i) forming the metal complex catalyst directly on the NP surface instead of utilising an in-situ approach, (ii) testing metal-to-ligand ratios that might be beneficial and (iii) more cautiously considering the impact of different ligand functional groups. The formation of a surface-supported metal complex using $\mathbf{3}@\text{TiO}_2$ NPs as a surface-bound ligand requires extended reaction times and reaction conditions compared to those optimised for related ‘free’ metal complexes. This was also reported in **Chapter II** when it was found that metal complex formation could be critically dependent upon the solvent, and often required several minutes while the homogeneous counterpart was almost instantaneous. Hence, identical experimental adaptation from homogeneous to NP systems is often unsuccessful. Ignoring this important point in favour of easier, faster experiment setups can be disadvantageous. Further, NP surface conditions are very difficult to precisely characterize especially when functionalization takes place. Ligand orientation, surface coverage, anchor binding and metal complex formation are parameters that are difficult to characterize. Hence, it is difficult to predict the activity of the catalyst during a reaction.

One potential problem identified in this Chapter was that TiO_2 NPs can exhibit large amounts of surface-adsorbed and chemisorbed water which created problems.^{17,155} Hence, catalytic processes in which it is crucial to avoid exposure to water and redox-related species such as dioxygen should not be investigated. While this might sound very limiting, “green” catalytic systems that can tolerate water and air are of increasing popularity and importance.¹⁶⁵ Investing time in transforming these systems onto a heterogeneous platform to take benefit from their advantages is of significance.

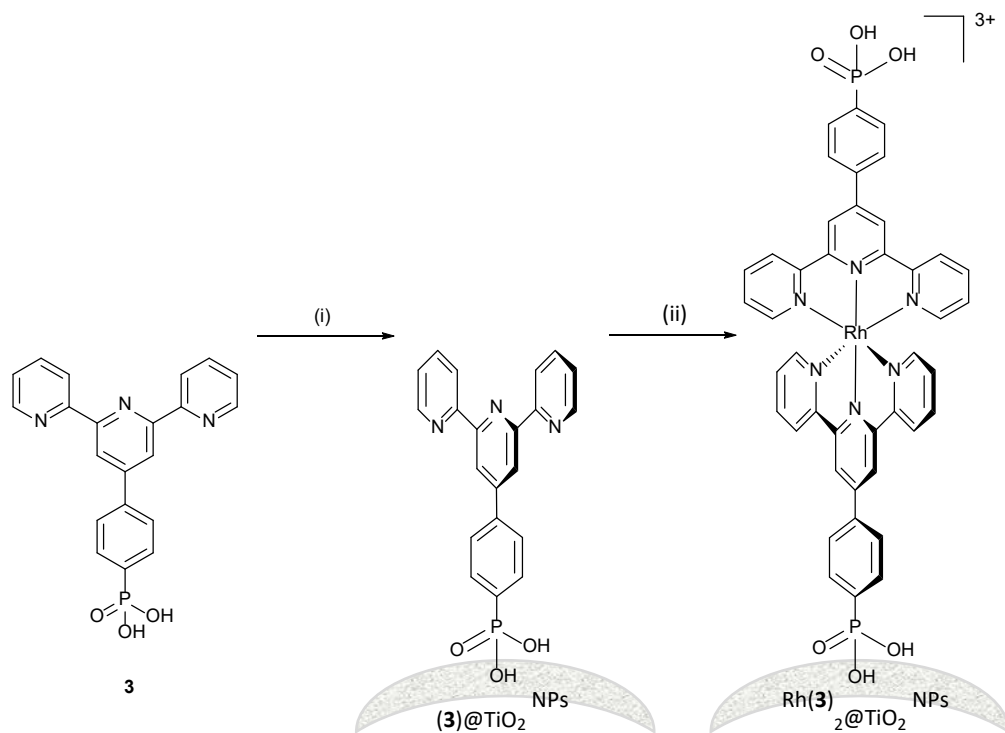
CHAPTER IV: TURNING OVER ON STICKY BALLS

PREPARATION AND CATALYTIC STUDIES OF SURFACE-FUNCTIONALIZED TiO₂ NANOPARTICLES

4.1 Summary

The limited success with transferring catalyst activity to f-NPs reported in **Chapter III** indicated that moisture-sensitive reactions could be problematic with the f-NPs. Hence, a new catalysed reaction was chosen that could be performed in water and under air and which would have a better chance of success using the NP platform. Catalytic reactions using $[\text{Rh}_2\text{Cl}_2(\mu\text{-OAc})(\text{tpy})_2]^+$ reported by Wang et al. seemed appealing because they were active under aqueous conditions.¹⁶⁵ However, it was challenging to form this complex on an NP surface.

The paper that resulted from this project²³ took a slightly unexpected turn as an analogous complex to $[\text{Rh}_2\text{Cl}_2(\mu\text{-OAc})(\text{tpy})_2]^+$ using anchoring ligand **3** (shown in Scheme 9) could not be formed. Instead of the rhodium dimer, the homoleptic complex $[\text{Rh}(\mathbf{3})_2]\text{Cl}_3$ was isolated in solution. This complex was then resynthesized by a more straightforward method using $\text{RhCl}_3 \cdot 3\text{H}_2\text{O}$ instead of $[\text{Rh}_2(\mu\text{-OAc})_4(\text{H}_2\text{O})_2]$. $[\text{Rh}(\mathbf{3})_2]\text{Cl}_3$ was shown to be able to homogeneously catalyse the intended alcohol oxidation and was able to bind to the NPs.¹⁷ Hence, $[\text{Rh}(\mathbf{3})_2]\text{Cl}_3$ was a primary candidate to use for proof-of-principle experiments even if it exhibited lower catalytic activity than $[\text{Rh}_2\text{Cl}_2(\mu\text{-OAc})(\text{tpy})_2]^+$.



Scheme 9: Anchoring ligand **3**, functionalization and complexation with (i) being NPs for 3 h in a microwave reactor at 130 °C in H₂O and (ii) being RhCl₃·3H₂O for 5 h at reflux (95 °C) in H₂O:EtOH.

The investigation was initiated with the formation of the complex on the TiO₂ NP surface using **3**@TiO₂ NPs. The direct functionalization with [Rh(**3**)₂]Cl₃ might have been possible but since the ligand functionalization with **3** had already been established, a stepwise approach was chosen. The resulting Rh(**3**)₂@TiO₂ NPs (shown in Scheme 9) were used to compare their catalytic activity in contrast to the homogeneous counterpart. It was confirmed that catalytic activity was not lost upon surface-binding. The stability of Rh(**3**)₂@TiO₂ NPs was remarkable as they were able to withstand reaction temperatures of up to 100 °C for 24 days without degradation. Reaction kinetics and recyclability of the NP-supported catalyst were followed using ¹H NMR spectroscopy.

The f-NPs were characterized using solid-state absorption spectroscopy, TGA-MS, MALDI, ¹H NMR and FTIR spectroscopies. The single crystal structures of [Rh(**3**)₂][NO₃]₃·1.25[H₃O][NO₃]₂·2.75H₂O and of a phosphonate ester derivative **10** were determined. The table of contents illustration is given in Figure 15 and showed a very simplified version of the overall process described.

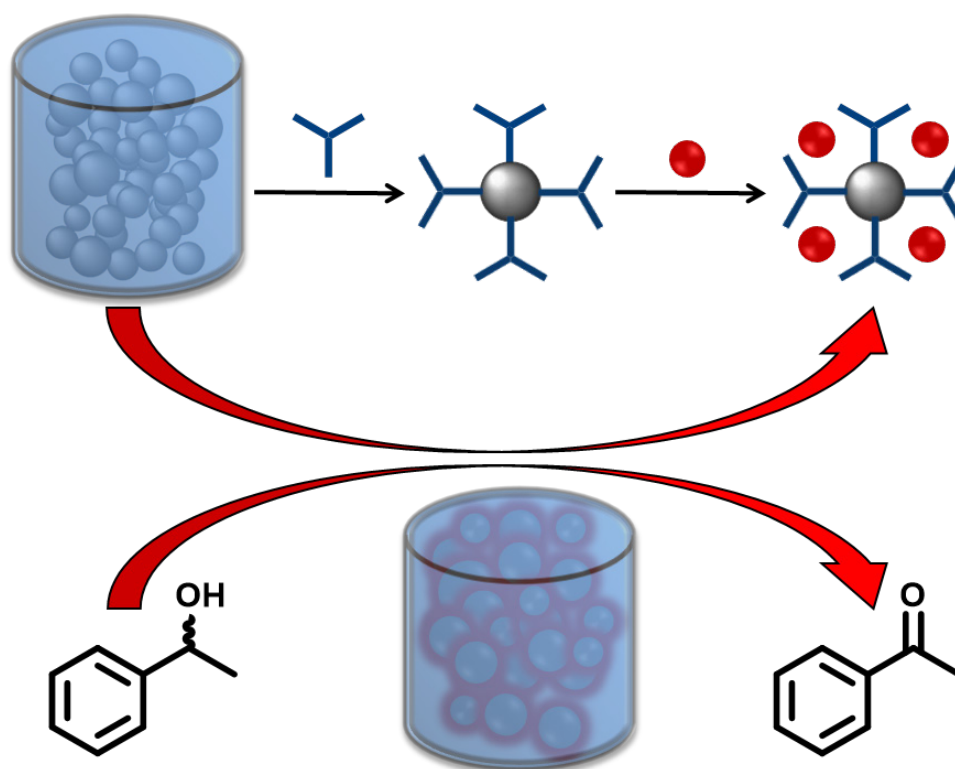



Figure 15: Table of contents image of the publication for Chapter IV.²³


 Cite this: *RSC Adv.*, 2021, 11, 5537

Turning over on sticky balls: preparation and catalytic studies of surface-functionalized TiO₂ nanoparticles†

 Sven A. Freimann,  Alessandro Prescimone,  Catherine E. Housecroft  and Edwin C. Constable *

We have investigated the reactivity of rhodium(III) complex-functionalized TiO₂ nanoparticles and demonstrate a proof-of-principle study of their catalytic activity in an alcohol oxidation carried out under aqueous conditions water in air. TiO₂ nanoparticles (NPs) have been treated with (4-((2,2':6',2''-terpyridin)-4'-yl)phenyl)phosphonic acid, **1**, to give the functionalized NPs (**1**)@TiO₂. Reaction between (**1**)@TiO₂ NPs and either RhCl₃·3H₂O or [Rh₂(μ-OAc)₄(H₂O)₂] produced the rhodium(III) complex-functionalized NPs Rh(**1**)₂@TiO₂. The functionalized NPs were characterized using thermogravimetric analysis (TGA), matrix-assisted laser desorption ionization (MALDI) mass spectrometry, ¹H NMR and FT-IR spectroscopies; the single crystal structures of [Rh(**1**)₂][NO₃]₃·1.25[H₃O][NO₃]·2.75H₂O and of a phosphonate ester derivative were determined. ¹H NMR spectroscopy was used to follow the reaction kinetics and to assess the recyclability of the NP-supported catalyst. The catalytic activity of the Rh(**1**)₂@TiO₂ NPs was compared to that of a homogeneous system containing [Rh(**1**)₂]³⁺, confirming that no catalytic activity was lost upon surface-binding. Rh(**1**)₂@TiO₂ NPs were able to withstand reaction temperatures of up to 100 °C for 24 days without degradation.

 Received 2nd November 2020
 Accepted 22nd January 2021

DOI: 10.1039/d0ra09319j

rsc.li/rsc-advances

Introduction

In general, catalytic processes are categorized as homogeneous or heterogeneous. Homogeneous catalysts have the advantage that all of the catalytic centres are potentially active, whereas in heterogeneous catalysts only the surface catalytic sites of solid phases are active as interior sites are inactive.¹ With solid phase heterogeneous catalysts, reaction only takes place at the interface rather than in the bulk of the reactant volume. On the other hand, it is often easier to separate the products of heterogeneous catalysis from the spent catalyst than in the case of homogeneous catalysis.^{2,3} Heterogeneous catalysts also have significant benefits in terms of catalyst recovery, a feature gaining increasing environmental and economic importance.

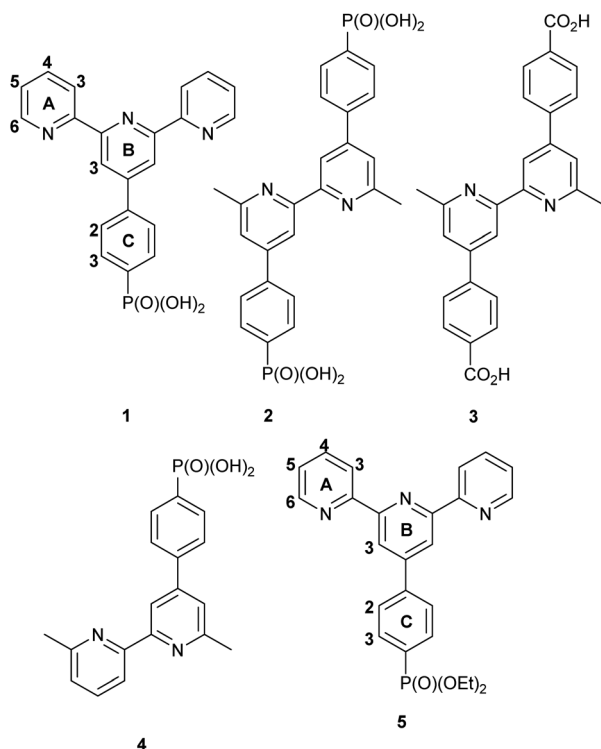
Nanoparticle (NP) immobilized catalysts have the potential of bridging the gap between these two extreme types of catalysis. Firstly, NPs exhibit greater surface-to-volume ratios than bulk heterogeneous catalysts and the catalyst loading capacity, catalytic activity and turnover will be enhanced, in particular the catalytic site-to-volume ratio will be high.⁴ Secondly, the ability to disperse NPs in solution gives some of the benefits of homogeneous catalysts. NP-supported catalysts have attracted great interest and offer already outstanding diversity and range in the chemical and pharmaceutical field.⁵⁻⁷

The advantages of NP supported catalysts have been demonstrated for a number of key reactions. For the Suzuki–Miyaura coupling reaction, palladium-decorated benzene-1,2-diamine-functionalized Fe₃O₄/SiO₂ magnetic NPs were utilized and showed excellent yields within short reaction times.¹ Gold NP-supported ruthenium catalysts have been used for ring-opening metathesis polymerization of bicyclo[2.2.1]hept-2-ene (norbornene) and show a higher activity than the unsupported counterparts.⁸ Nickel NP-based catalysts were active in the steam–reformation reaction of methane showing excellent conversion, H₂ selectivity and thermal stability.⁹ These reactions often make use of valuable and rare elements that cannot be efficiently recovered in the case of homogeneous catalysis. Recyclability of a catalyst is essential and conventional heterogeneous catalysts have the benefit that they can be easily recovered compared to homogeneous catalysts. Dispersed NPs are more challenging to separate than conventional

Department of Chemistry, University of Basel, BPR 1096, Mattenstrasse 24a, CH-4058 Basel, Switzerland. E-mail: edwin.constable@unibas.ch

† Electronic supplementary information (ESI) available: Fig. S1–S2: Mass and ¹H NMR spectra of [Rh(**1**)₂]Cl₃; Fig. S3: Precipitation of AgCl from [Rh(**1**)₂]Cl₃; Fig. S4–S13: Mass, ¹H NMR and 2D NMR spectra of [Rh(**1**)₂]Cl₃; Fig. S14–S21: ¹H NMR, 2D NMR, solution absorption spectra and ORTEP representation of [Rh(**5**)₂][PF₆]₃; Fig. S22–S27: solid-state IR and absorption spectra, TGA curves and Mass spectra of NP-[Rh(**1**)₂]³⁺; Fig. S28 and S29: ¹H NMR and solid-state IR comparison spectra, Fig. S30 and S31 TGA curves from commercial NPs and (**1**)@TiO₂ NPs, Fig. S32–S35: Mass and solid-state IR spectra of [Rh(**5**)₂][PF₆]₃; Fig. S36: ¹H NMR spectrum of [Rh(**1**)₂]Cl₃. CCDC 2040345 and 2025772. For ESI and crystallographic data in CIF or other electronic format see DOI: 10.1039/d0ra09319j





Scheme 1 Structures of compounds 1–5.

heterogeneous catalysts but the recoverability is still greater than with most homogenous catalysts. Furthermore, NPs can be modified to boost recoverability by introducing additional characteristics such as magnetic properties.

The benefits of NPs are well-established in the oxidation of alcohols, a key step in the synthesis of many organic compounds.⁷ The transformation of alcohols to aldehydes, ketones or carboxylic acids generally needs stoichiometric quantities of hazardous, environmentally damaging and toxic oxidants such as chromium trioxide, dichromate, permanganate and chromic acid.¹⁰

We have recently demonstrated¹⁴ the functionalization of TiO₂ NPs with ligands **1**, **2**, **3** and **4** (see Scheme 1) which bind to the metal oxide surface through their phosphonate or phosphonic acid groups and we were interested in investigating the activity of complexes incorporating these surface-bound ligands. We report here the assembly of surface-bound rhodium complexes of ligand **1** related to [Rh₂Cl₂(μ-OAc)(tpy)₂]⁺ reported by Wang *et al.*¹² We compare the catalytic behaviour of functionalized TiO₂ NPs to the homogeneous catalytic performance of [Rh(1)₂]Cl₃ and [Rh(5)₂][PF₆]₃. We have also investigated the kinetics of these reactions, the recyclability of the NP catalyst over 5 cycles, and the influence of the concentration of base on the catalytic activity of the functionalized nanoparticles.

Experimental

General

Instrumentation details are given in the ESI.†

Ligands **1** and **5** (Scheme 1),¹³ were prepared according to the literature and their spectroscopic data matched those

previously reported. TiO₂ NP activation and functionalization with ligand **1** were carried out according to our previously published procedure.¹¹ MALDI mass spectra were recorded using α-cyano-4-hydroxycinnamic acid (CHCA) as the matrix.

[Rh₂(μ-OAc)₄(H₂O)₂] and *rac*-(1*R*)-1-phenylethanol were purchased from Acros Organics and Sigma Aldrich respectively. RhCl₃·3H₂O was purchased from Johnson Matthey, Materials Technology UK. Microwave vials (5 mL and 20 mL) were from Biotage and were selected depending on the required solvent volume.

TiO₂ NPs (AEROXIDE TiO₂ P25) were purchased from Evonik Industries. The spherical NPs have an average radius of 10.5 nm (ref. 14) and an average surface area-to-volume ratio of 28%. The number of equivalents of NPs is defined as 0.28 × the total number of TiO₂ formula equivalents in the mass given, *i.e.* the effective surface concentration of TiO₂.¹¹ Similarly, when clarifying equivalents or mmol of functionalized NPs, it refers to the estimated amount of ligand or complex bound to the surface.

Activation of commercial P25 TiO₂ NPs

The commercial NPs were activated as previously described¹¹ but the procedure was scaled up as follows. Commercial P25 TiO₂ NPs (2.00 g) were dispersed by sonication for 15 min in dilute aqueous HNO₃ (30 mL, 3 M). The mixture was then stirred for 30 min. The NPs were separated from the acid by centrifugation (10 min, 9000 rpm) and washed once with milliQ water (30 mL). The NPs were again dispersed in milliQ water (20 mL) through sonication for 10 min and the suspension was then stirred overnight. The NPs were separated by centrifugation (10 min, 9000 rpm) and washed with milliQ water (2 × 20 mL). The activated NPs (1.85 g) were stored in a sealed vial under N₂ after drying over high vacuum.

Preparation of (1)@TiO₂ NPs

The functionalization was done as previously reported¹¹ but the procedure was scaled up as follows. Ligand **1** (29.2 mg, 0.075 mmol, 1 eq.) and milliQ water (18 mL) were added to a microwave vial and dispersed through sonication for 1 min. Activated TiO₂ NPs (660 mg, 30.8 TiO₂ eq.) were added to the solution and the mixture was dispersed with sonication for 10 min. The microwave vial was sealed and the reaction mixture heated for 3 h at 130 °C in the microwave reactor. The (1)@TiO₂ NPs were separated from the solvent by centrifugation (30 min, 9000 rpm) after cooling to room temperature. The white (1)@TiO₂ NPs (674 mg) were stored in a sealed vial under N₂ after drying under high vacuum. For NMR measurements, (1)@TiO₂ NPs (5–10 mg) were dispersed in 500 μL D₂O in an NMR tube.

Attempted synthesis of [Rh₂(μ-OAc)(1)₂]Cl

Compound **1** (81.8 mg, 0.210 mmol, 2 eq.) was dispersed with NaCl (61.4 mg, 1.05 mmol, 10 eq.) through sonication for 10 min in ethanol (5 mL). [Rh₂(μ-OAc)₄(H₂O)₂] (50.2 mg, 0.105 mmol, 1 eq.) was added. Argon was bubbled through the suspension for 5 minutes while stirring. The suspension was stirred under argon at 80 °C for 18 h. The reaction mixture was allowed to cool down to room temperature and recrystallized



from water to yield a dark solid. The product analysed as $[\text{Rh}(\text{1})_2\text{Cl}_3]$ (71.9 mg, 0.0728 mmol, 69.3%). ^1H NMR (500 MHz, D_2O) δ/ppm : 9.31 (s, 4H, $\text{H}^{\text{B}3}$), 8.84 (d, $J = 8.1$ Hz, 4H, $\text{H}^{\text{A}3}$), 8.35 (ddd, 4H, $J = 8.9, 6.8, 1.5$ Hz, $\text{H}^{\text{A}4}$), 8.22–8.15 (m, 4H, $\text{H}^{\text{C}2}$), 8.11–8.05 (m, 4H, $\text{H}^{\text{C}3}$), 7.82 (d, $J = 5.6$ Hz, 4H, $\text{H}^{\text{A}6}$), 7.57 (ddd, $J = 7.3, 5.6, 1.5$ Hz, 4H, $\text{H}^{\text{A}5}$). ^1H NMR (500 MHz, TFA-*d*) δ/ppm : 9.27 (s, 4H, $\text{H}^{\text{B}3}$), 8.90 (d, $J = 8.0$ Hz, 4H, $\text{H}^{\text{A}3}$), 8.34–8.27 (m, 12H, $\text{H}^{\text{A}4+\text{C}2+\text{C}3}$), 7.87 (d, $J = 5.7$ Hz, 4H, $\text{H}^{\text{A}6}$), 7.59 (ddd, $J = 7.5, 5.7, 1.3$ Hz, 4H, $\text{H}^{\text{A}5}$). $^{13}\text{C}\{^1\text{H}\}$ NMR (126 MHz, TFA-*d*) δ/ppm : 156.7 ($\text{C}^{\text{B}4}$), 156.6 ($\text{C}^{\text{A}2}$), 154.3, ($\text{C}^{\text{B}2}$) 152.1 ($\text{C}^{\text{A}6}$), 143.4 ($\text{C}^{\text{A}4}$), 138.6 ($\text{C}^{\text{C}1}$), 132.7 ($\text{C}^{\text{C}3}$), 132.0 ($\text{C}^{\text{C}4}$), 130.8 ($\text{C}^{\text{A}5}$), 128.0 ($\text{C}^{\text{C}2}$), 127.8 ($\text{C}^{\text{A}3}$), 124.8 ($\text{C}^{\text{B}3}$). MALDI: m/z 390.1 $[(1) + \text{H}]^+$ (calc. 390.1), 492.0 $[\text{Rh}(1)]^+$ (calc. 492.0), 681.0 $[\text{Rh}(1) + \text{CHCA}]^+$ (calc. 681.0), 881.0 $[\text{Rh}(1)_2]^+$ (calc. 881.1), 903.0 $[\text{Rh}(1)((1)\text{-H})\text{Na}]^+$ (calc. 903.1).

Synthesis of $[\text{Rh}(1)_2]\text{Cl}_3$

$[\text{Rh}(1)_2]\text{Cl}_3$ was prepared in an analogous manner to $[\text{Rh}(4'\text{-Phtpy})_2][\text{PF}_6]_3$.¹⁵ Ligand 1 (300 mg, 0.771 mmol, 2 eq.) was dispersed through sonication for 10 min in ethanol: water (1 : 1, 50 mL). $\text{RhCl}_3 \cdot 3\text{H}_2\text{O}$ (101 mg, 0.384 mmol, 1 eq.) was added. The solution was stirred at reflux (95 °C) for 5 h. The reaction mixture was allowed to cool down to room temperature and a precipitate formed which was filtered off and washed with water (3 × 10 mL), ethanol (3 × 10 mL) and Et_2O (3 × 10 mL). $[\text{Rh}(1)_2]\text{Cl}_3$ (285 mg, 0.288 mmol, 75.0%) was collected as a black solid. ^1H NMR (500 MHz, D_2O) δ/ppm : 9.31 (s, 4H, $\text{H}^{\text{B}3}$), 8.84 (d, $J = 8.1$ Hz, 4H, $\text{H}^{\text{A}3}$), 8.35 (ddd, 4H, $J = 8.1, 5.6, 1.4$ Hz, $\text{H}^{\text{A}4}$), 8.22–8.16 (m, 4H, $\text{H}^{\text{C}2}$), 8.12–8.04 (m, 4H, $\text{H}^{\text{C}3}$), 7.82 (d, $J = 5.6$ Hz, 4H, $\text{H}^{\text{A}6}$), 7.57 (ddd, $J = 7.5, 5.7, 1.4$ Hz, 4H, $\text{H}^{\text{A}5}$). ^1H NMR (500 MHz, TFA-*d*) δ/ppm : 9.31 (s, 4H, $\text{H}^{\text{B}3}$), 8.94 (d, $J = 8.0$ Hz, 4H, $\text{H}^{\text{A}3}$), 8.41–8.29 (m, 12H, $\text{H}^{\text{A}4+\text{C}2+\text{C}3}$), 8.01 (d, $J = 5.5$ Hz, 4H, $\text{H}^{\text{A}6}$), 7.64 (dd, $J = 8.0, 5.6, 1.4$ Hz, 4H, $\text{H}^{\text{A}5}$). $^{13}\text{C}\{^1\text{H}\}$ NMR (126 MHz, TFA-*d*) δ/ppm : 159.1 ($\text{C}^{\text{B}4}$), 158.9 ($\text{C}^{\text{A}2}$), 156.4, ($\text{C}^{\text{B}2}$) 154.5 ($\text{C}^{\text{A}6}$), 145.5 ($\text{C}^{\text{A}4}$), 141.2 ($\text{C}^{\text{C}1}$), 134.9 (d, $J_{\text{PC}} = 11.4$ Hz, $\text{C}^{\text{C}3}$), 133.1 (d, $J_{\text{PC}} = 194$ Hz, $\text{C}^{\text{C}4}$), 132.9 ($\text{C}^{\text{A}5}$), 130.3 (d, $J_{\text{PC}} = 16.4$ Hz, $\text{C}^{\text{C}2}$), 130.0 ($\text{C}^{\text{A}3}$), 127.3 ($\text{C}^{\text{B}3}$). MALDI: m/z 390.2 $[(1) + \text{H}]^+$ (calc. 390.1), 492.0 $[\text{Rh}(1)]^+$ (calc. 492.0), 527.0 $[\text{Rh}(1) + \text{Cl}]^+$ (calc. 527.0), 681.1 $[\text{Rh}(1) + \text{CHCA}]^+$ (calc. 681.0), 881.1 $[\text{Rh}(1)_2]^+$ (calc. 881.1), 903.2 $[\text{Rh}(1)((1)\text{-H}) + \text{Na}]^+$ (calc. 903.1). Found C 48.85, H 3.54, N 7.99; $\text{C}_{42}\text{H}_{38}\text{Cl}_3\text{N}_6\text{O}_9\text{P}_2\text{Rh}$ ($[\text{Rh}_2]\text{Cl}_3 \cdot 3\text{H}_2\text{O}$), requires C 48.41, H 3.68, N 8.07.

Synthesis of $[\text{Rh}(5)_2][\text{PF}_6]_3$

$[\text{Rh}(5)_2]\text{Cl}_3$ was prepared in an analogous manner to $[\text{Rh}(4'\text{-Phtpy})_2][\text{PF}_6]_3$.¹⁵ Compound 5 (150 mg, 0.337 mmol, 2 eq.) was dispersed through sonication for 10 min in ethanol : water (1 : 1, 35 mL). $\text{RhCl}_3 \cdot 3\text{H}_2\text{O}$ (44.2 mg, 0.168 mmol, 1 eq.) was added. The solution was stirred at reflux (95 °C) for 5 h. The reaction mixture was allowed to cool down to room temperature. The solution was filtered and NH_4PF_6 (82.2 mg, 0.504 mmol, 3 eq.) was added to the filtrate under stirring. A precipitate formed which was filtered off and washed with cold water (3 × 1 mL), cold EtOH (3 × 1 mL) and cold Et_2O (3 × 1 mL). $[\text{Rh}(5)_2][\text{PF}_6]_3$ (198 mg, 0.139 mmol, 82.7%) was collected as a pale pink solid. ^1H NMR (500 MHz, CD_3CN) δ/ppm : 9.14 (s, 4H, $\text{H}^{\text{B}3}$), 8.77 (dd, $J = 8.1, 1.4$ Hz, 4H, $\text{H}^{\text{A}3}$), 8.36–8.28 (m, 8H, $\text{H}^{\text{A}4+\text{C}2}$), 8.21–8.15 (m, 4H, $\text{H}^{\text{C}3}$), 7.75 (d, $J = 5.6$ Hz, 4H,

$\text{H}^{\text{A}6}$), 7.53 (ddd, $J = 7.4, 5.6, 1.4$ Hz, 4H, $\text{H}^{\text{A}5}$). $^{13}\text{C}\{^1\text{H}\}$ NMR (126 MHz, CD_3CN) δ/ppm : 157.7 ($\text{C}^{\text{A}2}$), 156.4 ($\text{C}^{\text{B}4}$), 154.9, ($\text{C}^{\text{B}2}$) 153.9 ($\text{C}^{\text{A}6}$), 143.8 ($\text{C}^{\text{A}4}$), 140.0 ($\text{C}^{\text{C}1}$), 133.7 (d, $J_{\text{PC}} = 9.9$ Hz, $\text{C}^{\text{C}3}$), 133.5 (d, $J_{\text{PC}} = 187$ Hz, $\text{C}^{\text{C}1}$), 131.2 ($\text{C}^{\text{A}5}$), 129.6 (d, $J_{\text{PC}} = 14.9$ Hz, $\text{C}^{\text{C}2}$), 128.6 ($\text{C}^{\text{A}3}$), 126.3 ($\text{C}^{\text{B}3}$), 63.4 (C^{A}), 16.7 (C^{B}). $^{31}\text{P}\{^1\text{H}\}$ NMR (200 MHz, CD_3CN) δ/ppm : 16.06 (s, 2P, $\text{P}(\text{O})(\text{OEt})_2$), −144.66 (heptet, $J_{\text{PF}} = 707$ Hz, 3P, $[\text{PF}_6]^-$). MALDI: m/z , 446.1 $[(5) + \text{H}]^+$ (calc. 446.2), 548.0 $[\text{Rh}(5)]^+$ (calc. 548.1), 737.1 $[\text{Rh}(5) + \text{CHCA}]^+$ (calc. 737.1) 993.1 $[\text{Rh}(5)_2]$ (calc. 993.2), 1283.9 $[\text{Rh}(5)_2 + (\text{PF}_6)_2]^+$ (calc. 1283.2). ESI-MS: negative mode: m/z 145.06 $[\text{PF}_6]^-$ (calc. 144.96); positive mode: 331.26 $[\text{Rh}(5)_2]^{3+}$ (calc. 331.07), 569.27 $[\text{Rh}(5)_2 + (\text{PF}_6)]^{2+}$ (calc. 569.09), 993.15 $[\text{Rh}(5)_2]^+$ (calc. 993.22), 1283.08 $[\text{Rh}(5)_2 + (\text{PF}_6)_2]^+$ (calc. 1283.14). HR ESI-MS: m/z , 331.0721 $[\text{Rh}(5)_2]^{3+}$ (calc. 331.0716), 496.1035 $[\text{Rh}(5)((5)\text{-H})]^{2+}$ (calc. 493.1038), 569.0895 $[\text{Rh}(5)_2 + (\text{PF}_6)]^{2+}$ (calc. 569.0898), 1283.1423 $[\text{Rh}(5)_2 + (\text{PF}_6)_2]^+$ (calc. 1283.1444). UV-VIS (MeCN, 2.25×10^{-5} mol dm^{-3} , λ/nm ($\epsilon/\text{dm}^3 \text{ mol}^{-1} \text{ cm}^{-1}$): 243 (39 600), 284 (sh, 53 500), 295 (60 500), 329 (35 400), 342 (sh, 28 500), 361 (17 400).

Crystallography

Single crystal data were collected on a Bruker APEX-II diffractometer (CuK α radiation) with data reduction, solution and refinement using the programs APEX,¹⁶ ShelXT,¹⁷ Olex2 (ref. 18) and ShelXL v. 2014/7.¹⁹ Structure analysis including the ORTEP representation, used CSD Mercury 2020.1.²⁰ In the structure of $[\text{Rh}(1)_2][\text{NO}_3]_3 \cdot 1.25[\text{H}_3\text{O}][\text{NO}_3] \cdot 2.75\text{H}_2\text{O}$, there are a large number of disordered water molecules, and one $[\text{NO}_3]^-$ position is partially occupied. For charge balance, $1.25\text{H}_2\text{O}$ were treated as $[\text{H}_3\text{O}]^+$; this is reasonable because crystals were grown from concentrated HNO_3 . In $[\text{Rh}(5)_2][\text{PF}_6]_3 \cdot \text{MeCN}$, due to high thermal motion, restraints were applied to two disordered ethoxy groups. Each phenylene ring was disordered and was modelled over two positions, 0.5 : 0.5 and 0.75 : 0.25 site occupancies, respectively. Each MeCN molecule was modelled with an occupancy of 0.5.

Crystal data for $[\text{Rh}(1)_2][\text{NO}_3]_3 \cdot 1.25[\text{H}_3\text{O}][\text{NO}_3] \cdot 2.75\text{H}_2\text{O}$. $\text{C}_{42}\text{H}_{41.25}\text{N}_{10.25}\text{O}_{22.75}\text{P}_2\text{Rh}$, $M_r = 1218.45$, brown block, triclinic, $P\bar{1}$, $a = 12.5277(7)$, $b = 14.3560(8)$, $c = 15.7458(9)$ Å, $\alpha = 91.845(2)^\circ$, $\beta = 110.580(2)^\circ$, $\gamma = 110.494(2)^\circ$, $V = 2444.1(2)$ Å³, $T = 150$ K, $Z = 2$, $\mu(\text{CuK}\alpha) = 4.300$ mm^{-1} . Total 23 158 reflections, 8879 unique ($R_{\text{int}} = 0.0238$). Refinement of 8743 reflections (712 parameters) with $I > 2\sigma(I)$ converged at final $R_1 = 0.0486$ (R_1 all data = 0.0490), $wR_2 = 0.1365$ (wR_2 all data = 0.1371), $\text{gof} = 1.085$. CCDC 2040345.

Crystal data for $[\text{Rh}(5)_2][\text{PF}_6]_3 \cdot \text{MeCN}$. $\text{C}_{52}\text{H}_{51}\text{F}_{18}\text{N}_7\text{O}_6\text{P}_5\text{Rh}$, $M_r = 1469.76$, colourless plate, triclinic, $P\bar{1}$, $a = 12.2477(7)$, $b = 14.0636(8)$, $c = 19.8182(11)$ Å, $\alpha = 73.903(4)^\circ$, $\beta = 83.442(4)^\circ$, $\gamma = 82.315(3)^\circ$, $V = 3239.6(3)$ Å³, $T = 150$ K, $Z = 2$, $\mu(\text{CuK}\alpha) = 4.223$ mm^{-1} . Total 37 630 reflections, 11 469 unique ($R_{\text{int}} = 0.0431$). Refinement of 9490 reflections (845 parameters) with $I > 2\sigma(I)$ converged at final $R_1 = 0.1061$ (R_1 all data = 0.1189), $wR_2 = 0.2968$ (wR_2 all data = 0.3092), $\text{gof} = 1.071$. CCDC 2025772.

Synthesis of $\text{Rh}(1)_2@ \text{TiO}_2$ NPs

Method 1. $(1)@ \text{TiO}_2$ NPs (440 mg, 0.05 mmol, 2 eq.) were dispersed through sonication for 10 min in ethanol: water (1 : 1,



5 mL). $\text{RhCl}_3 \cdot 3\text{H}_2\text{O}$ (6.58 mg, 0.0250 mmol, 1 eq.) was added. The suspension was stirred at reflux (95 °C) for 5 h. The reaction mixture was allowed to cool down to room temperature. The $\text{Rh}(\mathbf{1})_2@/\text{TiO}_2$ NPs were separated from the solvent by centrifugation (10 min, 9000 rpm) and then washed with water (2 × 8 mL) and ethanol (2 × 8 mL) and then dried under high vacuum yielding a light red powder (428 mg). $\text{Rh}(\mathbf{1})_2@/\text{TiO}_2$ NPs (5–10 mg) was dispersed in 500 μL D_2O in an NMR tube. MALDI spectrum of dried $\text{Rh}(\mathbf{1})_2@/\text{TiO}_2$ NPs: m/z 390.1 [(1) + H]⁺ (calc. 390.1), 492.0 [Rh(1)]⁺ (calc. 492.0), 527.0 [Rh(1) + Cl]⁺ (calc. 527.0), 681.1 [Rh(1) + CHCA]⁺ (calc. 681.0), 881.1 [Rh(1)₂]⁺ (calc. 881.1). Solid-state UV-VIS (λ/nm): 411, 608, 669.

Method 2. (1)@TiO₂ NPs (440 mg, 0.05 mmol, 2 eq.) were dispersed with NaCl (14.6 mg, 0.25 mmol, 10 eq.) through sonication for 10 min in ethanol (5 mL). [Rh₂(μ-OAc)₄(H₂O)₂] (12 mg, 0.0251 mmol, 1 eq.) was added. Argon was bubbled through the suspension for 5 min while stirring. The suspension was stirred under argon at 80 °C for 18 h. The reaction mixture was allowed to cool down to room temperature. The $\text{Rh}(\mathbf{1})_2@/\text{TiO}_2$ NPs were separated from the solvent by centrifugation (10 min, 9000 rpm) and then washed with water (2 × 8 mL) and ethanol (2 × 8 mL). The $\text{Rh}(\mathbf{1})_2@/\text{TiO}_2$ NPs were dried under high vacuum yielding a light brown powder (430 mg). $\text{Rh}(\mathbf{1})_2@/\text{TiO}_2$ NPs (5–10 mg) was dispersed in 500 μL D_2O in an NMR tube. MALDI spectrum of dried $\text{Rh}(\mathbf{1})_2@/\text{TiO}_2$ NPs: m/z 390.1 [(1) + H]⁺ (calc. 390.1), 492.1 [Rh(1)]⁺ (calc. 492.0), 527.1 [Rh(1) + Cl]⁺ (calc. 527.0), 681.1 [Rh(1) + CHCA]⁺ (calc. 681.0). Solid-state UV-VIS (λ/nm): 444, 539, 609, 664.

Oxidation of *rac*-(1R)-1-phenylethanol to acetophenone in water under air

$\text{Rh}(\mathbf{1})_2@/\text{TiO}_2$ NPs (72.7 mg, 0.5 mol%) and milliQ water (1.67 mL) were added to a microwave vial. The contents were sonicated (1 min) and then aqueous NaOH (25 mM, 0.331 mL) and *rac*-(1R)-1-phenylethanol (0.1 mL, 0.827 mmol, 1 eq.) were added to the suspension. The vial was sealed and the reaction mixture was heated to 100 °C for 24 h. A small amount of the reaction mixture (*ca.* 50 μL) was removed by syringe and dispersed in 500 μL D_2O in an NMR tube. ¹H NMR spectra were measured to determine product : reactant ratios. The NMR spectroscopic data revealed that after 18 h, the ratio of product to reactant was 1.0 : 5.7 (14.9% product). The sampling procedure was repeated with 24 h and 38 h reaction time yielding a ratio of 1 : 3.3 (23.2% product, Table S1†) and 1 : 2.9 (25.7% product) respectively. The procedure yielded similar conversions independent of the synthetic route of the catalytic NPs.

Recyclability of $\text{Rh}(\mathbf{1})_2@/\text{TiO}_2$ NPs

$\text{Rh}(\mathbf{1})_2@/\text{TiO}_2$ NPs (72.7 mg, 0.5 mol%) and milliQ water (1.67 mL) were added to a microwave vial. The suspension was sonicated (1 min) and then aqueous NaOH (25 mM, 0.331 mL) was added. The pH of the mixture was determined to be 7.8. *rac*-(1R)-1-Phenylethanol (0.1 mL, 0.827 mmol, 1 eq.) was added to the suspension after which the vial was sealed and the reaction

mixture heated to 100 °C for 24 h. After cooling, the reaction mixture was washed with Et₂O (6 × 3 mL). A small amount of the collected Et₂O fractions (*ca.* 50 μL) was removed by syringe and the solvent was evaporated. The residue was dissolved in 500 μL D_2O and added to an NMR tube. The ¹H NMR spectrum was measured to determine product : reactant ratios. The pH of the reaction mixture was measured using a pH electrode and adjusted to the initial value of 7.8 by adding aqueous NaOH (25 mM). The vial was resealed and the reaction mixture was heated again to 100 °C for 24 h. The reaction was performed with this procedure 5 times in total. The product conversions were as follows: 20.3, 20.1, 18.3, 20.9 and 19.9%.

Kinetics of oxidation

$\text{Rh}(\mathbf{1})_2@/\text{TiO}_2$ NPs (145.4 mg, 0.5 mol%) and D_2O (3.33 mL) were added into a microwave vial. The contents were sonicated (1 min) and then NaOH (25 mM in D_2O , 0.667 mL) and *rac*-(1R)-1-phenylethanol (0.2 mL, 1.65 mmol, 1 eq.) were added to the suspension. The vial was sealed and the reaction mixture was heated to 100 °C for two weeks (*ca.* 300 h). At varying time intervals, a small amount of the reaction mixture (*ca.* 50 μL) was removed by syringe and dispersed in 500 μL D_2O in an NMR tube. The ¹H NMR spectrum was recorded to determine the product : reactant ratios at any point. Overall, data for 27 points were recorded over 12 days.

Control experiment 1: catalyst influence on reaction rate

Activated NPs (72.7 mg) and milliQ water (1.67 mL) were added to a microwave vial. The contents were sonicated (1 min) and then aqueous NaOH (25 mM, 0.331 mL) and *rac*-(1R)-1-phenylethanol (0.1 mL, 0.827 mmol, 1 eq.) were added to the suspension. The vial was sealed and the reaction mixture was heated to 100 °C for 24 h. A small amount of the reaction mixture (*ca.* 50 μL) was removed by syringe and dispersed in 500 μL D_2O in an NMR tube. The ¹H NMR spectrum was recorded and revealed that no acetophenone had formed. Further control experiments were conducted using either unactivated commercial NPs, activated NPs, (1)@TiO₂ NPs or [Rh₂(μ-OAc)₄(H₂O)₂]. The control experiment using (1)@TiO₂ NPs and [Rh₂(μ-OAc)₄(H₂O)₂] showed 7% product conversion while all other experiments showed less than 1% product conversion after 24 hours (Table S1†).

Control experiment 2: temperature influence on reaction rate

$\text{Rh}(\mathbf{1})_2@/\text{TiO}_2$ NPs (72.7 mg, 0.5 mol%) and milliQ water (1.67 mL) were added to a microwave vial. The contents were sonicated (1 min) and then aqueous NaOH (25 mM, 0.331 mL) and *rac*-(1R)-1-phenylethanol (0.1 mL, 0.827 mmol, 1 eq.) were added to the suspension. The vial was sealed and the reaction mixture was left stirring at room temperature for 72 h. A small amount of the reaction mixture (*ca.* 50 μL) was removed by syringe and dispersed in 500 μL D_2O in an NMR tube. The ¹H NMR spectrum was recorded which revealed no acetophenone had formed (Table S1†).



Control experiment 3: NaOH influence on functionalization stability

Rh(1)₂@TiO₂ NPs (72.7 mg, 0.5 mol%) and milliQ water (1.67 mL) were added to a microwave vial. The contents were sonicated (1 min) and then aqueous NaOH (25 mM, 0.331 mL) was added to the suspension. The vial was sealed and the reaction mixture was heated to 100 °C for 72 h. The supernatant solution was separated from the NPs by centrifugation (30 min, 17 500 rpm). The supernatant solution was filtered and added into a separate microwave vial and *rac*-(1*R*)-1-phenylethanol (0.1 mL, 0.827 mmol, 1 eq.) was added to the solution. The vial was sealed and the reaction mixture was heated to 100 °C for 24 hours. A small amount of the reaction mixture (*ca.* 500 μL) was removed by syringe and dispersed in 500 μL D₂O in an NMR tube. The ¹H NMR spectrum was recorded and revealed that no acetophenone had formed. The separated NPs were added together with milliQ water (1.67 mL) into a separate microwave vial. The contents were sonicated (1 min) and then aqueous NaOH (25 mM, 0.331 mL) *rac*-(1*R*)-1-phenylethanol (0.1 mL, 0.827 mmol, 1 eq.) were added to the suspension. The vial was sealed and the reaction mixture was heated to 100 °C for 24 hours. A small amount of the reaction mixture (*ca.* 50 μL) was removed by syringe and dispersed in 500 μL D₂O in an NMR tube. The ¹H NMR spectrum was recorded and showed acetophenone had been formed. This experiment was repeated without any base and yielded the same result. The reaction using the separated supernatant solution did not show acetophenone formation (<1%) while the reaction containing the separated NPs showed normal product conversion (19.9%).

Control experiment 4: NaOH concentration influence on reaction rate

Rh(1)₂@TiO₂ NPs (72.7 mg, 0.5 mol%) and milliQ water (1.67 mL) were added to a microwave vial. The contents were sonicated (1 min) and then aqueous NaOH (25 mM, 0.331 mL) *rac*-(1*R*)-1-phenylethanol (0.1 mL, 0.827 mmol, 1 eq.) were added to the suspension. Simultaneously three other vials were prepared under the same conditions with different NaOH (0.331 mL, 50 mM, 0.25 M, 2.5 M) concentrations. The vials were sealed and the reaction mixtures were heated to 100 °C for 3 weeks. A small amount of each reaction mixture (*ca.* 50 μL) was removed from each vial by syringe and dispersed in 500 μL D₂O in separate NMR tubes. The ¹H NMR spectrum of each sample was recorded to determine the product : reactant ratios at any point. Overall, 11 data points were recorded over 24 days.

Control experiment 5: oxidation using free rhodium complexes

[Rh(1)₂]Cl₃ (3.79 mg, *ca.* 0.5 mol%) and milliQ water (1.67 mL) were added to a microwave vial. The contents were sonicated (1 min) and then aqueous NaOH (25 mM, 0.331 mL) and *rac*-(1*R*)-1-phenylethanol (0.1 mL, 0.827 mmol, 1 eq.) were added to the suspension. The vial was sealed and the reaction mixture was left stirring at 100 °C for 24 h. A small amount of the reaction mixture (*ca.* 50 μL) was removed by syringe and dispersed in 500

μL D₂O in an NMR tube. The NMR data revealed that after 24 h, the ratio of product to reactant was 1.0 : 5.3 (15.8% product, Table S1†). The procedure was repeated using [Rh(5)₂][PF₆]₃ and showed a ratio of product to reactant of 1.0 : 4.2 (19.2% product, Table S1†).

Control experiment 6: inert atmosphere and light influence on reaction rate

Four microwave vials were prepared to all of them Rh(1)₂@TiO₂ NPs (72.7 mg, 0.5 mol%) and milliQ water (1.67 mL) was added. The contents were sonicated (1 min) and then aqueous NaOH (25 mM, 0.331 mL) and *rac*-(1*R*)-1-phenylethanol (0.1 mL, 0.827 mmol, 1 eq.) were added to the suspensions. The suspensions in two vials were bubbled with Argon for 15 minutes. The vials were sealed and one under inert atmosphere and one under air were covered from light with alumina foil. Leading to vials having inert atmosphere, no light, inert atmosphere and no light, and a control with air not covered from light. The four vials were left stirring at 100 °C for 72 h. A small amount of each reaction mixture (*ca.* 50 μL) was removed by syringe and dispersed in 500 μL D₂O in separate NMR tubes. The NMR data revealed that after 72 h, the ratio of product to reactant for the control vial was 1.0 : 2.4 (29.3% product, Table S1†) while the ratio of product to reactant when using inert gas was 1.0 : 5.0 (16.5% product, Table S1†). Performing the reaction without light had no effects on the product formation.

Results and discussion

Choice of anchoring ligand and substrate

2,2':6',2''-Terpyridines (tpy) are well-established chelating ligands which undergo a conformational change from the equilibrium transoid-arrangement upon coordination to metal centres.²¹ The tpy metal-binding domain acts as a good σ-donor and a strong π-acceptor, making tpy ligands excellent candidates for the stabilization of low oxidation state metal centres. This leads to their applications in a wide range of homogeneous catalytic reactions involving metals such as Ni, Cu, Ru, Pd, Rh, Fe, Mg and Co.²²

The functionalization of metal chalcogenide NPs with carboxylic and phosphonic acids is well-established.^{23–32} We have extended surface-modification strategies developed for dye-sensitized solar cells to nanoparticles and have illustrated that TiO₂ NPs can be functionalized with bpy or tpy ligands bearing carboxylic or phosphonic acid anchoring units.¹¹ We further demonstrated the preferential binding of phosphonic acids over carboxylic acids, and the ability of ligand-functionalized NPs to complex metal ions such as copper(i) and iron(ii) to form robust coordination-complex functionalized NPs.¹¹

TiO₂ NPs have benefits beyond being able to strongly bind anchoring ligands (carboxylic or phosphonic acids): they comprise earth abundant elements, are relatively cheap, non-toxic, thermodynamically stable and temperature resistant. TiO₂ NPs can also be specifically prepared in a wide variety of



sizes and shapes. This makes them a desirable choice for further investigation as a substrate for catalysis.

One potential problem with TiO₂ NPs is that they can exhibit large amounts of surface-adsorbed water creating problems for catalytic processes in which it is crucial to avoid exposure to water and redox-related species such as dioxygen.^{11,22} It is therefore of significant interest to investigate catalytic systems that can tolerate both water and air.¹² These “green” conditions are in any case desirable. The rhodium(III) complexes selected for the present investigation are tolerant of both water and air.

Attempted synthesis of [Rh₂Cl₂(μ-OAc)(1)₂]Cl and synthesis of [Rh(1)₂]Cl₃

Wang and coworkers have reported the catalytic behaviour of the water-soluble complex [Rh₂Cl₂(μ-OAc)(tpy)₂]Cl in the dehydrogenation and oxidation of alcohols in aqueous aerobic conditions to carboxylic acids or ketones.¹² Our initial aim, was to prepare a TiO₂ NP surface-bound version of this catalyst containing [Rh₂Cl₂(μ-OAc)(1)₂]⁺. Before investigating the metallation of (1)@TiO₂ NP, we decided to prepare [Rh₂(μ-OAc)(1)₂Cl₂]Cl following the general procedure of Wang and coworkers, starting from [Rh₂(μ-OAc)₄(H₂O)₂] and **1** in the presence of NaCl in EtOH. A black product was isolated and the MALDI mass spectrum (Fig. S1†) showed peaks at *m/z* 492.0, 681.0, 881.1 and 903.0 corresponding to [Rh(1)]⁺, [Rh(1) + CHCA]⁺, [Rh(1)₂]⁺ and [Rh(1)((1)-H) + Na]⁺. No peaks assigned to acetato species were observed in the mass spectrum and the ¹H NMR spectrum (Fig. S2†) showed no signals arising from an acetate group.

A comparison of the ¹H NMR spectrum of **1** with that of the black product suggested the formation of a homoleptic [Rh(1)₂]³⁺ complex. The shift to lower frequency for the signal assigned to proton A6 (see Scheme 1) is consistent with this proton lying over the ring of a second tpy domain and the spectrum (which shows only one set of tpy signals) indicates the formation of a homoleptic bis(tpy) complex. We therefore concluded that the product was [Rh(1)₂]Cl₃. In order to confirm this proposal, we adapted the protocol described by Thomas and coworkers¹⁵ for the preparation of [Rh(4'-Phtpy)₂][PF₆]₃ to prepare [Rh(1)₂]Cl₃ from RhCl₃·3H₂O and **1**. The presence of chloride counter ion in the product was established by dissolving the compound in concentrated HNO₃ and adding a drop of silver nitrate which lead to the precipitation of white silver chloride (Fig. S3†). The MALDI mass spectrum of [Rh(1)₂]Cl₃ (Fig. S4†) was similar to that described above (Fig. S2†) with peaks at *m/z* 492.0, 527.0, 681.1, 881.1 and 903.2 arising from [Rh(1)]⁺, [Rh(1)Cl]⁺, [Rh(1) + CHCA]⁺, [Rh(1)₂]⁺ and [Rh(1)((1)-H) + Na]⁺. The ¹H and ¹³C NMR spectra of [Rh(1)₂]Cl₃ (Fig. S5 and S6†) were assigned using 2D methods (Fig. S7–S9†) and were identical to those of the product from the attempted synthesis of [Rh₂(μ-OAc)(1)₂Cl₂]Cl (Fig. S10–S13†). We speculate that the acidic phosphonic acid substituents on ligand **1** labilize the acetato ligands and prevent the isolation of [Rh₂Cl₂(μ-OAc)(1)₂]⁺.

The compound [Rh(1)₂]Cl₃ formed during the synthesis was insoluble in most solvents and could only be dissolved in

concentrated HNO₃ or in water under very basic conditions. This pH dependent solubility suggested the formation of a zwitterionic species in basic conditions.

Crystal structure of [Rh(1)₂][NO₃]₃·1.25[H₃O][NO₃]₃·2.75H₂O

Single crystals of [Rh(1)₂][NO₃]₃·1.25[H₃O][NO₃]₃·2.75H₂O grew from a solution of [Rh(1)₂]Cl₃ dissolved in a small amount of concentrated aqueous HNO₃ which, after the addition of water, was left to stand at room temperature (*ca.* 22 °C) for 4 weeks. The complex crystallizes in the triclinic space group *P* $\bar{1}$ and the single crystal structure confirmed the fully protonated phosphonic acid substituents. The crystal lattice contained a large number of disordered H₂O molecules, as well as [H₃O]⁺ and [NO₃]⁻ in addition to the nitrate ions required to balance the charge on the [Rh(1)₂]³⁺ cation. Because of the disorder, we focus only on the structure of the cation (Fig. 1a). An ORTEP

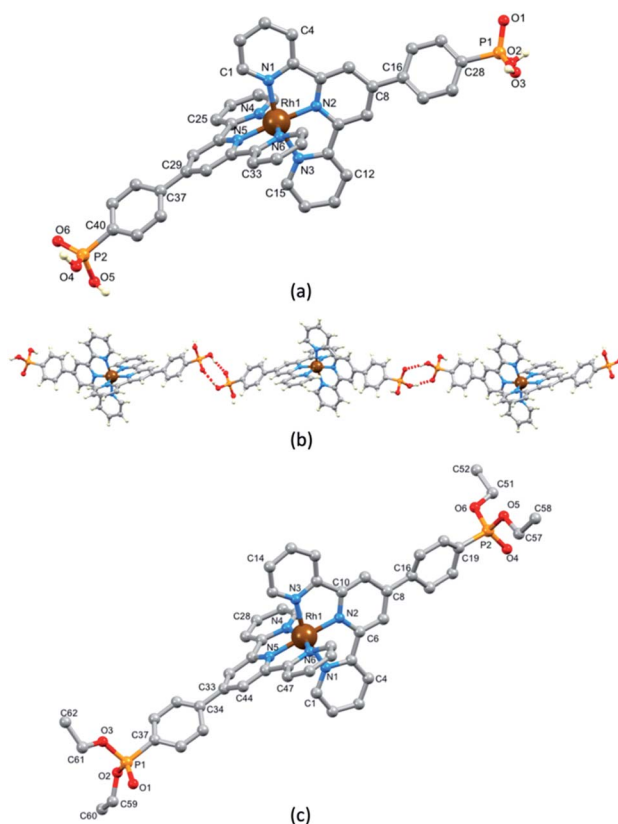


Fig. 1 (a) The structure of the [Rh(1)₂]³⁺ cation in the complex [Rh(1)₂][NO₃]₃·1.25[H₃O][NO₃]₃·2.75H₂O; H atoms except those in the phosphonic acid groups are omitted for clarity. Selected bond distances: Rh1–N1 = 2.047(3), Rh1–N2 = 1.962(3), Rh1–N3 = 2.055(3), Rh1–N4 = 2.055(3), Rh1–N5 = 1.964(3), Rh1–N6 = 2.043(3), P1–O1 = 1.501(3), P1–O2 = 1.544(3), P1–O3 = 1.552(3), P1–C28 = 1.786(4), P2–O4 = 1.550(3), P2–O5 = 1.546(4), P2–O6 = 1.489(3), P2–C40 = 1.800(4) Å. (b) Part of one hydrogen-bonded chain of [Rh(1)₂]³⁺ cations. (c) The structure of the [Rh(5)₂]³⁺ cation in [Rh(5)₂][PF₆]₃·MeCN; H atoms are omitted for clarity. Selected bond parameters: Rh1–N1 = 2.040(6), Rh1–N2 = 1.964(6), Rh1–N3 = 2.046(7), Rh1–N4 = 2.047(7), Rh1–N5 = 1.984(6), Rh1–N6 = 2.050(7), P1–O1 = 1.471(10), P1–O2 = 1.540(15), P1–O3 = 1.605(14), P1–C37 = 1.803(11), P2–O4 = 1.453(8), P2–O5 = 1.707(15), P2–O6 = 1.634(13), P2–C19 = 1.787(9) Å.



representation of the cation is displayed in Fig. S21a.† The octahedral coordination environment with two chelating tpy domains is unexceptional with the $[\text{Rh}(\text{tpy})_2]^{3+}$ core closely resembling that observed in other $[\text{Rh}(\text{Xtpy})_2]^{3+}$ cations ($X = 4'$ -phenyl, $4'$ -(pyridin-4-yl), 4-ferrocenyl (DAHDA,¹⁵ DAHDIA,¹⁵ DAHDEW,¹⁵ XIFTIS³⁴). The Rh–N bond lengths are given in the caption to Fig. 1a, and the chelate N–Rh–N bond angles are in the range $79.84(13)$ – $80.60(13)^\circ$. Each P atom is tetrahedrally sited and P–O and P–C bond lengths are given in the caption to Fig. 1a; the bond angles centred on P1 and P2 lie in the range $104.20(17)$ – $114.96(18)^\circ$. The most dominant packing interaction involving the $[\text{Rh}(\mathbf{1})_2]^{3+}$ cations is hydrogen bonding between $\text{PO}(\text{OH})_2$ units leading to the assembly of 1D-chains (Fig. 1b). For the centrosymmetric hydrogen-bonded motifs, pertinent parameters are $\text{O1}\cdots\text{O2}^{\text{i}} = 2.485(5)$ Å, $\text{O1}\cdots\text{H}-\text{O2}^{\text{i}} = 1.68$ Å, angle $\text{O1}\cdots\text{H}-\text{O2}^{\text{i}} = 159^\circ$ (symmetry code $i = -1 - x, -1 - y, 2 - z$), $\text{O4}\cdots\text{O6}^{\text{ii}} = 2.534(5)$ Å, $\text{O4}\cdots\text{HA}-\text{O6}^{\text{ii}} = 1.70$ Å, angle $\text{O4}\cdots\text{HA}-\text{O6}^{\text{ii}} = 171^\circ$ (symmetry code $ii = 1 - x, 2 - y, 1 - z$). Although the $[\text{Rh}(\mathbf{1})_2]^{3+}$ cations pack in the lattice with head-to-tail pairings of ligands on adjacent complexes, there are no significant π -stacking interactions between phenyl and tpy domains.

Synthesis and characterization of $[\text{Rh}(\mathbf{5})_2][\text{PF}_6]_3$

Because of initial uncertainties regarding the protonation state of the homoleptic complex obtained with **1**, we prepared an analogous compound with a phosphonate ester. Compound **5** (Scheme 1) was prepared according to the literature¹⁵ and its reaction with $\text{RhCl}_3 \cdot 3\text{H}_2\text{O}$ followed by anion exchange using NH_4PF_6 yielded $[\text{Rh}(\mathbf{5})_2][\text{PF}_6]_3$ as a pale pink solid in 82.7% yield. Mass spectrometric and ^1H , ^{13}C and ^{31}P NMR spectroscopic data (see the Experimental section, Fig. S14–S16†) were consistent with the formation of the homoleptic complex. ^1H and ^{13}C NMR spectra were assigned using NOESY, HMQC and HMBC spectra (Fig. S17–S19†). The solution absorption spectrum (in MeCN) of $[\text{Rh}(\mathbf{5})_2][\text{PF}_6]_3$ (Fig. S20†) exhibits intense bands below 370 nm which are assigned to ligand-centred $\pi^* \leftarrow \pi$ transitions similar to that reported for $[\text{Rh}(\text{tpy})_2](\text{PF}_6)_3$.³³ The lack of absorptions in the visible region arising from metal-to-ligand charge transfer is consistent with the low-spin d^6 configuration of the Rh(III) centre. X-ray quality crystals of $[\text{Rh}(\mathbf{5})_2][\text{PF}_6]_3 \cdot \text{MeCN}$ were grown by vapour diffusion of Et_2O into a MeCN solution and the structure of the $[\text{Rh}(\mathbf{5})_2]^{3+}$ cation is shown in Fig. 1c; an ORTEP representation is displayed in Fig. S21b.† Important bond lengths and angles are given in the caption to Fig. 1c. As anticipated, the Rh(III) centre is octahedral, bound by two bis-chelating tpy domains. The structure is unexceptional but serves to confirm the formation of the homoleptic complex, and there are no noteworthy packing interactions.

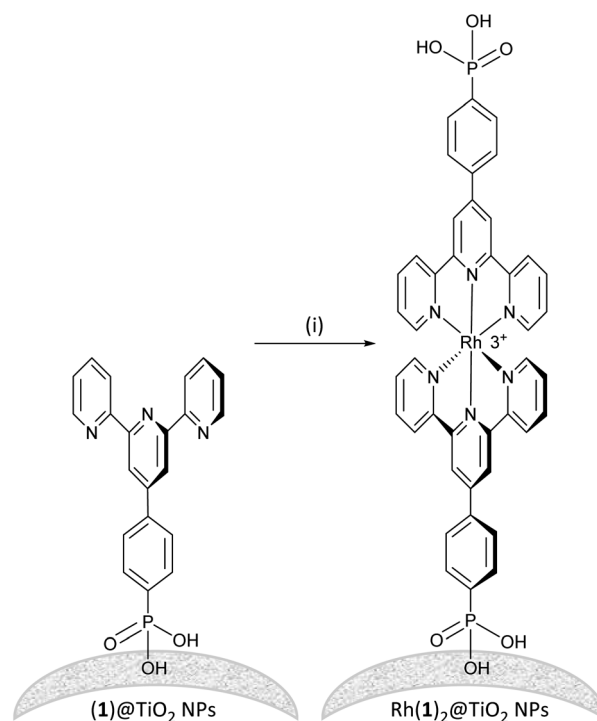
Assembly of a homoleptic rhodium(III) complex on TiO_2 NPs

Established procedures for TiO_2 NP activation involve HNO_3 (ref. 35) treatment and sonication to optimize surface functionalization and particle dispersion respectively.³⁶ Commercial P25 TiO_2 NPs were activated using aqueous HNO_3 and then functionalized with ligand **1** (see the Experimental section). For

the functionalization, an aqueous suspension of dispersed ligand **1** and activated NPs was heated to 130°C for 3 h under microwave conditions. The $(\mathbf{1})@\text{TiO}_2$ NPs were separated from the liquid phase by centrifugation. The functionalization procedure differs only from that previously described¹¹ in that it was scaled up and the ratio TiO_2 to **1** had to be increased by 10% to ensure binding of all the ligand.

To form the NP-supported complex $\text{Rh}(\mathbf{1})_2@\text{TiO}_2$ (Scheme 2), $(\mathbf{1})@\text{TiO}_2$ NPs were dispersed with $\text{RhCl}_3 \cdot 3\text{H}_2\text{O}$ in ethanol and water under air at 95°C for 5 h. The NPs changed colour from white to pale red. The $\text{Rh}(\mathbf{1})_2@\text{TiO}_2$ NPs were separated from the solvent using centrifugation (see Experimental section, Method 1). The conjugate $\text{Rh}(\mathbf{1})_2@\text{TiO}_2$ was also prepared using $[\text{Rh}_2(\mu\text{-OAc})_4(\text{H}_2\text{O})_2]$ as a precursor (see Experimental, Method 2). $(\mathbf{1})@\text{TiO}_2$ NPs were dispersed with NaCl and $[\text{Rh}_2(\mu\text{-OAc})_4(\text{H}_2\text{O})_2]$ in EtOH at 80°C , and a colour change from pale blue to brown was observed during the reaction. The $\text{Rh}(\mathbf{1})_2@\text{TiO}_2$ NPs were separated using centrifugation. The overall charge associated with each $\{\text{Rh}(\mathbf{1})_2\}$ moiety in the $\text{Rh}(\mathbf{1})_2@\text{TiO}_2$ is uncertain as the protonation state and binding mode is typically not well defined.^{37–39} However, assuming that all **1** ligands are fully protonated, the $\text{Rh}(\mathbf{1})_2@\text{TiO}_2$ NPs should bear a +3 charge per surface-bound $\{\text{Rh}(\mathbf{1})_2\}$.

The $\text{Rh}(\mathbf{1})_2@\text{TiO}_2$ NPs from both methods 1 and 2 were characterized using MALDI mass spectrometry and FTIR, ^1H NMR and solid-state UV-VIS spectroscopies. FTIR spectra



Scheme 2 Assembly of $[\text{Rh}(\mathbf{1})_2]^{3+}$ on TiO_2 NPs starting from NPs functionalized with **1**. Conditions: (i) RhCl_3 , EtOH : H_2O , 95°C , 6 h or $[\text{Rh}_2(\mu\text{-OAc})_4(\text{H}_2\text{O})_2]$, NaCl, EtOH, 80°C , 18 h. NP surfaces are rough and could potentially provide two binding sites for the rhodium metal complex or two NPs could come together to form the rhodium metal complex.



(Fig. S22[†]), solid-state absorption spectra (Fig. S23[†]), TGA measurements (Fig. S24 and S25[†]), MALDI mass spectra (Fig. S26 and S27[†]) and ¹H NMR spectra (Fig. S28[†]) confirmed that both methods yielded similar Rh(1)₂@TiO₂ NPs. The characterization details are discussed further below.

Characterization of Rh(1)₂@TiO₂ NPs

The MALDI mass spectrum of Rh(1)₂@TiO₂ NPs⁺ (Fig. S26 and S27[†]) showed peaks at *m/z* 492.1, 527.0 and 681.1 arising from [Rh(1)]⁺, [Rh(1) + Cl]⁺ and [Rh(1) + CHCA]⁺, respectively. Additionally, a peak at *m/z* 881.1 assigned to [Rh(1)₂]⁺ was observed for Rh(1)₂@TiO₂ NPs prepared using method 1. The similarity between the mass spectrum of pristine [Rh(1)₂]Cl₃ and the mass spectra of Rh(1)₂@TiO₂ NPs is consistent with the assembly of the homoleptic [Rh(1)₂]³⁺ complex on the NP surface using both [Rh₂(μ-OAc)₄(H₂O)₂] and RhCl₃·3H₂O as metal source.

Fig. 2 compares the FT-IR spectra of activated NPs, (1)@TiO₂ NPs and Rh(1)₂@TiO₂ NPs together with the spectrum of the pristine compound [Rh(1)₂]Cl₃. The full spectra are presented in Fig. S29[†]. The activated NPs show weak absorption bands at 1613 and 1584 cm⁻¹ while the (1)@TiO₂ NPs exhibit bands at 1602, 1588, 1570, 1538, 1470, 1444, 1408 and 1387 cm⁻¹. The isolated complex [Rh(1)₂]Cl₃ has absorption bands at 1605, 1565, 1549, 1477, 1429, 1395, 1367, 1297, 1242, 1213, 1152, 1127, 1072, 1048, 1029 and 1015 cm⁻¹. Rh(1)₂@TiO₂ NPs shows bands at 1607, 1585, 1572, 1554, 1476, 1428, 1408, 1391 and 1136 cm⁻¹ and their relative intensities and energies resemble most of the major peaks seen in (1)@TiO₂ NPs and [Rh(1)₂]Cl₃.

Thus, the IR spectroscopic data provide evidence that (1)@TiO₂ NPs has undergone a change upon treatment with either [Rh₂(μ-OAc)₄(H₂O)₂] or RhCl₃·3H₂O consistent with the formation of Rh(1)₂@TiO₂ NPs.

Further evidence for the NP functionalization came from ¹H NMR spectroscopic data for Rh(1)₂@TiO₂ NPs dispersed in D₂O. TiO₂ NPs and their functionalized derivatives are insoluble in D₂O, and signals associated with the surface-bound species are not observed under typical acquisition conditions. Any observed resonances can be attributed to the released of compounds

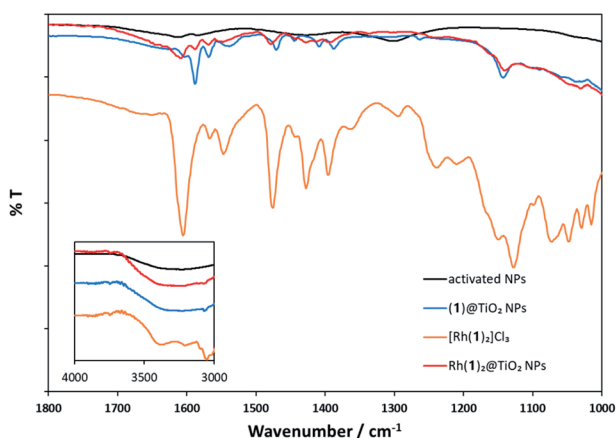


Fig. 2 Solid-state FT-IR spectra of activated NPs (black), (1)@TiO₂ NPs (blue), [Rh(1)₂]Cl₃ (orange), and Rh(1)₂@TiO₂ NPs (red).

from the surface. The ¹H NMR spectrum of Rh(1)₂@TiO₂ NPs synthesized from [Rh₂(μ-OAc)₄(H₂O)₂] (Fig. 3d) showed no signals in the aromatic region. The only signals recorded arose from residual HOD and EtOH (Fig. S28[†]). A similar result was obtained for Rh(1)₂@TiO₂ NPs synthesized with RhCl₃·3H₂O (Fig. 3g). Under very basic conditions with an excess of NaOH, it is possible to partially defunctionalize the surface leading to the appearance of signals arising from free complex and ligand. This can be seen with the Rh(1)₂@TiO₂ NPs synthesized from [Rh₂(μ-OAc)₄(H₂O)₂] (Fig. 3e) or RhCl₃·3H₂O (Fig. 3h). The ¹H NMR spectra of 1 (Fig. 3a), (1)@TiO₂ and [Rh(1)₂]Cl₃ made with [Rh₂(μ-OAc)₄(H₂O)₂] (Fig. 3c) or RhCl₃·3H₂O (Fig. 3f) were also recorded under basic conditions. Using these spectra for comparison, we observed that the spectra of Rh(1)₂@TiO₂ NPs (Fig. 3e and h) contained signals arising from both 1 and [Rh(1)₂]Cl₃. This is not surprising considering that not every surface-bound ligand will bind a metal ion. However the similarity between the spectra of the pristine [Rh(1)₂]Cl₃ (Fig. 3c and f) and those of the defunctionalized NPs (Fig. 3e and h) provides strong evidence that the surface was partially functionalized with [Rh(1)₂]³⁺ prior to treatment with base.

Thermogravimetric analysis (TGA) of activated NPs, (1)@TiO₂ and Rh(1)₂@TiO₂ NPs was carried out, and the results are presented in Fig. 4. All samples show a weight loss of 1.5–2% in two steps (isotherm maxima <120 °C and <330 °C). The two steps can be attributed to the loss of physisorbed followed by chemisorbed water. The mass of the non-functionalized NPs undergoes no further significant change (Fig. S30[†]) upon being heated to 900 °C for 30 minutes. The (1)@TiO₂ NPs and Rh(1)₂@TiO₂ NPs exhibit additional 3% and 4–5% weight losses above ca. 400 °C (Fig. S24 and S25[†]) ascribed to decomposition of the ligand. Additionally, Rh(1)₂@TiO₂ NPs show a weight increase occurring during the 30 minute 900 °C isotherm.

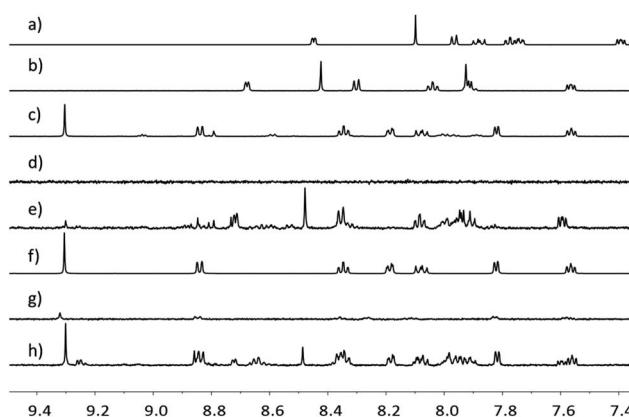


Fig. 3 ¹H NMR spectra (500 MHz, D₂O, 298 K) of 1 in D₂O and NaOH (a), (1)@TiO₂ in D₂O and NaOH (b), [Rh(1)₂]Cl₃ made using [Rh₂(μ-OAc)₄(H₂O)₂] in D₂O and NaOH (c), Rh(1)₂@TiO₂ NPs made using [Rh₂(μ-OAc)₄(H₂O)₂] in D₂O (d), Rh(1)₂@TiO₂ NPs made using [Rh₂(μ-OAc)₄(H₂O)₂] in D₂O and NaOH (e), [Rh(1)₂]Cl₃ made using RhCl₃·3H₂O in D₂O and NaOH (f), Rh(1)₂@TiO₂ NPs made using RhCl₃·3H₂O in D₂O and NaOH (g), Rh(1)₂@TiO₂ NPs made using RhCl₃·3H₂O in D₂O and NaOH (h). Chemical shifts in δ/ppm.



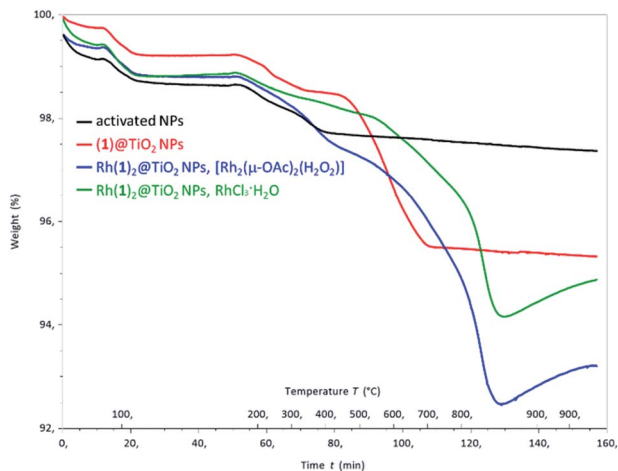


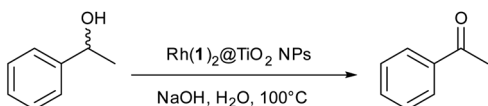
Fig. 4 TGA curves for activated NPs (black), (1)@TiO₂ NPs (red), Rh(1)₂@TiO₂ NPs made using [Rh₂(μ-OAc)₄(H₂O)₂] (blue) and for Rh(1)₂@TiO₂ NPs made using RhCl₃·3H₂O (green).

NP supported homoleptic rhodium complex for alcohol oxidation

Wang and coworkers¹² reported the dehydrogenation and aerobic oxidation of alcohols under air to produce carboxylic acids or ketones with [Rh₂Cl₂(μ-OAc)(tpy)₂]Cl as catalyst under aqueous conditions. We chose the reaction shown in Scheme 3 for a proof-of-principle investigation of the catalytic activity of Rh(1)₂@TiO₂ NPs.

For the alcohol oxidation, Rh(1)₂@TiO₂ NPs were dispersed by sonication in milliQ water. Aqueous NaOH and *rac*-(1*R*)-1-phenylethanol were added to the suspension and the mixture was again dispersed by sonication. A control (Control experiment 3) was carried out to check that NaOH (at the concentrations used in the reactions) did not strip the catalyst from the surface. The reaction was performed under air at 100 °C for 18 h, 24 h and 38 h. The product : reactant ratio was measured using ¹H NMR spectroscopy by removing a small amount of reaction solution and dispersing it in D₂O (see Experimental section). Since the reaction shown in Scheme 3 involves one reactant forming one product, it was possible to reliably determine the reactant to product ratio by comparing the peak area of the aromatic protons and the methyl protons (Fig. 5).

Control experiments (see Experimental section) were performed to investigate several key factors during the reaction. Control experiment 1 compared Rh(1)₂@TiO₂ NPs with pristine commercial NPs or activated NPs were added to the reaction vial. After the reaction, ¹H NMR spectroscopy revealed no acetophenone formation confirming that Rh(1)₂@TiO₂ NPs are the active catalyst. Control experiment 2 investigate the influence of



Scheme 3 Secondary alcohol oxidation of *rac*-(1*R*)-1-phenylethanol to acetophenone.

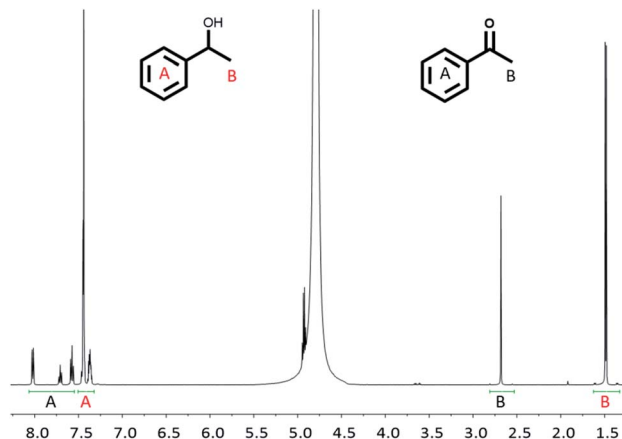


Fig. 5 ¹H NMR spectrum (500 MHz, D₂O, 298 K) of the reaction solution after alcohol oxidation (38 h) using Rh(1)₂@TiO₂ NPs as catalyst (see Experimental).

temperature with the reaction being performed at room temperature (*ca.* 22 °C) instead of 100 °C. ¹H NMR spectroscopy revealed <1% conversion to acetophenone, even after 72 h, at the lower temperature. Hence, elevated temperatures are important for product formation.

We also ensured that the reaction was catalysed by Rh(1)₂@TiO₂ NPs as opposed to [Rh(1)₂]³⁺ that had been removed from the surface. Control experiment 3 investigated if defunctionalization could occur under the basic reaction conditions. Firstly, Rh(1)₂@TiO₂ NPs and NaOH were dispersed in milliQ water. The mixture was then heated to 100 °C for 72 h to simulate the reaction conditions. Next, the NPs were separated from the solution by centrifugation, and the supernatant solution separated into two sample vials. The substrate *rac*-(1*R*)-1-phenylethanol was added to each vial (see Experimental section) and the reaction mixtures were then heated to 100 °C for 24 h. After the reaction, ¹H NMR spectroscopy revealed no acetophenone had formed in the vial containing the supernatant solution whereas it was found in the vial containing the NPs. The results of Control 3 indicated that under the basic conditions used in the reaction, little or no defunctionalization of the NPs occurred.

Control experiment 4 investigated the influence of the concentration of the base concentration on the oxidation and allowed us to determine at what point defunctionalization occurred. Reactions were performed with NaOH – *rac*-(1*R*)-1-phenylethanol ratios of 0.01, 0.02, 0.1 and 1 (see Experimental section). Fig. 6 illustrates the reaction course of each experiment, and shows that the base concentration does not strongly influence the activity of Rh(1)₂@TiO₂ NPs with 0.01, 0.02 or 0.1 equivalents of NaOH. The catalytic activity of the Rh(1)₂@TiO₂ NPs is only affected strongly basic conditions (Fig. 6, green line).

Control experiment 5 was performed to compare the differences in catalytic activities of to [Rh(1)₂]Cl₃. We can make a number of general observations: (i) the attempt to prepare an immobilized dinuclear catalyst analogous to the established homogeneous species was unsuccessful (ii) the presence of the



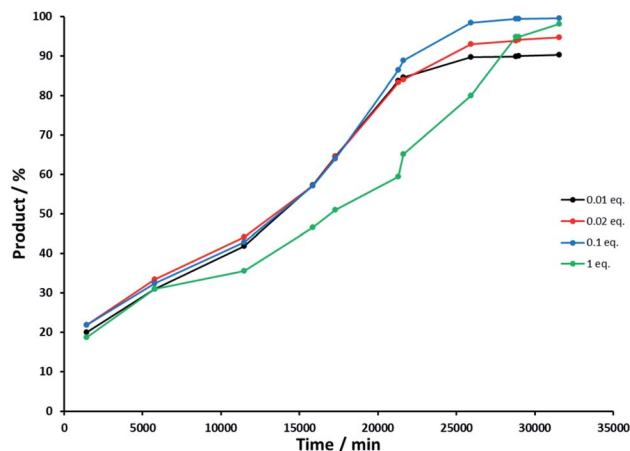


Fig. 6 Product concentration in percent against time in minutes during alcohol oxidation with varying NaOH base concentration, NaOH equivalents compared to starting material: 0.01 (black), 0.02 (red), 0.1 (blue) and 1 (green).

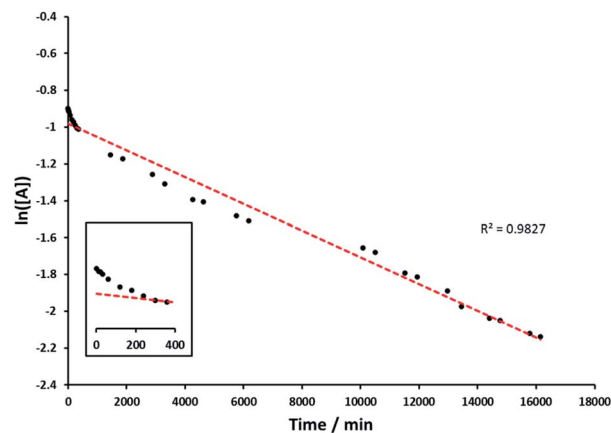


Fig. 7 1st order reaction graph, natural logarithm of starting material concentration during kinetic measurements of *rac*-(1*R*)-1-phenylethanol oxidation (see Experimental) against time in minutes (black), linear trendline through datapoints (red), insert of first 400 minutes illustrates incubation time.

phosphonate functionality hinders the formation of the homogeneous dinuclear species (iii) both solution and surface chemistry leads to mononuclear complexes with **1** ligands (iv) the catalytic activity of homogeneous species depends to some extent upon the synthetic route used and (v) the catalytic activity of Rh(**1**)₂@TiO₂ NPs is generally similar to the homogeneous species.

Although [Rh(tpy)₂]ⁿ⁺ species do not appear to have been used as photocatalysts, [Rh(bpy)₃]ⁿ⁺ (*n* = 2 or 3) are well-established in multicomponent systems for photocatalytic reduction. We do not speculate in detail upon the mechanism of the photo-oxidation but it seems likely that the observed photooxidation product arises from the alcohol acting as a sacrificial reductant. We note that the yield of the oxidation product is somewhat reduced when the reaction is performed under argon (Table S1†). We have not observed dihydrogen production.^{40–45}

Kinetics of Rh(**1**)₂@TiO₂ NP catalysed alcohol oxidation

The kinetics of the alcohol oxidation by Rh(**1**)₂@TiO₂ NPs was investigated. The Rh(**1**)₂@TiO₂ NPs were dispersed in D₂O, *rac*-(1*R*)-1-phenylethanol and aqueous NaOH were added and the mixture again dispersed by sonication. The alcohol oxidation was performed under air at 100 °C for two weeks. The product – reactant ratio was determined by measuring a small amount of reaction solution dispersed in D₂O at certain time intervals with ¹H NMR spectroscopy (see Experimental section).

Analysis of the data indicated first order kinetics (Fig. 7). The data further suggested an incubation time during the first 6 h in which the reaction rate was slower. However overall *rac*-(1*R*)-1-phenylethanol was able to perform linearly over an extended period of time yielding over 71% product after the reaction.

Recyclability of Rh(**1**)₂@TiO₂ NPs

The recyclability of the Rh(**1**)₂@TiO₂ NPs was studied. In contrast to the typical procedure described earlier, the pH was monitored using a pH electrode and was returned to pH 7.8 after each cycle. The conversion of each cycle was determined from the product and starting material extracted with Et₂O from

the reaction solution. This had the benefits of not removing any Rh(**1**)₂@TiO₂ NPs from the experiment with consequent distortion of the results from the next cycle. Five reaction cycles were measured under which the conversions stayed steady at a product to reactant ratio of 1.0 : 5 (20% product) after 24 hours reaction time.

Conclusions

In this work we have built upon our previously established metal binding ligand functionalized TiO₂ NPs and use their properties to form a surface bound homoleptic rhodium complex (Rh(**1**)₂@TiO₂ NPs). The functionalized NPs were investigated using TGA and ¹H NMR and FT-IR spectroscopies. We further demonstrate a proof-of-principle investigation of their catalytic activity in an alcohol oxidation in water and under air. By tracking the product conversion over time with ¹H NMR spectroscopy we were able to study the reaction kinetics and the recyclability of the catalyst. Rh(**1**)₂@TiO₂ NPs were further compared to their non-bound counterpart concluding that the NP-bound catalyst performs similarly if not slightly better. Rh(**1**)₂@TiO₂ NPs were able to withstand reactions at 100 °C for at least 24 days without showing decomposition or degradation. We further studied the resistance of the functionalization to higher base concentrations. Several other control experiments were performed to exclude influencing circumstances that could lead to unintentional product formation.

Conflicts of interest

There are no conflicts to declare.

Acknowledgements

We are grateful to the Swiss National Science Foundation (grantnumber 200020_182000) and the University of Basel financial support.



Notes and references

- 1 A. Maleki, R. Taheri-Ledari, R. Ghalavand and R. Firouzi-Haji, *J. Phys. Chem. Solids*, 2020, **136**, 109200.
- 2 A. F. Hassan and H. Elhadidy, *J. Phys. Chem. Solids*, 2019, **129**, 180–187.
- 3 S. Sajjadi, A. Khataee, R. D. C. Soltani and A. Hasanzadeh, *J. Phys. Chem. Solids*, 2019, **127**, 140–150.
- 4 P. D. Stevens, J. Fan, H. M. R. Gardimalla, M. Yen and Y. Gao, *Org. Lett.*, 2005, **11**, 2085–2088.
- 5 A. Zecchina, S. Bordiga and E. Groppo, *Selective Nanocatalysts and Nanoscience*, Wiley-VHC, Weinheim, 2011.
- 6 S. Bagheri and N. M. Julkapli, *Nanocatalysts in Environmental Applications*, Springer, Cham, 2018.
- 7 S. Albonetti, R. Mazzoni and F. Cavani, in *Transition Metal Catalysis in Aerobic Alcohol Oxidation*, Royal Society of Chemistry, Cambridge, UK, 2015, ch. 1, pp. 1–39.
- 8 M. Bartz, J. Küther, R. Seshadri and W. Tremel, *Angew. Chem., Int. Ed.*, 1998, **37**, 2466.
- 9 S. Ali, M. J. Al-Marri, A. G. Abdelmoneim, A. Kumar and M. M. Khader, *Int. J. Hydrogen Energy*, 2016, **41**, 22876–22885.
- 10 H. Göksu, H. Burhan, S. D. Mustafaov and F. Şen, *Sci. Rep.*, 2020, **10**, 5439.
- 11 S. A. Freimann, D. Zare, C. E. Housecroft and E. C. Constable, *Nanoscale Adv.*, 2020, **2**, 679–690.
- 12 X. Wang, C. Wang, Y. Liu and J. Xiao, *Green Chem.*, 2016, **18**, 4605.
- 13 V. Spampinato, N. Tuccitto, S. Quici, V. Calabrese, G. Marletta, A. Torrisi and A. Liccardello, *Langmuir*, 2010, **26**, 8400.
- 14 <https://www.aerosil.com/sites/lists/RE/DocumentsSI/TI-1243-Titanium-Dioxide-as-Photocatalyst-EN.pdf>, (accessed 05 April 2020).
- 15 J. Paul, S. Spey, H. Adams and J. A. Thomas, *Inorg. Chim. Acta*, 2004, **357**, 2827.
- 16 *Software for the Integration of CCD Detector System Bruker Analytical X-ray Systems*, Bruker axs, Madison, WI (after 2013).
- 17 G. M. Sheldrick, *Acta Crystallogr., Sect. A: Found. Adv.*, 2015, **71**, 3.
- 18 O. V. Dolomanov, L. J. Bourhis, R. J. Gildea, J. A. K. Howard and H. Puschmann, *J. Appl. Crystallogr.*, 2009, **42**, 339.
- 19 G. M. Sheldrick, *Acta Crystallogr., Sect. C: Struct. Chem.*, 2015, **27**, 3.
- 20 C. F. Macrae, I. Sovago, S. J. Cottrell, P. T. A. Galek, P. McCabe, E. Pidcock, M. Platings, G. P. Shields, J. S. Stevens, M. Towler and P. A. Wood, *J. Appl. Crystallogr.*, 2020, **53**, 226.
- 21 E. C. Constable, *Adv. Inorg. Chem.*, 1986, **30**, 69–121.
- 22 C. Wei, Y. He, X. Shi and Z. Song, *Coord. Chem. Rev.*, 2019, **385**, 1–19.
- 23 R. Calzada, C. M. Thompson, D. E. Westmoreland, K. Edme and E. A. Weiss, *Chem. Mater.*, 2016, **28**, 6716.
- 24 J. De Roo, K. De Keukeleere, Z. Hens and I. Van Driessche, *Dalton Trans.*, 2016, **45**, 13277.
- 25 J. De Roo, Z. Zhou, J. Wang, L. Deblock, A. J. Crosby, J. S. Owen and S. S. Nonnenmann, *Chem. Mater.*, 2018, **30**, 8034.
- 26 L. Du, W. Wang, C. Zhang, Z. Jin, G. Palui and H. Mattoussi, *Chem. Mater.*, 2018, **30**, 7269.
- 27 C. Goldmann, F. Ribot, L. F. Peiretti, P. Quaino, F. Tielens, C. Sanchez, C. Chanéac and D. Portehault, *Small*, 2017, **13**, 1604028.
- 28 V. Grigel, L. K. Sagar, K. De Nolf, Q. Zhao, A. Vantomme, J. De Roo, I. Infante and Z. Hens, *Chem. Mater.*, 2018, **30**, 7637.
- 29 M. L. Kessler, H. E. Starr, R. R. Knauf, K. J. Rountree and J. L. Dempsey, *Phys. Chem. Chem. Phys.*, 2018, **20**, 23649.
- 30 R. R. Knauf, J. C. Lennox and J. L. Dempsey, *Chem. Mater.*, 2016, **28**, 4762.
- 31 M. La Rosa, T. Avellini, C. Lincheneau, S. Silvi, I. A. Wright, E. C. Constable and A. Credi, *Eur. J. Inorg. Chem.*, 2017, **2017**, 5143.
- 32 A. Ritchhart and B. M. Cossairt, *Inorg. Chem.*, 2019, **58**, 2840.
- 33 C. M. Harris and E. D. McKenzie, *J. Inorg. Nucl. Chem.*, 1963, **25**, 171–174.
- 34 E. Botha, M. Landman, P. H. van Rooyen and E. Erasmus, *Inorg. Chim. Acta*, 2018, **482**, 514–521.
- 35 B. Kim, S. W. Park, J.-Y. Kim, K. Yoo, J. A. Lee, M.-W. Lee, D.-K. Lee, J. Y. Kim, B. S. Kim, H. Kim, S. Han, H. J. Son and M. J. Ko, *ACS Appl. Mater. Interfaces*, 2013, **5**, 5201.
- 36 See for example: A. Estrada-Monje, R. Zitzumbo-Guzmán, J. A. Bañuelos-Díaz and E. A. Zaragoza-Contreras, *Mater. Chem. Phys.*, 2019, **235**, 121760.
- 37 See for example: M. Nilsing, S. Lunell, P. Persson and L. Ojamäe, *Surf. Sci.*, 2005, **582**, 49; C. Queffélec, M. Petit, P. Janvier, D. A. Knight and B. Bujoli, *Chem. Rev.*, 2012, **112**, 3777.
- 38 V. Spampinato, N. Tuccitto, S. Quici, V. Calabrese, G. Marletta, A. Torrisi and A. Liccardello, *Langmuir*, 2010, **26**, 8400.
- 39 A. J. Stephens, F. J. Malzner, E. C. Constable and C. E. Housecroft, *Sustainable Energy Fuels*, 2018, **2**, 786.
- 40 M. Kirch, J. M. Lehn and J. P. Sauvage, *Helv. Chim. Acta*, 1979, **62**, 1345.
- 41 B. Hubsch and B. Mahieu, *Polyhedron*, 1985, **4**, 669.
- 42 B. Hubsch, B. Mahieu and J. Meunier-Piret, *Bull. Soc. Chim. Belg.*, 1985, **94**, 685.
- 43 H. Hukkanen and T. T. Pakkanen, *J. Mol. Catal.*, 1986, **37**, 297.
- 44 V. E. Maier and V. Y. Shafirovich, *Kinet. Katal.*, 1987, **28**, 839.
- 45 Y. Kataoka, K. Sato, Y. Miyazaki, Y. Suzuki, H. Tanaka, Y. Kitagawa, T. Kawakami, M. Okumura and W. Mori, *Chem. Lett.*, 2010, **39**, 358.



Supporting Information

Turning over on sticky balls: Preparation and catalytic studies of surface-functionalized TiO₂ nanoparticles

Sven A. Freimann,^a Alessandro Prescimone,^a Catherine E. Housecroft^a and Edwin C. Constable*^a

^a Department of Chemistry, University of Basel, BPR 1096, Mattenstrasse 24a, CH-4058 Basel, Switzerland. email: edwin.constable@unibas.ch

Experimental Details of Instruments

¹H NMR, ¹³C{¹H} NMR and ³¹P{¹H} NMR spectra were measured at 298 K on a Bruker Avance III-500 NMR spectrometer. ¹H, ¹³C and ³¹P chemical shifts were referenced to residual solvent peaks with respect to $\delta(\text{TMS}) = 0$ ppm for ¹H and ¹³C{¹H} and $\delta(\text{H}_3\text{PO}_4 \text{ 85\% aqueous}) = 0$ ppm for ³¹P{¹H}. A Gaussian fit to the diffusion peak intensity was done to determine the diffusion constant of the signal.

Reactions under microwave conditions were carried out in a Biotage Initiator 8 reactor. An Eppendorf Centrifuge 5415 R was used for 2 mL samples while a Hettich Centrifuge Universal 320 was used for 10 mL samples.

Solution absorption spectra were recorded on an Agilent Cary 5000 spectrophotometer and for solid-state absorption spectra, a Diffuse Reflectance Accessory was added to the spectrophotometer. For each solid-state absorption spectrum, a baseline correction was done with the respective nanoparticle precursor as the reference sample. FTIR spectra were recorded on a Perkin Elmer UATR Two spectrophotometer. Electrospray ionization (ESI) mass spectra and high resolution ESI MS were measured on a Shimadzu LCMS-2020 or a Bruker maXis 4G instrument, respectively. MALDI was measured on a Shimadzu MALDI-8020 with α -cyano-4-hydroxycinnamic acid (CHCA) solution as matrix for sample preparation.

Thermogravimetric analysis (TGA) was performed on a TGA5500 (TA Instruments) instrument under nitrogen. Initially, the temperature was held at 30 °C for 10 min before heating at a rate of 10 °C/min to 120 °C. This temperature was maintained for 30 min to remove all traces of water. Afterwards the sample was heated to 900 °C at a rate of 10 °C/min. After maintaining the temperature at 900 °C for 30 min, the sample was cooled to ambient temperature.

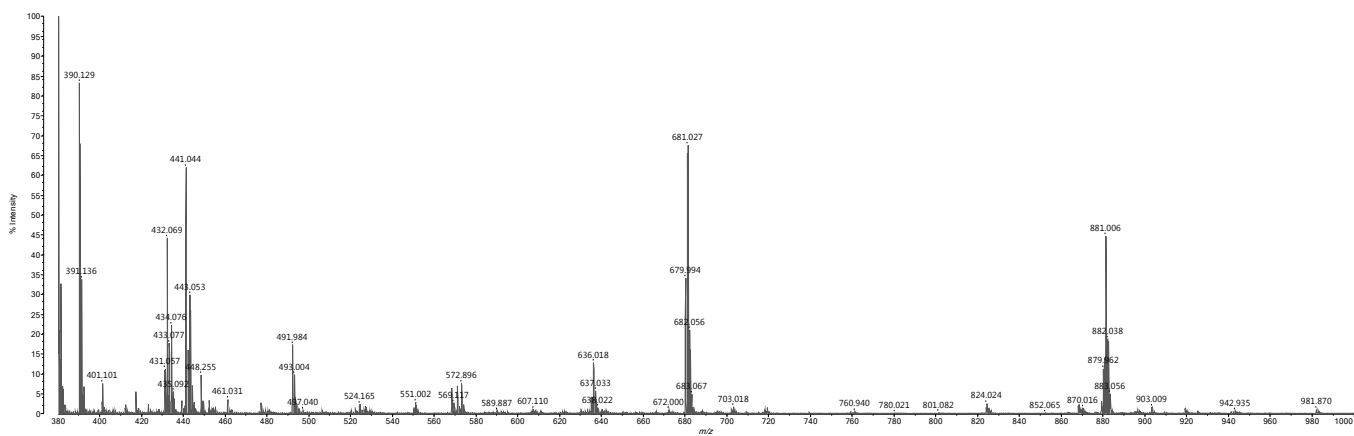


Fig. S1. MALDI mass spectrum (with CHCA matrix) of $[\text{Rh}(\mathbf{1})_2]\text{Cl}_3$ prepared from $[\text{Rh}_2(\mu\text{-OAc})_4(\text{H}_2\text{O})_2]$.

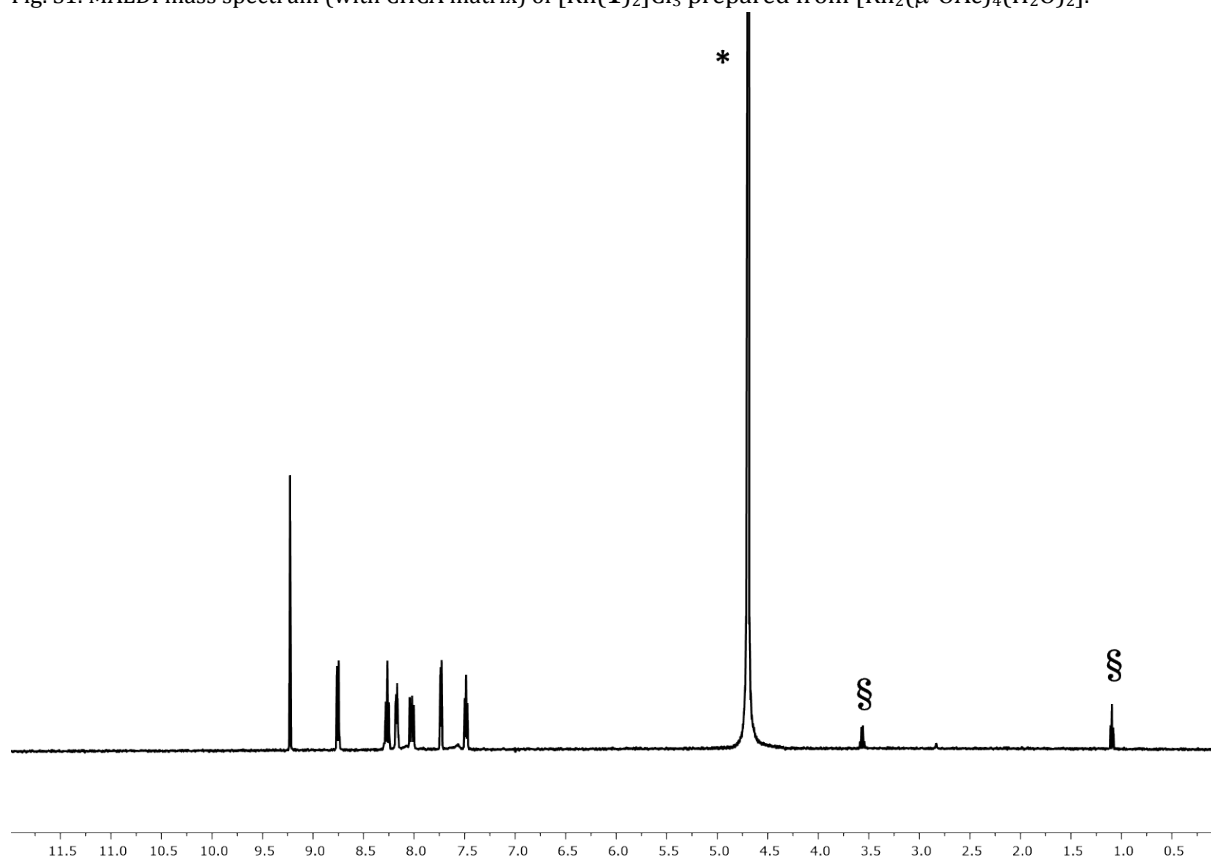


Fig. S2. ^1H NMR (500 MHz, D_2O , 298 K) spectrum of $[\text{Rh}(\mathbf{1})_2]\text{Cl}_3$ prepared from $[\text{Rh}_2(\mu\text{-OAc})_4(\text{H}_2\text{O})_2]$, * = HOD, § = residual EtOH. Chemical shifts in δ/ppm .

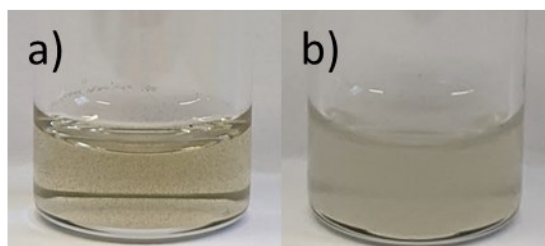


Fig. S3. a) $[\text{Rh}(\mathbf{1})_2]\text{Cl}_3$ dissolved in concentrated HNO_3 b) $[\text{Rh}(\mathbf{1})_2]\text{Cl}_3$ dissolved in concentrated HNO_3 after adding a drop of silver nitrate showing precipitation of AgCl .

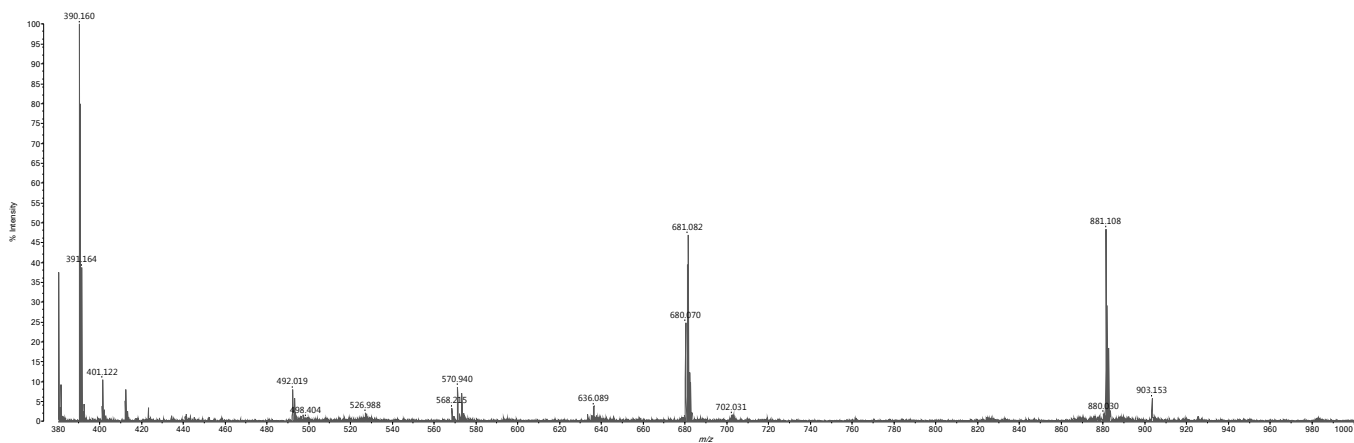


Fig. S4. MALDI mass spectrum (with CHCA matrix) of $[\text{Rh}(\mathbf{1})_2]\text{Cl}_3$ prepared from $\text{RhCl}_3 \cdot 3\text{H}_2\text{O}$.

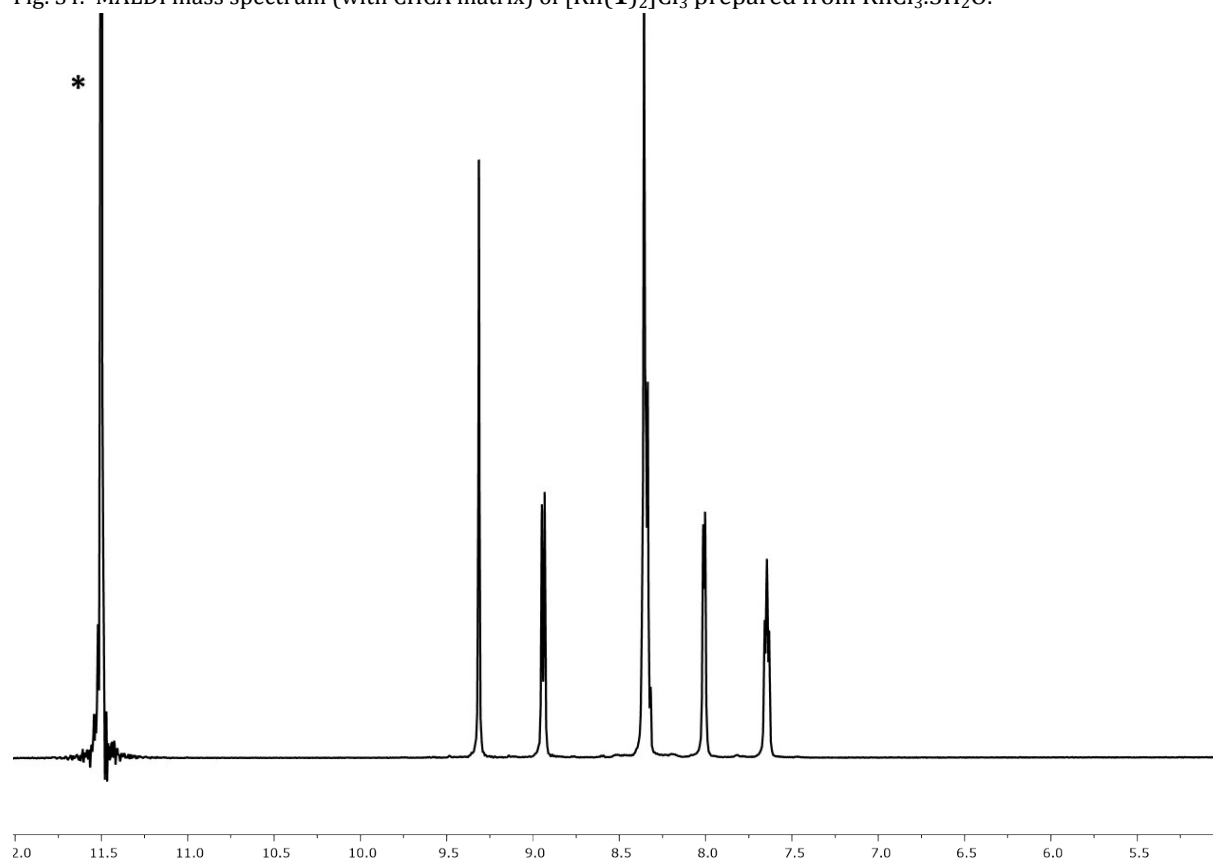


Fig. S5. ^1H NMR (500 MHz, TFA-d 298 K) spectrum of $[\text{Rh}(\mathbf{1})_2]\text{Cl}_3$ prepared from $\text{RhCl}_3 \cdot 3\text{H}_2\text{O}$, * = HOD. Chemical shifts in δ/ppm .

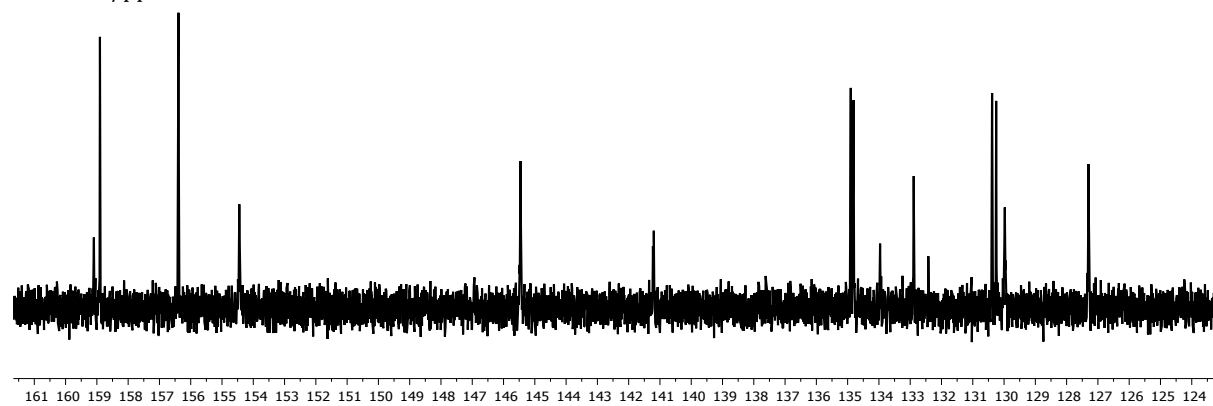


Fig. S6. $^{13}\text{C}\{^1\text{H}\}$ NMR (126 MHz, TFA-d 298 K) spectrum of $[\text{Rh}(\mathbf{1})_2]\text{Cl}_3$ prepared from $\text{RhCl}_3 \cdot 3\text{H}_2\text{O}$. Chemical shifts in δ/ppm .

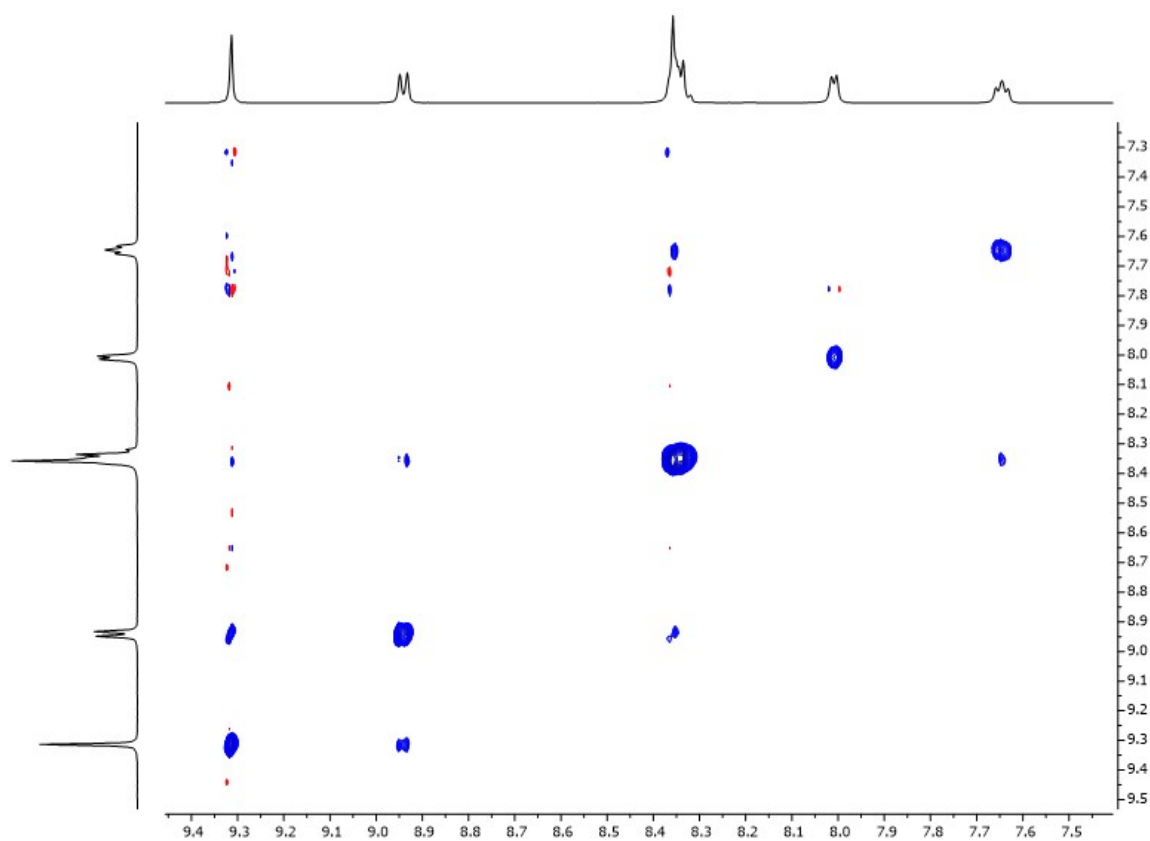


Fig. S7. NOESY (500 MHz, TFA-d 298 K) spectrum of $[\text{Rh}(\mathbf{1})_2]\text{Cl}_3$ prepared from $\text{RhCl}_3 \cdot 3\text{H}_2\text{O}$. Chemical shifts in δ/ppm .

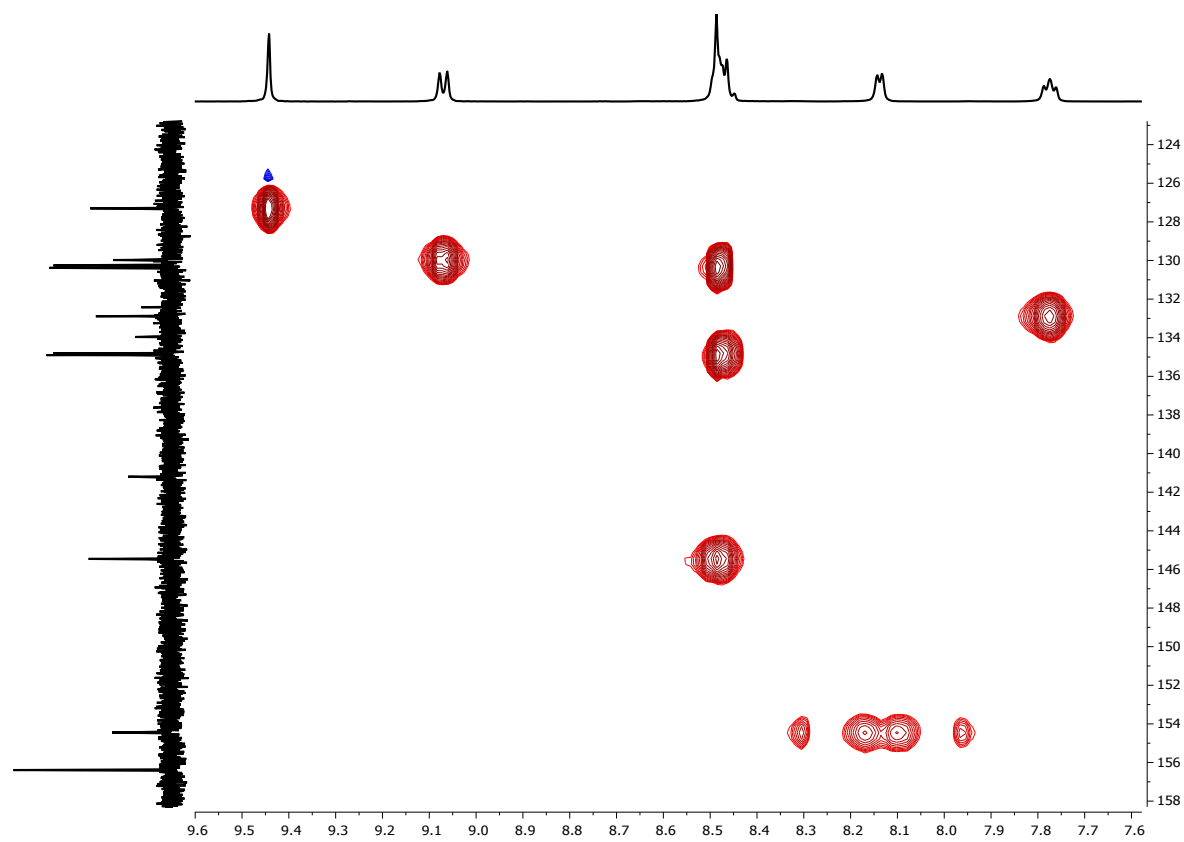


Fig. S8. HMBC (500 MHz ^1H , 126 MHz ^{13}C , TFA-d 298 K) spectrum of $[\text{Rh}(\mathbf{1})_2]\text{Cl}_3$ prepared from $\text{RhCl}_3 \cdot 3\text{H}_2\text{O}$. Chemical shifts in δ/ppm .

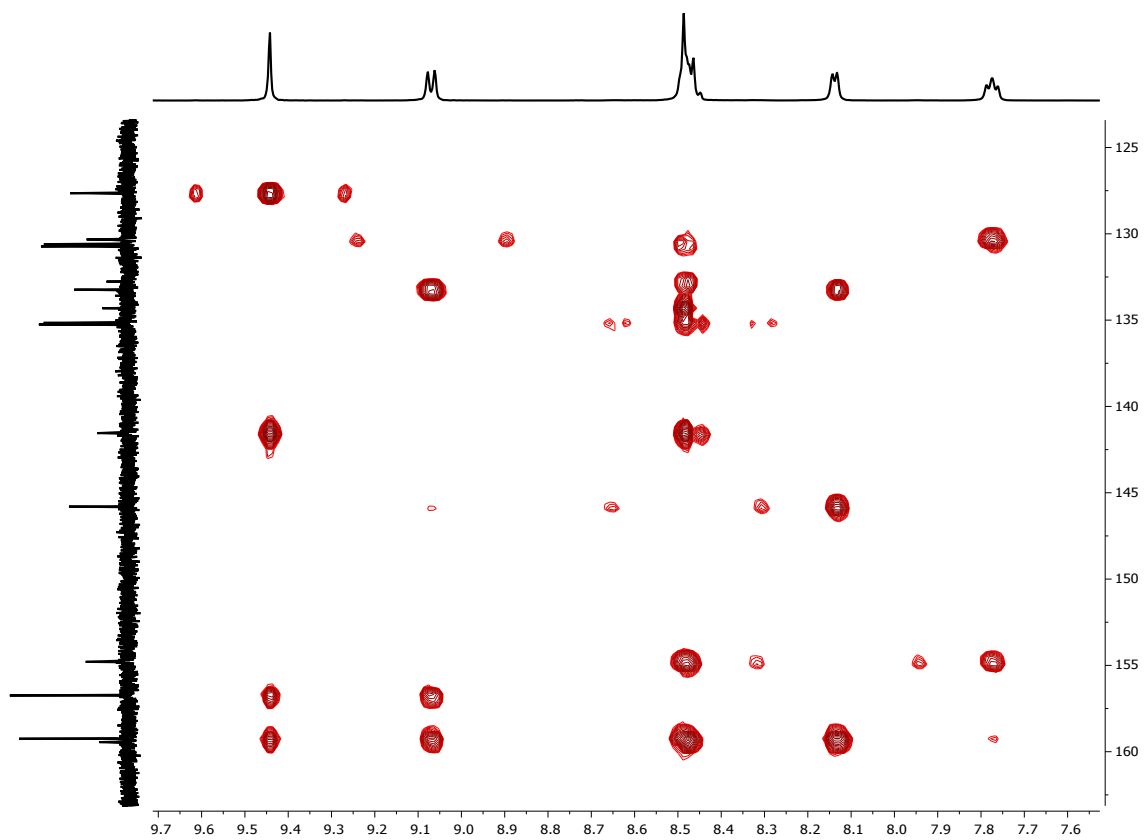


Fig. S9. HMBC (500 MHz ^1H , 126 MHz ^{13}C , TFA-d 298 K) spectrum of $[\text{Rh}(\mathbf{1})_2]\text{Cl}_3$ prepared from $\text{RhCl}_3 \cdot 3\text{H}_2\text{O}$. Chemical shifts in δ/ppm .

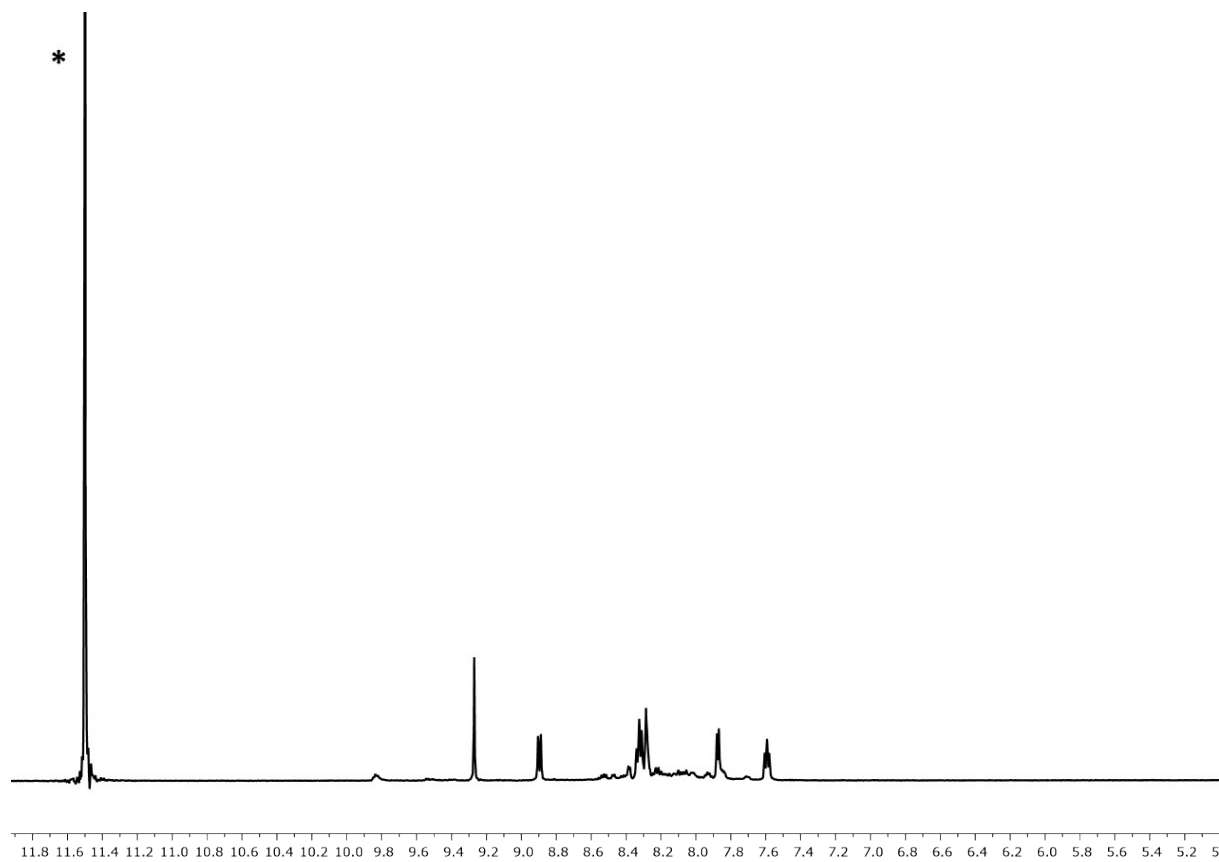


Fig. S10. ^1H NMR (500 MHz, TFA-d, 298 K) spectrum of $[\text{Rh}(\mathbf{1})_2]\text{Cl}_3$ prepared from $[\text{Rh}_2(\mu\text{-OAc})_4(\text{H}_2\text{O})_2]$, * = $\text{CF}_3\text{CO}_2\text{H}$. Chemical shifts in δ/ppm .

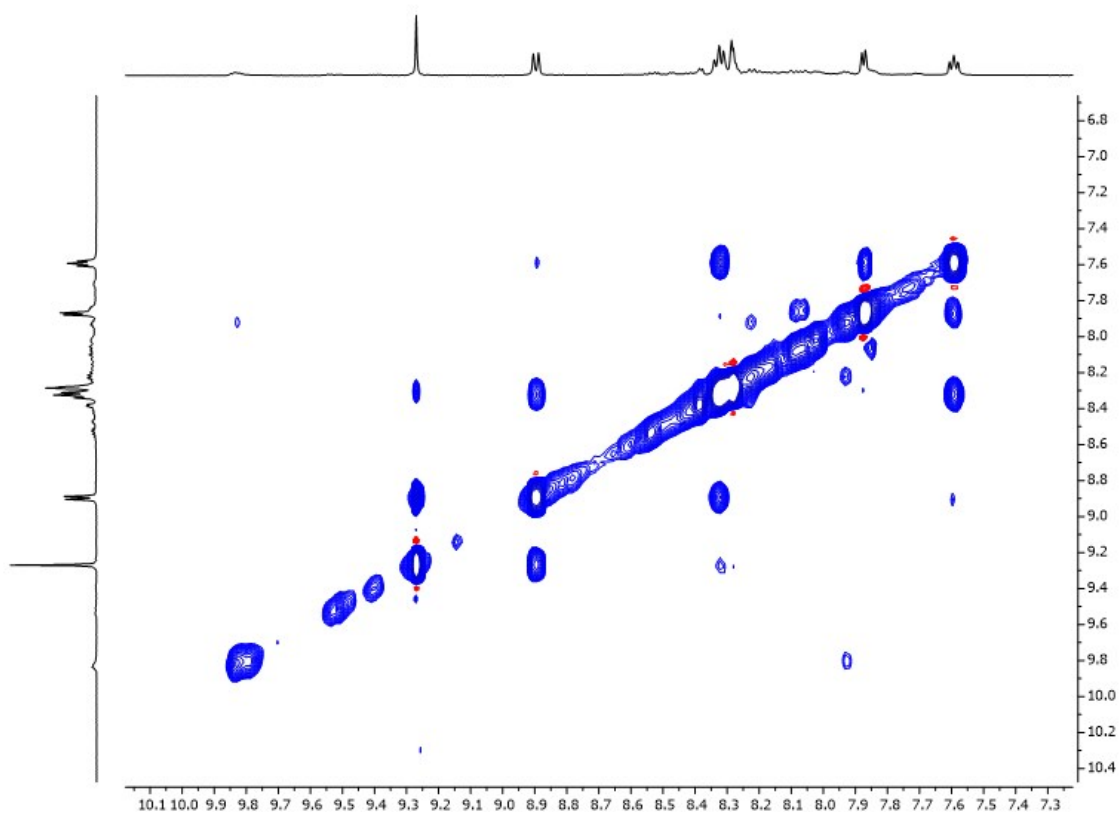


Fig. S11. NOESY (500 MHz, TFA-d 298 K) spectrum of $[\text{Rh}(\mathbf{1})_2]\text{Cl}_3$ prepared from $[\text{Rh}_2(\mu\text{-OAc})_4(\text{H}_2\text{O})_2]$. Chemical shifts in δ/ppm .

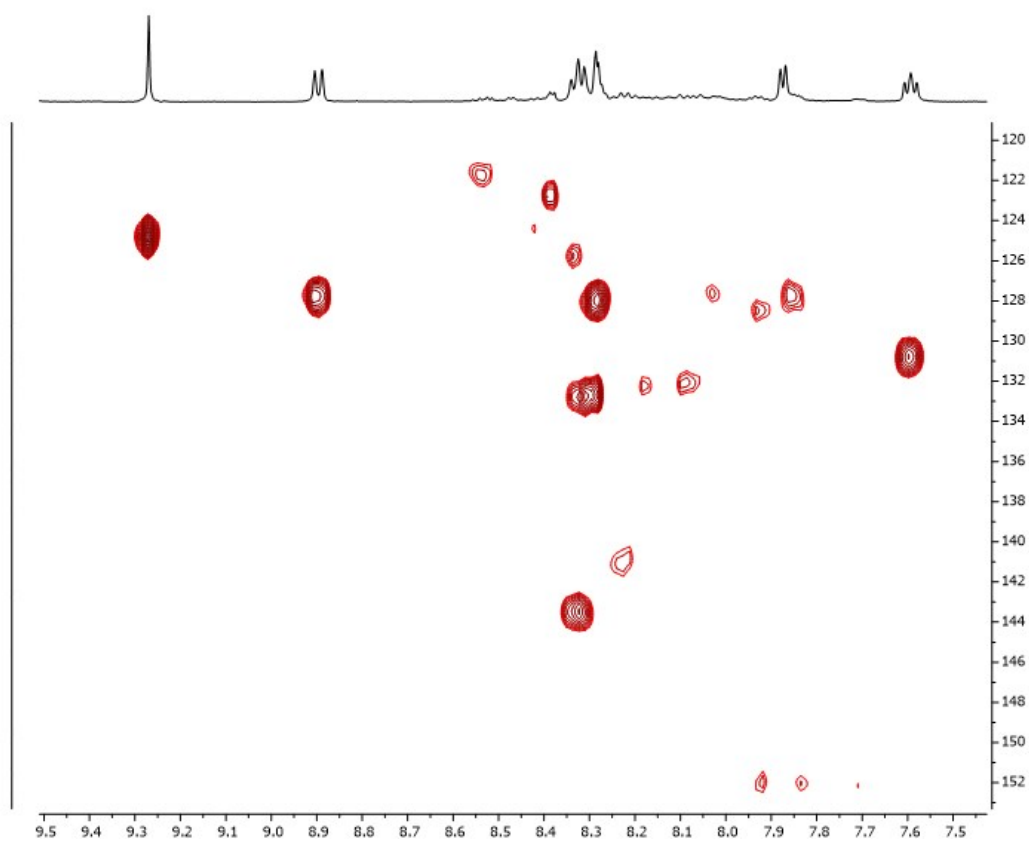


Fig. S12. HMQC (500 MHz ^1H , 126 MHz ^{13}C , TFA-d 298 K) spectrum of $[\text{Rh}(\mathbf{1})_2]\text{Cl}_3$ prepared from $[\text{Rh}_2(\mu\text{-OAc})_4(\text{H}_2\text{O})_2]$. Chemical shifts in δ/ppm .

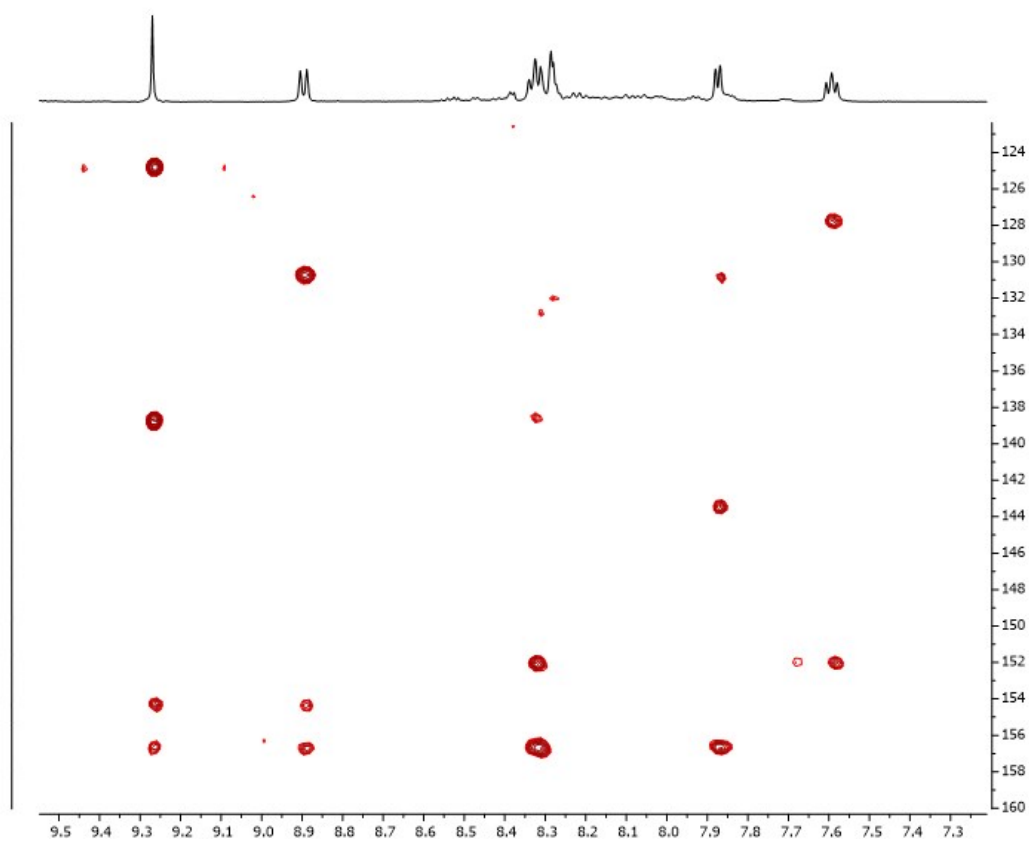


Fig. S13. HMBC (500 MHz ^1H , 126 MHz ^{13}C , TFA-d 298 K) spectrum of $[\text{Rh}(\mathbf{1})_2]\text{Cl}_3$ prepared from $[\text{Rh}_2(\mu\text{-OAc})_4(\text{H}_2\text{O})_2]$. Chemical shifts in δ/ppm .

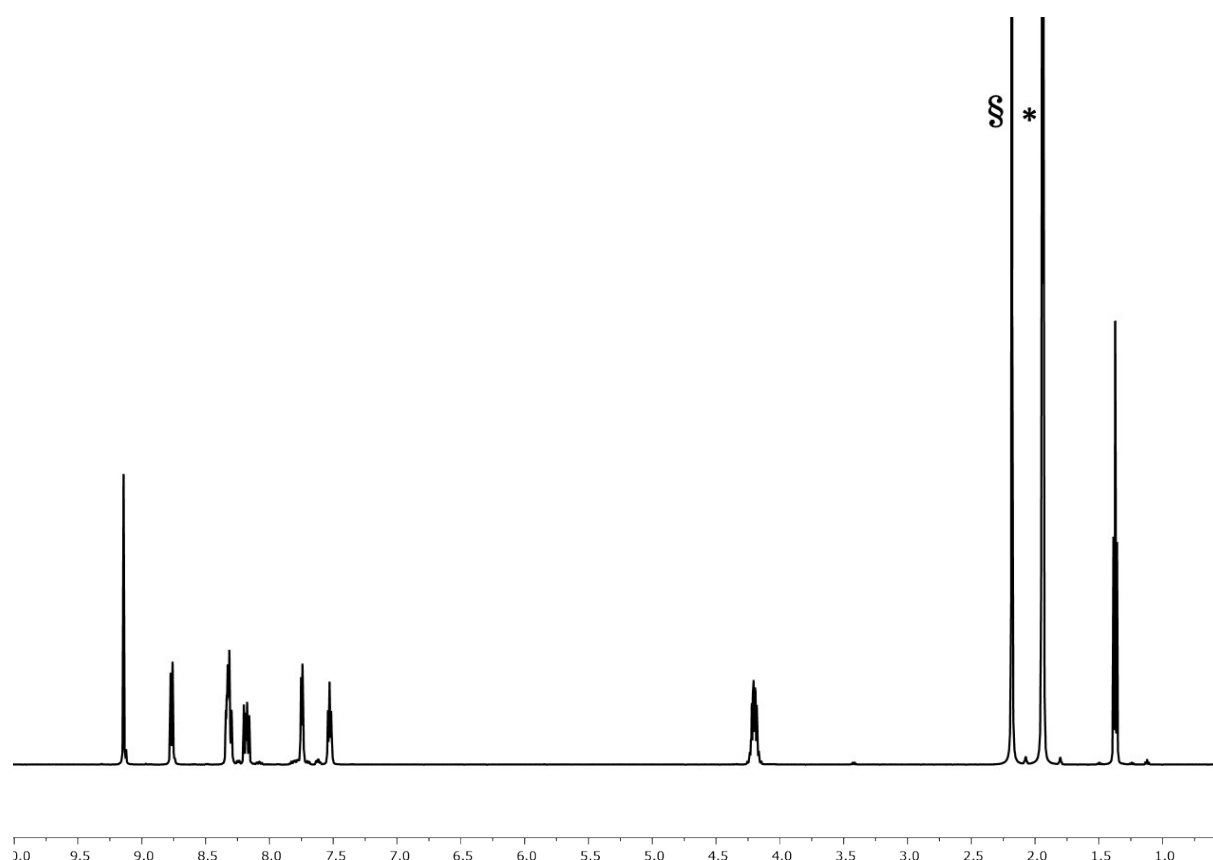


Fig. S14. ^1H NMR (500 MHz, CD_3CN , 298 K) spectrum of $[\text{Rh}(\mathbf{5})_2][\text{PF}_6]_3$, * = CHD_2CN , σ = HOD . Chemical shifts in δ/ppm .

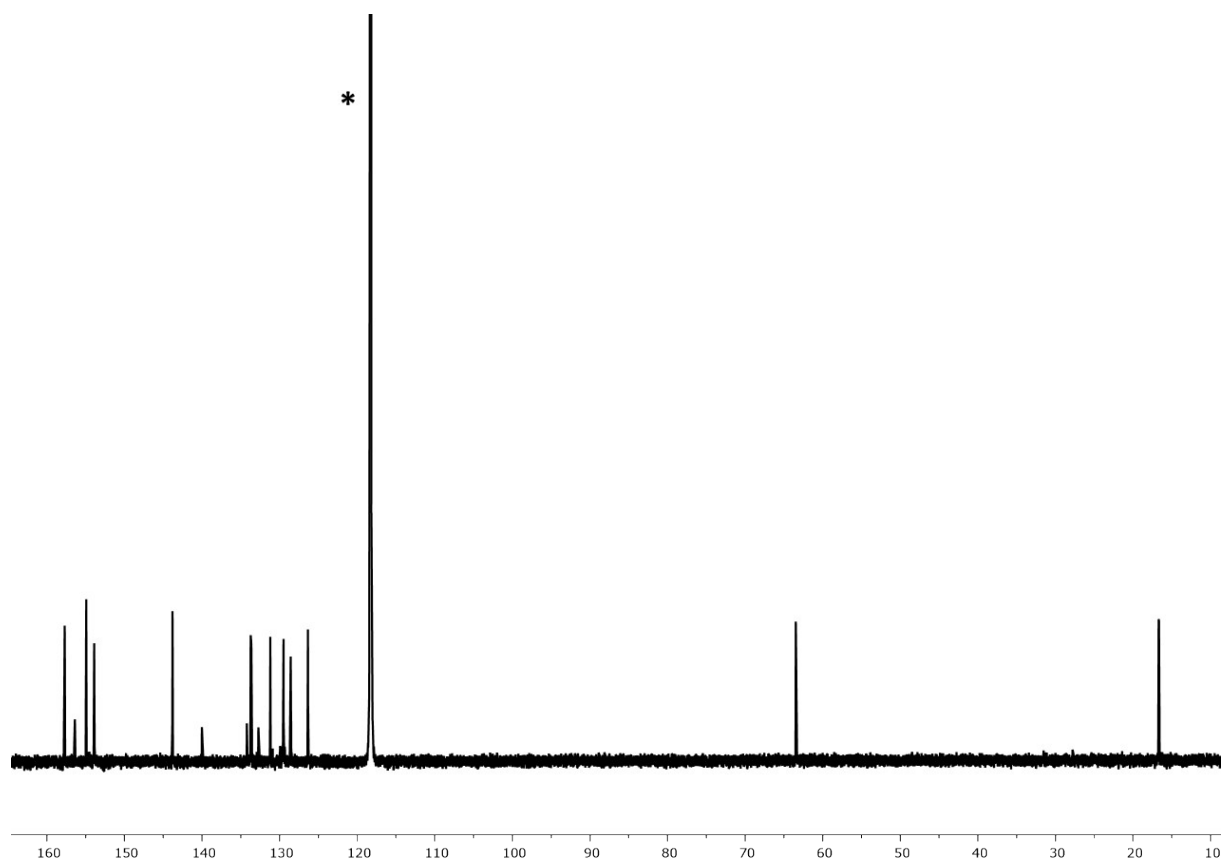


Fig. S15. $^{13}\text{C}\{^1\text{H}\}$ NMR (126 MHz, CD_3CN , 298 K) spectrum of $[\text{Rh}(\mathbf{5})_2][\text{PF}_6]_3$, * = CHD_2CN . Chemical shifts in δ/ppm .

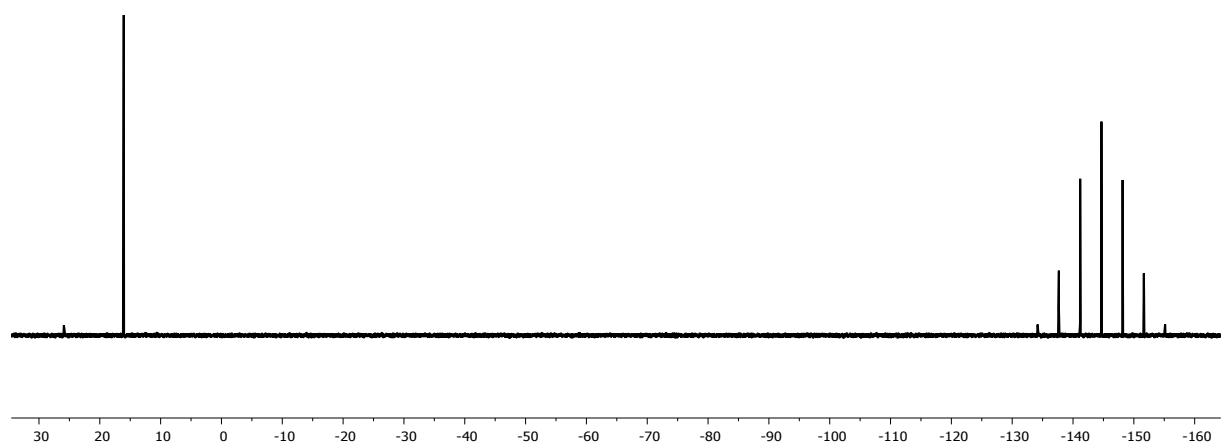


Fig. S16. $^{31}\text{P}\{^1\text{H}\}$ NMR (202 MHz, CD_3CN , 298 K) spectrum of $[\text{Rh}(\mathbf{5})_2][\text{PF}_6]_3$. Chemical shifts in δ/ppm .

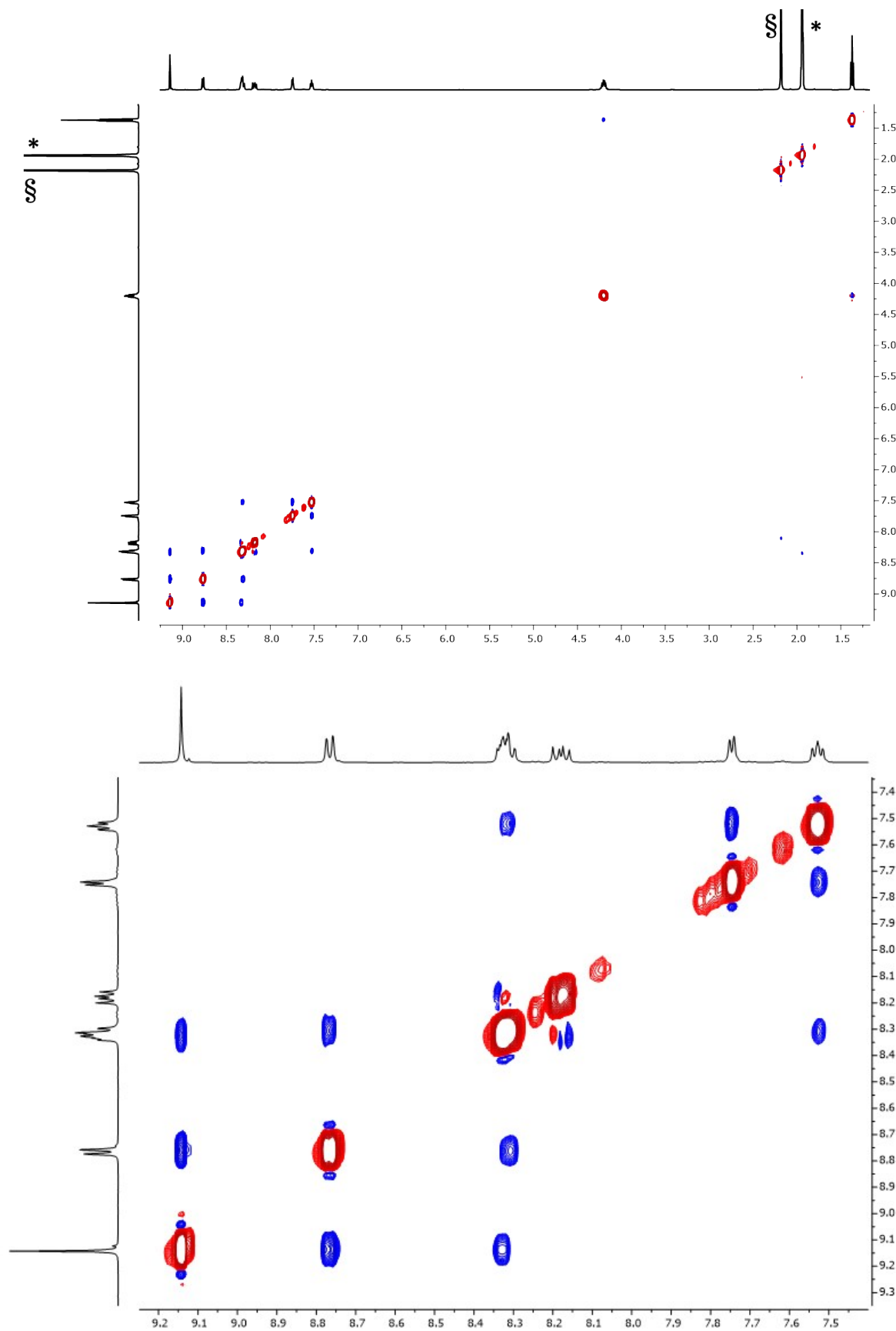


Fig. S17. NOESY (500 MHz, CD₃CN, 298 K) spectrum of [Rh(5)₂][PF₆]₃, * = CHD₂CN, § = HOD. Chemical shifts in δ/ppm.

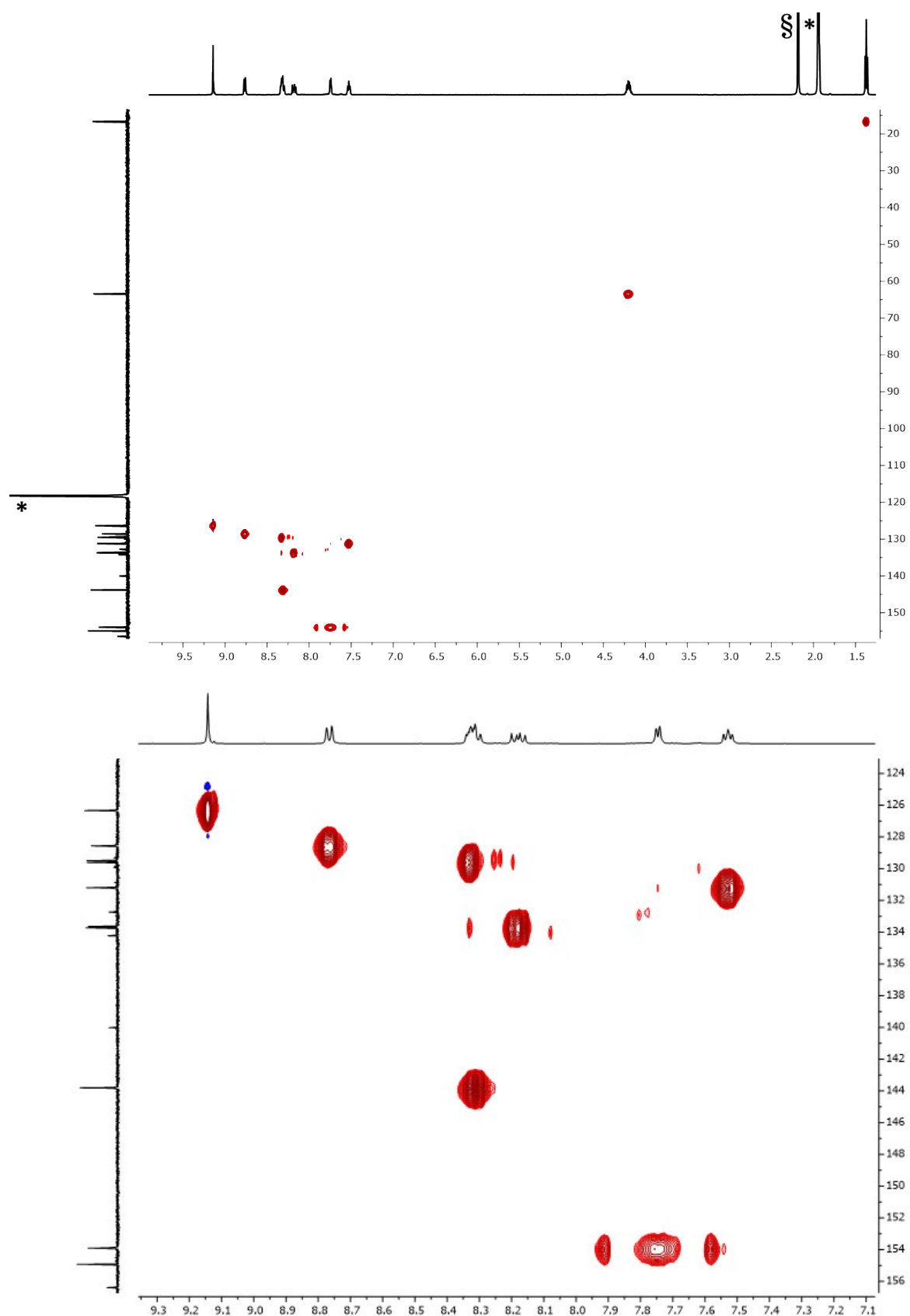


Fig. S18. HMQC (500 MHz ^1H , 126 MHz ^{13}C , CD_3CN , 298 K) spectrum of $[\text{Rh}(\mathbf{5})_2][\text{PF}_6]_3$, * = CHD_2CN , § = HOD . Chemical shifts in δ/ppm .

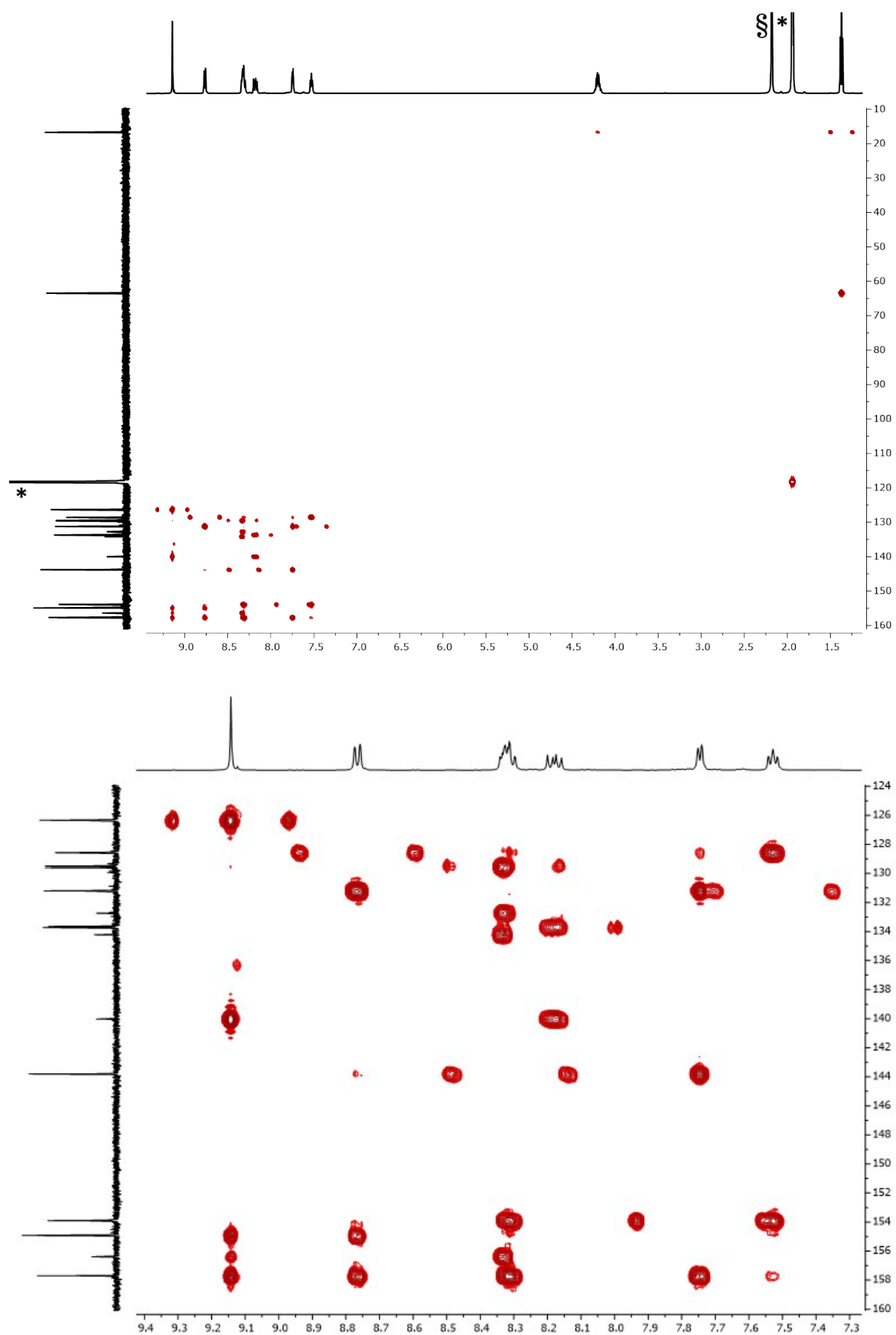


Fig. S19. HMBC (500 MHz ^1H , 126 MHz ^{13}C , CD_3CN , 298 K) spectrum of $[\text{Rh}(\mathbf{5})_2][\text{PF}_6]_3$, * = CHD_2CN , § = HOD . Chemical shifts in δ/ppm .

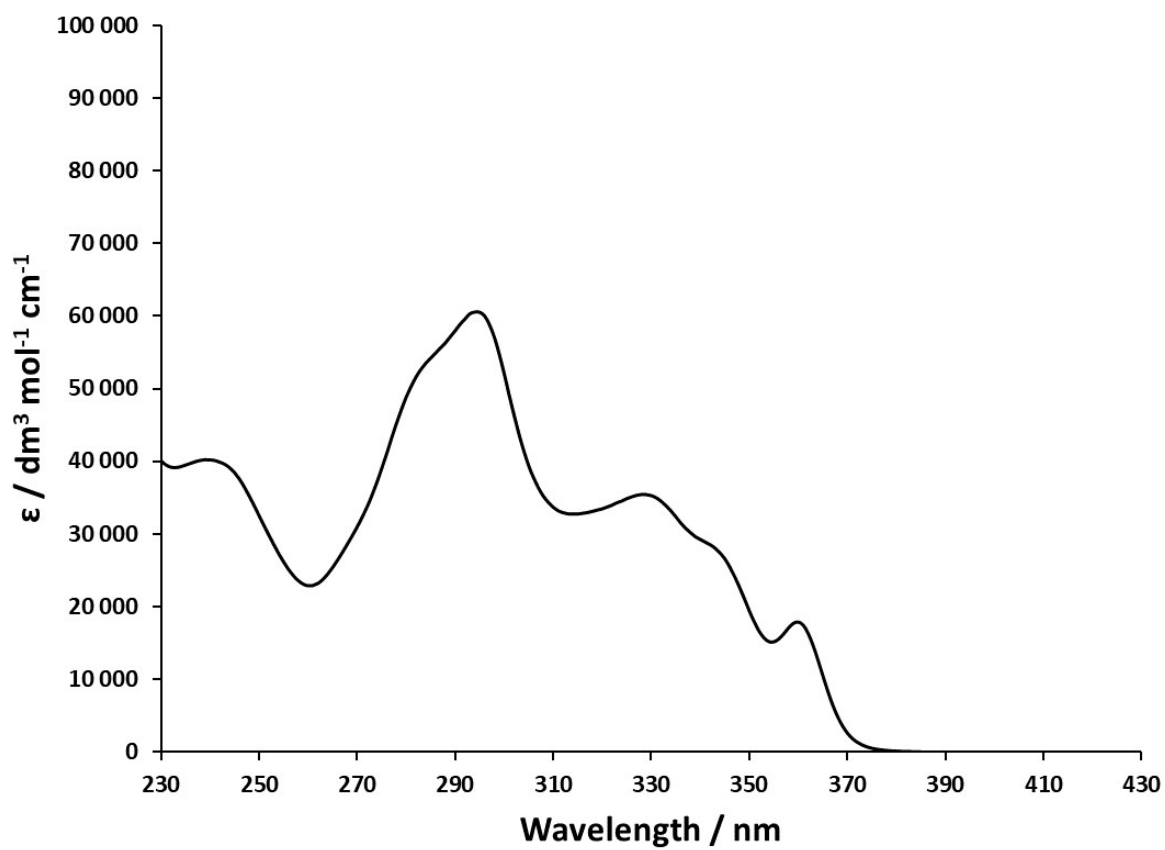
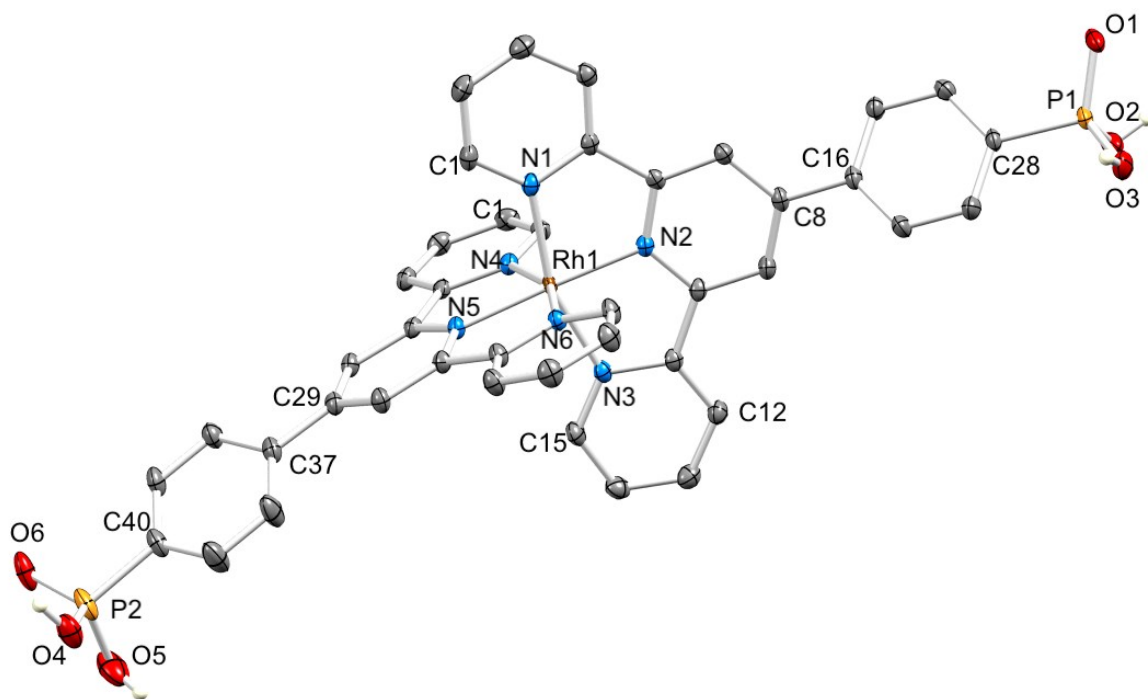
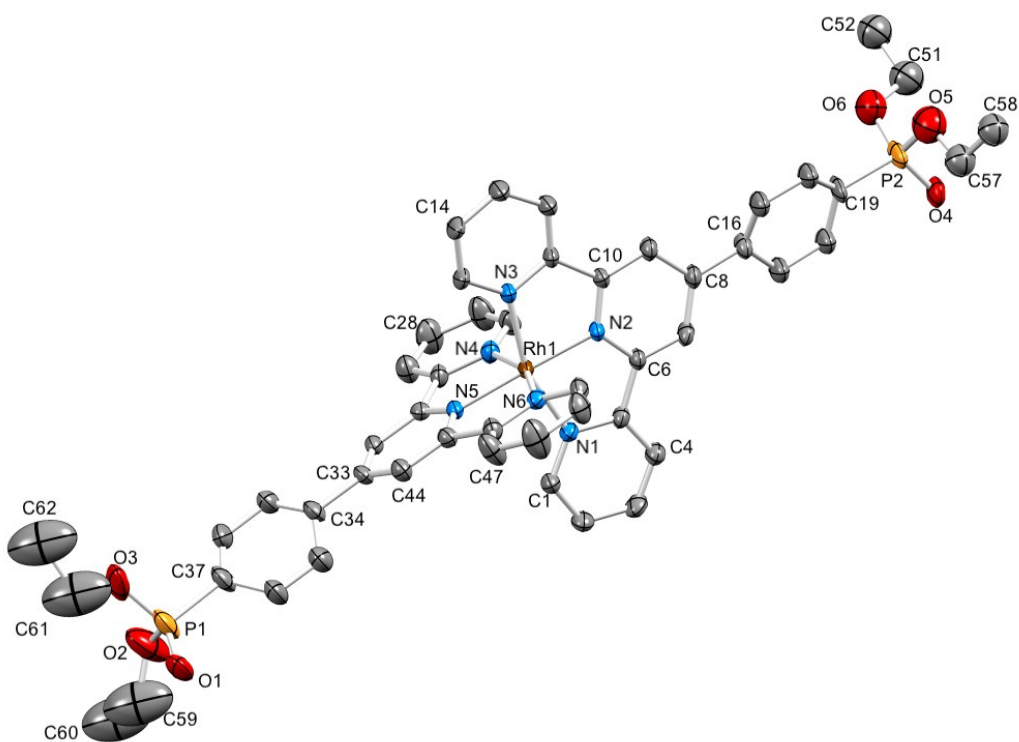


Fig. S20. Solution absorption spectra of $[\text{Rh}(\text{5})_2][\text{PF}_6]_3$ ($2.25 \times 10^{-5} \text{ mol dm}^{-3}$) in MeCN.



(a)



(b)

Fig. S21. (a) An ORTEP representation of the structure of the $[\text{Rh}(\mathbf{1})_2]^{3+}$ cation in $[\text{Rh}(\mathbf{1})_2][\text{NO}_3]_3 \cdot 1.25[\text{H}_3\text{O}][\text{NO}_3] \cdot 2.75\text{H}_2\text{O}$ with ellipsoids plotted at 50% probability level. H atoms except for those attached to the phosphonic acid groups are omitted for clarity. (b) An ORTEP representation of the structure of the $[\text{Rh}(\mathbf{5})_2]^{3+}$ cation in $[\text{Rh}(\mathbf{5})_2][\text{PF}_6]_3 \cdot \text{MeCN}$ with ellipsoids plotted at 30% probability level and H atoms omitted for clarity. Both phenylene rings and the $\text{PO}(\text{OEt})_2$ group including P2 were disordered (see Experimental section for details).

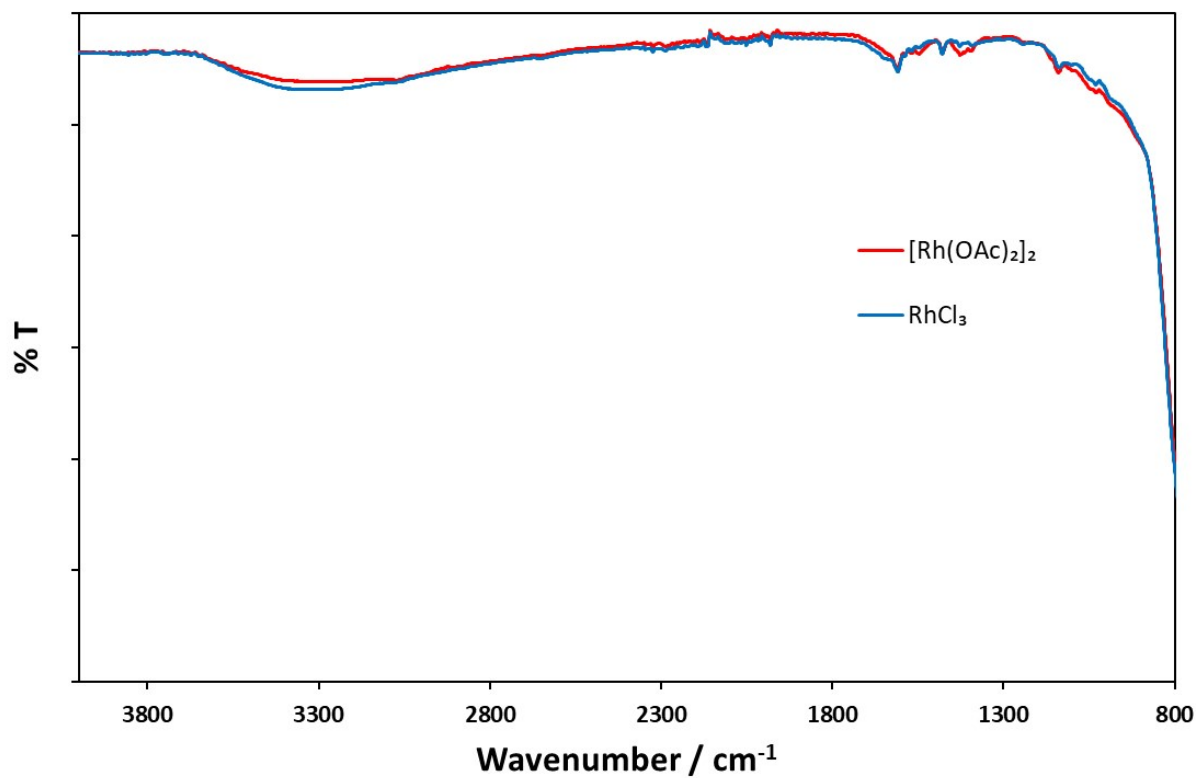


Fig. S22. Solid-state IR spectra of NP- $[\text{Rh}(\mathbf{1})_2]^{3+}$, prepared from $[\text{Rh}_2(\mu\text{-OAc})_4(\text{H}_2\text{O})_2]$ (red) or $\text{RhCl}_3 \cdot 3\text{H}_2\text{O}$ (blue) following the procedures in the Experimental Section.

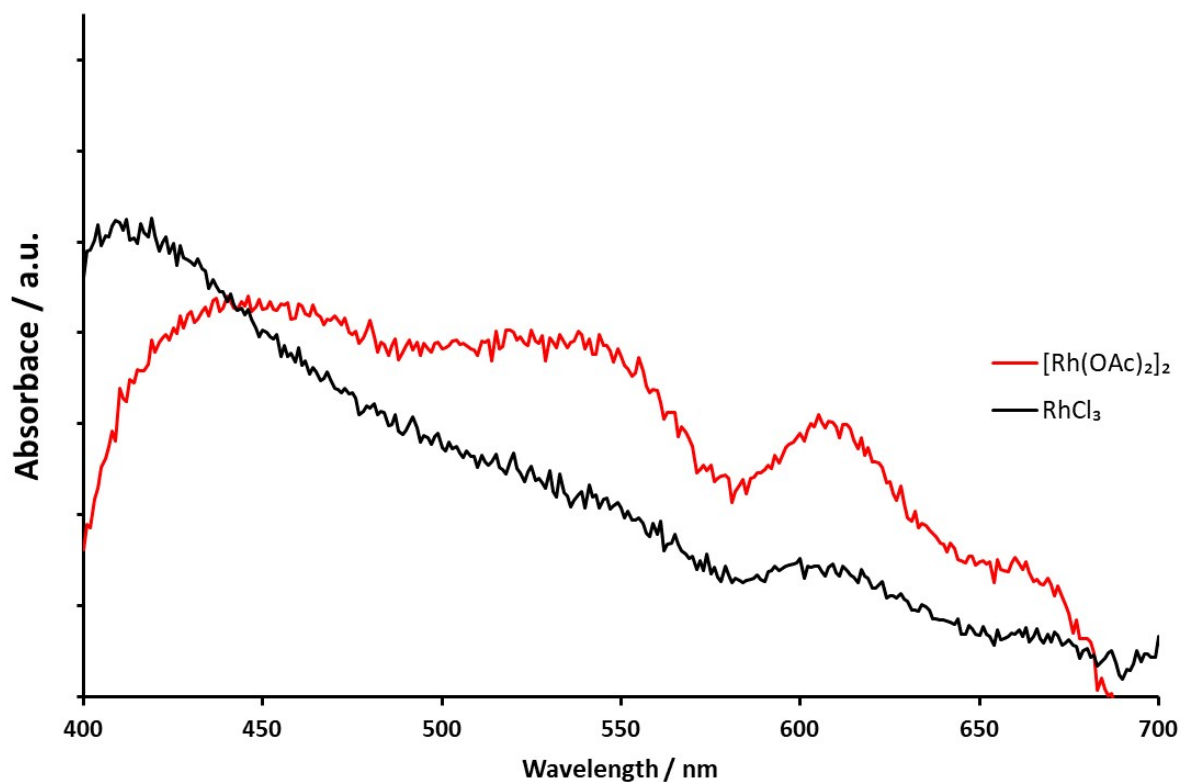


Fig. S23. Solid-state absorption spectra of NP- $[\text{Rh}(\mathbf{1})_2]^{3+}$ prepared from $[\text{Rh}_2(\mu\text{-OAc})_4(\text{H}_2\text{O})_2]$ (red) or $\text{RhCl}_3 \cdot 3\text{H}_2\text{O}$ (black); The spectra are background-corrected using an NP reference.

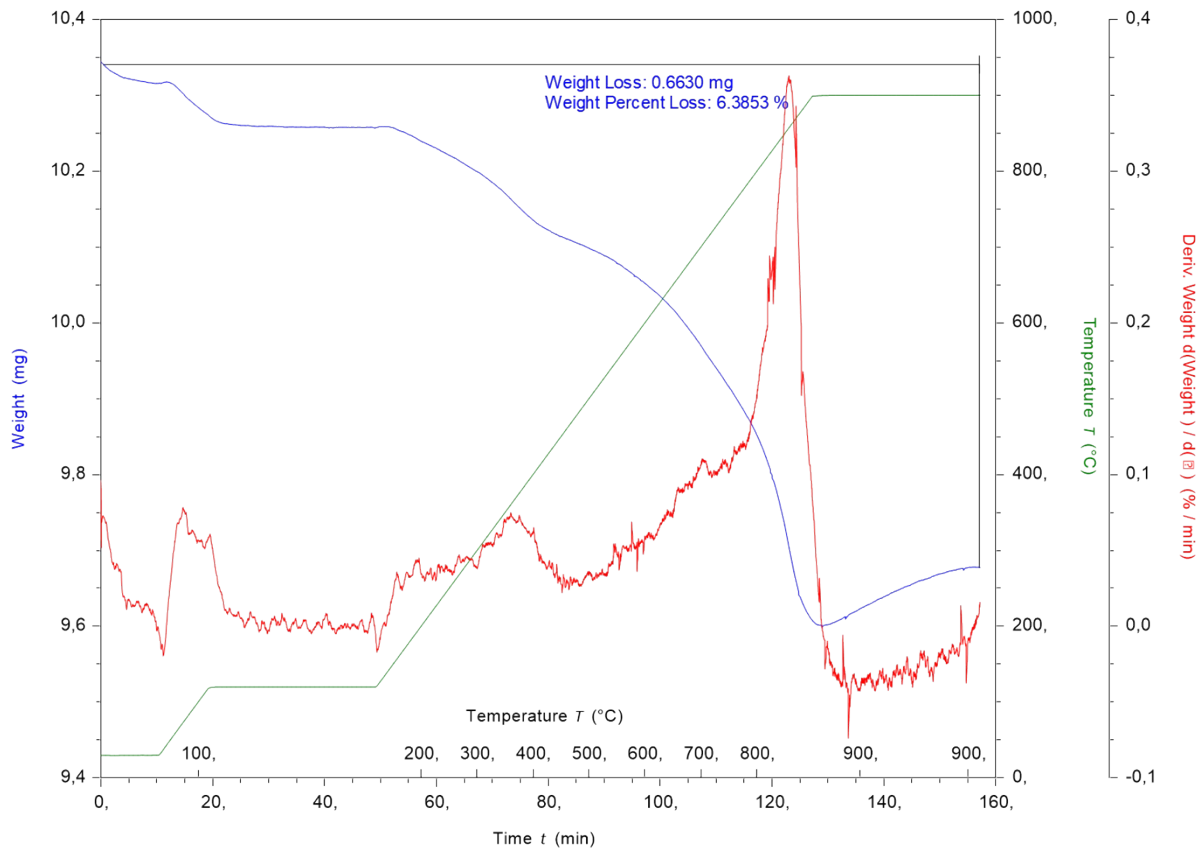


Fig. S24. TGA curve for NP-[Rh(1)₂]³⁺ prepared from [Rh₂(μ-OAc)₄(H₂O)₂]: Weight against time and temperature (blue), derivative of weight change against time (red).

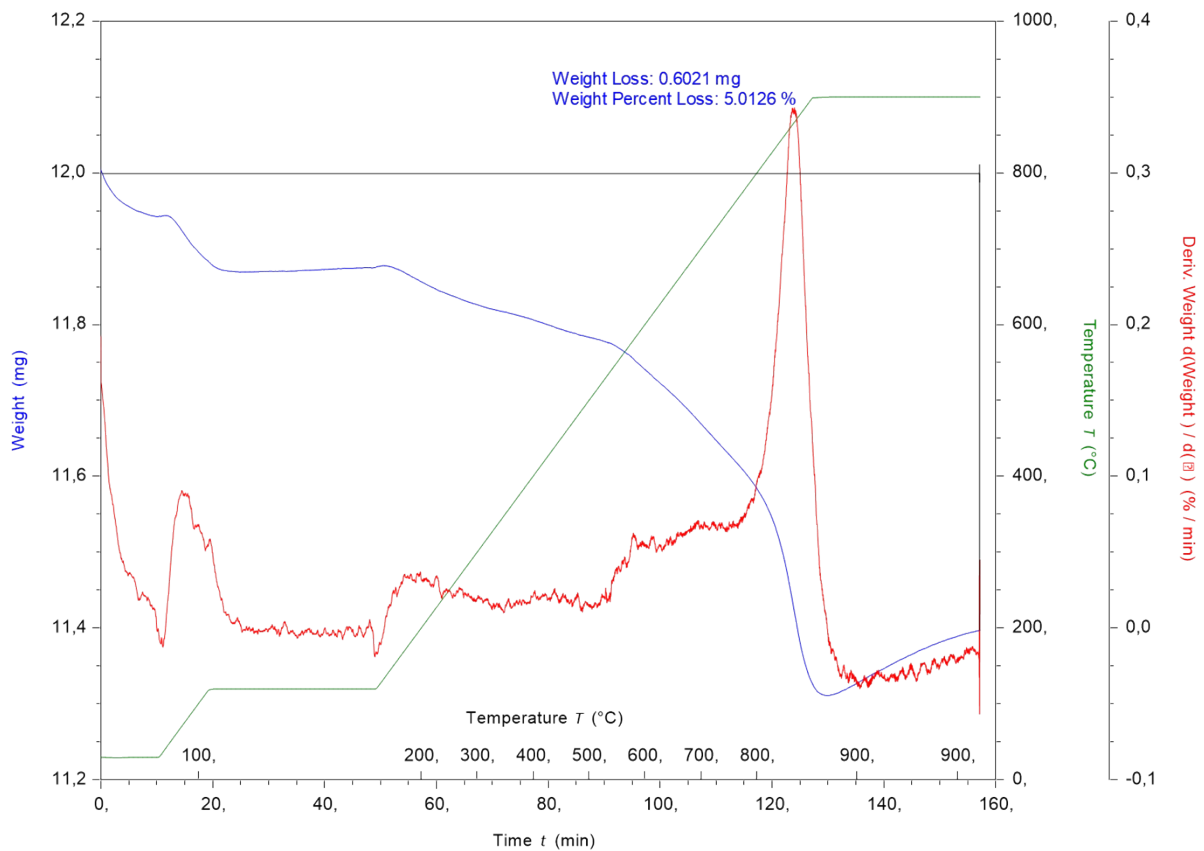


Fig. S25. TGA curve for NP-[Rh(1)₂]³⁺ prepared from RhCl₃·3H₂O: Weight against time and temperature (blue), derivative of weight change against time (red).

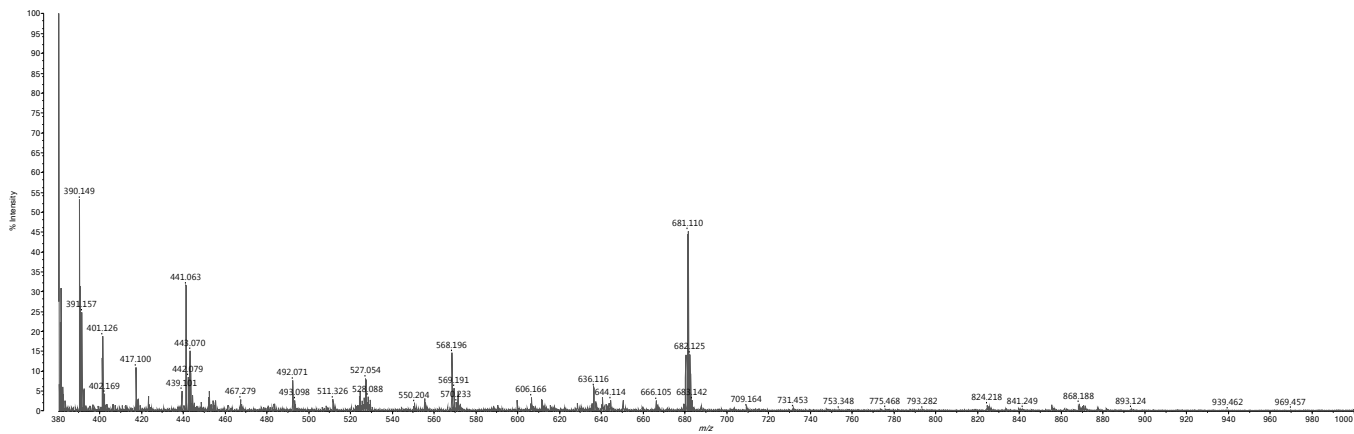


Fig. S26. MALDI mass spectrum (with CHCA matrix) of **(1)**@TiO₂ NPs prepared from [Rh₂(μ-OAc)₄(H₂O)₂].

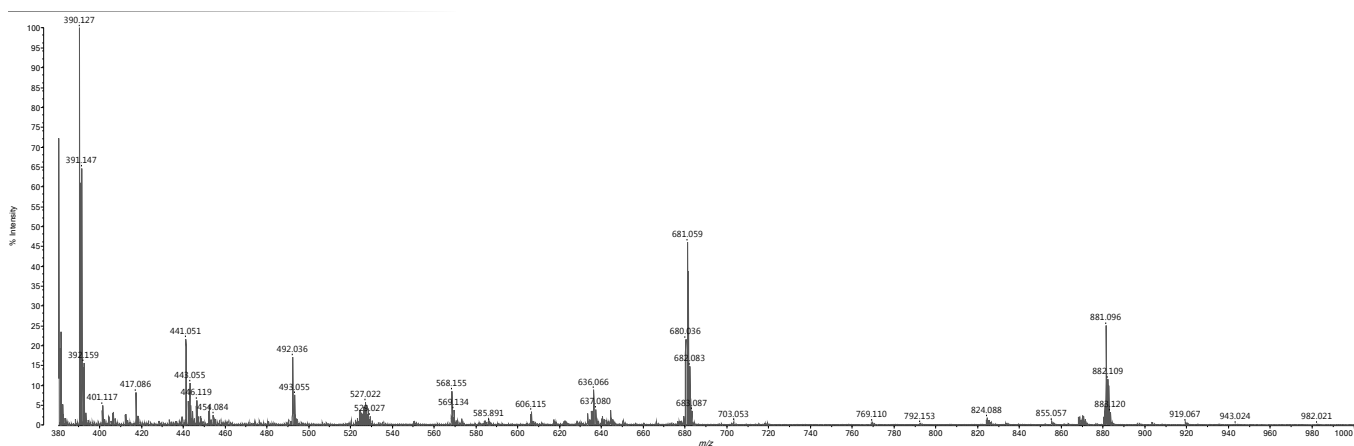


Fig. S27. MALDI mass spectrum (with CHCA matrix) of Rh(**1**)₂@TiO₂ NPs prepared from RhCl₃·3H₂O.

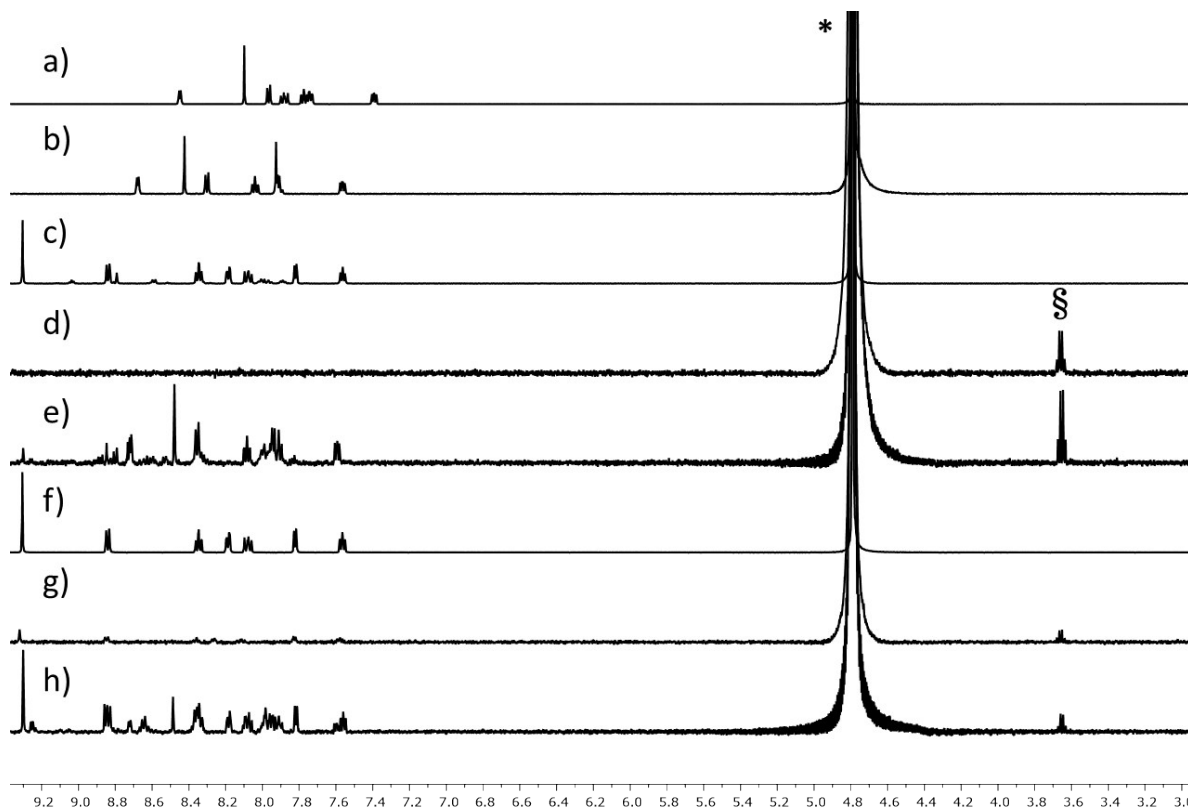


Fig. S28. ^1H NMR spectra (500 MHz, D_2O , 298 K) of **1** in D_2O and NaOH (a), (**1**)@ TiO_2 in D_2O and NaOH (b), $[\text{Rh}(\mathbf{1})_2]\text{Cl}_3$ made using $[\text{Rh}_2(\mu\text{-OAc})_4(\text{H}_2\text{O})_2]$ in D_2O and NaOH (c), $\text{Rh}(\mathbf{1})_2$ @ TiO_2 NPs made using $[\text{Rh}_2(\mu\text{-OAc})_4(\text{H}_2\text{O})_2]$ in D_2O (d), $\text{Rh}(\mathbf{1})_2$ @ TiO_2 NPs made using $[\text{Rh}_2(\mu\text{-OAc})_4(\text{H}_2\text{O})_2]$ in D_2O and NaOH (e), $[\text{Rh}(\mathbf{1})_2]\text{Cl}_3$ made using $\text{RhCl}_3 \cdot 3\text{H}_2\text{O}$ in D_2O and NaOH (f), $\text{Rh}(\mathbf{1})_2$ @ TiO_2 NPs made using $\text{RhCl}_3 \cdot 3\text{H}_2\text{O}$ in D_2O (g), $\text{Rh}(\mathbf{1})_2$ @ TiO_2 NPs made using $\text{RhCl}_3 \cdot 3\text{H}_2\text{O}$ in D_2O and NaOH (h). Chemical shifts in δ/ppm .

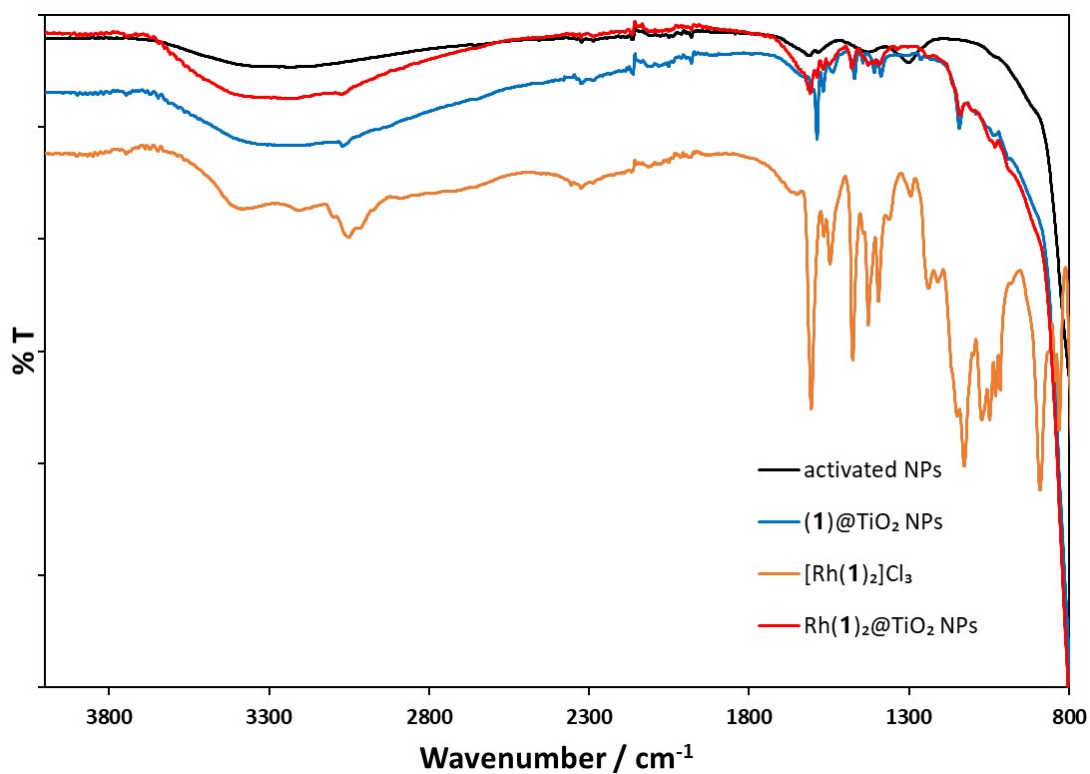


Fig. S29. Solid-state IR spectra of activated NPs (black), (**1**)@ TiO_2 NPs (blue), $[\text{Rh}(\mathbf{1})_2]\text{Cl}_3$ (orange) and $\text{Rh}(\mathbf{1})_2$ @ TiO_2 NPs (red) following the procedures in the Experimental Section.

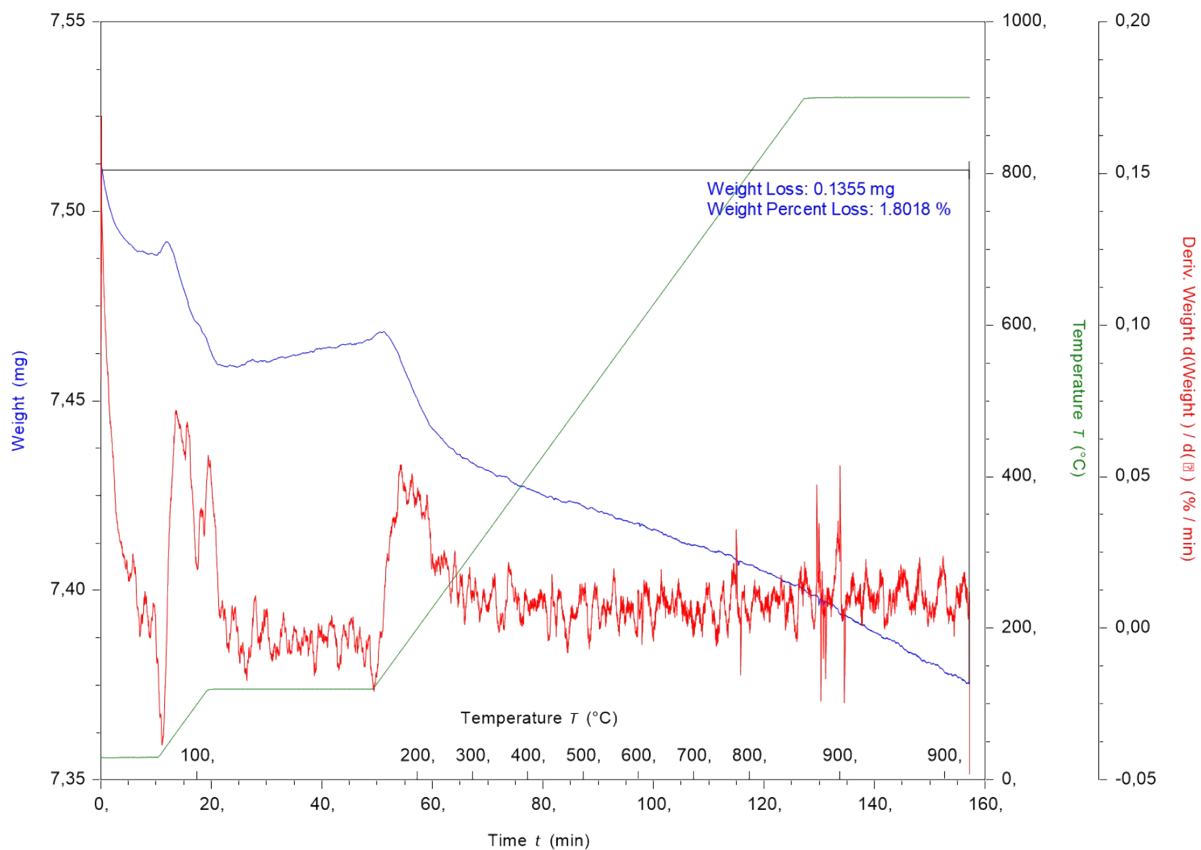


Fig. S30. TGA curve for commercial NPs: Weight against time and temperature (blue), derivative of weight change against time (red).

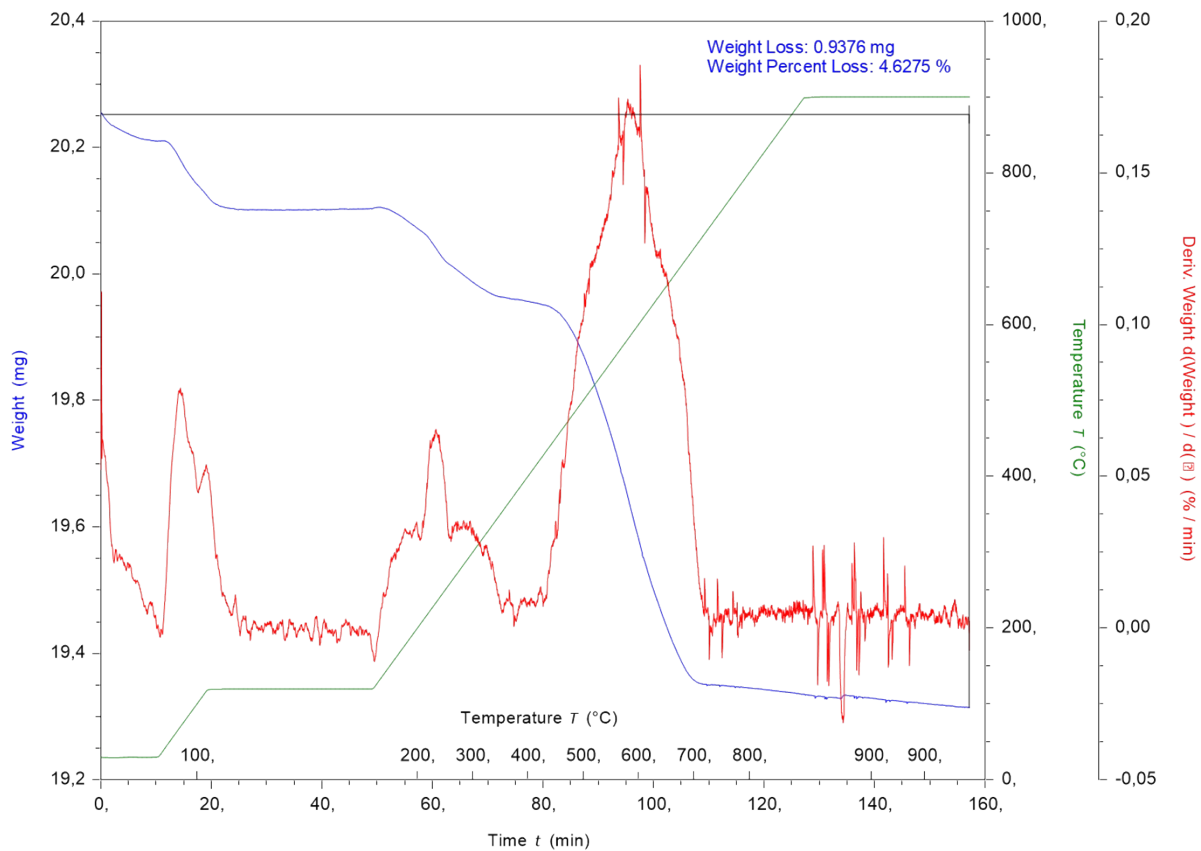


Fig. S31. TGA curve of (1)@TiO₂ NPs: Weight against time and temperature (blue), derivative of weight change against time (red).

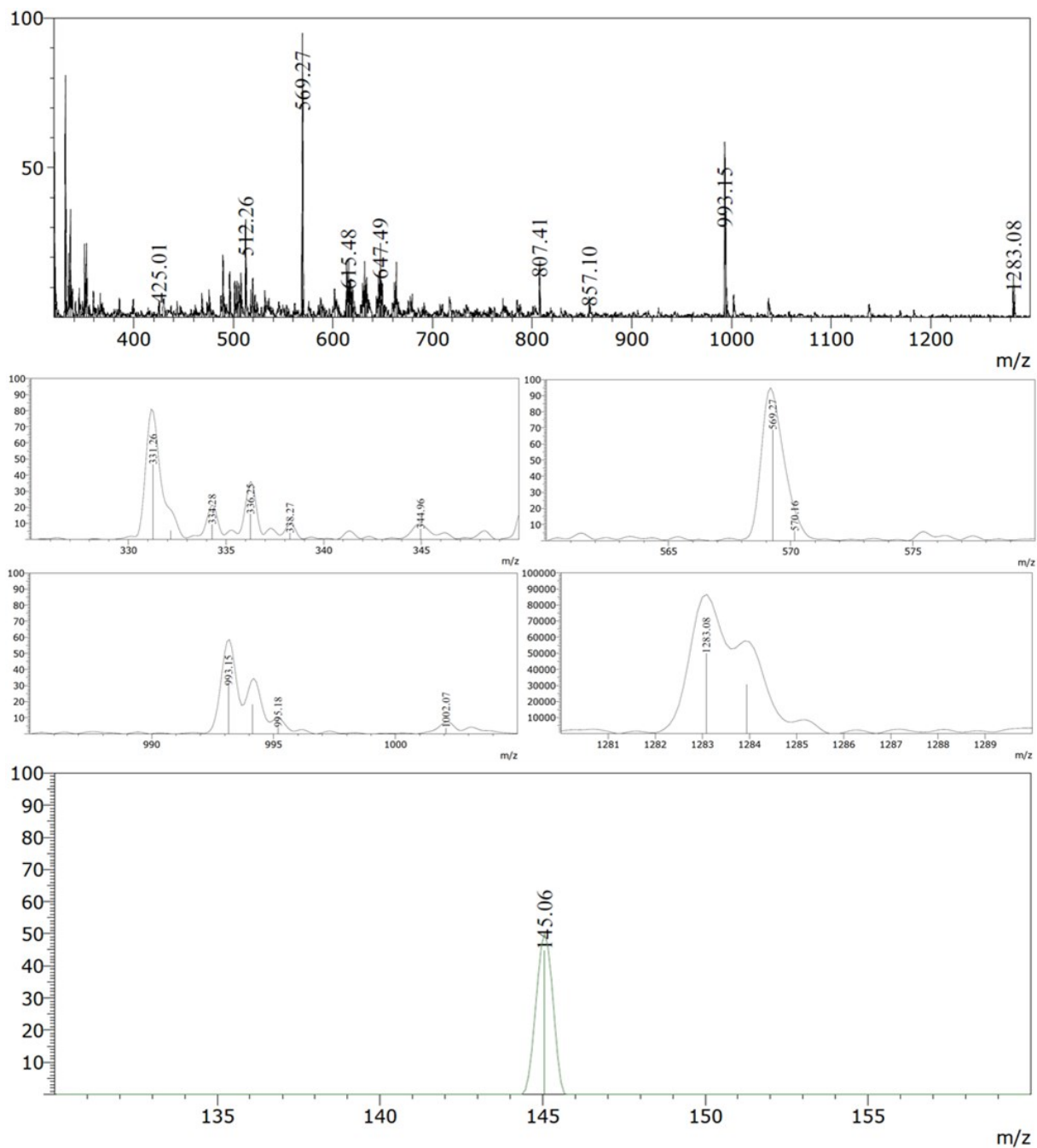
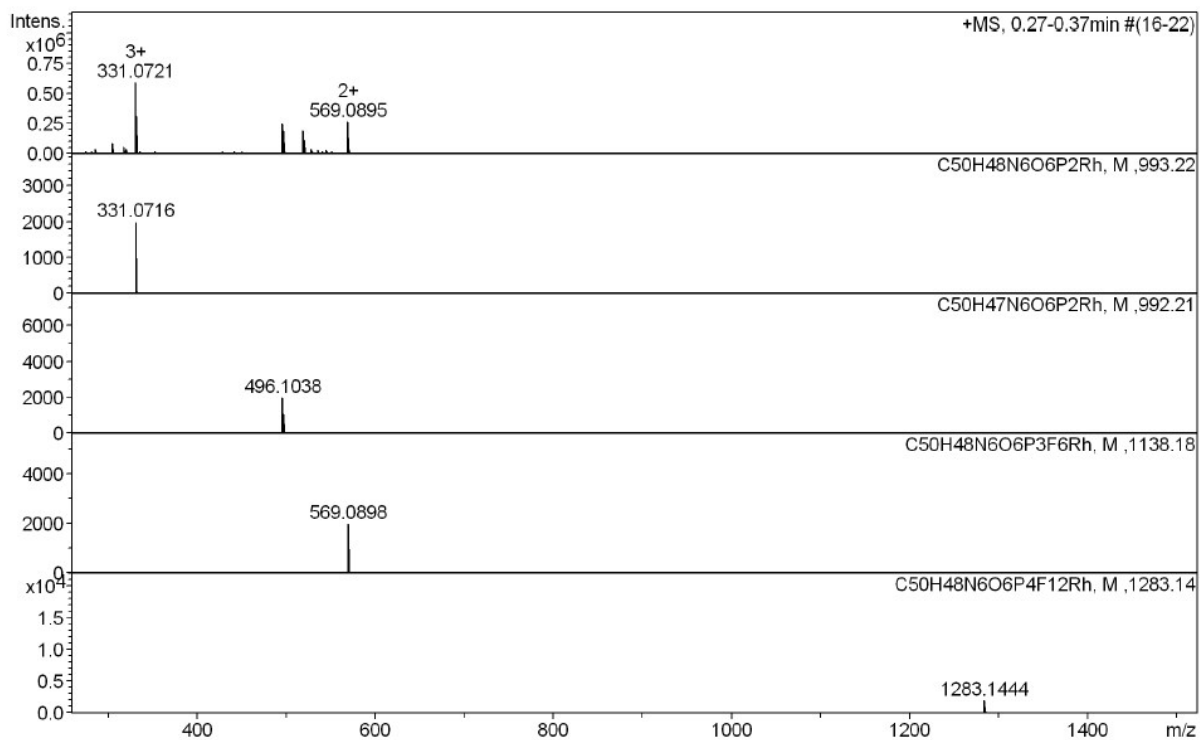
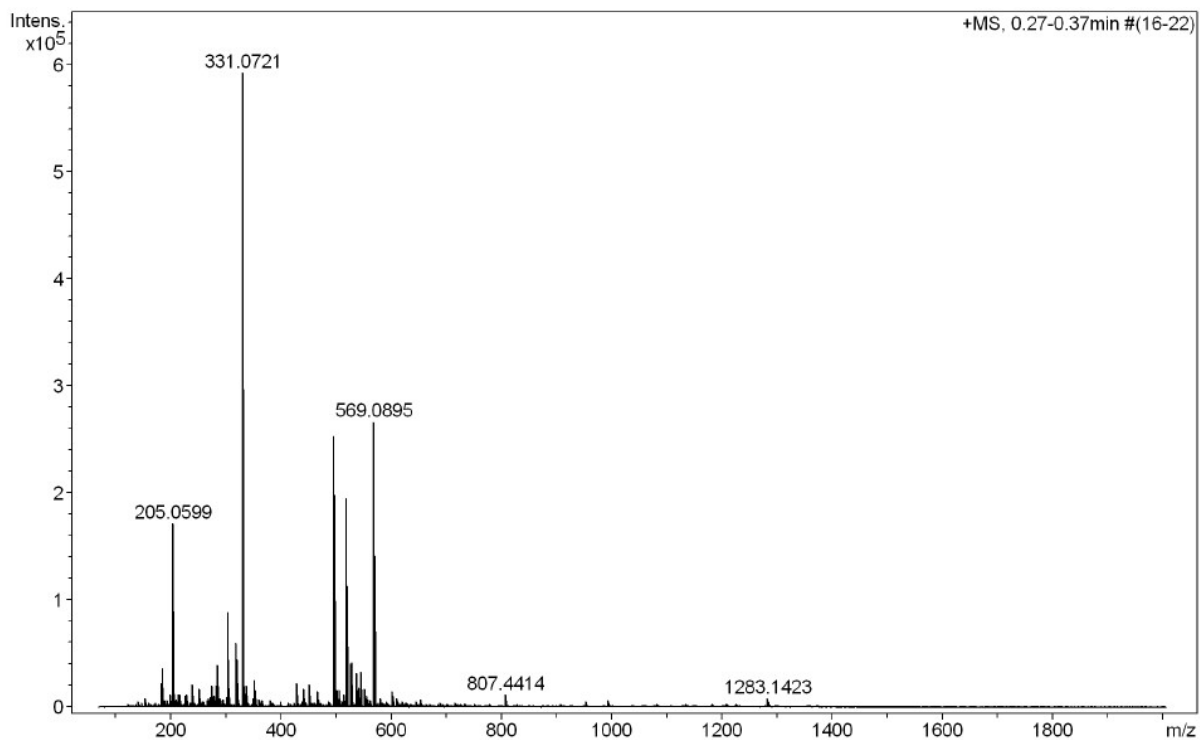


Fig. S32. Electrospray mass spectrum of $[\text{Rh}(\mathbf{5})_2][\text{PF}_6]_3$ (MeCN). Positive mode in black, negative mode in green.



Measured m/z vs. theoretical m/z

Meas. m/z	#	Formula	Score	m/z	err [mDa]	err [ppm]	mSigma	rdb	e ⁻ Conf	z
331.0721	1	C 50 H 48 N 6 O 6 P 2 Rh	100.00	331.0716	-0.5	-1.4	14.4	31.5	even	3+
496.1035	1	C 50 H 47 N 6 O 6 P 2 Rh	100.00	496.1038	0.3	0.6	126.5	32.0	even	2+
569.0895	1	C 50 H 48 F 6 N 6 O 6 P 3 Rh	100.00	569.0898	0.3	0.5	19.2	29.0	even	
1283.1423	1	C 50 H 48 F 12 N 6 O 6 P 4 Rh	100.00	1283.1444	2.1	1.7	40.2	26.5	even	1+

Fig. S33. High resolution electrospray mass spectrum of $[\text{Rh}(\text{5})_2][\text{PF}_6]_3$ (MeCN, positive mode). Calculated spectra are shown in the lower four traces.

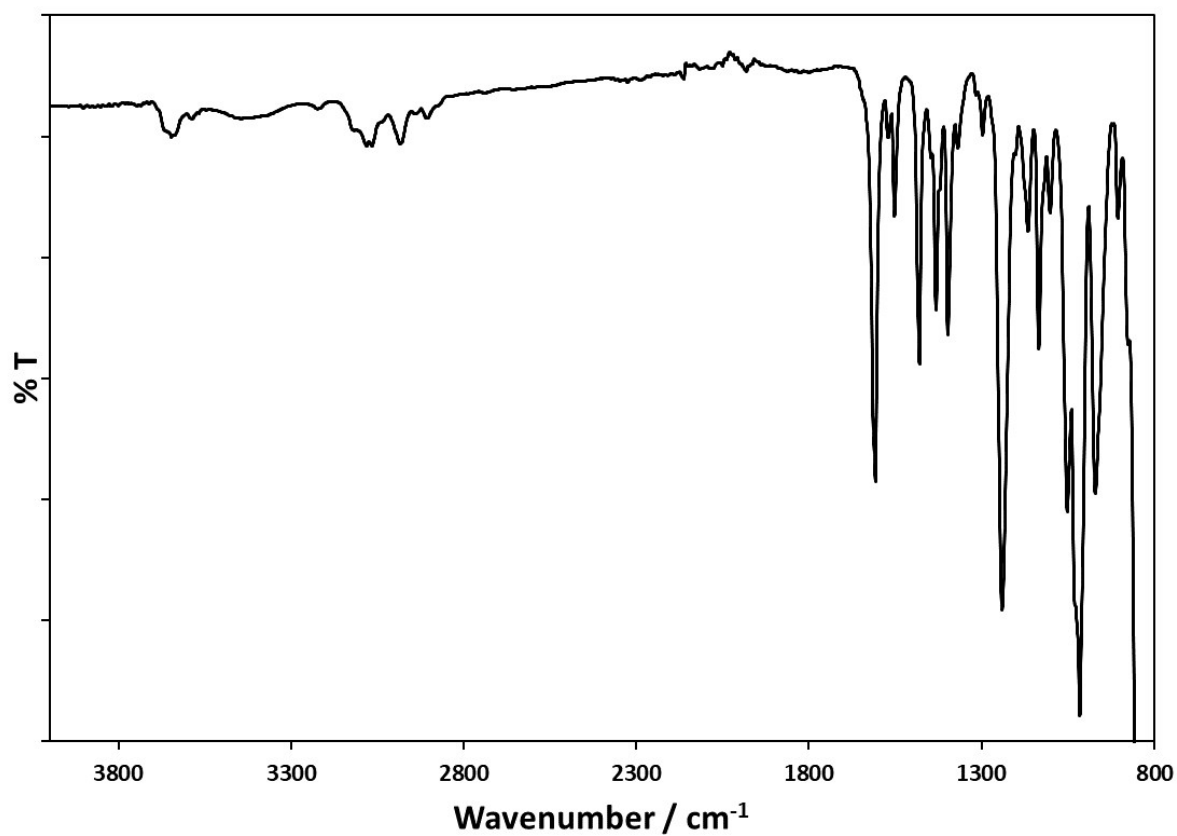


Fig. S34. Solid-state IR spectrum of $[\text{Rh}(\mathbf{5})_2][\text{PF}_6]_3$.

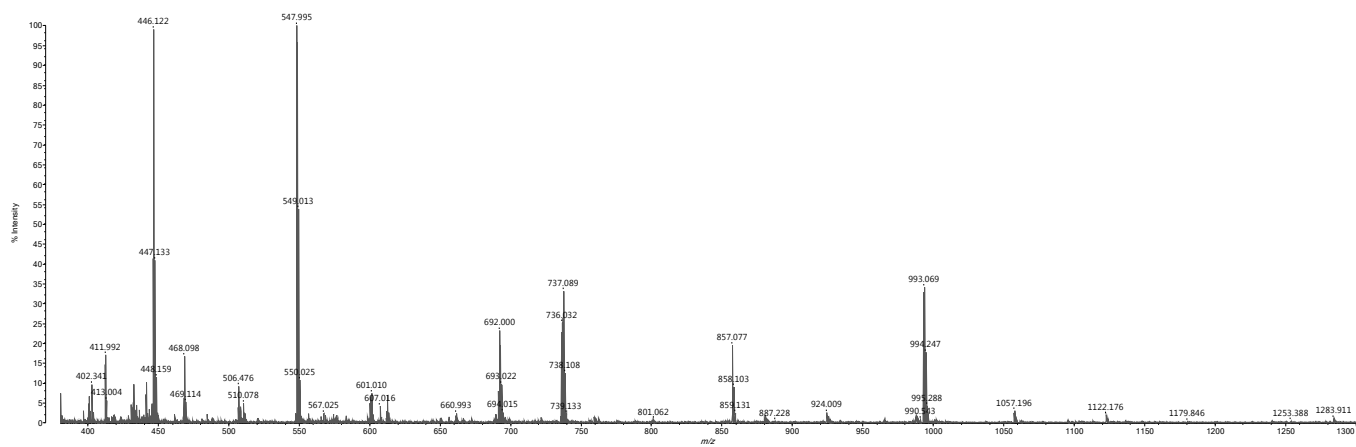


Fig. S35. MALDI mass spectrum (with CHCA matrix) of $[\text{Rh}(\mathbf{5})_2][\text{PF}_6]_3$

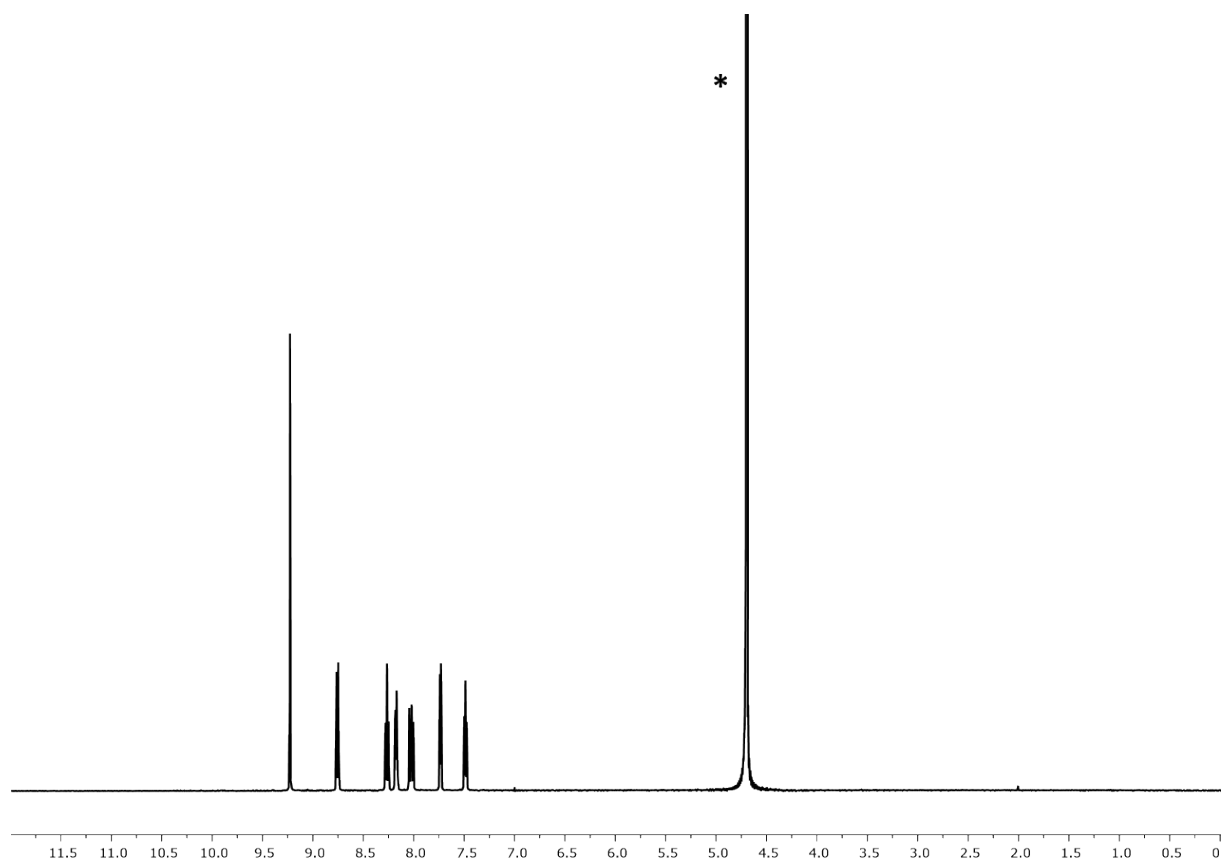


Fig. S36. ^1H NMR (500 MHz, D_2O , 298 K) spectrum of $[\text{Rh}(\mathbf{1})_2]\text{Cl}_3$ prepared from $\text{RhCl}_3 \cdot 3\text{H}_2\text{O}$, * = HOD. Chemical shifts in δ/ppm .

Table S1: Conditions and yields for the oxidation of *rac*-(1*R*)-1-phenylethanol to acetophenone.

Conditions	Yield (Product)
$\text{Rh}(\mathbf{1})_2@ \text{TiO}_2$ NPs (0.5 mol%), NaOH (25 mM), 100 °C, 24 h	23.2%
$\text{Rh}(\mathbf{1})_2@ \text{TiO}_2$ NPs (0.5 mol%), NaOH (50 mM), 100 °C, 24 h	21.9%
$\text{Rh}(\mathbf{1})_2@ \text{TiO}_2$ NPs (0.5 mol%), NaOH (0.25 M), 100 °C, 24 h	21.9%
$\text{Rh}(\mathbf{1})_2@ \text{TiO}_2$ NPs (0.5 mol%), NaOH (2.5 M), 100 °C, 24 h	18.7%
$\text{Rh}(\mathbf{1})_2@ \text{TiO}_2$ NPs (0.5 mol%), NaOH (25 mM), 22 °C, 72 h	< 1%
Commercial NPs (0.5 mol%), NaOH (25 mM), 100 °C, 24 h	< 1%
Activated NPs (0.5 mol%), NaOH (25 mM), 100 °C, 24 h	< 1%
Activated NPs (0.5 mol%), $[\text{Rh}_2(\mu\text{-OAc})_4(\text{H}_2\text{O})_2]$ (0.5 mol%), NaOH (25 mM), 100 °C, 24 h	< 1%
$(\mathbf{1})@ \text{TiO}_2$ NPs (0.5 mol%), NaOH (25 mM), 100 °C, 24 h	< 1%
$(\mathbf{1})@ \text{TiO}_2$ NPs (0.5 mol%), $[\text{Rh}_2(\mu\text{-OAc})_4(\text{H}_2\text{O})_2]$ (0.5 mol%), NaOH (25 mM), 100 °C, 24 h	7%
$[\text{Rh}(\mathbf{1})_2]\text{Cl}_3$ (0.5 mol%), NaOH (25 mM), 100 °C, 24 h	15.8%
$[\text{Rh}(\mathbf{5})_2][\text{PF}_6]_3$ (0.5 mol%), NaOH (25 mM), 100 °C, 24 h	19.2%
$\text{Rh}(\mathbf{1})_2@ \text{TiO}_2$ NPs (0.5 mol%), NaOH (25 mM), 100 °C, 72 h, air	29.3%
$\text{Rh}(\mathbf{1})_2@ \text{TiO}_2$ NPs (0.5 mol%), NaOH (25 mM), 100 °C, 72 h, argon	16.5%

CHAPTER V: ATTRACTION IN ACTION

REDUCTION OF WATER TO DIHYDROGEN USING SURFACE-FUNCTIONALIZED TiO₂ NANOPARTICLES

5.1 Summary

Chapter IV showed that by using an NP platform, it was possible to achieve catalytic activities comparable to homogenous catalytic counterpart given appropriate reaction conditions. In the published paper that comprises this Chapter,²⁵ focus centres on a previously reported system for water reduction under simulated sunlight irradiation.²⁴ Lehn and Sauvage utilized [Ru(bpy)₃]²⁺ and [Rh(bpy)₃]³⁺ as photo- and electrocatalysts, K₂[PtCl₄] as catalyst to facilitate dihydrogen formation, bpy as a catalyst regenerative additive, triethanolamine (TEOA) as sacrificial electron donor and aqueous H₂SO₄ for pH adjustments to achieve photochemical water reductions. Once again, the aim of the project for this thesis was to show the effect of immobilizing analogous metal complexes on TiO₂ NPs. Therefore, Rh(III) and Ru(II) complex-functionalized TiO₂ NPs were prepared within an autoclave and using this simple method, metal complexes with the desired complex ratio of rhodium to ruthenium were assembled directly on the NP surface using **9**@TiO₂ (Figure 16), bpy, RuCl₃ and RhCl₃ in H₂O:EtOH at 160 °C. The resulting bimetallic complex functionalized TiO₂ NPs (**rR**@TiO₂) worked both as photo- and electrocatalysts and were used to replace the two metal complexes while other reaction conditions reported in the original work were followed as closely as possible.²⁴

It was found that the ruthenium(II) and rhodium(III) metal complexes work almost twice as efficient in tandem when both metal complexes are functionalized onto the same TiO₂ NPs compared to using individual metal complex f-NPs (**Ru**@TiO₂ or **Rh**@TiO₂). Using these **rR**@TiO₂ NPs, greater efficiency for the immobilised systems over the previously reported homogeneous systems was demonstrated in terms of turnover number (TON) and frequency (TOF). The study also tested the influence of individual components such as additive, pH, and catalyst within the system.

The f-NPs were characterized using ¹H NMR spectroscopy, FTIR spectroscopy, solid absorption spectroscopy, TGA-MS and ICP-QQQ-MS yielding solid evidence for the material. Gas chromatography was used to determine the reaction kinetics by measuring dihydrogen yields which provided evidence of partial 1st and 2nd order reaction kinetics. The same method was used to determine the recyclability of the NP-supported photocatalyst which were able to withstand several cycles but showed considerable losses in efficiency after 10 cycles (4 h each cycle). Further studies were conducted with ZrO₂ NPs. The change from the semiconductor TiO₂ (band gap = 3.2 eV)¹⁶⁶ to the insulator ZrO₂ (band gap = 5.1 eV)¹⁶⁷ was expected to yield insights into metal complex to NP surface bonding and electronic interactions.

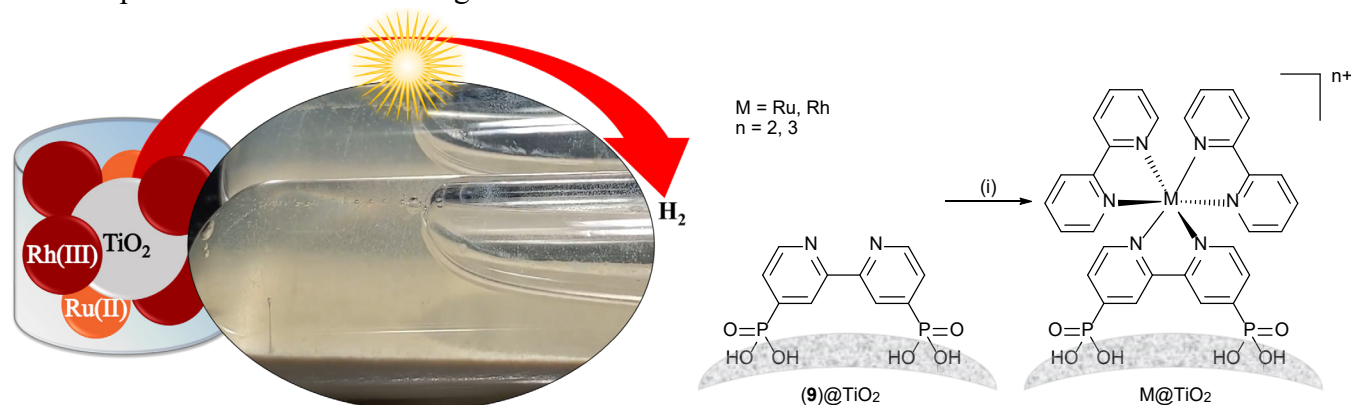


Figure 16: Table of contents image of the publication for **Chapter V** and scheme of ligand complexation, (i) MCl₃, bpy in H₂O:EtOH for 1 h at 160 °C in an autoclave, detailed conditions given in **Section 5.2**.²⁵

Article

Attraction in Action: Reduction of Water to Dihydrogen Using Surface-Functionalized TiO₂ Nanoparticles

Sven A. Freimann, Catherine E. Housecroft  and Edwin C. Constable * 

Department of Chemistry, University of Basel, Mattenstrasse 24a, BPR 1096, 4058 Basel, Switzerland; s.freimann@unibas.ch (S.A.F.); catherine.housecroft@unibas.ch (C.E.H.)

* Correspondence: edwin.constable@unibas.ch

Abstract: The reactivity of a heterogeneous rhodium(III) and ruthenium(II) complex-functionalized TiO₂ nanoparticle (NP) system is reported. The ruthenium and rhodium metal complexes work in tandem on the TiO₂ NPs surface to generate H₂ through water reduction under simulated and normal sunlight irradiation. The functionalized TiO₂ NPs outperformed previously reported homogeneous systems in turnover number (TON) and frequency (TOF). The influence of individual components within the system, such as pH, additive, and catalyst, were tested. The NP material was characterized using TGA-MS, ¹H NMR spectroscopy, FTIR spectroscopy, solid absorption spectroscopy, and ICP-MS. Gas chromatography was used to determine the reaction kinetics and recyclability of the NP-supported photocatalyst.

Keywords: nanoparticles; anchored-catalyst; heterogeneous catalysis; water reduction



Citation: Freimann, S.A.; Housecroft, C.E.; Constable, E.C. Attraction in Action: Reduction of Water to Dihydrogen Using Surface-Functionalized TiO₂ Nanoparticles. *Nanomaterials* **2022**, *12*, 789. <https://doi.org/10.3390/nano12050789>

Academic Editor: Chung-Li Dong

Received: 20 January 2022

Accepted: 24 February 2022

Published: 25 February 2022

Publisher's Note: MDPI stays neutral with regard to jurisdictional claims in published maps and institutional affiliations.



Copyright: © 2022 by the authors. Licensee MDPI, Basel, Switzerland. This article is an open access article distributed under the terms and conditions of the Creative Commons Attribution (CC BY) license (<https://creativecommons.org/licenses/by/4.0/>).

1. Introduction

The increasing energy demand of the world population has led to the unsustainable consumption of fossil fuels and emission of greenhouse gases [1–3]. Within the next century, fossil fuels will be substantially depleted if consumption rates or energy sources do not change [4]. The development of cleaner, renewable, available, and less-expensive energy solutions has become a central societal and research imperative [5].

Dihydrogen is an outstanding candidate as fuel, possessing key advantages, including long term storage and carbon-free combustion. Liquid or high-pressure gaseous dihydrogen has high gravimetric energy density while lacking volumetric energy density compared to liquid fossil fuels [6]. Hydrogen is the most abundant element in the universe and the tenth most abundant element in the earth's crust by weight percentage. Terrestrially, only small amounts of elemental H₂ occur, with most hydrogen found within molecules, most commonly water [7]. This means dihydrogen for use as fuel must be generated through chemical transformations.

The most common processes for large-scale dihydrogen preparation are water electrolysis and steam methane reforming [8]. Both technologies require high amounts of energy and work best with non-sustainable metal catalysts [8–10]. An imperative is improving energy efficiency and using sustainable, recyclable, or easily recoverable catalysts [11]. One option is to combine energy harvesting and dihydrogen evolution using photocatalysts that work under sunlight irradiation [12].

Homogeneous photocatalytic systems can be very efficient, although catalyst recovery can be extremely challenging and cost or energy-intensive [13,14]. In particular, multicomponent systems are problematic. Heterogeneous catalysts are often easier to recover but have the disadvantage of inactive interior volumes with only surface sites being catalytically active [13–15]. An alternative is to surface-functionalize nanoparticle (NP) scaffolds composed of cheap and abundant elements with photocatalysts. Such immobilized photocatalysts offer greater catalyst-to-volume ratios than bulk heterogeneous catalysts, which

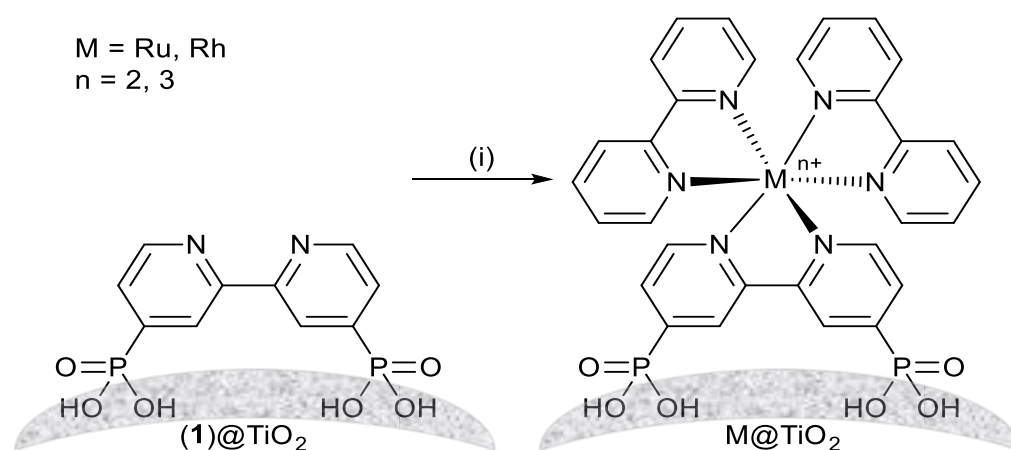
translates to enhanced catalytic activity and turnover. An additional benefit of NPs is the ability to disperse them in liquid phases [16–19]. A number of heterogeneous NP photocatalytic systems, including CdS NPs [20], Cu-doped TiO₂ NPs [21] or ZnO NPs [22], Pt-doped TiO₂ NPs [23] or ZnO NPs [24], Ti³⁺ doped TiO₂ NPs [25], and TiO₂ mediated ligand-capped RuO₂ NPs [26], have been reported as efficient systems for dihydrogen generation. Results of comparable systems are summarized in Table 1.

Table 1. Comparative H₂ evolution materials in the literature.

System	Cat _A / μmol	Cat _B / μmol	Irr./ h	Yield H ₂ / μmol	TON _A	TOF _A / h ⁻¹	TON _B	TOF _B / h ⁻¹
CdS ^a [20]	1730	-	6	283	0.2	0.0	-	-
TiO ₂ p25 ^a [20]	3130	-	6	62	0.0	0.0	-	-
0.25%Pt@TiO ₂ ^b [23]	1.3	-	3	432	337	112.4	-	-
0.75%Pt@ZnO ^c [24]	3.8	-	3	745	194	64.6	-	-
Ru@RuO ₂ PPTiO ₂ -RuP ^d [26]	0.6	-	10	111	176	17.6	-	-
Ru(bpy) ₃ ²⁺ , Rh(bpy) ₃ ³⁺ ^e [27]	1.8	11.7	32	1359	748	23.4	116	3.6

^a Using TEOA (0.67 M) as electron donor, ^b using TEOA (0.25 M) as electron donor and Eosin Y as dye at 1:83 to photocatalyst, ^c using TEOA (0.76 M) as electron donor and Eosin Y as dye at 1:2 to photocatalyst, ^d using TEOA (0.2 M) as electron donor, ^e using TEOA (0.42 M) as electron donor and K₂[PtCl₄] (0.28 mM) as catalyst.

We now describe the immobilization of components from a previously reported aqueous photochemical system for water reduction under simulated sunlight irradiation [27]. The system utilizes TiO₂ NPs supporting ruthenium(II) and rhodium(III) 2,2'-bipyridine (bpy) complexes as photosensitizer and relay species, respectively Scheme 1 [27]. The complexes at the desired surface ratio are assembled on [2,2'-bipyridine]-4,4'-diylbis(phosphonic acid) (**1**) functionalized NPs (**1**@TiO₂). Comparative studies with ZrO₂ NPs are also reported. ZrO₂ is an insulator and the NPs are commercially available. The change from TiO₂ (band gap = 3.2 eV) [28] to ZrO₂ (band gap = 5.1 eV) [29] was expected to yield insights into metal complex to NP surface bonding and electronic interactions.



Scheme 1. Assembly of metal complexes on TiO₂ NPs starting from NPs functionalized with **1**. Conditions: (i) MCl₃·3H₂O (M = Ru or Rh), bpy, EtOH: H₂O, 160 °C, autoclave, 1 h.

The NPs were characterized using Fourier-transform infrared (FTIR) and solid-state absorption spectroscopies, thermogravimetric analysis mass spectrometry (TGA-MS), triple quadrupole inductively coupled plasma mass spectrometry (ICP-QQQ-MS), and matrix-assisted laser desorption/ionization (MALDI) mass spectrometry while dihydrogen generation was analysed using gas chromatography (GC, see ESI† for details).

2. Materials and Methods

2.1. General

RuCl₃·3H₂O was purchased from Oxkem Ltd., Reading, UK. RhCl₃·3H₂O was purchased from Johnson Matthey, Materials Technology UK. 2,2'-Bipyridine and triethanolamine

(TEOA) were purchased from Apollo Scientific Ltd., Stockport, UK and Sigma-Aldrich Chemie GmbH, Buchs, Switzerland respectively while $K_2[PtCl_4]$ was purchased from Alfa Aesar GmbH & Co KG, Karlsruhe, Germany. TiO_2 NPs (AEROXIDE TiO_2 P25) were purchased from Evonik Industries, Essen, Germany or Sigma-Aldrich Chemie GmbH, Buchs, Switzerland. Pristine ZrO_2 NPs (<100 nm particle size) were purchased from Sigma-Aldrich Chemie GmbH, Buchs, Switzerland. For further characterization see ESI†. *cis*-[Ru(bpy) $_2$ Cl $_2$] and anchoring ligand (**1**) were prepared according to the literature (see ESI† for synthetic details) [30–35]. Instrumentation details are given in the ESI†. Calculated major MALDI peaks given in the experimental sections were calculated using the most abundant isotopes (e.g., ^{102}Ru , ^{35}Cl).

2.2. Synthetic Procedures

2.2.1. TiO_2 NPs Functionalization

NP activation and functionalization with ligand (**1**) were carried out according to our previously published procedure [36,37]. The procedures were adjusted according to the molecular weight for anchoring ligand (**1**) (see following section).

2.2.2. Activation of Commercial P25 TiO_2 NPs

The commercially available NPs were activated as previously reported [36]. The procedure was scaled up as follows. Commercial P25 TiO_2 NPs (5.00 g) were dispersed by sonication for 15 min in dilute aqueous HNO_3 (70 mL, 3 M). The mixture was then stirred for 30 min. The suspension was centrifuged (10 min, 7000 rpm) and the NPs were washed once with milliQ water (70 mL). The NPs were added to milliQ water (50 mL) and dispersed by sonication for 10 min. The suspension was then stirred overnight. The suspension was centrifuged (10 min, 7000 rpm) and the NPs were washed with milliQ water (2 × 50 mL). The activated NPs (4.83 g) were stored in a sealed vial under N_2 after drying under high vacuum. TGA: weight loss/%, 1.8 (<380 °C), 0.3 (380–900 °C). TGA-MS: amu, 18, 30 (<380 °C), 18, 44 (380–900 °C). FTIR spectroscopy: 1607, 1582, 1427, and 1298 cm^{-1} . ICP-MS: No ruthenium or rhodium were detected in either the pristine or activated NPs.

2.2.3. Preparation of $1@TiO_2$

The functionalization was performed as previously reported [36,37] with the procedure adjusted for the anchoring ligand 4,4'-bis(phosphonato)-2,2'-bipyridine as follows. (**1**) (25.0 mg, 0.079 mmol, 1 eq.) and milliQ water (18 mL) were added to a microwave vial and dispersed by sonication for 1 min. Activated TiO_2 NPs (727 mg, 33.9 TiO_2 eq.) were added. The suspension was dispersed by sonication for 10 min. The microwave vial was sealed, and the reaction mixture heated for 3 h at 130 °C in the microwave reactor. The suspension was centrifuged (20 min, 7000 rpm) after cooling to room temperature. The NPs were separated from the solvent. The white $1@TiO_2$ NPs (742 mg) were stored in a sealed vial under N_2 after drying under high vacuum. For NMR spectroscopic measurements, $1@TiO_2$ NPs (5–10 mg) were dispersed in 500 μ L D_2O in an NMR tube. TGA: weight loss/%, 0.7 (<380 °C), 2.9 (380–900 °C). TGA-MS: amu, 18 (<380 °C), 18, 44 (380–900 °C). FTIR spectroscopy: 1630, 1590, 1540, 1500, 1480, 1430 and 1160 cm^{-1} . ICP-MS: No ruthenium or rhodium was detected. Solid-state absorption spectroscopy: 400–670 nm (weak). MALDI *m/z*: 317.1 [(**1**) + H] $^+$ (calc. 317.0), 379.1 [(**1**) – H + TiO] $^+$ (calc. 378.9), 445.0 [(**1**) + H + Ti_2O_2] $^+$ (calc. 444.9) and 656.0 [(**1**) $_2$ + H + Na] $^+$ (calc. 656.0).

2.2.4. $Ru@TiO_2$

The metal complex was formed directly on the NP surface. Hence, $1@TiO_2$ (45.9 mg), $RuCl_3 \cdot 3H_2O$ (1.03 mg, 3.9 μ mol), and 2,2'-bipyridine (1.56 mg, 10.0 μ mol) were added to a vial. H_2O (5 mL) and EtOH (3 mL) were added, and the mixture was thoroughly dispersed using sonication and stirring. The suspension was transferred to an autoclave PTFE liner with additional EtOH (2 mL). The autoclave was sealed and then heated in an oven with 320 °C/h to 160 °C. The autoclave was left at 160 °C for 1 h. After cooling

down the autoclave was opened and the suspension was centrifuged (20 min, 7000 rpm). The resulting NPs were washed with H₂O (3 × 10 mL) and EtOH (1 × 10 mL). Ru@TiO₂ was isolated as dark orange powder. ¹H-NMR spectroscopy, MALDI, TGA-MS, FTIR spectroscopy, ICP-MS, and solid absorption spectroscopy were performed on the NPs. TGA: weight loss/%, 1.5 (<380 °C), 4.6 (380–900 °C). TGA-MS: amu, 18 (<380 °C), 18, 44 (380–900 °C). FTIR spectroscopy: 1640, 1604, 1465, 1447, 1423, 1398, 1156, and 1049 cm⁻¹. ICP-MS: ruthenium present. Solid-state absorption spectroscopy: 400–490 nm, 490–700 nm (weak). MALDI *m/z*: 414.1 [Ru(bpy)₂]⁺ (calc. 414.0), 535.1 [Ru(1) + TiO₂ + K – 2 H]⁺ (calc. 534.8), 570.1 [Ru(1)(bpy) – 4 H]⁺ (calc. 569.9), 602.1 [Ru(bpy)₂ + CHCA – H]⁺ (calc. 602.1), 728.9 [Ru(1)(bpy)₂ – H]⁺ (calc. 729.0). (CHCA = α-cyano-4-hydroxycinnamic acid).

2.2.5. Ru@TiO₂ Using [Ru(bpy)₂Cl₂]

1@TiO₂ (45.9 mg) and [Ru(bpy)₂Cl₂] (3.05 mg, 5.0 μmol) were added to a vial. H₂O (5 mL) and EtOH (3 mL) were added, and the mixture was thoroughly dispersed using sonication and stirring. The suspension was transferred to an autoclave PTFE liner with additional EtOH (2 mL). The autoclave was sealed and then heated in an oven at a rate of 320 °C/h to 160 °C. The autoclave was left at 160 °C for 1 h. After cooling down, the autoclave was opened and the suspension was centrifuged (20 min, 7000 rpm). The resulting NPs were washed with H₂O (3 × 10 mL) and EtOH (1 × 10 mL). Ru@TiO₂ was isolated as an orange powder. ¹H-NMR spectroscopy, MALDI, TGA-MS, FTIR and solid absorption spectroscopy were performed on the NPs. TGA: weight loss/%, 0.6 (<380 °C), 3.3 (380–900 °C). TGA-MS: amu, 18 (<380 °C), 18, 44 (380–900 °C). FTIR spectroscopy: 1626, 1591, 1544, 1465, 1447, 1428, 1376 and 1155 cm⁻¹. Solid-state absorption spectroscopy: 400–490 nm, 490–700 nm (weak). MALDI *m/z*: 414.0 [Ru(bpy)₂]⁺ (calc. 414.0), 535.0 [Ru(1) + TiO₂ + K – 2 H]⁺ (calc. 534.8), 570.1 [Ru(1)(bpy) – 4 H]⁺ (calc. 569.9), 602.0 [Ru(bpy)₂ + CHCA – H]⁺ (calc. 602.1).

2.2.6. Rh@TiO₂

The metal complex was formed directly on the NP surface. 1@TiO₂ (200 mg), RhCl₃·3H₂O (4.51 mg, 17.1 μmol) and 2,2'-bipyridine (6.81 mg, 4.36 μmol) were added to a vial. H₂O (5 mL) and EtOH (3 mL) were added, and the mixture was thoroughly dispersed using sonication and stirring. The suspension was transferred to an autoclave PTFE liner with additional EtOH (2 mL). The autoclave was sealed and then heated in an oven with 320 °C/h to 160 °C. The autoclave was left at 160 °C for 1 h. After cooling down the autoclave was opened and the suspension was centrifuged (20 min, 7000 rpm). The resulting NPs were washed with H₂O (3 × 10 mL) and EtOH (1 × 10 mL). Rh@TiO₂ was isolated as white powder. ¹H-NMR spectroscopy, MALDI, TGA-MS, FTIR spectroscopy, ICP-MS, and solid absorption spectroscopy were performed on the NPs. TGA: weight loss/%, 1.3 (<380 °C), 3.8 (380–900 °C). TGA-MS: amu, 18 (<380 °C), 18, 44 (380–900 °C). FTIR spectroscopy: 1633, 1607, 1544, 1500, 1470, 1453 1401, 1378, and 1153 cm⁻¹. ICP-MS: rhodium present. Solid-state absorption spectroscopy: 400–440 nm, 440–700 nm (weak). MALDI *m/z*: 415.0 [Rh(bpy)₂]⁺ (calc. 415.0), 450.0 [Rh(bpy)₂ + Cl]⁺ (calc. 450.0), 603.1 [Rh(bpy)₂ + CHCA – H]⁺ (calc. 603.1) and 656.1 [(1)₂ + H + Na]⁺ (calc. 656.0).

2.2.7. rR-TiO₂

The metal complex was formed directly on the NP surface. Hence, 1@TiO₂ (241 mg), RuCl₃·3H₂O (0.24 mg, 0.9 μmol), RhCl₃·3H₂O (5.16 mg, 19.6 μmol), and 2,2'-bipyridine (8.08 mg, 51.8 μmol) were added to a vial. H₂O (5 mL) and EtOH (3 mL) were added, and the mixture was thoroughly dispersed using sonication and stirring. The suspension was transferred to an autoclave PTFE liner with additional EtOH (2 mL). The autoclave was sealed and then heated in an oven at a rate of 320 °C/h to 160 °C. The autoclave was left at 160 °C for 1 h. After cooling down the autoclave was opened and the suspension was centrifuged (20 min, 7000 rpm). The resulting NPs were washed with H₂O (3 × 10 mL) and EtOH (1 × 10 mL). rR@TiO₂ was isolated as an orange powder. ¹H-NMR spectroscopy,

MALDI, TGA-MS, FTIR spectroscopy, ICP-MS and solid absorption spectroscopy were performed on the NPs. TGA: weight loss/%, 1.1 (<380 °C), 3.7 (380–900 °C). TGA-MS: amu, 18 (<380 °C), 18, 44 (380–900 °C). FTIR spectroscopy: 1627, 1608, 1546, 1500, 1470, 1453, 1412, 1373 and 1149 cm^{-1} . ICP-MS: ruthenium and rhodium present. Solid-state absorption spectroscopy: 400–490 nm, 490–700 nm (weak). MALDI m/z : 415.0 $[\text{Rh}(\text{bpy})_2]^+$ (calc. 415.0), 450.0 $[\text{Rh}(\text{bpy})_2 + \text{Cl}]^+$ (calc. 450.0) and 603.1 $[\text{Rh}(\text{bpy})_2 + \text{CHCA} - \text{H}]^+$ (calc. 603.1).

2.2.8. RR-TiO₂

The metal complex was formed directly on the NP surface. **1**@TiO₂ (340 mg), RuCl₃·3H₂O (2.39 mg, 9.1 μmol), RhCl₃·3H₂O (5.16 mg, 19.6 μmol) and 2,2'-bipyridine (11.3 mg, 72.3 μmol) were added to a vial. H₂O (5 mL) and EtOH (3 mL) were added, and the mixture was thoroughly dispersed using sonication and stirring. The suspension was transferred to an autoclave PTFE liner with additional EtOH (2 mL). The autoclave was sealed and then heated in an oven with 320 °C/h to 160 °C. The autoclave was left at 160 °C for 1 h. After cooling down, the autoclave was opened and the suspension was centrifuged (20 min, 7000 rpm). The resulting NPs were washed with H₂O (3 × 10 mL) and EtOH (1 × 10 mL). RR-TiO₂ was isolated as a dark orange powder. ¹H-NMR spectroscopy, MALDI, TGA-MS, FTIR spectroscopy, ICP-MS and solid absorption spectroscopy were performed on the NPs. TGA: weight loss/%, 1.5 (<380 °C), 3.5 (380–900 °C). TGA-MS: amu, 18 (<380 °C), 18, 44 (380–900 °C). FTIR spectroscopy: 1643, 1542, 1498, 1472, 1447, 1423, 1398, 1375 and 1149 cm^{-1} . ICP-MS: ruthenium and rhodium present. Solid-state absorption spectroscopy: 400–490 nm, 490–700 nm (weak). MALDI m/z : 415.1 $[\text{Rh}(\text{bpy})_2]^+$ (calc. 415.0), 450.1 $[\text{Rh}(\text{bpy})_2 + \text{Cl}]^+$ (calc. 450.0), 603.1 $[\text{Rh}(\text{bpy})_2 + \text{CHCA} - \text{H}]^+$ (calc. 603.1) and 656.1 $[(\text{I})_2 + \text{H} + \text{Na}]^+$ (calc. 656.0), 729.1 $[\text{Ru}(\text{I})(\text{bpy})_2 - \text{H}]^+$ (calc. 729.0).

2.2.9. Preparation of **1**@ZrO₂

The functionalization was performed as previously reported [36,37] without the acid treatment activation step. The procedure was further adjusted for the anchoring ligand 4,4'-bis(phosphonato)-2,2'-bipyridine and a different NP surface as follows. (**1**) (20.0 mg, 0.063 mmol, 1 eq.) and milliQ water (18 mL) were added to a microwave vial and dispersed by sonication for 1 min. ZrO₂ NPs (897 mg, 6.9 ZrO₂ eq.) were added. The suspension was dispersed by sonication for 10 min. The microwave vial was sealed, and the reaction mixture heated for 3 h at 130 °C in the microwave reactor. The suspension was centrifuged (20 min, 7000 rpm) after cooling to room temperature. The NPs were separated from the solvent and washed with H₂O (3 × 10 mL) and EtOH (1 × 10 mL). The white **1**@ZrO₂ NPs (856 mg) were stored in a sealed vial under N₂ after drying under high vacuum. For NMR spectroscopic measurements, **1**@ZrO₂ NPs (5–10 mg) were dispersed in 500 μL D₂O in an NMR tube. TGA: weight loss/%, 0.6 (<380 °C), 1.7 (380–900 °C). TGA-MS: amu, 18 (<380 °C), 18, 44 (380–900 °C). FTIR spectroscopy: 1625, 1590, 1542, 1496, 1473, 1432, 1376, 1223, 1152, 1038, 1000, 840, 744, 658, 562 and 480 cm^{-1} .

2.2.10. Ru@ZrO₂

The metal complex was formed directly on the NP surface. Hence, **1**@ZrO₂ (142 mg), RuCl₃·3H₂O (2.07 mg, 7.9 μmol), and 2,2'-bipyridine (2.50 mg, 16.0 μmol) were added to a vial. H₂O (5 mL) and EtOH (3 mL) were added, and the mixture was thoroughly dispersed using sonication and stirring. The suspension was transferred to an autoclave PTFE liner with additional EtOH (2 mL). The autoclave was sealed and then heated in an oven with 320 °C/h to 160 °C. The autoclave was left at 160 °C for 1 h. After cooling down the autoclave was opened and the suspension was centrifuged (20 min, 7000 rpm). The resulting NPs were washed with H₂O (3 × 10 mL) and EtOH (1 × 10 mL). Ru@ZrO₂ was isolated as an ochre powder. ¹H-NMR spectroscopy, MALDI, TGA-MS and FTIR spectroscopy were performed on the NPs. TGA: weight loss/%, 0.6 (<380 °C), 2.1 (380–900 °C). TGA-MS: amu, 18 (<380 °C), 18, 44 (380–900 °C). FTIR spectroscopy: 1644, 1604, 1544, 1465, 1447, 1422, 1398, 1223, 1160, 1122, 1057, 913, 744, 658, 562, and 480 cm^{-1} .

2.2.11. rR-ZrO₂

The metal complex was formed directly on the NP surface. Hence, 1@ZrO₂ (366 mg), RuCl₃·3H₂O (0.24 mg, 0.9 μmol), RhCl₃·3H₂O (5.16 mg, 19.6 μmol) and 2,2'-bipyridine (6.45 mg, 41.3 μmol) were added to a vial. H₂O (5 mL) and EtOH (3 mL) were added, and the mixture was thoroughly dispersed using sonication and stirring. The suspension was transferred to an autoclave PTFE liner with additional EtOH (2 mL). The autoclave was sealed and then heated in an oven with 320 °C/h to 160 °C. The autoclave was left at 160 °C for 1 h. After cooling down the autoclave was opened and the suspension was centrifuged (20 min, 7000 rpm). The resulting NPs were washed with H₂O (3 × 10 mL) and EtOH (1 × 10 mL). rR@ZrO₂ was isolated as light orange powder. ¹H-NMR spectroscopy, MALDI, TGA-MS and FTIR spectroscopy were performed on the NPs. TGA: weight loss/%, 0.4 (<380 °C), 2.1 (380–900 °C). TGA-MS: amu, 18 (<380 °C), 18, 44 (380–900 °C). FTIR spectroscopy: 1633, 1606, 1589, 1541, 1498, 1468, 1452, 1429, 1398, 1375, 1215, 1156, 1042, 1000, 910, 839, 744, 658, 562, and 480 cm⁻¹.

2.3. Dihydrogen Generation

2.3.1. General Procedure

The system for dihydrogen generation used metal complex functionalized NPs [38] as photo- and electrocatalysts, triethanolamine as a sacrificial electron donor, K₂[PtCl₄] as catalyst to facilitate dihydrogen formation (possibly by Pt NP formation), bpy as additive, aqueous H₂SO₄ for pH adjustment, and milliQ water as solvent. As [Ru(bpy)₃]²⁺ and [Rh(bpy)₃]³⁺ are somewhat photolabile under the operating conditions, the additional bpy was added to regenerate ruthenium and rhodium surface-bound complexes.

In a 5 mL microwave vial TEOA (2.52 mmol, 376 mg), K₂[PtCl₄] (1.7 μmol, 0.70 mg) and 2,2'-bipyridine (18.6 μmol, 2.91 mg) were added together with milliQ water and aqueous H₂SO₄ (1M) to modify the pH. Experiments performed at pH 10 used no aqueous H₂SO₄ (1M) and 6 mL milliQ water while experiments performed at pH 7.5 used 1 mL aqueous H₂SO₄ (1M) and 5 mL milliQ water. Metal complex-functionalized NPs were added (114.1 mg). The vial was flushed with nitrogen and then sealed. The suspension was sonicated (10 min) and thoroughly shaken. Nitrogen was bubbled through the suspension for 10 min. The vial was irradiated for 4–8 h at a slight angle (5°) with a sun simulator generating 1200 W m⁻². The suspension was shaken hourly. Headspace samples for gas chromatography were collected using a syringe and transferred to a 10 mL GC vial for analysis. The measured GC integral was converted to mL of H₂ with a calibration made by injecting several known volumes of dihydrogen.

2.3.2. Kinetic Measurements

Using the general procedure, a kinetic run was performed at pH 7.5 using rR@TiO₂ as photocatalyst. Two vials were prepared and the H₂ evolution was measured hourly by collecting the headspace by syringe and transferring it to a 10 mL GC vial for GC analysis. After each collection, the suspension was bubbled with N₂ for 5 min and then irradiation was continued. The vials were irradiated in total for 8 h and 9 h respectively.

2.3.3. Recycle Measurements

Using the general procedure, a recycling experiment was performed preparing two vials at pH 7.5 using rR@TiO₂ as photocatalyst with 4 h irradiation for each cycle. H₂ evolution was recorded after each cycle by collecting the headspace by syringe and transferring it to a 10 mL GC vial for GC analysis. After each collection, the suspension was centrifuged, the supernatant was removed, the NPs were washed with water (4 × 10 mL). Subsequently, the NPs were dried under high vacuum. Following the general procedure, the recycled NPs were used instead for the next cycle.

3. Results and Discussion

3.1. Ligand Functionalization, Surface Complexation and Material Characterisation

3.1.1. Anchoring Ligand Functionalization

We commenced by establishing a reliable method for the preparation of $1@TiO_2$ and its subsequent metallation. Anchoring ligand **1** was prepared according to the literature [31–35] with the phosphonic acid being chosen for stable binding to TiO_2 surfaces in neutral, slightly basic and slightly acidic conditions [36,37]. The bpy metal-binding domain in **1** is commensurate with the assembly of surface-bound $\{M(bpy)_3\}^{n+}$ ($M = Ru, n = 2; M = Rh, n = 3$) motifs. The previously developed method [36,37] for NP anchor functionalization with bpy metal-binding domains was adapted for anchoring ligand **1**. In this case, 32.2 eq. of activated NPs [38,39] were dispersed with anchoring ligand **1** in water and heated to 130 °C for 3 h in a microwave reactor (see Experimental section for full details).

The purchased ZrO_2 NPs were functionalized using similar techniques but without prior activation. The ZrO_2 NPs had a diameter of 100 nm changing the surface area to volume ratio significantly (from 28% to 6%). The functionalization method was optimized using our previously established formula [38] to give an adjusted ratio of 6.9 ZrO_2 eq. to 1 eq. anchoring ligand. The resulting NPs were carefully washed to avoid non-bound free ligand.

3.1.2. Ligand Functionalized NP Characterisation Methods

The $1@TiO_2$ NPs were analysed using TGA-MS (see Figure S1) and showed a small weight loss (<1%) in two steps (<120 °C, <380 °C) attributed to the loss of physisorbed and chemisorbed water. This was further seen in the coupled MS, which showed peaks with m/z of 17 and 18 for HO and H_2O respectively. A further weight loss of 2.9% over the range of 380–900 °C was measured and attributed to the decomposition of the anchoring ligand on the surface. The MS in this range showed the decomposition product of the ligand to be CO_2 . In contrast, activated NPs (see Figure S2) showed almost no weight loss over the range of 380–900 °C. To verify that the organic weight loss within the 380–900 °C range was not caused by non-covalently bound free ligand, the 1H NMR spectrum of $1@TiO_2$ was measured in D_2O (see Figure S3) and showed no significant amounts of free ligand in solution (ligand bound to the NPs is not observed) [36]. Further characterisation with FTIR spectroscopy (see Figure S4) and solid-state absorption spectroscopy (see Figure S5) revealed peaks at 1630, 1590, 1540, 1500, 1480, 1430, and 1160 cm^{-1} and 400–670 nm respectively which are not observed for pristine activated NPs. The additional peaks found for $1@TiO_2$ in FTIR spectroscopy did match to the pristine anchoring ligand. MALDI mass spectrometry showed peaks arising from species consistent with surface binding of the phosphonate ligand (See Figures S6–S8).

$1@ZrO_2$ was characterized similarly to $1@TiO_2$: TGA-MS, 1H NMR spectroscopy, and FTIR spectroscopy (see Figures S9–S12) were measured. $1@ZrO_2$ showed a weight loss of 1.7% over the range of 380–900 °C, which was attributed to the decomposition of the anchoring ligand on the surface. The MS in this range showed the decomposition product of the ligand to be CO_2 . The commercial NPs did not show any weight loss other than H_2O . 1H NMR spectroscopy in D_2O was used to verify absence of non-covalently bound free ligand and no significant amounts of free ligand in solution were observed. FTIR spectroscopy showed several weak additional peaks compared to the commercial NPs within the 1600 and 800 cm^{-1} region (see ESI† Figure S12) originating from the anchoring ligand.

3.1.3. Nanoparticle Surface Complexation

Metal complexes were assembled directly on the NP surface using methods derived from literature procedures for heteroleptic ruthenium(II) complexes, replacing free ligand by $1@TiO_2$ (Table 2) [35]. Orange $Ru@TiO_2$ was isolated from the reaction of $1@TiO_2$ NPs [38], $RuCl_3 \cdot 3H_2O$, and bpy in 1:1 water-ethanol in an autoclave at 160 °C for 1 h (see Experimental section for full details). $Ru@TiO_2$ can also be formed by replacing

RuCl₃·3H₂O and bpy with [Ru(bpy)₂Cl₂], giving a similar product (TGA-MS, ¹H NMR spectroscopy, FTIR and solid-state absorption spectroscopies, MALDI mass spectrometry see Figures S13–S27) differing only slightly in colour and small weight loss differences during the TGA measurement. All subsequent metal complex-functionalized NPs (Table 2) were prepared in the autoclave with H₂O/EtOH as solvent using the one-pot (MCl₃ + bpy) procedure described in the experimental. The abbreviation rR@TiO₂ describes metal complex functionalized NPs with a small amount of ruthenium vs. rhodium (1:20) on the surface, while for RR@TiO₂ ruthenium and rhodium surface concentrations are comparatively similar (1:2). The first letter in rR and RR always refers to ruthenium and the second to rhodium.

Table 2. Different metal complex functionalized nanoparticles.

Entry	1@TiO ₂ ^a	RuCl ₃	RhCl ₃	bpy
Ru@TiO ₂	1.0 eq.	0.79 eq.	0	2.0 eq.
Rh@TiO ₂	1.0 eq.	0	0.79 eq.	2.0 eq.
rR@TiO ₂	1.0 eq.	0.04 eq.	0.76 eq.	2.0 eq.
RR@TiO ₂	1.0 eq.	0.25 eq.	0.54 eq.	2.0 eq.

^a 1@TiO₂ equivalents represent estimated amount of 1 on the NP surface.

The metal complexes Ru@ZrO₂ and rR@ZrO₂ were prepared using 1@ZrO₂ as starting material and followed the procedure described above with TiO₂.

3.1.4. Complex Functionalized Characterisation Methods

All metal complex-functionalized NPs species were characterized using the same methods as 1@TiO₂. For both Ru@TiO₂ and Rh@TiO₂, TGA-MS (Figures S13 and S28) confirmed a higher weight loss (380–900 °C) than 1@TiO₂. ¹H NMR spectroscopy (Figures S15 and S29) showed that no labile species were adsorbed on the NPs. In contrast to 1@TiO₂, FTIR spectroscopy (Figures S16 and S30) showed absorptions between 1650 and 1590 cm⁻¹ in addition to 1540, 1470, 1450, 1400, and 1150 cm⁻¹ originating from the organic ligands. Solid-state absorption spectroscopy showed broad and weak absorptions between 400 and 670 nm. Additionally Rh@TiO₂ showed a more pronounced absorption band at 420 nm (Figure S31), whilst any surface bound ruthenium complex gave dominant absorptions between 410 and 490 nm (Figure S17). The MALDI mass spectrum of Rh@TiO₂ (see Figures S32–S35) showed masses with the correct isotope pattern at *m/z*: 415.0 [Rh(bpy)₂]⁺ (calc. 415.0), 450.0 [Rh(bpy)₂ + Cl]⁺ (calc. 450.0), 603.1 [Rh(bpy)₂ + CHCA – H]⁺ (calc. 603.1) and 656.1 [(1)₂ + H + Na]⁺ (calc. 656.0), while that of Ru@TiO₂ (Figures S18–S27) showed masses with the correct isotope patterns at *m/z*: 414.1 [Ru(bpy)₂]⁺ (calc. 414.0), 535.1 [Ru(1) + TiO₂ + K – 2 H]⁺ (calc. 534.8), 570.1 [Ru(1)(bpy) – 4 H]⁺ (calc. 569.9), 602.1 [Ru(bpy)₂ + CHCA – H]⁺ (calc. 602.1), 728.9 [Ru(1)(bpy)₂ – H]⁺ (calc. 729.0). For NPs containing both ruthenium and rhodium, the observed isotope distribution in the MALDI mass spectrum confirmed that the rhodium complex was dominant (Figures S36–S44). For full characterisation details, see Section 2 or ESI† Figures S36–S49.

Emission spectra of the metal complex functionalized NPs dispersed in water were recorded (Figure 1). The suspension was excited at 450 nm. Ru@TiO₂ showed a broad emission at 634 nm while RR@TiO₂ showed a broad emission at 630 nm. Both Rh@TiO₂ and rR@TiO₂ were non-emissive.

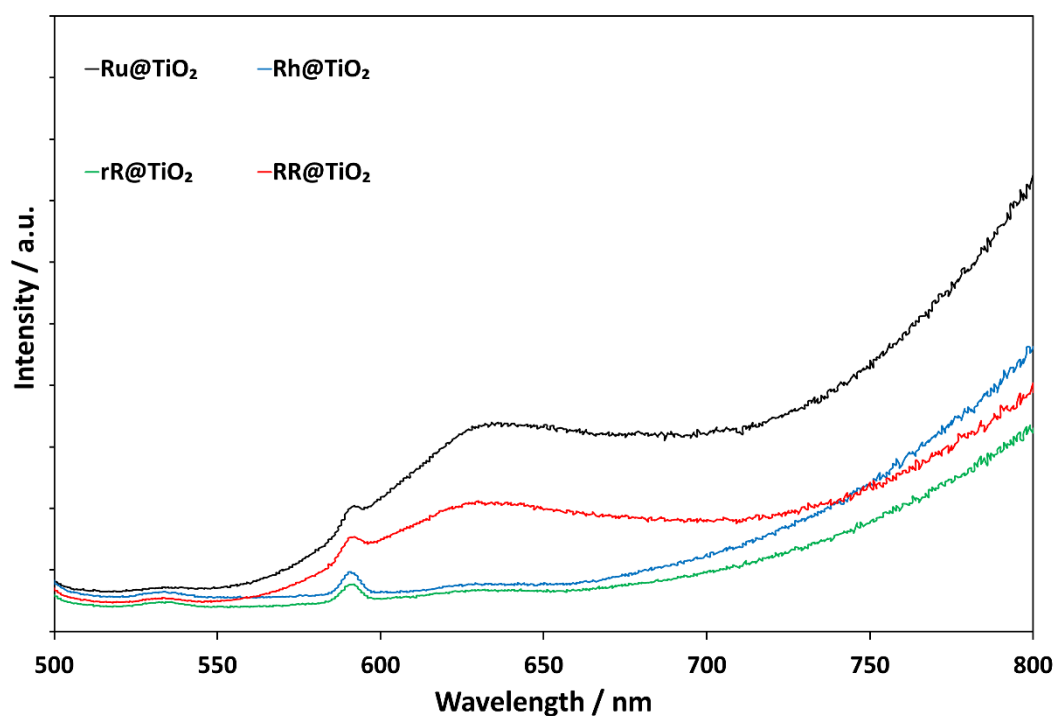


Figure 1. Emission spectra of complex-functionalized NPs after excitation at 450 nm. Excitation slit width 3 nm, emission slit width 10 nm.

The NPs were further investigated using ICP-MS (see Table 3). Ruthenium or rhodium functionalized NPs showed their respective elements. It was not possible to perform an exact surface concentration measurement of the elements with ICP-MS as even concentrated nitric acid did not remove all of the surface-bound species from the NP.

Table 3. ICP-MS concentration and standard deviation of functionalized TiO₂ NPs.

Sample	⁴⁷ Ti Conc. µg/L	⁴⁷ Ti Conc. RSD ^a	¹⁰¹ Ru Conc. µg/L	¹⁰¹ Ru Conc. RSD ^a	¹⁰³ Rh Conc. µg/L	¹⁰³ Rh Conc. RSD ^a	⁸⁹ Y (ISTD) Conc. µg/L	⁸⁹ Y (ISTD) Conc. RSD ^a
c-NPs	16,756.5	6.1	0.1	17.7	0.1	5.5	145,600.3	4.0
a-NPs	21,460.7	5.6	0.3	127.0	0.3	106.3	150,634.5	4.6
1@TiO ₂	20,492.8	4.7	0.1	12.8	0.1	2.9	146,834.6	5.6
Ru@TiO ₂	21,142.6	21.0	232.7	2.4	0.1	4.0	141,660.1	5.1
Rh@TiO ₂	21,879.5	5.7	0.2	9.6	117.7	3.6	148,959.7	5.3
rR@TiO ₂	20,350.4	2.6	22.2	3.1	89.6	2.5	142,814.2	5.4
RR@TiO ₂	18,659.6	5.9	62.0	4.2	53.5	2.9	146,352.9	5.9
rR@TiO ₂ ^b	13,466.9	2.9	3.5	3.2	3.1	4.5	142,412.9	6.5

^a Relative standard deviation in percentage, triplicate measurements, ⁸⁹Y used as internal standard to account for matrix effects, ^b rR@TiO₂ after 10 dihydrogen catalytic cycles were measured.

For Ru@ZrO₂ and rR@ZrO₂, characterization was performed using TGA-MS, ¹H NMR spectroscopy, and FTIR spectroscopy (see Figures S12, S50–S52). TGA-MS of Ru@ZrO₂ and rR@ZrO₂ revealed a smaller weight loss of 2.1% (380–900 °C) compared to the TiO₂ equivalents Ru@TiO₂ (4.6%) and rR@TiO₂ (3.7%). This was within expectations considering the weight loss seen for 1@ZrO₂. Importantly, an increase from 1@ZrO₂ to Ru@ZrO₂ or rR@ZrO₂ was still observed. ¹H NMR spectroscopy was used to verify the absence of non-bound anchoring ligand while the FTIR spectra showed only minor differences to 1@ZrO₂ within 1600–800 cm⁻¹.

3.2. Dihydrogen Generation

3.2.1. Performance and Influence of Individual Components during Dihydrogen Generation

Experimental details are given in Section 2.3.1. The study revealed that 1@TiO₂, Ru@TiO₂, and Rh@TiO₂ all produce H₂ under irradiation (Table 4) but the gas generation is significantly higher when both ruthenium and rhodium are present on the surface. It is especially interesting that when a single batch of NPs was functionalized with both metal complexes (rR@TiO₂ or RR@TiO₂), the H₂ production was more than double compared to that using an equivalent mixture of Ru@TiO₂ and Rh@TiO₂. We propose that the additional efficiency for rR@TiO₂ and RR@TiO₂ can be explained by an energy transfer from Ru to Rh which promotes the dihydrogen generation [27,40]. The recorded emission spectra of each species support this proposal as rR@TiO₂ is not emissive. It has to be noted that the energy transfer must be relatively inefficient since with higher ruthenium concentrations on the surface (RR@TiO₂ vs. rR@TiO₂) the metal complex functionalized NPs are emissive again.

Table 4. Performed dihydrogen generating experiments; see Table 2 for NP abbreviations.

Entry No.	NPs / μmol	Byp / μmol	pH	Time /h	GCI ^a /a. u.	H ₂ /mL (mL h ⁻¹)
1	Ru@TiO ₂ /1.5	18.6	10	8	152,250	3.14 (0.39)
2	Rh@TiO ₂ /9.3	18.6	10	8	199,140	4.11 (0.51)
3 ^b	Ru@TiO ₂ + Rh@TiO ₂ /9.7	18.6	10	8	255,530	5.27 (0.66)
4	rR@TiO ₂ /9.7	18.6	10	8	451,170	9.30 (1.16)
5	rR@TiO ₂ /9.7	18.6	7.5	4	455,940	9.40 (2.34)
6	rR@TiO ₂ /9.7	0	7.5	4	332,280	6.85 (1.71)
7 ^c	rR@TiO ₂ /9.7	18.6	7.5	4	34,720	0.50 (0.13)
8	RR@TiO ₂ /9.7	18.6	7.5	4	384,200	7.92 (1.98)
9 ^d	RR@TiO ₂ /13.0	18.6	7.5	4	398,860	8.23 (2.06)
10 ^d	RR@TiO ₂ /13.0	210	7.5	4	397,710	8.20 (2.05)
11 ^e	a-NP	18.6	7.5	4	138,600	2.86 (0.71)
12	1@TiO ₂ /12.2	18.6	7.5	4	134,050	2.76 (0.69)
13	0	18.6	7.5	4	0	0.00 (0.00)
14 ^f	rR@TiO ₂ /9.7	18.6	7.5	4	533,930	11.0 (2.75)
15 ^g	rR@TiO ₂ /9.7	18.6	7.5	4	318,210	6.5 (1.64)
16 ^f	rR@ZrO ₂ /9.7	18.6	7.5	4	29,720	0.6 (0.15)
17 ^h	rR@TiO ₂ /9.7	0	7.5	4	88,360	1.82 (0.46)

^a GC integral (GCI) was adjusted for pre-existing nitrogen headspace in the reaction vial and partial sampling during the GC measurement, ^b using Ru@TiO₂ (5.1 mg) and Rh@TiO₂ (109 mg), ^c no K₂[PtCl₄] used, ^d vial headspace was measured after 2 h and 4 h irradiation, generated H₂ was added together, ^e 114.1 mg a-NP were used, ^f vial was stirred instead of shaken hourly, ^g vial was irradiated using normal sunlight instead, ^h using 18.6 mmol phen as additive.

Further experiments were performed to test the influence of each component in the system. In the absence of K₂[PtCl₄], there was a strong decrease in efficiency while K₂[PtCl₄] on its own gave no H₂ generation. Removing bpy had a less significant influence on the H₂ generation but slightly lowered the efficiency. In contrast, increasing the bpy concentration had no effect on the efficiency. TEOA was essential for dihydrogen formation. Another important parameter was the pH; at pH 10 the system generated dihydrogen at half the rate observed at pH 7.5. A pH dependence is expected as the formal driving force of the reaction (ΔG) will depend upon pH according to the Nernst equation ($\Delta G = -nFE$) since the key step in the formation of H₂ involves a proton. A significant improvement in H₂ formation (17%, $\text{TOF}_{\text{Rh}} = 3.4 \times 10^{-3} \text{ s}^{-1}$, $\text{TOF}_{\text{Ru}} = 7.4 \times 10^{-2} \text{ s}^{-1}$) could be observed by simple stirring of the suspension instead of periodic shaking. This shows when the metal complex functionalized NPs settle and block the light, they partially hinder a successful water reduction on covered NPs. For this observation to be possible, a successful surface

functionalization must have happened. A further experiment was performed by using normal sunlight, resulting in respectable dihydrogen generation (see Table 4, Entry 15^g), especially since the weather conditions were not bright sunlight.

The dihydrogen generation experiment was expanded using ZrO₂ NPs as the metal complex carrier material. Since ZrO₂ is an insulator, the change from TiO₂ (band gap = 3.2 eV) [28] to ZrO₂ (band gap = 5.1 eV) [29] was expected to hinder the H₂ generation during the experiment if the metal complex is surface-bound and interacting electronically with the NP. Hence, the experiment (see Table 4, Entry 16^f) yielding almost no H₂ generation during the irradiation was interesting and strongly implies mediation by the semiconducting TiO₂ nanoparticles.

3.2.2. Kinetics of rR@TiO₂ during Light Irradiation

The kinetics of the H₂ formation when using rR@TiO₂ in the general setup was investigated and the experimental results are plotted in Figure 2a) and shown in Table 5. Experimental details are given in Section 2.3.2. Analysis of the data in Figure 2 when TEOA was considered as a reactant (see Figure 2b) indicated first order kinetics ($R_2 = 0.986$) or second order kinetics ($R_2 = 0.995$). This observation is consistent with the mechanism proposed by Kirch et al. [27]. Using these data, a minimal TON of 86 ($\text{TOF} = 2.7 \times 10^{-3} \text{ s}^{-1}$) and TON 1844 ($\text{TOF} = 5.7 \times 10^{-2} \text{ s}^{-1}$) can be calculated for the rhodium and ruthenium surface-bound complexes respectively. Furthermore, the amount of H₂ produced after 9 h irradiation corresponds to a depletion of 32% of TEOA.

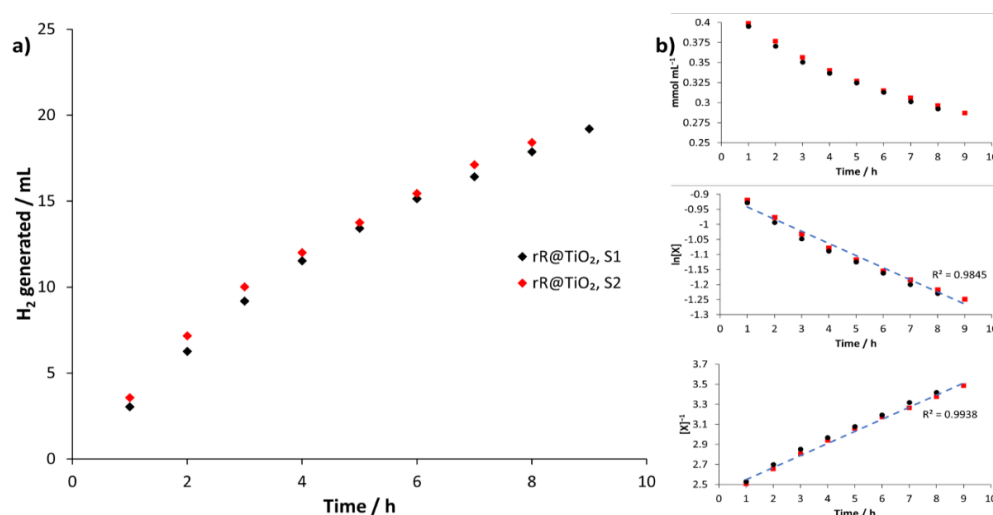


Figure 2. (a) Graphical representation of H₂ generated using rR@TiO₂ in mL during light irradiation experiments versus time for two samples. (b) Zeroth order reaction graph (top), concentration (mmol per mL) starting material during kinetic irradiation measurements of two samples (red and black) against time (hours); 1st order reaction graph (middle), natural logarithm of starting material concentration [X] during kinetic irradiation measurements of two samples (red and black) against time (hours), linear trendline through datapoints (blue); 2nd order reaction graph (bottom), One over concentration [X] of starting material during kinetic irradiation measurements of two samples (red and black) against time (hours), linear trendline through data points (blue).

3.2.3. Recyclability of rR@TiO₂

Our motivation was to develop a system that could be recycled multiple times and still generate dihydrogen upon irradiation (see Video 1 in the ESI[†] for visual representation). After an initial run, the NPs were separated from the solution and washed several times with water to ensure the complete removal of the solution components. The NPs were then dried under high vacuum and redispersed in milliQ water at pH 7.5 with fresh TEOA, bpy and K₂[PtCl₄]. After each run, the headspace was collected and measured using GC analysis (see Table 6). Overall, rR@TiO₂ NPs were most suitable for multiple cycles with only a

slight decline in efficiency (see Figure 3). We believe that the decline in efficiency is due to the loss of NPs in the recycling processing (10 wt.% after 8 cycles) and defunctionalization of the NP surface. Using the data, a minimal TON of 300 ($\text{TOF} = 1.9 \times 10^{-3} \text{ s}^{-1}$) and TON 6424 ($\text{TOF} = 4.1 \times 10^{-2} \text{ s}^{-1}$) can be calculated for the rhodium(III) and ruthenium(II) surface bound complexes, respectively.

Table 5. Performed hourly kinetic dihydrogen generating experiment of two sample vials.

Runtime/h	GC Integral ^a S1 /a. u.	H ₂ Generated S1 /mL	GC Integral ^a S2 /a. u.	H ₂ Generated S2 /mL
1	146,050	3.04	171,190	3.57
2	154,530	3.22	172,650	3.60
3	143,060	2.92	136,850	2.85
4	112,380	2.34	95,670	1.99
5	90,960	1.89	83,770	1.75
6	82,450	1.72	81,480	1.70
7	61,900	1.29	80,410	1.67
8	69,260	1.44	62,050	1.29
9	52,740	1.33	-	-

^a GC integrals were adjusted for pre-existing nitrogen headspace in the reaction vial and partial sampling during the GC measurement.

Table 6. Performed recycle dihydrogen generating experiments of two sample vials.

Cycle/N	GC Integral ^a /a. u.	NPs Runtime/h	H ₂ /mL (mL h ⁻¹)
0	455,940	4	9.40 (2.35)
1	463,320	8	9.55 (2.38)
2	372,850	12	7.68 (1.92)
3	344,720	16	7.10 (1.77)
4	277,740	20	5.73 (1.43)
5	258,630	24	5.33 (1.33)
6	257,160	28	5.30 (1.33)
7	228,530	32	4.71 (1.18)
8	209,710	36	4.32 (1.08)
9	191,940	40	3.96 (0.99)
10	181,590	44	4.75 (0.94)

^a GC integrals were adjusted for pre-existing nitrogen headspace in the reaction vial and partial sampling during the GC measurement.

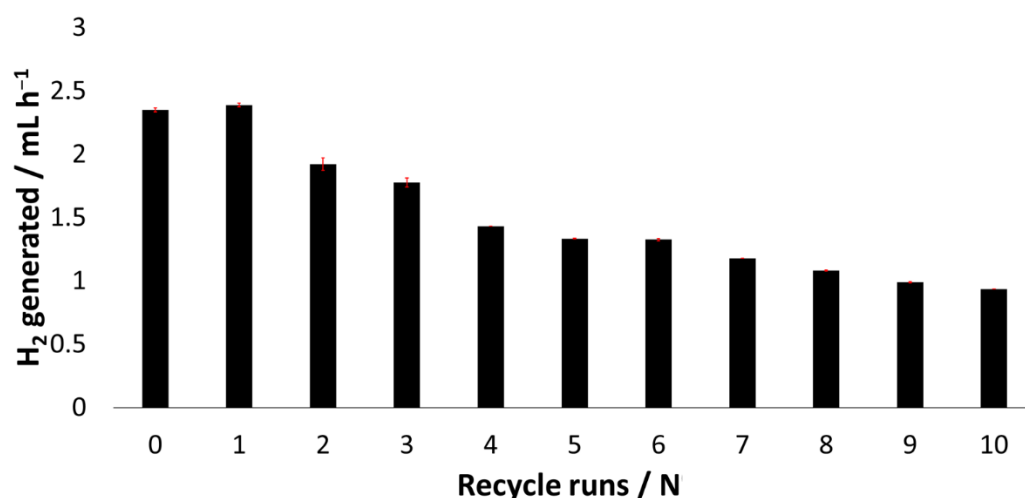


Figure 3. Graphical representation of dihydrogen generated measured through GC analysis after each cycle using rR@TiO₂ as photocatalyst, standard deviation indicated with red error bars.

4. Conclusions

We have demonstrated the immobilization of an established photochemical system for the solar generation of dihydrogen using sunlight by binding photo- and redox-active Rh and Ru complexes to TiO₂ NP surfaces. We further show that binding both metal complexes to the same NP improves the photocatalytic efficiency. The kinetic rate order and recyclability were determined. The NPs could be recycled multiple times and retain dihydrogen generation capacity. TON and TOF of the system were determined and exceeded the previous reported similar homogenous system. The dihydrogen generation was monitored using GC while the NPs were characterized using various methods, including MALDI, FTIR spectroscopy, TGA-MS, solid-absorption spectroscopy, fluorescence emission spectroscopy, and ICP-MS.

Supplementary Materials: The following supporting information can be downloaded at: <https://www.mdpi.com/article/10.3390/nano12050789/s1>. Details of instrumentation and procedure, experimental to anchoring synthesis. Video S1: Visible H₂ formation during irradiation. Scheme S1: Anchoring Ligand Synthesis route. Figures S1–S8: TGA-MS (activated NPs, 1@TiO₂), ¹H NMR spectroscopy (1@TiO₂), solid state IR spectra (activated NPs, 1@TiO₂, 1), solid state absorption spectra (1@TiO₂) and MALDI mass spectra (1@TiO₂). Figures S9–S12: TGA-MS (pristine ZrO₂, 1@ZrO₂), ¹H NMR spectroscopy (1@ZrO₂), solid state IR spectra (pristine ZrO₂, 1@ZrO₂, Ru@ZrO₂ and rR@ZrO₂). Figures S13–S27: TGA-MS, ¹H NMR spectroscopy, solid state IR spectra, solid state absorption spectra and MALDI mass spectra for Ru@TiO₂ made with RuCl₃·3 H₂O and *cis*-[Ru(bpy)₂Cl₂]. Figures S28–S35: TGA-MS, ¹H NMR spectroscopy, solid state IR spectra, solid state absorption spectra and MALDI mass spectra for Rh@TiO₂. Figures S36–S49: MALDI mass spectra (rR@TiO₂, RR@TiO₂) TGA-MS (rR@TiO₂, RR@TiO₂), ¹H NMR spectroscopy (rR@TiO₂, RR@TiO₂), solid state IR spectra (activated NPs, 1@TiO₂, rR@TiO₂, RR@TiO₂) and solid state absorption spectra (1@TiO₂, Ru@TiO₂, Rh@TiO₂, rR@TiO₂, RR@TiO₂). Figures S50–S52: TGA-MS (Ru@ZrO₂ and rR@ZrO₂) and ¹H NMR spectroscopy (Ru@ZrO₂ and rR@ZrO₂).

Author Contributions: Methodology, investigation, formal analysis, writing—original draft, S.A.F.; writing review and editing, C.E.H. and E.C.C.; supervision, project management, funding acquisition, C.E.H. and E.C.C. All authors have read and agreed to the published version of the manuscript.

Funding: This research was funded by Swiss National Science Foundation, grant number 200020_182000.

Data Availability Statement: Data are available from the authors on request.

Acknowledgments: We acknowledge support from the University of Basel. We would like to thank Markus Lenz (FHNW, Muttenz, Basel) for carrying out the ICP-MS measurements.

Conflicts of Interest: The authors declare no conflict of interest.

References

1. Omer, A.M. Energy, environment and sustainable development. *Renew. Sustain. Energy Rev.* **2008**, *12*, 2265–2300. [[CrossRef](#)]
2. Bölük, G.; Mert, M. Fossil & renewable energy consumption, GHGs (greenhouse gases) and economic growth: Evidence from a panel of EU (European Union) countries. *Energy* **2014**, *74*, 439–446. [[CrossRef](#)]
3. Letcher, T.M. 1—Introduction With a Focus on Atmospheric Carbon Dioxide and Climate Change. In *Future Energy: Improved, Sustainable and Clean Options for Our Planet*, 3rd ed.; Letcher, T.M., Ed.; Elsevier: Amsterdam, The Netherlands, 2020; pp. 3–17.
4. Metzger, J.O.; Hüttermann, A. Sustainable global energy supply based on lignocellulosic biomass from afforestation of degraded areas. *Sci. Nat.* **2009**, *96*, 279–288. [[CrossRef](#)] [[PubMed](#)]
5. Kang, J.-N.; Wei, Y.-M.; Liu, L.-C.; Han, R.; Yu, B.-Y.; Wang, J.-W. Energy systems for climate change mitigation: A systematic review. *Appl. Energy* **2020**, *263*, 114602. [[CrossRef](#)]
6. Rivard, E.; Trudeau, M.; Zaghib, K. Hydrogen Storage for Mobility: A Review. *Materials* **2019**, *12*, 1973. [[CrossRef](#)] [[PubMed](#)]
7. Available online: <https://www.rsc.org/periodic-table/element/1/hydrogen> (accessed on 14 June 2021).
8. Timmerberg, S.; Kaltschmitt, M.; Finkbeiner, M. *Hydrogen and Hydrogen-Derived Fuels through Methane Decomposition of Natural Gas—GHG Emissions and Costs*; Elsevier: Amsterdam, The Netherlands, 2020; Volume 7, p. 100043.
9. Wang, S.; Lu, A.; Zhong, C.-J. Hydrogen production from water electrolysis: Role of catalysts. *Nano Converg.* **2021**, *8*, 4. [[CrossRef](#)]
10. Chen, L.; Qi, Z.; Zhang, S.; Su, J.; Somorjai, G.A. Catalytic Hydrogen Production from Methane: A Review on Recent Progress and Prospect. *Catalysts* **2020**, *10*, 858. [[CrossRef](#)]
11. Dovì, V.G.; Friedler, F.; Huisingh, D.; Klemeš, J.J. Cleaner energy for sustainable future. *J. Clean. Prod.* **2009**, *17*, 889–895. [[CrossRef](#)]

12. Johnson, T.C.; Morris, D.J.; Wills, M. Hydrogen generation from formic acid and alcohols using homogeneous catalysts. *Chem. Soc. Rev.* **2010**, *39*, 81–88. [[CrossRef](#)]
13. Sajjadi, S.; Khataee, A.; Darvishi Cheshmeh Soltani, R.; Hasanzadeh, A. N, S co-doped graphene quantum dot-decorated Fe₃O₄ nanostructures: Preparation, characterization and catalytic activity. *J. Phys. Chem.* **2019**, *127*, 140–150. [[CrossRef](#)]
14. Hassan, A.F.; Elhadidy, H. Effect of Zr⁴⁺ doping on characteristics and sonocatalytic activity of TiO₂/carbon nanotubes composite catalyst for degradation of chlorpyrifos. *J. Phys. Chem.* **2019**, *129*, 180–187. [[CrossRef](#)]
15. Maleki, A.; Taheri-Ledari, R.; Ghalavand, R.; Firouzi-Haji, R. Palladium-decorated o-phenylenediamine-functionalized Fe₃O₄/SiO₂ magnetic nanoparticles: A promising solid-state catalytic system used for Suzuki–Miyaura coupling reactions. *J. Phys. Chem.* **2020**, *136*, 109200. [[CrossRef](#)]
16. Stevens, P.D.; Fan, J.; Gardimalla, H.M.R.; Yen, M.; Gao, Y. Superparamagnetic Nanoparticle-Supported Catalysis of Suzuki Cross-Coupling Reactions. *Org. Lett.* **2005**, *7*, 2085–2088. [[CrossRef](#)] [[PubMed](#)]
17. Zecchina, A.; Bordiga, S.; Groppo, E. *Selective Nanocatalysts and Nanoscience: Concepts for Heterogeneous and Homogeneous Catalysis*; Wiley-VHC: Weinheim, Germany, 2011.
18. Samira Bagheri, N.M.J. *Nanocatalysts in Environmental Applications*; Springer: Cham, Switzerland, 2018.
19. Albonetti, S.; Mazzoni, R.; Cavani, F. CHAPTER 1 Homogeneous, Heterogeneous and Nanocatalysis. In *Transition Metal Catalysis in Aerobic Alcohol Oxidation*; Green Chemistry Series; Cardona, F., Parmeggiani, C., Eds.; RSC: London, UK, 2015; pp. 1–39.
20. Kumaravel, V.; Imam, M.D.; Badreldin, A.; Chava, R.K.; Do, J.Y.; Kang, M.; Abdel-Wahab, A. Photocatalytic Hydrogen Production: Role of Sacrificial Reagents on the Activity of Oxide, Carbon, and Sulfide Catalysts. *Catalysts* **2019**, *9*, 276. [[CrossRef](#)]
21. Yoong, L.S.; Chong, F.K.; Dutta, B.K. Development of copper-doped TiO₂ photocatalyst for hydrogen production under visible light. *Energy* **2009**, *34*, 1652–1661. [[CrossRef](#)]
22. Kanade, K.G.; Kale, B.B.; Baeg, J.-O.; Lee, S.M.; Lee, C.W.; Moon, S.-J.; Chang, H. Self-assembled aligned Cu doped ZnO nanoparticles for photocatalytic hydrogen production under visible light irradiation. *Mater. Chem. Phys.* **2007**, *102*, 98–104. [[CrossRef](#)]
23. Chowdhury, P.; Goma, H.; Ray, A.K. Sacrificial hydrogen generation from aqueous triethanolamine with Eosin Y-sensitized Pt/TiO₂ photocatalyst in UV, visible and solar light irradiation. *Chemosphere* **2015**, *121*, 54–61. [[CrossRef](#)]
24. Popugaeva, D.; Tian, T.; Ray, A.K. Hydrogen production from aqueous triethanolamine solution using Eosin Y-sensitized ZnO photocatalyst doped with platinum. *Int. J. Hydrog. Energy* **2020**, *45*, 11097–11107. [[CrossRef](#)]
25. Zuo, F.; Wang, L.; Wu, T.; Zhang, Z.; Borchardt, D.; Feng, P. Self-Doped Ti³⁺ Enhanced Photocatalyst for Hydrogen Production under Visible Light. *J. Am. Chem. Soc.* **2010**, *132*, 11856–11857. [[CrossRef](#)]
26. Romero, N.; Guerra, R.B.; Gil, L.; Drouet, S.; Salmeron-Sánchez, I.; Illa, O.; Philippot, K.; Natali, M.; García-Antón, J.; Sala, X. TiO₂-mediated visible-light-driven hydrogen evolution by ligand-capped Ru nanoparticles. *Sustain. Energy Fuels* **2020**, *4*, 4170–4178. [[CrossRef](#)]
27. Kirch, M.; Lehn, J.-M.; Sauvage, J.-P. Hydrogen Generation by Visible Light Irradiation of Aqueous Solutions of Metal Complexes. An approach to the photochemical conversion and storage of solar energy. *Helv. Chim. Acta* **1979**, *62*, 1345–1384. [[CrossRef](#)]
28. Ansari, S.A.; Cho, M.H. Highly Visible Light Responsive, Narrow Band gap TiO₂ Nanoparticles Modified by Elemental Red Phosphorus for Photocatalysis and Photoelectrochemical Applications. *Sci. Rep.* **2016**, *6*, 25405. [[CrossRef](#)] [[PubMed](#)]
29. Singh, H.; Sunaina; Yadav, K.K.; Bajpai, V.K.; Jha, M. Tuning the bandgap of m-ZrO₂ by incorporation of copper nanoparticles into visible region for the treatment of organic pollutants. *Mater. Res. Bull.* **2020**, *123*, 110698. [[CrossRef](#)]
30. Lenis-Rojas, O.A.; Fernandes, A.R.; Roma-Rodrigues, C.; Baptista, P.V.; Marques, F.; Pérez-Fernández, D.; Guerra-Varela, J.; Sánchez, L.; Vázquez-García, D.; Torres, M.L.; et al. Heteroleptic mononuclear compounds of ruthenium(II): Synthesis, structural analyses, in vitro antitumor activity and in vivo toxicity on zebrafish embryos. *Dalton Trans.* **2016**, *45*, 19127–19140. [[CrossRef](#)] [[PubMed](#)]
31. Zhang, D.; Telo, J.P.; Liao, C.; Hightower, S.E.; Clennan, E.L. Experimental and Computational Studies of Nuclear Substituted 1,1'-Dimethyl-2,2'-Bipyridinium Tetrafluoroborates. *J. Phys. Chem. A* **2007**, *111*, 13567–13574. [[CrossRef](#)] [[PubMed](#)]
32. Maerker, G.; Case, F.H. The Synthesis of Some 4,4'-Disubstituted 2,2'-Bipyridines. *J. Am. Chem. Soc.* **1958**, *80*, 2745–2748. [[CrossRef](#)]
33. Han, W.-S.; Han, J.-K.; Kim, H.-Y.; Choi, M.J.; Kang, Y.-S.; Pac, C.; Kang, S.O. Electronic Optimization of Heteroleptic Ru(II) Bipyridine Complexes by Remote Substituents: Synthesis, Characterization, and Application to Dye-Sensitized Solar Cells. *Inorg. Chem.* **2011**, *50*, 3271–3280. [[CrossRef](#)] [[PubMed](#)]
34. Montalti, M.; Wadhwa, S.; Kim, W.Y.; Kipp, R.A.; Schmehl, R.H. Luminescent Ruthenium(II) Bipyridyl–Phosphonic Acid Complexes: pH Dependent Photophysical Behavior and Quenching with Divalent Metal Ions. *Inorg. Chem.* **2000**, *39*, 76–84. [[CrossRef](#)]
35. Norris, M.R.; Concepcion, J.J.; Glasson, C.R.K.; Fang, Z.; Lapidés, A.M.; Ashford, D.L.; Templeton, J.L.; Meyer, T.J. Synthesis of Phosphonic Acid Derivatized Bipyridine Ligands and Their Ruthenium Complexes. *Inorg. Chem.* **2013**, *52*, 12492–12501. [[CrossRef](#)]
36. Freimann, S.A.; Zare, D.; Housecroft, C.E.; Constable, E.C. The SALSAC approach: Comparing the reactivity of solvent-dispersed nanoparticles with nanoparticulate surfaces. *Nanoscale Adv.* **2020**, *2*, 679–690. [[CrossRef](#)]
37. Freimann, S.A.; Prescimone, A.; Housecroft, C.E.; Constable, E.C. Turning over on sticky balls: Preparation and catalytic studies of surface-functionalized TiO₂ nanoparticles. *RSC Adv.* **2021**, *11*, 5537–5547. [[CrossRef](#)]

38. The surface area-to-volume ratio of NPs with an average radius of 10.5 nm is 28%. Surface concentrations were calculated as 0.28 times the number of TiO₂ formula equivalents. When describing experiments using functionalized NPs, the number of equivalents or moles refer to the estimated amount of anchoring ligand or complex bound to the surface using the above formula.
39. Available online: <https://www.aerosil.com/sites/lists/RE/DocumentsSI/TI-1243-Titanium-Dioxide-as-Photocatalyst-EN.pdf>. (accessed on 5 April 2020).
40. Cooke, M.W.; Santoni, M.-P.; Loiseau, F.; Hasenknopf, B.; Hanan, G.S. Energy transfer in rhodium–ruthenium dimer-of-dimer assemblies. *Inorg. Chim. Acta* **2017**, *454*, 208–215. [[CrossRef](#)]

Supplementary Materials

Attraction in Action: Reduction of Water to Dihydrogen Using Surface-Functionalized TiO₂ Nanoparticles

Sven A. Freimann, Catherine E. Housecroft and Edwin C. Constable *

Department of Chemistry, University of Basel, Mattenstrasse 24a, BPR 1096, 4058 Basel, Switzerland; s.freimann@unibas.ch (S.A.F.); catherine.housecroft@unibas.ch (C.E.H.)

* Correspondence: edwin.constable@unibas.ch

1. Experimental Details

1.1 Instruments

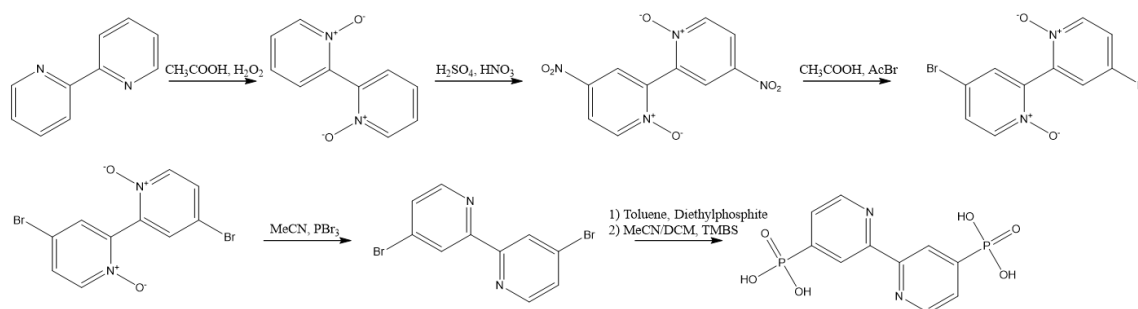
¹H NMR spectra were measured at 298 K on a Bruker Avance III-500 NMR spectrometer. ¹H chemical shifts were referenced to residual solvent peaks with respect to $\delta(\text{TMS}) = 0$ ppm for ¹H. Reactions and procedures under microwave conditions were carried out in a Biotage Initiator 8 reactor. Microwave vials (5 mL and 20 mL) were from Biotage and were selected depending on the required solvent volume. For centrifugation an Eppendorf Centrifuge 5415 R was used with 2-, 10- and 50 mL samples. Irradiation experiments were done in a Biotage 5 mL microwave vial with a LOT Quantum Design LS0811 instrument as light source at 1200 W m⁻². The simulated light power was calibrated with a silicon reference cell. Solid-state absorption spectra were recorded on an Agilent Cary 5000 spectrophotometer with a Diffuse Reflectance Accessory. For each solid-state absorption spectrum, a baseline correction was done with activated NPs as the reference sample. FTIR spectra were recorded on a Perkin Elmer UATR Two spectrophotometer. MALDI mass spectra were measured using a Shimadzu MALDI-8020 with α -cyano-4-hydroxycinnamic acid (CHCA) solution as matrix for sample preparation. Thermogravimetric analysis (TGA) was performed on a TGA5500 (TA Instruments) instrument under nitrogen and coupled to a MKII mass spectrometer. Initially, the temperature was held at 30 °C for 10 min before heating at a rate of 10 °C/min to 120 °C. This temperature was maintained for 30 min to remove all traces of water. Afterwards the sample was heated to 900 °C at a rate of 10 °C/min. After maintaining the temperature at 900 °C for 30 min, the sample was cooled to ambient temperature. Autoclave reactions were done in a 23 mL Acid digestion vessel (Parr Instrument Company) using a forced convection chamber furnace (Nabertherm NA15/65).

Gas chromatography was performed on a Model 8610C Gas Chromatograph from SRI instruments equipped with a flame ionization detector (FID/meth 300C hi gain), thermal conductivity detector (TCD100C low current), Haysep D 3 m 1/8" AD 2 mm ID Mesh 80/100 column and a HT2000H headspace autosampler from HTA S.R.L. The method used a constant column temperature of 90°C, 3 minutes event time, N₂ carrier gas at 10 mL min⁻¹ and 1 mL isocratic sampling. The GC integral was measured, adjusted for pre-existing nitrogen volume, sampling amount and then converted to volume in mL using a H₂ GC measured blank curve. Fluorescence emission spectra were measured on a Shimadzu RF-6000 spectrofluorometer with an excitation slit width of 3 – 10 nm and an emission slit width of 3 – 10 nm. For the emission spectroscopy, the NPs were dispersed in water with a concentration of 0.1 mg / mL. NP sample analysis with triple quadrupole inductively coupled plasma mass spectrometry (ICP-QQQ-MS) was performed on an 8800 ICP-QQQ MS system (Agilent) using the general-purpose operational settings. Samples were digested in aqueous HNO₃ (69%, semiconductor grade, PanReac AppliChem), diluted with milliQ water to a final HNO₃ concentration of 3 % and quantification was performed via multi-element standards (Sigma-Aldrich). To account for matrix effects ⁸⁹Y was used as an internal standard. ⁴⁷Ti, ¹⁰¹Ru and ¹⁰³Rh were quantified operating the ICP-MS system in single-quad mode using helium as the collision gas. Commercial ZrO₂ NPs (Sigma-Aldrich, <100 nm TEM) were further characterized using TGA-MS and

FTIR spectroscopy. TGA: weight loss / %, 0.8 (200–900°C). TGA-MS: amu, 18 (200–900 °C). FTIR spectroscopy: 1629, 766, 683, 582 and 467 cm⁻¹.

1.2 Anchoring Ligand Synthesis

The anchoring ligand (**1**) and its precursors were prepared according to the literature (see Scheme S1 and following sections). The respective spectroscopic data matched those previously reported.



Scheme S1. Anchoring ligand synthesis route.

2,2'-Bipyridine *N,N'*-dioxide[1]

H₂O₂ (35%, 35 mL) was added to 2,2'-bipyridine (12.0 g, 76.8 mmol) in glacial acetic acid (80 mL) and then stirred at 75°C for 48 h. After cooling to room temperature acetone (1 L) was added and the suspension was cooled to 4°C for 3h. The precipitate was filtered off, washed with acetone (5 x 25 mL) and then dried at high vacuum. 2,2'-bipyridine *N,N'* dioxide (13.4 g, 70.9 mmol, 92%) was isolated as white solid. ¹H NMR (600 MHz, D₂O, 298 K) δ /ppm: 8.45(m, 2H), 7.83 (m, 2H), 7.74 (m, 2H).

4,4'-Dinitro-2,2'-bipyridine *N,N'*-dioxide[1]

2,2'-Bipyridine *N,N'* dioxide (13.4 g, 70.9 mmol) dissolved in fuming sulphuric acid (39 mL). The solution was cooled to 0°C and then fuming nitric acid (30 mL) was slowly added. The mixture was then stirred at 100°C for 7h and then slowly poured on ice (300 g). The precipitate was filtered off, washed with water (5 x 100 mL) and then dried at high vacuum. The product 4,4'-dinitro-2,2'-bipyridine *N,N'* dioxide (16.4 g, 59.0 mmol, 83%) was isolated as beige powder. ¹H NMR (600 MHz, DMSO-*d*₆, 298 K) δ /ppm: 8.70 (d, *J* = 3.3, 2H), 8.60 (d, *J* = 7.2, 2H), 8.38 (dd, *J* = 7.2, 3.3, 2H).

4,4'-Dibromo-2,2'-bipyridine *N,N'*-dioxide[2]

4,4'-Dinitro-2,2'-bipyridine *N,N'* dioxide (8.40 g, 30.2 mmol) was added to glacial acetic acid (120 mL) and stirred at 60°C. Acetyl bromide (65.5 mL, 884 mmol) was added and the solution was stirred at reflux for 2h. The solution was cooled to r.t. and then poured on ice (500 g). After neutralisation with NaOH the precipitate was filtered off and washed with water exhaustively. The crude beige product (8.19 g) was used for the next step without further purification.

4,4'-Dibromo-2,2'-bipyridine[3]

4,4'-Dibromo-2,2'-bipyridine *N,N'* dioxide (8.00 g, 23.1 mmol) was added to anhydrous acetonitrile (100 mL) and cooled down to 0°C. PBr₃ (32 mL, 341 mmol) was added and the solution was refluxed while stirring for 4h. After cooling down the reaction was carefully poured on ice (200 g) and then NaOH was added till pH 11 was reached. The suspension was extracted with CHCl₃ (5 x 100 mL), dried with MgSO₄, the solvent was then evaporated under reduced pressure and the solid was dried at high vacuum. 4,4'-dibromo-2,2'-bipyridine (6.58 g, 20.9 mmol, 91%) was isolated as off white powder. ¹H NMR (500 MHz, CDCl₃, 298 K) δ /ppm: 8.62 (dd, *J* = 2.0, 0.6, 2H), 8.49 (d, *J* = 5.2, 0.6 2H), 7.51 (dd, *J* = 5.2, 2.0, 2H).

Tetraethyl [2,2'-bipyridine]-4,4'-diylbis(phosphonate)[4]

4,4'-Dibromo-2,2'-bipyridine (4.01 g, 12.7 mmol) and tetrakis(triphenylphosphine) palladium(0) (1.37 g, 1.19 mmol) were added to dry under flask under nitrogen. The solids were dissolved with anhydrous toluene (40 mL). Diethylphosphine (4.68 mL, 36.3 mmol) and triethylamine (5.19 mL, 37.3 mmol) were added to the reaction under stirring with a syringe. The solution was stirred at 110°C for 3.5 h, filtered hot to remove trimethylamine hydrobromide and then filtered again after the reaction cooled down. The solvent was removed under reduced pressure and the residue was recrystallized from hexanes. Tetraethyl [2,2'-bipyridine]-4,4'-diylbis(phosphonate) (4.56g, 10.7 mmol, 83%) was isolated as white crystals. ¹H NMR

(500 MHz, CDCl₃, 298 K) δ /ppm: 8.84 (td, $J = 4.8, 1.4, 2\text{H}$), 8.78 (dd, $J = 13.5, 1.4, 2\text{H}$), 7.73 (ddd, $J = 13.5, 4.8, 1.4, 2\text{H}$), 4.19 (m, 8H), 1.36 (t, $J = 7.1, 12\text{H}$).

[2,2'-Bipyridine]-4,4'-diylbis(phosphonic acid), (1)[5]

Tetraethyl [2,2'-bipyridine]-4,4'-diylbis(phosphonate) (1.50 g, 3.50 mmol) was dissolved in dry acetonitrile, dichloromethane (50 mL, 1:1) under nitrogen. Bromotrimethylsilane (6 mL, 45.5 mmol) was added and the solution was refluxed under nitrogen overnight. A pink precipitate formed and the reaction mixture was cooled to room temperature. Water was added dropwise to the reaction mixture while stirring, the precipitate was filtered off and washed with cold MeOH (3 x 2 mL) and cold Ether (3 x 10 mL). [2,2'-Bipyridine]-4,4'-diylbis(phosphonic acid) was isolated as off white powder (0.95 g, 3.00 mmol, 86%). ¹H NMR (500 MHz, D₂O, 298 K) δ /ppm: 8.92 (m, 2H), 8.68 (d, $J = 12.3, 2\text{H}$), 8.12 (m, 2H).

1.3 Supporting Figures

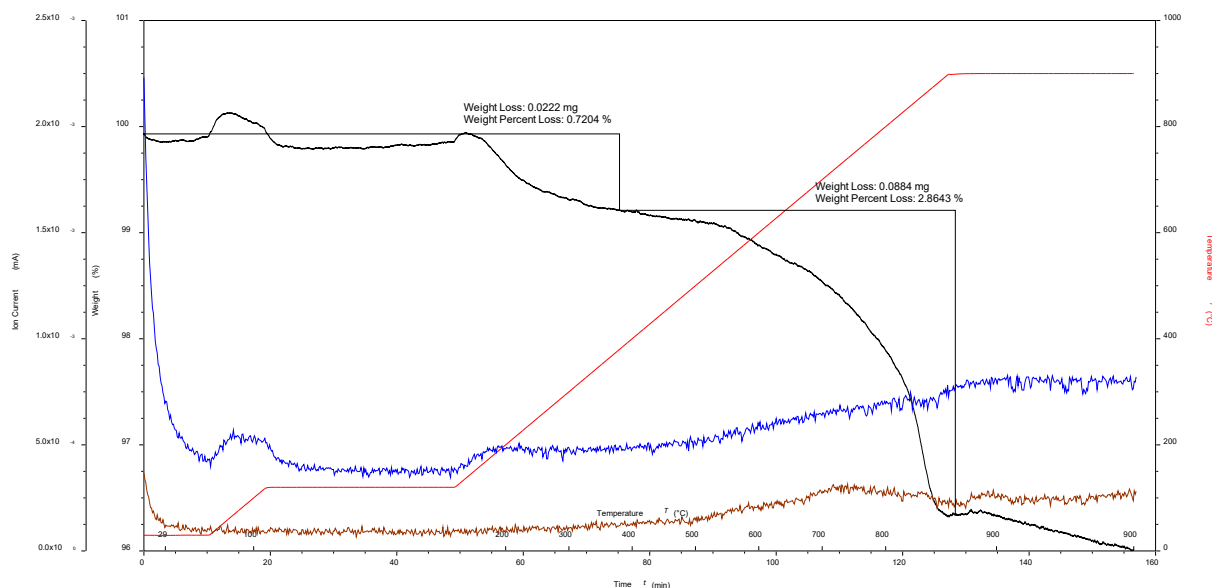


Figure S1. TGA-MS curves for 1@TiO₂: Weight against time and temperature (black), temperature (red), amu 18 (blue), amu 44 (brown).

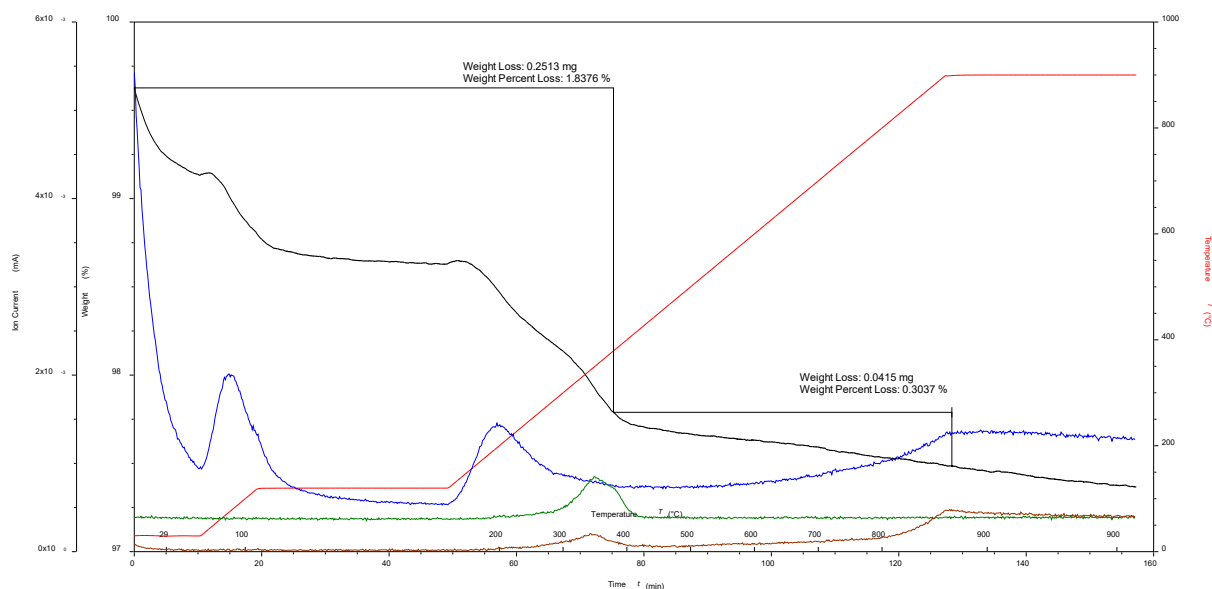


Figure S2. TGA-MS curves for a-NPs: Weight against time and temperature (black), temperature (red), amu 18 (blue), amu 30 (green), amu 44 (brown). Adapted figure from previous work.[6]

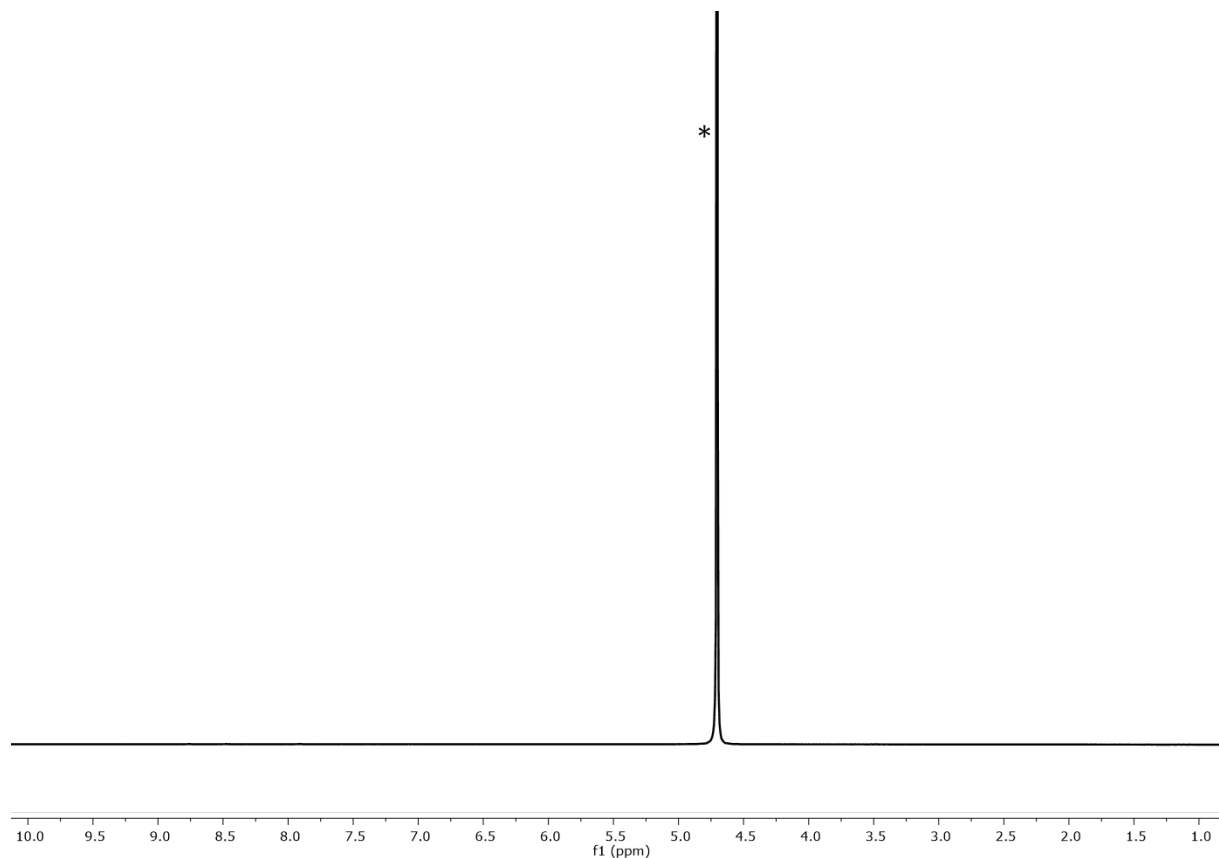


Figure S3. ¹H NMR (500 MHz, D₂O, 298 K) spectrum of **1**@TiO₂, * = HOD. Chemical shifts in ppm.

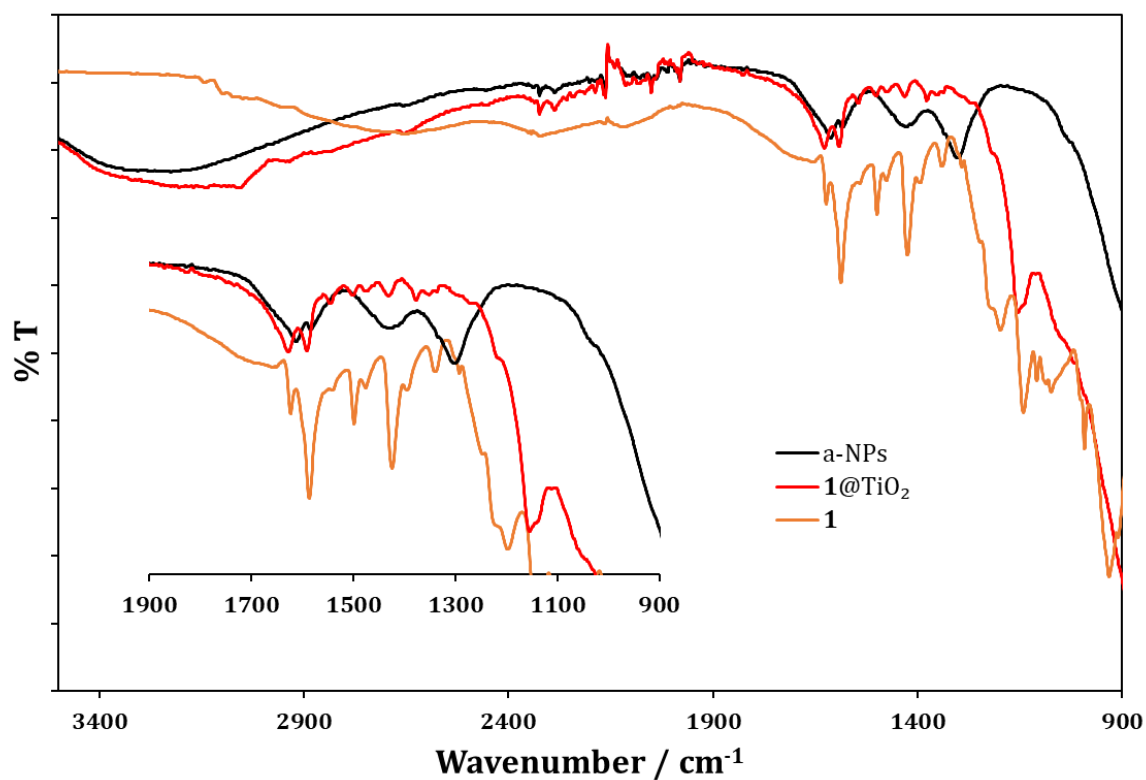


Figure S4. Solid-state IR spectra of **1**@TiO₂ (red), a-NPs (black) and pristine anchoring ligand **1** (orange) with expansion of the low energy regions.

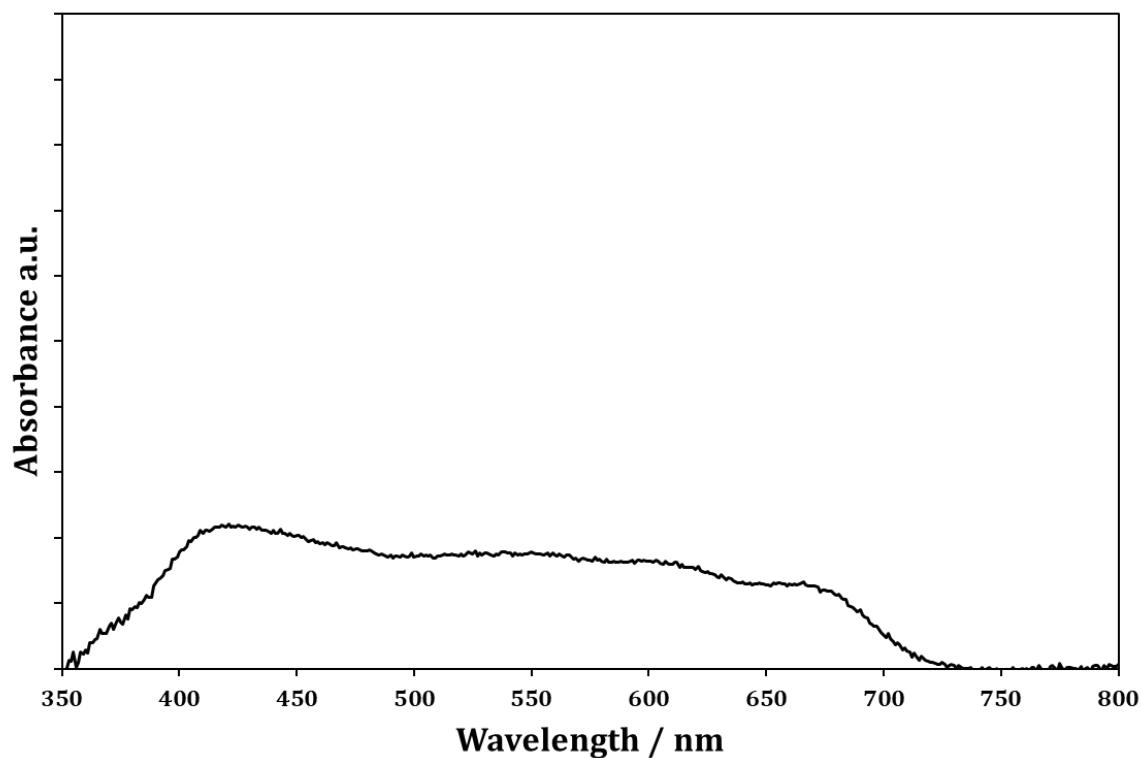


Figure S5. Solid-state absorption spectra of **1**@TiO₂ using a-NP as reference.

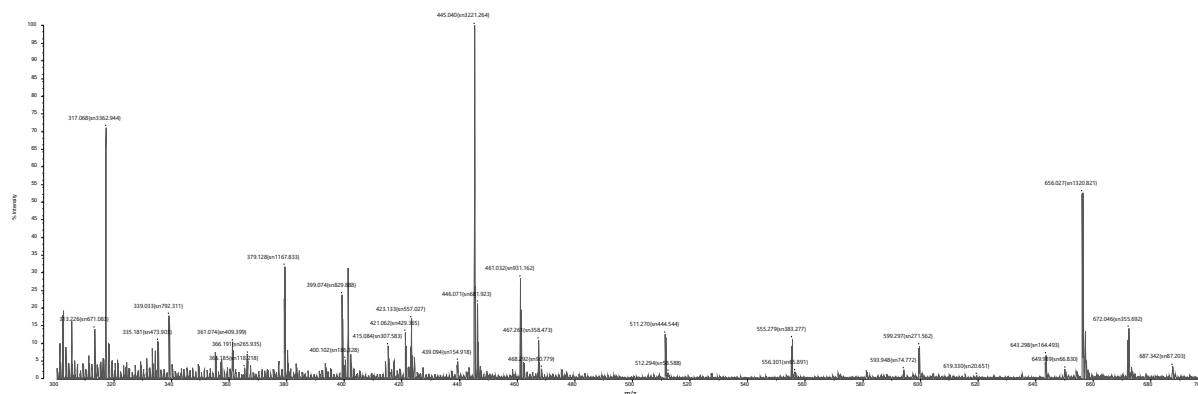


Figure S6. MALDI mass spectrum (with CHCA matrix) of **1**@TiO₂.

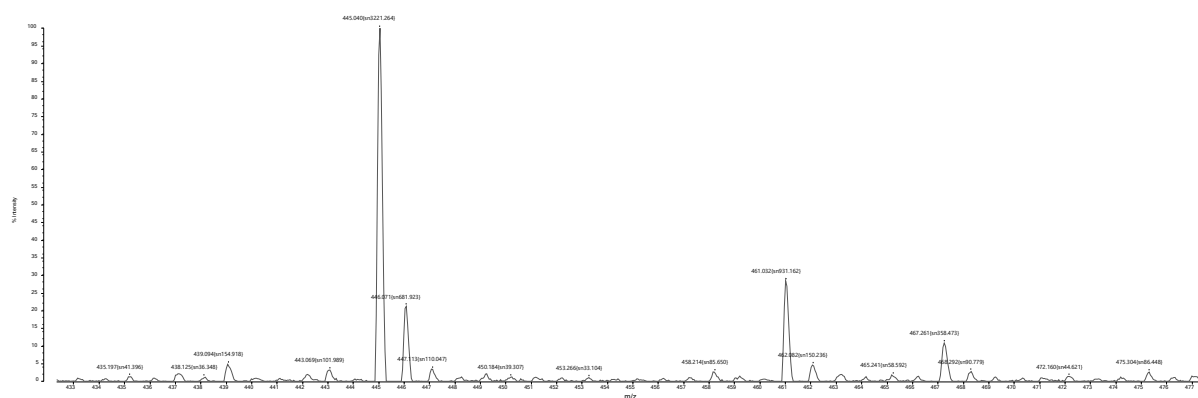


Figure S7. MALDI mass spectrum (with CHCA matrix) of **1**@TiO₂.

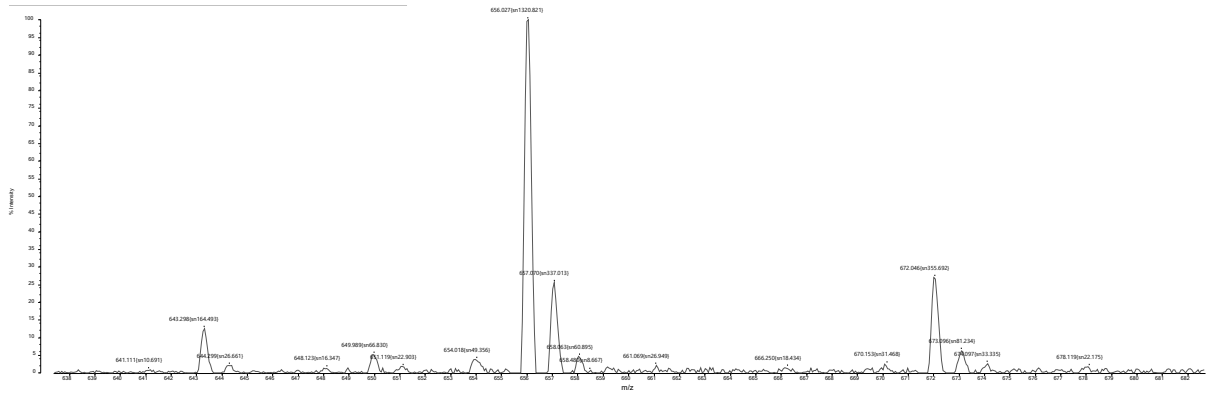
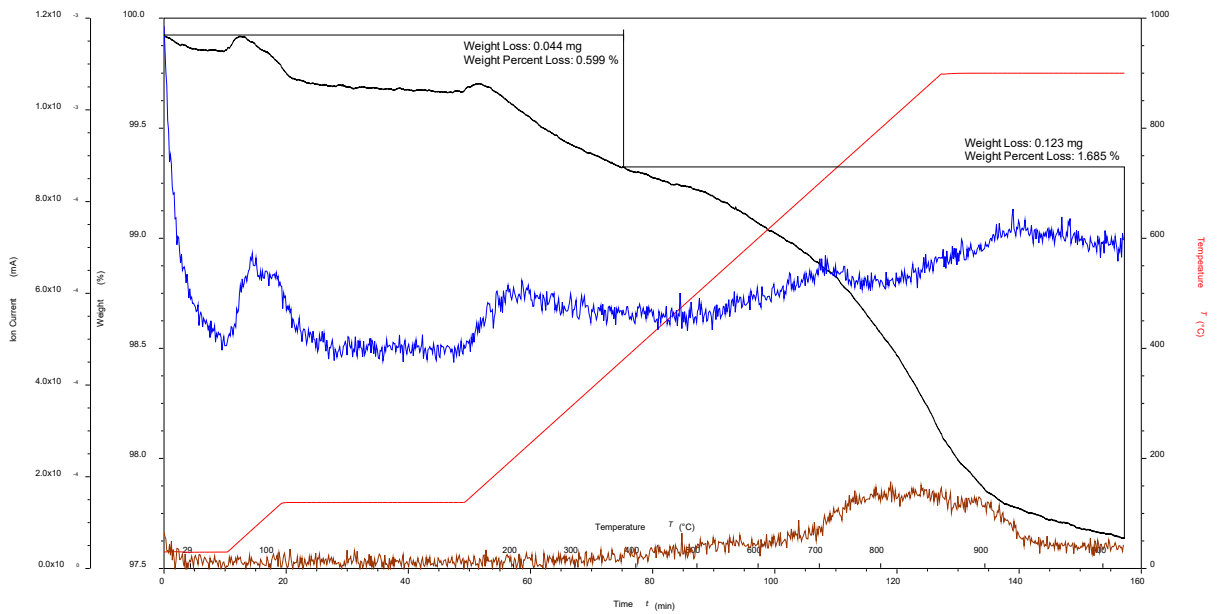
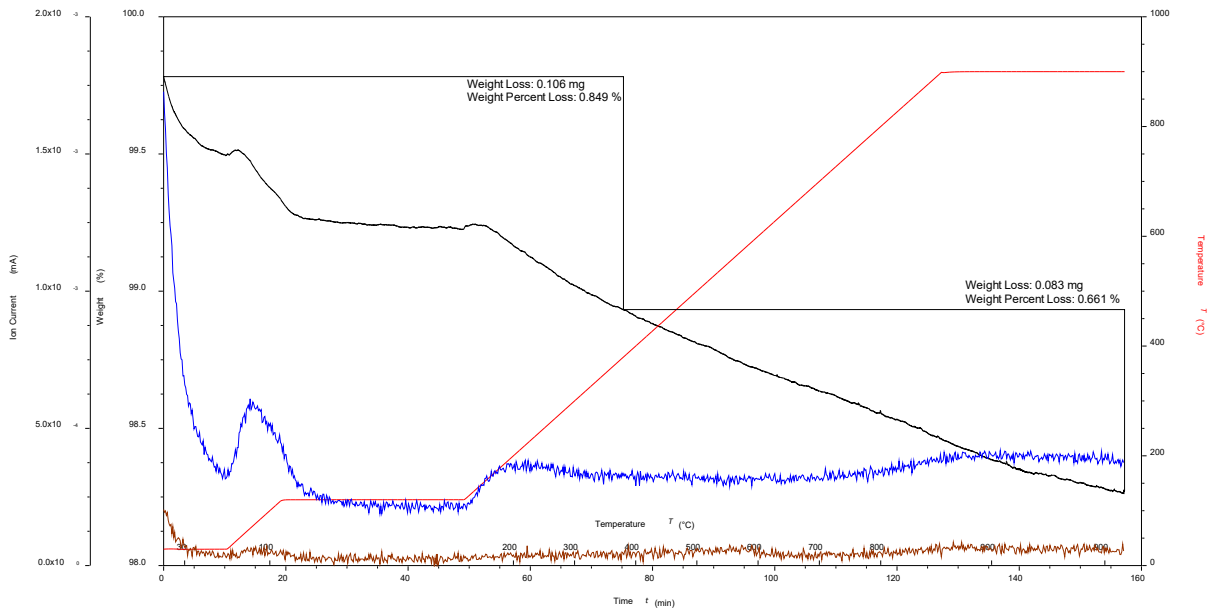


Figure S8. MALDI mass spectrum (with CHCA matrix) of 1@TiO₂.



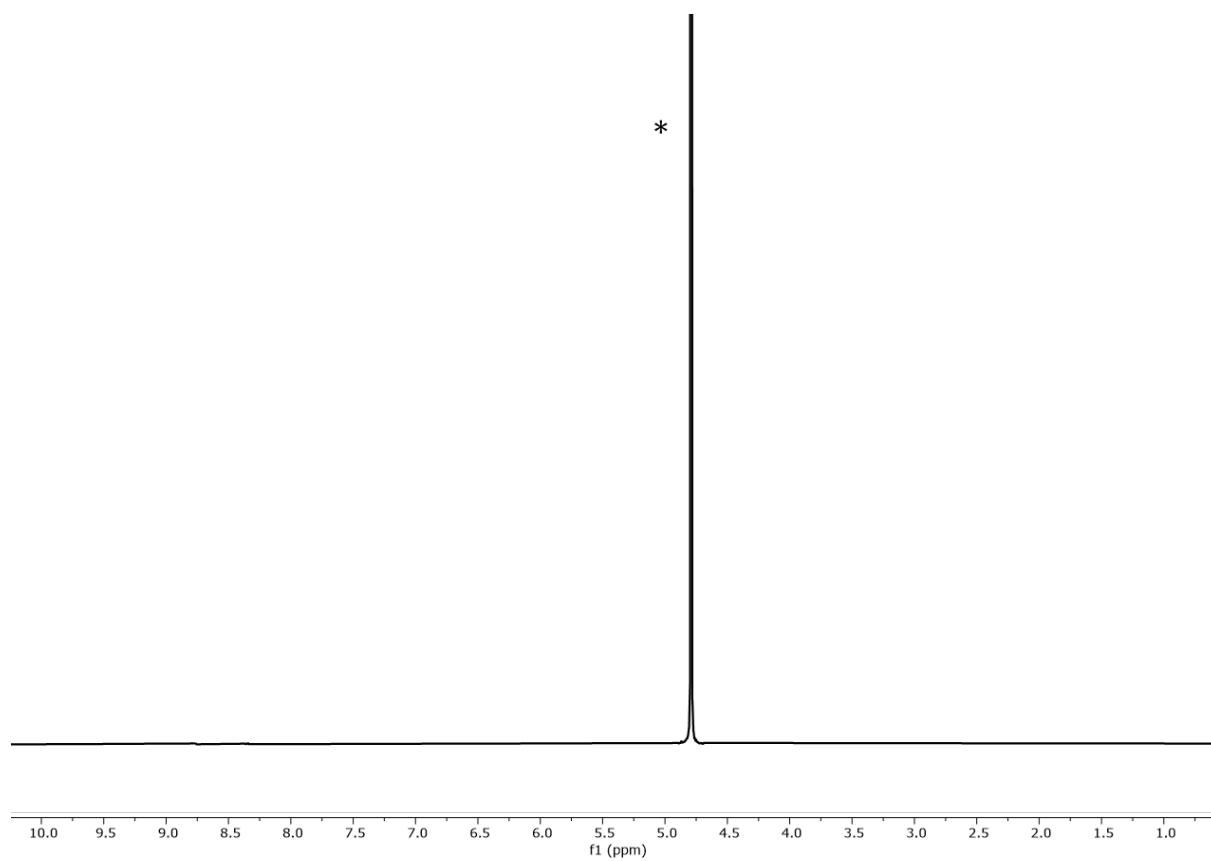


Figure S11. ^1H NMR (500 MHz, D_2O , 298 K) spectrum of $1@ZrO_2$, * = HOD. Chemical shifts in δ /ppm.

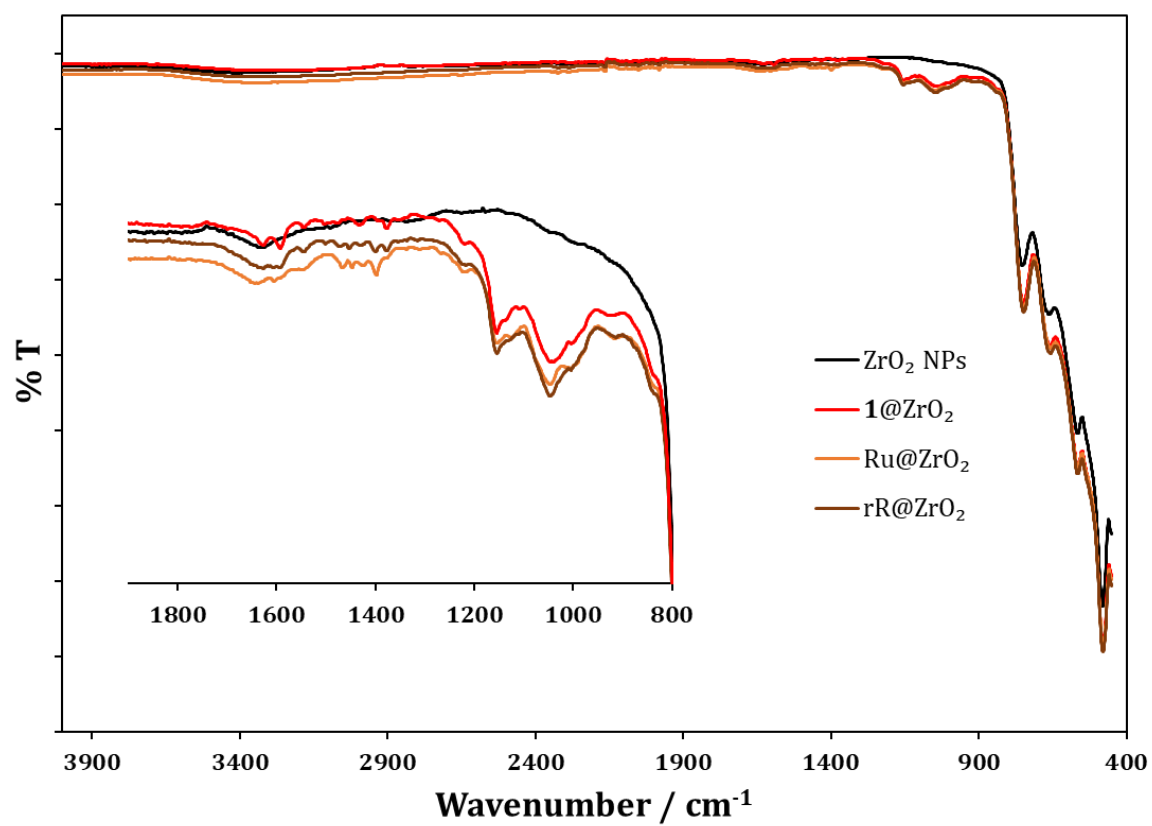


Figure S12. Solid-state IR spectra of pristine ZrO₂ NPs (black), $1@ZrO_2$ (red), Ru@ZrO₂ (orange), rR@ZrO₂ (brown) with expansion of the low energy regions.

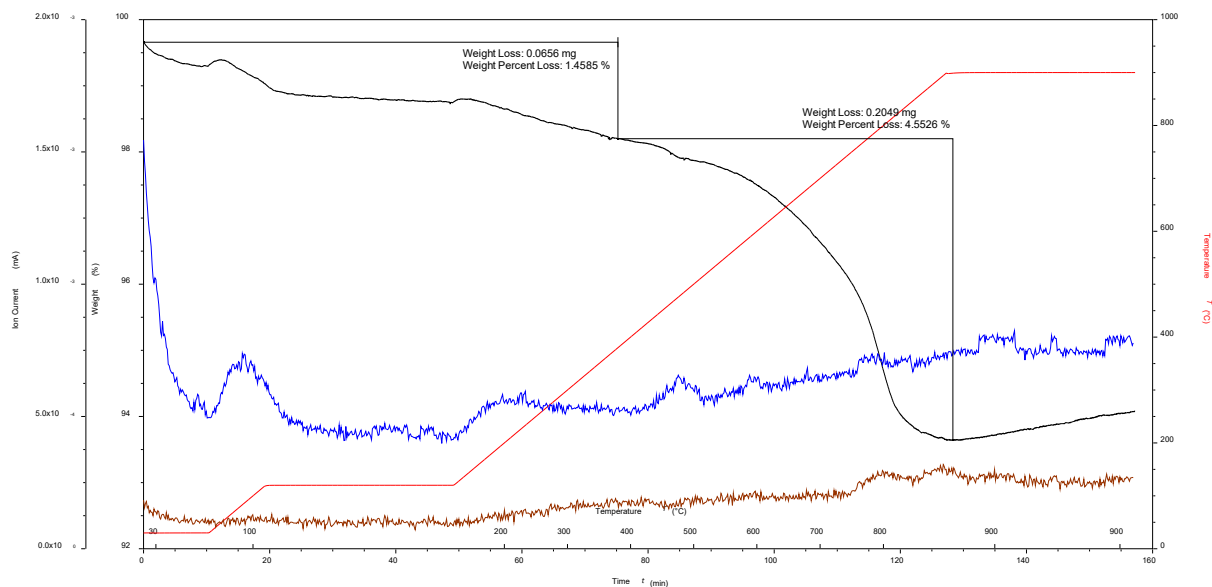


Figure S13. TGA curves for Ru@TiO₂ made with RuCl₃·3H₂O and bpy: Weight against time and temperature (black), temperature (red), amu 18 (blue), amu 44 (brown).

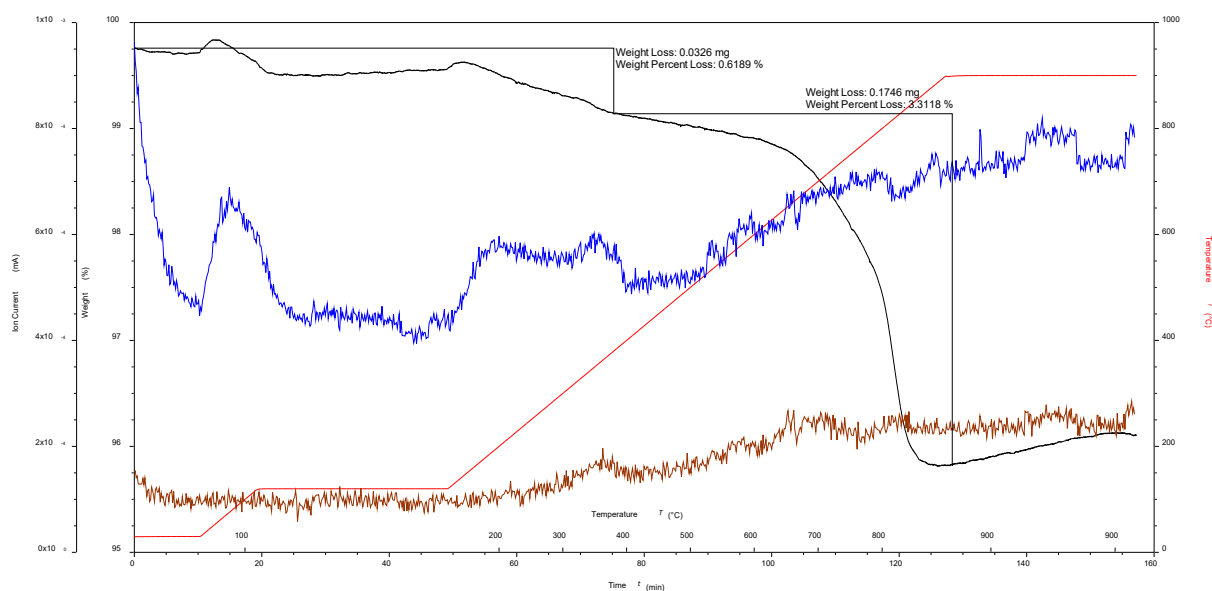


Figure S14. TGA curves for Ru@TiO₂ made with *cis*-[Ru(bpy)₂Cl₂]: Weight against time and temperature (black), temperature (red), amu 18 (blue), amu 44 (brown).

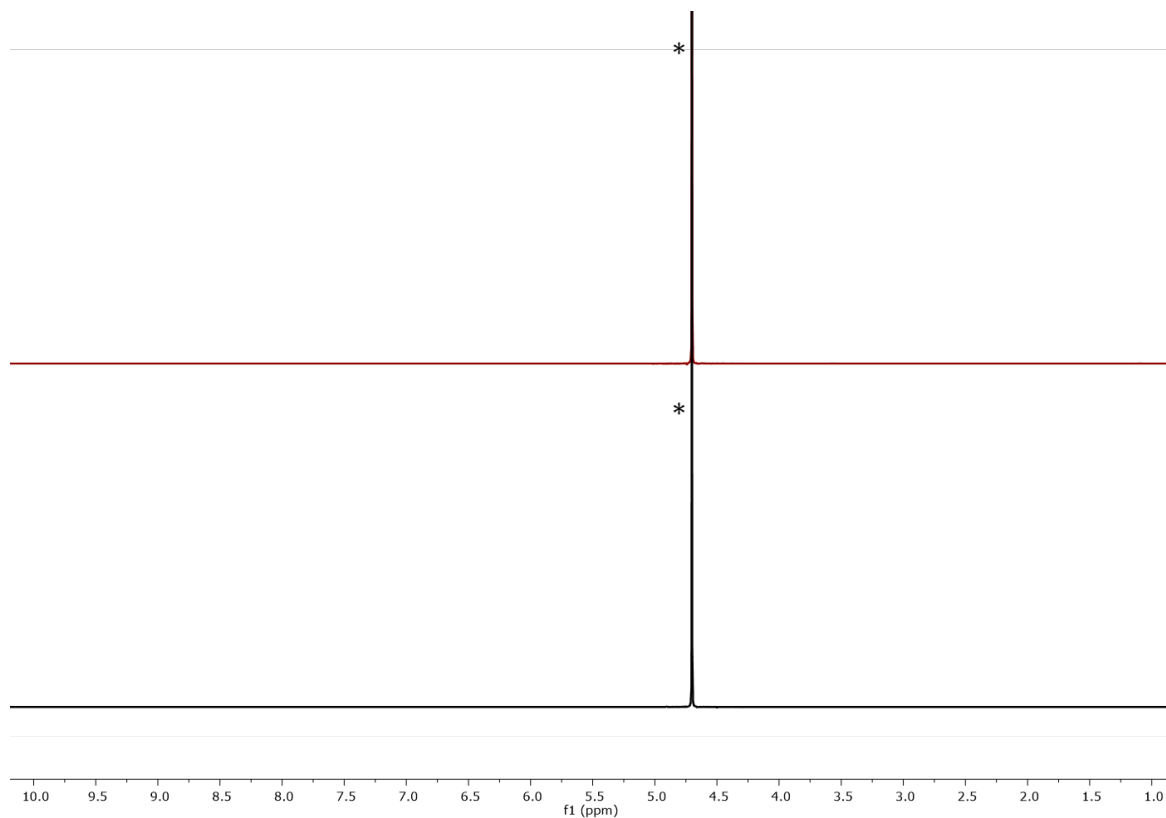


Figure S15. ^1H NMR (500 MHz, D_2O , 298 K) spectrum of Ru@TiO_2 made with: $\text{RuCl}_3 \cdot 3\text{H}_2\text{O}$ and bpy (black), *cis*- $[\text{Ru}(\text{bpy})_2\text{Cl}_2]$ (red); * = HOD. Chemical shifts in δ /ppm.

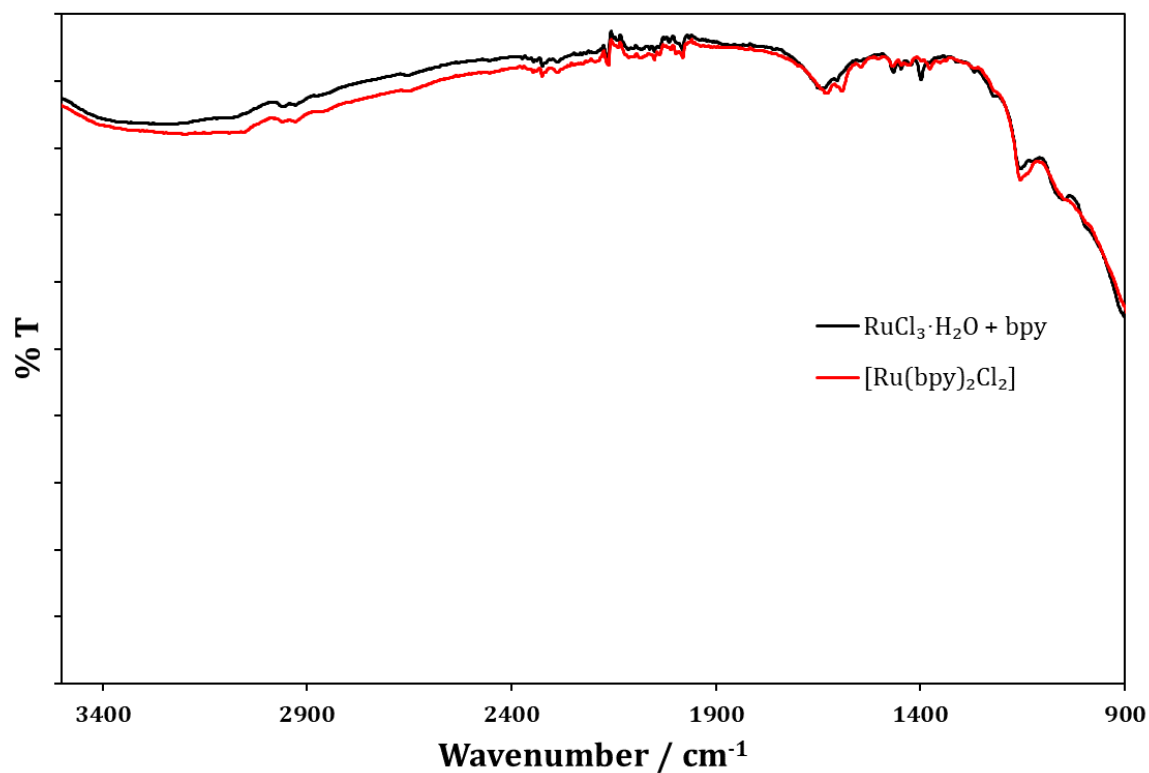


Figure S16. Solid-state IR spectra of Ru@TiO_2 made with: $\text{RuCl}_3 \cdot 3\text{H}_2\text{O}$ and bpy (black), *cis*- $[\text{Ru}(\text{bpy})_2\text{Cl}_2]$ (red).

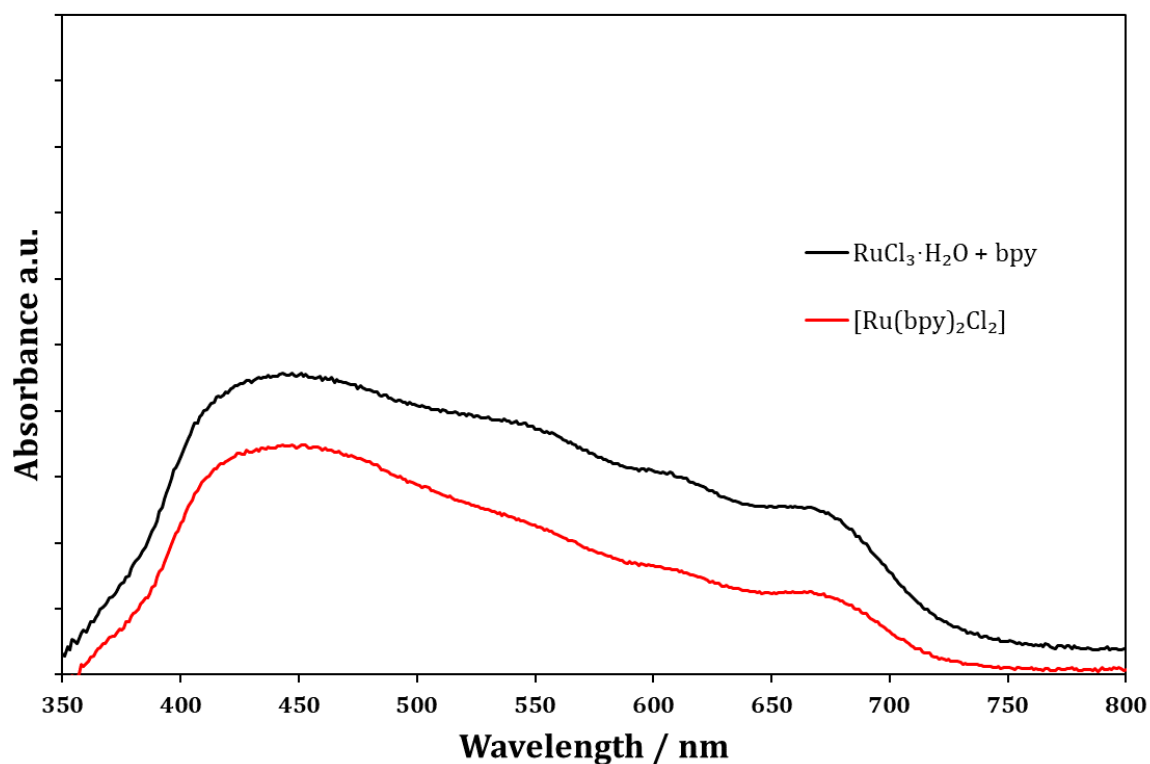


Figure S17. Solid-state absorption spectra of Ru@TiO₂ made with: RuCl₃·3H₂O and bpy (black), *cis*-[Ru(bpy)₂Cl₂] (red) using a-NP as reference.

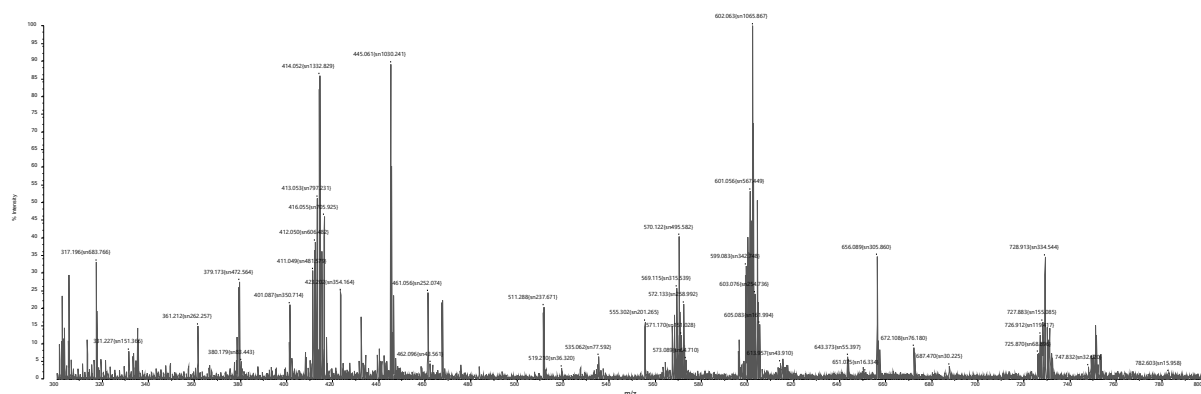


Figure S18. MALDI mass spectrum (with CHCA matrix) of Ru@TiO₂ with RuCl₃·3H₂O.

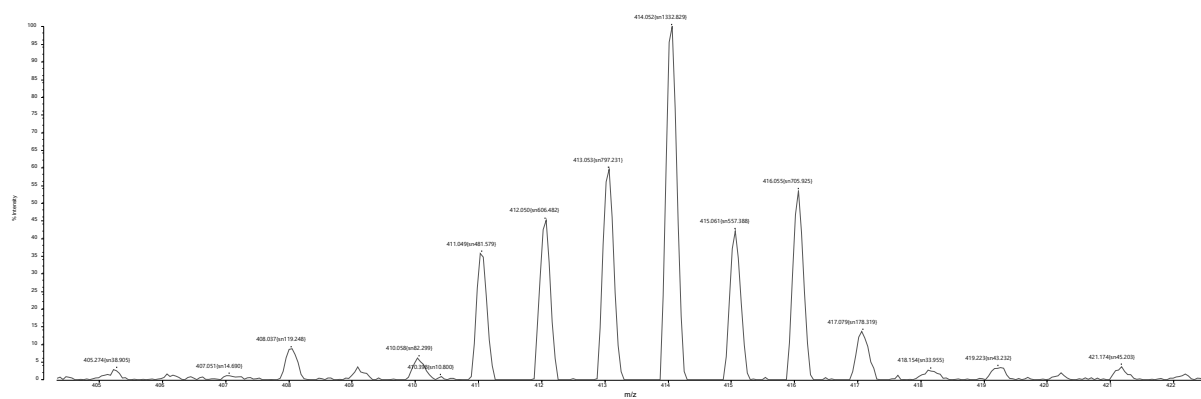


Figure S19. MALDI mass spectrum (with CHCA matrix) of Ru@TiO₂ with RuCl₃·3H₂O.

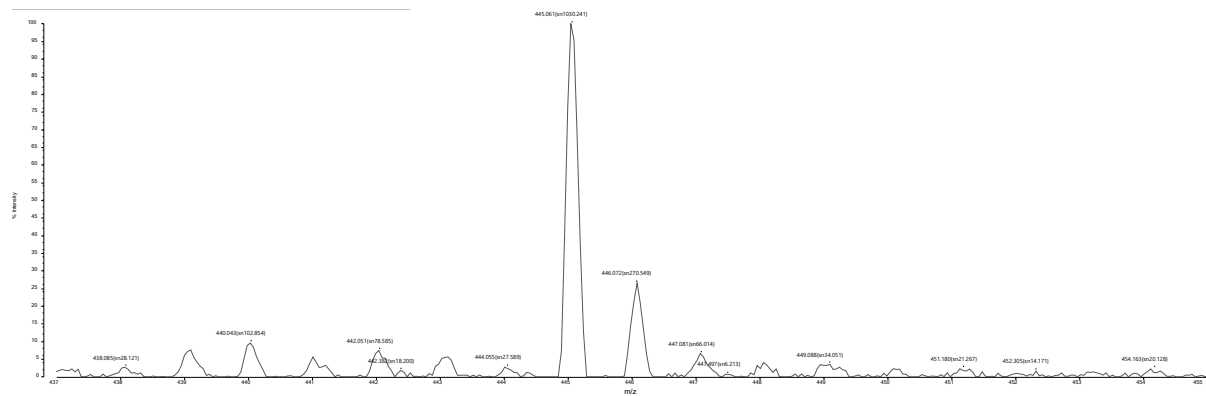


Figure S20. MALDI mass spectrum (with CHCA matrix) of Ru@TiO₂ with RuCl₃·3H₂O.

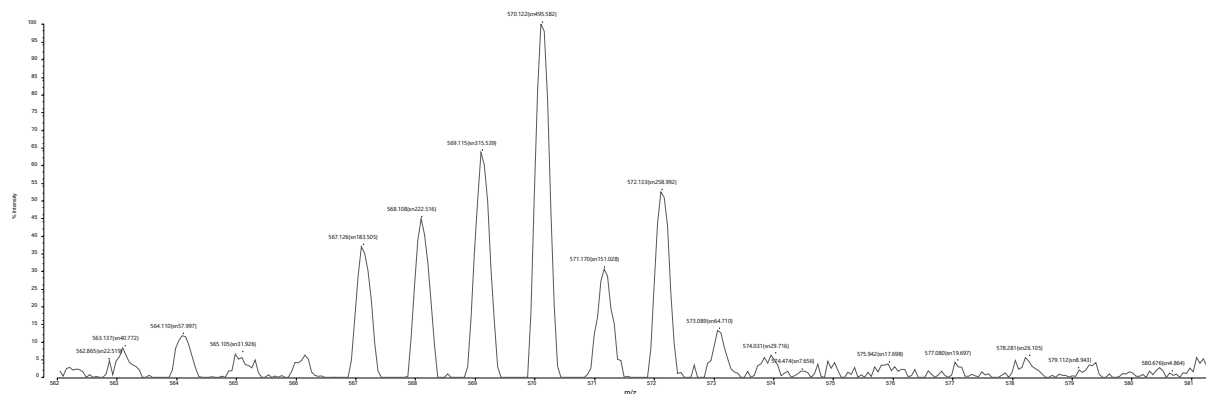


Figure S21. MALDI mass spectrum (with CHCA matrix) of Ru@TiO₂ with RuCl₃·3H₂O.

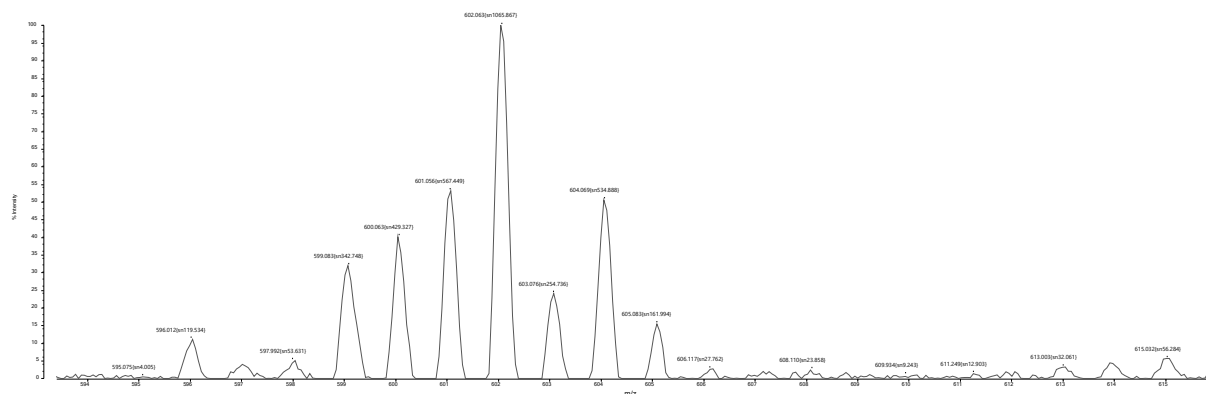


Figure S22. MALDI mass spectrum (with CHCA matrix) of Ru@TiO₂ with RuCl₃·3H₂O.

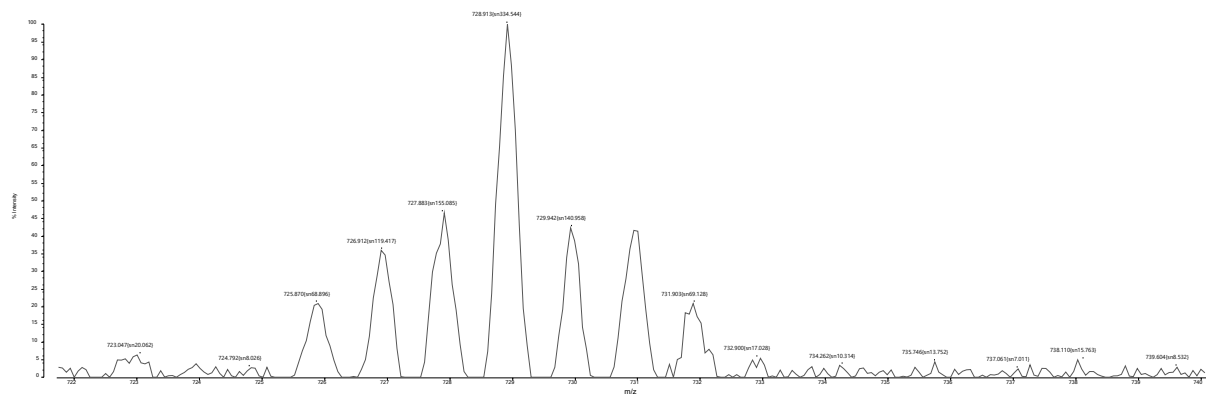


Figure S23. MALDI mass spectrum (with CHCA matrix) of Ru@TiO₂ with RuCl₃·3H₂O.

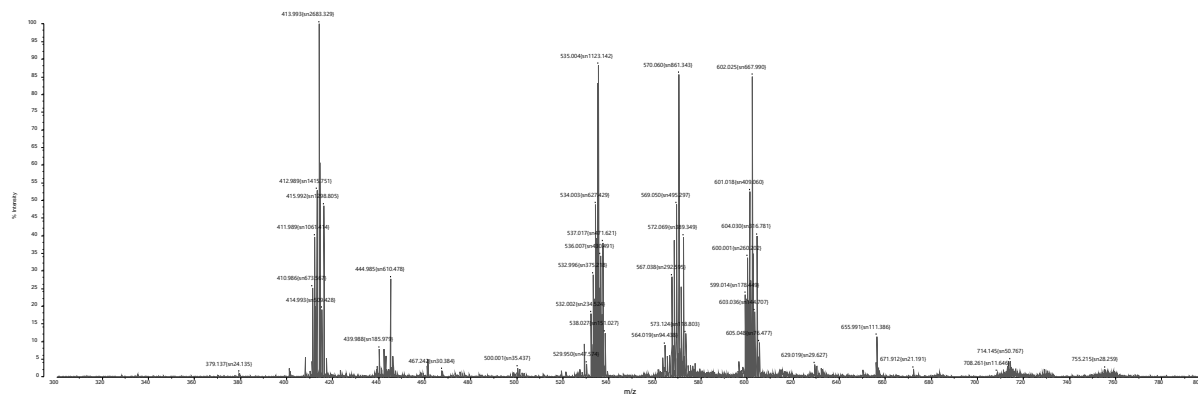


Figure S24. MALDI mass spectrum (with CHCA matrix) of Ru@TiO₂ with *cis*-[Ru(bpy)₂Cl₂].

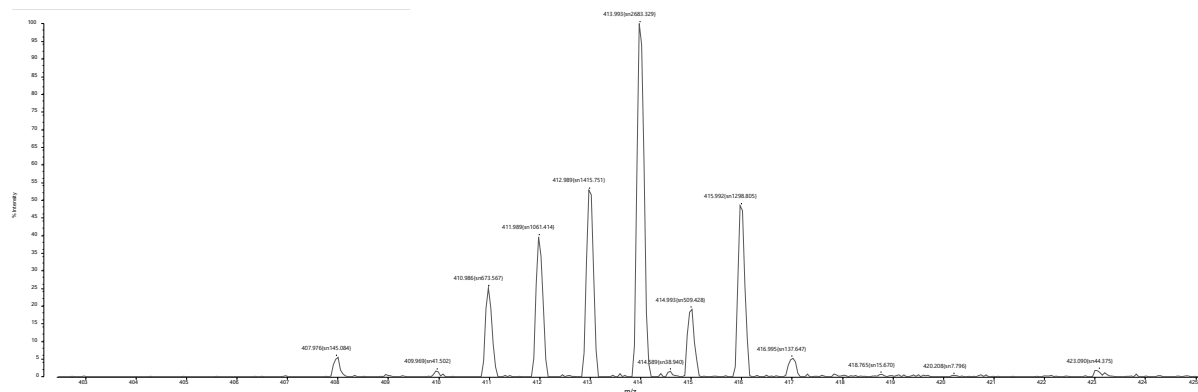


Figure S25. MALDI mass spectrum (with CHCA matrix) of Ru@TiO₂ with *cis*-[Ru(bpy)₂Cl₂].

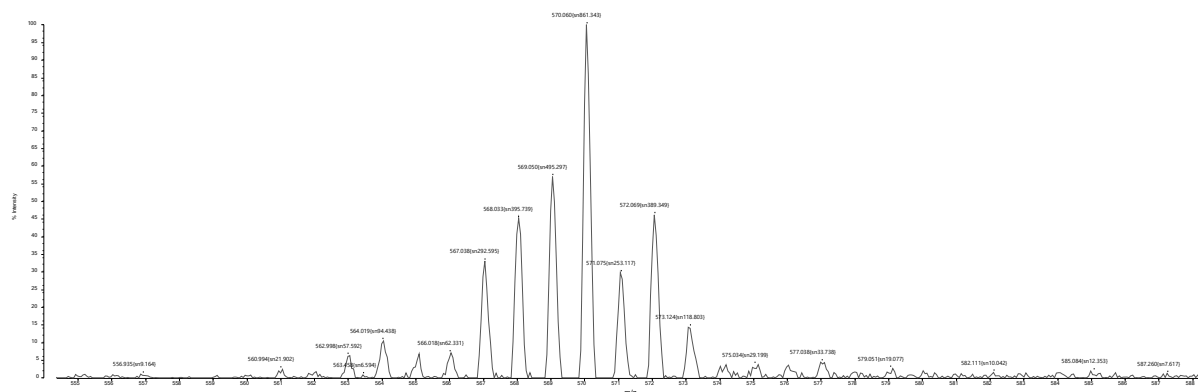


Figure S26. MALDI mass spectrum (with CHCA matrix) of Ru@TiO₂ with *cis*-[Ru(bpy)₂Cl₂].

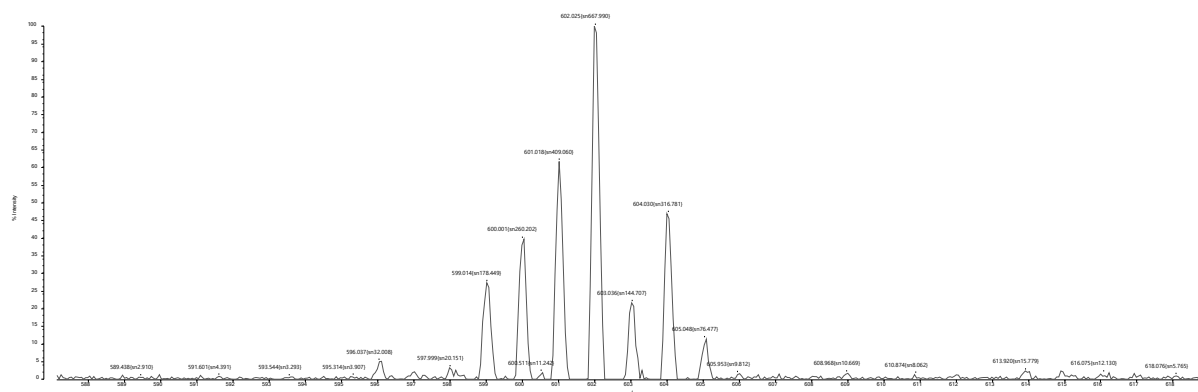


Figure S27. MALDI mass spectrum (with CHCA matrix) of Ru@TiO₂ with *cis*-[Ru(bpy)₂Cl₂].

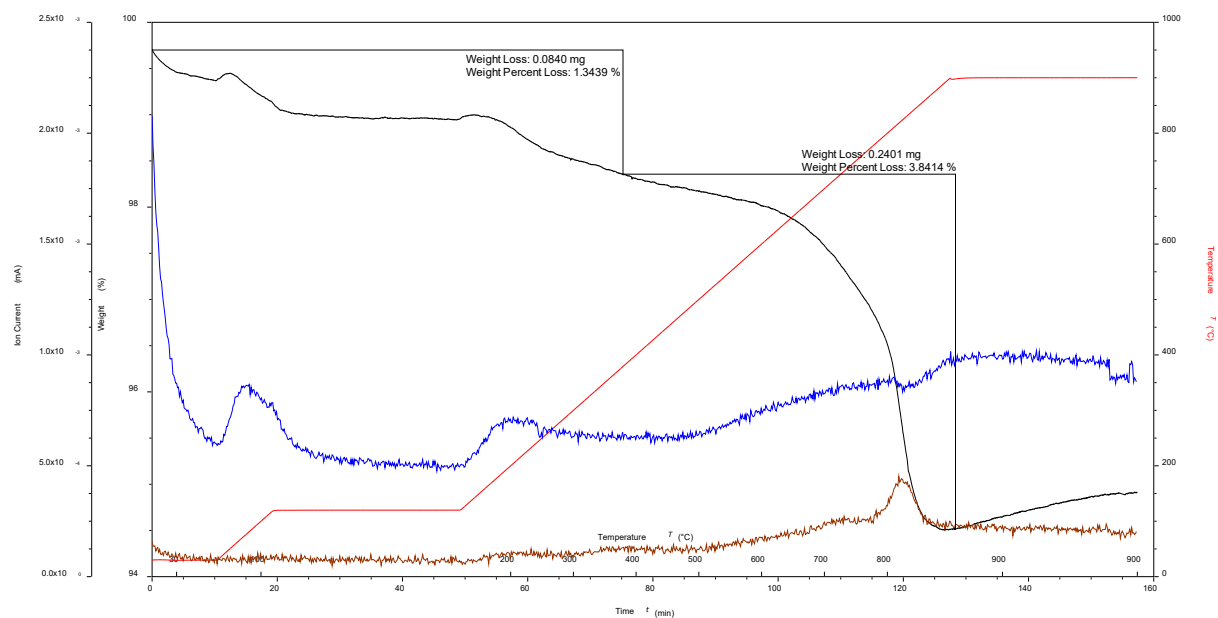


Figure S28. TGA curves for Rh@TiO₂: Weight against time and temperature (blue), derivative of weight change against time (red).

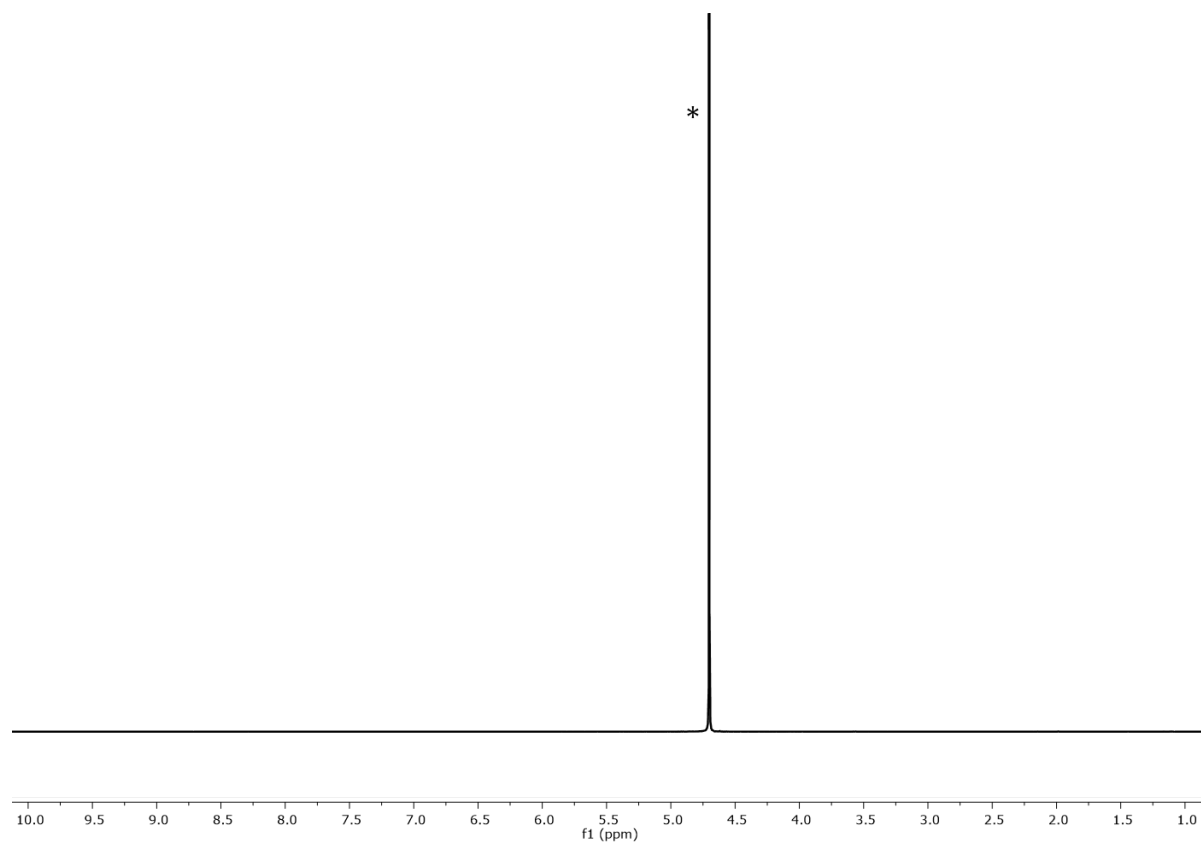


Figure S29. ¹H NMR (500 MHz, D₂O, 298 K) spectrum of Rh@TiO₂, * = HOD. Chemical shifts in ppm.

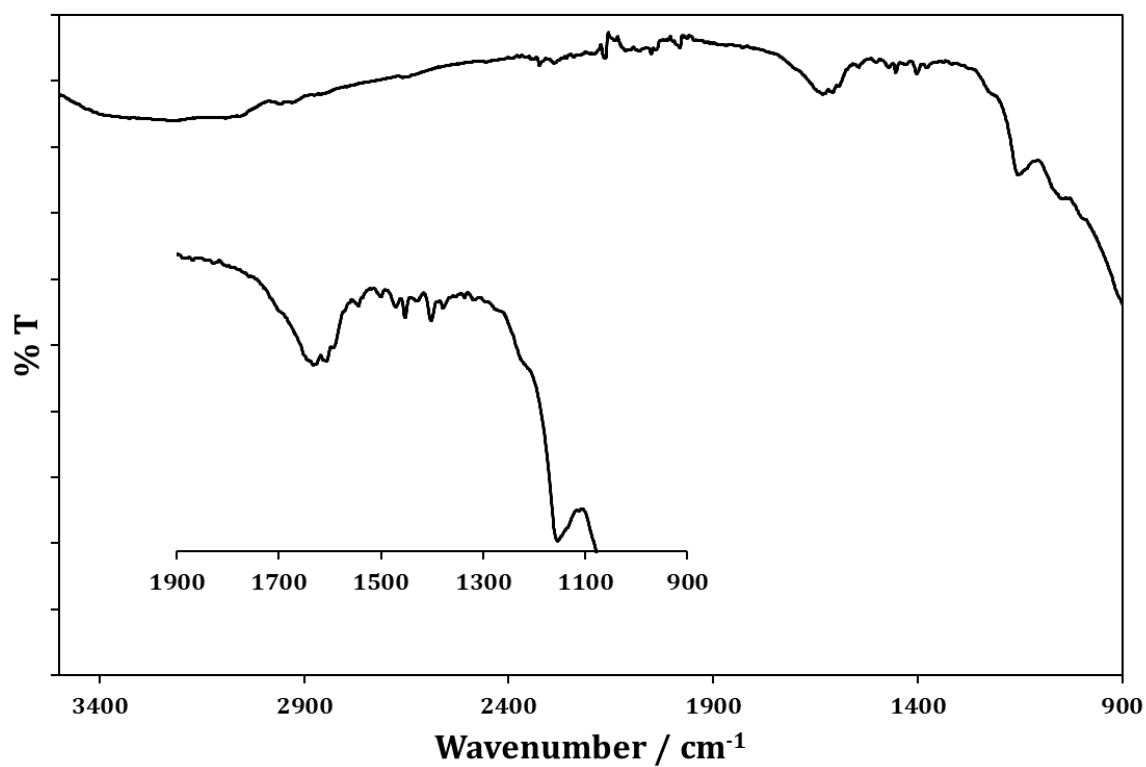


Figure S30. Solid-state IR spectrum of Rh@TiO₂ with expansion of the low energy regions.

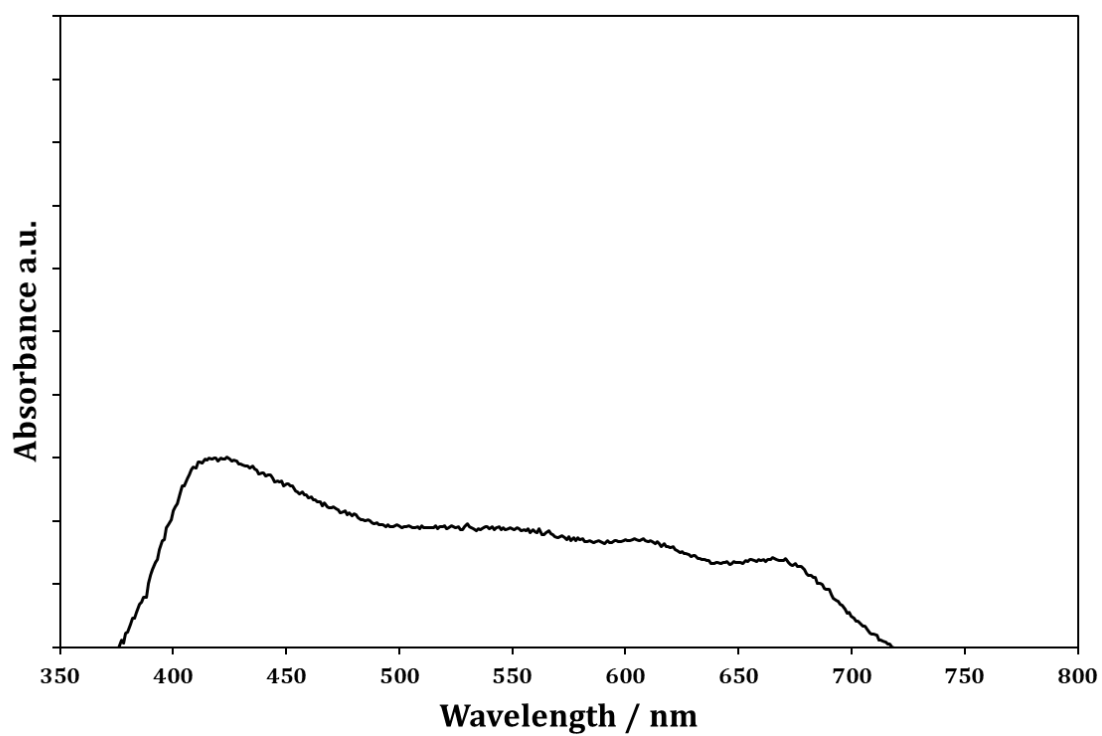


Figure S31. Solid-state absorption spectra of Rh@TiO₂ using a-NP as reference.

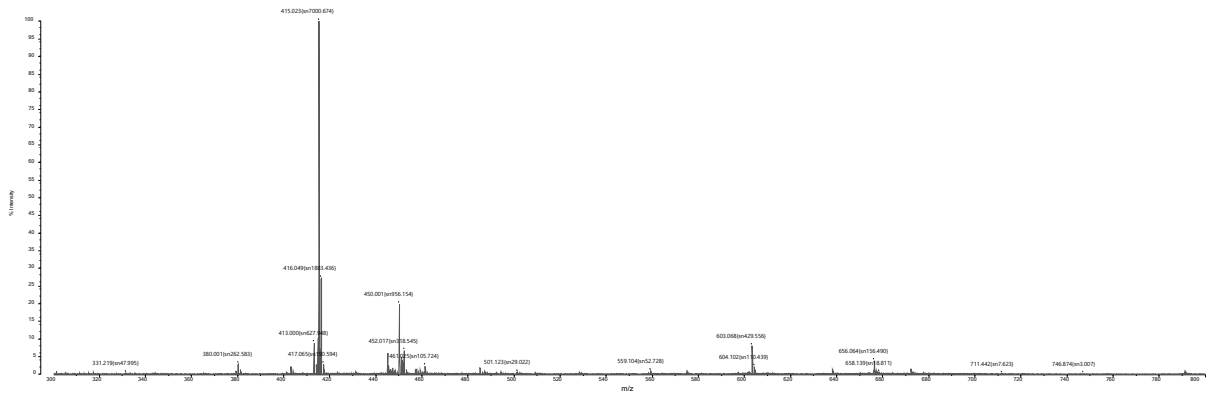


Figure S32. MALDI mass spectrum (with CHCA matrix) of Rh@TiO₂.

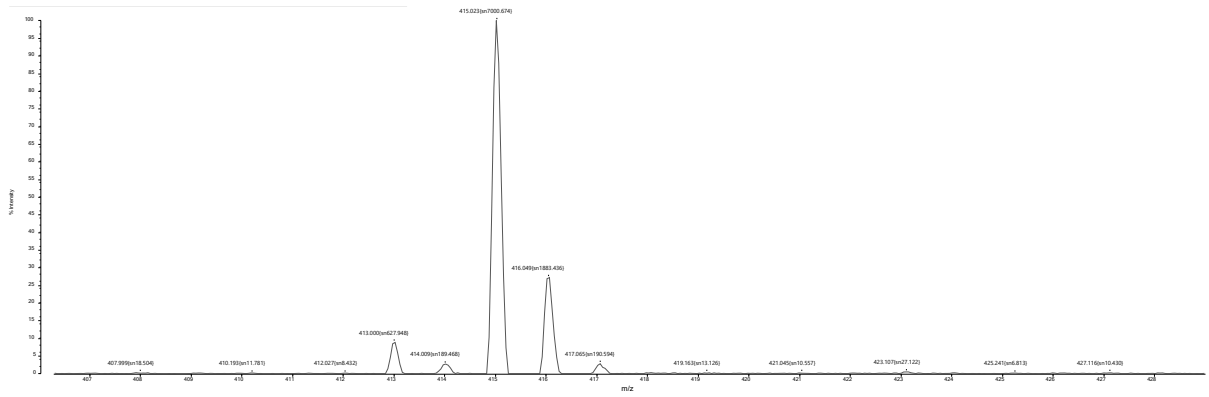


Figure S33. MALDI mass spectrum (with CHCA matrix) of Rh@TiO₂.

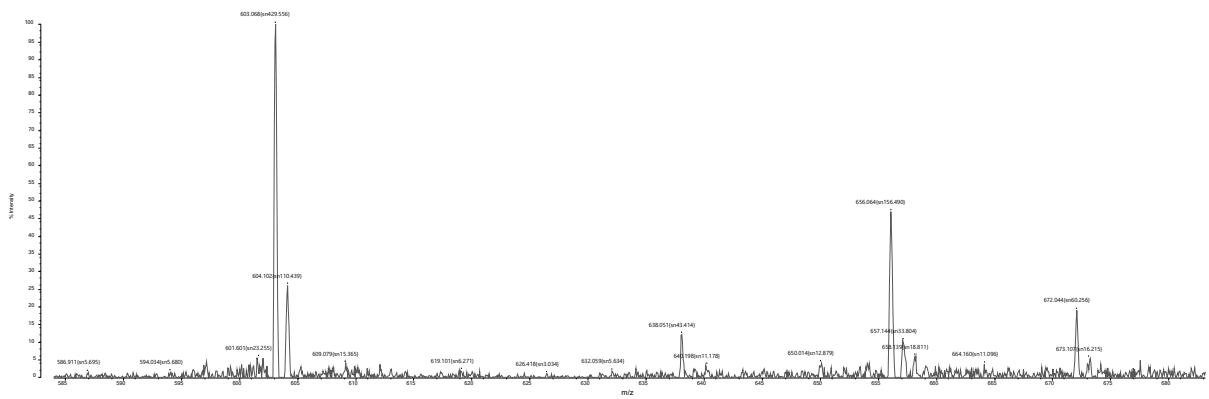


Figure S34. MALDI mass spectrum (with CHCA matrix) of Rh@TiO₂.

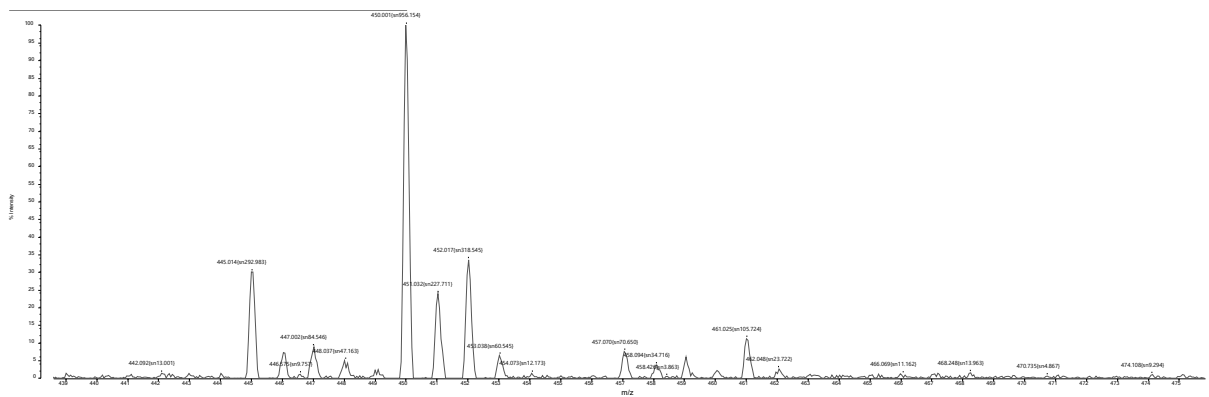


Figure S35. MALDI mass spectrum (with CHCA matrix) of Rh@TiO₂.

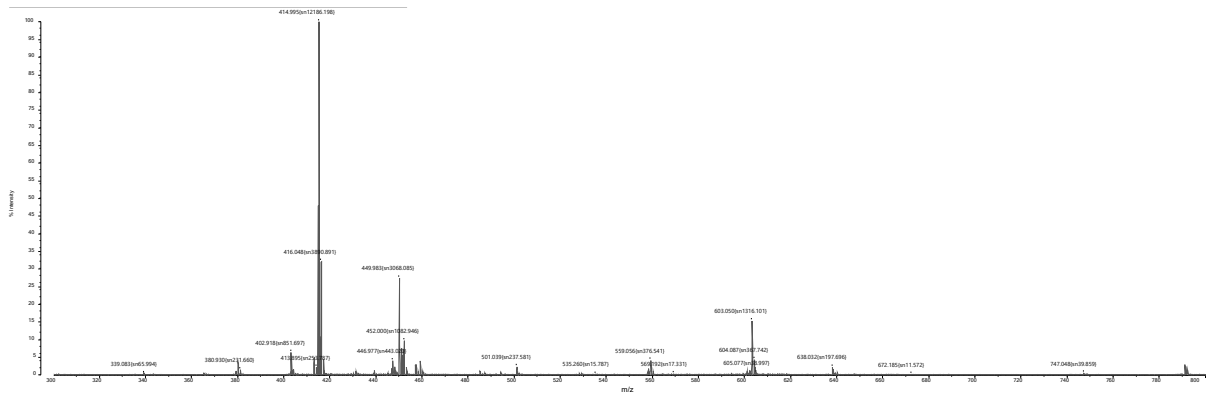


Figure S36. MALDI mass spectrum (with CHCA matrix) of rR@TiO₂.

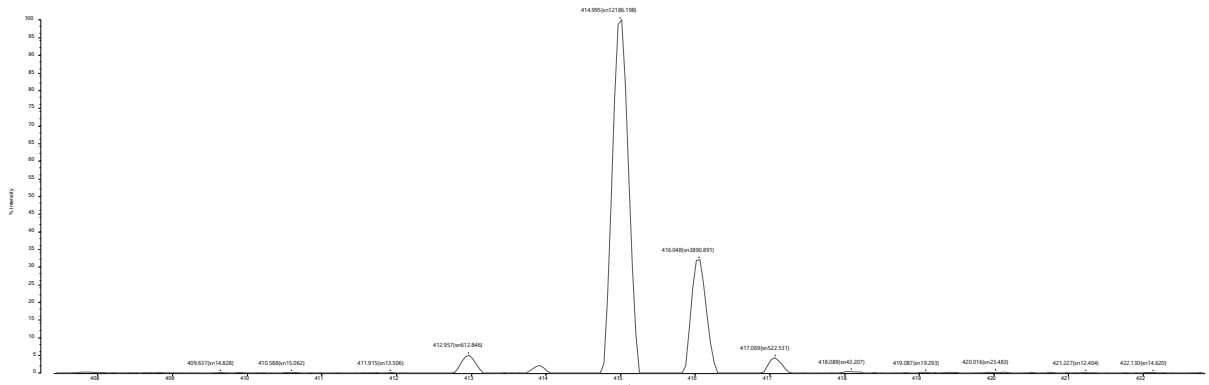


Figure S37. MALDI mass spectrum (with CHCA matrix) of rR@TiO₂.

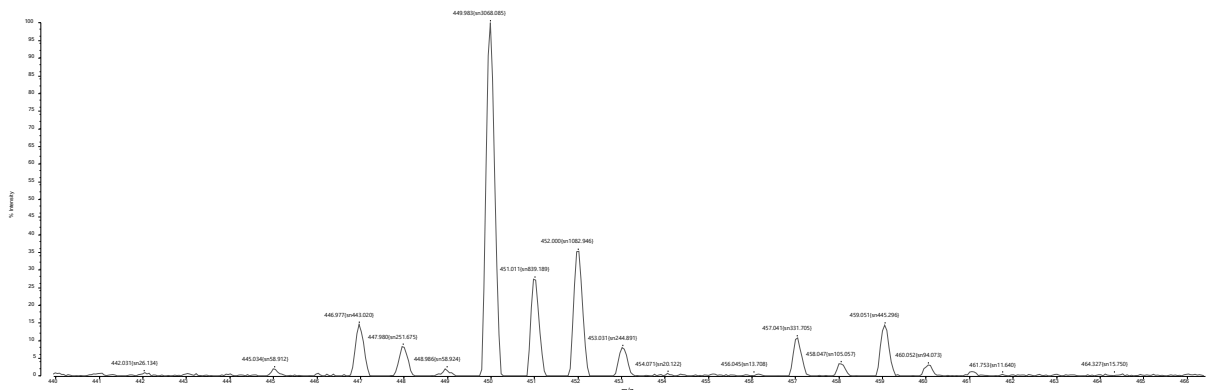


Figure S38. MALDI mass spectrum (with CHCA matrix) of rR@TiO₂.

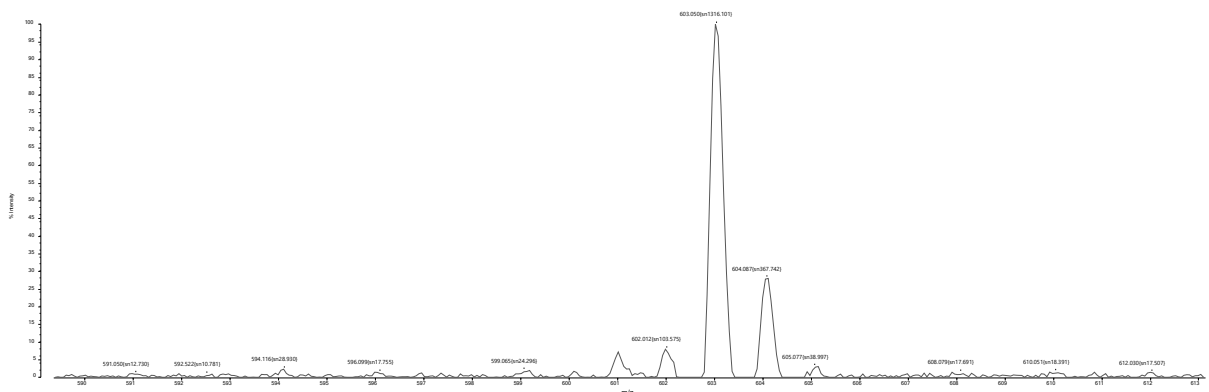


Figure S39. MALDI mass spectrum (with CHCA matrix) of rR@TiO₂.

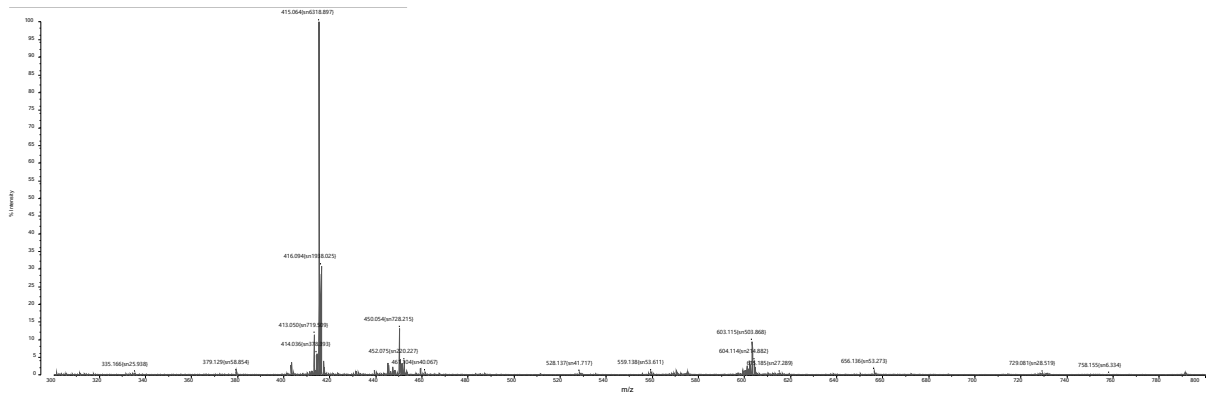


Figure S40. MALDI mass spectrum (with CHCA matrix) of RR@TiO₂.

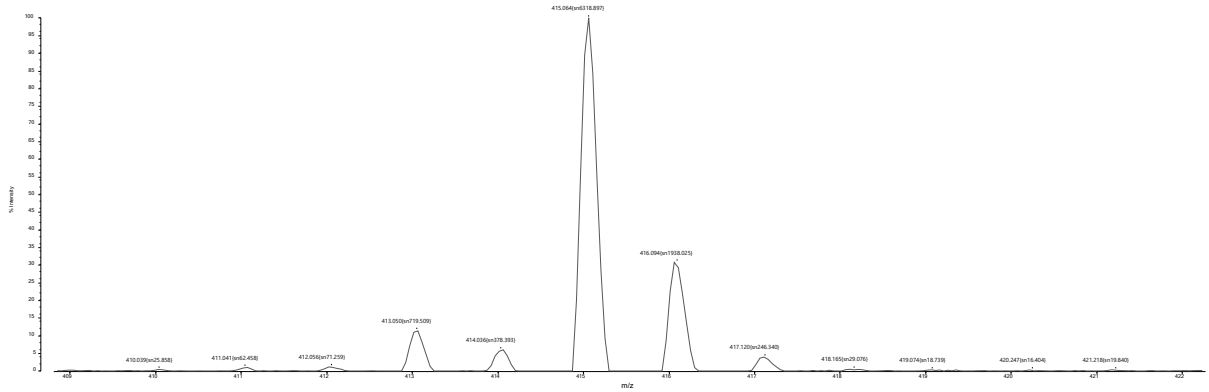


Figure S41. MALDI mass spectrum (with CHCA matrix) of RR@TiO₂.

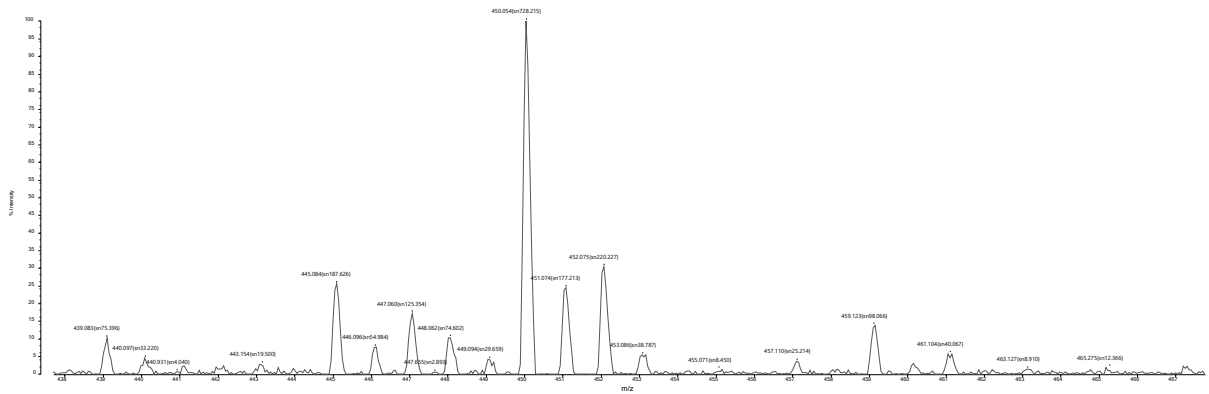


Figure S42. MALDI mass spectrum (with CHCA matrix) of RR@TiO₂.

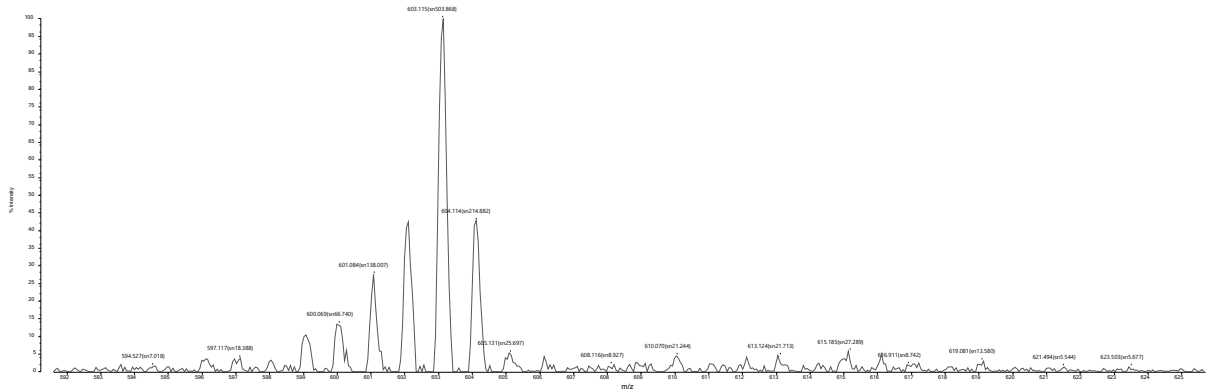


Figure S43. MALDI mass spectrum (with CHCA matrix) of RR@TiO₂.

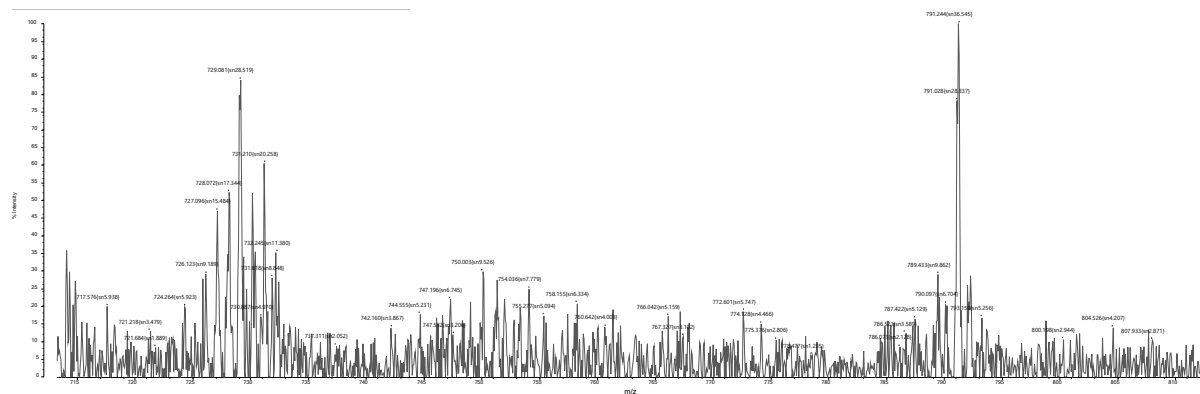


Figure S44. MALDI mass spectrum (with CHCA matrix) of RR@TiO₂.

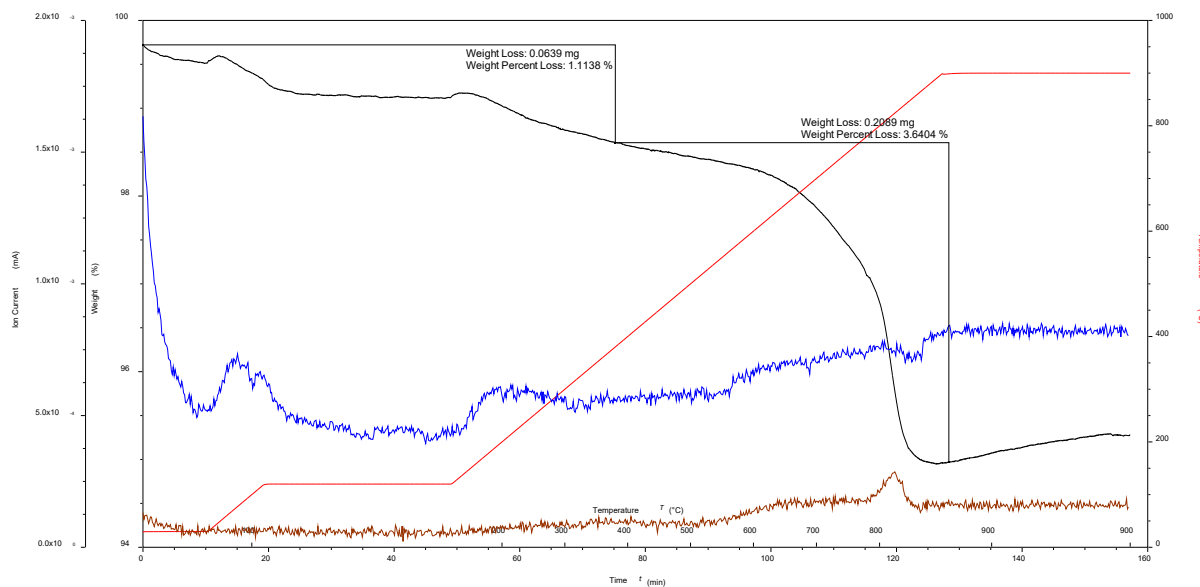


Figure S45. TGA curves for rR@TiO₂: Weight against time and temperature (blue), derivative of weight change against time (red).

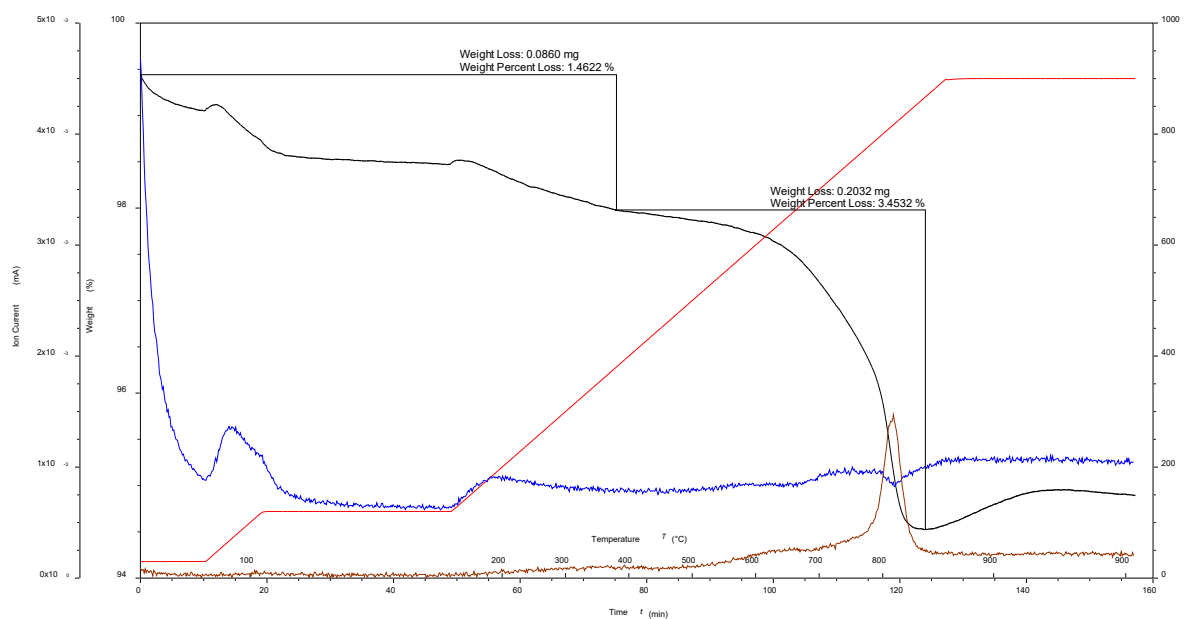


Figure S46. TGA curves for RR@TiO₂: Weight against time and temperature (blue), derivative of weight change against time (red).

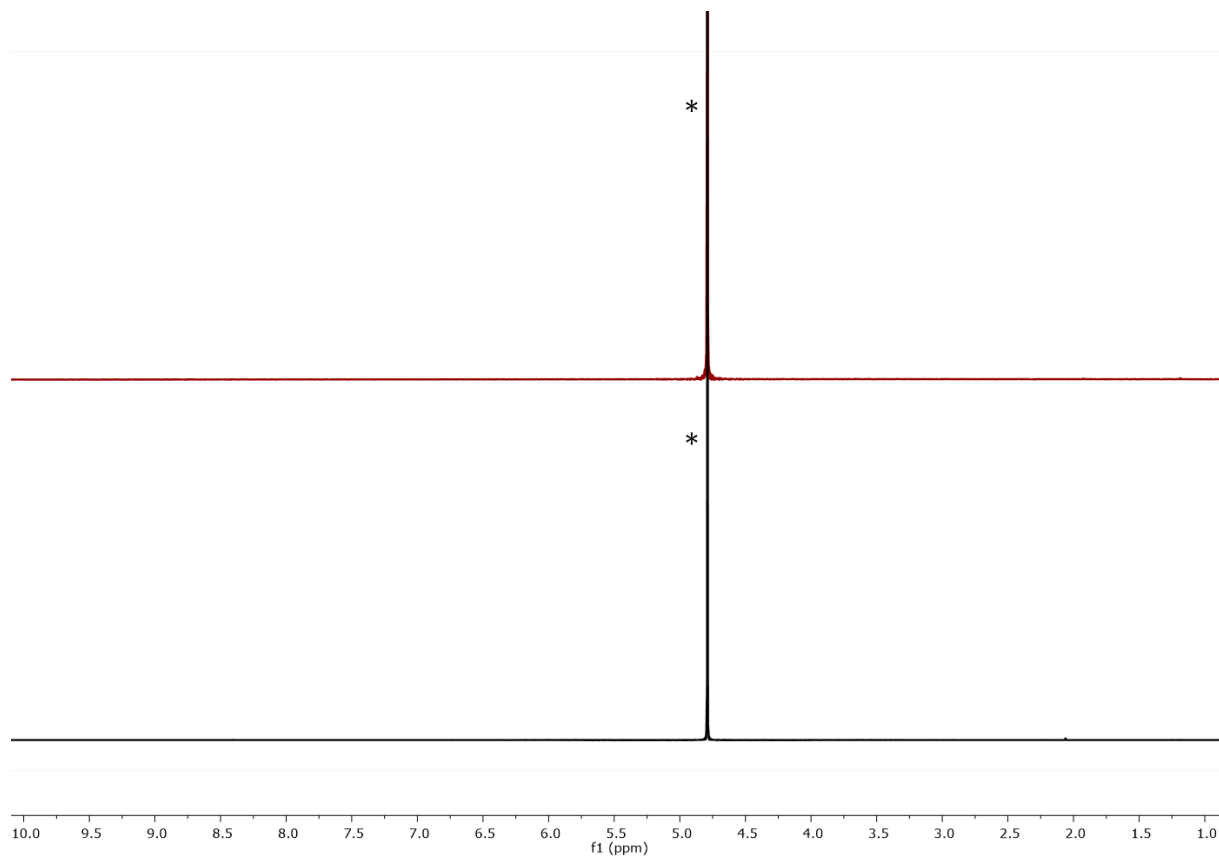


Figure S47. ^1H NMR (500 MHz, D_2O , 298 K) spectrum of rR@TiO_2 (black) and RR@TiO_2 (red), * = HOD. Chemical shifts in δ /ppm.

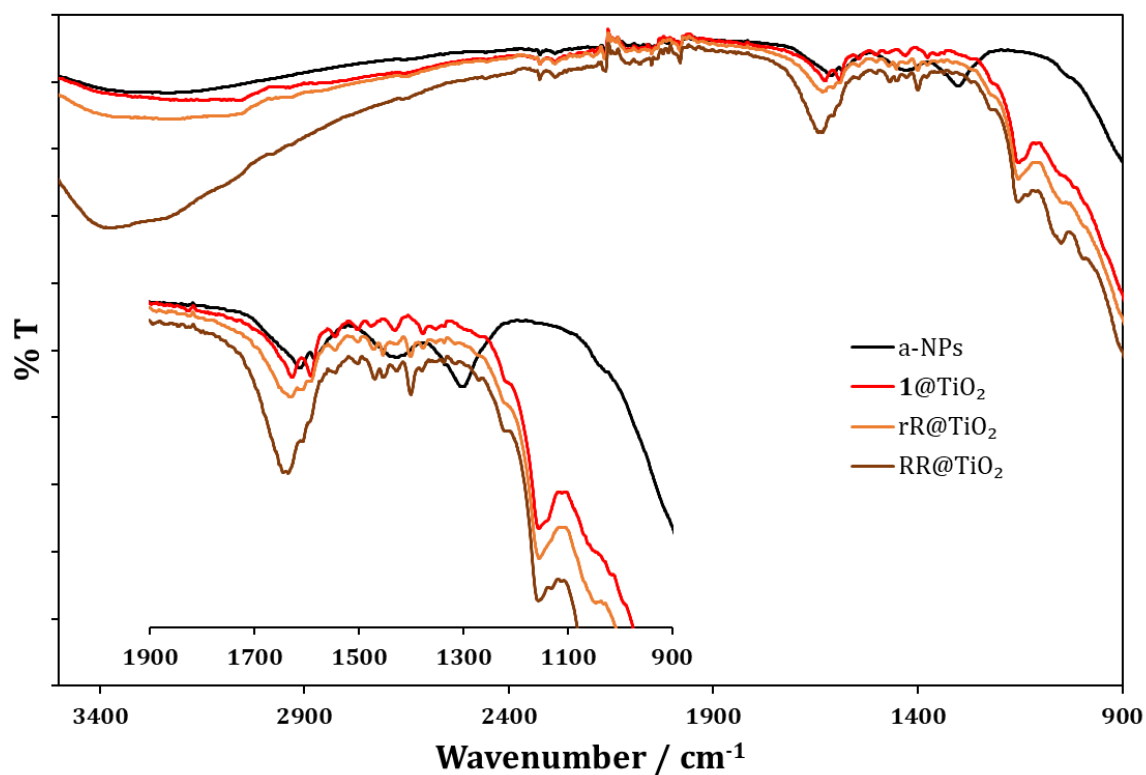


Figure S48. Solid-state IR spectra of a-NPs (black), $\mathbf{1@TiO}_2$ (red), rR@TiO_2 (orange) and RR@TiO_2 (brown) with expansion of the low energy regions.

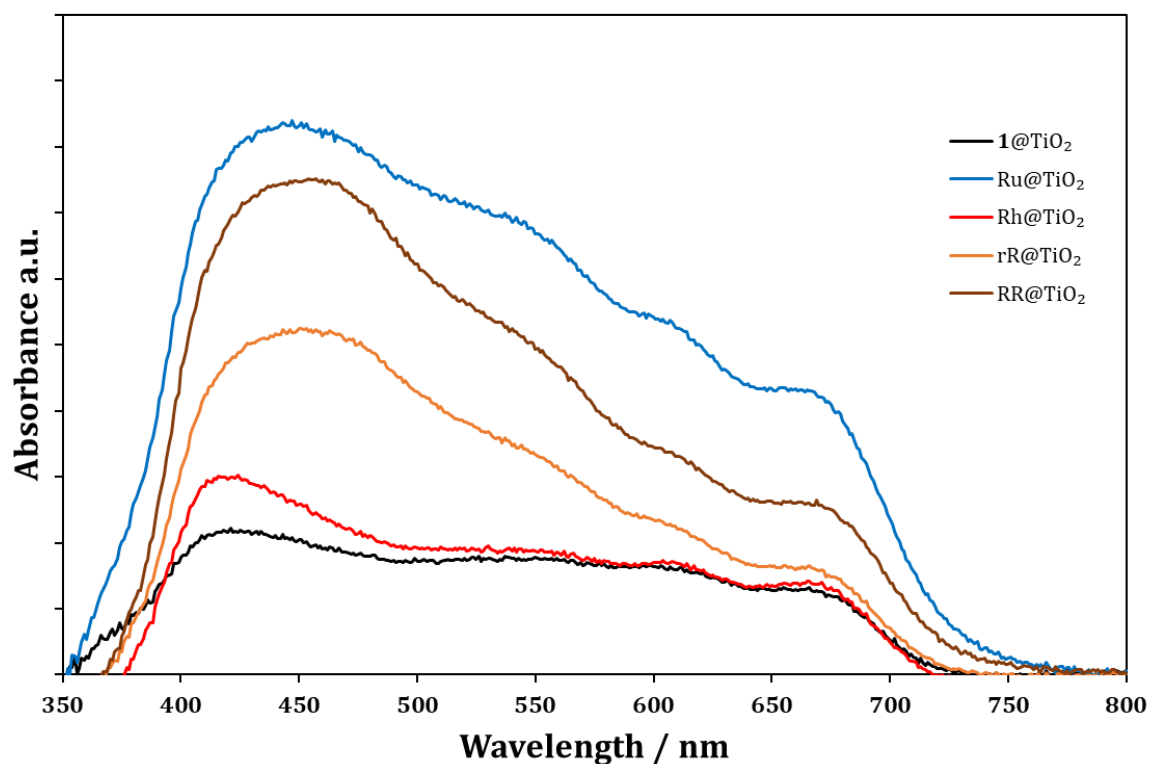


Figure S49. Solid-state absorption spectra of 1@TiO₂ (black), Ru@TiO₂ (blue), Rh@TiO₂ (red), rR@TiO₂ (orange) and RR@TiO₂ (brown) using a-NP as reference.

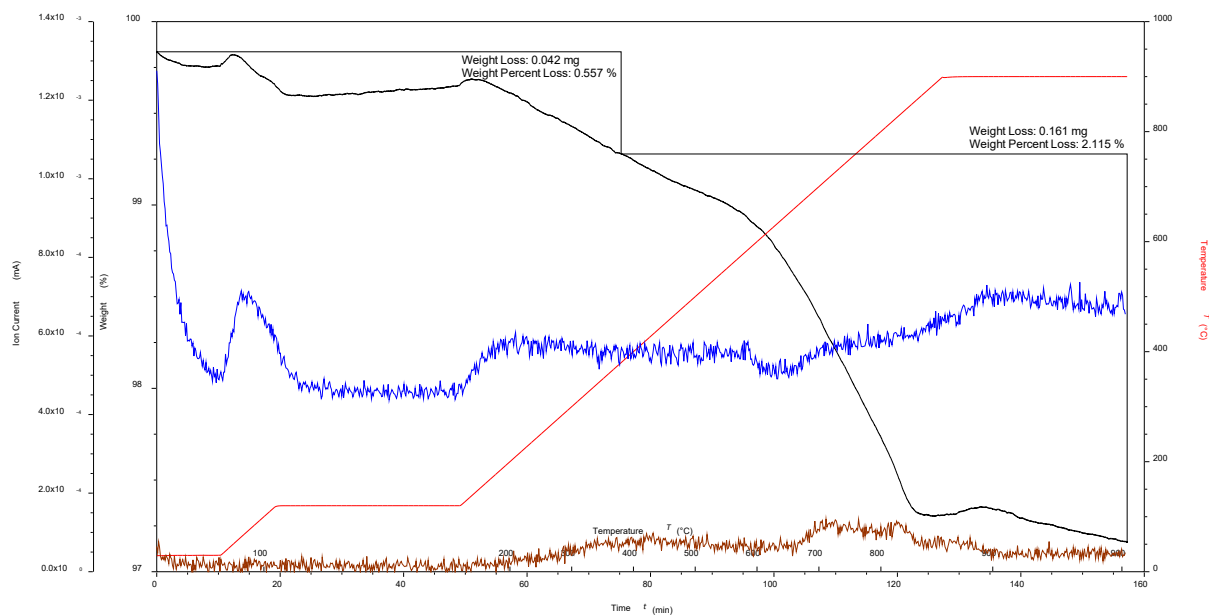


Figure S50. TGA curves for Ru@ZrO₂: Weight against time and temperature (blue), derivative of weight change against time (red).

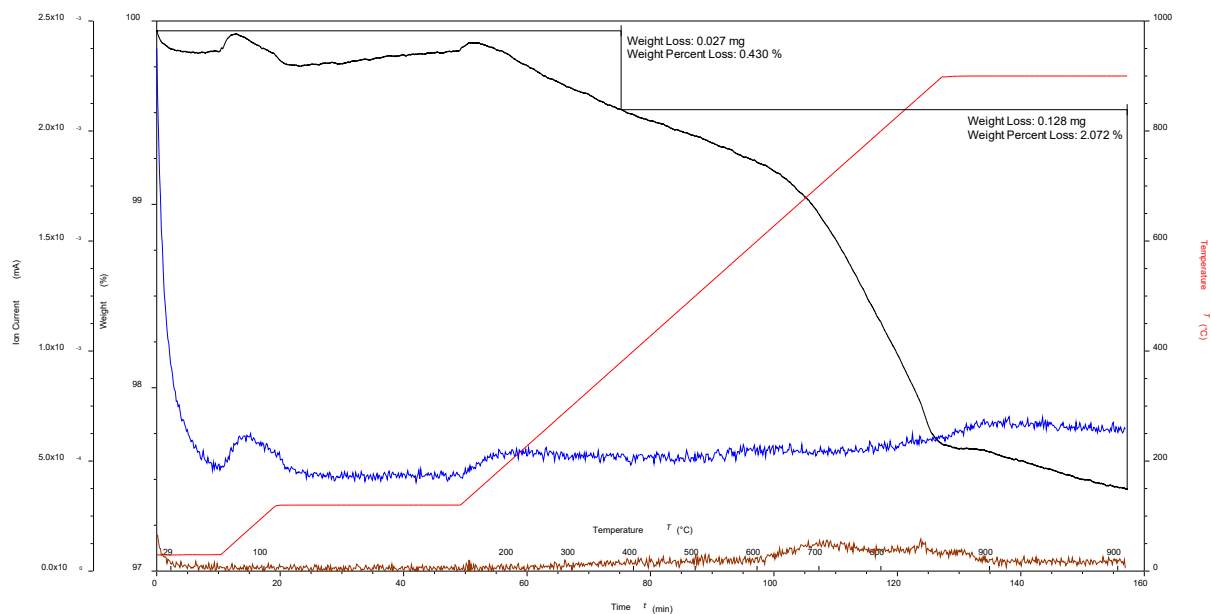


Figure S51. TGA curves for rR@ZrO₂: Weight against time and temperature (blue), derivative of weight change against time (red).

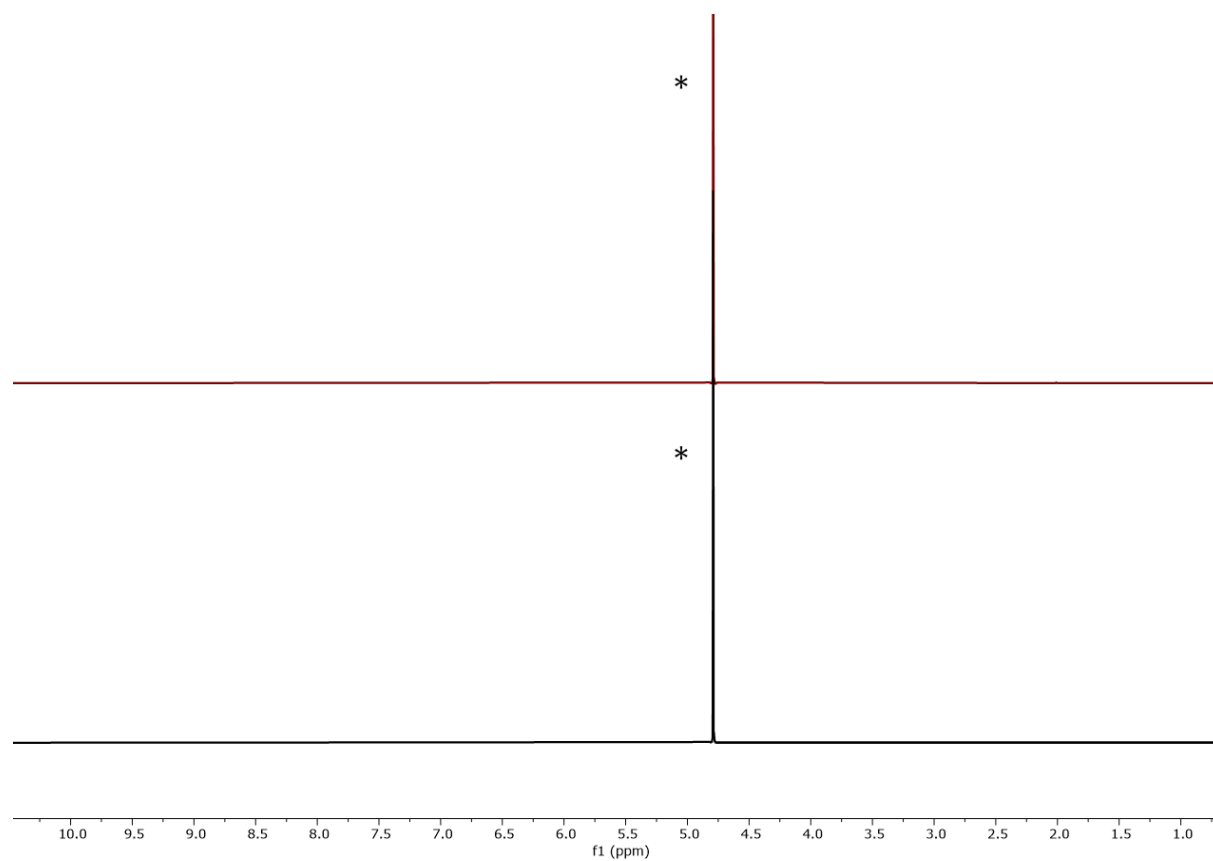


Figure S52. ¹H NMR (500 MHz, D₂O, 298 K) spectrum of rR@ZrO₂ (black) and RR@ZrO₂ (red), * = HOD. Chemical shifts in ppm.

References

1. Zhang, D.; Telo, J.P.; Liao, C.; Hightower, S.E.; Clennan, E.L. Experimental and Computational Studies of Nuclear Substituted 1,1'-Dimethyl-2,2'-Bipyridinium Tetrafluoroborates. *J. Phys. Chem. A* **2007**, *111*, 13567-13574, doi:10.1021/jp074323u.
2. Maerker, G.; Case, F.H. The Synthesis of Some 4,4'-Disubstituted 2,2'-Bipyridines. *J. Am. Chem. Soc.* **1958**, *80*, 2745-2748, doi:10.1021/ja01544a042.
3. Han, W.-S.; Han, J.-K.; Kim, H.-Y.; Choi, M.J.; Kang, Y.-S.; Pac, C.; Kang, S.O. Electronic Optimization of Heteroleptic Ru(II) Bipyridine Complexes by Remote Substituents: Synthesis, Characterization, and Application to Dye-Sensitized Solar Cells. *Inorg. Chem.* **2011**, *50*, 3271-3280, doi:10.1021/ic101909e.
4. Norris, M.R.; Concepcion, J.J.; Glasson, C.R.K.; Fang, Z.; Lapidus, A.M.; Ashford, D.L.; Templeton, J.L.; Meyer, T.J. Synthesis of Phosphonic Acid Derivatized Bipyridine Ligands and Their Ruthenium Complexes. *Inorg. Chem.* **2013**, *52*, 12492-12501, doi:10.1021/ic4014976.
5. Montalti, M.; Wadhwa, S.; Kim, W.Y.; Kipp, R.A.; Schmehl, R.H. Luminescent Ruthenium(II) Bipyridyl-Phosphonic Acid Complexes: pH Dependent Photophysical Behavior and Quenching with Divalent Metal Ions. *Inorg. Chem.* **2000**, *39*, 76-84, doi:10.1021/ic991143t.
6. Freimann, S.A.; Prescimone, A.; Housecroft, C.E.; Constable, E.C. Turning over on sticky balls: preparation and catalytic studies of surface-functionalized TiO₂ nanoparticles. *RSC Adv.* **2021**, *11*, 5537-5547, doi:10.1039/D0RA09319J.

CHAPTER VI: WHERE THE SUN DOES SHINE

WATER REDUCTION USING SURFACE-FUNCTIONALIZED BaTiO₃ AND SrTiO₃ NANOPARTICLES

6.1 Motivation

The results reported in **Chapter V** were a major contributor to the motivation of this next project. They showed that the TiO₂ NP platform could be used successfully and even competitively for catalysis. While there were many more catalytic examples for potential exploration, there was also interest in applying the same functionalization methods to other NPs and investigate their use in catalysis. Hence, this **Chapter** and the following **Chapter VII** describe studies to find how easy it was to apply the previously established functionalization methods to other semiconducting NPs. Further interest lay in finding the differences when water reduction reactions were performed with semiconductors having different band gaps to TiO₂. SrTiO₃ and BaTiO₃ were suitable candidates to continue the study as they share many traits with TiO₂. SrTiO₃ and BaTiO₃ NPs are composed of cheap, earth abundant elements,¹⁶⁸⁻¹⁷⁰ are thermodynamically stable, temperature resistant and water insoluble. SrTiO₃ and BaTiO₃ exhibit relatively similar pH dependent zeta potentials and have only ~0.2 eV larger band gaps than TiO₂.¹⁷¹⁻¹⁷⁶ The literature also showed the possibility of functionalizing these compounds with various anchoring groups including phosphonic acids, carboxylic acids or even hydroxy groups.^{177,178}

This Chapter reports the surface activation of commercial SrTiO₃ and BaTiO₃ NPs both with either HNO₃ or H₂O₂ giving SrTiO₃-a, BaTiO₃-a or SrTiO₃-OH, BaTiO₃-OH respectively. It further compares the functionalization of SrTiO₃, BaTiO₃, SrTiO₃-a, BaTiO₃-a, SrTiO₃-OH or BaTiO₃-OH NPs using [2,2'-bipyridine]-4,4'-diylbis(phosphonic acid) (**9**). The f-NPs were used for direct surface metal complex assembly with bpy, RuCl₃ and RhCl₃ in H₂O:EtOH at 160 °C in an autoclave. The Chapter also describes an experiment to highlight the importance of pH control for successful metal complex assembly on the NP surface and uses the NPs for water reduction as described previously in **Chapter V**.

The NPs were characterized using Fourier-transform infrared (FTIR) and solid-state absorption spectroscopies, thermogravimetric analysis mass spectrometry (TGA-MS), while dihydrogen generation was analysed using gas chromatography mass spectrometry (GC-MS).

6.2 Results

6.2.1 Nanoparticle surface activation

Surface activation for NPs can be a crucial step for successful and stable surface functionalization. **Chapter II** reported the benefits of acid activation of TiO₂ NPs which was then applied throughout this thesis prior to NP functionalization with an anchoring ligand. However, in the literature many other methods are described including the use of other acids or hydrogen peroxide for activation.¹⁷⁹⁻¹⁸¹ These methods are used to enhance the surface reactivity and make them more susceptible to functionalization. TiO₂ and SrTiO₃ NPs are very acid resistant while BaTiO₃ NPs are rather sensitive to mineral acids. Hence, as reported in the experimental **Section 6.3.1**, during acid activation with aqueous HNO₃ (3 M) BaTiO₃ NPs partially dissolved or were lost during washing (70%). It is interesting to note that the NPs mainly seemed to dissolve during washing with H₂O after removing them from the aqueous HNO₃ (3 M). Hence, acid activation seemed less suitable for BaTiO₃ NPs and other activation methods were explored. As such, H₂O₂ activation of BaTiO₃ as described in the literature¹⁸¹ seemed a good alternative. The method should saturate the surface with hydroxyl groups and simultaneously strip the surface of adsorbed carbonates. Although the literature protocol¹⁸¹ required hydroxyl

groups for a silanization reaction, the hydroxyl groups should also be favourable for condensation with the phosphonic acid from the anchoring ligand.

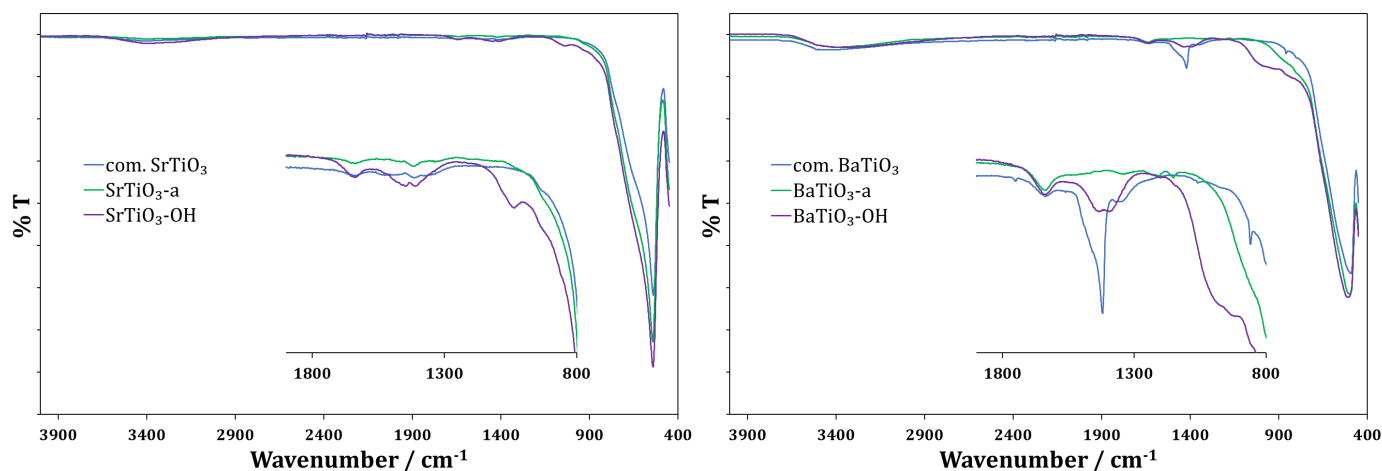


Figure 17: FTIR spectra of commercial SrTiO₃ NPs (left, blue), SrTiO₃-a NPs (left, green), SrTiO₃-OH NPs (left, violet); commercial BaTiO₃ (right, blue), BaTiO₃-a NPs (right, green), BaTiO₃-OH NPs (right, violet).

The activation was performed with both SrTiO₃ and BaTiO₃ by boiling the dispersed NPs under N₂ in 30% H₂O₂. The particles were washed with water and then dried for an extended period of time (72 h) under high vacuum to remove any excess water or H₂O₂. The commercial and activated NPs were characterized using FTIR and TGA-MS. FTIR differences shown in Figure 17 were limited to the fingerprint region. For SrTiO₃ the H₂O₂ activation caused an additional peak at 1446 cm⁻¹ while for BaTiO₃ a prominent peak at 1420 cm⁻¹ either disappeared or shifted and broadened when activated with acid or with H₂O₂ respectively.

Table 1: TGA-MS results of non-activated and activated SrTiO₃ and BaTiO₃ NPs.

Entry	NP	30 – 380 °C / %	Mass found / amu	380 – 900 °C / %	Mass found / amu
1	Commercial SrTiO ₃	0.5	18, 44 ^a	0.4	18, 44
2	SrTiO ₃ -a	0.6	18	1.0	18, 44 ^b , 81 ^b
3	SrTiO ₃ -OH	1.8	18, 44	0.6	18, 44
4	Commercial BaTiO ₃	1.0	18, 44	0.6	18, 44
5	BaTiO ₃ -a	1.4	18	0.5	18, 44 ^b
6	BaTiO ₃ -OH	3.6	18, 44	0.8	18, 44

^aAmu 44 was recorded as traces slightly above baseline, ^bamu 44 was only recorded within a very limited temperature range of 500 – 600 °C, (-a) represents HNO₃ activated NPs and (-OH) represents H₂O₂ activated NPs.

TGA-MS results are reported in Table 1. A comparison of commercial SrTiO₃ or commercial BaTiO₃ NPs with acid activated NPs (SrTiO₃ and BaTiO₃) shows that there is a slight weight loss increase (0.1 – 0.4%) in the lower temperature region (<380 °C). The activation using H₂O₂ showed a greater weight loss compared to the commercial NPs, with an increase of 1.2% or 2.2% for SrTiO₃ and BaTiO₃ respectively in the lower temperature region (<380 °C). Using the mass spectrometer coupled to the TGA, a peak with amu 18 (H₂O) was found in each sample and assigned to physisorbed and chemisorbed water. For H₂O₂ activated NPs this

further increase could possibly be due to the loss of hydroxyl groups decomposing to water and oxygen. Furthermore, commercial NPs and H₂O₂ activated NPs showed organic decomposition products (amu 44, CO₂) throughout the TGA experiment possibly due to impurities from the manufacturer; this was especially visible for BaTiO₃.

In the higher temperature region (380 – 900 °C), H₂O₂ activated SrTiO₃ and BaTiO₃ NPs also showed slightly higher weight losses (0.2%) compared to the commercial NPs. The acid-activated SrTiO₃ and BaTiO₃ NPs showed slightly higher (0.6%) and lower (0.1%) weight losses respectively. In both cases, the TGA-MS experiment recorded a sharp weight loss at ~550 °C attributed to amu 44 (CO₂) and, in the case of SrTiO₃-a, a mass loss at amu 81 was also observed. The TGA-MS experiment of SrTiO₃-a is illustrated in Figure 18 as an example of the sharp weight loss. The origin of this weight loss is unclear. Although the mass of 81 would fit to TiO₂H, it is rather difficult to justify how this fragment only occurs with acid-activated NPs.

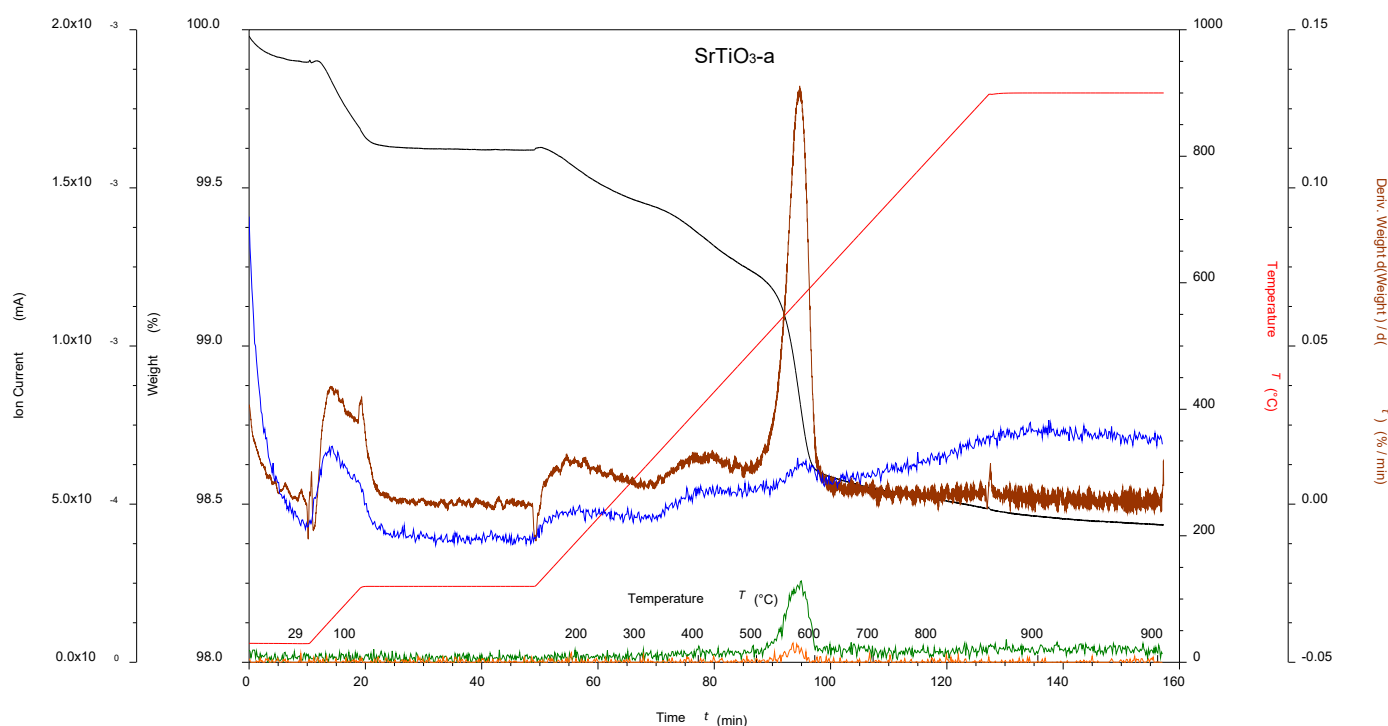
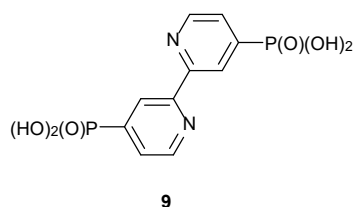


Figure 18: TGA-MS of acid activated SrTiO₃ NPs; SrTiO₃-a where black is the weight loss, red is the temperature, brown is the derivative weight against time, blue is the ion current of amu 18, green is the ion current of amu 44 and orange is the ion current of amu 81.

6.2.2 Nanoparticle surface ligand functionalization



Scheme 10: Anchoring ligand **9**.

For BaTiO₃ and SrTiO₃ NPs, the method described in **Chapter V** using anchoring ligand **9** (Scheme 10) was modified. The bpy metal-binding domain in ligand **9** would be useful for the later surface assembly of {M(bpy)₃}ⁿ⁺ (M = Ru, n = 2; M = Rh, n = 3) analogues. Phosphonic acids have been shown to bind strongly

to BaTiO₃ NP surfaces and it was assumed they would behave similarly with SrTiO₃.¹⁷⁷ The commercial BaTiO₃ and SrTiO₃ NPs had diameters of 50 and 100 nm, respectively, making them larger than the TiO₂ NPs used in **Chapters II-V**. This difference in size changes the surface area to volume ratio significantly from 0.28 nm⁻¹ for TiO₂, to 0.12 nm⁻¹ and 0.06 nm⁻¹ for BaTiO₃ and SrTiO₃, respectively. This reduces the available surface area and requires some adjustments to the functionalization method to avoid physisorbed free ligand. In this case 4.6 eq. or 7.3 eq. of commercial or activated SrTiO₃ or BaTiO₃ NPs^{17,181} were dispersed with anchoring ligand **9** in milliQ water (18 mL) and then heated to 130 °C for 3 h in a microwave reactor. It was found that washing of the NPs after reaction sufficed to remove unreacted ligand **9**. Based on the recorded ¹H NMR spectra of the dried NPs after functionalization and washing with EtOH or H₂O, it was confirmed that this procedure was enough to remove non-bound ligand **9** completely. The experimental **Section 6.3.3** describes the functionalization method in full detail. The NPs were characterized using ¹H NMR spectroscopy, FTIR, TGA-MS and solid-state absorption spectroscopy. TGA-MS results are shown in Table 2 and showed higher weight losses than the corresponding unfunctionalized NPs in the high temperature region (380 – 900 °C) indicating successful surface functionalization. The additional weight loss was significant (0.2 – 0.7%) but smaller than observed in **Chapter V** with functionalized TiO₂ (2.6%).

Table 2: TGA-MS results of **9**@SrTiO₃ and **9**@BaTiO₃ NPs using non-activated and activated NPs.

Entry	NP	30 – 380 °C / %	Mass found / amu	380 – 900 °C / %	Mass found / amu
1	9 @SrTiO ₃	0.8	18	1.0	18, 44
2	9 @SrTiO ₃ -a	0.6	18	1.2	18, 44, 81
3	9 @SrTiO ₃ -OH	1.6	18	1.3	18, 44
4	9 @BaTiO ₃	1.4	18	1.0	18, 44
5	9 @BaTiO ₃ -a	1.5	18	1.2	18, 44, 81
6	9 @BaTiO ₃ -OH	3.3	18	1.5	18, 44

(**9**@) represents anchoring ligand **9** bound to the surface of the NPs while (-a) represents using HNO₃ activated NPs during the functionalization and (-OH) using H₂O₂ activated NPs during the functionalization.

A lower absolute additional weight loss was to be expected since SrTiO₃ and BaTiO₃ have considerably larger particle sizes than the TiO₂ NPs. The NPs all showed carbon-containing impurities before the functionalization as described in **Section 6.3.1**. These impurities, based on TGA-MS experiments in the low temperature region, were lost during the functionalization and it is possible that the functionalization method augmented the low recorded weight loss. Figure 19 shows the TGA-MS measurement of **9**@SrTiO₃-a and it is clear where ligand **9** decomposes as the decomposition processes do not overlap. The TGA-MS measurement of **9**@SrTiO₃ still showed the peak recorded for SrTiO₃-a at ~550 °C with now an additional weight loss between 700 °C and 880 °C. The mass spectrometric trace in this region showed amu 18 (H₂O) and 44 (CO₂) further fitting to a decomposition of the anchoring ligand **9**.

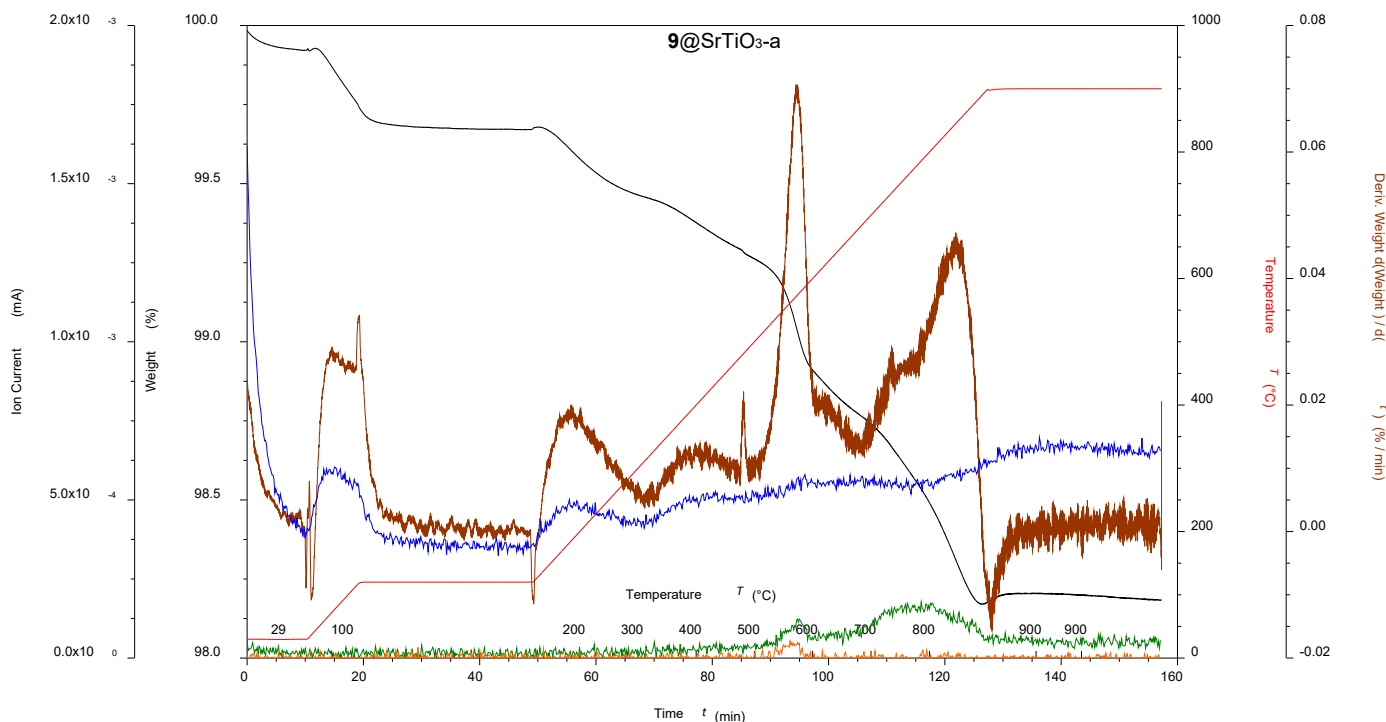


Figure 19: TGA-MS of acid activated with ligand **9** functionalized SrTiO₃ NPs; **9**@SrTiO₃-a where black is the weight loss, red is the temperature, brown is the derivative weight against time, blue is the ion current of amu 18, green is the ion current of amu 44 and orange is the ion current of amu 81.

FTIR spectra of the f-NPs (Figure 20) showed a broad, weak absorption around 3300 cm⁻¹ in accordance with the TGA-MS results confirming the presence of hydroxy groups. The measured NPs showed a strong absorption at 540 cm⁻¹ and 500 cm⁻¹ for SrTiO₃ and BaTiO₃, respectively. Compared to the unfunctionalized NPs, **9**@SrTiO₃ and **9**@BaTiO₃ (independent of prior activation) showed a number of absorptions in the range 1900 cm⁻¹ to 900 cm⁻¹ indicating either a bound ligand or traces of free ligand left on the surface. ¹H NMR spectroscopy however showed no indication of adsorbed labile species being present on the NP surface after the functionalization.

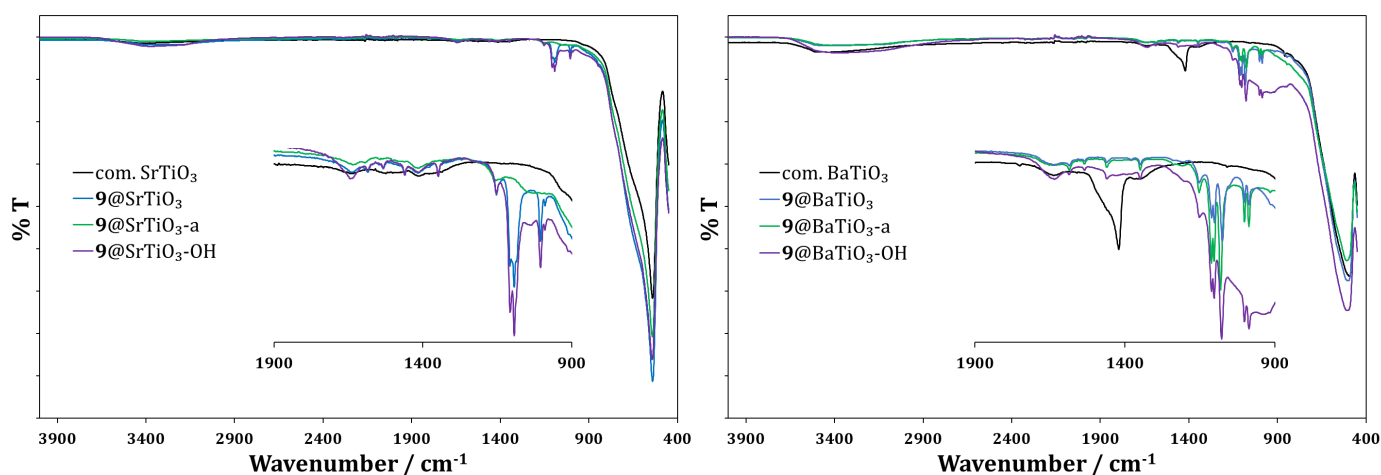


Figure 20: FTIR spectra of commercial SrTiO₃ (left, black), **9**@SrTiO₃ NPs (left, blue), **9**@SrTiO₃-a NPs (left, green), **9**@SrTiO₃-OH NPs (left, violet); commercial BaTiO₃ (right, black), **9**@BaTiO₃ NPs (right, blue), **9**@BaTiO₃-a NPs (right, green), **9**@BaTiO₃-OH NPs (right, violet).

Solid-state absorption spectra used the commercial NPs (SrTiO₃ or BaTiO₃) as 100% baseline and the results are shown in Figure 21. With the exception of **9**@SrTiO₃, the f-NPs showed a broad weak absorption

between 400 and 700 nm. These results were similar to the recorded solid-state absorption spectra of ligand **9** functionalized TiO₂ NPs in **Chapter V**. **9@SrTiO₃** was the only exception, possibly due to a very low amount of ligand on the surface.

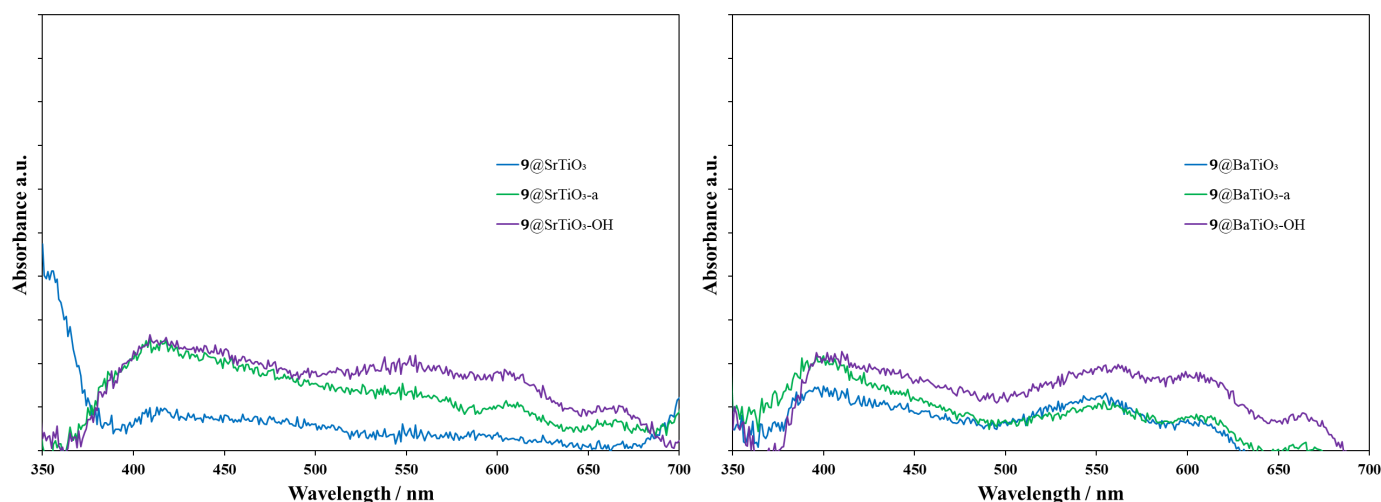


Figure 21: Solid-state absorption spectra of **9@SrTiO₃** NPs (left, blue), **9@SrTiO₃-a** NPs (left, green), **9@SrTiO₃-OH** NPs (left, violet); **9@BaTiO₃** NPs (right, blue), **9@BaTiO₃-a** NPs (right, green), **9@BaTiO₃-OH** NPs (right, violet).

6.2.3 Nanoparticle surface complexation

Metal complexes were assembled directly on the NP surface using procedures described in **Chapter V**. These procedures were initially a modified version of a literature one pot procedure for the formation of heteroleptic ruthenium(II) complexes.¹⁰ The method was adjusted by replacing the free ligand by **9@SrTiO₃** or **9@BaTiO₃**. For all complexations, f-NPs were dispersed in a 1:1 mixture of H₂O:EtOH together with RuCl₃·3H₂O, RhCl₃·3H₂O and bpy in an autoclave at 160 °C for 1 h. The abbreviations, for example **rR@SrTiO₃**, describe metal complex-functionalized NPs with a small amount of ruthenium vs. rhodium (1:20) on the surface. The method was also performed for testing purposes with only RuCl₃·3H₂O yielding **Ru@SrTiO₃** and **Ru@BaTiO₃**. The full experimental details are described in **Section 6.3.4** and **Section 6.3.5**, respectively. Depending on the activation of the NPs and pH during the complexation, differently coloured NPs with different catalytic activities were isolated. The ruthenium and rhodium metal complex bearing NPs were tested for their capability to catalyse dihydrogen production during an artificial sun irradiated water reduction experiment. The isolated f-NPs are shown in Figure 22 and were characterized using ¹H NMR spectroscopy, FTIR, TGA-MS and solid-state absorption spectroscopy.



Figure 22: Isolated f-NPs; from left to right **rR@SrTiO₃**, **rR@SrTiO₃-a**, **rR@SrTiO₃-OH**, **rR@SrTiO₃-OH-A**, **Ru@SrTiO₃**, **Ru@BaTiO₃**, **rR@BaTiO₃-a**, **rR@BaTiO₃-OH**, **rR@BaTiO₃-OH-A**.

TGA-MS revealed an increased weight loss of the complex bearing NPs when comparing them to the f-NPs discussed in the previous section. The results are shown in Table 3. The weight loss increase for the isolated metal complexed f-NPs compared to only ligand f-NPs in the high temperature region (380 – 900 °C)

was rather low (0.2 – 0.5%). This provided evidence for the lower degree of functionalization compared to TiO₂ reported in **Chapter V**.

Table 3: TGA-MS results of **rR@SrTiO₃** and **rR@BaTiO₃** NPs using non-activated and activated NPs.

Entry	NP	30 – 380 °C / %	Mass found / amu	380 – 900 °C / %	Mass found / amu
1	rR@SrTiO₃	0.9	18, 44	1.5	18, 44
2	rR@SrTiO₃-a	0.7	18, 44	1.4	18, 44
3	rR@SrTiO₃-OH	1.5	18, 44	1.6	18, 44
4	rR@SrTiO₃-OH-A	1.2	18	5.3	18, 44, 48, 64
5	rR@BaTiO₃	0.9	18, 44	1.2	18, 44
6	rR@BaTiO₃-a	1.6	18, 44	1.5	18, 44
7	rR@BaTiO₃-OH	3.2	18, 44	1.6	18, 44
8	rR@BaTiO₃-OH-A	2.9	18	7.6	18, 44, 48, 64

(**rR@**) represents anchoring ligand **9** f-NPs bound to the surface of the NPs and complexed with RuCl₃ and RhCl₃ at a ratio of roughly 1:20; (-a) represents using HNO₃ activated NPs during the functionalization; (-OH) means H₂O₂ activated NPs during the functionalization; (-OH-A) refers to additionally adjusting the pH to 1.5 during the complexation.

A successful complexation was expected to result in additional decomposition in the TGA-MS. Hence, the TGA-MS data of SrTiO₃-a (Figure 18) and **9@SrTiO₃-a** (Figure 19) to **rR@SrTiO₃-a** (Figure 23) were used to identify new decomposition processes. As decomposition processes often overlap in the TGA, they can be very difficult to differentiate. Figure 23 of **rR@SrTiO₃-a** is an instructive example for this as it showed increased weight loss. However, identifying an additional decomposition based on only the TGA curves was not possible as the curve associated with the weight loss was broad. Using the TGA coupled to a mass spectrometer and following the ion current of CO₂, amu 44 (Figure 23, green) the separate decompositions can be differentiated. The decomposition was at a slightly lower temperature (~650 °C) than the recorded decomposition for **9@SrTiO₃-a** (~800 °C) and higher than the impurity recorded with SrTiO₃-a (~550 °C).

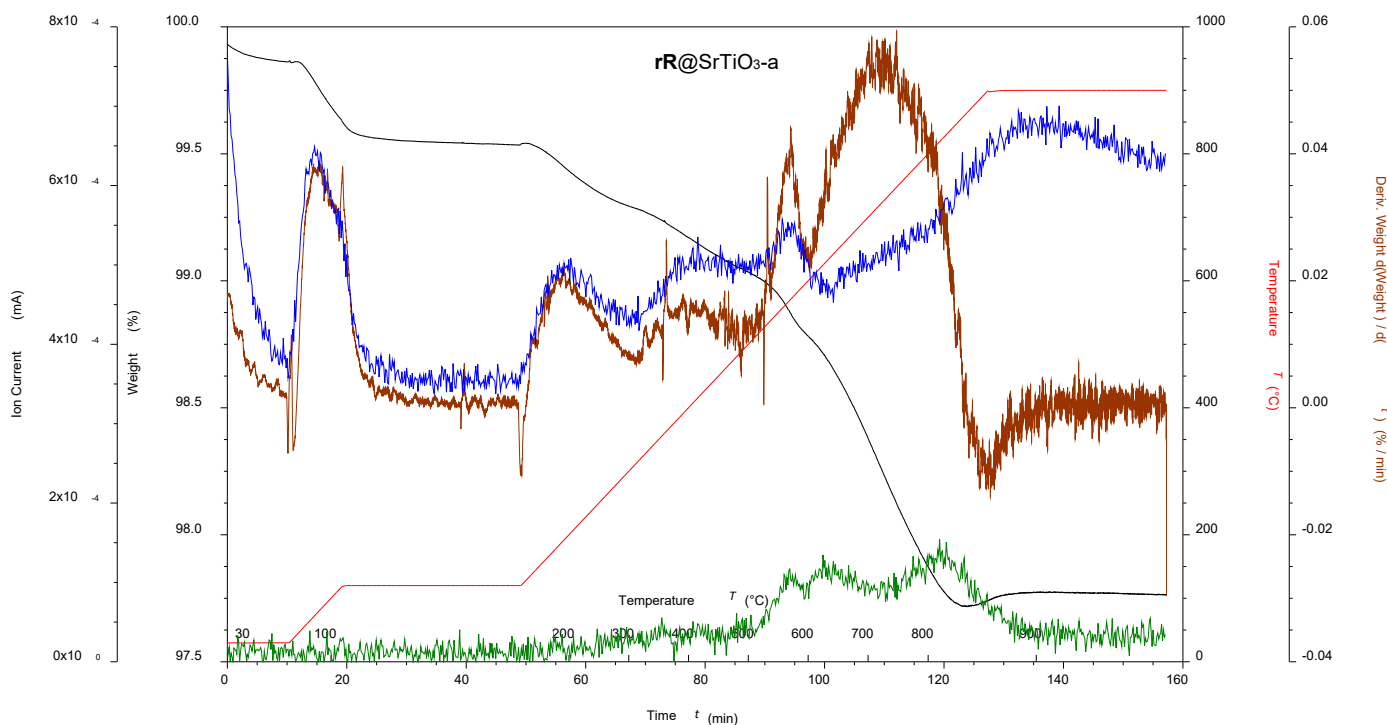


Figure 23: TGA-MS of acid activated with ligand **9** functionalized and ruthenium, rhodium and bpy complexed SrTiO₃ NPs; **rR@SrTiO₃-a** where black is the weight loss, red is the temperature, brown is the derivative weight against time, blue is the ion current of amu 18 and green is the ion current of amu 44.

In a further experiment with **9@SrTiO₃-OH** or **9@BaTiO₃-OH**, the complexation in the autoclave was pH adjusted (from 6.9 to 1.5) with aqueous H₂SO₄ (3M). The resulting NPs showed a large weight loss increase in the high temperature region of 4.0% (Figure 24, bottom) and 6.1% (Figure 24, top) and were labelled **rR@SrTiO₃-OH-A** and **rR@BaTiO₃-OH-A** respectively. However, the mass spectrometric data showed peaks at amu 48 (SO) and 64 (SO₂) at 750 °C suggesting surface binding of H₂SO₄.¹⁸² However, Figure 24 shows that the decomposition of H₂SO₄ is not the main cause of the weight loss, because the main peak at amu 44 (CO₂) suggests an organic decomposition. The main weight loss occurs at ~700 °C corresponding to the decomposition observed for **rR@SrTiO₃-a**. The earlier decomposition at ~550 °C and ~800 °C was not observed for **rR@SrTiO₃-OH-A**. For **rR@BaTiO₃-OH-A** an additional decomposition at ~900 °C was observed. ¹H NMR spectroscopy was used to verify the absence of non-bound anchoring ligand in all cases.

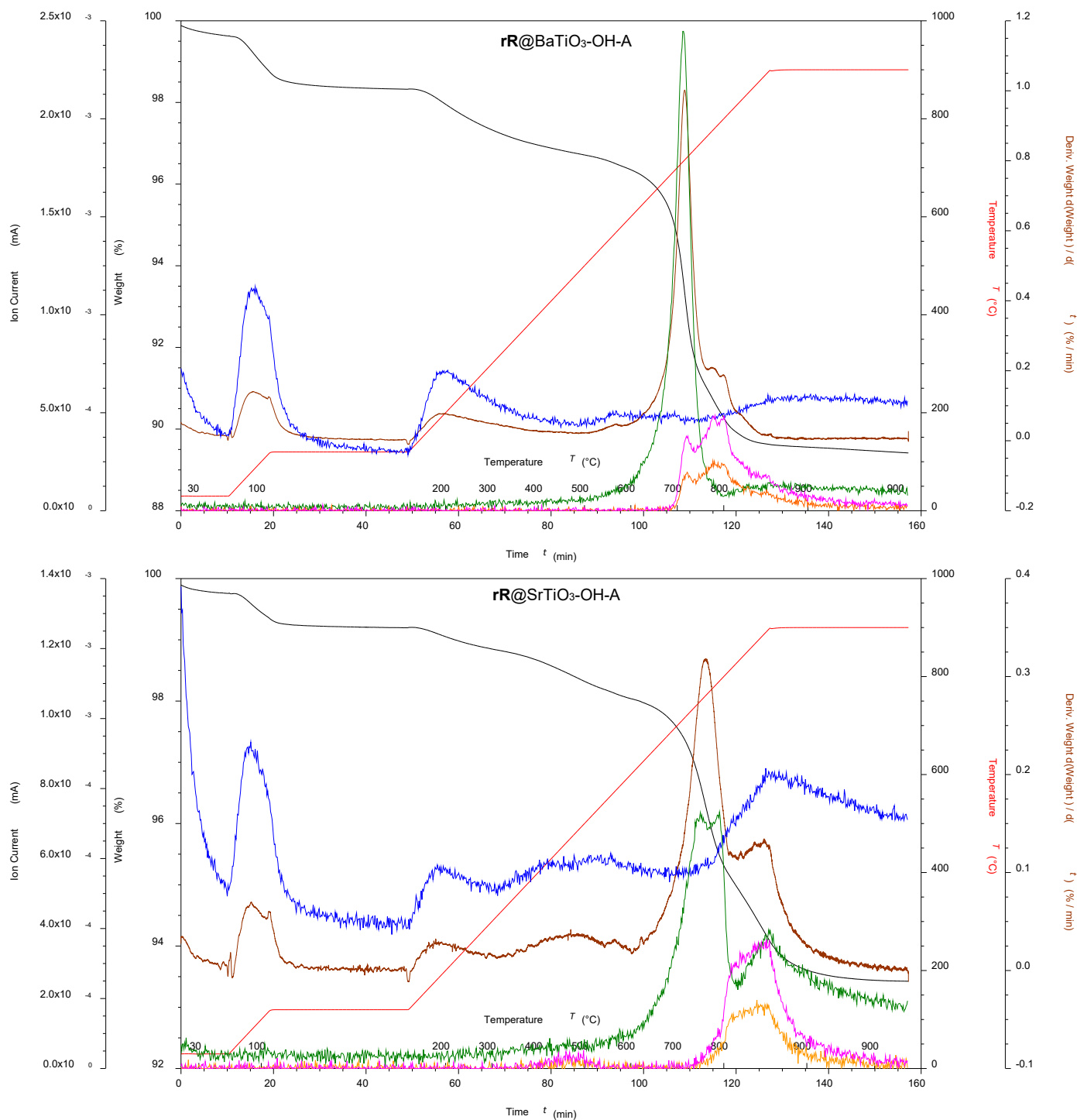


Figure 24: TGA-MS of H_2O_2 activated with ligand **9** functionalized and ruthenium, rhodium and bpy under adjusted pH complexed SrTiO_3 NPs (top) and BaTiO_3 NPs (bottom); $\mathbf{rR@SrTiO}_3\text{-OH-A}$ and $\mathbf{rR@SrTiO}_3\text{-OH-A}$ where black is the weight loss, red is the temperature, brown is the derivative weight against time, blue is the ion current of amu 18, green is the ion current of amu 44, yellow is the ion current of amu 48 and pink is the ion current of amu 64.

Solid-state absorption spectra of complexed NPs used commercial NPs (SrTiO_3 or BaTiO_3) for correction of the baseline as 100% during the measurement and are shown in Figure 25. In the case of SrTiO_3 the spectrum of the metal complex f-NPs (Figure 25, left) shows a broad absorption between 410 nm and 480 nm with weaker absorptions between 500 and 700 nm. These solid-state absorption spectra (while less intense) generally agreed with the absorption spectra reported in **Chapter V** for TiO_2 NPs. However, $\mathbf{rR@SrTiO}_3\text{-OH}$ NPs (Figure 25, left, violet) behaved differently, as they showed more intense absorptions in the regions 540 – 570,

600 – 620 and 660 – 680 nm. This was reasonable as these NPs were grey to black and a panchromatic absorption was to be expected. Metal complex f-NPs in the case of BaTiO₃ NPs (Figure 25, right) showed a similar panchromatic adsorption resembling the grey **rR@SrTiO₃-OH** NPs. The only exception was **rR@BaTiO₃-OH-A** (Figure 25, right, red) that had a strong absorption between 400 and 470 nm with 600 – 620 and 660 – 680 nm being weaker absorptions, which was in accordance with its pale orange colour.

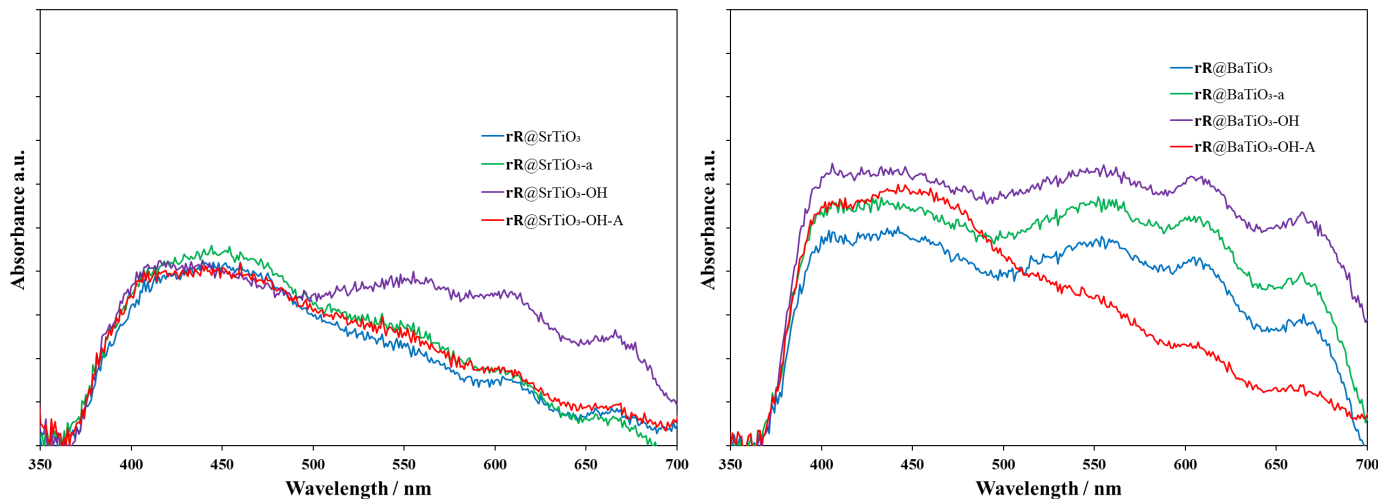


Figure 25: Solid-state absorption spectra of **rR@SrTiO₃** NPs (left, blue), **rR@SrTiO₃-a** NPs (left, green), **rR@SrTiO₃-OH** NPs (left, violet), **rR@SrTiO₃-OH-A** NPs (left, red); **rR@BaTiO₃** NPs (right, blue), **rR@BaTiO₃-a** NPs (right, green), **rR@BaTiO₃-OH** NPs (right, violet), **rR@BaTiO₃-OH-A** NPs (right, red).

Figure 26 shows the FTIR spectra of **rR@SrTiO₃** (left, blue) and **rR@BaTiO₃** (right, blue) and their variants (-a, green; -OH, violet; -OH-A, red). Overall, the IR spectra of all metal complex f-NPs of SrTiO₃ and BaTiO₃ were similar with the exception of **rR@SrTiO₃-OH-A** and **rR@BaTiO₃-OH-A**. In addition, the spectra were very similar to that of the anchoring ligand f-NPs described in the previous **Section 6.3.2** with only small differences in the fingerprint region (1900 to 900 cm⁻¹). In contrast, FTIR spectra of **rR@SrTiO₃-OH-A** and **rR@BaTiO₃-OH-A** showed strong absorptions at 1219, 1141, 1100 and 1200, 1091 cm⁻¹ respectively possibly caused by the presence of H₂SO₄ on the NP surface. This was confirmed by recording a FTIR spectrum of a mixture of commercial SrTiO₃ NPs and aqueous H₂SO₄ (see **Section 6.3.5** or Figure 27).

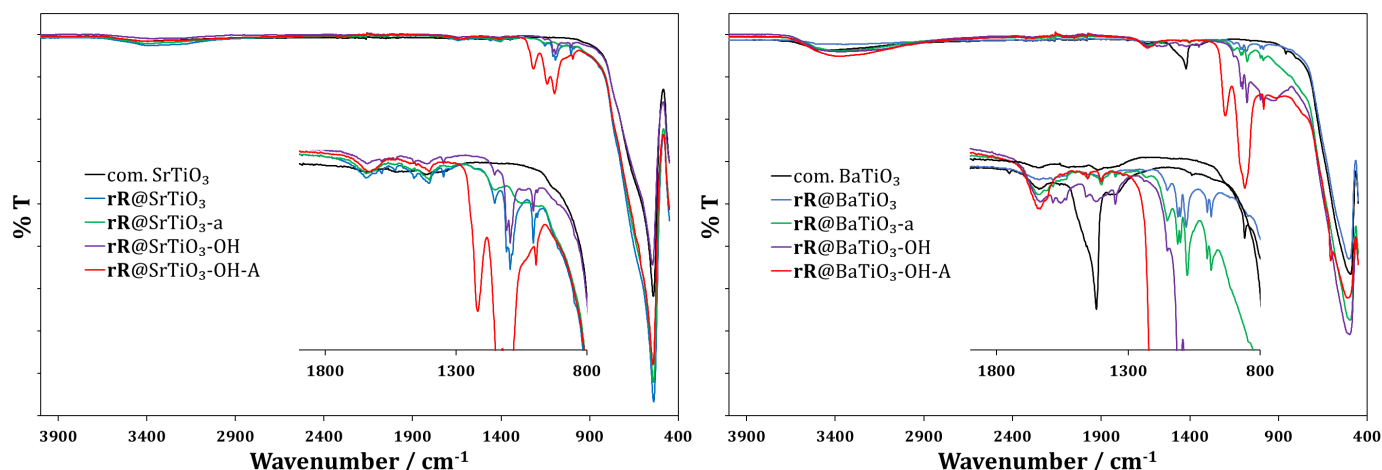


Figure 26: FTIR spectra of **rR@SrTiO₃** NPs (left, blue), **rR@SrTiO₃-a** NPs (left, green), **rR@SrTiO₃-OH** NPs (left, violet), **rR@SrTiO₃-OH-A** NPs (left, red); **rR@BaTiO₃** NPs (right, blue), **rR@BaTiO₃-a** NPs (right, green), **rR@BaTiO₃-OH** NPs (right, violet), **rR@BaTiO₃-OH-A** NPs (right, red).

6.2.4 Dihydrogen generation

Experimental details for these studies are given in **Section 6.3.6**. The study revealed that **rR@SrTiO₃**, **rR@SrTiO₃-a**, **rR@SrTiO₃-OH-A**, **rR@BaTiO₃-a** and **rR@BaTiO₃-OH-A** all produce H₂ under irradiation while **rR@SrTiO₃-OH** and **rR@BaTiO₃-OH** were rather inactive (see Table 4). **rR@SrTiO₃-a** yielded the best results with 1.1 mL dihydrogen per hour, with **rR@SrTiO₃** roughly ²/₃ as efficient with 0.77 mL dihydrogen per hour. **rR@BaTiO₃-a** was tested for photocatalysis and yielded dihydrogen at an even lower rate than **rR@SrTiO₃** with 0.46 mL dihydrogen per hour. **rR@SrTiO₃-OH-A** NPs were less active than **rR@SrTiO₃** with 0.49 mL dihydrogen per hour, while **rR@BaTiO₃-OH-A** performed better (with 0.56 mL dihydrogen) than **rR@BaTiO₃-a**.

The f-NPs that produced dihydrogen showed the characteristic red colour of a [Ru(bpy)₃]²⁺ chromophore while f-NPs that were either grey or black either did not produce dihydrogen or did so with less efficiency. BaTiO₃ NPs and SrTiO₃ NPs activated with H₂O₂, functionalized with ligand **9** and then complexed with RuCl₃·3H₂O and RhCl₃·3H₂O were less active for water reduction. This indicated minimal or no formation of the required photocatalyst(s) on the surface.

Table 4: Dihydrogen generating experiments.

Entry	NP	GCI ^a / a. u.	H ₂ / mL	Rate / mL h ⁻¹
1	rR@SrTiO₃	150100	3.10	0.77
2	rR@SrTiO₃-a	216900	4.47	1.12
3	rR@SrTiO₃-OH	31800	0.66	0.16
4	rR@SrTiO₃-OH-A	94900	1.96	0.49
5	rR@BaTiO₃-a	90000	1.86	0.46
6	rR@BaTiO₃-OH	0	0	0
7	rR@BaTiO₃-OH-A	108600	2.24	0.56

^a GC integral (GCI) was adjusted for pre-existing nitrogen headspace in the reaction vial and partial sampling during the GC measurement.

6.3 Experimental

6.3.1 Nanoparticle surface activation using HNO₃ (SrTiO₃-a, BaTiO₃-a)

Commercially available SrTiO₃ or BaTiO₃ NPs were activated as previously reported.¹⁷ NPs (2.00 g) were dispersed by sonication for 15 min in dilute aqueous HNO₃ (30 mL, 3.0 M). The mixture was then stirred for 30 min. The suspension was centrifuged (10 min, 7,000 rpm) and the NPs were washed once with milliQ water (40 mL). The NPs were added to milliQ water (40 mL) and dispersed by sonication for 10 min. The suspension was then stirred for 72 h. The suspension was centrifuged (10 min, 7,000 rpm) and the NPs were washed with milliQ water (2 × 40 mL). The activated NPs (SrTiO₃-a, 1.67 g and BaTiO₃-a, 0.60 g) were stored in a sealed vial under N₂ after drying the NPs under high vacuum. SrTiO₃-a: TGA: weight loss / %, 0.6 (<380 °C), 1.0 (380 – 900 °C). TGA-MS: amu, 18 (<380 °C), 18, 44, 81 (380 – 900 °C). FTIR spectroscopy: 3384, 1635, 1414, and 534 cm⁻¹.

BaTiO₃-a: TGA: weight loss / %, 1.5 (<380 °C), 0.5 (380 – 900 °C). TGA-MS: amu, 18 (<380 °C), 18, 44 (380 – 900 °C). FTIR spectroscopy: 3367, 1638, 1337, 1207, 1151 and 497 cm⁻¹.

6.3.2 Nanoparticle surface activation using H₂O₂ (SrTiO₃-OH, BaTiO₃-OH)

Commercially available SrTiO₃ or BaTiO₃ NPs were activated as reported in the literature.¹⁸¹ NPs (1.05 g) were dispersed by sonication for 20 min in H₂O₂ (50 mL, 30%). The mixture was then stirred for 4 h at 110 °C under N₂. The suspension was cooled down, centrifuged (10 min, 7,000 rpm) and the NPs were washed with milliQ water (40 mL). The activated NPs (1.05 g and 1.05 g) were stored in a sealed vial under N₂ after drying the NPs under high vacuum for 72 h. SrTiO₃-OH: TGA: weight loss / %, 1.6 (<380 °C), 1.3 (380 – 900 °C). TGA-MS: amu, 18, 44 (<380 °C), 18, 44 (380 – 900 °C). FTIR spectroscopy: 3396, 1638, 1446, 1404, 1037 and 543 cm⁻¹.

BaTiO₃-OH: TGA: weight loss / %, 3.6 (<380 °C), 0.8 (380 – 900 °C). TGA-MS: amu, 18, 44 (<380 °C), 18, 44 (380 – 900 °C). FTIR spectroscopy: 3348, 1635, 1435, 1392, 974, 924 and 506 cm⁻¹.

6.3.3 Nanoparticle surface ligand functionalization (9@SrTiO₃-a, 9@SrTiO₃-OH, 9@BaTiO₃-a, 9@BaTiO₃-OH)

The functionalization was performed as previously reported. Anchoring ligand **9** (10.0 mg, 31.6 μmol, 1.0 eq.) and milliQ water (18 mL) were added to a microwave vial and dispersed by sonication for 1 min. Acid or H₂O₂ activated NPs (449.0 mg, 4.6 SrTiO₃ eq. or 7.3 BaTiO₃) were added. The suspension was dispersed by sonication for 10 min. The microwave vial was sealed and the reaction mixture heated for 3 h at 130 °C in the microwave reactor. The suspension was centrifuged (20 min, 7,000 rpm) after cooling to room temperature. The NPs were separated from the solvent and washed with EtOH (2 × 15 mL). This procedure gave white f-NPs with following yields: 9@SrTiO₃-a NPs (418.3 mg), 9@SrTiO₃-OH NPs (422.6 mg), 9@BaTiO₃-a NPs (409.9 mg), 9@BaTiO₃-OH NPs (425.1 mg) were stored in a sealed vial under N₂ after drying the NPs under high vacuum. This reaction was repeated using commercial SrTiO₃ and BaTiO₃ NPs (224 mg, 4.6 SrTiO₃ eq. or 7.3 BaTiO₃ eq.) and **9** (5.0 mg, 15.8 μmol) yielding 9@SrTiO₃ NPs (218.1 mg, 221.6 mg) and 9@BaTiO₃ NPs (210.7 mg, 219.4 mg). For NMR spectroscopic measurements, NPs (5 – 10 mg) were dispersed in 500 μL D₂O in an NMR tube.

9@SrTiO₃: TGA: weight loss / %, 0.8 (<380 °C), 1.0 (380 – 900 °C). TGA-MS: amu, 18 (<380 °C), 18, 44 (380 – 900 °C). FTIR spectroscopy: 3376, 3171, 1637, 1583, 1535, 1459, 1411, 1349, 1154, 1108, 1094, 1006 and 540 cm⁻¹. Solid-state absorption spectroscopy: no absorption bands within 350–700 nm.

9@SrTiO₃-a: TGA: weight loss / %, 0.6 (<380 °C), 1.2 (380 – 900 °C). TGA-MS: amu, 18 (<380 °C), 18, 44, 81 (380 – 900 °C). FTIR spectroscopy: 3368, 1623, 1589, 1407, 1161, 1028 and 541 cm⁻¹. Solid-state absorption spectroscopy: 390 – 450 (broad) and 590 – 630 nm (broad).

9@SrTiO₃-OH: TGA: weight loss / %, 1.6 (<380 °C), 1.3 (380 – 900 °C). TGA-MS: amu, 18 (<380 °C), 18, 44 (380 – 900 °C). FTIR spectroscopy: 3366, 1635, 1585, 1530, 1463, 1411, 1350, 1151, 1106, 1093, 1033, 1006 and 541 cm⁻¹. Solid-state absorption spectroscopy: 390 – 450 (broad), 530 – 570 (broad), 590 – 620 (broad) and 660 – 680 nm (broad).

9@BaTiO₃: TGA: weight loss / %, 1.4 (<380 °C), 1.0 (380 – 900 °C). TGA-MS: amu, 18 (<380 °C), 18, 44 (380 – 900 °C). FTIR spectroscopy: 3488, 3102, 1647, 1589, 1538, 1459, 1347, 1151, 1103, 1085, 1080, 988, 1000, 988 and 500 cm⁻¹. Solid-state absorption spectroscopy: 380 – 440 (broad), 530 – 570 (broad) and 600 – 620 nm (broad).

9@BaTiO₃-a: TGA: weight loss / %, 1.5 (<380 °C), 1.2 (380 – 900 °C). TGA-MS: amu, 18 (<380 °C), 18, 44, 81 (380 – 900 °C). FTIR spectroscopy: 3359, 1639, 1583, 1531, 1462, 1374, 1351, 1149, 1103, 1101, 1074, 989, 984 and 508 cm⁻¹. Solid-state absorption spectroscopy: 380 – 420 (broad), 540 – 580 (broad) and 600 – 620 nm (broad).

9@BaTiO₃-OH: TGA: weight loss / %, 3.3 (<380 °C), 1.2 (380 – 900 °C). TGA-MS: amu, 18 (<380 °C), 18, 44 (380 – 900 °C). FTIR spectroscopy: 3361, 1636, 1585, 1538, 1459, 1348, 1149, 1101, 1103, 1078, 983, 985, 931 and 500 cm⁻¹. Solid-state absorption spectroscopy: 390 – 430 (broad), 540 – 580 (broad), 590 – 620 (broad) and 660 – 670 nm (broad).

6.3.4 Nanoparticle surface complexation (**Ru@SrTiO₃**, **Ru@BaTiO₃**)

The metal complex was formed directly on the NP surface. **9@SrTiO₃** (70.9 mg), RuCl₃·3H₂O (1.03 mg, 3.94 μmol), and 2,2'-bipyridine (1.25 mg, 8.00 μmol) were added to a vial. H₂O (5.0 mL) and EtOH (3.0 mL) were added and the mixture was thoroughly dispersed using sonication and stirring. The suspension was transferred into an autoclave PTFE liner with additional EtOH (2.0 mL). The autoclave was sealed and then heated in an oven with 320 °C/h to 160 °C. The autoclave was left at 160 °C for 1 h. After cooling, the autoclave was opened and the suspension centrifuged (20 min, 7000 rpm). The resulting NPs were washed with H₂O (3 × 10 mL) and EtOH (1 × 10 mL). **Ru@SrTiO₃** (65.8 mg) was obtained as pale orange powder after drying the NPs under high vacuum. TGA: weight loss / %, 1.0 (<380 °C), 1.8 (380 – 900 °C). TGA-MS: amu, 18, 44 (<380 °C), 18, 44 (380 – 900 °C). FTIR spectroscopy: 3386, 3203, 2651, 1639, 1534, 1462, 1400, 1348, 1152, 1107, 1093, 1005 and 541 cm⁻¹. Solid-state absorption spectroscopy: 430 – 470, 540 – 560 (broad), 600 – 620 (broad) and 660 – 670 nm.

This experiment was repeated with **9@BaTiO₃** (70.9 mg), RuCl₃·3H₂O (1.03 mg, 3.95 μmol), and 2,2'-bipyridine (1.25 mg, 8.00 μmol) yielding **Ru@BaTiO₃** (67.0 mg) as dark brown powder. TGA: weight loss / %, 1.5 (<380 °C), 1.6 (380 – 900 °C). TGA-MS: amu, 18, 44 (<380 °C), 18, 44 (380 – 900 °C). FTIR spectroscopy: 3369, 1636, 1400, 1152, 1113, 1081, 981, 985 and 494 cm⁻¹. Solid-state absorption spectroscopy: 400 – 480, 540 – 560, 600 – 620 and 660 – 670 nm.

6.3.5 Nanoparticle surface complexation (**rR@SrTiO₃-a**, **rR@SrTiO₃-OH**, **rR@SrTiO₃-OH-A**, **rR@BaTiO₃-a**, **rR@BaTiO₃-OH**, **rR@BaTiO₃-OH-A**)

The metal complex was formed directly on the NP surface. This reaction was done with each isolated NP from Section 6.3.3. **9@SrTiO₃**, **9@SrTiO₃-a** NPs, **9@SrTiO₃-OH**, **9@BaTiO₃**, **9@BaTiO₃-a** or **9@BaTiO₃-OH** (365.6 mg) were added into a vial with RuCl₃·3H₂O (0.24 mg, 0.9 μmol), RhCl₃·3H₂O (5.15 mg, 19.6 μmol) and 2,2'-bipyridine (6.45 mg, 41.3 μmol). H₂O (5.0 mL) and EtOH (3.0 mL) were added and the mixture was thoroughly dispersed using sonication and stirring. The suspension was transferred to an autoclave with a PTFE liner with additional EtOH (2.0 mL). The autoclave was sealed and then heated in an oven with 320 °C/h to 160 °C. The autoclave was left at 160 °C for 1 h. After cooling, the autoclave was opened and the suspension centrifuged (20 min, 7000 rpm). The resulting NPs were washed with H₂O (3 × 10 mL) and EtOH (1 × 10 mL). After drying the NPs under high vacuum, the reaction yielded **rR@SrTiO₃** (354.2 mg) as pale orange powder, **rR@SrTiO₃-a** (358.2 mg) as pale orange powder, **rR@SrTiO₃-OH** (358.4 mg) as grey powder, **rR@BaTiO₃** (349.9 mg) as grey powder, **rR@BaTiO₃-a** (356.9 mg) as dark brown powder or **rR@BaTiO₃-OH** (357.4 mg) as dark grey powder.

rR@SrTiO₃: TGA: weight loss / %, 0.9 (<380 °C), 1.5 (380 – 900 °C). TGA-MS: amu, 18, 44 (<380 °C), 18, 44 (380 – 900 °C). FTIR spectroscopy: 3380, 3177, 1636, 1625, 1608, 1531, 1463, 1402, 1347, 1154, 1083, 1058 and 987 cm⁻¹. Solid-state absorption spectroscopy: 410 – 480, 540 – 570 (broad), 600 – 620 (broad) and 660 – 670 nm (broad).

rR@SrTiO₃-a: TGA: weight loss / %, 0.7 (<380 °C), 1.4 (380 – 900 °C). TGA-MS: amu, 18, 44 (<380 °C), 18, 44 (380 – 900 °C). FTIR spectroscopy: 3404, 3236, 1634, 1404, 1158, 1008, 1003 and 538 cm⁻¹. Solid-state absorption spectroscopy: 410 – 480, 540 – 570 (broad), 600 – 620 (broad) and 660 – 670 nm (broad).

rR@SrTiO₃-OH: TGA: weight loss / %, 1.5 (<380 °C), 1.6 (380 – 900 °C). TGA-MS: amu, 18, 44 (<380 °C), 18, 44 (380 – 900 °C). FTIR spectroscopy: 3382, 1636, 1583, 1534, 1457, 1402, 1350, 1152, 1108, 1092, 1005 and 543 cm⁻¹. Solid-state absorption spectroscopy: 410 – 480, 540 – 570, 600 – 620 and 660 – 680 nm.

rR@BaTiO₃: TGA: weight loss / %, 0.9 (<380 °C), 1.2 (380 – 900 °C). TGA-MS: amu, 18, 44 (<380 °C), 18, 44 (380 – 900 °C). FTIR spectroscopy: 3325, 1632, 1457, 1402, 1345, 1152, 1110, 1082, 983 and 493 cm⁻¹. Solid-state absorption spectroscopy: 400 – 480, 540 – 570, 600 – 620 and 660 – 670 nm.

rR@BaTiO₃-a: TGA: weight loss / %, 1.6 (<380 °C), 1.5 (380 – 900 °C). TGA-MS: amu, 18, 44 (<380 °C), 18, 44 (380 – 900 °C). FTIR spectroscopy: 3346, 1634, 1450, 1401, 1345, 1148, 1103, 1075, 984, and 493 cm⁻¹. Solid-state absorption spectroscopy: 400 – 480, 540 – 570, 600 – 620 and 660 – 670 nm.

rR@BaTiO₃-OH: TGA: weight loss / %, 3.2 (<380 °C), 1.6 (380 – 900 °C). TGA-MS: amu, 18, 44 (<380 °C), 18, 44 (380 – 900 °C). FTIR spectroscopy: 3346, 1635, 1584, 1556, 1420, 1349, 1103, 1078, 986 and 493 cm⁻¹. Solid-state absorption spectroscopy: 400 – 480, 540 – 570, 600 – 620 and 660 – 670 nm.

This reaction was repeated with **9@SrTiO₃-OH** and **9@BaTiO₃-OH** with a pH adjusted to 1.5 using 4.0 mL H₂O, 1.0 mL aqueous H₂SO₄ (1M) and the same amount of EtOH (5 mL). Other reaction conditions were kept the same. **rR@SrTiO₃-OH-A** (356.0 mg) and **rR@BaTiO₃-OH-A** (355.1 mg) were both isolated as pale orange powder. As reference for FTIR spectroscopy, a sample was prepared by mixing commercial SrTiO₃ NPs (500 mg) with aqueous H₂SO₄ (200 μL, 3M) using a mortar. The spectrum is given in Figure 27. FTIR spectroscopy: 3243, 1637, 1199, 1141, 1091, 1051 and 534 cm⁻¹.

rR@SrTiO₃-OH-A: TGA: weight loss / %, 1.1 (<380 °C), 5.3 (380 – 900 °C). TGA-MS: amu, 18 (<380 °C), 18, 44, 48, 64 (380 – 900 °C). FTIR spectroscopy: 3405, 1640, 1403, 1219, 1141, 1100, 996 and 541 cm⁻¹. Solid-state absorption spectroscopy: 410 – 480, 540 – 570 (broad), 600 – 620 (broad) and 660 – 670 nm (broad).

rR@BaTiO₃-OH-A: TGA: weight loss / %, 2.9 (<380 °C), 7.6 (380 – 900 °C). TGA-MS: amu, 18 (<380 °C), 18, 44, 48, 64 (380 – 900 °C). FTIR spectroscopy: 3377, 1632, 1454, 1403, 1200, 1091, 984, 606 and 503 cm⁻¹. Solid-state absorption spectroscopy: 400 – 470, 600 – 620 (broad) and 660 – 680 nm (broad).

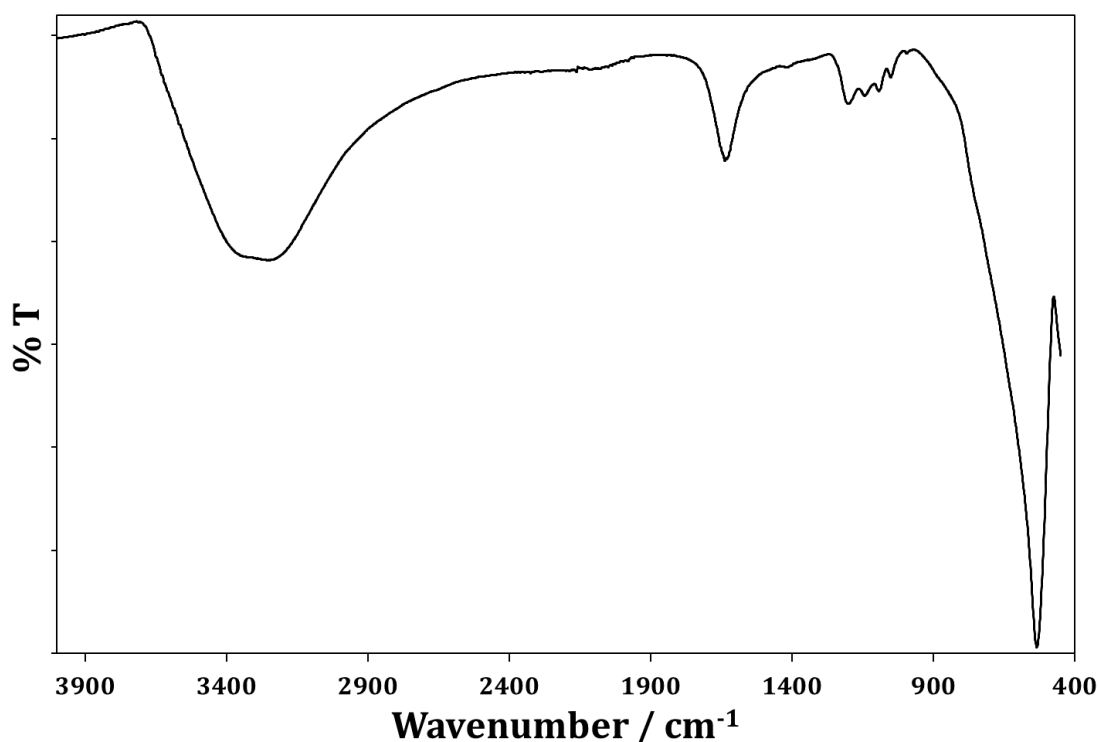


Figure 27: FTIR spectra of commercial SrTiO₃ NPs (500 mg) mixed with 200 μL aqueous H₂SO₄ (3M).

6.3.6 Dihydrogen generation

The water reduction reaction conditions are given in **Chapter V**²⁵ and are again reported here for convenience. In a 5 mL microwave vial TEOA (2.52 mmol, 376 mg), K₂[PtCl₄] (1.7 μmol, 0.70 mg) and 2,2'-bipyridine (18.6 μmol, 2.91 mg) were added together with milliQ water and aqueous H₂SO₄ (1M) to modify the pH. Experiments were performed at pH 7.5 and used 1 mL aqueous H₂SO₄ (1M) and 5 mL milliQ water. Metal complex-functionalized NPs were added (114.1 mg). The vial was flushed with nitrogen and then sealed. The suspension was sonicated (10 min) and thoroughly shaken. Nitrogen was bubbled through the suspension for 10 minutes. The vial was irradiated for 4 h at a slight angle (5°) with a sun simulator (see Materials and Methods section) generating 1200 W m⁻². The suspension was stirred throughout the irradiation and periodically shaken. Headspace samples for gas chromatography were collected using a syringe and transferred into a 10 mL GC vial for analysis. The measured GC integral was converted to mL of H₂ with a calibration made by injecting several known volumes of dihydrogen.

6.4 Conclusion

This Chapter explored activation methods for SrTiO₃ and BaTiO₃ NPs with a literature protocol¹⁸¹ using H₂O₂ and with the method established in **Chapter II** using aqueous HNO₃. Commercial and activated SrTiO₃ and BaTiO₃ NPs were functionalized using anchoring ligand **9**. Using methods published in **Chapter V** the f-NPs were complexed using 2,2'-bipyridine and either RuCl₃·3H₂O or RuCl₃·3H₂O and RhCl₃·3H₂O. When using H₂O₂ for activation the resulting SrTiO₃ and BaTiO₃ NPs were isolated as dark grey powders. Commercial NPs and acid activated SrTiO₃ yielded pale orange NPs while the counter part with BaTiO₃ gave grey or dark brown NPs. The potentially photo- and redox- active Rh and Ru surface-bound metal complex f-NPs were used in a photochemical system for the solar generation of dihydrogen using sunlight. BaTiO₃ NPs and SrTiO₃ NPs activated with H₂O₂ and functionalized with ligand **9** and then complexed with RuCl₃·3H₂O and RhCl₃·3H₂O yielded f-NPs inactive for water reduction. This indicated no successful formation of the desired photocatalytic metal complex on the surface. **rR@SrTiO₃-a** was the most efficient giving 1.1 mL dihydrogen per hour with **rR@SrTiO₃** being roughly ²/₃ as efficient. The complexation method of H₂O₂ activated and functionalized NPs was modified by adjusting the pH to 1.5 with aqueous H₂SO₄. The resulting SrTiO₃ and BaTiO₃ metal complex pale orange f-NPs were active for water reduction and produced dihydrogen. **rR@SrTiO₃-OH-A** were considerably less active than **rR@SrTiO₃** or **rR@SrTiO₃-a**, while **rR@BaTiO₃-OH-A** performed better than **rR@BaTiO₃-a**. Hence, it seems that pH is more important during complexation than previously thought and that adjusting it can play a major role. It is unclear if the drop in efficiency for **rR@SrTiO₃-OH-A** was due to remaining H₂SO₄ influencing the pH of the suspension during the water reduction or if the complexation itself was impacted. For **rR@BaTiO₃-OH-A**, solid-state absorption spectroscopic data and the general red colour of the functionalized NPs further suggest that the complexation went more towards the characteristic [Ru(bpy)₃]²⁺ chromophore with one bpy being replaced by ligand **9**.

It can be concluded that SrTiO₃ or BaTiO₃ NPs may perform better than TiO₂ NPs. However, the former are more expensive than TiO₂ which is a disadvantage, and additional experiments are required to confirm if the added cost is justified. At present, parameters such as particle size have not been explored. Furthermore, particle size might play a major role for surface loading and the commercial BaTiO₃ and SrTiO₃ NPs had 2 to 4 times greater radii than the TiO₂ NPs, respectively. The Chapter further included characterization of activated, f-NPs and metal complex f-NPs using with FTIR spectroscopy, solid-state absorption spectroscopy and TGA-MS, providing evidence for successful functionalization. Certainly, TEM-EDX, ICP-MS or MALDI spectroscopy could yield further substantiated results for this project, but the time limitations of the investigations precluded these additional measurements.

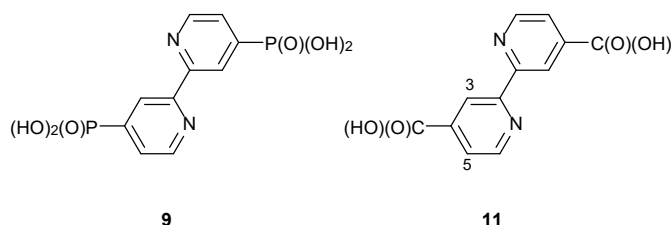
CHAPTER VII: A PEEK AT TRANSITION METAL OXIDES

FUNCTIONALIZATION OF TUNGSTEN, TIN, ZIRCONIUM AND ZINC OXIDE NANOPARTICLES

7.1 Motivation

Semiconducting TiO_2 is a versatile metal oxide for the production of NPs; however, metal oxides in general have uses in many fields as they can be cheap and composed of the most abundant d-block metals in the Earth's crust.^{168,170,183} Properties such as a superconductivity, high dielectric constant, good optical or electrical characteristics are desirable in a material, especially when combined with high chemical and thermal stability.¹⁸³⁻¹⁸⁵ Thus, metal oxides find use in applications including optoelectronics,¹⁸⁶ gas sensors,¹⁸⁷ solid fuel cells,¹⁸⁸ electron and hole transporting layers in light-emitting diodes, solar cells and perovskites^{183,189} or as described in **Chapters III-VI** in catalysis. In many of these applications, surface functionalization is used to optimize their characteristics. The diversity of the methods described in **Chapter II** inspired to extend this work to the surface-binding of the ligands and complexes to other NPs of interest and WO_3 , SnO_2 , ZrO_2 and ZnO were selected to study as typical metal oxides.

The project commenced by establishing the behaviour of each metal oxide under the activation and functionalization methods described in **Chapter II** and, metal oxide NPs were functionalized with anchoring ligands **9** and **11** shown in Scheme 11. To test the anchoring ligand specificity, competition experiments between **9** and **11** were performed using ^1H NMR spectroscopy to quantify binding. The length of the functionalization time was studied with each metal oxide type, a parameter not explored in earlier Chapters.



Scheme 11: Anchoring ligands used for functionalization and competition experiments.

The NPs were characterized using mainly thermogravimetric analysis mass spectrometry (TGA-MS) and ^1H NMR spectroscopy. Ligand **9** functionalized ZnO NPs were used with bpy-d_8 and $\text{RuCl}_3 \cdot 3\text{H}_2\text{O}$ to form a metal complex on the surface for further analysis with TGA-MS. Preliminary complexation experiments with WO_3 , SnO_2 were performed, and colour changes were observed but the hybrid NPs were not further characterized.

7.2 Results and discussion

7.2.1 Anchoring ligand functionalization

The methods described in **Chapters II** and **V** were used to functionalize WO_3 , ZrO_2 , SnO_2 , TiO_2 and ZnO NPs (experimental details given in **Section 7.3.1**) using anchoring ligands **9** or **11** (see Scheme 1 or Scheme 11). Given that the particle sizes of WO_3 , ZrO_2 , SnO_2 , and ZnO NPs were 100 nm in radii compared to TiO_2 NPs radii of 25 nm, the amounts of ligand used had to be adjusted. After functionalization, the NPs were carefully washed and tested for traces of free ligand using ^1H NMR spectroscopy. When using anchoring ligand **11** a further washing with DMSO was required to remove traces of free ligand from WO_3 and SnO_2 NPs after functionalization. Successful complexation was verified using mainly TGA-MS. TGA-MS results

are shown in Table 5 and generally exhibited higher weight losses in the high temperature region (380 – 900 °C) compared to commercial NPs indicating successful surface functionalization. This was supported by the mass spectrometer recording amu 44 (CO₂) assigned to ligand decomposition. Increased reaction times (from 3 h to 12 h) had little or effect on the weight loss.

Table 5: TGA-MS results of functionalized WO₃, SnO₂, ZrO₂, TiO₂ and ZnO NPs.

Entry	NP	30 – 380 °C / %	Mass found / amu	380 – 900 °C / %	Mass found / amu
1	Commercial WO ₃	0.0	18	0.2	18, 44 ^a
2	9 @WO ₃	0.3	18	0.3	18, 44
3	9 @WO ₃ -L	0.3	18	0.4	18, 44
4	11 @WO ₃	0.3	18, 44	0.2	18, 44
5	Commercial SnO ₂	0.6	18, 44	0.2 ^b / 0.4 ^c	18, 44 / 18, 44
6	9 @SnO ₂	0.6	18, 44 ^a	1.6 ^d / 2.0 ^e	18, 44 / 44 ^a
7	9 @SnO ₂ -L	0.3	18, 44 ^a	1.6 ^d / 2.3 ^e	18, 44 / 44 ^a
8	11 @SnO ₂	0.5	18, 44	1.4 ^d / 1.9 ^e	18, 44 / 18, 44
9	Commercial ZrO ₂	0.9	18, 44 ^a	0.7	18, 44 ^a
10	9 @ZrO ₂ ^f	0.7	18, 44 ^a	1.6	18, 44
11	9 @ZrO ₂ -L	0.8	18, 44 ^a	1.4	18, 44
12	11 @ZrO ₂	0.5	18, 44 ^a	1.7	18, 44
13	9 @TiO ₂ ^f	1.1	18	2.7	18, 44
14	11 @TiO ₂	1.4	18, 44	2.5	18, 44
15	Commercial ZnO ^g	0.7	18, 44 ^a	0.5	18, 44
16	9 @ZnO	1.6	18	26.5	18, 44
17	9 @ZnO-L	0.8	18	30.1	18, 44
18	9 @ZnO-air	1.7	-	3.75	-

^a Traces only found, ^b temperature range 380 – 600 °C, ^c temperature range 600 – 900 °C ^d temperature range 380 – 800 °C, ^e temperature range 800 – 900 °C, ^f prepared according to **Chapter V**, ^g NPs were heat treated at 550 °C, (**9**@ or **11**@) represents anchoring ligand **9** or **11** functionalized NPs while (-L) describes longer functionalization time of 12 h and (-air) was used for NPs analysed with TGA under air.

It was only possible to functionalize WO₃ NPs (Table 5, entries 1 – 4) to a small extent with an increase over the commercial NPs of only 0.1% in the high temperature region with ligand **9** and even less with **11**. The TGA-MS (shown in Figure 28, top) showed two clear new decomposition peaks between 300 – 750 °C with **11**@WO₃ NPs. It has to be noted that at such low weight losses, trace amounts of free ligand could still

have an effect even with testing using ^1H NMR spectroscopy. However, the decomposition recorded for **11**@ WO_3 NPs (shown in Figure 28, bottom) was different from the free ligand **11** which showed the main decomposition occurring sharply between only 300 – 400 °C. A parallel, standard mass spectrometer measurement of the sample showed several decomposition products between 700 – 800 °C including amu 44, 51, 78, 156. It is unclear why these masses were recorded offset (as shown in Figure 28) to the main weight loss of the sample.

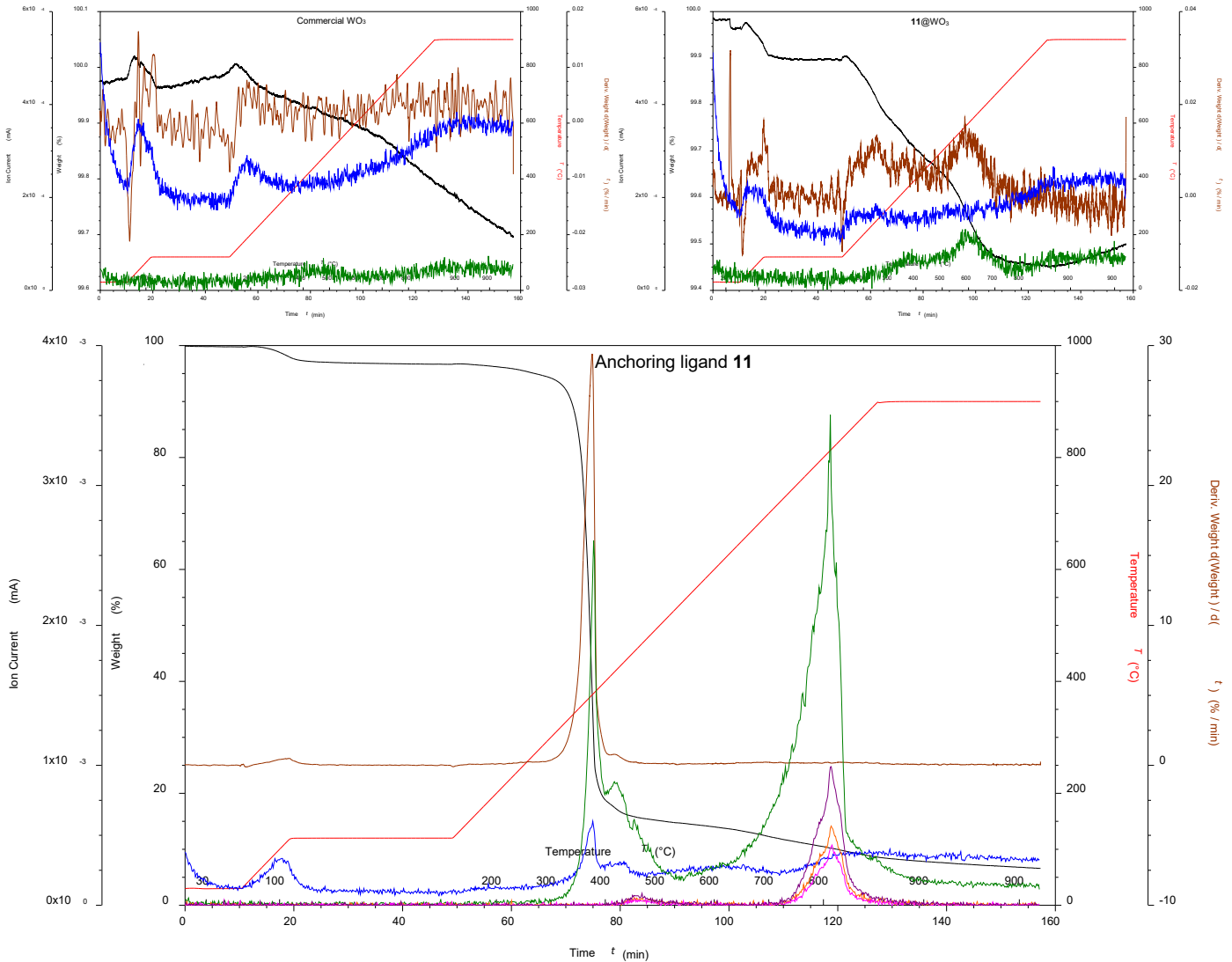


Figure 28: TGA-MS of commercial WO_3 NPs (top left), ligand **11** functionalized WO_3 NPs (top, right) and anchoring ligand **11** (bottom); where black is the weight loss, red is the temperature, brown is the derivative weight against time, blue is the ion current of amu 18, green is the ion current of amu 44, orange is the ion current of amu 51, pink is the ion current of 78 and violet is the ion current of 156.

SnO_2 NPs needed to be analysed in a different manner (see Table 5, entries 5 – 8), as the commercial NPs themselves showed two main weight losses between 200 – 400 °C and between 600 – 900 °C. Hence, the high temperature region as previously described had to be split. For commercial SnO_2 NPs, the regions analysed were low temperature (<380 °C, 0.6%), medium temperatures (380 – 600 °C, 0.2%) and high temperatures (600 – 900 °C, 0.4%) while for functionalized NPs these regions had to be redefined to medium temperature (380 – 800 °C) and high temperature (800 – 900 °C) ranges. Independent of functionalization reaction time, **9**@ SnO_2 NPs showed a sharp weight loss at 650 °C of overall 1.6% for the medium temperature region and between 2.0 and 2.3% in the high temperature region. The mass loss in the medium temperature region was mainly associated with amu 44. The high temperature region did not yield any significant signal in the mass

spectrometer. This was interpreted as a mass higher than the region observable (amu 300), hidden by the carrier gas (amu 14, 15, 27, 28, 29) or within general measurement impurities at high temperatures (amu 16, 32). **11**@SnO₂ NPs (Figure 29) showed the same phenomenon in the high temperature range and a weight loss of 1.7% in the medium temperature range over several peaks assigned to mainly amu 44 (CO₂).

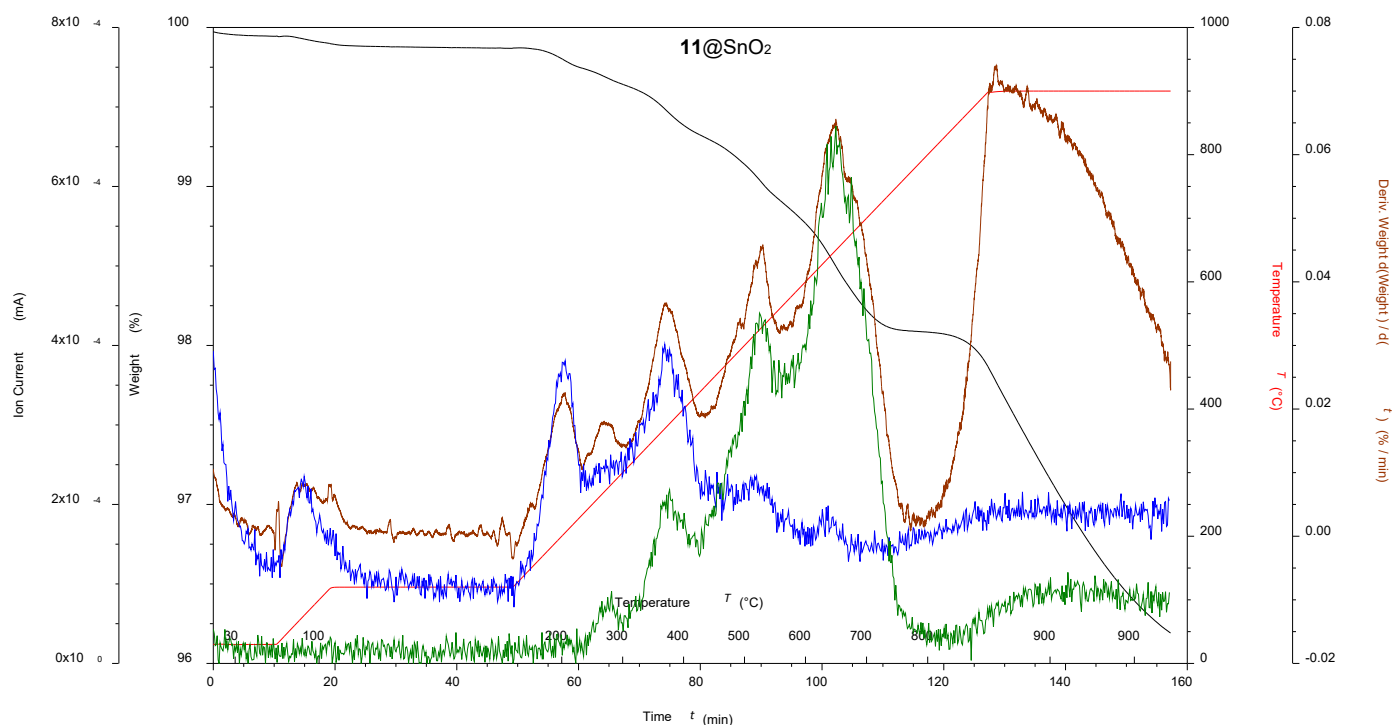


Figure 29: TGA-MS of ligand **11** functionalized SnO₂ NPs; where black is the weight loss, red is the temperature, brown is the derivative weight against time, blue is the ion current of amu 18, green is the ion current of amu 44.

ZrO₂ NPs were already functionalized and described in **Chapter V** but were remade for this project to compare the results with anchoring ligand **11**. The data are shown in Table 5, entries 9 – 12. In the high temperature region (380 – 900 °C), the TGA-MS of **9**@ZrO₂ NPs showed a sharp weight loss at 900 °C, which was 0.9% higher when compared to the commercial ZrO₂ NPs. Longer functionalization times (**9**@ZrO₂-L) yielded 0.7% higher weight losses compared to the commercial ZrO₂ NPs. **11**@ZrO₂ NPs showed a 1.0% higher weight loss compared to the commercial NPs. The anchoring ligand **9** functionalized NPs showed the decomposition to amu 18 and 44 between 650 – 900 °C in two peaks. NPs functionalized with anchoring ligand **11** also showed amu 18 and 44, with amu 44 occurring from 400 – 900 °C in three steps shown in Figure 30. Similar observations were made when functionalizing TiO₂ with anchoring ligand **11**. Hence, a weight loss over three steps assigned to amu 18 and 44 of 2.5% in the high temperature region (380 – 900 °C) was recorded. The weight loss in the high temperature region (380 – 900 °C) was lower compared to the reported results for **9**@TiO₂ in **Chapter V**.

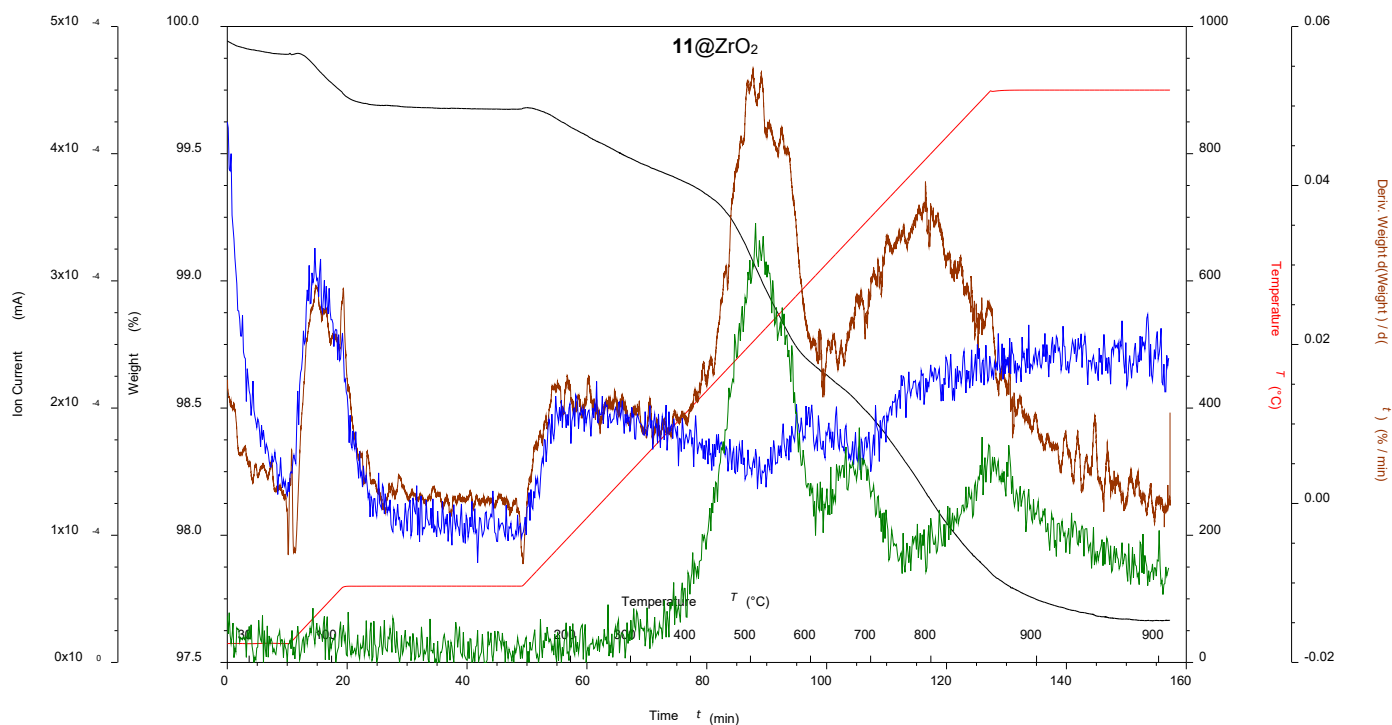


Figure 30: TGA-MS of ligand **11** functionalized ZrO_2 NPs; where black is the weight loss, red is the temperature, brown is the derivative weight against time, blue is the ion current of amu 18, green is the ion current of amu 44.

Commercial ZnO NPs were heat treated to remove organic impurities before functionalization. Anchoring ligand f-NPs yielded suspiciously high weight losses when using N_2 as carrier gas for TGA-MS measurements and it seemed that the ZnO itself was decomposing or volatilizing giving weight losses greater than the attached ligand. A further concern was the use of a phosphonic acid bearing anchoring ligand because ZnO can form zinc phosphates in the presence of phosphoric acid. Hence, the NPs after the functionalization (Figure 31, right) were studied using TEM and were compared with commercial heat treated ZnO NPs (Figure 31, left) for their integrity. The ZnO NPs after functionalization observed under the microscope looked relatively similar to the starting material although surface etching could not be ruled out.

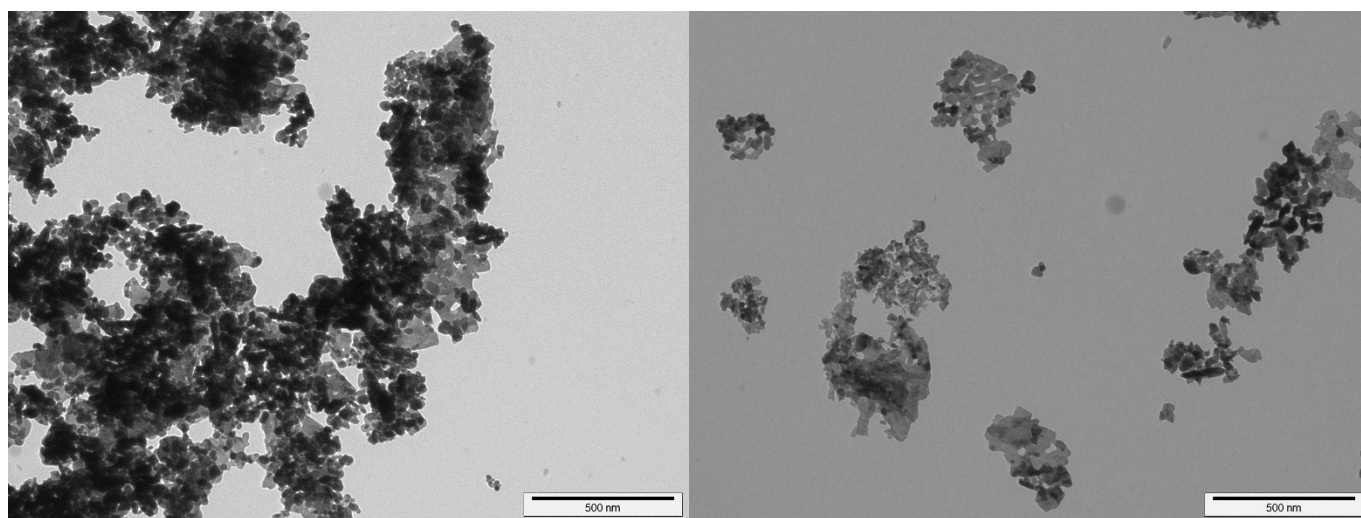


Figure 31: TEM image of heat treated ZnO NPs (left) and ligand **9**@ZnO (right).

The TGA data showed that the main weight loss (Table 5) of **9**@ZnO and **9**@ZnO-L were 26.5 and 30.1% respectively. The main weight loss was observed at 800 °C and was accompanied with a depletion of the underlying O_2 (amu 32) baseline in the mass spectrometer (Figure 32, orange trace). An O_2 (amu 32) baseline

was typically seen in every measurement but never before with a decrease in ion current. ZnO NPs themselves were relatively inert in to the TGA experiment showing only 0.7% and 0.5% weight losses for the low and high temperature region respectively. Hence, it was assumed that the decomposition of the ligand and the resulting carbon reduces the ZnO NPs under inert conditions during the TGA experiment yielding elemental zinc and CO₂ (amu 44). Due to the high temperature and mostly inert atmosphere, zinc would partially evaporate and react with any oxygen explaining the high weight loss, the decrease in the O₂ baseline and strong CO₂ signal.

Table 6: TGA-MS results of functionalized elemental zinc.

Entry	Sample	30 – 380 °C	380 – 900 °C
		/ %	/ %
1	Zn(0)	0.6	88.3
2	Zn(0)-air	0.4	-22.6

This result was supported by measuring elemental zinc (shown in Table 6) under the same conditions which showed a weight loss of 88.3% and the previously observed decrease in ion current for O₂ (amu 32). When measuring elemental zinc under air the oxidation of the material was observed instead, yielding a weight increase of 22.6% which corresponds to a conversion to ZnO. **9**@ZnO-L measured under air (shown in Figure 33) yielded a low temperature region weight loss of 1.7% and a high temperature region weight loss of 3.7% with the main decomposition in two steps starting at 450 °C. The weight curve of **9**@ZnO-L during the experiment looked surprisingly comparable to previous anchoring ligand functionalized samples using ZrO₂ or TiO₂ NPs.

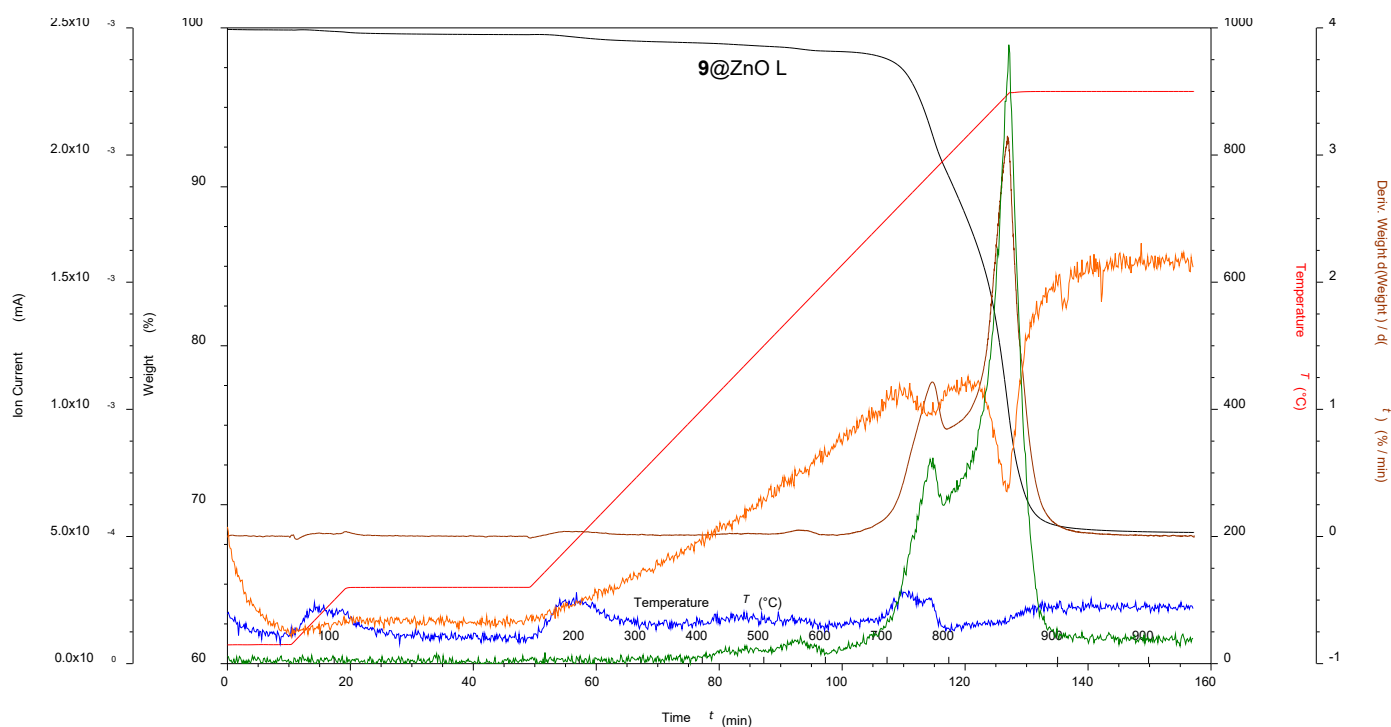


Figure 32: TGA-MS of ligand **9** 12 h functionalized ZnO NPs under N₂; where black is the weight loss, red is the temperature, brown is the derivative weight against time, blue is the ion current of amu 18, orange is the ion current of 32, green is the ion current of amu 44.

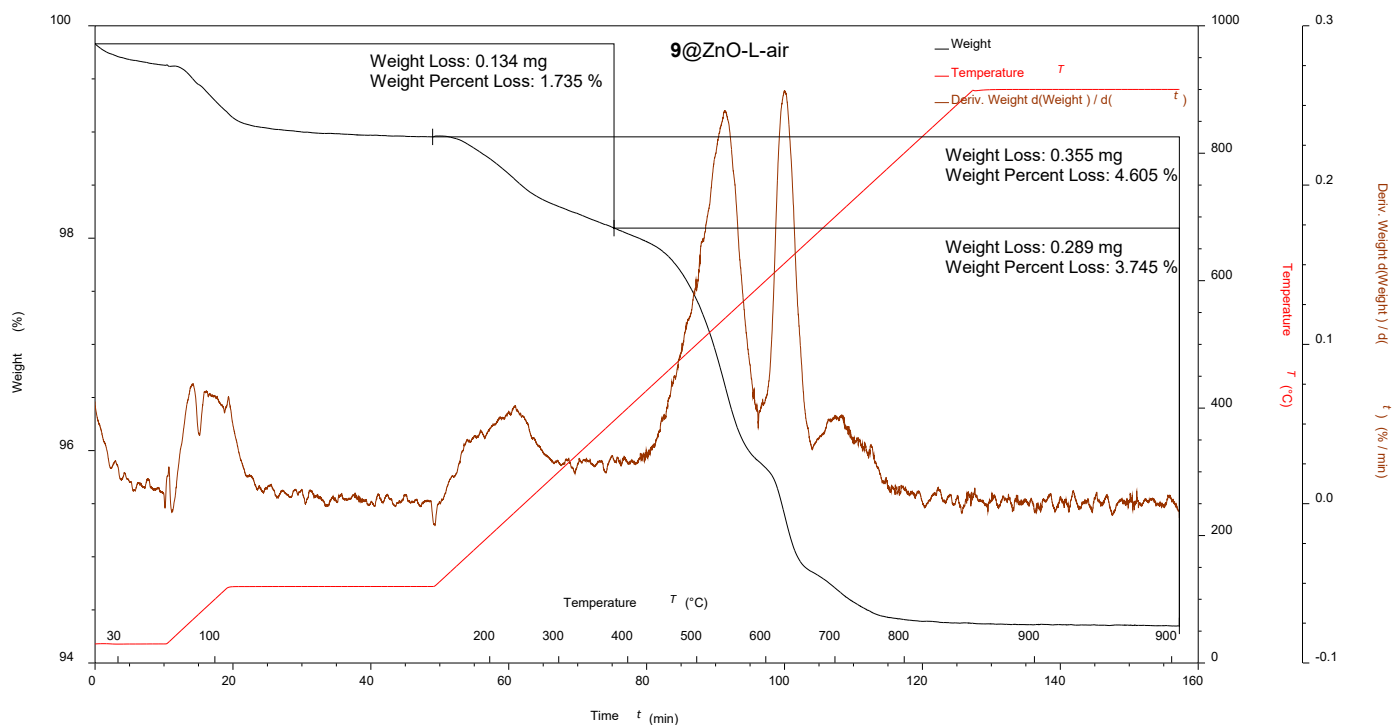


Figure 33: TGA-MS of ligand **9** 12 h functionalized ZnO NPs under air; where black is the weight loss, red is the temperature and brown is the derivative weight against time.

Preliminary complexation experiments as described in **Chapters V** and **VI (Section 6.3.4)** were performed with WO_3 , SnO_2 and colour changes were observed but further characterization was not performed. ZnO NPs were unusual in that it bound ruthenium independent of functionalization with the anchoring ligand. Using the method described in **Section 7.3.3** the NPs coloured dark blue to black indicating at least partial ruthenium oxide formation instead of the desired metal complex.¹⁹⁰ These materials show a 6.3% and 26.0% weight loss in the low and high temperature region respectively. Remeasuring TGA for these NPs in air yielded 4.3% and 4.7% in the low and high temperature regions respectively which were higher than only anchoring ligand **9** f-NPs indicating successful complex formation. When using *cis*-[Ru(bpy)₂Cl₂] for complex formation instead of bpy and $\text{RuCl}_3 \cdot 3\text{H}_2\text{O}$, pale pink NPs were isolated (see Figure 34). This would also suggest successful complexation, although TGA-MS showed no significant difference compared to **9**@ZnO NPs over the temperature range of 30 – 800 °C. The high temperature region for the isolated pink NPs gave a lower weight loss of 25.2% instead of 26.5%. The dominant weight loss from the ZnO reduction and zinc evaporation might explain why differences between the samples were not found.



Figure 34: Photograph of commercial heat treated ZnO NPs (left), **9**@ZnO (middle) and *cis*-Ru(bpy)₂Cl₂ complexed **9**@ZnO (right).

Further investigations of the functionalized ZnO NPs involved using bpy-d₈ during the complexation with RuCl₃·3H₂O. The deuterated bpy had the benefit that it would be directly visible during the TGA-MS experiment. 9@ZnO NPs complexed with bpy-d₈ and RuCl₃·3H₂O in D₂O:EtOH showed an additional weight loss between 120 – 380 °C of 4.4% (Figure 35, black and black dashed) that could be assigned to amu 18, 19 and 44 using the coupled mass spectrometer. This decomposition provided evidence for a deuterated compound (amu 19, HDO) being present on the surface. However, the temperature region in which this decomposition took place was unusual and would suggest no complex formation and instead some kind of other attachment to the surface.

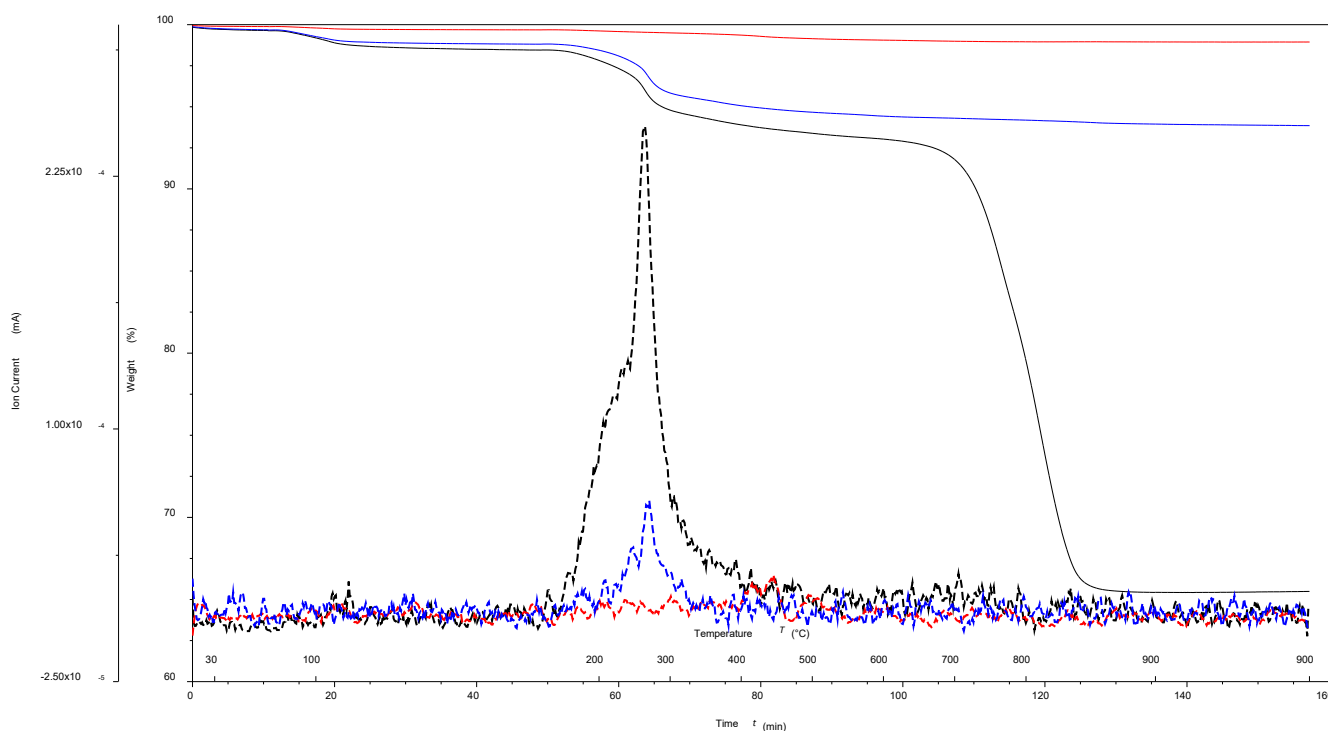


Figure 35: TGA-MS of ligand **9** functionalized ZnO NPs complexed with RuCl₃·3H₂O and bpy-d₈ in D₂O:EtOH (black) and its mass spectrometer data of amu 19 (black dashed) compared to unfunctionalized ZnO NPs after control reaction with bpy in D₂O:EtOH (red) and its mass spectrometer data of amu 19 (red, dashed) compared to unfunctionalized ZnO NPs after control reaction with bpy and RuCl₃·3H₂O in D₂O:EtOH (blue) and its mass spectrometer data of amu 19 (blue dashed).

Control experiments were performed to rule out bpy surface absorption or RuCl₃·3H₂O surface deuteration as the cause of the deuterated peak within the mass spectrometer. Weight losses or mass spectrometer signals belonging to deuterated decompositions (amu 19) were not found when unfunctionalized ZnO NPs and bpy were used during the “complexation” in D₂O:EtOH (Figure 35, red and red dashed), confirming no surface absorption occurring without anchoring ligand or metal chloride. When RuCl₃·3H₂O was used with bpy in D₂O:EtOH (see **Section 7.3.3** for experimental details) even unfunctionalized ZnO NPs showed a weight loss of 3.6% from 120 – 380 °C (Figure 35, blue and blue dashed) with traces of amu 19 (HDO). This was to be expected to some extent as RuCl₃ has been used in the literature before to perform deuterations.¹⁹¹ ¹H NMR spectroscopy (Figure 36) of the extracted bpy after the reaction provided further evidence, as a clear difference in coupling within the aromatic protons and a drastic integral difference of the aromatic H6 proton was seen, indicating a partially deuterated compound. Keeping this in mind deuteration of the surface anchored ligand might also explain the TGA-MS results shown in Figure 35.

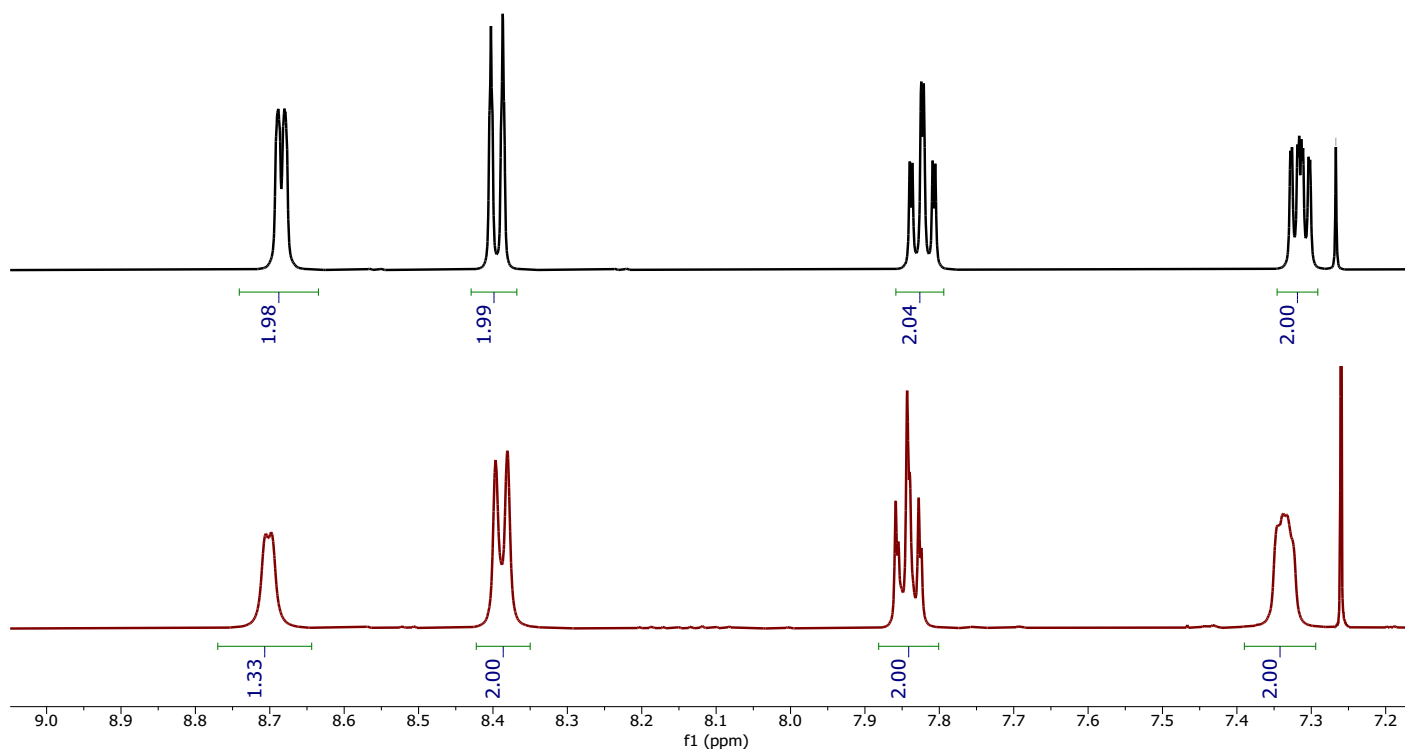


Figure 36: ^1H -NMR spectroscopy in CDCl_3 of bpy extracted from the supernatant after control reaction with: ZnO NPs and bpy in $\text{D}_2\text{O}:\text{EtOH}$ (black), ZnO NPs, $\text{RuCl}_3\cdot 3\text{H}_2\text{O}$ and bpy in $\text{D}_2\text{O}:\text{EtOH}$ (red).

Results obtained in a subsequent project, described in **Chapter VIII** indicate an unknown process occurring. In this case unfunctionalized ZnO NPs and $\text{RuCl}_3\cdot 3\text{H}_2\text{O}$ was reacted in $\text{H}_2\text{O}:\text{EtOH}$ to form a catalyst. The performed characterization with TGA-MS revealed an unexpected similar weight loss (3.3 – 5.8%) in the low temperature region that was assigned to amu 18 and 44. These later obtained results aligned with the suspicion of less interaction of the used bpy- d_8 with the surface and rather deuteration of the surface functionalization occurring explaining the that the higher amu 19 peak measured with TGA-MS (Figure 35). Hence, how the $\text{RuCl}_3\cdot 3\text{H}_2\text{O}$ and bpy interacts with the ZnO NP surface remains unclear.

7.2.2 Competition between different pairs of anchors on NPs

The NPs selectivity between two anchoring ligands was tested using compounds **9** and **11**. The competition experiments (see **Section 7.3.2**) were performed using the same method used for the general functionalization described in **Section 7.3.1**. Anchoring ligand to NP ratios during the functionalization were chosen to have the ligands in a minor excess to allow a clear measurement of the remaining free ligands by ^1H NMR spectroscopy. This was achieved by using roughly 90 mg of NPs with $6.33\ \mu\text{mol}$ of both ligands (overall twice the amount of ligand used in the general functionalization). Attempts using smaller amounts of ligands gave insufficient resolution with NMR spectroscopy to identify the ratio between ligand **9** and **11**. The ratio was determined by evaporating the reaction solution after the functionalization and dispersing the remaining material in $\text{DMSO}-d_6$. The suspension was then transferred into an NMR tube, a drop of TFA- d was added, and the NPs allowed to settle before ^1H NMR spectroscopy was performed. TFA- d was added as partial protonation of anchoring ligand **9** caused a broadening of signals making interpretation difficult. The baseline was corrected to accommodate the broad peaks from TFA. The competition experiment resulted in anchoring ligand concentration on the NP surface for **9** to **11** being 1.0:1.0 for WO_3 NPs, 1.6:1.0 for SnO_2 NPs, 19.9:1.0 for ZrO_2 NPs and 10.6:1.0 for TiO_2 NPs. However, results of WO_3 NPs were questionable as the overall functionalization was very low.

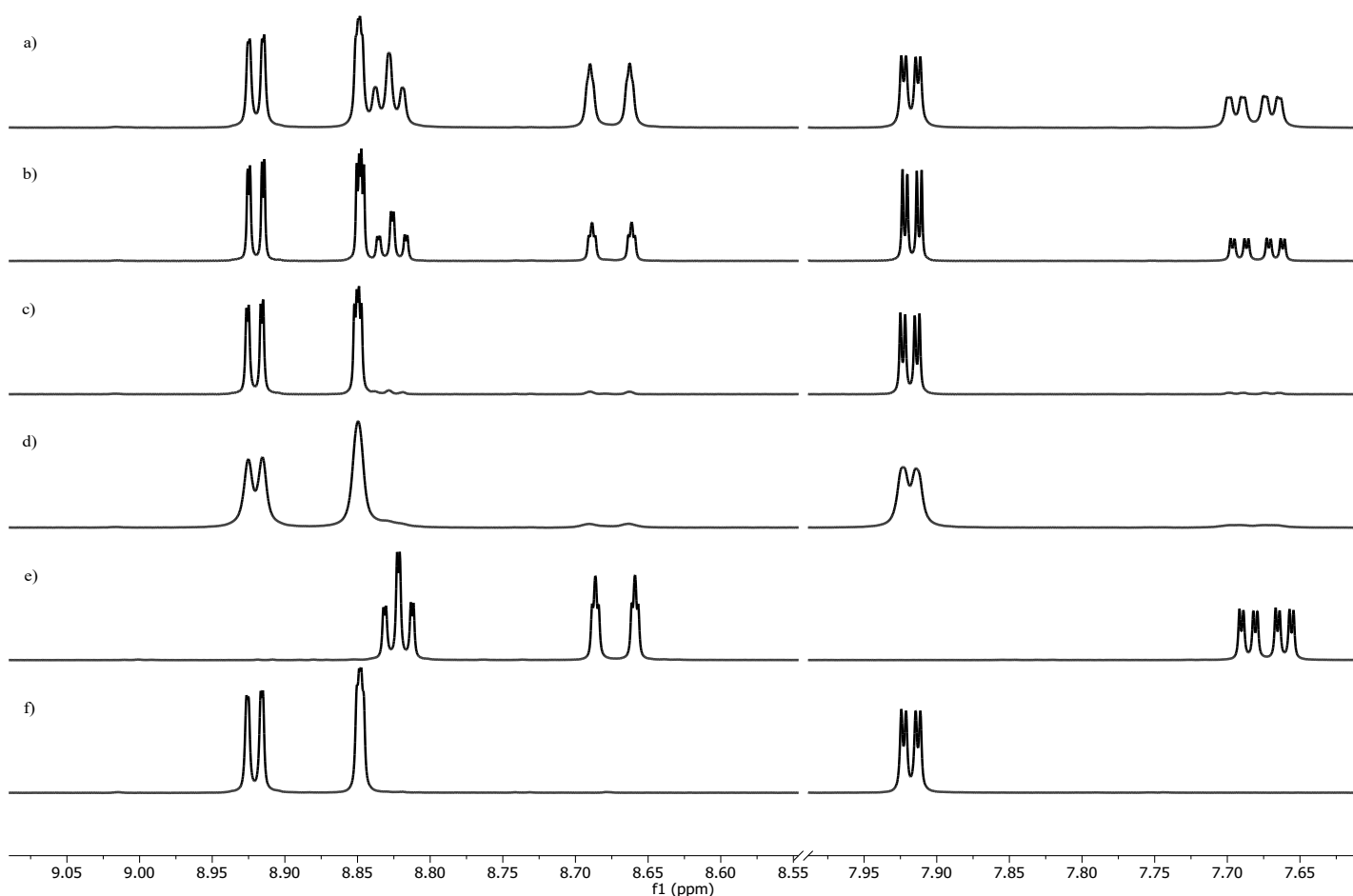


Figure 37: ^1H NMR spectra in DMSO-d_6 of competition experiments between anchoring ligand **9** and **11** showing the results for: a) WO_3 NPs; b) SnO_2 NPs; c) ZrO_2 NPs; d) TiO_2 NPs; e) only anchoring ligand **9**; f) only anchoring ligand **11**.

7.3 Experimental

7.3.1 General functionalization method

The functionalization was performed as previously reported. Anchoring ligand **9** or **11** (15.8 μmol , 1.0 eq.) and milliQ water (18 mL) was added to a microwave vial and dispersed by sonication for 1 min. Commercial NPs (224.0 mg) were added. The suspension was dispersed by sonication for 10 min. The microwave vial was sealed and the reaction mixture heated for 3 – 12 h at 130 $^\circ\text{C}$ in the microwave reactor. The suspension was centrifuged (20 min, 7,000 rpm) after cooling to room temperature. The NPs were separated from the solvent. f-NPs were isolated as powder and stored in a sealed vial under N_2 after drying the NPs under high vacuum. For NMR spectroscopic measurements, NPs (5 – 10 mg) were dispersed in 500 μL D_2O in an NMR tube. For yields and equivalents or changes to the general procedure see Table 7.

Table 7: NP functionalization conditions and yields.

Entry	NP	NP amount / mg (NP eq.)	Ligand	Ligand / μmol	Time / h	Washing	Yield / mg	TGA-MS
								30 – 380 $^\circ\text{C}$ (amu)
1	WO_3	224.0 (3.67)	9	15.8	3	3 \times H_2O , 1 \times EtOH	198.8	0.3 (18)
							9@WO₃	0.3 (18, 44)
2	WO_3	224.0 (3.67)	9	15.8	12	3 \times H_2O , 1 \times EtOH	201.2	0.3 (18)
							9@WO₃-L	0.4 (18, 44)

3 ^a	WO ₃	897.0 (3.67)	11	63.3	3	3×H ₂ O, 1×EtOH 3×DMSO 4×EtOH	825.4 11@WO₃	0.3 (18, 44) 0.2 (18, 44)
4 ^c	SnO ₂	224.0 (5.64)	9	15.8	3	3×H ₂ O, 1×EtOH	216.0 9@SnO₂	0.7 (18, 44 ^b) 1.6 (18, 44), 2.0 (44 ^b)
5 ^c	SnO ₂	224.0 (5.64)	9	15.8	12	3×H ₂ O, 1×EtOH	215.5 9@SnO₂-L	0.3 (18, 44) 1.6 (18, 44), 2.3 (44 ^b)
6 ^{a, c}	SnO ₂	897.0 (5.64)	11	63.3	3	3×H ₂ O, 1×EtOH 3×DMSO 4×EtOH	881.6 11@SnO₂	0.5 (18, 44) 1.4 (18, 44), 1.9 (18, 44)
7	ZrO ₂	224.0 (6.90)	9	15.8	3	3×H ₂ O, 1×EtOH	209.5 9@ZrO₂	0.7 (18, 44 ^b) 1.6 (18, 44)
8	ZrO ₂	224.0 (6.90)	9	15.8	12	3×H ₂ O, 1×EtOH	217.1 9@ZrO₂-L	0.8 (18, 44 ^b) 1.4 (18, 44)
9	ZrO ₂	897.0 (6.90)	11	63.3	3	3×H ₂ O 1×EtOH	878.9 11@ZrO₂	0.5 (18, 44 ^b) 1.7 (18, 44)
10	TiO ₂	727.0 (32.2)	9	79.2	3	1×H ₂ O 1×EtOH	721.5 9@TiO₂	1.1 (18) 2.7 (18, 44)
12	TiO ₂	727.0 (32.2)	11	79.2	3	3×H ₂ O 1×EtOH	714.5 11@TiO₂	1.4 (18, 44) 2.5 (18, 44)
7	ZnO ^d	149.0 (3.48)	9	31.6	3	3×H ₂ O, 1×EtOH	138.9 9@ZnO	1.6 (18) 26.5 (18, 44)
8	ZnO ^d	149.0 (3.48)	9	31.6	12	3×H ₂ O, 1×EtOH	142.4 9@ZnO-L	0.8 (18) 30.1 (18, 44)

^a ¹H NMR spectroscopy was recorded after H₂O and EtOH washing which showed additional washing was required, ^b only traces found, ^c high temperature ranges for SnO₂ NPs were separated into 380 – 800 °C and 800 – 900 °C, ^d heat treated (550 °C) ZnO NPs were used.

7.3.2 General competitions experiment method

The competition experiments were performed in a similar manner to the functionalization described in **Section 7.3.1**. However, two anchoring ligands were added and deliberately chosen to be present in a minor excess to the amount that can be bound to the NP surface. Hence, anchoring ligand **9** (6.33 μmol, 1 eq.), **11** (6.33 μmol, 1 eq.) and milliQ water (13 mL) were added to a microwave vial and dispersed by sonication for 1 min. Commercial NPs (89.7 mg) were added. The suspension was dispersed by sonication for 10 min. The microwave vial was sealed, and the reaction mixture heated for 3 h at 130 °C in the microwave reactor. The solvent was evaporated and 600 μL DMSO-d₆ were added to the vial. The suspension was dispersed for 10 minutes, transferred into an NMR tube and 5 μL TFA-d were added. Before the NMR spectroscopic measurements, the NPs within the suspension were allowed settle. Results are given in Table 8.

Table 8: Competition experiments conditions and ¹H NMR spectroscopy results.

Entry	NP	Amount / mg (NP eq.)	Ligand 1	Ligand 1 / μmol	Ligand 2	Ligand 2 / μmol	Ligand 1 : 2
1	WO ₃	150.0 (6.13)	9	6.33	11	6.33	n.d.
2	WO ₃	89.7 (3.67)	9	6.33	11	6.33	1 : 1
3	SnO ₂	150.0 (9.43)	9	6.33	11	6.33	n.d.

4	SnO ₂	89.7 (5.64)	9	6.33	11	6.33	1.6 : 1
5	ZrO ₂	150.0 (11.54)	9	6.33	11	6.33	n.d.
6	ZrO ₂	89.7 (6.90)	9	6.33	11	6.33	19.9 : 1
7	TiO ₂	100.0 (32.20)	9	6.33	11	6.33	n.d.
8	TiO ₂	60.0 (28.00)	9	7.51	11	7.51	10.6 : 1

7.3.3 Functionalized ZnO NP complexation

9@ZnO-L NPs (45.9 mg) were added into a vial with RuCl₃·3H₂O (9.68 mg, 37.0 μmol) and 2,2'-bipyridine (9.68 mg, 75.0 μmol). H₂O (5.0 mL) and EtOH (3.0 mL) were added and the mixture was thoroughly dispersed using sonication and stirring. The suspension was transferred into an autoclave with a PTFE liner with additional EtOH (2.0 mL). The autoclave was sealed and then heated in an oven with 320 °C/h to 160 °C. The autoclave was left at 160 °C for 1 h. After cooling down, the autoclave was opened and the suspension was centrifuged (20 min, 7000 rpm). The resulting NPs were washed with H₂O (3 × 10 mL) and EtOH (1 × 10 mL). Ru@ZnO-L NPs were isolated as dark blue powder (41.2 mg). TGA: weight loss / %, 6.3 (<380 °C), 26.0 (380 – 900 °C). TGA-MS: amu, 18, 44 (<380 °C), 18, 44 (380 – 900 °C). TGA under air: weight loss / %, 4.3 (<380 °C), 4.7 (380 – 900 °C). The reaction was repeated with 2,2'-bipyridine-d₈ (12.3 mg, 75.0 μmol) and D₂O:EtOH instead of bpy and H₂O:EtOH yielding a dark blue powder (40.1 mg). TGA: weight loss / %, 5.8 (<380 °C), 28.6 (380 – 900 °C). TGA-MS: amu, 18, 19, 44 (<380 °C), 18, 44 (380 – 900 °C). A further reaction was done using **9**@ZnO (45.9 mg) and *cis*-Ru(bpy)₂Cl (3.1 mg, 6.3 μmol) in H₂O:EtOH yielding pale pink NPs (42.9 mg). TGA: weight loss / %, 1.5 (<380 °C), 25.2 (380 – 900 °C). TGA-MS: amu, 18, 44 only traces (<380 °C), 18, 44 (380 – 900 °C).

Three control experiments were performed using the same method described with RuCl₃·3H₂O with following replacing modifications: control 1, using ZnO NPs with no bpy or RuCl₃·3H₂O in D₂O:EtOH yielding a white powder (41.3 mg); control 2, ZnO NPs with bpy and no RuCl₃·3H₂O in D₂O:EtOH yielding a white powder (41.5 mg); control 3, ZnO NPs with bpy in D₂O:EtOH yielding a dark blue powder (43.2 mg). For ¹H NMR analysis the first separated supernatant solution was extracted with CHCl₃, evaporated and measured with CDCl₃. For NMR spectroscopy characterization the integral value was given if a significant (more than 0.1) difference from the expected integral was recorded.

TGA: weight loss of control 1 / %, 0.6 (<380 °C), 0.5 (380 – 900 °C). TGA-MS: amu, 18 (<380 °C), 18, 44 (380 – 900 °C). TGA: weight loss of control 2 / %, 0.5 (<380 °C), 0.5 (380 – 900 °C). TGA-MS: amu, 18 (<380 °C), 18, 44 (380–900 °C). ¹H NMR (500 MHz, CDCl₃) δ / ppm: 8.68 (ddd, *J* = 4.8, 1.9, 1.0 Hz, 2 H, H6), 8.39 (dt, *J* = 8.0, 1.1 Hz, 2 H, H3), 7.82 (td, *J* = 7.7, 1.8 Hz, 2 H, H4), 7.31 (ddd, *J* = 7.5, 4.8, 1.2 Hz, 2 H, H5). TGA: weight loss of control 3 / %, 4.7 (<380 °C), 1.3 (380 – 900 °C). TGA-MS: amu, 18, 19 only traces, 44 (<380 °C), 18, 44 (380 – 900 °C). ¹H NMR (500 MHz, CDCl₃) δ / ppm: 8.70 (d, *J* = 3.8 Hz, (1.3) 2 H, H6), 8.39 (d, *J* = 7.8 Hz, 2 H, H3), 7.84 (td, *J* = 7.7, 1.9 Hz, 2 H, H4), 7.39 – 7.29 (m, 2 H, H5).

7.7 Conclusion

This Chapter provided results for the functionalization of commercial WO₃, ZrO₂, SnO₂, TiO₂ and ZnO NPs with anchoring ligand **9** or **11** using methods established in **Chapter II**. The investigation included longer reaction times during functionalization and concluded that previous reaction times of 3 h were sufficient.

Overall, successful functionalization was established with each type of metal oxide NPs, although the functionalization degree was rather limited in some cases. Characterization of the NPs in this Chapter was mostly limited to TGA-MS experiments although further characterization would definitely be beneficial to solidify the gathered evidence (e.g. FTIR spectroscopy, XPS spectroscopy, ICP-MS spectrometry).

Working with ZnO NPs was especially complicated as these were sensitive to acids and problematic during regular TGA-MS experiments under N₂. Anchoring ligand binding preferences were studied by carrying out ¹H NMR spectroscopy competition experiments. Binding preferences were determined and showed phosphonic acid bearing anchoring ligand **9** preferable to carboxylic acid anchoring ligand **11** in all cases except WO₃ NPs. The result with WO₃ NPs was questionable as the overall degree of functionalization was very limited. Preliminary tests to complex these anchoring ligand f-NPs were made and gave coloured NPs however due to the rather low functionalization degree and time constraints no characterization was done with WO₃ NPs and SnO₂ NPs.

Functionalized ZnO NPs were analysed with TGA-MS under N₂ showed large weight losses in the region of interest. The weight loss was justified by the reduction of ZnO to elemental zinc and its evaporation. The complexation approach with *cis*-[Ru(bpy)₂Cl₂] and **9**@ZnO resulted in pale pink-coloured NPs. This would suggest successful complexation which would require successful anchoring ligand functionalization. However, TGA-MS results were very similar to **9**@ZnO under N₂. One explanation for these TGA results could be that the prominent weight loss from the ZnO reduction and zinc evaporation might have obscured further differences between the samples.

Complexation of functionalized ZnO NPs together with RuCl₃·3H₂O and bpy yielded dark blue NPs with an increased weight loss in the low and large weight loss high temperature region when running TGA-MS under N₂. A possible workaround to characterize these NPs was to run the TGA experiment under air, concluding weight losses exceeding measured weight losses for anchoring ligand **9** functionalized ZnO NPs. Interestingly, control experiments revealed RuCl₃·3H₂O would react independently of functionalization with ZnO NPs yielding dark blue NPs.

Additional control experiments using **9**@ZnO NPs or ZnO NPs together with RuCl₃·3H₂O and bpy-d₈ under various conditions were performed to find the role of the RuCl₃·3H₂O and bpy during the complexation. However, based on the gathered results RuCl₃·3H₂O and ZnO NPs undergo an unexplained process during the complexation conditions independent if functionalized ZnO-NPs were used or not. This process leads to a significant weight loss in the low temperature region, showing amu 18, 44 when using the coupled mass spectrometer. It has to be further noted, that results gathered using bpy-d₈ were less helpful to determine the presence of bpy on the NP surface after the complexation since RuCl₃ in the presence of D₂O can deuterate organic compounds. This was both demonstrated in this Chapter and reported in the literature.¹⁹¹ Hence, a deuteration of the anchored ligand **9** might have occurred. Therefore, the gathered TGA-MS results did not necessarily demonstrate the presence of bpy-d₈ but rather a deuteration of the anchoring ligand **9** instead. Generally, the obtained results aligned more with the suspicion that the used bpy or bpy-d₈ did not significantly bind to the NPs surface during the complexation conditions. As such, how the RuCl₃·3H₂O and bpy interacts with the ZnO NP surface remains unclear.

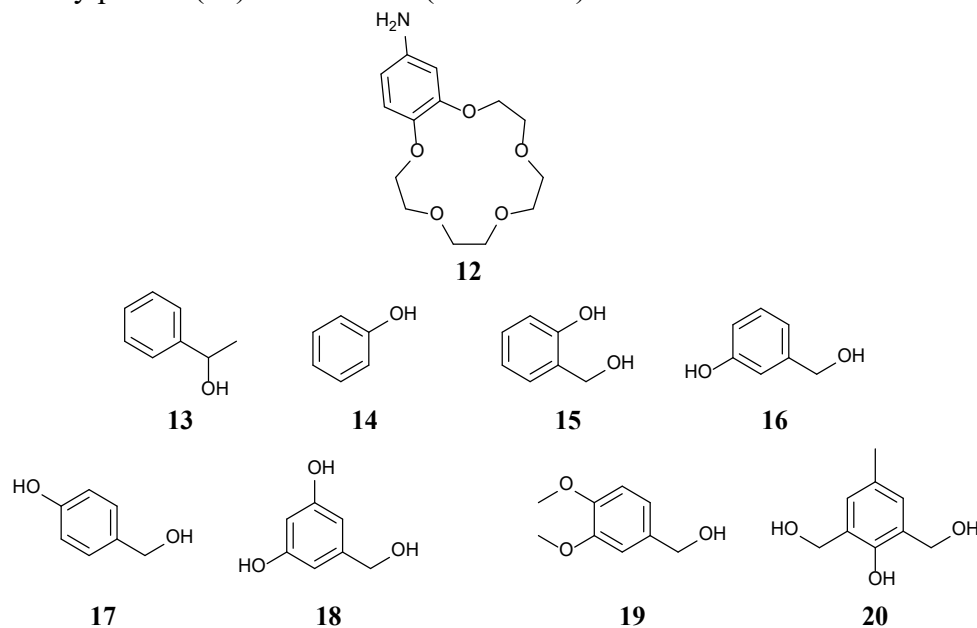
CHAPTER VIII: CATALYSIS AND DEUTERATION USING METAL OXIDE DEPOSITED ZNO NANOPARTICLES

8.1 Motivation

In **Chapter VII** it was observed that during functionalization using $\text{RuCl}_3 \cdot 3\text{H}_2\text{O}$, ruthenium would deposit onto the ZnO NP surfaces. As ZnO and ruthenium or ruthenium oxide are effective catalysts that can promote several reactions such as the Sumitomo-Deacon process, Fischer-Tropsch process or the Haber-Bosch process, the materials catalytic potential was briefly screened.¹⁹²⁻¹⁹⁴

In **Chapter VII** catalytic deuteration was observed in the preparation of f-NPs. This raised the question of whether the f-NPs catalysed the deuteration or if deuteration was caused only by the RuCl_3 , a phenomenon noted before in the literature.¹⁹¹ Deuteration of organic molecules is often an expensive procedure and commercial materials are frequently hundreds of times more expensive^{195,196} but find use in numerous areas (e. g. spectroscopic studies, reaction mechanism studies, drug studies) and occupy an irreplaceable position in science.¹⁹⁷⁻²⁰³ On this basis, further investigation of the catalytic potential of the $\text{RuCl}_3 \cdot 3\text{H}_2\text{O}$ functionalized ZnO NPs ($\text{Ru}@u\text{ZnO}$ NPs) was decided. The project commenced by establishing a procedure to form the f-NPs without any additional organic material. The resulting f-NPs were then used to carry out deuteration experiments using bpy and 4'-aminobenzo-15-crown-5 (**12**, Scheme 12) as substrates. Results using bpy were compared to common deuteration catalysts used in the literature. Results were studied using ^1H and ^2H NMR spectroscopy as well as ESI-MS.

A second aspect of the project focused on extending the alcohol oxidation studies described in **Chapter IV** using these ruthenium functionalized ZnO NPs, and this forms the topic of **Chapter VIII**. Although, ruthenium is expensive, it is roughly 20 times cheaper than rhodium, the basis of the most commonly used catalysts.^{204,205} Alcohol oxidation was studied using 1-phenylethanol (**13**) and subsequently ethanol, hexyl alcohol, 3-octanol, phenol (**14**), 2-hydroxybenzyl alcohol (**15**), 3-hydroxybenzyl alcohol (**16**), 4-hydroxybenzyl alcohol (**17**), 3,5-dihydroxybenzyl alcohol (**18**), 3,4-dimethoxybenzyl alcohol (**19**) and 2,6-bis-(hydroxymethyl)-4-methylphenol (**20**) as substrates (Scheme 12).



Scheme 12: Starting materials used for deuteration and alcohol oxidations in **Chapter VIII**.

8.2 Results and discussion

8.2.1 Functionalization of ZnO NPs using $\text{RuCl}_3 \cdot 3\text{H}_2\text{O}$

The synthesis of Ru@uZnO NPs was similar to previous complexation procedures in other Chapters using commercial ZnO NPs and $\text{RuCl}_3 \cdot 3\text{H}_2\text{O}$. ZnO NPs and $\text{RuCl}_3 \cdot 3\text{H}_2\text{O}$ were dispersed in $\text{H}_2\text{O}:\text{EtOH}$ and placed in a PTFE liner which then was sealed into an autoclave. This was heated to 160 °C for 1 h. Afterwards, the contents were separated by centrifugation and then washed and dried under high vacuum. The characterization of this material was minimal because time was limited and the first initial TGA-MS characterization yielded unexpected results. As described in **Chapter VII** a weight loss of 5.8% was recorded showing both masses amu 18 and 44 (Figure 38). These results were difficult to explain as the only organic material within the whole procedure was EtOH. In both cases the NPs were dried under high vacuum for 72 h. Hence, EtOH should not have been present after 72 drying. When measured using ^1H NMR spectroscopy no notable peaks were found. The reaction was repeated using a new PTFE liner, yielding a 3.3% weight loss in the low temperature region. It is unclear why a repetition of the procedure would yield deviating results.

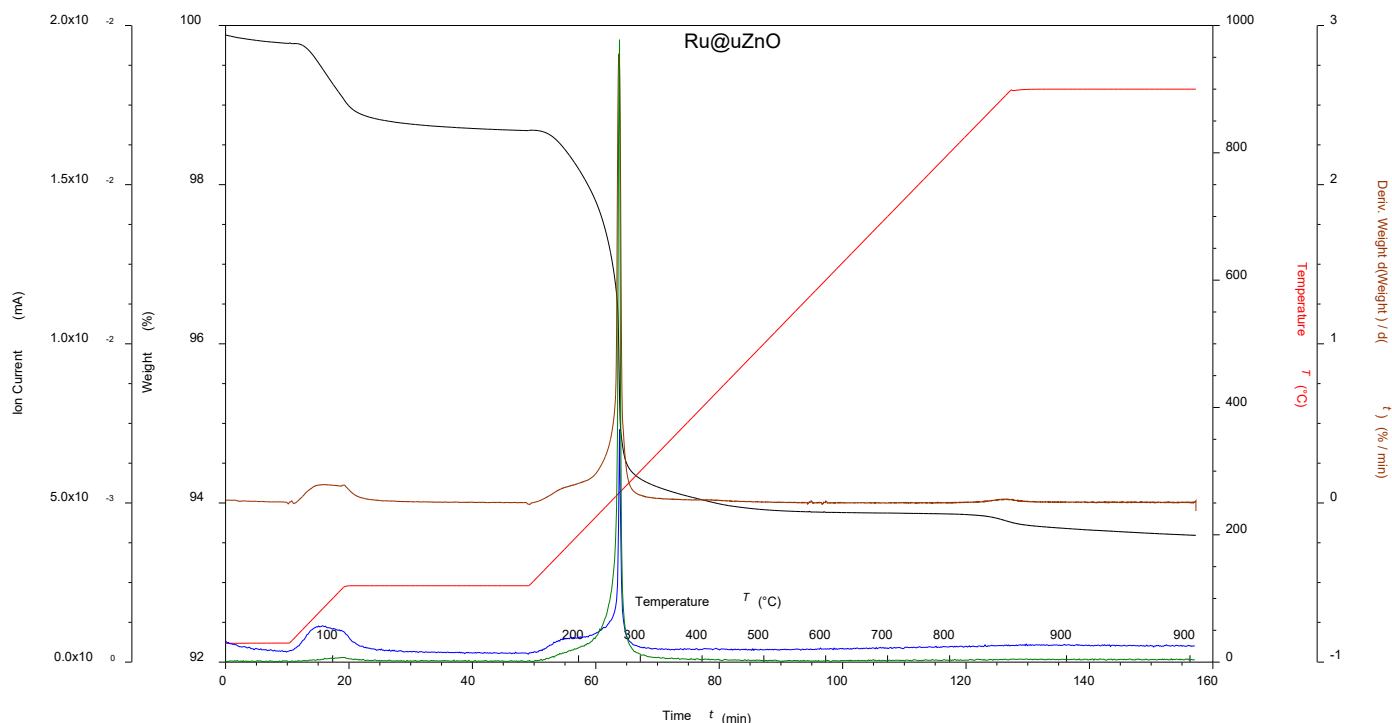


Figure 38: TGA-MS of Ru@uZnO NPs; where black is the weight loss, red is the temperature, brown is the derivative weight against time, blue is the ion current of amu 18, green is the ion current of amu 44.

8.2.2 Deuteration experiments

The procedure for deuteration was modified from a literature procedure used with aromatic hydrocarbons with PtO_2 , Pd/C or CaO as catalysts.^{206,207} Initially, bpy was chosen as a substrate and comparisons with deuteration using PtO_2 , Pd/C or CaO were made. The amount of Ru@uZnO NPs was determined by estimating the ruthenium on the NP surface and using an equivalent to the established systems. Further deuteration experiments were performed with **12** as substrate. Ru@uZnO NPs were added into a PTFE liner with bpy (312.0 mg, 2.0 mmol) and D_2O (10 mL). The mixture was thoroughly dispersed using sonication (10 minutes). The PTFE liner was put into an autoclave, sealed and heated in an oven to 250 °C and left at 250 °C for 24 h. After cooling and removal of NPs by centrifugation, the product was isolated by extraction with CHCl_3 . The isolated bpy was characterized and compared with material from PtO_2 , Pd/C or CaO catalysis using ^1H NMR and ^2H NMR, ESI and high-resolution ESI-MS.

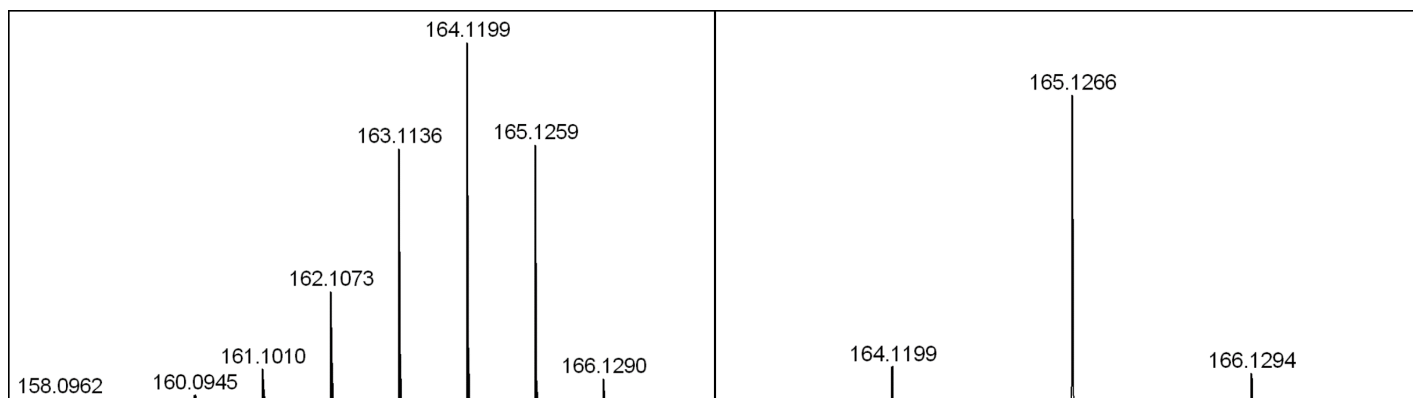


Figure 39: High-resolution ESI-MS of bpy deuterated using Ru@uZnO NPs (left) or PtO₂ (right) as catalyst.

High-resolution ESI-MS results, with bpy deuterated using either Ru@uZnO NPs or PtO₂ as catalyst are shown in Figure 39 on the left and right respectively while results of Pd/C or CaO are shown in Figure 40 on the left and right respectively. With Ru@uZnO NPs as catalyst, a main base peak was observed at *m/z* 164 corresponding to a predominant isotopomer of bpy-d₇. As shown in Figure 39 (left) the deuteration yielded a range of products from bpy-d₄ to bpy-d₈. This observation corresponded with ¹H NMR spectroscopy data given in **Section 8.3.2**. By comparing the aromatic protons of the bpy the exchange rate was shown to be H₆>H₃>H₄>H₅. The pattern recorded with high-resolution ESI-MS and the integrals measured with ¹H NMR spectroscopy were different for each used catalyst. With PtO₂, mainly bpy-d₈ was present. The base peaks for Pd/C and CaO in high-resolution ESI-MS were 160 and 159 respectively corresponding to bpy-d₃ and bpy-d₂. For these samples ¹H NMR spectroscopy showed a dominant deuteration of the H₆ position. CaO even selectively deuterated this position with other aromatic protons not being observed in ²H NMR spectroscopy. Interestingly, Pd/C did not show the same deuteration affinity seen with Ru@uZnO NPs but instead showed H₆>>H₃=H₄=H₅.

After deuteration, the ESI-MS of ligand **12** showed predominantly **12**-d₂ and ¹H NMR spectroscopic signals for H₂ and H₅ had vanished whilst crown-ether and H₄ (less intense) signals remained. ²H NMR spectroscopy was performed and while the spectra yielded very broad signals it could be seen that all aromatic positions were partially deuterated with H₄ to about half the extent of H₂ and H₅. Aliphatic sites were not visible within ²H NMR spectroscopy which was expected as they should be much more difficult to deuterate.

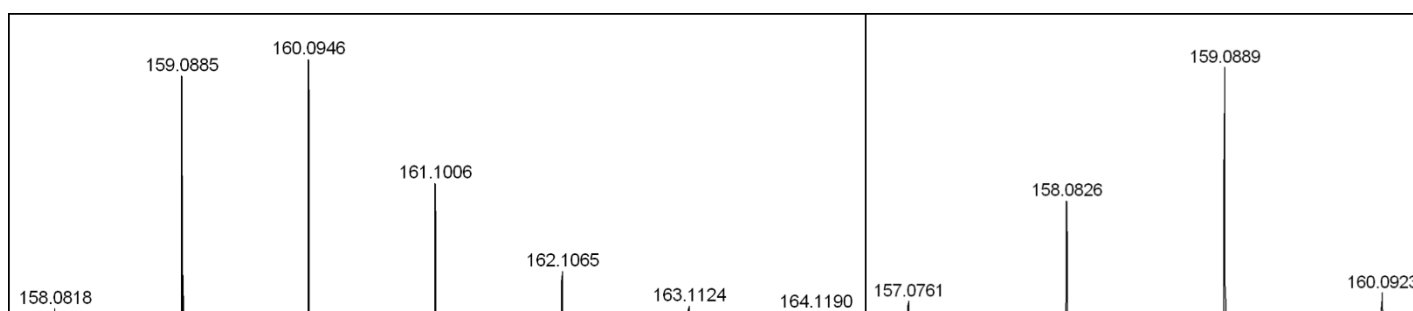


Figure 40: High-resolution ESI-MS of bpy deuterated using Pd/C (left) or CaO (right) as catalyst.

8.2.3 Alcohol oxidation

To further investigate the catalytic potential of ruthenium-functionalized ZnO NPs alcohol oxidation studied in **Chapter IV** was tested with the materials. A similar performance of the new material would make the new method over 20 times less expensive based on prices for ruthenium versus rhodium.^{204,205} Treatment of the ZnO NPs with RuCl₃·3H₂O solution results in complete binding to the NP surface (based on complete decolourization of the aqueous solution). This corresponds to a roughly 15 times higher functionalization degree compared to the previous catalytic studies with Rh(**3**)₂@TiO₂ NPs in **Chapter IV**, allowing low NP to

substrate ratios. Using 10 mg of Ru@uZnO NPs would achieve this which is equivalent to using double the amount of rhodium used in **Chapter IV** but with the benefit of metal costs being 10 times cheaper. The reaction conditions are described in **Section 8.3.3** and Table 9. Generally the alcohol oxidation worked best with **13** as substrate, showing a 1 : 1.7 starting material to aldehyde ratio. This result slightly outperformed the reaction setup in **Chapter IV**. Although a broad range of other precursors were tested, efforts to use the catalyst NPs with other alcohols were less successful. Alcohols without aromatic groups attached lead to incredibly low yields while precursors **14 – 20** showed either no conversion (**14, 18**) or product and side product mixtures (**15 – 17, 19, 20**). Analysis of these complex reactions with only ^1H NMR and ESI-MS was rather inadequate. Nevertheless, **15, 17** and **19** yielded the most conversion although the full range of products other than the aldehyde was not identified.

8.3 Experimental

8.3.1 ZnO NP functionalization (Ru@uZnO NPs)

Heat treated ZnO NPs (213.5 mg) were added into a vial with $\text{RuCl}_3 \cdot 3\text{H}_2\text{O}$ (45 mg, 170.0 μmol). H_2O (5 mL) and EtOH (3 mL) were added, and the mixture was thoroughly dispersed using sonication (10 min) and shaking. The suspension was transferred into an autoclave with a PTFE liner with additional EtOH (2 mL). The autoclave was sealed and then heated in an oven with 320 $^\circ\text{C}/\text{h}$ to 160 $^\circ\text{C}$. The autoclave was left at 160 $^\circ\text{C}$ for 1 h. After cooling down, the autoclave was opened and the suspension was centrifuged (20 min, 7000 rpm). The resulting NPs were washed with H_2O (3×10 mL) and EtOH (3×10 mL) and dried under high vacuum for 72 h. Ru@uZnO NPs were isolated as dark blue powder (226.1 mg). TGA: weight loss / %, 5.8 (<380 $^\circ\text{C}$), 0.5 (380 – 900 $^\circ\text{C}$). TGA-MS: amu, 12, 16, 18, 22, 44 (<380 $^\circ\text{C}$), no masses found (380 – 900 $^\circ\text{C}$). For NMR spectroscopic measurements, NPs (5 – 10 mg) were dispersed in 500 μL D_2O in an NMR tube.

8.3.2 General procedure for deuteration experiments

This procedure was derived from a literature reaction previously used for aromatic hydrocarbons.^{206,207} Ru@uZnO NPs (50.0 mg, 0.04 mmol) were added into a PTFE liner with bpy (312.0 mg, 2.0 mmol). D_2O (10 mL) were added, and the mixture was thoroughly dispersed using sonication (10 minutes). The PTFE liner was put into an autoclave, was sealed and then heated in an oven with 320 $^\circ\text{C}/\text{h}$ to 250 $^\circ\text{C}$. The autoclave was left at 250 $^\circ\text{C}$ for 24 h. After cooling down, the autoclave was opened transferred into a 50 mL Eppendorf tube and 10 mL CHCl_3 was added. The suspension was centrifuged (20 min, 7000 rpm) after thoroughly shaking it. The resulting supernatant was removed and extracted with CHCl_3 (3×10 mL). The collected organic phases were dried over Na_2SO_4 and the solvent was evaporated. The solid was dried under high vacuum for 10 minutes yielding partially deuterated bpy (271.5 mg) as beige powder. The general procedure was repeated with **12** as starting material yielding partially deuterated **12** as viscous dark brown oil (555.1 mg). For NMR characterization the integral value was given in brackets if a significant (more than 0.1) difference from the expected integral was recorded. ESI-MS of bpy after deuteration using Ru@uZnO NPs; $\text{C}_{10}\text{H}_1\text{D}_7\text{N}_2$: m/z 164.24 $[\text{M}+\text{H}]^+$ (calc. 164.12). HR ESI-MS: m/z 164.1199 $[\text{M}+\text{H}]^+$ (calc. 164.1200). ^1H NMR (500 MHz, CD_2Cl_2) δ / ppm: 8.68 – 8.64 (m, (0.15) 2 H, H6), 8.45 – 8.41 (m, (0.52) 2 H, H3), 7.85 – 7.80 (m, (1.39) 2 H, H4), 7.35 – 7.29 (m, 2 H, H5).

ESI-MS of **12** after deuteration using Ru@uZnO NPs; $\text{C}_{14}\text{H}_{19}\text{D}_2\text{NO}_5$: m/z 308.15 $[\text{M}+\text{Na}]^+$ (calc. 308.14). ^1H NMR (500 MHz, CD_3CN) δ / ppm: 6.68 (s, (0.63) 1 H, H4), 4.01 – 3.92 (m, 4 H, a), 3.79 – 3.73 (m, 4 H, b), 3.65 – 3.59 (m, 8 H, c,d). ^1H NMR (600 MHz, CH_3CN) δ / ppm: 6.62 (s, (0.57) 1 H, H4), 4.02 – 3.84 (m, 4 H, a), 3.82 – 3.65 (m, 4 H, b), 3.63 – 3.50 (m, 8 H, c,d). ^2H NMR (92.12 MHz, CH_3CN) δ / ppm: 6.79 – 6.53 (m, (0.44) 1 H, H4), 6.49 – 6.22 (m, 1 H, H2), 6.23 – 5.97 (m, 1 H, H5).

For comparison the general procedure was repeated using PtO₂ or Pd/C or CaO as catalyst. The method was adjusted with CaO according to the literature.²⁰⁸ Hence, the general procedure was repeated at reduced temperature (180 °C) four times in succession adding the bpy from the previous reaction and replenishing the CaO and D₂O. This yielded partially deuterated bpy (298.3 mg, 285.5 mg, 260.1 mg) for the catalysts PtO₂, Pd/C and CaO. ¹H and ²H NMR spectroscopy was used to study the deuteration degree. CD₃OD was used as NMR standard but due to the higher room temperatures the results seemed to be compromised. ESI-MS was performed for all compounds. High resolution ESI-MS was performed for all bpy compounds. ESI-MS of bpy after deuteration using PtO₂; C₁₀D₈N₂: m/z 187.07 [M+Na]⁺ (calc. 187.11). HR ESI-MS: m/z 165.1266 [M+H]⁺ (calc. 164.1262). ¹H NMR (600 MHz, CD₂Cl₂) δ / ppm: 8.66 (s, (1.46) 2 H, H6), 8.45 – 8.41 (m, (1.97) 2 H, H3), 7.86 – 7.80 (m, (2.04) 2 H, H4), 7.35 – 7.29 (m, (2.00) 2 H, H5). ²H NMR (92.12 MHz, CD₂Cl₂) δ / ppm: 8.59 (s, 2 H, H6), 8.47 (s, 2 H, H3), 7.87 (s, 2 H, H4), 7.36 (s, 2 H, H5).

ESI-MS of bpy after deuteration using Pd/C; C₁₀H₅D₃N₂: m/z 182.07 [M+Na]⁺ (calc. 182.08). HR ESI-MS: m/z 160.0946 [M+H]⁺ (calc. 160.0949). ¹H NMR (600 MHz, CD₂Cl₂) δ / ppm: 8.69 – 8.64 (m, (0.05) 2 H, H6), 8.47 – 8.39 (m, 2 H, H3), 7.87 – 7.79 (m, 2 H, H4), 7.35 – 7.28 (m, 2 H, H5). ²H NMR (92.12 MHz, CD₂Cl₂) δ / ppm: 8.69 (s, 2 H, H6), 8.47 (s, (0.32) 2 H, H3), 7.87 (s, (0.40) 2 H, H4), 7.36 (s, (0.34) 2 H, H5).

ESI-MS of bpy after deuteration using CaO; C₁₀H₆D₂N₂: m/z 181.01 [M+Na]⁺ (calc. 181.07). HR ESI-MS: m/z 159.0889 [M+H]⁺ (calc. 159.0886). ¹H NMR (600 MHz, CD₂Cl₂) δ / ppm: 8.66 (ddd, *J* = 4.8, 1.8, 0.9 Hz, (0.42) 2 H, H6), 8.43 (dd, *J* = 8.0, 1.3 Hz, 2 H, H3), 7.86 – 7.79 (m, 2 H, H4), 7.36 – 7.28 (m, 2 H, H5). ²H NMR (92.12 MHz, CD₂Cl₂) δ / ppm: 8.69 (s, 2 H, H6).

8.3.3 Alcohol oxidation

Ru@uZnO NPs (10.0 mg) and milliQ water (1.67 mL) were added to a microwave vial. The contents were sonicated (1 min) and then aqueous NaOH (25 mM, 0.331 mL) and precursor (0.827 mmol, 1 eq.) were added to the suspension. The vial was sealed, and the reaction mixture was heated to 100 °C for 72 h. A small amount of the reaction mixture (ca. 50 μL) was removed by syringe and dispersed in 500 μL D₂O in an NMR tube. ¹H NMR spectroscopy and ESI-MS were measured to determine reactant to product ratios and are given in Table 9.

Table 9: Reaction conditions, yields and ESI MS characterization.

Entry	Starting material	Reaction time / h	Number of products identified ^a	Reactant:product ratio	ESI MS / amu
1	EtOH	72	1	1 : 95.2 (1.0%)	n.d. ^b
2	Hexyl alcohol	72	1	1 : 19.8 (4.8%)	n.d.
3	3-Octanol	72	1	1 : 26.9 (3.6%)	n.d.
4	13	72	1	1 : 1.7 (37.5%)	n.d.
5	14	72	0	n.d.	n.d.
6	15	72	3 ^c	1 : 2.9 1 : n.d. 1 : n.d.	123.1 [15 – H] ⁻ , 137.0, 229.1, 243.0, 297.0
7 ^d	16	72	1	1 : 5.9 (14.4 %)	121.1 [Aldehyde – H] ⁻ , 123.2 [16 – H] ⁻ , 137.1, 245.1, 351.1

8	17	72	2	1 : 2.1 (28.8%) 1 : 4.2 (13.7%) ^e	121.1 [Aldehyde – H] ⁻ , 227.1
9 ^f	18	72	0	n.d.	139.1 [18 – H] ⁻
10 ^d	19	72	1	1 : 5.0 (16.7%)	product peak not found
11 ^d	20	72	1	1 : 8.7 (11.5%)	167.1 [20 – H] ⁻

^a This value is an assumption based on ¹H NMR spectroscopy and ESI MS, separation and complete characterization of each compound within the mixture were not performed, ^b n.d. = not defined, ^c number refers to estimated minimal amount of products present within ¹H NMR spectroscopy, product that could be evaluated used the separate aldehyde peak for calculations, ^d ¹H NMR suggests 1 main product other small unidentified impurities were present, ^e unidentified sideproduct, ^f small (<1%) conversion to unidentified product.

8.4 Conclusion

Ru@uZnO NPs were an interesting material to work with, since they were able to perform two catalytic reactions relatively well, namely the deuteration of bpy or **12**, and the oxidation of **13**. The characterization of Ru@uZnO NPs using TGA-MS was insufficient to fully characterize the material and further measurements are required to provide insights into the catalytic activity.

In the case of the deuteration, control experiments using literature catalysts were performed and comparisons would put the efficiency of Ru@uZnO NPs in the deuteration of organic compounds somewhere in between Pd/C and PtO₂. The catalyst showed a preference for exchanging aromatic protons of bpy in the order H6>H3>H4>H5 compared to PtO₂ and Pd/C (H6>H3=H4=H5) while CaO only deuterated the H6 position.

When comparing the alcohol oxidation of **13** with the method used in **Chapter IV**, Ru@uZnO NPs slightly outperformed the earlier method in yield but not efficiency. However, considering the cost of both catalysts Ru@uZnO NPs appears better in comparison. Overall, 10 further substrates for oxidation were tested. Alcohols without aromatic groups attached gave very low yields while aromatic alcohols (**14** – **20**) showed either no conversion (**14**, **18**) or product and side product mixtures (**15** – **20**). Both problems made analysis with only ¹H NMR and ESI-MS rather inadequate. Nevertheless, **15**, **17** and **19** yielded the most conversion even though the products formed cannot be sufficiently confirmed.

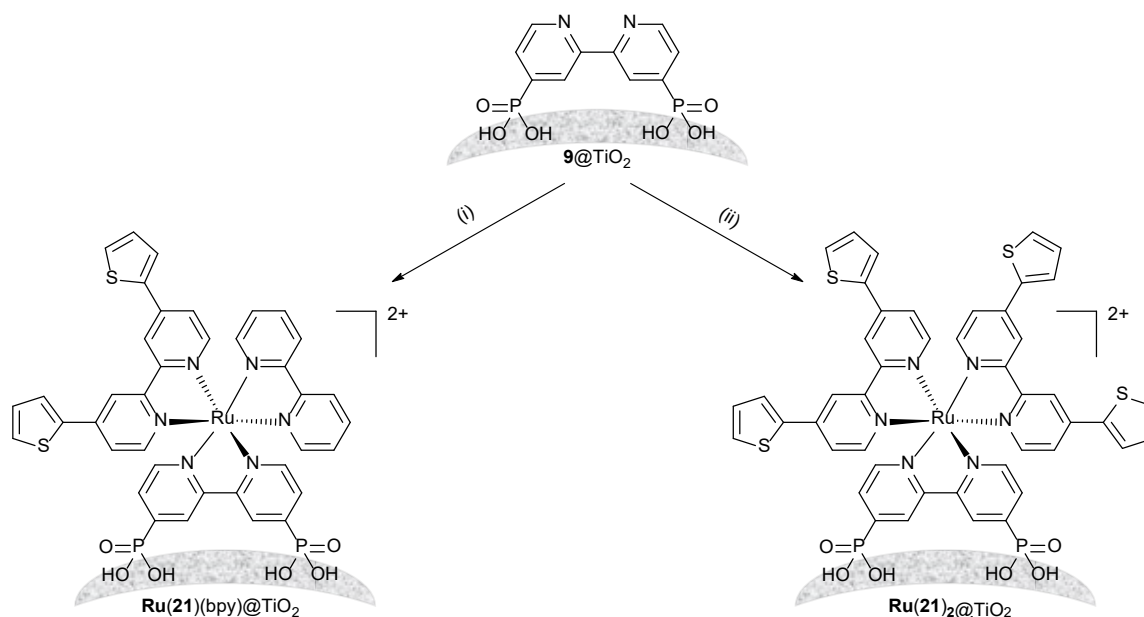
CHAPTER IX: MODIFYING SURFACE CHARACTERISTICS

INTRODUCTION OF POLYMERIZABLE THIOPHENES

9.1 Motivation

One project idea was to use metal complex functionalized TiO₂ NPs to perform a polymerization using a surface-bound complex to initiate polymerization of (oligo)thiophenes to create a surface functionalization resembling PEDOT (poly(3,4-ethylenedioxythiophene)). The project's main goal was the proof of principle of reacting a surface-bound complex containing a pendant thienyl group to generate a pendant polythienyl chain. Poly(3,4-ethylenedioxythiophene):poly(styrenesulfonate) (PEDOT:PSS) has been used as an electrode in optoelectronic devices for flexible electronics because of its high conductivity and transmittance.²⁰⁹ It is also attractive as it is low-cost and offers a high optical transparency.²¹⁰ Good mobility of electrons through TiO₂ NP materials is usually achieved by sintering the NPs which decreases the electrical resistivity of the material.²¹¹ However, this renders the material brittle and makes it difficult or impossible to perform prior surface functionalization. Hence, a second objective was to study the surface characteristics of polymer functionalized NPs to ascertain if functionalization would have enough influence so that the NPs would attain electronic characteristics associated with PEDOT.

In this Chapter initial attempts were made using thiophene in combination with oxidants in solution (FeCl₃ or FeCl₃ and H₂O₂) to try and polymerize thiophene at a TiO₂ NP surface bound complex. The reaction of the RuCl₃·3H₂O complexed NPs shown in Scheme 13 with either 2-(thiophen-2-yl)-2,2'-bipyridine (**21**) and 2,2'-bipyridine (bpy) or only **21** yielded Ru(**21**)(bpy)@TiO₂ NPs or Ru(**21**)₂@TiO₂ NPs. Of course the formulation as Ru(**21**)(bpy)@TiO₂ NPs describes the statistical mixture of surface bound homoleptic and heteroleptic species. A further study was made utilizing vapour phase polymerization (VPP) with Ru(**21**)(bpy)@TiO₂ and FeCl₃ or *p*-toluenesulfonic acid (PTSA) as oxidant and 2,2':5',2''-terthiophene (TTh) as building block. Several control experiments were conducted, and characterization was made with TGA-MS, solid-absorptions spectroscopy and FTIR spectroscopy.



Scheme 13: Complexed NPs Ru(**21**)(bpy)@TiO₂ and Ru(**21**)₂@TiO₂ from **9@TiO₂** where (i) used 1.0 eq. **21** and 1.0 eq. bpy while (ii) used 2.0 eq. **21** both reactions were conducted in an autoclave at 160 °C for 1 h in H₂O:EtOH.

9.2. Results and discussion

9.2.1 TiO_2 NP complexation forming $\text{Ru}(\mathbf{21})(\text{bpy})@\text{TiO}_2$ and $\text{Ru}(\mathbf{21})_2@\text{TiO}_2$

Metal complexes were assembled directly on the NP surface using procedures described in **Chapter V**. The procedure for complex formation used $\mathbf{9}@\text{TiO}_2$ NPs, $\text{RuCl}_3 \cdot 3\text{H}_2\text{O}$ and either ligand $\mathbf{21}$ and bpy in equimolar amounts (see (i) in Scheme 13) or only ligand $\mathbf{21}$ (see (ii) in Scheme 13). The experimental details are described in **Section 9.3.1**. For all complexations, f-NPs and ligand(s) were dispersed in a 1:1 mixture of $\text{H}_2\text{O}:\text{EtOH}$ together with $\text{RuCl}_3 \cdot 3\text{H}_2\text{O}$ in at 160°C for 1 h. This procedure yielded two types of NPs, abbreviated $\text{Ru}(\mathbf{21})(\text{bpy})@\text{TiO}_2$ and $\text{Ru}(\mathbf{21})_2@\text{TiO}_2$. In all cases the pendant thienyl group of ligand $\mathbf{21}$ of the surface-bound complex is the site of initiation for the polymerization. Ligand $\mathbf{21}$ was synthesized according to the literature.¹² The NPs were studied after testing various conditions to establish if a successful polymerization had occurred. The isolated f-NPs were characterized using ^1H NMR spectroscopy, FTIR, TGA-MS and solid-state absorption spectroscopy.

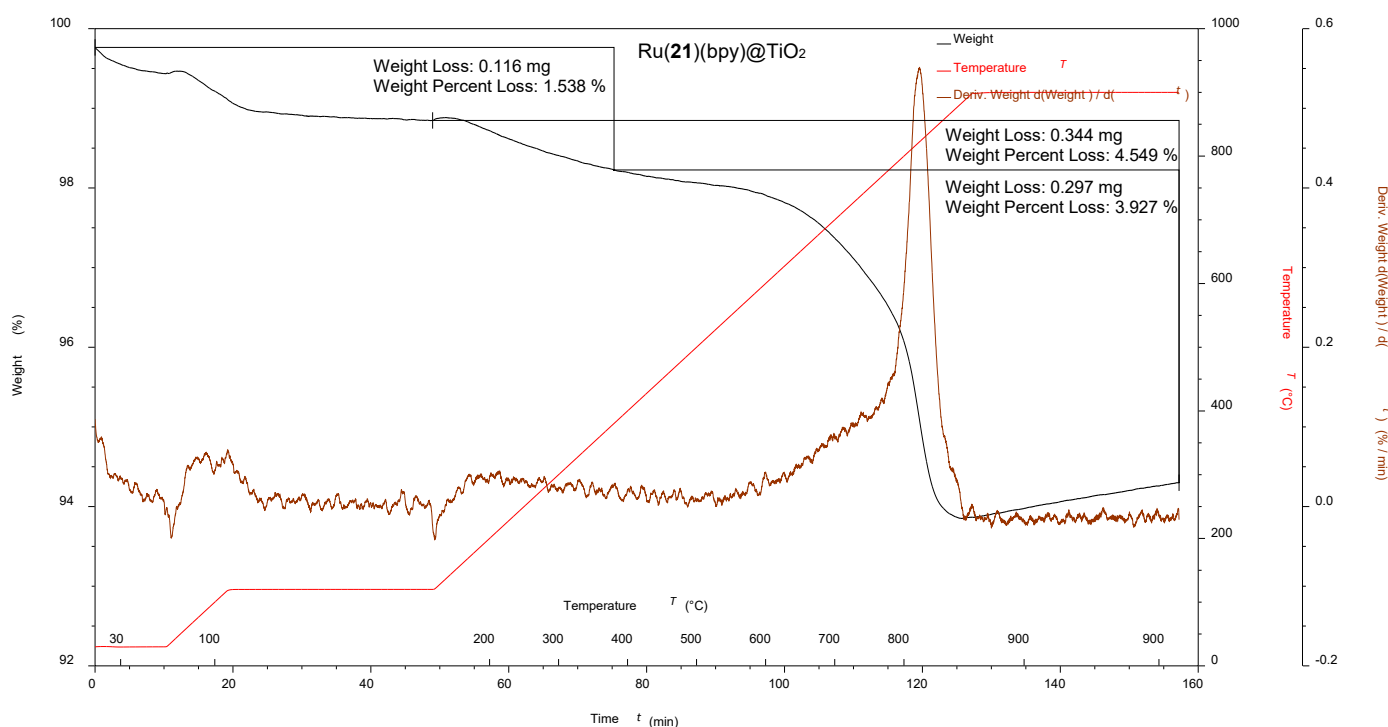


Figure 41: TGA-MS of ligand $\text{Ru}(\mathbf{21})(\text{bpy})@\text{TiO}_2$ where black is the weight loss, red is the temperature and brown is the derivative weight against time.

TGA-MS revealed an increased weight loss of the complex functionalized NPs when comparing them to the f-NPs discussed in **Chapter V**. The weight loss for the isolated metal complexed f-NPs $\text{Ru}(\mathbf{21})(\text{bpy})@\text{TiO}_2$ and $\text{Ru}(\mathbf{21})_2@\text{TiO}_2$ was 1.5% and 1.1% in the low temperature region ($30 - 380^\circ\text{C}$) and 3.9 and 4.1% in the high temperature region ($380 - 900^\circ\text{C}$) respectively. The TGA of $\text{Ru}(\mathbf{21})(\text{bpy})@\text{TiO}_2$ NPs is shown in Figure 41. The TGA coupled mass spectrometer showed amu 18 (H_2O) and 44 (CO_2) throughout the measurement with a peak in the ion current of amu 44 (CO_2) around 800°C , providing evidence for a successful functionalization. FTIR spectroscopy of both NPs resembled $\text{Ru}@\text{TiO}_2$ closely and a comparison of the spectra is shown in Figure 42. The main difference between the newly prepared NPs and $\text{Ru}@\text{TiO}_2$ from **Chapter V** was a less intense peak at 1640 cm^{-1} and a more intense peak at 1540 cm^{-1} . Only minor differences were to be expected, as the NPs are extremely similar. Between the $\text{Ru}(\mathbf{21})(\text{bpy})@\text{TiO}_2$ and $\text{Ru}(\mathbf{21})_2@\text{TiO}_2$ the differences in FTIR spectroscopy were less significant with only slight intensity changes in the fingerprint. Solid-state absorption spectroscopy of $\text{Ru}(\mathbf{21})(\text{bpy})@\text{TiO}_2$ NPs showed peaks between $430 - 520\text{ nm}$ and a broad absorption between $660 - 700\text{ nm}$. Overall, the spectra were similar to $\text{Ru}@\text{TiO}_2$.

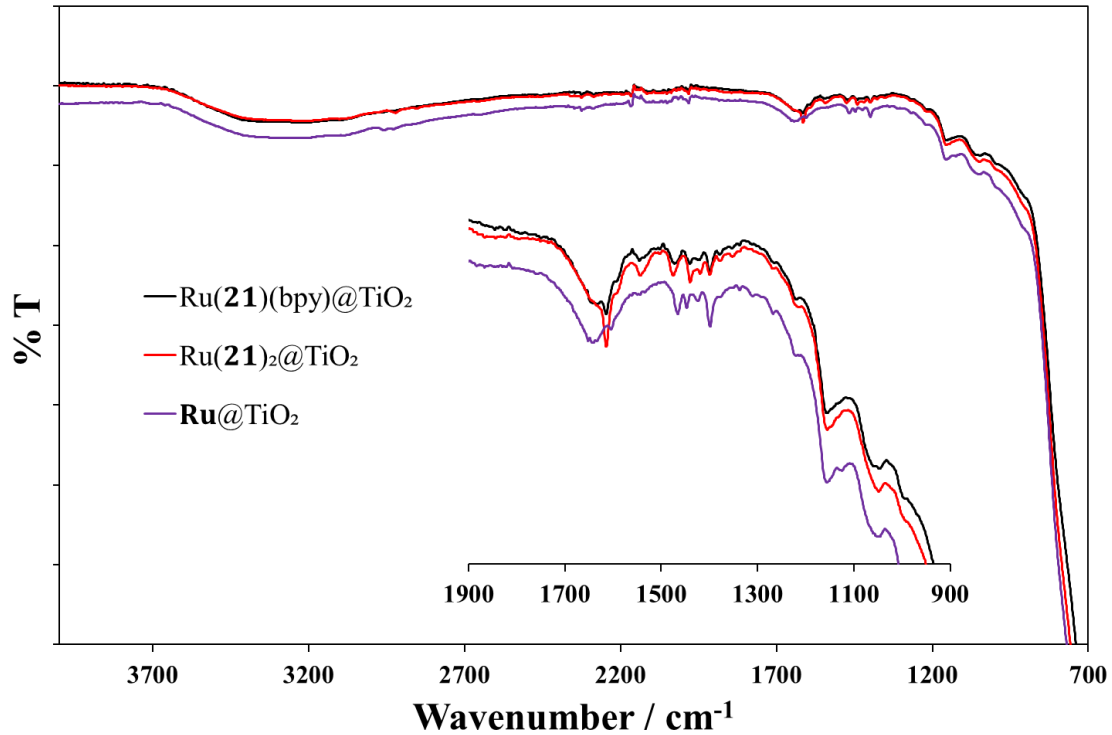
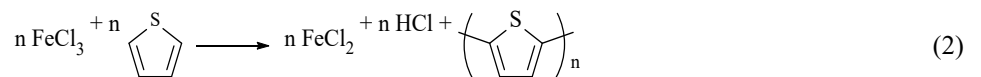


Figure 42: FTIR spectroscopy where black is Ru(21)(bpy)@TiO₂, red is Ru(21)₂@TiO₂ and violet is Ru@TiO₂.

9.2.2 9@TiO₂ NPs polymerization attempts using FeCl₃ or FeCl₃ and H₂O₂ in suspension



The literature reports various thiophene polymerization (Equation (2) and (3)) methods using FeCl₃ or FeCl₃ and H₂O₂ as oxidizers.^{212,213} The reaction conditions were adapted with the purpose of growing a polythienyl from the thiophene group of the NP-anchored ligand **21**. The f-NPs (Ru(21)(bpy)@TiO₂ and Ru(21)₂@TiO₂) were dispersed in a solution of thiophene in CHCl₃ then either an excess of FeCl₃ or FeCl₃ and H₂O₂ was added. The ratio of thiophene to NPs was determined by the estimated number of thiophene groups on the NP surface. In practise, when Ru(21)(bpy)@TiO₂ NPs were used half the equivalents of thiophene was used than with Ru(21)₂@TiO₂ NPs. The detailed reaction conditions are described in **Section 9.3.2** and **9.3.3**. However, using an excess of FeCl₃ as oxidant had almost no effect on the f-NPs while traces of FeCl₃ and H₂O₂ as oxidant seemed to deteriorate the functionalization.

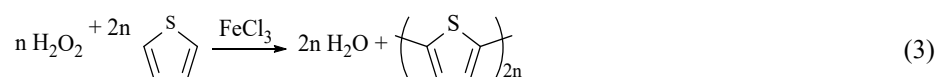


Table 10: TGA-MS data from f-NPs and polymerization attempts using either FeCl₃ or FeCl₃ and H₂O₂.

Entry	NP	30 – 380 °C / %	Mass found / amu	380 – 900 °C / %	Mass found / amu
1	Ru@TiO ₂	1.5	18, 44	3.5	18, 44
2	Ru(21)(bpy)@TiO ₂	1.5	18, 44	3.9	18, 44
3	Ru(21) ₂ @TiO ₂	1.1	18, 44	4.1	18, 44
4	Ru(21)(bpy)@TiO ₂ polymerization attempt, FeCl ₃	2.2	18, 44	3.7	18, 44
5	Ru(21)(bpy)@TiO ₂ polymerization attempt, FeCl ₃ , H ₂ O ₂	2.1	18, 44	2.0	18, 44
6	Ru(21) ₂ @TiO ₂ polymerization attempt, FeCl ₃	2.4	18, 44	4.6	18, 44
7	Ru(21) ₂ @TiO ₂ polymerization attempt, FeCl ₃ , H ₂ O ₂	2.1	18, 44	2.0	18, 44

The TGA measurements (Table 10) revealed that the weight loss generally increased in the lower temperature region (<380 °C) while the weight loss in the higher temperature region (380 – 900 °C) was slightly lower for Ru(21)(bpy)@TiO₂ and higher for Ru(21)₂@TiO₂ using only FeCl₃ as oxidant. Using FeCl₃ and H₂O₂ as oxidizing agent leads to lower weight loss in the high temperature region (see Table 10, entries 2, 3 vs 5, 7) which was most likely caused by either defunctionalization of the f-NPs or degradation of the surface bound complex.

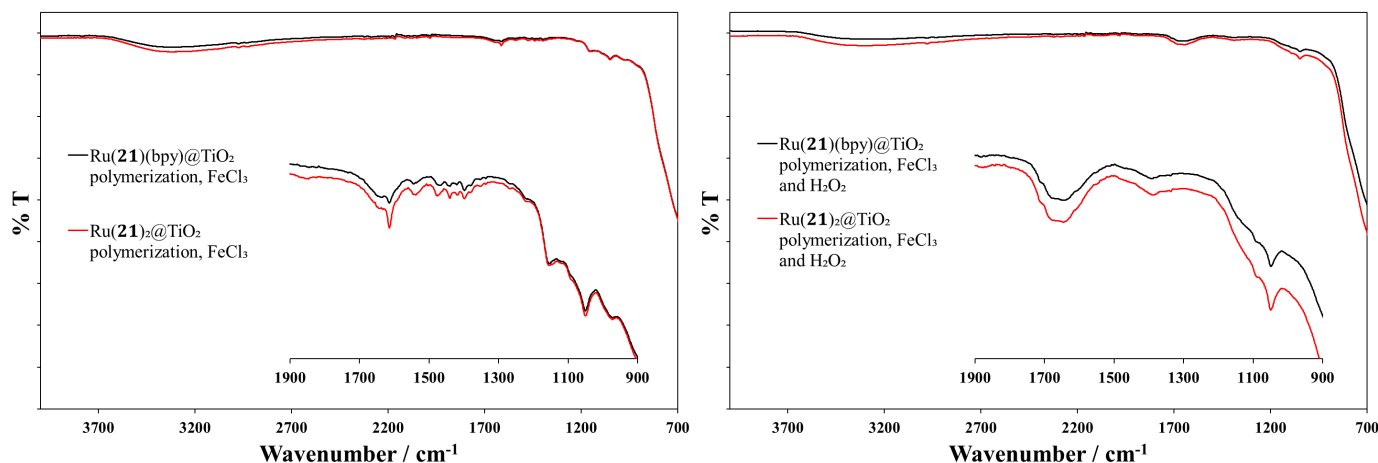


Figure 43: FTIR spectra of attempted polymerizations with FeCl₃ (left) or FeCl₃ and H₂O₂ (right) of Ru(21)(bpy)@TiO₂ NPs (black) or Ru(21)₂@TiO₂ NPs (red).

When comparing FTIR spectra of Ru(21)(bpy)@TiO₂ and Ru(21)₂@TiO₂ (Figure 42) with the NPs collected after the attempted polymerizations (Figure 43) there were almost no differences using only FeCl₃ as oxidant while FeCl₃ and H₂O₂ seemed to significantly alter the fingerprint within the spectra. Gauging differences and their effect of the rather plain FTIR spectra of f-NPs was, however, difficult as the FTIR spectra have only slight differences (Figure 43, left). It is difficult to establish if a polymerization occurred or whether the broadening in the fingerprint region (Figure 43, right) could be caused by defunctionalization or degradation, in accord with the TGA-MS results. Using only FeCl₃ as oxidant seemed not to modify the f-NPs in a major way while using FeCl₃ and H₂O₂ changed them significantly. A similar pattern was observed when comparing the NPs using solid-state absorption spectroscopy (Figure 44). Using FeCl₃ as oxidant, almost no changes were observed while using FeCl₃ and H₂O₂ showed significant changes in the 400 – 500 nm region.

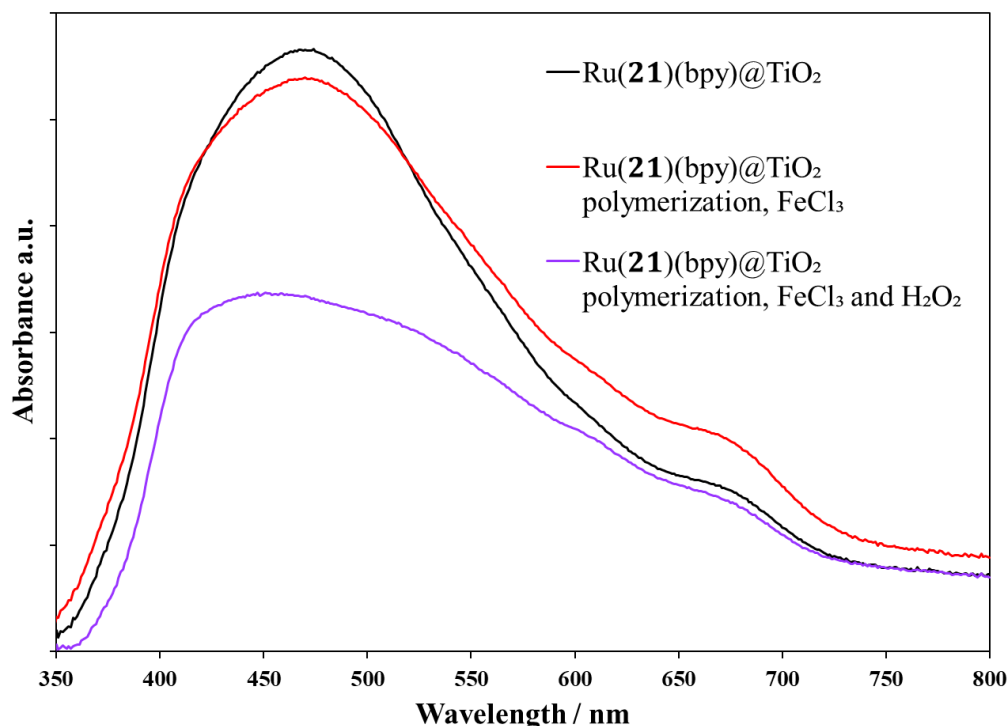
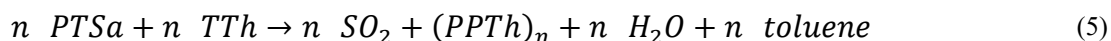


Figure 44: Solid-state absorption spectra where Ru(21)(bpy)@TiO₂ NPs (black), attempted polymerization of Ru(21)(bpy)@TiO₂ NPs using FeCl₃ as oxidant (red) and using FeCl₃ and H₂O₂ as oxidant (violet).

9.2.3 9@TiO₂ NPs vapour phase polymerization using FeCl₃ or PTSa

After the data from Section 9.2.2 were analysed, a different approach was followed. The idea was to move from solution-based functionalization to vapour phase polymerization (VPP). A literature protocol (see Equations (4) and (5)) using VPP with either FeCl₃ or PTSa as oxidant to polymerize TThs onto solid surfaces was modified for NPs.²¹⁴ Since NPs are a powder and not a solid block (as used in the literature), the sample preparation had to be considered. The NPs were dispersed in an oxidant solution of either FeCl₃ or PTSa (0.01 M, EtOH) and the suspension evaporated to give a relatively thin film on the inside of a flask. The use of FeCl₃ coloured the NPs. The flask was then connected to a vial containing TTh and kept in an oven for 22 h at 95 °C.



In addition to VPP with Ru(21)(bpy)@TiO₂, several control experiments were conducted. Detailed experimental descriptions are given in Section 9.3.4. Initial controls used commercial or activated NPs with either FeCl₃ or PTSa and on two different reaction scales. The controls were done to compare the effects of activation, functionalization and complexation on the polymerization. Further controls were performed using Ru@TiO₂ (prepared according to Chapter V) using the same reaction conditions and method. The polymerization procedure with commercial and activated NPs showed organic material being deposited on the NPs surface. It was important to further study if the thiophene groups in Ru(21)(bpy)@TiO₂ were beneficial to the process. Control experiments revealed that using FeCl₃ the NPs remained coloured even after washing (solid-state absorption spectroscopy, Figure 45, left). A control experiment using only Ru(21)(bpy)@TiO₂ and FeCl₃ with no TTh (Figure 45, green) was conducted to identify which absorptions stem only from the FeCl₃ derived colouration. This revealed that most absorptions were due to the use of FeCl₃ but the shape and intensity in certain regions were different. Solid-state absorption spectroscopy of the NPs after polymerization using PTSa

of Ru(21)(bpy)@TiO₂ NPs was vastly different than for the controls using a-NPs (Figure 45, right). Most absorptions observed for Ru(21)(bpy)@TiO₂ after polymerization were broadened compared to the starting NPs. Interestingly, when Ru@TiO₂ NPs were used the broadening did not occur and the effects of the FeCl₃ were less pronounced. Hence, the broadening could be an indication of a successful polymerization.

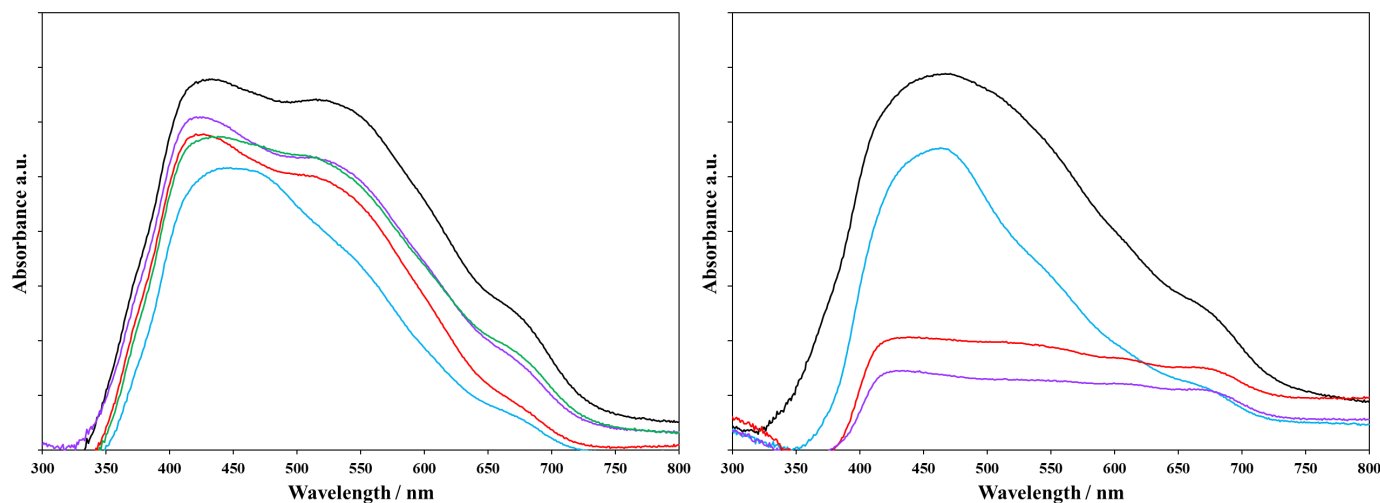


Figure 45: Solid-state absorption spectra of VPP reactions using TTh and either FeCl₃ (left) or PTSA (right) as oxidant, with Ru(21)(bpy)@TiO₂ NPs (black), a-NPs (red), a-NPs polymerized on a larger scale (violet), Ru@TiO₂ NPs (blue) and Ru(21)(bpy)@TiO₂ NPs without TTh (green).

The TGA measurements (Table 11) were in accord with polymerization. There was generally a larger weight loss recorded after the VPP within the low (<380 °C) and high (380 – 900 °C) temperature regions. When using Ru(21)(bpy)@TiO₂ NPs in the VPP with FeCl₃ (Figure 46, left) weight losses were 6.5% and 6.4% while with PTSA the weight losses were 1.8% and 4.4% for the low and high temperature regions respectively. Weight losses at and below 120 °C were assigned to amu 18 (H₂O) while weight losses from 120 – 380 °C and 380 – 900 °C contained amu 18 (H₂O) and 44 (CO₂). It is plausible that shorter chain polymers were able to bind to the surface causing the weight loss at lower temperatures. This was confirmed as the controls using only a-NPs, oxidant and TTh showed higher weight losses after the VPP (Table 11, entries 2 – 5, 7 – 9) especially when increasing the reaction scale (Figure 46, right).

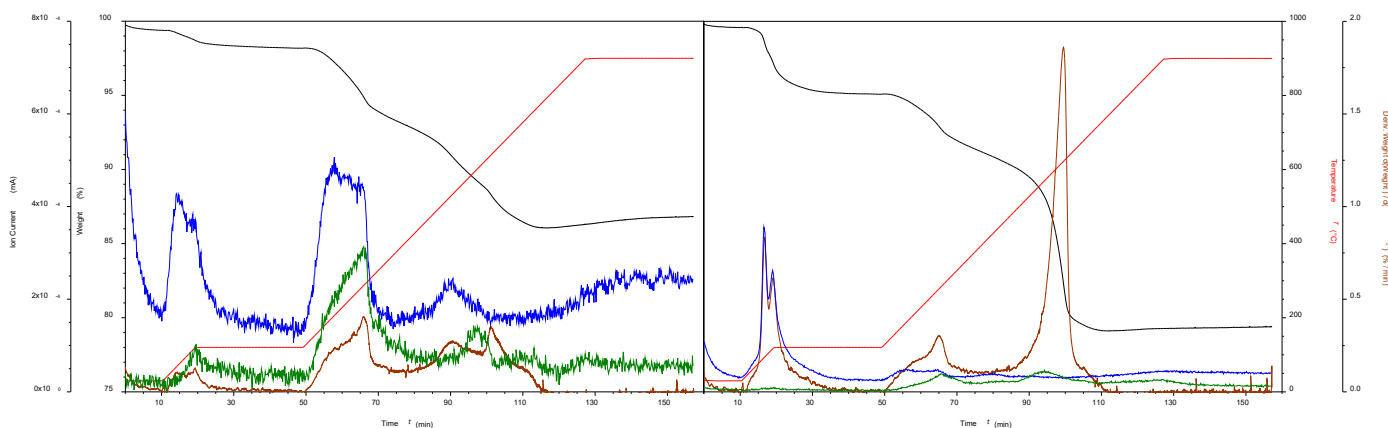


Figure 46: TGA-MS NPs after VPP using Ru(21)(bpy)@TiO₂ (left) using FeCl₃ and TTh and a-NPs using FeCl₃ and TTh in a larger reaction scale (right), where black is the weight loss, red is the temperature and brown is the derivative weight against time.

The increased weight loss in the low temperature region was associated with amu 18 and 44. The control performing VPP on a larger scale (5 times the general method, see Section 9.3.4) using a-NPs and FeCl₃ showed unusually high weight losses at 120 °C which was somewhat baffling as the NPs underwent a long

drying (24 – 72 h) under high vacuum. It must be noted that the largest weight loss (12.0%) in the high temperature region was measured with these NPs (Table 11, entry 4). This could mean linear scaling of the reaction conditions can lead to different results. A similar although less pronounced observation was made with a-NPs using PTSa (Table 11, entry 8) as oxidant. As the controls always showed polymerization (best indicated by the grey colour of PTSa polymerized a-NPs) occurring independent of the functionalization a longer or different washing method to remove this unwanted material would be very beneficial to better study the process.

Further results were gathered by testing the VPP with FeCl₃ or PTSa on **Ru@TiO₂**. If the polymerization occurred independently of the NP functionalization this sample should have shown a similar pattern as observed with Ru(**21**)(bpy)**@TiO₂**. Hence, the weight loss (Table 11, entries 5, 9) in the low temperature region (<380 °C) for both VPP using FeCl₃ or PTSa increased while the weight loss in the high temperature region (380 – 900 °C) was either lower when using FeCl₃ or higher when using PTSa. It has to be noted that ¹H NMR of these samples using PTSa as oxidant showed traces of the acid after the washing process which could contribute to the weight loss. The observation from the FeCl₃ polymerized NPs was promising and suggested that either the thiophene groups in Ru(**21**)(bpy)**@TiO₂** were beneficial to the overall polymerization process or a polymerization at the thiophene groups and chain elongation occurred.

Table 11: TGA-MS data of NPs after VPP using either FeCl₃ or PTSa as oxidant.

Entry	NP	30 – 380 °C / %	Mass found / amu	380 – 900 °C / %	Mass found / amu
1	Ru(21)(bpy) @TiO₂ VPP, FeCl ₃	6.5	18, 44	6.4	18, 44
2	Commercial NPs VPP, FeCl ₃	2.3	18, 44	1.0	18, 44
3	a-NPs VPP, FeCl ₃	2.8	18, 44	1.7	18, 44
4	a-NPs larger scale VPP, FeCl ₃	8.4	18, 44	12.0	18, 44
5	Ru@TiO₂ VPP, FeCl ₃	3.7	18, 44	3.2	18, 44
6	Ru(21)(bpy) @TiO₂ VPP, PTSa	1.8	18, 44	4.4	18, 44
7	a-NPs VPP, PTSa	1.6	18, 44	2.3	18, 44
8	a-NPs larger scale VPP, PTSa	2.5	18, 44	3.1	18, 44
9	Ru@TiO₂ VPP, PTSa	1.6	18, 44	4.5	18, 44

The FTIR spectra shown in Figure 47 depict material prepared using FeCl₃ (left) or PTSa (right). Both oxidants yielded similar spectra with most differences being in the intensity of peaks in the fingerprint region. Specifically, the measurements resulting from a-NPs polymerized at a larger scale showed disparities. For FeCl₃ (violet, left) the peaks at 3400 and 1600 cm⁻¹ were either new or increased in intensity and shifted while for PTSa (violet, right) peaks around 1150 cm⁻¹ increased in intensity. It must be noted that using FeCl₃ with Ru(**21**)(bpy)**@TiO₂** NPs without TTh leads to a slight decrease in intensity of the observed peaks within the fingerprint of the spectra (Figure 47, green). This was observed previously in solid-state absorption spectroscopy and is most likely due to FeCl₃ being adsorbed by the NP surface. Using **Ru@TiO₂** NPs as reaction

partner for the VPP resulted in broadened peaks (Figure 47, blue) compared to Ru(**21**)(bpy)@TiO₂ NPs (Figure 47, black) as reaction partner.

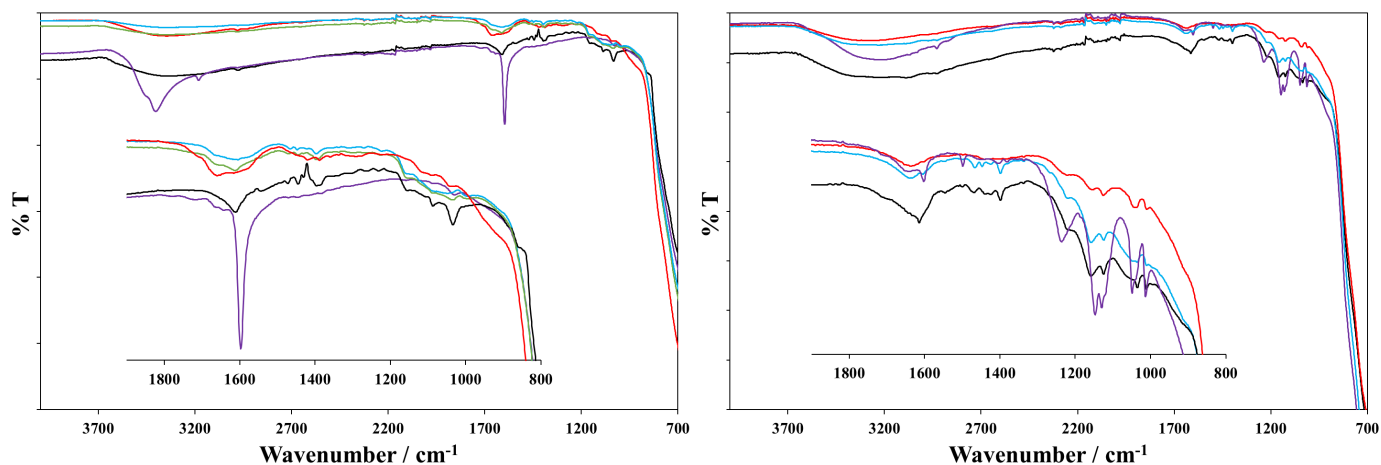


Figure 47: FTIR spectra of VPP reactions using TTh and either FeCl₃ (left) or PTSa (right) as oxidant, with Ru(**21**)(bpy)@TiO₂ NPs (black), a-NPs (red), a-NPs polymerized on a larger scale (violet), Ru@TiO₂ NPs (blue) and Ru(**21**)(bpy)@TiO₂ NPs without TTh (green).

9.3 Experimental

9.3.1 TiO₂ NPs complexation with bpy and ligand **21**

9@TiO₂ NPs (91.8 mg) were added into a vial with RuCl₃·3H₂O (2.0 mg, 7.9 μmol, 1.0 eq.), bpy (1.2 mg, 7.9 μmol, 1.0 eq.) and **21** (2.5 mg, 7.9 μmol, 1.0 eq.). H₂O (5.0 mL) and EtOH (3.0 mL) were added, and the mixture was dispersed using sonication (5 min) and shaking. The suspension was transferred into an autoclave with a PTFE liner with additional EtOH (2.0 mL). The autoclave was sealed and then heated in an oven with 320 °C/h to 160 °C. The autoclave was left at 160 °C for 1 h. After cooling down, the autoclave was opened and the suspension was centrifuged (20 min, 7000 rpm). The resulting NPs were washed with H₂O (3 × 10 mL) and EtOH (1 × 10 mL) and dried under high vacuum. Ru(**21**)(bpy)@TiO₂ NPs were isolated as ochre powder (92.1 mg, Figure 48 left). TGA: weight loss / %, 1.5 (<380 °C), 3.9 (380 – 900 °C). TGA-MS: amu, 18, 44 (<380 °C), 18, 44 (380 – 900 °C). FTIR spectroscopy: 3356, 3228, 3090, 1634, 1615, 1546, 1472, 1441, 1399, 1157 and 1048 cm⁻¹. Solid-state absorption spectroscopy: 430 – 520 and 660 – 700 (broad).



Figure 48: Dried Ru(**21**)(bpy)@TiO₂ (left) and Ru(**21**)₂@TiO₂ NPs (right).

The reaction was repeated using no bpy and double the amount of ligand **21** (5.0 mg, 16 μmol, 2.0 eq.) yielding Ru(**21**)₂@TiO₂ NPs (89.9 mg, Figure 48, right) as red orange powder. TGA: weight loss / %, 1.1 (<380 °C), 4.1 (380 – 900 °C). TGA-MS: amu, 18, 44 (<380 °C), 18, 44 (380 – 900 °C). FTIR spectroscopy: 3359, 3208, 3084, 2922, 2852, 1615, 1544, 1473, 1440, 1419, 1400, 1155 and 1049 cm⁻¹.

9.3.2 Attempt at thiophene surface polymerization using $FeCl_3$

$Ru(21)(bpy)@TiO_2$ NPs (46.0 mg) were added to a solution of thiophene (8.0 μ L, 0.10 mmol) in 2.5 mL $CHCl_3$. The suspension was dispersed through sonication and stirring (10 min). $FeCl_3$ (35.7 mg, 0.220 mmol) were added, and the suspension was stirred at room temperature for 72 h. The suspension was centrifuged (20 min, 7000 rpm) and washed with $CHCl_3$ (3×8 mL) and EtOH (3×8 mL). After drying the NPs under high vacuum, an ochre powder (44.3 mg, Figure 49, left) was obtained. TGA: weight loss / %, 2.2 (<380 $^{\circ}C$), 3.7 (380 – 900 $^{\circ}C$). TGA-MS: amu, 18, 44 (<380 $^{\circ}C$), 18, 44 (380 – 900 $^{\circ}C$). FTIR spectroscopy: 3310, 2975, 2929, 1638, 1615, 1543, 1467, 1440, 1397, 1379, 1153, 1050 and 953 cm^{-1} . Solid-state absorption spectroscopy: 410 – 520 and 660 – 700 (broad).



Figure 49: Dried $Ru(21)(bpy)@TiO_2$ (left) and $Ru(21)_2@TiO_2$ NPs (right) after polymerization attempt with $FeCl_3$.

The reaction was repeated using the same method with $Ru(21)_2@TiO_2$ NPs (46.0 mg), thiophene (16 μ L, 0.20 mmol) and $FeCl_3$ (71.4 mg, 0.440 mmol) yielding red orange NPs (42.5 mg, Figure 49, right). TGA: weight loss / %, 2.4 (<380 $^{\circ}C$), 4.6 (380 – 900 $^{\circ}C$). TGA-MS: amu, 18, 44 (<380 $^{\circ}C$), 18, 44 (380 – 900 $^{\circ}C$). FTIR spectroscopy: 3315, 3231, 2976, 2926, 1639, 1615, 1539, 1475, 1440, 1399, 1154 and 1053 cm^{-1} .

9.3.3 Attempt at thiophene surface polymerization using $FeCl_3$ and H_2O_2

$Ru(21)(bpy)@TiO_2$ NPs (37.0 mg) were added to a solution of thiophene (12.8 μ L, 0.100 mmol) in 3.0 mL H_2O . The suspension was dispersed through sonication and stirring (10 min). H_2O_2 (83.1 μ L, 0.880 mmol, 30% aqueous solution) and $FeCl_3$ (0.26 mg, 1.6 μ mol) were added, and the suspension was stirred at 50 $^{\circ}C$ for 15 h. The suspension was centrifuged (20 min, 7000 rpm) and washed with $CHCl_3$ (3×8 mL) and EtOH (3×8 mL). After drying the NPs under high vacuum, a pale red powder (34.3) was obtained. TGA: weight loss / %, 2.1 (<380 $^{\circ}C$), 2.0 (380 – 900 $^{\circ}C$). TGA-MS: amu, 18, 44 (<380 $^{\circ}C$), 18, 44 (380 – 900 $^{\circ}C$). FTIR spectroscopy: 3240, 2978, 2935, 1674, 1639, 1391 and 1047 cm^{-1} . Solid-state absorption spectroscopy: 410 – 580 (broad) and 660 – 710 nm (broad).



Figure 50: Dried $Ru(21)(bpy)@TiO_2$ (left) and $Ru(21)_2@TiO_2$ NPs (right) after polymerization attempt with $FeCl_3$ and H_2O_2 .

The reaction was repeated using the same method with Ru(**21**)₂@TiO₂ NPs (37.0 mg), thiophene (25.6 μ L, 0.200 mmol), H₂O₂ (166 μ L, 1.76 mmol, 30% aqueous solution) and FeCl₃ (0.52 mg, 3.2 μ mol) yielding a pale red powder (35.1 mg). TGA: weight loss / %, 2.1 (<380 °C), 2.0 (380 – 900 °C). TGA-MS: amu, 18, 44 (<380 °C), 18, 44 (380 – 900 °C). FTIR spectroscopy: 3275, 2978, 1657, 1647, 1389 and 1050 cm⁻¹.

9.3.4 Vapor-phase surface polymerization using TTh

Ru(**21**)(bpy)@TiO₂ (10 mg) was dispersed in FeCl₃ (3.8 mL, 0.01 M in EtOH) and was slowly evaporated to coat a 10 mL flask. The flask was dried under high vacuum for 30 min and then connected to a second flask with TTh (10.0 mg, 40.3 μ mol) and secured with a metal clamp. The setup was covered in an unsealed steel container and kept in an oven for 22 h at 95 °C. After cooling down the NPs were removed and washed with CHCl₃ (2 \times 10 mL) and EtOH (3 \times 10 mL). The NPs were dried under high vacuum yielding a dark red powder (8.8 mg, Figure 51, left). TGA: weight loss / %, 6.5 (<380 °C), 6.4 (380 – 900 °C). TGA-MS: amu, 18, 44 (<380 °C), 18, 44 (380 – 900 °C). FTIR spectroscopy: 3316, 2972, 1607, 1538, 1472, 1443, 1393, 1143, 1085 and 1032 cm⁻¹. Solid-state absorption spectroscopy: 410 – 450, 510 – 550 and 670 – 700 nm (broad). The reaction was repeated using p-toluene sulfonic acid (PTSa, 3.8 mL, 0.01 M in EtOH) instead of FeCl₃ (3.8 mL, 0.01 M in EtOH) yielding dark red NPs (9.3 mg, Figure 51, middle). TGA: weight loss / %, 1.8 (<380 °C), 4.4 (380 – 900 °C). TGA-MS: amu, 18, 44 (<380 °C), 18, 44 (380 – 900 °C). FTIR spectroscopy: 3230, 3079, 2957, 2928, 1614, 1545, 1470, 1426, 1400, 1220, 1157, 1125, 1035 and 1011 cm⁻¹. Solid-state absorption spectroscopy: 420 – 530, and 670 – 700 nm (broad).



Figure 51: Dried Ru(**21**)(bpy)@TiO₂ after VPP with TTh and FeCl₃ (left) and PTSa (middle), control reaction using commercial NPs, TTh and FeCl₃ (right).

Control reactions were performed using commercial NPs (10 mg) with FeCl₃ solution and TTh (10.0 mg, 40.3 μ mol) or a-NPs (10.0 mg) with either FeCl₃ solution or PTSa solution (3.8 mL, 0.01 M in EtOH) and TTh (10.0 mg, 40.3 μ mol). The control reactions were repeated on a larger scale using a-NPs (50.0 mg) and either FeCl₃ solution or PTSa solution (19.0 mL, 0.01 M in EtOH) as oxidant with TTh (50 mg, 0.20 mmol). Another control was performed using Ru@TiO₂ (10 mg) with either FeCl₃ solution or PTSa solution (3.8 mL, 0.01 M in EtOH) and TTh (10 mg, 40.3 μ mol). Control using commercial NPs and FeCl₃ yielded pale yellow NPs (9.3 mg, Figure 51, right): TGA: weight loss / %, 2.3 (<380 °C), 1.0 (380 – 900 °C). TGA-MS: amu, 18, 44 (<380 °C), 18, 44 (380 – 900 °C). FTIR spectroscopy: 3342, 1663, 1599, 1419, 1388, 1277, 1111 and 1038 cm⁻¹. Control using a-NPs and FeCl₃, lower scale yielded red NPs (9.1 mg, Figure 52, middle left): TGA: weight loss / %, 2.8 (<380 °C), 1.7 (380 – 900 °C). TGA-MS: amu, 18, 44 (<380 °C), 18, 44 (380 – 900 °C). FTIR spectroscopy: 3346, 2980, 2932, 1659, 1616, 1419, 1388, 1359, 1290, 1086 and 1038 cm⁻¹. Solid-state absorption spectroscopy: 410 – 440 and 520 – 550. Control using a-NPs and FeCl₃, larger scale yielded brown NPs (47.5 mg, Figure 52, left): TGA: weight loss / %, 8.4 (<380 °C), 12.0 (380 – 900 °C). TGA-MS: amu,

18, 44 (<380 °C), 18, 44 (380 – 900 °C). FTIR spectroscopy: 3447, 3403, 3179, 2978, 1719, 1655, 1598 and 1029 cm^{-1} . Solid-state absorption spectroscopy: 410 – 440, 520 – 560, and 680 – 700 nm (broad).

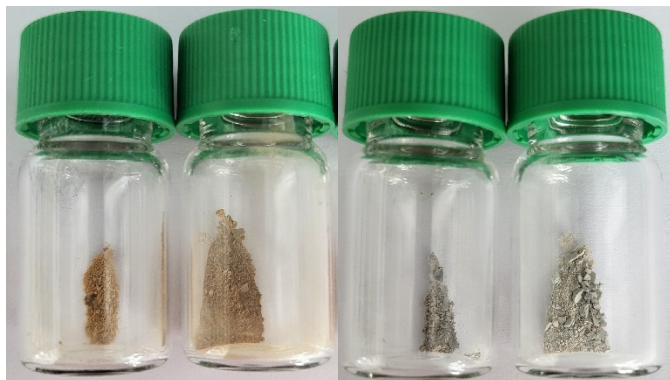


Figure 52: a-NPs after VPP with TTh using general and larger scale with FeCl_3 (left) or with PTSa (right).

Control using a-NPs and PTSa, lower scale yielding grey NPs (8.5 mg, Figure 52, middle right): TGA: weight loss / %, 1.6 (<380 °C), 2.3 (380 – 900 °C). TGA-MS: amu, 18, 44 (<380 °C), 18, 44 (380 – 900 °C). FTIR spectroscopy: 3261, 2980, 2931, 2635, 1661, 1439, 1218, 1154, 1125, 1038 and 1010 cm^{-1} . Solid-state absorption spectroscopy: 400 – 700 nm (broad). Control using a-NPs and PTSa, larger scale yielding grey NPs (46.1 mg, Figure 52, right): TGA: weight loss / %, 2.5 (<380 °C), 3.1 (380 – 900 °C). TGA-MS: amu, 18 (<380 °C), 18, 44 (380 – 900 °C). FTIR spectroscopy: 3220, 3069, 2930, 1639, 1602, 1498, 1443, 1402, 1380, 1236, 1146, 1130, 1049 and 1013 cm^{-1} . Solid-state absorption spectroscopy: 410 – 670 nm (broad).



Figure 53: $\text{Ru}(\mathbf{21})(\text{bpy})@\text{TiO}_2$ after VPP using FeCl_3 without TTh (left) and $\text{Ru}@\text{TiO}_2$ after VPP with TTh using FeCl_3 (middle) or PTSa (right).

Control using $\text{Ru}@\text{TiO}_2$ (10 mg) and FeCl_3 yielding orange NPs (8.7 mg, Figure 53, middle): TGA: weight loss / %, 3.7 (<380 °C), 3.1 (380 – 900 °C). TGA-MS: amu, 18, 44 (<380 °C), 18, 44 (380 – 900 °C). FTIR spectroscopy: 3327, 2976, 1603, 1466, 1446, 1398, 1311, 1270, 1220, 1148, 1074 and 1048 cm^{-1} . Solid-state absorption spectroscopy: 410 – 500, 530 – 560 (broad) and 660 – 670 nm (broad). Control using $\text{Ru}@\text{TiO}_2$ (10 mg) and PTSa yielding orange NPs (9.2 mg, Figure 53, right): TGA: weight loss / %, 3.7 (<380 °C), 3.2 (380 – 900 °C). TGA-MS: amu, 18, 44 (<380 °C), 18, 44 (380 – 900 °C). FTIR spectroscopy: 3233, 3083, 2973, 2926, 1634, 1603, 1465, 1446, 1426, 1399, 1219, 1159, 1123 and 1035 cm^{-1} . Solid-state absorption spectroscopy: 430 – 490 and 660 – 700 nm (broad). A further control reaction was performed using only $\text{Ru}(\mathbf{21})(\text{bpy})@\text{TiO}_2$ (10 mg) and FeCl_3 (3.8 mL, 0.01 M in EtOH) with no TTh in the attached vial yielding red NPs (8.9 mg, Figure 53, left). FTIR spectroscopy: 3308, 2976, 1649, 1610, 1469, 1446, 1396, 1224, 1192, 1080, 1033 and 994 cm^{-1} . Solid-state absorption spectroscopy: 410 – 480, 510 – 550 and 670 – 700 nm (broad).

9.4 Conclusion

In this Chapter, $\mathbf{9@TiO_2}$ NPs were used to prepare $\text{Ru}(\mathbf{21})(\text{bpy})@\text{TiO}_2$ or $\text{Ru}(\mathbf{21})_2@\text{TiO}_2$ NPs with 2-(thiophen-2-yl)-2,2'-bipyridine (**21**) and/or 2,2'-bipyridine (bpy) as ancillary ligands. Ligand **21** was selected with the aim of using the pendant thienyl groups to investigate solution or vapour polymerizations. Solution based polymerizations were conducted in CHCl_3 using thiophene as building block and FeCl_3 or FeCl_3 and H_2O_2 as oxidant. Characterization with TGA-MS, FTIR spectroscopy and solid-absorption spectroscopy showed that the solution polymerization was unsuccessful with either with $\text{Ru}(\mathbf{21})(\text{bpy})@\text{TiO}_2$ or $\text{Ru}(\mathbf{21})_2@\text{TiO}_2$ NPs. The project was more successful in using vapour phase polymerization (VPP) and with $\text{Ru}(\mathbf{21})(\text{bpy})@\text{TiO}_2$ NPs using either FeCl_3 or *p*-toluenesulfonic acid (PTSa) as oxidant and 2,2':5',2''-terthiophene (TTh) as building block. TGA-MS showed promising results with higher weight losses being recorded across the measurement indicating a polymerization. FTIR and solid-state absorption spectroscopy revealed a general broadening of peaks in the new f-NPs. FeCl_3 was determined to be more effective at polymerization but also problematic as the removal of the oxidant or side products after the reaction was not simple.

Several control experiments with both oxidants were conducted using commercial, activated or $\mathbf{Ru@TiO_2}$ NPs instead of $\text{Ru}(\mathbf{21})(\text{bpy})@\text{TiO}_2$ NPs under the same reaction conditions. Further controls included a larger scale VPP with a-NPs using TTh. The control using a-NPs, FeCl_3 and no TTh showed the presence of the oxidant or side products after VPP. Controls using TTh in the presence of an oxidant revealed additional organic material on the NP surface independent of surface functionalization. Measuring the NPs with TGA-MS after the larger scale reaction showed that linear scaling of the reaction conditions would lead to more organic material on NP surface. Improved purification methods to remove this material would be very beneficial to better study how and in what way thiophene groups of $\text{Ru}(\mathbf{21})(\text{bpy})@\text{TiO}_2$ NPs are involved in the polymerization.

The TGA-MS of NPs after VPP of $\mathbf{Ru@TiO_2}$ using FeCl_3 or PTSa as oxidant showed weight losses in the high temperature region (380 – 900 °C) that were either lower (FeCl_3) or higher (PTSa) compared to pure $\mathbf{Ru@TiO_2}$. ^1H NMR spectroscopy of extracts of samples using PTSa as oxidant showed traces of PTSa after washing process which could contribute to the weight loss. These observations suggest that either the thiophene groups in $\text{Ru}(\mathbf{21})(\text{bpy})@\text{TiO}_2$ were beneficial to the overall polymerization process or a polymerization at the thiophene groups of the metal complex occurred. Other results such as FTIR spectroscopy and solid-state absorptions spectroscopy are in accord with to this suggestion. Further experiments are however required to come to a definitive conclusion.

CHAPTER X: CONCLUSIONS

After introducing the thesis motivation and synthesis, functionalization and application of NPs in **Chapter I**, **Chapter II** summarized published work which investigated NP surface activation with HNO₃, and established functionalization methods with carboxylic acid or phosphonic acid anchoring ligands. Suitable characterization methods for TiO₂ NPs were found.¹⁷ The work in **Chapter II** was a cornerstone for subsequent Chapters of this thesis. **Chapter II** further studied the application of the SALSAC 'surface-as-ligand, surface-as-complex' method using several homoleptic copper(I) and iron(II) complexes with f-NPs.

Chapter III attempted to transfer literature homogeneous catalytic reactions onto TiO₂ f-NPs. It showed that in many cases, transferring reactions from homogeneous to heterogeneous conditions can bring new and unexpected challenges. Although the projects in **Chapter III** did not yield publishable results, they helped immensely in understanding the limitations of the systems, but more importantly, they aided the development of techniques for analysis of the NP-supported systems. The methods and lessons learned included (i) forming the metal complex catalyst directly on the NP surface instead of utilising an in-situ approach, (ii) testing metal-to-ligand ratios to optimize conditions, (iii) more cautiously considering the impact of different ligand functional groups, and (iv) moisture-sensitive reactions can be problematic when working with TiO₂ NPs.

Chapter IV summarized published work²³ which resulted from these lessons. Hence, a new catalysed reaction that could be performed in water and under air with a better chance of success using the NP platform was chosen. This project used stepwise synthesised Rh(3)₂@TiO₂ NPs as the catalyst to perform an alcohol oxidation with 1-phenylethanol. The Rh(3)₂@TiO₂ NPs were used to compare their catalytic activity in contrast to the homogeneous counterpart, [Rh(3)₂]Cl₃. It was confirmed that catalytic activity was not lost upon surface-binding. The stability of Rh(3)₂@TiO₂ NPs was remarkable as they were able to withstand reaction temperatures of up to 100 °C for 24 days without degradation. Reaction kinetics and recyclability of the NP-supported catalyst were followed using ¹H NMR spectroscopy.

In the published paper that comprises **Chapter V**,²⁵ the focus centres on a previously reported system for water reduction under simulated sunlight irradiation.²⁴ Lehn and Sauvage utilized [Ru(bpy)₃]²⁺ and [Rh(bpy)₃]³⁺ as photo- and electrocatalysts, K₂[PtCl₄] as catalyst to facilitate dihydrogen formation, bpy as a catalyst regenerative additive, triethanolamine as sacrificial electron donor and aqueous H₂SO₄ for pH adjustments to achieve photochemical water reductions. Once again, the homogeneous catalysts were replaced with a heterogeneous analogue anchored onto TiO₂ NPs. It was found that the ruthenium(II) and rhodium(III) metal complexes acting as photo- and electrocatalysts function almost twice as efficient in tandem when both metal complexes are functionalized onto the same TiO₂ NPs compared to using individual metal complex f-NPs (**Ru@TiO₂** or **Rh@TiO₂**). Using these ruthenium(II) and rhodium(III) metal complex f-NPs (**rR@TiO₂** NPs), greater efficiency for the immobilised systems over the previously reported homogeneous systems was demonstrated in terms of turnover number and frequency. The f-NPs were further able to withstand several reaction cycles, but they showed considerable losses in efficiency after 10 cycles (4 h each cycle). The study also tested the influence of individual components such as additive, pH, and catalyst within the system.

Chapter VI explored the same water reduction catalysis and metal complex preparation as described in **Chapter V** but using SrTiO₃ and BaTiO₃ NPs instead of TiO₂. The Chapter further investigated H₂O₂ surface activation compared to previous studies with HNO₃ activation. The commercial, acid or peroxide activated NPs were used to form bimetallic complexes with ruthenium(II) and rhodium(III) (**rR@SrTiO₃**, **rR@SrTiO₃-a**, **rR@SrTiO₃-OH** and **rR@BaTiO₃**, **rR@BaTiO₃-a**, **rR@BaTiO₃-OH**). It was found H₂O₂ activated metal complex NPs (**rR@BaTiO₃-OH** NPs and **rR@SrTiO₃-OH**) were inactive for water reduction. This result and the colour of the NPs indicated no successful formation of the desired photocatalytic metal complex on the surface. **rR@SrTiO₃-a** and **rR@BaTiO₃-a** NPs were both active during water reduction with **rR@SrTiO₃-a** being the most efficient while no activation of SrTiO₃ NPs was roughly 2/3 as efficient. The

project further tested the influence of pH during complexation with peroxide activated NPs and concluded that adjusting it can play a major role in this procedure. Both NPs created ($\mathbf{rR@SrTiO_3-OH-A}$, $\mathbf{rR@BaTiO_3-OH-A}$) resulted in active NPs while $\mathbf{rR@SrTiO_3-a}$ remained the most efficient, while underperforming with respect to the results gathered in **Chapter V**. Overall, it was concluded that $\mathbf{SrTiO_3}$ and $\mathbf{BaTiO_3}$ NPs may perform better than $\mathbf{TiO_2}$ NPs. However, the former are more expensive than $\mathbf{TiO_2}$ which is a disadvantage, and additional experiments are required to confirm if the added cost is justified. At present, parameters such as particle size have not been explored.

Chapter VII focused on functionalization of commercial $\mathbf{WO_3}$, $\mathbf{ZrO_2}$, $\mathbf{SnO_2}$, $\mathbf{TiO_2}$ and \mathbf{ZnO} NPs with anchoring ligands bearing phosphonic or carboxylic acids using methods established in **Chapter II**. The investigation included longer reaction times during functionalization and concluded that previous reaction times of 3 h were sufficient. Overall, successful functionalization was established with each type of metal oxide NPs, although the functionalization degree was rather limited in some cases. \mathbf{ZnO} NPs was especially complicated as these were sensitive to acids and problematic during regular TGA-MS experiments under $\mathbf{N_2}$. Anchoring ligand binding preferences were studied by carrying out ^1H NMR spectroscopy competition experiments concluding a better binding with phosphonic acid bearing anchors in most cases. Preliminary tests to complex these anchoring ligand f-NPs were made and gave coloured NPs. However, due to the rather low functionalization degree and time constraints no characterization was done with $\mathbf{WO_3}$ NPs and $\mathbf{SnO_2}$ NPs.

Chapter VIII took a closer look at ruthenium functionalized \mathbf{ZnO} ($\mathbf{Ru@uZnO}$) NPs which were an interesting material to work with. They were able to perform two catalytic reactions relatively well, namely the deuteration of bpy or 4'-aminobenzo-15-crown-5 (**12**), and the oxidation of 1-phenylethanol (**13**). However, the material characterization of $\mathbf{Ru@uZnO}$ NPs using TGA-MS was insufficient to fully characterize the material and further measurements are required to provide insights into the catalytic activity. In the case of the deuteration, control experiments using literature catalysts were performed and comparisons would put the efficiency of $\mathbf{Ru@uZnO}$ NPs in the deuteration of organic compounds somewhere in between Pd/C and PtO₂. When comparing the alcohol oxidation of **13** with the method used in **Chapter IV**, $\mathbf{Ru@uZnO}$ NPs slightly outperformed the earlier method in yield, but not efficiency. However, considering the cost of both catalysts, $\mathbf{Ru@uZnO}$ NPs appear to be a better choice.

In **Chapter IX**, f-NPs were used to prepare ruthenium complex functionalized NPs $\mathbf{Ru(21)(bpy)@TiO_2}$ or $\mathbf{Ru(21)_2@TiO_2}$ NPs with 2-(thiophen-2-yl)-2,2'-bipyridine (**21**) and/or 2,2'-bipyridine (bpy) as ancillary ligands. Ligand **21** was selected with the aim of using the pendant thienyl groups to investigate solution or vapour polymerizations. Solution-based polymerizations were conducted in $\mathbf{CHCl_3}$ using thiophene as a building block and $\mathbf{FeCl_3}$ or $\mathbf{FeCl_3}$ and $\mathbf{H_2O_2}$ as oxidants. Characterization showed that the polymerization was unsuccessful. The project was more successful in using vapour phase polymerization (VPP) and with $\mathbf{Ru(21)(bpy)@TiO_2}$ NPs using either $\mathbf{FeCl_3}$ or *p*-toluenesulfonic acid as oxidant and 2,2':5',2''-terthiophene (TTh) as a building block. TGA-MS showed promising results with higher weight losses being recorded indicating polymerization. $\mathbf{FeCl_3}$ was determined to be more effective for polymerization but it was also problematic since the removal of the oxidant or side products after the reaction was far from simple. Several control experiments with both oxidants were conducted using commercial, activated or $\mathbf{Ru@TiO_2}$ NPs instead of $\mathbf{Ru(21)(bpy)@TiO_2}$ NPs under the same reaction conditions. Further controls included a larger scale VPP with a-NPs using TTh. The results suggest that either the thiophene groups in $\mathbf{Ru(21)(bpy)@TiO_2}$ were beneficial to the overall polymerization process or a polymerization at the thiophene groups of the metal complex occurred. Further experiments are however required to come to a definitive conclusion.

SUPPLEMENTARY MATERIALS:

Supplementary materials and complete open data documentation for published work **Chapter II**, **Chapter IV** and **Chapter V** are linked here or can be found directly using the links:

<https://zenodo.org/record/6510796#.Y24QGS8w2X0>

<https://zenodo.org/record/6626665#.Y24QIS8w2X0>

<https://zenodo.org/record/7014339#.Y24PxC8w2X0>

REFERENCES

1. Schönhofer, E.; Bozic-Weber, B.; Martin, C.J.; Constable, E.C.; Housecroft, C.E.; Zampese, J.A. 'Surfaces-as-ligands, surfaces-as-complexes' strategies for copper(I) dye-sensitized solar cells. *Dyes and Pigm.* **2015**, *115*, 154-165, 10.1016/j.dyepig.2014.12.022.
2. Bozic-Weber, B.; Brauchli, S.Y.; Constable, E.C.; Furer, S.O.; Housecroft, C.E.; Malzner, F.J.; Wright, I.A.; Zampese, J.A. Improving the photoresponse of copper(i) dyes in dye-sensitized solar cells by tuning ancillary and anchoring ligand modules. *Dalton Trans.* **2013**, *42*, 12293-12308, 10.1039/C3DT51416A.
3. Spampinato, V.; Tuccitto, N.; Quici, S.; Calabrese, V.; Marletta, G.; Torrisi, A.; Licciardello, A. Functionalization of Oxide Surfaces by Terpyridine Phosphonate Ligands: Surface Reactions and Anchoring Geometry. *Langmuir* **2010**, *26*, 8400-8406, 10.1021/la9048314.
4. Redondo, A.H. Copper(I) polypyridine complexes. the sensitizers of the future for dye-sensitized solar cells (DSSCs). PhD Thesis, University of Basel, Basel, 2009.
5. Brunner, F.; Graber, S.; Baumgartner, Y.; Häussinger, D.; Prescimone, A.; Constable, E.C.; Housecroft, C.E. The effects of introducing sterically demanding aryl substituents in [Cu(N^N)(P^P)]⁺ complexes. *Dalton Trans.* **2017**, *46*, 6379-6391, 10.1039/C7DT00782E.
6. Wang, J.; Hanan, G.S. A Facile Route to Sterically Hindered and Non-Hindered 4'-Aryl-2,2':6',2''-Terpyridines. *Synlett* **2005**, *2005*, 1251-1254.
7. Zhang, D.; Telo, J.P.; Liao, C.; Hightower, S.E.; Clennan, E.L. Experimental and Computational Studies of Nuclear Substituted 1,1'-Dimethyl-2,2'-Bipyridinium Tetrafluoroborates. *J. Phys. Chem. A* **2007**, *111*, 13567-13574, 10.1021/jp074323u.
8. Maerker, G.; Case, F.H. The Synthesis of Some 4,4'-Disubstituted 2,2'-Bipyridines. *J. Am. Chem. Soc.* **1958**, *80*, 2745-2748, 10.1021/ja01544a042.
9. Han, W.-S.; Han, J.-K.; Kim, H.-Y.; Choi, M.J.; Kang, Y.-S.; Pac, C.; Kang, S.O. Electronic Optimization of Heteroleptic Ru(II) Bipyridine Complexes by Remote Substituents: Synthesis, Characterization, and Application to Dye-Sensitized Solar Cells. *Inorg. Chem.* **2011**, *50*, 3271-3280, 10.1021/ic101909e.
10. Norris, M.R.; Concepcion, J.J.; Glasson, C.R.K.; Fang, Z.; Lapidés, A.M.; Ashford, D.L.; Templeton, J.L.; Meyer, T.J. Synthesis of Phosphonic Acid Derivatized Bipyridine Ligands and Their Ruthenium Complexes. *Inorg. Chem.* **2013**, *52*, 12492-12501, 10.1021/ic4014976.
11. Montalti, M.; Wadhwa, S.; Kim, W.Y.; Kipp, R.A.; Schmechl, R.H. Luminescent Ruthenium(II) Bipyridyl-Phosphonic Acid Complexes: pH Dependent Photophysical Behavior and Quenching with Divalent Metal Ions. *Inorg. Chem.* **2000**, *39*, 76-84, 10.1021/ic991143t.
12. Mishra, A.; Pootrakulchote, N.; Fischer, M.K.R.; Klein, C.; Nazeeruddin, M.K.; Zakeeruddin, S.M.; Bäuerle, P.; Grätzel, M. Design and synthesis of a novel anchoring ligand for highly efficient thin film dye-sensitized solar cells. *Chem. Commun.* **2009**, 7146-7148, 10.1039/B912506J.
13. Kubas, G.J.; Monzyk, B.; Crumbliss, A.L. Tetrakis(Acetonitrile)Copper(I) Hexafluorophosphate. *Inorg. Synth.* **1979**, *90*-92, 10.1002/9780470132500.ch18.
14. Constable, E.C.; Lewis, J.; Liptrot, M.C.; Raithby, P.R. The coordination chemistry of 4'-phenyl-2,2':6', 2''-terpyridine; the synthesis, crystal and molecular structures of 4'-phenyl-2,2':6',2''-terpyridine and bis(4'-phenyl-2,2':6',2''-terpyridine)nickel(II) chloride decahydrate. *Inorganica Chim. Acta* **1990**, *178*, 47-54, 10.1016/S0020-1693(00)88132-3.
15. Lenis-Rojas, O.A.; Fernandes, A.R.; Roma-Rodrigues, C.; Baptista, P.V.; Marques, F.; Pérez-Fernández, D.; Guerra-Varela, J.; Sánchez, L.; Vázquez-García, D.; Torres, M.L.; et al. Heteroleptic mononuclear compounds of ruthenium(ii):

- synthesis, structural analyses, in vitro antitumor activity and in vivo toxicity on zebrafish embryos. *Dalton Trans.* **2016**, 45, 19127-19140, 10.1039/C6DT03591D.
16. Available online: <https://www.sigmaaldrich.com/CH/de/product/aldrich/718467>. (accessed on 14.11.2022).
 17. Freimann, S.A.; Zare, D.; Housecroft, C.E.; Constable, E.C. The SALSAC approach: comparing the reactivity of solvent-dispersed nanoparticles with nanoparticulate surfaces. *Nanoscale Adv.* **2020**, 2, 679-690, 10.1039/C9NA00488B.
 18. Software for the Integration of CCD Detector System Bruker Analytical X-ray Systems, Bruker axs, Madison, WI (after 2013). *Software for the Integration of CCD Detector System Bruker Analytical X-ray Systems, Bruker axs, Madison, WI (after 2013)*.
 19. Sheldrick, G. SHELXT - Integrated space-group and crystal-structure determination. *Acta Crystallogr., Sect. A: Found. Adv.* **2015**, 71, 3-8, 10.1107/S2053273314026370.
 20. Dolomanov, O.V.; Bourhis, L.J.; Gildea, R.J.; Howard, J.A.K.; Puschmann, H. OLEX2: a complete structure solution, refinement and analysis program. *J. Appl. Crystallogr.* **2009**, 42, 339-341, 10.1107/S0021889808042726.
 21. Sheldrick, G. Crystal structure refinement with SHELXL. *Acta Crystallogr., Sect. C: Struct. Chem.* **2015**, 71, 3-8, 10.1107/S2053229614024218.
 22. Macrae, C.F.; Sovago, I.; Cottrell, S.J.; Galek, P.T.A.; McCabe, P.; Pidcock, E.; Platings, M.; Shields, G.P.; Stevens, J.S.; Towler, M.; et al. Mercury 4.0: from visualization to analysis, design and prediction. *J. Appl. Crystallogr.* **2020**, 53, 226-235, 10.1107/S1600576719014092.
 23. Freimann, S.A.; Prescimone, A.; Housecroft, C.E.; Constable, E.C. Turning over on sticky balls: preparation and catalytic studies of surface-functionalized TiO₂ nanoparticles. *RSC Adv.* **2021**, 11, 5537-5547, 10.1039/D0RA09319J.
 24. Kirch, M.; Lehn, J.-M.; Sauvage, J.-P. Hydrogen Generation by Visible Light Irradiation of Aqueous Solutions of Metal Complexes. An approach to the photochemical conversion and storage of solar energy. *Helv. Chim. Acta* **1979**, 62, 1345-1384, 10.1002/hlca.19790620449.
 25. Freimann, S.A.; Housecroft, C.E.; Constable, E.C. Attraction in Action: Reduction of Water to Dihydrogen Using Surface-Functionalized TiO₂ Nanoparticles. *Nanomater.* **2022**, 12, doi:10.3390/nano12050789.
 26. Available online: <https://www.ipcc.ch/sr15/download/#full>. (accessed on 04.11.22).
 27. Available online: <https://www.metoffice.gov.uk/about-us/press-office/news/weather-and-climate/2022/2021-hadcrut5-wmo-temperature-statement>. (accessed on 04.11.22).
 28. Available online: <https://www.giss.nasa.gov/projects/impacts/>. (accessed on 04.11.22).
 29. Available online: <https://public.wmo.int/en/media/press-release/more-bad-news-planet-greenhouse-gas-levels-hit-new-highs>. (accessed on 04.11.22).
 30. Available online: https://library.wmo.int/doc_num.php?explnum_id=11352. (accessed on 04.11.22).
 31. Available online: <https://climate.nasa.gov/news/2865/a-degree-of-concern-why-global-temperatures-matter>. (accessed on 04.11.22).
 32. Raftery, A.E.; Zimmer, A.; Frierson, D.M.W.; Startz, R.; Liu, P. Less than 2 °C warming by 2100 unlikely. *Nat. Clim. Change* **2017**, 7, 637-641, 10.1038/nclimate3352.
 33. Solomon, S.; Plattner, G.-K.; Knutti, R.; Friedlingstein, P. Irreversible climate change due to carbon dioxide emissions. *Proc. Natl. Acad. Sci. U.S.A.* **2009**, 106, 1704-1709, 10.1073/pnas.0812721106.
 34. Fahlman, B.D. *Materials Chemistry*, 3 ed.; Springer: Dordrecht, 2018.
 35. Available online: https://en.wikipedia.org/wiki/File:Elemental_abundances.svg. (accessed on 11.11.22).
 36. Jeevanandam, J.; Barhoum, A.; Chan, Y.S.; Dufresne, A.; Danquah, M.K. Review on nanoparticles and nanostructured materials: history, sources, toxicity and regulations. *Beilstein J. Nanotechnol.* **2018**, 9, 1050-1074, 10.3762/bjnano.9.98.
 37. You, H.; Yang, S.; Ding, B.; Yang, H. Synthesis of colloidal metal and metal alloy nanoparticles for electrochemical energy applications. *Chem. Soc. Rev.* **2013**, 42, 2880-2904, 10.1039/C2CS35319A.

38. Auffan, M.; Rose, J.; Wiesner, M.R.; Bottero, J.-Y. Chemical stability of metallic nanoparticles: A parameter controlling their potential cellular toxicity in vitro. *Environ. Pollut.* **2009**, *157*, 1127-1133, 10.1016/j.envpol.2008.10.002.
39. Tahir, M.B.; Sohaib, M.; Sagir, M.; Rafique, M. Role of Nanotechnology in Photocatalysis. In *Encyclopedia of Smart Materials*, Olabi, A.-G., Ed.; Elsevier: Oxford, 2022; pp. 578-589.
40. Bahnemann, D.W. Ultrasmall Metal Oxide Particles: Preparation, Photophysical Characterization, and Photocatalytic Properties. *Isr. J. Chem.* **1993**, *33*, 115-136, 10.1002/ijch.199300017.
41. Anu Mary Ealia, S.; Saravanakumar, M.P. A review on the classification, characterisation, synthesis of nanoparticles and their application. *IOP Conf. Ser.: Mater. Sci. Eng.* **2017**, *263*, 032019, 10.1088/1757-899X/263/3/032019.
42. Jamkhande, P.G.; Ghule, N.W.; Bamer, A.H.; Kalaskar, M.G. Metal nanoparticles synthesis: An overview on methods of preparation, advantages and disadvantages, and applications. *J. Drug Deliv. Sci. Technol.* **2019**, *53*, 101174, 10.1016/j.jddst.2019.101174.
43. Available online: <https://www.acsmaterial.com/fullerene-c60.html>. (accessed on 04.11.22).
44. Bartelmess, J.; Giordani, S. Carbon nano-onions (multi-layer fullerenes): chemistry and applications. *Beilstein Journal of Nanotechnology* **2014**, *5*, 1980-1998, 10.3762/bjnano.5.207.
45. Kazemzadeh, H.; Mozafari, M. Fullerene-based delivery systems. *Drug Discov. Today* **2019**, *24*, 898-905, 10.1016/j.drudis.2019.01.013.
46. Murata, H.; Nakajima, Y.; Saitoh, N.; Yoshizawa, N.; Suemasu, T.; Toko, K. High-Electrical-Conductivity Multilayer Graphene Formed by Layer Exchange with Controlled Thickness and Interlayer. *Sci. Rep.* **2019**, *9*, 4068, 10.1038/s41598-019-40547-0.
47. Available online: https://commons.wikimedia.org/wiki/File:Eight_Allotropes_of_Carbon.png. (accessed on 11.11.22).
48. Available online: [https://commons.wikimedia.org/wiki/File:Colloidal_nanoparticle_of_lead_sulfide_\(selenide\)_with_complete_passivation.png](https://commons.wikimedia.org/wiki/File:Colloidal_nanoparticle_of_lead_sulfide_(selenide)_with_complete_passivation.png). (accessed on 11.11.22).
49. Available online: https://commons.wikimedia.org/wiki/File:Phospholipids_aqueous_solution_structures-ca.svg. (accessed on 11.11.22).
50. Wang, S.; McQuirk, C.M.; d'Aquino, A.; Mason, J.A.; Mirkin, C.A. Metal–Organic Framework Nanoparticles. *Adv. Mater.* **2018**, *30*, 1800202, 10.1002/adma.201800202.
51. Rytwo, G. Clay Minerals as an Ancient Nanotechnology: Historical Uses of Clay Organic Interactions, and Future Possible Perspectives. *MACLA revista de la sociedad española de mineralogía* **2008**, *9*, 15-17, 10.13140/2.1.4481.0884.
52. Heiligtag, F.J.; Niederberger, M. The fascinating world of nanoparticle research. *Mater. Today* **2013**, *16*, 262-271, 10.1016/j.mattod.2013.07.004.
53. Walter, P.; Welcomme, E.; Hallégot, P.; Zaluzec, N.J.; Deeb, C.; Castaing, J.; Veyssièrre, P.; Brénioux, R.; Lévêque, J.-L.; Tsoucaris, G. Early Use of PbS Nanotechnology for an Ancient Hair Dyeing Formula. *Nano Lett.* **2006**, *6*, 2215-2219, 10.1021/nl061493u.
54. Artioli, G.; Angelini, I.; Polla, A. Crystals and phase transitions in protohistoric glass materials. *Phase Transit.* **2008**, *81*, 233-252, 10.1080/01411590701514409.
55. Johnson-McDaniel, D.; Barrett, C.A.; Sharafi, A.; Salguero, T.T. Nanoscience of an Ancient Pigment. *J. Am. Chem. Soc.* **2013**, *135*, 1677-1679, 10.1021/ja310587c.
56. Leonhardt, U. Invisibility cup. *Nat. Photonics.* **2007**, *1*, 207-208, 10.1038/nphoton.2007.38.
57. Freestone, I.; Meeks, N.; Sax, M.; Higgitt, C. The Lycurgus Cup — A Roman nanotechnology. *Gold Bull.* **2007**, *40*, 270-277, 10.1007/BF03215599.
58. Available online: <https://www.flickr.com/photos/dandiffendale/30416460551>. (accessed on 11.11.22).
59. Available online: https://en.wikipedia.org/wiki/File:Actinolite_Portugal.jpg. (accessed on 11.11.22).
60. Available online: https://commons.wikimedia.org/wiki/File:Lycurgus_cup-_Dionysus.jpg. (accessed on 11.11.22).

61. Available online: https://commons.wikimedia.org/wiki/File:British_Museum_The_Lycurgus_Cup_02_15022019_4362.jpg. (accessed on 11.11.22).
62. Mie, G. Beiträge zur Optik trüber Medien, speziell kolloidaler Metallösungen. *Ann. Phys. (Leipzig)* **1908**, *330*, 377-445, 10.1002/andp.19083300302.
63. Bogner, A.; Jouneau, P.H.; Thollet, G.; Basset, D.; Gauthier, C. A history of scanning electron microscopy developments: Towards “wet-STEM” imaging. *Micron* **2007**, *38*, 390-401, 10.1016/j.micron.2006.06.008.
64. Talapin, D.V.; Shevchenko, E.V. Introduction: Nanoparticle Chemistry. *Chem. Rev.* **2016**, *116*, 10343-10345, 10.1021/acs.chemrev.6b00566.
65. Gilroy, K.D.; Ruditskiy, A.; Peng, H.-C.; Qin, D.; Xia, Y. Bimetallic Nanocrystals: Syntheses, Properties, and Applications. *Chem. Rev.* **2016**, *116*, 10414-10472, 10.1021/acs.chemrev.6b00211.
66. Rajput, N. Methods of Preparation of Nanoparticles - A Review. *J. Adv. Eng. Technol.* **2015**, *7*, 1806-1811.
67. Ullah, M.; Ali, M.E.; Hamid, S.B.A. Surfactant-assisted ball milling: A novel route to novel materials with controlled nanostructure-A review. *Rev. Adv. Mater. Sci.* **2014**, *37*, 1-14.
68. Saravanan, P.; Deepika, D.; Hsu, J.-H.; Vinod, V.T.P.; Černík, M.; Kamat, S.V. A surfactant-assisted high energy ball milling technique to produce colloidal nanoparticles and nanocrystalline flakes in Mn–Al alloys. *RSC Adv.* **2015**, *5*, 92406-92417, 10.1039/C5RA16550D.
69. Tavakoli, A.; Sohrabi, M.; Kargari, A. A review of methods for synthesis of nanostructured metals with emphasis on iron compounds. *Chem. Pap.* **2007**, *61*, 151-170, 10.2478/s11696-007-0014-7.
70. Seyedi, M.; Haratian, S.; Khaki, J.V. Mechanochemical Synthesis of Fe₂O₃ Nanoparticles. *Procedia Mater. Sci.* **2015**, *11*, 309-313, 10.1016/j.mspro.2015.11.093.
71. Chen, Y.; Soler, L.; Armengol-Profítos, M.; Xie, C.; Crespo, D.; Llorca, J. Enhanced photoproduction of hydrogen on Pd/TiO₂ prepared by mechanochemistry. *Appl. Catal., B* **2022**, *309*, 121275, 10.1016/j.apcatb.2022.121275.
72. Simakin, A.V.; Voronov, V.V.; Kirichenko, N.A.; Shafeev, G.A. Nanoparticles produced by laser ablation of solids in liquid environment. *Appl. Phys. A* **2004**, *79*, 1127-1132, 10.1007/s00339-004-2660-8.
73. Abou El-Nour, K.M.M.; Eftaiha, A.a.; Al-Warthan, A.; Ammar, R.A.A. Synthesis and applications of silver nanoparticles. *Arab. J. Chem.* **2010**, *3*, 135-140, 10.1016/j.arabjc.2010.04.008.
74. Ghorbani, H.R. A Review of Methods for Synthesis of Al Nanoparticles. *Orient. J. Chem.* **2014**, *30*, 1941-1949, <http://dx.doi.org/10.13005/ojc/300456>.
75. Levoska, J.; Tyunina, M.; Leppävuori, S. Laser ablation deposition of silicon nanostructures. *Nanostruct. Mater.* **1999**, *12*, 101-106, 10.1016/S0965-9773(99)00074-4.
76. Swihart, M.T. Vapor-phase synthesis of nanoparticles. *Curr. Opin. Colloid Interface Sci.* **2003**, *8*, 127-133, 10.1016/S1359-0294(03)00007-4.
77. Chandra, R.; Chawla, A.K.; Ayyub, P. Optical and Structural Properties of Sputter-Deposited Nanocrystalline Cu₂O Films: Effect of Sputtering Gas. *J. Nanosci. Nanotechnol.* **2006**, *6*, 1119-1123, 10.1166/jnn.2006.176.
78. Hawkes, P.W. *Advances in imaging and electron physics*, 1 ed.; Academic Press, Elsevier: Radarweg 29, Amsterdam, Netherlands, 2010; Volume 164.
79. Available online: <https://www.asml.com/en/technology/lithography-principles>. (accessed on 07.11.22).
80. Available online: <https://www.asml.com/en/products/euv-lithography-systems>. (accessed on 07.11.22).
81. Available online: <https://www.asml.com/en/investors/annual-report>. (accessed on 07.11.22).
82. Hulteen, J.C.; Treichel, D.A.; Smith, M.T.; Duval, M.L.; Jensen, T.R.; Van Duyne, R.P. Nanosphere Lithography: Size-Tunable Silver Nanoparticle and Surface Cluster Arrays. *J. Phys. Chem. B* **1999**, *103*, 3854-3863, 10.1021/jp9904771.

83. Hufschmid, R.; Arami, H.; Ferguson, R.M.; Gonzales, M.; Teeman, E.; Brush, L.N.; Browning, N.D.; Krishnan, K.M. Synthesis of phase-pure and monodisperse iron oxide nanoparticles by thermal decomposition. *Nanoscale* **2015**, *7*, 11142-11154, 10.1039/C5NR01651G.
84. Odularu, A.T. Metal Nanoparticles: Thermal Decomposition, Biomedical Applications to Cancer Treatment, and Future Perspectives. *Bioinorg. Chem. Appl.* **2018**, *2018*, 9354708, 10.1155/2018/9354708.
85. Chen, S.-C.; Hsieh, D.-H.; Jiang, H.; Liao, Y.-K.; Lai, F.-I.; Chen, C.-H.; Luo, C.W.; Juang, J.-Y.; Chueh, Y.-L.; Wu, K.-H.; et al. Growth and characterization of Cu(In,Ga)Se₂ thin films by nanosecond and femtosecond pulsed laser deposition. *Nanoscale Res. Lett.* **2014**, *9*, 280, 10.1186/1556-276X-9-280.
86. Pandey, P.A.; Bell, G.R.; Rourke, J.P.; Sanchez, A.M.; Elkin, M.D.; Hickey, B.J.; Wilson, N.R. Physical Vapor Deposition of Metal Nanoparticles on Chemically Modified Graphene: Observations on Metal–Graphene Interactions. *Small* **2011**, *7*, 3202-3210, 10.1002/sml.201101430.
87. Adachi, M.; Tsukui, S.; Okuyama, K. Nanoparticle Synthesis by Ionizing Source Gas in Chemical Vapor Deposition. *Jpn. J. Appl. Phys.* **2003**, *42*, L77, 10.1143/JJAP.42.L77.
88. Huang, G.; Lu, C.-H.; Yang, H.-H. Chapter 3 - Magnetic Nanomaterials for Magnetic Bioanalysis. In *Novel Nanomaterials for Biomedical, Environmental and Energy Applications*, Wang, X., Chen, X., Eds.; Elsevier: 2019; pp. 89-109.
89. Ghawade, S.P.; Pande, K.N.; Dhoble, S.J.; Deshmukh, A.D. 11 - Tuning the properties of ZnS semiconductor by the addition of graphene. In *Nanoscale Compound Semiconductors and their Optoelectronics Applications*, Pawade, V.B., Dhoble, S.J., Swart, H.C., Eds.; Woodhead Publishing: 2022; pp. 351-381.
90. Ong, W.-J.; Tan, L.-L.; Chai, S.-P.; Yong, S.-T.; Mohamed, A.R. Highly reactive {001} facets of TiO₂-based composites: synthesis, formation mechanism and characterization. *Nanoscale* **2014**, *6*, 1946-2008, 10.1039/C3NR04655A.
91. Xiang, Q.; Yu, J.; Jaroniec, M. Graphene-based semiconductor photocatalysts. *Chem. Soc. Rev.* **2012**, *41*, 782-796, 10.1039/C1CS15172J.
92. Farha, O.K.; Hupp, J.T. Rational Design, Synthesis, Purification, and Activation of Metal–Organic Framework Materials. *Acc. Chem. Res.* **2010**, *43*, 1166-1175, 10.1021/ar1000617.
93. Xia, Y.; Gilroy, K.D.; Peng, H.-C.; Xia, X. Seed-Mediated Growth of Colloidal Metal Nanocrystals. *Angew. Chem., Int. Ed. Engl.* **2017**, *56*, 60-95, 10.1002/anie.201604731.
94. Patarroyo, J.; Delgado, J.A.; Merkoçi, F.; Genç, A.; Sauthier, G.; Llorca, J.; Arbiol, J.; Bastus, N.G.; Godard, C.; Claver, C.; et al. Hollow PdAg-CeO₂ heterodimer nanocrystals as highly structured heterogeneous catalysts. *Sci. Rep.* **2019**, *9*, 18776, 10.1038/s41598-019-55105-x.
95. Ghaffarian, H.R.; Saiedi, M.; Sayyadnejad, M.A.; Rashidi, A.M. Synthesis of ZnO Nanoparticles by Spray Pyrolysis Method. *Iran. J. Chem. Chem. Eng.* **2011**, *30*, 1-6, 10.30492/ijcce.2011.6250.
96. Petri Ahonen, P.; Joutsensaari, J.; Richard, O.; Tapper, U.; P. Brown, D.; K. Jokiniemi, J.; I. Kauppinen, E. Mobility size development and the crystallization path during aerosol decomposition synthesis of TiO₂ particles. *J. Aerosol Sci.* **2001**, *32*, 615-630, 10.1016/S0021-8502(00)00107-5.
97. Deplanche, K.; Caldeleri, I.; Mikheenko, I.P.; Sargent, F.; Macaskie, L.E. Involvement of hydrogenases in the formation of highly catalytic Pd(0) nanoparticles by bioreduction of Pd(II) using Escherichia coli mutant strains. *Microbiology* **2010**, *156*, 2630-2640, 10.1099/mic.0.036681-0.
98. Kalimuthu, K.; Suresh Babu, R.; Venkataraman, D.; Bilal, M.; Gurunathan, S. Biosynthesis of silver nanocrystals by Bacillus licheniformis. *Colloids Surf. B* **2008**, *65*, 150-153, 10.1016/j.colsurfb.2008.02.018.
99. Nikolaos, P.; Louise, E.H. Biological Synthesis of Metallic Nanoparticles by Bacteria, Fungi and Plants. *J. Nanomed. Nanotechnol.* **2014**, *05*, 10.4172/2157-7439.1000233.
100. Ahmad, A.; Mukherjee, P.; Senapati, S.; Mandal, D.; Khan, M.I.; Kumar, R.; Sastry, M. Extracellular biosynthesis of silver nanoparticles using the fungus Fusarium oxysporum. *Colloids Surf. B* **2003**, *28*, 313-318, 10.1016/S0927-7765(02)00174-1.

101. Kuppusamy, P.; Yusoff, M.M.; Maniam, G.P.; Govindan, N. Biosynthesis of metallic nanoparticles using plant derivatives and their new avenues in pharmacological applications – An updated report. *Saudi Pharm. J.* **2016**, *24*, 473-484, 10.1016/j.jsps.2014.11.013.
102. Irvani, S. Green synthesis of metal nanoparticles using plants. *Green Chem.* **2011**, *13*, 2638-2650, 10.1039/C1GC15386B.
103. Furneaux, R.C.; Rigby, W.R.; Davidson, A.P. The formation of controlled-porosity membranes from anodically oxidized aluminium. *Nature* **1989**, *337*, 147-149, 10.1038/337147a0.
104. Dikumar, A.I.; Globa, P.G.; Belevskii, S.S.; Sidel'nikova, S.P. On limiting rate of dimensional electrodeposition at meso- and nanomaterial manufacturing by template synthesis. *Surf. Eng. Appl. Electrochem.* **2009**, *45*, 171-179, 10.3103/S1068375509030016.
105. Mohanty, U.S. Electrodeposition: a versatile and inexpensive tool for the synthesis of nanoparticles, nanorods, nanowires, and nanoclusters of metals. *J. Appl. Electrochem.* **2011**, *41*, 257-270, 10.1007/s10800-010-0234-3.
106. Wang, B.; Zhuang, X.; Deng, W.; Cheng, B. Microwave-Assisted Synthesis of Silver Nanoparticles in Alkaline Carboxymethyl Chitosan Solution. *Engineering* **2010**, *02*, 387-390, 10.4236/eng.2010.25050.
107. Ali, A.; Zafar, H.; Zia, M.; ul Haq, I.; Phull, A.R.; Ali, J.S.; Hussain, A. Synthesis, characterization, applications, and challenges of iron oxide nanoparticles. *Nanotechnol., Sci. Appl.* **2016**, *9*, 49.
108. Seku, K.; Kishore Kumar, K.; Narasimha, G.; Bhagavanth Reddy, G. Chapter 7 - Bio-mediated synthesis of silver nanoparticles via microwave-assisted technique and their biological applications. In *Green Synthesis of Silver Nanomaterials*, Abd-Elsalam, K.A., Ed.; Elsevier: 2022; pp. 149-188.
109. Bang, J.H.; Suslick, K.S. Applications of Ultrasound to the Synthesis of Nanostructured Materials. *Adv. Mater.* **2010**, *22*, 1039-1059, 10.1002/adma.200904093.
110. Dalodière, E.; Virost, M.; Morosini, V.; Chave, T.; Dumas, T.; Hennig, C.; Wiss, T.; Dieste Blanco, O.; Shuh, D.K.; Tylliszczak, T.; et al. Insights into the sonochemical synthesis and properties of salt-free intrinsic plutonium colloids. *Sci. Rep.* **2017**, *7*, 43514, 10.1038/srep43514.
111. Philippot, G.; Elissalde, C.; Maglione, M.; Aymonier, C. Supercritical fluid technology: A reliable process for high quality BaTiO₃ based nanomaterials. *Adv. Powder Technol.* **2014**, *25*, 1415-1429, 10.1016/j.apt.2014.02.016.
112. Thiruppathi, R.; Mishra, S.; Ganapathy, M.; Padmanabhan, P.; Gulyás, B. Nanoparticle Functionalization and Its Potentials for Molecular Imaging. *Adv. Sci.* **2017**, *4*, 1600279, 10.1002/advs.201600279.
113. Ahmad, F.; Salem-Bekhit, M.M.; Khan, F.; Alshehri, S.; Khan, A.; Ghoneim, M.M.; Wu, H.-F.; Taha, E.I.; Elbagory, I. Unique Properties of Surface-Functionalized Nanoparticles for Bio-Application: Functionalization Mechanisms and Importance in Application. *Nanomater.* **2022**, *12*, doi:10.3390/nano12081333.
114. Bei, H.P.; Yang, Y.; Zhang, Q.; Tian, Y.; Luo, X.; Yang, M.; Zhao, X. Graphene-Based Nanocomposites for Neural Tissue Engineering. *Molecules* **2019**, *24*, doi:10.3390/molecules24040658.
115. Sanità, G.; Carrese, B.; Lamberti, A. Nanoparticle Surface Functionalization: How to Improve Biocompatibility and Cellular Internalization. *Front. Mol. Biosci.* **2020**, *7*, 10.3389/fmolb.2020.587012.
116. Kango, S.; Kalia, S.; Celli, A.; Njuguna, J.; Habibi, Y.; Kumar, R. Surface modification of inorganic nanoparticles for development of organic-inorganic nanocomposites—A review. *Prog. Polym. Sci.* **2013**, *38*, 1232-1261, 10.1016/j.progpolymsci.2013.02.003.
117. Hood, M.A.; Mari, M.; Muñoz-Espí, R. Synthetic Strategies in the Preparation of Polymer/Inorganic Hybrid Nanoparticles. *Materials* **2014**, *7*, 4057-4087, doi:10.3390/ma7054057.
118. Conde, J.; Dias, J.T.; Grazú, V.; Moros, M.; Baptista, P.V.; de la Fuente, J.M. Revisiting 30 years of biofunctionalization and surface chemistry of inorganic nanoparticles for nanomedicine. *Front. Chem.* **2014**, *2*, 10.3389/fchem.2014.00048.
119. Wagner, C.S.; Shehata, S.; Henzler, K.; Yuan, J.; Wittmann, A. Towards nanoscale composite particles of dual complexity. *J. Colloid Interface Sci.* **2011**, *355*, 115-123, 10.1016/j.jcis.2010.12.017.

120. Zhan, J.; Lei, Z.; Zhang, Y. Non-covalent interactions of graphene surface: Mechanisms and applications. *Chem* **2022**, *8*, 947-979, 10.1016/j.chempr.2021.12.015.
121. Clark, S.L.; Hammond, P.T. Engineering the Microfabrication of Layer-by-Layer Thin Films. *Adv. Mater.* **1998**, *10*, 1515-1519, 10.1002/(SICI)1521-4095(199812)10:18<1515::AID-ADMA1515>3.0.CO;2-E.
122. Sukhorukov, G.B.; Donath, E.; Lichtenfeld, H.; Knippel, E.; Knippel, M.; Budde, A.; Möhwald, H. Layer-by-layer self assembly of polyelectrolytes on colloidal particles. *Colloids Surf. A: Physicochem. Eng. Asp.* **1998**, *137*, 253-266, 10.1016/S0927-7757(98)00213-1.
123. Caruso, F.; Caruso, R.A.; Möhwald, H. Nanoengineering of Inorganic and Hybrid Hollow Spheres by Colloidal Templating. *Science* **1998**, *282*, 1111-1114, 10.1126/science.282.5391.1111.
124. Takahashi, H.; Niidome, T.; Kawano, T.; Yamada, S.; Niidome, Y. Surface modification of gold nanorods using layer-by-layer technique for cellular uptake. *J. Nanoparticle Res.* **2008**, *10*, 221-228, 10.1007/s11051-007-9227-5.
125. Nakamura, M.; Katagiri, K.; Koumoto, K. Preparation of hybrid hollow capsules formed with Fe₃O₄ and polyelectrolytes via the layer-by-layer assembly and the aqueous solution process. *J. Colloid Interface Sci.* **2010**, *341*, 64-68, 10.1016/j.jcis.2009.09.014.
126. Wu, P.; Zhang, H.; Du, N.; Ruan, L.; Yang, D. A Versatile Approach for the Synthesis of ZnO Nanorod-Based Hybrid Nanomaterials via Layer-by-Layer Assembly. *J. Phys. Chem. C* **2009**, *113*, 8147-8151, 10.1021/jp901896u.
127. Sperling, R.A.; Parak, W.J. Surface modification, functionalization and bioconjugation of colloidal inorganic nanoparticles. *Philos. Trans. Royal Soc.* **2010**, *368*, 1333-1383, 10.1098/rsta.2009.0273.
128. Jiang, S.; Chen, Q.; Tripathy, M.; Luijten, E.; Schweizer, K.S.; Granick, S. Janus Particle Synthesis and Assembly. *Adv. Mater.* **2010**, *22*, 1060-1071, 10.1002/adma.200904094.
129. Plueddemann, E.P. Adhesion Through Silane Coupling Agents. In *Fundamentals of Adhesion*, Lee, L.-H., Ed.; Springer US: Boston, MA, 1991; pp. 279-290.
130. Ukaji, E.; Furusawa, T.; Sato, M.; Suzuki, N. The effect of surface modification with silane coupling agent on suppressing the photo-catalytic activity of fine TiO₂ particles as inorganic UV filter. *Appl. Surf. Sci.* **2007**, *254*, 563-569, 10.1016/j.apsusc.2007.06.061.
131. Tang, E.; Liu, H.; Sun, L.; Zheng, E.; Cheng, G. Fabrication of zinc oxide/poly(styrene) grafted nanocomposite latex and its dispersion. *Eur. Polym. J.* **2007**, *43*, 4210-4218, 10.1016/j.eurpolymj.2007.05.015.
132. Galoppini, E. Linkers for anchoring sensitizers to semiconductor nanoparticles. *Coord. Chem. Rev.* **2004**, *248*, 1283-1297, 10.1016/j.ccr.2004.03.016.
133. Macchione, M.A.; Biglione, C.; Strumia, M. Design, Synthesis and Architectures of Hybrid Nanomaterials for Therapy and Diagnosis Applications. *Polymers* **2018**, *10*, doi:10.3390/polym10050527.
134. Tchoul, M.N.; Fillery, S.P.; Koerner, H.; Drummy, L.F.; Oyerokun, F.T.; Mirau, P.A.; Durstock, M.F.; Vaia, R.A. Assemblies of Titanium Dioxide-Polystyrene Hybrid Nanoparticles for Dielectric Applications. *Chem. Mater.* **2010**, *22*, 1749-1759, 10.1021/cm903182n.
135. Fu, R.; Fu, G.-D. Polymeric nanomaterials from combined click chemistry and controlled radical polymerization. *Polym. Chem.* **2011**, *2*, 465-475, 10.1039/C0PY00174K.
136. Rosilo, H.; Kontturi, E.; Seitsonen, J.; Kolehmainen, E.; Ikkala, O. Transition to Reinforced State by Percolating Domains of Intercalated Brush-Modified Cellulose Nanocrystals and Poly(butadiene) in Cross-Linked Composites Based on Thiol-ene Click Chemistry. *Biomacromolecules* **2013**, *14*, 1547-1554, 10.1021/bm400185z.
137. Agrawal, M.; Rubio-Retama, J.; Zafeiropoulos, N.E.; Gaponik, N.; Gupta, S.; Cimrova, V.; Lesnyak, V.; López-Cabarcos, E.; Tzavalas, S.; Rojas-Reyna, R.; et al. Switchable Photoluminescence of CdTe Nanocrystals by Temperature-Responsive Microgels. *Langmuir* **2008**, *24*, 9820-9824, 10.1021/la801347d.
138. Krovi, S.A.; Smith, D.; Nguyen, S.T. "Clickable" polymer nanoparticles: a modular scaffold for surface functionalization. *Chem. Commun.* **2010**, *46*, 5277-5279, 10.1039/C0CC00232A.

139. Sidorenko, A.; Minko, S.; Gafijchuk, G.; Voronov, S. Radical Polymerization Initiated from a Solid Substrate. 3. Grafting from the Surface of an Ultrafine Powder. *Macromolecules* **1999**, *32*, 4539-4543, 10.1021/ma981355u.
140. Wang, X.; Song, X.; Lin, M.; Wang, H.; Zhao, Y.; Zhong, W.; Du, Q. Surface initiated graft polymerization from carbon-doped TiO₂ nanoparticles under sunlight illumination. *Polymer* **2007**, *48*, 5834-5838, 10.1016/j.polymer.2007.08.017.
141. Rong, M.Z.; Zhang, M.Q.; Wang, H.B.; Zeng, H.M. Surface modification of magnetic metal nanoparticles through irradiation graft polymerization. *Appl. Surf. Sci.* **2002**, *200*, 76-93, 10.1016/S0169-4332(02)00620-7.
142. Fan, X.; Lin, L.; Messersmith, P.B. Surface-initiated polymerization from TiO₂ nanoparticle surfaces through a biomimetic initiator: A new route toward polymer–matrix nanocomposites. *Compos. Sci. Technol.* **2006**, *66*, 1198-1204, 10.1016/j.compscitech.2005.10.001.
143. Yokoyama, R.; Suzuki, S.; Shirai, K.; Yamauchi, T.; Tsubokawa, N.; Tsuchimochi, M. Preparation and properties of biocompatible polymer-grafted silica nanoparticle. *Eur. Polym. J.* **2006**, *42*, 3221-3229, 10.1016/j.eurpolymj.2006.08.015.
144. Hansen, S.F.; Hansen, O.F.H.; Nielsen, M.B. Advances and challenges towards consumerization of nanomaterials. *Nat. Nanotechnol.* **2020**, *15*, 964-965, 10.1038/s41565-020-00819-7.
145. Available online: <https://www.nanodb.dk>. (accessed on 11.11.22).
146. Available online: <https://product.statnano.com/>. (accessed on 11.11.22).
147. Available online: <https://www.economist.com/leaders/2011/10/01/asias-new-model-company>. (accessed on 11.11.22).
148. Pietryga, J.M.; Park, Y.-S.; Lim, J.; Fidler, A.F.; Bae, W.K.; Brovelli, S.; Klimov, V.I. Spectroscopic and Device Aspects of Nanocrystal Quantum Dots. *Chem. Rev.* **2016**, *116*, 10513-10622, 10.1021/acs.chemrev.6b00169.
149. Jing, L.; Kershaw, S.V.; Li, Y.; Huang, X.; Li, Y.; Rogach, A.L.; Gao, M. Aqueous Based Semiconductor Nanocrystals. *Chem. Rev.* **2016**, *116*, 10623-10730, 10.1021/acs.chemrev.6b00041.
150. Reiss, P.; Carrière, M.; Lincheneau, C.; Vaure, L.; Tamang, S. Synthesis of Semiconductor Nanocrystals, Focusing on Nontoxic and Earth-Abundant Materials. *Chem. Rev.* **2016**, *116*, 10731-10819, 10.1021/acs.chemrev.6b00116.
151. Wu, L.; Mendoza-Garcia, A.; Li, Q.; Sun, S. Organic Phase Syntheses of Magnetic Nanoparticles and Their Applications. *Chem. Rev.* **2016**, *116*, 10473-10512, 10.1021/acs.chemrev.5b00687.
152. Wei, D. *Int. J. Mol. Sci. International Journal of Molecular Sciences* **2010**, *11*, 1103-1113, doi:10.3390/ijms11031103.
153. O'Regan, B.; Grätzel, M. A low-cost, high-efficiency solar cell based on dye-sensitized colloidal TiO₂ films. *Nature* **1991**, *353*, 737-740, 10.1038/353737a0.
154. Yu, X.; Zhang, C.; Luo, Z.; Zhang, T.; Liu, J.; Li, J.; Zuo, Y.; Biendicho, J.J.; Llorca, J.; Arbiol, J.; et al. A low temperature solid state reaction to produce hollow Mn_xFe_{3-x}O₄ nanoparticles as anode for lithium-ion batteries. *Nano Energy* **2019**, *66*, 104199, 10.1016/j.nanoen.2019.104199.
155. Wei, C.; He, Y.; Shi, X.; Song, Z. Terpyridine-metal complexes: Applications in catalysis and supramolecular chemistry. *Coord. Chem. Rev.* **2019**, *385*, 1-19, 10.1016/j.ccr.2019.01.005.
156. Maleki, A.; Taheri-Ledari, R.; Ghalavand, R.; Firouzi-Haji, R. Palladium-decorated o-phenylenediamine-functionalized Fe₃O₄/SiO₂ magnetic nanoparticles: A promising solid-state catalytic system used for Suzuki–Miyaura coupling reactions. *J. Phys. Chem.* **2020**, *136*, 109200, 10.1016/j.jpccs.2019.109200.
157. Ennaert, T.; Van Aelst, J.; Dijkmans, J.; De Clercq, R.; Schutyser, W.; Dusselier, M.; Verboekend, D.; Sels, B.F. Potential and challenges of zeolite chemistry in the catalytic conversion of biomass. *Chem. Soc. Rev.* **2016**, *45*, 584-611, 10.1039/C5CS00859J.
158. Perot, G.; Guisnet, M. Advantages and disadvantages of zeolites as catalysts in organic chemistry. *J. Mol. Catal.* **1990**, *61*, 173-196, 10.1016/0304-5102(90)85154-A.
159. Hassan, A.F.; Elhadidy, H. Effect of Zr⁺⁴ doping on characteristics and sonocatalytic activity of TiO₂/carbon nanotubes composite catalyst for degradation of chlorpyrifos. *J. Phys. Chem.* **2019**, *129*, 180-187, 10.1016/j.jpccs.2019.01.018.

160. Sajjadi, S.; Khataee, A.; Darvishi Cheshmeh Soltani, R.; Hasanzadeh, A. N. S co-doped graphene quantum dot-decorated Fe₃O₄ nanostructures: Preparation, characterization and catalytic activity. *J. Phys. Chem.* **2019**, *127*, 140-150, 10.1016/j.jpccs.2018.12.014.
161. Duong, H.A.; Wu, W.; Teo, Y.-Y. Cobalt-Catalyzed Cross-Coupling Reactions of Arylboronic Esters and Aryl Halides. *Organometallics* **2017**, *36*, 4363-4366, 10.1021/acs.organomet.7b00726.
162. Prinsell, M.R.; Everson, D.A.; Weix, D.J. Nickel-catalyzed, sodium iodide-promoted reductive dimerization of alkyl halides, alkyl pseudohalides, and allylic acetates. *Chem. Commun* **2010**, *46*, 5743-5745, 10.1039/C0CC01716G.
163. Nicholls, T.P.; Caporale, C.; Massi, M.; Gardiner, M.G.; Bissember, A.C. Synthesis and characterisation of homoleptic 2,9-diaryl-1,10-phenanthroline copper(i) complexes: influencing selectivity in photoredox-catalysed atom-transfer radical addition reactions. *Dalton Trans.* **2019**, *48*, 7290-7301, 10.1039/C8DT04116D.
164. Bagal, D.B.; Kachkovskiy, G.; Knorn, M.; Rawner, T.; Bhanage, B.M.; Reiser, O. Trifluoromethylchlorosulfonylation of Alkenes: Evidence for an Inner-Sphere Mechanism by a Copper Phenanthroline Photoredox Catalyst. *Angew. Chem. Int. Ed.* **2015**, *54*, 6999-7002, 10.1002/anie.201501880.
165. Wang, X.; Wang, C.; Liu, Y.; Xiao, J. Acceptorless dehydrogenation and aerobic oxidation of alcohols with a reusable binuclear rhodium(ii) catalyst in water. *Green Chem.* **2016**, *18*, 4605-4610, 10.1039/C6GC01272H.
166. Ansari, S.A.; Cho, M.H. Highly Visible Light Responsive, Narrow Band gap TiO₂ Nanoparticles Modified by Elemental Red Phosphorus for Photocatalysis and Photoelectrochemical Applications. *Sci. Rep.* **2016**, *6*, 25405, 10.1038/srep25405.
167. Singh, H.; Sunaina; Yadav, K.K.; Bajpai, V.K.; Jha, M. Tuning the bandgap of m-ZrO₂ by incorporation of copper nanoparticles into visible region for the treatment of organic pollutants. *Mater. Res. Bull.* **2020**, *123*, 110698, 10.1016/j.materresbull.2019.110698.
168. Emsley, J. *The Elements*, 3 ed.; Oxford University Press Inc.: New York, United States, 1994.
169. Available online: <https://pubs.usgs.gov/pp/0440d/report.pdf>. (accessed on 17.10.22).
170. *Mineral commodity summaries 2021*; Reston, VA, 2021; p. 200.
171. Fujisawa, J.-i.; Eda, T.; Hanaya, M. Comparative study of conduction-band and valence-band edges of TiO₂, SrTiO₃, and BaTiO₃ by ionization potential measurements. *Chem. Phys. Lett.* **2017**, *685*, 23-26, 10.1016/j.cplett.2017.07.031.
172. Liao, D.L.; Wu, G.S.; Liao, B.Q. Zeta potential of shape-controlled TiO₂ nanoparticles with surfactants. *Colloids Surf.* **2009**, *348*, 270-275, 10.1016/j.colsurfa.2009.07.036.
173. Bhagya, N.P.; Prashanth, P.A.; Raveendra, R.S.; Sathyanarayani, S.; Ananda, S.; Nagabhushana, B.M.; Nagabhushana, H. Adsorption of hazardous cationic dye onto the combustion derived SrTiO₃ nanoparticles: Kinetic and isotherm studies. *J. Asian Ceram. Soc.* **2016**, *4*, 68-74, 10.1016/j.jascers.2015.11.005.
174. Cai, J.; Wei, H.; Zhang, Y.; Cai, R.; Zhang, X.; Wang, Y.; Liu, J.; Tan, H.H.; Xie, T.; Wu, Y. Designed Construction of SrTiO₃/SrSO₄/Pt Heterojunctions with Boosted Photocatalytic H₂ Evolution Activity. *Eur. J. Chem.* **2021**, *27*, 7300-7306, 10.1002/chem.202100101.
175. Olhero, S.M.; Kaushal, A.; Ferreira, J.M.F. Preventing hydrolysis of BaTiO₃ powders during aqueous processing and of bulk ceramics after sintering. *J. Eur. Ceram. Soc.* **2015**, *35*, 2471-2478, 10.1016/j.jeurceramsoc.2015.03.007.
176. Luan, W.; Gao, L. Influence of pH value on properties of nanocrystalline BaTiO₃ powder. *Ceram. Int.* **2001**, *27*, 645-648, 10.1016/S0272-8842(01)00012-8.
177. Ye, H.-J.; Shao, W.-Z.; Zhen, L. Tetradecylphosphonic acid modified BaTiO₃ nanoparticles and its nanocomposite. *Colloids Surf. A Physicochem Eng. Asp.* **2013**, *427*, 19-25, 10.1016/j.colsurfa.2013.02.068.
178. Rechberger, F.; Ilari, G.; Willa, C.; Tervoort, E.; Niederberger, M. Processing of Cr doped SrTiO₃ nanoparticles into high surface area aerogels and thin films. *Mater. Chem. Front.* **2017**, *1*, 1662-1667, 10.1039/C7QM00155J.
179. Pujari, S.P.; Scheres, L.; Marcelis, A.T.M.; Zuilhof, H. Covalent Surface Modification of Oxide Surfaces. *Angew. Chem., Int. Ed. Engl.* **2014**, *53*, 6322-6356, 10.1002/anie.201306709.

180. Kim, B.; Park, S.W.; Kim, J.-Y.; Yoo, K.; Lee, J.A.; Lee, M.-W.; Lee, D.-K.; Kim, J.Y.; Kim, B.; Kim, H.; et al. Rapid Dye Adsorption via Surface Modification of TiO₂ Photoanodes for Dye-Sensitized Solar Cells. *ACS Appl. Mater. Interfaces* **2013**, *5*, 5201-5207, 10.1021/am401034r.
181. Čulić-Viskota, J.; Dempsey, W.P.; Fraser, S.E.; Pantazis, P. Surface functionalization of barium titanate SHG nanoprobe for in vivo imaging in zebrafish. *Nat. Protoc.* **2012**, *7*, 1618-1633, 10.1038/nprot.2012.087.
182. Available online: <https://webbook.nist.gov/cgi/cbook.cgi?ID=C7664939&Mask=200#Mass-Spec> (accessed on 17.10.22).
183. Shin, S.S.; Lee, S.J.; Seok, S.I. Exploring wide bandgap metal oxides for perovskite solar cells. *APL Mater.* **2018**, *7*, 022401, 10.1063/1.5055607.
184. Gutowski, M.; Jaffe, J.E.; Liu, C.-L.; Stoker, M.; Hegde, R.I.; Rai, R.S.; Tobin, P.J. Thermodynamic stability of high-K dielectric metal oxides ZrO₂ and HfO₂ in contact with Si and SiO₂. *Appl. Phys. Lett.* **2002**, *80*, 1897-1899, 10.1063/1.1458692.
185. Takada, K.; Sakurai, H.; Takayama-Muromachi, E.; Izumi, F.; Dilanian, R.A.; Sasaki, T. Superconductivity in two-dimensional CoO₂ layers. *Nature* **2003**, *422*, 53-55, 10.1038/nature01450.
186. Yu, X.; Marks, T.J.; Facchetti, A. Metal oxides for optoelectronic applications. *Nature Mater.* **2016**, *15*, 383-396, 10.1038/nmat4599.
187. Wang, C.; Yin, L.; Zhang, L.; Xiang, D.; Gao, R. Metal Oxide Gas Sensors: Sensitivity and Influencing Factors. *Sensors* **2010**, *10*, 2088-2106, doi:10.3390/s100302088.
188. Stambouli, A.B.; Traversa, E. Solid oxide fuel cells (SOFCs): a review of an environmentally clean and efficient source of energy. *Renew. Sust. Energ. Rev.* **2002**, *6*, 433-455, 10.1016/S1364-0321(02)00014-X.
189. Liang, X.; Bai, S.; Wang, X.; Dai, X.; Gao, F.; Sun, B.; Ning, Z.; Ye, Z.; Jin, Y. Colloidal metal oxide nanocrystals as charge transporting layers for solution-processed light-emitting diodes and solar cells. *Chem. Soc. Rev.* **2017**, *46*, 1730-1759, 10.1039/C6CS00122J.
190. Duvigneaud, P.H.; Reinhard-Derie, D. DTA study of RuO₂ formation from the thermal decomposition of ruthenium(III) hydrate. *Thermochim. Acta* **1981**, *51*, 307-314, 10.1016/0040-6031(81)85168-4.
191. Smart, K.A.; Mothes-Martin, E.; Annaka, T.; Grellier, M.; Sabo-Etienne, S. Silane Deuteration Catalyzed by Ruthenium Bis(dihydrogen) Complexes or Simple Metal Salts. *Adv. Synth. Catal.* **2014**, *356*, 759-764, 10.1002/adsc.201300902.
192. Over, H.; Schomäcker, R. What Makes a Good Catalyst for the Deacon Process? *ACS Catal.* **2013**, *3*, 1034-1046, 10.1021/cs300735e.
193. Available online: <https://www.netl.doe.gov/research/coal/energy-systems/gasification/gasifipedia/ftsynthesis>. (accessed on 18.10.22).
194. Humphreys, J.; Lan, R.; Tao, S. Development and Recent Progress on Ammonia Synthesis Catalysts for Haber-Bosch Process. *Adv. Energy and Sustainability Res.* **2021**, *2*, 2000043, 10.1002/aesr.202000043.
195. Available online: <https://www.sigmaaldrich.com/CH/de/product/sial/d216305>. (accessed on 17.10.22).
196. Available online: <https://www.sigmaaldrich.com/CH/de/product/aldrich/491306>. (accessed on 17.10.22).
197. Kunishige, S.; Katori, T.; Baba, M.; Hayashi, M.; Hasegawa, H.; Ohshima, Y. Spectroscopic study on deuterated benzenes. II. High-resolution laser spectroscopy and rotational structure in the S₁ state. *Chem. Phys.* **2015**, *143*, 244303, 10.1063/1.4937950.
198. Hostetler, M.J.; Bergman, R.G. Secondary .beta.-deuterium isotope effects on the rates and equilibria of organometallic oxidative addition/reductive elimination reactions. *J. Am. Chem. Soc.* **1992**, *114*, 7629-7636, 10.1021/ja00046a004.
199. DeWitt, S.H.; Maryanoff, B.E. Deuterated Drug Molecules: Focus on FDA-Approved Deutetabenazine. *Biochemistry* **2018**, *57*, 472-473, 10.1021/acs.biochem.7b00765.
200. Gant, T.G. Using Deuterium in Drug Discovery: Leaving the Label in the Drug. *J. Med. Chem.* **2014**, *57*, 3595-3611, 10.1021/jm4007998.

201. Patel, M.; Saunthwal, R.K.; Verma, A.K. Base-Mediated Deuteration of Organic Molecules: A Mechanistic Insight. *ACS Omega* **2018**, *3*, 10612-10623, 10.1021/acsomega.8b01329.
202. Yang, X.; Ben, H.; Ragauskas, A.J. Recent Advances in the Synthesis of Deuterium-Labeled Compounds. *Asian J. Org. Chem* **2021**, *10*, 2473-2485, 10.1002/ajoc.202100381.
203. Prakash, G.; Paul, N.; Oliver, G.A.; Werz, D.B.; Maiti, D. C–H deuteration of organic compounds and potential drug candidates. *Chem. Soc. Rev.* **2022**, *51*, 3123-3163, 10.1039/D0CS01496F.
204. Available online: <https://www.dailymetalprice.com/metalprices.php?c=ru&u=kg&d=1>. (accessed on 17.10.22).
205. Available online: <https://www.dailymetalprice.com/metalprices.php?c=rh&u=kg&d=1>. (accessed on 17.10.22).
206. Matsubara, S.; Asano, K.; Kajita, Y.; Yamamoto, M. C-H Bond Activation by Water on a Palladium or Platinum Metal Surface. *Synthesis* **2007**, *2007*, 2055-2059.
207. Matsubara, M.Y.K.O.S. Platinum Catalyzed H-D Exchange Reaction of Various Aromatic Compounds under Hydrothermal Condition. *Heterocycles* **2005**, *67*, 353-359, 10.3987/COM-05-S(T)36.
208. Neto, N.; Muniz-Miranda, M.; Angeloni, L.; Castellucci, E. Normal mode analysis of 2,2'-bipyridine—I. Internal modes. *Spectrochim. Acta, Part A* **1983**, *39*, 97-106, 10.1016/0584-8539(83)80063-4.
209. Ramadhan, Z.R.; Han, J.W.; Hong, J.; Park, S.B.; Kim, J.H.; Wibowo, A.F.; Prameswati, A.; Kim, S.Y.; Lee, J.; Kim, S.; et al. Conductive PEDOT:PSS on surface-functionalized chitosan biopolymers for stretchable skin-like electronics. *Org. Electron.* **2021**, *94*, 106165, 10.1016/j.orgel.2021.106165.
210. Huseynova, G.; Hyun Kim, Y.; Lee, J.-H.; Lee, J. Rising advancements in the application of PEDOT:PSS as a prosperous transparent and flexible electrode material for solution-processed organic electronics. *J. Inf. Disp.* **2020**, *21*, 71-91, 10.1080/15980316.2019.1707311.
211. Chao, S.; Petrovsky, V.; Dogan, F. Effects of sintering temperature on the microstructure and dielectric properties of titanium dioxide ceramics. *J. Mater. Sci.* **2010**, *45*, 6685-6693, 10.1007/s10853-010-4761-4.
212. Tsuchiya, K.; Ogino, K. Catalytic oxidative polymerization of thiophene derivatives. *Polym. J.* **2013**, *45*, 281-286, 10.1038/pj.2012.146.
213. Lee, S.J.; Lee, J.M.; Cheong, I.W.; Lee, H.; Kim, J.H. A facile route of polythiophene nanoparticles via Fe³⁺-catalyzed oxidative polymerization in aqueous medium. *J. Polym. Sci.* **2008**, *46*, 2097-2107, 10.1002/pola.22544.
214. So, J.H.; Mayevsky, D.; Winther-Jensen, O.; Winther-Jensen, B. A novel route for polymerisation of thiophene based conducting polymers using trace-free oxidants. *Polym. Chem.* **2014**, *5*, 361-364, 10.1039/C3PY01265D.